

AD 665427

AD

USAAVLABS TECHNICAL REPORT 67-44

INVESTIGATION OF COMPOUND HELICOPTER AERODYNAMIC INTERFERENCE EFFECTS

By

Lawrence J. Bain
Anton J. Landgrebe

November 1967

**U. S. ARMY AVIATION MATERIEL LABORATORIES
FORT EUSTIS, VIRGINIA**

CONTRACT DA 44-177-AMC-203(T)

**UNITED AIRCRAFT CORPORATION
SIKORSKY AIRCRAFT DIVISION
STRATFORD, CONNECTICUT**

This document has been approved
for public release and sale; its
distribution is unlimited.



R
FEB 21 1968

Reproduced by the
CLEARINGHOUSE
for Federal Scientific & Technical
Information Springfield Va. 22151



DEPARTMENT OF THE ARMY
U. S. ARMY AVIATION MATERIEL LABORATORIES
FORT EUSTIS, VIRGINIA 23604

**This report has been reviewed by the U. S. Army
Aviation Materiel Laboratories and is considered
to be technically sound. The report is published
for the exchange of information and the stimula-
tion of ideas.**

Task 1F125901A13903
Contract DA 44-177-AMC-203(T)
USAAVLABS Technical Report 67-44
November 1967

**INVESTIGATION OF COMPOUND HELICOPTER AERODYNAMIC
INTERFERENCE EFFECTS**

SER-50474

By

**Lawrence J. Bain
Anton J. Landgrebe**

Prepared by

**United Aircraft Corporation
Sikorsky Aircraft Division
Stratford, Connecticut**

for

**U. S. ARMY AVIATION MATERIEL LABORATORIES
FORT EUSTIS, VIRGINIA**

**This document has been approved
for public release and sale; its
distribution is unlimited.**

SUMMARY

The presence of multiple lifting and propulsive components on a compound helicopter results in mutual aerodynamic interference between them. Two investigations were undertaken to study these effects.

In the first, a generalized model of a compound helicopter was tested in the United Aircraft 18-foot wind tunnel to determine the nature of interferences between the rotor, the fuselage, and various wings, as well as the effects of these components on the downwash at the tail. A number of the results of this test were correlated with published theories. In addition, a theoretical method for calculating the wing induced flow through the rotor is presented, and the theoretical results are correlated with the experimental results. It was concluded from this work that:

1. Although definite measurable interferences do exist, none were found that would seriously compromise the compound helicopter concept.
2. In general, existing theories for predicting aerodynamic interference effects due to a wing produce reasonable correlation with measured effects. However, correlation is lacking for rotor induced interference effects.

In the second test, the mutual interferences between a rotor and various propeller configurations were investigated in the 18-foot tunnel with the compound helicopter model. It was concluded from this work that:

1. The vibratory bending moments on wing-mounted tractor propellers are a direct function of the sum of the rotor momentum downwash angle and the geometric angle of attack.
2. The vibratory bending moments on a tail-mounted pusher propeller are related to the rotor lift. The exact relationship is dependent on the presence or absence of empennage forward of the propeller.
3. Increasing thrust on the wing-mounted tractor propellers generally causes increased rotor blade vibratory bending moments.

FOREWORD

• This program was sponsored by the U. S. Army Aviation Materiel Laboratories, Fort Eustis, Virginia, and was monitored by Mr. Patrick Cancro.

• The theoretical analysis was performed by Mr. Anton J. Landgrebe (coauthor) of the United Aircraft Research Laboratories. Mr. Edmond F. Kiely of Sikorsky Aircraft supervised the development of the compound helicopter model and shared the responsibility for the conduct of the wind tunnel tests.

TABLE OF CONTENTS

	<u>Page</u>
• SUMMARY	iii
FOREWORD	v
• LIST OF ILLUSTRATIONS	viii
LIST OF SYMBOLS	xxvii
INTRODUCTION	1
DESCRIPTION OF MODEL AND TEST FACILITIES . .	3
EXPERIMENTAL PROCEDURE	9
EVALUATION OF RESULTS, ROTOR-WING-FUSELAGE INTERFERENCE EFFECTS	10
THEORETICAL ANALYSIS AND CORRELATION OF ROTOR- WING-FUSELAGE INTERFERENCE EFFECTS . . .	22
EVALUATION OF RESULTS, ROTOR-PROPELLER INTERFERENCE EFFECTS	49
CONCLUSIONS	60
REFERENCES CITED	64
APPENDIXES	
I Wing Aerodynamic Characteristics . . .	297
II Rotor Aerodynamic Characteristics . . .	313
III Aerodynamic Characteristics of Wing With Propellers	328
DISTRIBUTION	352

LIST OF ILLUSTRATIONS

<u>Figure</u>		<u>Page</u>
1	S-61F Research Aircraft	66
2	Sikorsky Compound Helicopter Model	67
3	Model Operating Characteristics	71
4	United Aircraft Subsonic Wind Tunnel	74
5	Isolated Propeller Test Fixture	75
6	Effect of Rotor Lift on Wing Lift for Various Wing Sizes and Positions, Forward Speeds, and Fuselage Angles of Attack	76
7	Effect of Forward Speed on Effective Rotor Downwash Angle for the Large Wing at Various Wing Positions	81
8	Effect of Forward Speed on Effective Rotor Downwash Angle for the Medium Wing at Various Wing Positions	82
9	Effect of Wing Position on Downwash Factor for the Large and Medium Wings	83
10	Effect of Rotor Lift on Wing Drag for Various Wing Sizes and Positions, Forward Speeds, and Fuselage Angles of Attack	84
11	Effect of Rotor Lift and Fuselage Angle of Attack on Wing Lift and Drag for the Medium Wing, Mid Position at Two Forward Speeds	89
12	Chordwise Wing Static Pressure Distributions for the Medium Wing, High Position, $V_s = 120$ Knots at Two Spanwise Locations and Two Rotor Lift Conditions .	91

<u>Figure</u>		<u>Page</u>
13	Spanwise Wing Normal Force Coefficient Distributions for the Medium Wing, High Position, $V_s = 200$ Knots, at Two Rotor Lift Conditions and $\alpha_f = 8^\circ$	93
14	Spanwise Wing Normal Force Coefficient Distributions for the Medium Wing, High Position, $V_s = 120$ Knots, at Two Fuselage Angles of Attack and Various Rotor Lift Conditions	94
15	Spanwise Wing Normal Force Coefficient Distributions for the Medium Wing, Mid Position, $V_s = 120$ Knots, at Two Fuselage Angles of Attack and Various Rotor Lift Conditions	95
16	A Sample of Wing Oscillatory Pressure Harmonic Components Taken From Tests With and Without the Rotor on the Medium Wing, High Position, Quarter Chord, $\alpha_f = 0^\circ$, $\theta_c = 4^\circ$, $V_s = 300$ Knots	96
17	Effect of Rotor Angle of Attack on Fourth Harmonic Oscillatory Wing Pressure at Various Wing Chord Locations for the Medium Wing, High Position, $V_s = 300$ Knots	97
18	Effect of Rotor Angle of Attack on Fourth Harmonic Oscillatory Wing Pressure at Various Wing Chord Locations for the Medium Wing, Mid Position, $V_s = 300$ Knots	99
19	Effect of Rotor Angle of Attack on Fourth Harmonic Oscillatory Wing Pressure at Various Wing Chord Locations for the Medium Wing, Low Position, $V_s = 300$ Knots	101
20	Effect of Rotor Lift on Wing Rolling Moment for the Medium Wing, Mid Position at Various Forward Speeds and Fuselage Angles of Attack	103
21	Wing Rolling Moment-Rotor Lift Derivative for the Medium Wing at Various Forward Speeds, Collective Pitch Settings, and Fuselage Angles of Attack	108

<u>Figure</u>		<u>Page</u>
22	Effect of Rotor Lift on Wing Pitching Moment for the Medium Wing, High Position, $V_s = 120$ Knots, at Various Fuselage Angles of Attack	111
23	Effect of Rotor Lift on Fuselage Lift With the Medium Wing at Two Wing Positions, Two Forward Speeds, and Various Fuselage Angles of Attack . . .	112
24	Effect of Rotor Lift on Fuselage Drag With the Medium Wing at Two Wing Positions, Two Forward Speeds, and Various Fuselage Angles of Attack . . .	115
25	Effect of Rotor Lift on Fuselage Pitching Moment With the Medium Wing at Two Wing Positions and Various Forward Speeds and Fuselage Angles of Attack	118
26	Effect of Rotor Lift on Fuselage Pitching Moment With the Medium Wing, High Position, $V_s = 120$ Knots, at Various Collective Pitch Settings and Fuselage Angles of Attack	122
27	Effect of Forward Speed on Fuselage Pitching Moment Per Unit Change in C_{LR}/σ With the Medium Wing at Two Wing Positions and $\alpha_f = 4^\circ$	125
28	Effect of Wing Size and Position on Rotor Lift and Angle of Attack at Various Fuselage Angles of Attack and $V_s = 120$ Knots	126
29	Effect of Wing Size and Position on Rotor Lift and Angle of Attack at Various Fuselage Angles of Attack and $V_s = 200$ Knots	128
30	Effect of Wing Size and Position on Rotor Lift and Angle of Attack for Various Fuselage Angles of Attack and $V_s = 300$ Knots	130
31	Effect of the Large Wing, High Position on Rotor Lift and Drag for Various Fuselage Angles of Attack and Forward Speeds	132

<u>Figure</u>		<u>Page</u>
32	Effect of the Large Wing, High Position on Rotor Torque for Two Forward Speeds and Various Fuselage Angles of Attack	135
33	Effect of Rotor Lift, Wing Position, and Fuselage Angle of Attack on Rotor Blade Flapwise Vibratory Moments at $V_s = 120$ Knots, Medium Wing, Blade #1, 60%R.	136
34	Effect of Rotor Lift, Wing Position, and Fuselage Angle of Attack on Rotor Blade Flapwise Vibratory Moments at $V_s = 200$ Knots, Medium Wing, Blade #1, 60%R.	137
35	Effect of Rotor Lift, Wing Position, and Fuselage Angle of Attack on Rotor Blade Flapwise Vibratory Moments at $V_s = 300$ Knots, Medium Wing, Blade #1, 60%R.	138
36	Effect of Rotor Lift, Wing Position, and Fuselage Angle of Attack on Rotor Blade Flapwise Vibratory Moments at $V_s = 120$ Knots, Large Wing, Blade #2, 60%R.	139
37	Effect of Rotor Lift, Wing Position, and Fuselage Angle of Attack on Rotor Blade Flapwise Vibratory Moments at $V_s = 200$ Knots, Large Wing, Blade #2, 60%R.	140
38	Effect of Rotor Lift, Wing Position, and Fuselage Angle of Attack on Rotor Blade Flapwise Vibratory Moments at $V_s = 232$ Knots, Large Wing, Blade #2, 60%R.	141
39	Effect of Rotor Lift, Wing Position, and Fuselage Angle of Attack on Rotor Blade Flapwise Vibratory Moments at $V_s = 300$ Knots, Large Wing, Blade #2, 60%R.	142
40	Effect of Wing Position on Rotor Blade Flapwise Moment Azimuthal Variation for the Large Wing at $V_s = 200$ Knots, $\alpha_f = -4^\circ$, $\theta_c = 4^\circ$, $CL_R/\sigma = 0.005$ Blade #2, 60%R	143

<u>Figure</u>		<u>Page</u>
41	Effect of Wing Position on Rotor Blade Flapwise Moment Azimuthal Variation for the Large Wing at $V_s = 200$ Knots, $\alpha_f = 4^\circ$, $\theta_c = 8^\circ$, $CL_R/\sigma = 0.065$, Blade #2, 60%R.	144
42	Effect of Wing Position on Rotor Blade Flapwise Moment Azimuthal Variation for the Large Wing at $V_s = 300$ Knots, $\alpha_f = 0^\circ$, $\theta_c = 0^\circ$, $CL_R/\sigma \approx 0.020$, Blade #1, 60%R.	145
43	Effect of Wing Position on Rotor Blade Chordwise Moment Azimuthal Variation for the Large Wing at $V_s = 200$ Knots, $\alpha_f = -4^\circ$, $\theta_c = 4^\circ$, $CL_R/\sigma = 0.005$, Blade #2, 20%R.	146
44	Effect of Wing Position on Rotor Blade Chordwise Moment Azimuthal Variation for the Large Wing at $V_s = 200$ Knots, $\alpha_f = 4^\circ$, $\theta_c = 8^\circ$, $CL_R/\sigma = 0.065$, Blade #2, 20%R.	147
45	Effect of Wing Position on Rotor Blade Chordwise Moment Azimuthal Variation for the Large Wing at $V_s = 300$ Knots, $\alpha_f = 0^\circ$, $\theta_c = 0^\circ$, $CL_R/\sigma \approx 0.020$, Blade #1, 20%R.	148
46	Effect of Wing Position on Rotor Blade Torsional Moment Azimuthal Variation for the Large Wing at $V_s = 200$ Knots and Two Rotor Operating Conditions, Blade #2, 18%R	149
47	Effect of Wing Position on Rotor Blade Torsional Moment Azimuthal Variation for the Large Wing at $V_s = 300$ Knots, $\alpha_f = 0^\circ$, $\theta_c = 0^\circ$, $CL_R/\sigma \approx 0.020$, Blade #1, 18%R	150
48	Effect of Fuselage Angle of Attack on Downwash Angle at the Tail for Various Size Wings at the Mid Position, Without Rotor	151
49	Effect of Rotor Lift on Downwash Angle at the Tail at Various Forward Speeds and $\alpha_f = 4^\circ$, Wing Off	152
50	Effect of Rotor Lift on Downwash Angle at the Tail for Various Size Wings at the Mid Position, Various Forward Speeds, and $\alpha_f = 4^\circ$	153

<u>Figure</u>		<u>Page</u>
51	Effect of Rotor Lift on Downwash Angle at the Tail for the Medium and Large Wings at the Mid Position, $V_s = 200$ Knots, and $\alpha_f = -4^\circ$	156
52	Comparison of the Effect of Fuselage Angle of Attack on Measured Downwash and Downwash Obtained by Superposition for the Medium Wing, Mid Position, $V_s = 200$ Knots	157
53	Aerodynamic Characteristics of the Small, Medium, and Large Wings at the Mid Position for Various Forward Speeds.	158
54	Fuselage Aerodynamic Characteristics With the Small, Medium, and Large Wings at the Mid Position for Various Forward Speeds	161
55	Fuselage Aerodynamic Characteristics With the Medium Wing at the Mid Position for Various Wing Incidence Angles, $V_s = 200$ Knots, and $\alpha_f = 0^\circ$	163
56	Effect of Wing Position on Fuselage Lift for the Large and Medium Wings and Various Fuselage Angles of Attack.	164
57	Parameters for the Effect of Wing Interference on Rotor Performance	166
58	Rotor-Wing-Wing Wake Geometry	167
59	Longitudinal Projection of Rotor-Wing-Wing Wake Geometry	168
60	Rotor-Wing Configurations	169
61	Vortex Representation of Wing Wake	170
62	Wing Circulation Distribution, Large Wing.	171
63	Comparison of Loading Distribution Between Full-Span Wing and Wing-Fuselage Configuration, Medium Wing, Mid Position	172

<u>Figure</u>		<u>Page</u>
64	Theoretical Wing Induced Velocity Normal to Rotor Plane, Large Wing, High Position, $V_s = 200$ Knots . . .	173
65	Theoretical Linearity of Wing Induced Flapping With Wing Lift Coefficient for Fixed Rotor Controls and Two Values of Pitch-Flap Coupling	174
66	Azimuth Distribution of Wing Effect on Rotor Blade Flapping, Large Wing, High Position, $\mu = 0.51$. . .	175
67	Theoretical Effect of Wing Size and Position on Rotor Blade Flapping, $\delta_3 = 0^\circ$, Fixed Rotor Controls . .	176
68	Theoretical Effect of Wing Size and Position on Rotor Blade Flapping, $\delta_3 = 45^\circ$, Fixed Rotor Controls . .	178
69	Theoretical Effect of Wing Size and Position on Coning and Cyclic Pitch Required to Trim Out Wing Induced First Harmonic Flapping, $\delta_3 = 45^\circ$	179
70	Theoretical Rotor Air Load Distribution Induced by the Large Wing at the High Position, $\mu = 0.51$. . .	180
71	Linearity of Wing Induced Rotor Lift With Wing Lift Coefficient, $\mu = 0.51$	183
72	Theoretical Effect of Wing Size and Position on Rotor Lift at Various Advance Ratios, Two Values of Pitch-Flap Coupling, and With Trimmed and Untrimmed Rotor Blade Flapping	184
73	Comparison of Sample Results of Linearized Equations With Computer Results	187
74	Comparison of Theoretical and Experimental Effect of Wing Interference on Rotor Lift Versus Advance Ratio	188
75	Fuselage Load Distribution	190
76	Wing-Fuselage Angles	191

<u>Figure</u>		<u>Page</u>
77	Components of Lift Distribution on Wing Alone and on Wing-Body Combinations at the Mid Wing Position	192
78	Theoretical Lift Coefficients on the Medium Wing, Mid Position at Various Fuselage Angles of Attack	193
79	Comparison of Theoretical and Experimental Lift Characteristics of the Fuselage and Large Wing at the Mid Position for Various Angles of Attack, Without Rotor	194
80	Comparison of Theoretical and Experimental Lift Characteristics of the Fuselage and Medium Wing at the Mid Position for Various Fuselage Angles of Attack, Without Rotor	195
81	Comparison of Theoretical and Experimental Lift Characteristics of the Fuselage and Small Wing at the Mid Position for Various Fuselage Angles of Attack, Without Rotor	196
82	Comparison of Experimental and Theoretical Combined Wing-Fuselage Lift Characteristics for Various Wing Sizes	197
83	Comparison of Experimental and Theoretical Wing Lift Characteristics for Various Wing Sizes	198
84	Comparison of Experimental and Theoretical Fuselage Lift Characteristics for Various Wing Sizes	199
85	Comparison of Experimental and Theoretical Lift Carry-Over on Fuselage for Various Wing Sizes	200
86	Wing-Tail Geometry for Reference 16 Theory	201
87	Theoretical Effect of Vertical Distance Between Wing Wake Centerline and Tail Pivot on Tail Downwash Angle Per Unit C_{LW} , Large Wing	202

<u>Figure</u>		<u>Page</u>
88	Experimental Wing Lift Coefficient and Vertical Distance Between Wing Wake Centerline and Tail Pivot Versus Fuselage Angle of Attack; Large Wing at Two Positions	203
89	Comparison of Theoretical and Experimental Tail Downwash Angles for the Large Wing at Various Fuselage Angles of Attack	204
90	Effect of Rotor Lift and Angle of Attack on Rotor Wake Skew Angle for Several Advance Ratios	205
91	Rotor Wake Skew Angle Boundaries for Zero Rotor Blade Flapping	206
92	Local Downwash Factor Distributions for Skew Angles of Reference 17	207
93	Theoretical Effect of Rotor Loading Distribution on Downwash Factor for Various Wing Sizes and Positions	208
94	Comparison of Theoretical and Experimental Effects of Wing Position on Downwash Factor for the Large and Medium Wings	209
95	Comparison of Previous Experimental Results With Theoretical and Experimental Effects of Wing Position on Downwash Factor for the Large Wing	210
96	Isolated Propeller Blade Vibratory Moment Characteristics at Various Propeller Angles of Attack, $N_{PROP} = 3500$ rpm, $V_s = 120$ Knots, $\beta_{.75} = 41^\circ$	211
97	Isolated Propeller Blade Vibratory Moment Characteristics at Various Propeller Angles of Attack, $N_{PROP} = 4200$ rpm, $V_s = 200$ Knots, $\beta_{.75} = 41^\circ$	212
98	Isolated Propeller Blade Vibratory Moment Characteristics at Various Propeller Angles of Attack, $N_{PROP} = 5100$ rpm, $V_s = 300$ Knots, $\beta_{.75} = 41^\circ$	213

<u>Figure</u>		<u>Page</u>
99	Isolated Propeller Blade Vibratory Moment Characteristics at Various Propeller Angles of Attack, $N_{PROP} = 5250$ rpm, $V_S = 120$ Knots, $\beta_{.75} = 30^\circ$	214
100	Isolated Propeller Blade Vibratory Moment Characteristics at Various Propeller Angles of Attack, $N_{PROP} = 5560$ rpm, $V_S = 200$ Knots, $\beta_{.75} = 30^\circ$	215
101	Isolated Propeller Blade Vibratory Moment Characteristics at Various Propeller Angles of Attack, $N_{PROP} = 5560$ rpm, $V_S = 300$ Knots, $\beta_{.75} = 30^\circ$	216
102	Effect of Fuselage Angle of Attack on Inboard Tractor Propeller Blade Vibratory Moments, Without Rotor, $V_S = 120$ Knots, $\beta_{.75} = 41^\circ$	217
103	Effect of Fuselage Angle of Attack on Inboard Tractor Propeller Blade Vibratory Moments, Without Rotor, $V_S = 200$ Knots, $\beta_{.75} = 41^\circ$	218
104	Effect of Fuselage Angle of Attack on Inboard Tractor Propeller Blade Vibratory Moments, Without Rotor, $V_S = 300$ Knots, $\beta_{.75} = 41^\circ$	220
105	Effect of Fuselage Angle of Attack on Outboard Tractor Propeller Blade Vibratory Moments, Without Rotor, $V_S = 120$ Knots, $\beta_{.75} = 41^\circ$	221
106	Effect of Fuselage Angle of Attack on Outboard Tractor Propeller Blade Vibratory Moments, Without Rotor, $V_S = 200$ Knots, $\beta_{.75} = 41^\circ$	222
107	Effect of Fuselage Angle of Attack on Outboard Tractor Propeller Blade Vibratory Moments, Without Rotor, $V_S = 300$ Knots, $\beta_{.75} = 41^\circ$	224
108	Effect of Fuselage Angle of Attack on Pusher Propeller Blade Vibratory Moments, Without Empennage or Rotor, $V_S = 120$ Knots, $\beta_{.75} = 41^\circ$	225

<u>Figure</u>		<u>Page</u>
109	Effect of Fuselage Angle of Attack on Pusher Propeller Blade Vibratory Moments, Without Empennage or Rotor, $V_s = 300$ Knots, $\beta_{.75} = 41^\circ$	226
110	Effect of Fuselage Angle of Attack on Pusher Propeller Blade Vibratory Moments With Empennage, Without Rotor, $V_s = 120$ Knots, $\beta_{.75} = 41^\circ$	227
111	Effect of Fuselage Angle of Attack on Pusher Propeller Blade Vibratory Moments With Empennage, Without Rotor, $V_s = 200$ Knots, $\beta_{.75} = 41^\circ$	228
112	Effect of Fuselage Angle of Attack on Pusher Propeller Blade Vibratory Moments With Empennage, Without Rotor, $V_s = 300$ Knots, $\beta_{.75} = 41^\circ$	230
113	Effect of Rotor Lift on Inboard Tractor Propeller Blade Vibratory Moments for Various Fuselage Angles of Attack and Collective Pitch Settings, $V_s = 120$ Knots, $\beta_{.75} = 41^\circ$	232
114	Comparison of Experimental and Empirical Effects of Rotor Lift on Inboard Tractor Propeller Blade Flatwise Vibratory Moments for Various Fuselage Angles of Attack and Collective Pitch Settings, $V_s = 120$ Knots, $\beta_{.75} = 41^\circ$, 29%R	234
115	Effect of Rotor Lift on Inboard Tractor Propeller Blade Vibratory Moments for Various Fuselage Angles of Attack and Collective Pitch Settings, $V_s = 120$ Knots, $\beta_{.75} = 30^\circ$	236
116	Effect of Rotor Lift on Inboard Tractor Propeller Blade Vibratory Moments for Various Fuselage Angles of Attack and Collective Pitch Settings, $V_s = 200$ Knots, $\beta_{.75} = 41^\circ$	239

<u>Figure</u>		<u>Page</u>
117	Effect of Rotor Lift on Inboard Tractor Propeller Blade Vibratory Moments for Various Fuselage Angles of Attack and Collective Pitch Settings, $V_s = 300$ Knots, $\beta_{.75} = 41^\circ$	242
118	Effect of Rotor Lift on Outboard Tractor Propeller Blade Vibratory Moments for Various Fuselage Angles of Attack and Collective Pitch Settings, $V_s = 120$ Knots, $\beta_{.75} = 41^\circ$	245
119	Comparison of Experimental and Empirical Effects of Rotor Lift on Outboard Tractor Propeller Blade Flatwise Vibratory Moments for Various Fuselage Angles of Attack and Collective Pitch Settings, $V_s = 120$ Knots, $\beta_{.75} = 41^\circ$, 29%R	247
120	Effect of Rotor Lift on Outboard Tractor Propeller Blade Vibratory Moments for Various Fuselage Angles of Attack and Collective Pitch Settings, $V_s = 200$ Knots, $\beta_{.75} = 41^\circ$	249
121	Effect of Rotor Lift on Outboard Tractor Propeller Blade Vibratory Moments for Various Fuselage Angles of Attack and Collective Pitch Settings, $V_s = 300$ Knots, $\beta_{.75} = 41^\circ$	252
122	Comparison of Experimental and Empirical Effects of Rotor Lift on Inboard Tractor Propeller Blade Flatwise Vibratory Moments at Two Rotor Tip Path Plane Angles of Attack, $V_s = 120$ Knots, $\beta_{.75} = 41^\circ$, Starboard, 29%R	254
123	Effect of Rotor Lift on Pusher Propeller Blade Vibratory Moments for Various Fuselage Angles of Attack and Collective Pitch Settings, Without Empennage, $V_s = 120$ Knots, $\beta_{.75} = 41^\circ$	256
124	Effect of Rotor Lift and Fuselage Angle of Attack on Pusher Propeller Blade Flatwise Vibratory Moments, Without Empennage, $V_s = 120$ Knots, $\beta_{.75} = 41^\circ$, 29%R	257

<u>Figure</u>		<u>Page</u>
125	Effect of Rotor Lift on Pusher Propeller Blade Flatwise Vibratory Moments for Three Collective Pitch Settings and Propeller Speeds, Without Empennage, $V_s = 300$ Knots, $\beta_{.75} = 41^\circ$, 58%R	258
126	Effect of Rotor Lift on Pusher Propeller Blade Vibratory Moments for Various Fuselage Angles of Attack and Collective Pitch Settings, With Empennage, $V_s = 120$ Knots, $\beta_{.75} = 41^\circ$. . .	259
127	Effect of Rotor Lift on Pusher Propeller Blade Vibratory Moments for Various Fuselage Angles of Attack and Collective Pitch Settings, With Empennage, $V_s = 200$ Knots, $\beta_{.75} = 41^\circ$. .	260
128	Effect of Rotor Lift on Pusher Propeller Blade Flatwise Vibratory Moments for Various Collective Pitch Settings, With Empennage, $V_s = 300$ Knots, $\beta_{.75} = 41^\circ$, 58%R	261
129	Effect of Rotor Lift on Pusher Propeller Blade Flatwise Vibratory Moments for Various Fuselage Angles of Attack and Collective Pitch Settings, With Empennage, $V_s = 120$ Knots, $\beta_{.75} = 30^\circ$	262
130	Effect of Propeller Configuration on Rotor Blade Flapwise Vibratory Moment Amplitudes for Various Fuselage Angles of Attack, Collective Pitch Settings, and Forward Speeds, 60%R	263
131	Effect of Propeller Configuration on Rotor Blade Chordwise Vibratory Moment Amplitudes for Various Fuselage Angles of Attack, Collective Pitch Settings, and Forward Speeds	266
132	Effect of Propeller Configuration on Rotor Blade Torsional Vibratory Moment Amplitudes for Various Fuselage Angles of Attack, Collective Pitch Settings, and Forward Speeds	269

<u>Figure</u>		<u>Page</u>
133	Effect of Collective Pitch Setting on Rotor Blade Torsional Moment Azimuthal Variation, With Pusher Propeller and Empennage, $\beta_{.75} = 30^\circ$, $V_s = 120$ Knots, $\alpha_f = 8^\circ$, 18%R	272
134	Rotor Blade Torsional Moment Azimuthal Variation With Outboard Tractor Propellers, $\beta_{.75} = 41^\circ$, $V_s = 300$ Knots, $\alpha_f = 4^\circ$, $\theta_c = 4^\circ$, 35%R	273
135	Effect of Inboard Tractor Propeller Thrust on Rotor Blade Flapwise Vibratory Moment Amplitudes at Various Rotor Angles of Attack and Collective Pitch Settings and Two Forward Speeds, 60%R	274
136	Effect of Tractor Propeller Location on Rotor Blade Flapwise Vibratory Moment Amplitudes at Various Rotor Angles of Attack, Collective Pitch Settings, and Forward Speeds, 60%R, $\beta_{.75} = 41^\circ$	275
137	Effect of Pusher Propeller Thrust on Rotor Blade Flapwise Vibratory Moment Amplitudes at Various Rotor Angles of Attack and Collective Pitch Settings, With Empennage, $V_s = 120$ Knots, 60%R . . .	276
138	Effect of Pusher Propeller Thrust on Rotor Blade Flapwise Vibratory Moment Amplitudes at Various Rotor Angles of Attack and Collective Pitch Settings, Without Empennage, $V_s = 300$ Knots, 60%R.	277
139	Effect of Tractor Propeller Location on Rotor Blade Flapping at $V_s = 300$ Knots, $\alpha_f = 4^\circ$, $\theta_c = 8^\circ$, $\beta_{.75} = 41^\circ$	278
140	Effect of Inboard Tractor Propeller Thrust on Rotor Blade Chordwise Vibratory Moment Amplitudes at Various Rotor Angles of Attack and Collective Pitch Settings and Two Forward Speeds, 60%R	279

<u>Figure</u>		<u>Page</u>
141	Effect of Tractor Propeller Location on Rotor Blade Chordwise Vibratory Moment Amplitudes at Various Rotor Angles of Attack, Collective Pitch Settings and Forward Speeds, 30%R, $\beta_{.75} = 41^\circ$	280
142	Effect of Pusher Propeller Thrust on Rotor Blade Chordwise Vibratory Moment Amplitudes at Various Rotor Angles of Attack and Collective Pitch Settings and Two Forward Speeds, With Empennage	281
143	Effect of Pusher Propeller Thrust on Rotor Blade Chordwise Vibratory Moment Amplitudes at Various Rotor Angles of Attack and Collective Pitch Settings, Without Empennage, $V_s = 300$ Knots, $\beta_{.75} = 41^\circ$	282
144	Effect of Inboard Tractor Propeller Thrust on Azimuthal Variation of Rotor Blade Chordwise Moment at $V_s = 120$ Knots, $\alpha_i = 0^\circ$, $\theta_c = 8^\circ$, 30%R, $\beta_{.75} = 41^\circ$	283
145	Effect of Inboard Tractor Propeller Thrust on Rotor Blade Torsional Vibratory Moment Amplitudes at Various Rotor Angles of Attack and Collective Pitch Settings and Two Forward Speeds, 18%R	284
146	Effect of Tractor Propeller Location on Rotor Blade Torsional Vibratory Moment Amplitudes at Various Rotor Angles of Attack, Collective Pitch Settings, and Forward Speeds, 35%R, $\beta_{.75} = 41^\circ$	285
147	Effect of Pusher Propeller Thrust on Rotor Blade Torsional Vibratory Moment Amplitudes at Various Rotor Angles of Attack and Collective Pitch Settings, With Empennage, $V_s = 120$ Knots, 35%R	286

<u>Figure</u>		<u>Page</u>
148	Effect of Forward Speed, Rotor Lift, and Collective Pitch Setting on Rotor Blade Flapwise Vibratory Moment Amplitudes With the Inboard Tractor Propellers, $\beta_{.75} = 41^\circ$, $\alpha_f = 4^\circ$, 60%R . . .	287
149	Effect of Forward Speed, Rotor Lift, and Collective Pitch Setting on Rotor Blade Chordwise Vibratory Moment Amplitudes With the Inboard Tractor Propellers, $\beta_{.75} = 41^\circ$, $\alpha_f = 4^\circ$, 30%R . . .	288
150	Effect of Forward Speed, Rotor Lift, and Collective Pitch Setting on Rotor Blade Torsional Vibratory Moment Amplitudes With the Inboard Tractor Propellers, $\beta_{.75} = 41^\circ$, $\alpha_f = 4^\circ$, 18%R	289
151	Effect of Forward Speed, Rotor Lift, and Collective Pitch Setting on Rotor Blade Flapwise Vibratory Moment Amplitudes Without Propellers, $\alpha_f = 4^\circ$, 60%R	290
152	Effect of Forward Speed, Rotor Lift, and Collective Pitch Setting on Rotor Blade Chordwise Vibratory Moment Amplitudes Without Propellers, $\alpha_f = 4^\circ$, 30%R	291
153	Effect of Forward Speed, Rotor Lift, and Collective Pitch Setting on Rotor Blade Torsional Moment Amplitudes Without Propellers, $\alpha_f = 4^\circ$, 35%R	292
154	Effect of Forward Speed, Rotor Lift, Collective Pitch Setting, and Fuselage Angle of Attack on Rotor Blade Flapwise Vibratory Moment Amplitudes With Inboard Tractor Propellers, $\beta_{.75} = 41^\circ$, 60%R	293
155	Effect of Propeller Thrust and Rotor Lift on Downwash Angle at the Tail for the Pusher and Inboard Tractor Propellers at $V_s = 120$ Knots, $\alpha_f = -4^\circ$	295

<u>Figure</u>		<u>Page</u>
156	Effect of Propeller Location and Rotor Lift on Downwash Angle at the Tail at $V_s = 200$ Knots, $\alpha_f = 8^\circ$, $\beta_{75} = 41^\circ$	296
157	Effect of Fuselage Angle of Attack and Wing Position on Wing Lift and Drag at Various Rotor Lifts, Medium Wing, $V_s = 120$ Knots	297
158	Effect of Fuselage Angle of Attack and Wing Position on Wing Lift and Drag at Various Rotor Lifts, Large Wing, $V_s = 120$ Knots	299
159	Effect of Fuselage Angle of Attack and Wing Position on Wing Lift and Drag at Various Rotor Lifts, Large and Medium Wings, $V_s = 160$ Knots	301
160	Effect of Fuselage Angle of Attack and Wing Position on Wing Lift and Drag at Various Rotor Lifts, Medium Wing, $V_s = 200$ Knots	304
161	Effect of Fuselage Angle of Attack and Wing Position on Wing Lift and Drag at Various Rotor Lifts, Large Wing, $V_s = 200$ Knots	306
162	Effect of Fuselage Angle of Attack on Wing Lift and Drag at Various Rotor Lifts, Large Wing, High Position, $V_s = 232$ Knots	309
163	Effect of Fuselage Angle of Attack and Wing Position on Wing Lift and Drag at Various Rotor Lifts, Large and Medium Wings, $V_s = 300$ Knots	311
164	Effect of Rotor Angle of Attack and Collective Pitch Setting on Rotor Aerodynamic Characteristics at $V_s = 120$ Knots	313
165	Effect of Rotor Angle of Attack and Collective Pitch Setting on Rotor Aerodynamic Characteristics at $V_s = 160$ Knots	316

<u>Figure</u>		<u>Page</u>
166	Effect of Rotor Angle of Attack and Collective Pitch Setting on Rotor Aerodynamic Characteristics at $V_s = 200$ Knots	319
167	Effect of Rotor Angle of Attack and Collective Pitch Setting on Rotor Aerodynamic Characteristics at $V_s = 232$ Knots	322
168	Effect of Rotor Angle of Attack and Collective Pitch Setting on Rotor Aerodynamic Characteristics at $V_s = 300$ Knots	325
169	Effect of Fuselage Angle of Attack on the Aerodynamic Characteristics of the Large Wing, Without Rotor, Nacelles, or Propellers, $i_w = 0^\circ$	328
170	Effect of Fuselage Angle of Attack on the Aerodynamic Characteristics of the Large Wing, Without Propellers or Nacelles and With Rotor at Various Collective Pitch Settings and Forward Speeds, $i_w = 0^\circ$	329
171	Effect of Fuselage Angle of Attack on the Aerodynamic Characteristics of the Large Wing, Without Propellers or Rotor and With Inboard Nacelles, $i_w = 0^\circ$	332
172	Effect of Fuselage Angle of Attack on the Aerodynamic Characteristics of the Large Wing, Without Rotor and With Inboard Tractor Propellers at Various Forward Speeds, $\beta_{.75} = 41^\circ$, $i_w = 0^\circ$	333
173	Effect of Fuselage Angle of Attack on the Aerodynamic Characteristics of the Large Wing, Without Propellers or Rotor and With Outboard Nacelles, $i_w = 0^\circ$	336
174	Effect of Fuselage Angle of Attack on the Aerodynamic Characteristics of the Large Wing, Without Rotor and With Outboard Tractor Propellers at Various Forward Speeds, $\beta_{.75} = 41^\circ$, $i_w = 0^\circ$	337

<u>Figure</u>		<u>Page</u>
156	Effect of Propeller Location and Rotor Lift on Downwash Angle at the Tail at $V_s = 200$ Knots, $\alpha_f = 8^\circ$, $\beta_{.75} = 41^\circ$	296
157	Effect of Fuselage Angle of Attack and Wing Position on Wing Lift and Drag at Various Rotor Lifts, Medium Wing, $V_s = 120$ Knots	297
158	Effect of Fuselage Angle of Attack and Wing Position on Wing Lift and Drag at Various Rotor Lifts, Large Wing, $V_s = 120$ Knots	299
159	Effect of Fuselage Angle of Attack and Wing Position on Wing Lift and Drag at Various Rotor Lifts, Large and Medium Wings, $V_s = 160$ Knots	301
160	Effect of Fuselage Angle of Attack and Wing Position on Wing Lift and Drag at Various Rotor Lifts, Medium Wing, $V_s = 200$ Knots	304
161	Effect of Fuselage Angle of Attack and Wing Position on Wing Lift and Drag at Various Rotor Lifts, Large Wing, $V_s = 200$ Knots	306
162	Effect of Fuselage Angle of Attack on Wing Lift and Drag at Various Rotor Lifts, Large Wing, High Position, $V_s = 232$ Knots	309
163	Effect of Fuselage Angle of Attack and Wing Position on Wing Lift and Drag at Various Rotor Lifts, Large and Medium Wings, $V_s = 300$ Knots	311
164	Effect of Rotor Angle of Attack and Collective Pitch Setting on Rotor Aerodynamic Characteristics at $V_s = 120$ Knots	313
165	Effect of Rotor Angle of Attack and Collective Pitch Setting on Rotor Aerodynamic Characteristics at $V_s = 160$ Knots	316

<u>Figure</u>		<u>Page</u>
166	Effect of Rotor Angle of Attack and Collective Pitch Setting on Rotor Aerodynamic Characteristics at $V_s = 200$ Knots	319
167	Effect of Rotor Angle of Attack and Collective Pitch Setting on Rotor Aerodynamic Characteristics at $V_s = 232$ Knots	322
168	Effect of Rotor Angle of Attack and Collective Pitch Setting on Rotor Aerodynamic Characteristics at $V_s = 300$ Knots	325
169	Effect of Fuselage Angle of Attack on the Aerodynamic Characteristics of the Large Wing, Without Rotor, Nacelles, or Propellers, $i_w = 0^\circ$	328
170	Effect of Fuselage Angle of Attack on the Aerodynamic Characteristics of the Large Wing, Without Propellers or Nacelles and With Rotor at Various Collective Pitch Settings and Forward Speeds, $i_w = 0^\circ$	329
171	Effect of Fuselage Angle of Attack on the Aerodynamic Characteristics of the Large Wing, Without Propellers or Rotor and With Inboard Nacelles, $i_w = 0^\circ$	332
172	Effect of Fuselage Angle of Attack on the Aerodynamic Characteristics of the Large Wing, Without Rotor and With Inboard Tractor Propellers at Various Forward Speeds, $\beta_{.75} = 41^\circ$, $i_w = 0^\circ$	333
173	Effect of Fuselage Angle of Attack on the Aerodynamic Characteristics of the Large Wing, Without Propellers or Rotor and With Outboard Nacelles, $i_w = 0^\circ$	336
174	Effect of Fuselage Angle of Attack on the Aerodynamic Characteristics of the Large Wing, Without Rotor and With Outboard Tractor Propellers at Various Forward Speeds, $\beta_{.75} = 41^\circ$, $i_w = 0^\circ$	337

<u>Figure</u>		<u>Page</u>
175	Effect of Fuselage Angle of Attack on the Aerodynamic Characteristics of the Large Wing, Without Rotor and With Pusher Propeller Without Empennage at $V_s = 300$ Knots, $\beta_{.75} = 41^\circ$, $i_w = 0^\circ$	340
176	Effect of Fuselage Angle of Attack on the Aerodynamic Characteristics of the Large Wing, With Rotor and Inboard Tractor Propellers at Various Forward Speeds and Collective Pitch Settings, $\beta_{.75} = 41^\circ$, $i_w = 0^\circ$	341
177	Effect of Fuselage Angle of Attack on the Aerodynamic Characteristics of the Large Wing, With Rotor and Inboard Tractor Propellers at $V_s = 120$ Knots and Various Collective Pitch Settings, $\beta_{.75} = 30^\circ$, $i_w = 0^\circ$	344
178	Effect of Fuselage Angle of Attack on the Aerodynamic Characteristics of the Large Wing, With Rotor and Outboard Tractor Propellers at Various Forward Speeds and Collective Pitch Settings, $\beta_{.75} = 41^\circ$, $i_w = 0^\circ$	345
179	Effect of Fuselage Angle of Attack on the Aerodynamic Characteristics of the Large Wing, With Rotor, Pusher Propeller, and Empennage at Various Forward Speeds and Collective Pitch Settings, $\beta_{.75} = 41^\circ$, $i_w = 0^\circ$	348
180	Effect of Fuselage Angle of Attack on the Aerodynamic Characteristics of the Large Wing, With Rotor, Pusher Propeller, and Empennage at $V_s = 120$ Knots and Various Collective Pitch Settings, $\beta_{.75} = 30^\circ$, $i_w = 0^\circ$	351

LIST OF SYMBOLS

Dimensional

α_0	rotor coning angle, degrees
α_{00}	rotor coning angle for configuration without wing, degrees
α_{0W}	rotor coning angle increment induced by the wing, degrees
α_{1s}	first harmonic longitudinal flapping angle with respect to the shaft axis, degrees
α_{1sW}	first harmonic longitudinal flapping angle increment induced by the wing, degrees
A_f	fuselage frontal area, square feet
A_W	wing area, square feet
A_{1s}	first harmonic lateral cyclic pitch angle with respect to the shaft axis, degrees
$A_{1s\text{TRIM}}$	first harmonic lateral cyclic pitch angle increment required to trim out wing induced first harmonic flapping, degrees
b_{1s}	first harmonic lateral flapping angle with respect to the shaft axis, degrees
b_{1s0}	first harmonic lateral flapping angle for configuration without wing, degrees
b_{1sW}	first harmonic lateral flapping angle increment induced by the wing, degrees
b_W	wing span, feet
B_{1s}	first harmonic longitudinal cyclic pitch angle with respect to the shaft axis, degrees
$B_{1s\text{TRIM}}$	first harmonic longitudinal cyclic pitch angle increment required to trim out wing induced first harmonic flapping, degrees

c	rotor blade chord, feet
c_w	wing section chord, feet
c_{wm}	wing mean geometric chord, $\frac{c_{wr} + c_{wt}}{2}$, feet
c_{wr}	wing root chord, projected to fuselage centerline, feet
c_{wt}	wing tip chord, feet
d	rotor diameter, feet
D	drag, pounds
h	downward displacement, normal to relative wind, of the centerline of the wing wake from the wing trailing edge, feet
i_{fzll}	angle between fuselage zero lift line and fuselage axis, degrees
i_{rw}	angle between wing wake and longitudinal projection of line parallel to rotor tip path plane, degrees
i_s	angle between fuselage axis and normal to rotor shaft ($i_s = 0^\circ$ on model), degrees
i_w	wing incidence, with respect to fuselage centerline, degrees
i_{wzll}	angle between wing section zero lift line and wing chord, degrees
l	rolling moment, foot-pounds
l_f	fuselage length, feet
l_w	wing lift per unit spanwise distance, pounds per foot
L	lift, pounds

m	vertical distance of tail pivot axis from wing trailing edge (normal to relative wind), feet
M	pitching moment, foot-pounds
N_{PROP}	propeller speed, rpm
p	static pressure, pounds per square foot
q	dynamic pressure, $\rho v^2/2$, pounds per square foot
Q	rotor torque, foot-pounds
R	rotor radius, feet
V	forward speed (appears only in equations), feet per second
$v_{i_{BD}}$	velocity induced at a point on the rotor by a single bound wake element of the wing, feet per second
$v_{i_{RMOM}}$	inflow velocity at the rotor based on momentum theory, feet per second
V_S	simulated forward speed (always specified), knots
$v_{i_{TRL}}$	velocity induced at a point on the rotor by a single trailing wake filament of the wing, feet per second
v_{i_W}	local downwash velocity induced at the wing by the rotor, feet per second
\bar{v}_{i_z}	effective value of the normal component of velocity induced by the wing at the rotor (linearized theory), feet per second
$v_{i_{z_{BD}}}$	normal component of velocity induced at a point on the rotor by a single bound wake element of the wing, feet per second

v_{iZ_0}	local spanwise normal component of velocity induced at the rotor by the wing (averaged azimuthally), feet per second
$v_{iZ_{r,\psi}}$	total normal component of induced velocity at a point on the rotor due to the wing, feet per second
$v_{iZ_{TRL}}$	normal component of velocity induced at a point on the rotor by a single trailing wake filament of the wing, feet per second
x	distance of tail pivot from wing quarter chord (parallel to relative wind), feet
y	spanwise position from center of fuselage, feet
y_F	spanwise position of fuselage boundary from center of fuselage, feet
y_T	spanwise position of wing tip from center of fuselage, feet
z	vertical distance from tail pivot axis to fuselage axis, feet
z	vertical distance from rotor to wing, feet
α_c	rotor (control axis) angle of attack, degrees
α_f	fuselage angle of attack ($= \alpha_s$ on model), degrees
α_{f_0}	fuselage zero lift line angle of attack, degrees
α_{iw}	induced angle of attack at the wing, degrees

α_p	propeller angle of attack (isolated propeller configuration), degrees
α_s	rotor shaft angle of attack ($= \alpha_f$ on model), degrees
α_{TPP}	rotor tip path plane angle of attack, degrees
α_w	wing angle of attack, degrees
α_{w0}	wing zero lift line angle of attack, degrees
α_{wy}	local effective wing angle of attack, degrees
β	rotor blade flapping angle, degrees
β_{75}	propeller pitch at 75% radius, degrees
Γ_{80}	circulation of wing bound wake element, feet squared per second
Γ_{TRL}	circulation of wing trailing wake filament, feet squared per second
Γ_y	local spanwise circulation, feet squared per second
δ_3	pitch-flap coupling angle, degrees
ϵ_t	downwash angle at the tail, degrees
ϵ_w	wing downwash angle, degrees
η	distance of tail pivot axis from wing quarter chord (parallel to fuselage axis), feet
θ	propeller blade twist, degrees
θ_1	angle between most negative boundary of the wing bound wake element and a point on the rotor, degrees

θ_2	angle between most positive boundary of the wing bound wake element and a point on the rotor, degrees
θ_c	collective pitch, degrees
θ_{TRL}	angle between the intersection of the trailing wake filament with the wing quarter chord and a point on the blade, degrees
ρ	air density, slugs per cubic foot
σ_{BD}	angle between the resultant velocity at a point on the rotor induced by a bound wake element and the normal component (see Figures 58 and 59), degrees
σ_{TRL}	angle between a component of velocity at a point on the rotor induced by a trailing wake filament and the normal component (see Figure 58), degrees
χ_{TPP}	rotor wake skew angle (measured with respect to the normal to the rotor tip path plane), degrees
ψ	blade azimuth angle (measured from downwind position in direction of rotation), degrees
Ω	rotor angular velocity, radians per second
<u>Nondimensional</u>	
a	blade section lift curve slope
AR	wing aspect ratio
b	number of rotor blades
c_l	wing section lift coefficient, $\frac{l_w}{\frac{1}{2} \rho v^2 c_w}$

c_{l_1}	component of local spanwise lift coefficient due to fuselage angle of attack
c_{l_2}	component of local spanwise lift coefficient due to wing angle increment over the fuselage angle of attack
c_p	static pressure coefficient, $\frac{p_{U',L'} - p}{q}$
C_{Df}	fuselage drag coefficient, $\frac{D_f}{\frac{1}{2} \rho V^2 A_f}$
C_{DR}	rotor drag coefficient, $\frac{D_R}{\pi R^2 \rho (\Omega R)^2}$
C_{DW}	wing drag coefficient, $\frac{D_W}{\frac{1}{2} \rho V^2 A_W}$
C_{l_W}	wing rolling moment coefficient, $\frac{l}{\frac{1}{2} \rho V^2 A_W b_W}$
C_{L_f}	fuselage lift coefficient, $\frac{L_f}{\frac{1}{2} \rho V^2 A_f}$
C_{LR}	rotor lift coefficient, $\frac{L_R}{\pi R^2 \rho (\Omega R)^2}$
C_{LW}	wing lift coefficient, $\frac{L_W}{\frac{1}{2} \rho V^2 A_W}$
C_{LW_f}	combined wing-fuselage lift coefficient, $C_{LW} + \frac{A_f C_{L_f}}{A_W}$

$C_{m_{c/4}}$	wing pitching moment coefficient, $\frac{M_W}{\frac{1}{2} \rho V^2 A_W c_{wm}}$
C_{m_f}	fuselage pitching moment coefficient, $\frac{M_f}{\frac{1}{2} \rho V^2 A_f l_f}$
C_{m_W}	wing pitching moment coefficient (measured with respect to mid wing quarter chord position), $C_{m_{c/4}} - \frac{C_{D_W}(z - 1.4)}{c_{wm}}$
C_n	local normal force coefficient, $\int_0^{c_W} \frac{p_U - p_L'}{q} dc_W$
C_Q	rotor torque coefficient, $\frac{Q}{\pi R^2 \rho (\Omega R)^2 R}$
e	rotor blade flapping hinge offset (nondimensionalized by rotor radius)
G_1	local lift coefficient factor (Reference 7)
G_2	local lift coefficient factor (Reference 7)
h_{BD}	distance between bound wake element and point on blade (nondimensionalized by rotor radius)
h_{TRL}	distance between trailing wake filament and point on blade (nondimensionalized by rotor radius)
k	downwash factor
$M_{(1.0,90)}$	equivalent advancing tip Mach number
r	rotor blade radial distance from center of rotation (nondimensionalized by rotor radius)

TR	wing taper ratio
(X,Y,Z)	tip path plane coordinate axis system (nondimensionalized by rotor radius)
\bar{y}	spanwise distance from center of fuselage (nondimensionalized by wing semispan)
y_1	boundary of starboard wing bound wake element (nondimensionalized by rotor radius)
y_2	boundary of port wing bound wake element (nondimensionalized by rotor radius)
y_{TRL}	lateral coordinate of wing trailing wake filament (nondimensionalized by rotor radius)
z_0	rotor-wing separation (nondimensionalized by rotor radius)
λ_s	rotor inflow ratio (with respect to shaft), $\frac{V \sin \alpha_s - V_{iR_{MOM}}}{\Omega R}$
μ	rotor advance ratio, $V/\Omega R$
σ	rotor solidity: $b c / \pi R$
σ_f	fuselage width to wing-span ratio

Subscripts

f	fuselage
R	rotor
w	wing
u'	upper wing surface
L'	lower wing surface

INTRODUCTION

It is generally recognized that the low speed advantages of the pure helicopter and a speed capability in the 200-to 300-knot range can be effectively achieved with a compound helicopter. The successful marriage of fixed wing and helicopter technologies in the development of the compound helicopter, however, requires an understanding of the aerodynamic interactions among the aircraft's lifting and propulsive components. The relative effects of a number of design and operating parameters such as wing size and vertical position, rotor-wing lift sharing, and placement of auxiliary propulsive devices on performance and handling characteristics must be determined before the concept can be fully developed.

At the present time, the state of the art pertaining to compound helicopter interference theory is quite limited. A complete theoretical approach for predicting the mutual interference effects of the compound helicopter components does not exist, and design has been based on experimental results or on theoretical methods developed for conventional helicopters and fixed-wing aircraft. However, departures of the winged helicopter design and flight regime from those of conventional aircraft, such as the presence of a wing-rotor combination, shorter span wings, differing fuselage shape, and higher flight speeds, have raised questions concerning the accuracy and applicability of the few existing theories.

The existence of rotor-wing-fuselage interference effects was revealed in small-scale wind tunnel tests which were conducted by Sikorsky Aircraft as early as 1955 and more recently in the United Aircraft Corporation's (UAC) 4-by-6-foot subsonic wind tunnel. In addition, Sikorsky flight research in this area began with the addition of wings to an S-55 (UH-19C) helicopter in 1957 and is continuing with the S-61F (NH-3A) research aircraft shown in Figure 1. The S-61F program and other flight research investigations of compound helicopters have helped to define the effects of rotor-wing lift sharing, but none has provided the flexibility or precision which is obtainable in the wind tunnel. The purpose of the present investigation was to perform comprehensive wind tunnel tests to study the aerodynamic characteristics and interference effects of rotor-wing-fuselage-propeller combinations. The data were obtained from tests of a wind tunnel model incorporating dynamically scaled rotor and propeller blades; independent strain gage balances to measure rotor, wing, and fuselage forces and moments; and a floating horizontal stabilizer. The tests were conducted in two parts, the first to study rotor-wing-fuselage interference effects and the second to study rotor-propeller interference effects.

An analytical study was performed as a part of this investigation in which some existing theories were applied to the compound helicopter model configuration. The theoretical results were compared with the experimental results obtained from the wind tunnel tests to evaluate the applicability of the theories to the compound helicopter interference problem and the necessity of extending them.

DESCRIPTION OF MODEL AND TEST FACILITIES

The compound helicopter wind tunnel model (Figure 2), as tested in the UAC main wind tunnel, was supported by a single main support strut and a pitch strut, both of which extended through the tunnel floor and attached to the main tunnel balance. The tunnel balance was locked out, and all forces and moments were measured on three internal balances that were mounted on the model keel. The keel was enclosed by, but free of, the fuselage.

A general description of the major systems of the model follows.

ROTOR SYSTEM

The four-bladed rotor is powered by a 19-horsepower electric motor through a transmission which provides a speed reduction of approximately 13.5 to 1. The rotor hub is fully articulated with flapping and lagging hinges at the 5.6 - percent radial station and incorporates a 1:1 pitch flap coupling ratio ($\delta_3 = 45$ degrees) to reduce flapping sensitivity at high advance ratios. Lagging motion is restrained by rotary viscous dampers, and flapping motion is sensed by a rotary potentiometer.

The rotor blades have a 54-inch radius, a 4.24-inch chord, and a resultant solidity of 0.10. When operated at approximately one-half full-scale tip speed, they are dynamically similar in flapwise, chordwise, and torsional stiffness properties to a full-scale design for high-speed operation. Construction is fiber glass, and except for increased chord, the blades are similar to those described in Reference 1 and tested under corporate and U. S. Army programs (References 2 and 3). On these blades, a 60-inch-pound flapwise moment at the radial stations presented herein corresponds to a 10,000-psi stress on an equivalent blade constructed of aluminum. Likewise, a 125-inch-pound chordwise moment corresponds to 10,000-psi stress and an 85-inch-pound torsional moment corresponds to 10,000-psi stress. The flight conditions tested in this investigation are shown in Figure 3a, which is a plot of rotor tip speed versus forward speed. The five test speeds simulate operation from 120 knots to high speed compound flight at 300 knots. The simulated forward speeds and rotor tip speeds and the corresponding advance ratios are as follows:

Simulated ΩR , ft/sec	V_s , Knots	μ
700	120	0.29
700	160	0.39
663	200	0.51
614	232	0.64
500	300	1.01

Rotor blade natural frequencies are shown in Figure 3b as functions of rotor speed.

Rotor cyclic and collective pitch angles are remotely controlled by the model operator through a hydraulic servo system. Blade vibratory bending moments are measured by complete strain gage bridges located at 5 flapwise, 4 chordwise, and 2 torsional stations. The radial locations of the gages are as follows:

<u>Gages</u>	<u>Percent Radius</u>				
Flapwise	20	30	45	60	80
Chordwise	20	30	45	60	
Torsional	12	35			

Bending moment and flapping signals are transmitted from the rotating system through 46 slip rings mounted at the base of the rotor shaft. The complete rotor system, including drive motor, transmission, and all hydraulic system components, is mounted on a six-component strain gage balance that is attached to the keel and is independent of the wing and fuselage balances.

WINGS

Design parameters for the three sets of wings are shown in Figure 2c. Each wing may be tested at a high, mid, and low position; the respective z/d values are 0.109, 0.156, and 0.205, and the medium wing has a remotely variable incidence range of ± 15 degrees at the mid fuselage position. In this report, the wing incidence relative to the fuselage is $+4$ degrees unless otherwise specified. All wings are constructed of cherry wood over a steel structure and have a NACA 642-415 airfoil section. Wing tips are generated by revolving an airfoil section about the blade tip chord line.

Each wing half contains oscillatory pressure transducers at one spanwise station (80 percent semispan) and at several chordwise locations to

measure differential pressures between upper and lower surfaces of the wing. The chordwise locations are as follows:

<u>Wing Size</u>	<u>Percent Chord From Leading Edge</u>					
Small	10	20	40	70		
Medium	5	10	15	25	40	70
Large	5	10	15	25	40	70

In addition, the medium wing has static pressure taps in two spanwise positions as follows:

Spanwise: 40 and 70 percent semispan

	<u>Percent Chord From Leading Edge</u>							
Chordwise: Upper Surface:	2	4	8	15	30	45	55	65
Lower Surface:	4	15	30	40	50			

The wings are attached to the model through the wing support frame which transmits aerodynamic loads from any mounting position to the wing strain gage balance. The balance is attached to the keel and is independent of the rotor and fuselage balances.

The large wing was modified to support propeller-nacelle assemblies on the lower surface, as shown in Figure 2d. Cover plates were provided to permit testing with and without the nacelles.

FUSELAGE

The fuselage is a streamlined fiber glass shell mounted on a separate strain gage balance. It is completely isolated from the wing and rotor balance systems to allow independent measurement of fuselage aerodynamic loads. The aft section of the fuselage is fitted to support the pusher propeller assembly (Figure 2d). The fuselage frontal area is 1.25 square feet and the total fuselage length is 9 feet.

FLOATING TAIL

A floating horizontal tail with a span equal to 30 percent of the rotor diameter is mounted with a tail pylon to the aft fuselage. It has a NACA 0012 airfoil section and is mass balanced about the pivot point

which is well forward of the center of pressure. A rotary viscous damper is provided to reduce oscillation. The tail angle of attack is sensed by a rotary potentiometer. The tail and tail pylon are removable to permit testing without the tail.

BALANCES

The three balances are of the internal strain gage, floating frame type. They are highly linear, are temperature compensated, and have small or negligible interactions between various components. Balance interactions and those inherent in the model design were determined experimentally during the model calibration and were included in the data reduction program coefficients.

PROPELLERS

The two four-bladed propellers are 16.5 inches in diameter and are powered by 9-horsepower variable speed electric motors. The propeller blades are constructed of fiber glass and are scaled in flatwise and edgewise stiffness properties to be dynamically similar to a full-scale design. Blade characteristics are shown in Figure 3c. The blade pitch is manually adjustable, and one blade of each propeller is instrumented to measure flatwise bending moments at the 29- and 58-percent radial stations and edgewise bending moments at the 29-percent radial station. The signals from the strain gage bridges are transmitted to the stationary system through special slip-ring assemblies mounted on the aft ends of the motors. On these blades, a 10-inch-pound flatwise moment at the 29-percent radial station corresponds to an 8,200-psi stress on the full-scale aluminum blade, and a 10-inch-pound moment at the 58-percent radial station corresponds to a 16,200-psi stress on the full-scale aluminum blade.

WIND TUNNEL

The UAC main wind tunnel (Figure 4) is a closed return, single passage type powered by a 9,000-horsepower drive motor and has a speed capability of 175 knots with the 18-foot test section installed. Control of the tunnel and the compound helicopter model is accomplished from a control room adjacent to the test section. Windows in the section allow the model operator to see the model at all times.

ISOLATED PROPELLER

A special fixture consisting of a vertical strut mounted on the tunnel yaw table was fabricated to test a propeller isolated from the interferences of the model. The propeller and motor were fixed to the strut, and changes in angle of attack were accomplished by rotation of the yaw table. The installation is shown in Figure 5.

DATA ACQUISITION SYSTEM

Dynamic data from the compound helicopter model were recorded on a 20-channel Epsco data acquisition system. Each incoming channel was scanned 30 times per rotor revolution for 6 revolutions. The information is received from the model in analog form, digitized, and recorded on magnetic tape. These data are transmitted to an IBM 7094 data processing unit and reduced. During the first part of the test, the fuselage balance data and the tail incidence were read from Baldwin strain indicators. The former data were reduced in a separate program and the latter were manually set into the Epsco system. The data reduction programs reduce all performance data to dimensional and coefficient form. Tare forces and moments are subtracted from the measured data so that rotor performance corresponds to that from blades alone, and gravity effect variations with angle of attack are eliminated from the performance data. Blade flapping and bending moments are reduced to average and peak-to-peak values. The oscillatory pressures on the wings were sensed with Scientific Advances SDT-7 differential pressure transducers. The output of these was fed directly into the Epsco system.

The static pressure data were obtained with standard U-tube manometers. Photographic records of the manometer levels were reduced with telereader equipment, and the resulting data were converted to coefficient form on the IBM 7094 unit.

The propeller bending moments were recorded with a system separate from the Epsco system which utilized 6 channels of a 24-channel Heiland Visicorder. Peak-to-peak values were manually reduced from the Visicorder records. To account for the difference in orientation between the calibration loads and the chord line at the 29-percent radial station due to blade twist, the measured bending moment values were transformed to principal structural directions through the following relation.

$$\begin{Bmatrix} \text{Flatwise} \\ \text{Edgewise} \end{Bmatrix} \text{ Principal} = \begin{bmatrix} 0.883 & -0.025 \\ -0.174 & 0.993 \end{bmatrix} \begin{Bmatrix} \text{Flatwise} \\ \text{Edgewise} \end{Bmatrix} \text{ Measured}$$

This transformation assumes that the peak values in the flatwise and edgewise directions are in phase. The nature of the data acquisition system was such that the actual phase relationship could not be determined because of the high frequency of the signal from the propeller blade.

DATA ACCURACY AND REPEATABILITY

The accuracy of all the data is within 1 percent of the maximum measured values except for the wing oscillatory pressures and the propeller blade bending moments. Signals from the oscillatory pressure transducers were processed through the Epsco system, but the data show a large amount of unexplained scatter (approximately 10 percent). The method of recording the propeller blade bending moments limited the measurements to a tolerance of ± 1 inch-pound, and the method of reduction introduced an equal amount of uncertainty for a net uncertainty of ± 2 inch-pounds (approximately 4 percent).

To determine whether or not random oscillatory pitching and yawing of the model was of a magnitude sufficient to affect the propeller blade moments, graduated scales were placed on the wing tips and tail cone and were observed with a surveyor's transit at all test conditions. From these observations, it was found that such oscillations were negligibly small, and it was concluded that the propeller moment data were free of effects introduced by model motions.

The repeatability of the various data elements is indicated by multiple points on the appropriate figures in the body of this report. The repeatability is generally good except for a hysteresis-type effect exhibited by the propeller blade moments under some operating conditions.

EXPERIMENTAL PROCEDURE

ROTOR-WING-FUSELAGE INTERFERENCE EFFECTS

In this part of the investigation, the wind tunnel testing procedure was to locate each of the three wings at each of the three vertical positions on the model. At each wing size-position combination, the rotor tip speed and the tunnel speed were set to each of the five advance ratios shown in Figure 3, and the fuselage angle of attack then varied in 4-degree increments. At each α_i setting, the collective pitch angle was set to 0, 4, and 8 degrees and the cyclic pitch control was employed to obtain first harmonic longitudinal flapping with respect to the rotor shaft angle of 0, +4, and -4 degrees, the first case defining trimmed rotor operation. This procedure was also repeated for the wingless configuration. Since the data were taken within the limits of rotor blade bending moments and control system kinematics, the actual number of test points obtainable varied somewhat with advance ratio. With each wing at the mid position and the rotor blades removed, the fuselage angle of attack was varied at $V_s = 120, 200, \text{ and } 300$ knots to obtain wing aerodynamic characteristics.

ROTOR-PROPELLER INTERFERENCE EFFECTS

The procedure for setting the rotor operating conditions in this part of the testing was fundamentally the same as that described above at each of the propeller pitch-configuration combinations. After the rotor tip speed was set for each data run, the wind tunnel speed was increased, allowing the propeller to windmill. The propeller was then brought up to speed and checks were made for the existence of modal coupling between the rotor and the propellers. No rotor-propeller dynamic coupling was observed. In the pusher propeller configuration, an additional set of runs was made in which the rotor conditions were varied at each of three selected propeller speeds. The propeller-fuselage combinations were also tested with the rotor blades removed by varying α_i at each forward speed.

EVALUATION OF RESULTS, ROTOR-WING-FUSELAGE INTERFERENCE EFFECTS

EFFECTS OF ROTOR LIFT ON WING AND FUSELAGE PERFORMANCE

The effect of rotor downwash on wing loading and performance was investigated for the nine configurations throughout the forward speed range. Wing lift and drag for constant values of rotor lift are presented in Appendix I for all forward speed configuration combinations. As was anticipated, the most significant measured effect was a decrease in wing lift which was approximately proportional to the rotor momentum downwash. This effect is shown in Figure 6, which includes plots of C_{LW} as a function of C_{LR}/σ for various values of α_f , V_s , and wing-fuselage combination. Each combination of α_f and θ_c includes the three flapping trim conditions as discussed in the section on experimental procedures. The first harmonic longitudinal flapping increases from -4 through 0 to +4 degrees as rotor lift increases. For reference, three such trim points are labeled in Figure 6a at $\alpha_f = 4$ degrees and $\theta_c = 0$ degrees. Point A corresponds to $\alpha_{1s} = -4$ degrees, point B to $\alpha_{1s} = 0$ degrees, and point C to $\alpha_{1s} = +4$ degrees.

The linear relationship between wing and rotor lift is well defined in these plots, but it is also evident that the rotor trim condition affects the magnitude of the wing lift, although it does not affect the rate of decrease with C_{LR}/σ . For example, in Figure 6e, at $C_{LR}/\sigma = 0.04$ and $\alpha_f = 4$ degrees, an increase in θ_c from 0 degrees (point A) where the rotor tip path plane is tilted rearward and is near autorotation to 8 degrees (point B) where the rotor is tilted forward, results in an increase in C_{LW} of 0.06. The effect is clearly not a function of rotor lift but could be the result of the change in rotor loading distribution or the repositioning of the rotor wake caused by the change in α_{TPP} .

The linear decrease in wing lift can be examined in terms of rotor momentum theory where the velocity induced at the rotor disk is given by

$$V_{i_{R_{MOM}}} = \frac{\Omega R}{2 \mu} C_{LR} \quad (1)$$

The change in effective wing angle of attack can then be expressed in the form

$$\Delta \alpha_w = k \frac{\sigma}{2\mu^2} \left[C_{LR}/\sigma \right] \quad (57.3) \quad (2)$$

where k is the proportionality factor which accounts for the spacing between the wing and the rotor. The validity of this expression is shown in Figures 7 and 8 for the large and medium wings respectively; the effective rotor downwash at the wing per unit change in C_{LR}/σ is shown as a function of V_s . The experimental values were obtained from the cross plots presented in Appendix I and compare well with momentum theory. The average experimental downwash factor, k , was determined for the medium and large wings and is shown in Figure 9 as a function of the nondimensional vertical separation between the wing and the rotor, z/d .

Although the effect of rotor downwash on the total wing lift was expressed as a simple angle of attack change, the effect on wing drag was found to be more complex. Figure 10 shows C_{DW} as a function of C_{LR}/σ for the same conditions as those of Figure 6. Longitudinal flapping trim settings of -4, 0, and +4 degrees are labeled in Figure 10a as A, B, and C. Increasing rotor downwash causes an increase in wing drag as a result of the rearward inclination of the resultant force vector. This effect, when combined with the rotor-induced loss of wing lift, tends to cause a deterioration of the wing lift-drag ratio. Figure 11 shows the nature of this effect for the medium wing at the mid position for $V_s = 120$ knots and $V_s = 300$ knots. Since the wing L/D is given by the inverse of the slope of a line from the origin to the operating point, it is clear from Figure 11 that increasing rotor lift at constant α_f increases the slope of this line and therefore decreases wing L/D . Comparing parts a and b of Figure 11 reveals that this change in slope for a given change in C_{LR}/σ is greatly diminished as forward speed increases and enters the region where wing performance is of major importance. In addition, at the high speeds, the rotor is usually operated at a low C_{LR}/σ , so the net L/D loss is not a significant factor. Wing lift-drag polars for other test configurations are given in Appendix I.

The static pressures measured on the medium wing were analyzed to obtain a more complete picture of the rotor downwash effects. Samples of the static pressure records are shown in Figure 12 for $\alpha_f = 0$ and 8 degrees at $V_s = 120$ knots. The pressures have been nondimensionalized by the dynamic pressure and integration of distributions such as these yielded normal force coefficients, C_n . Figures 13 through 15 present

spanwise plots of C_n values determined in this manner. In Figure 13, which shows the medium wing in the high position, it can be seen that rotor lift has essentially no effect on the spanwise distribution of normal force coefficient at $V_s = 200$ knots. However, Figure 14, which is a similar plot for the 120-knot condition, shows that the lift on the starboard wing is substantially decreased as the rotor lift is increased, while the lift on the port wing remains relatively constant. The unbalance seen in this figure becomes less pronounced as the wing is moved away from the rotor; this can be seen in Figure 15, where the wing is in the mid position. It can be reasoned that the rotor bound wake system possibly provides the mechanism for the unsymmetrical phenomenon just discussed. This system induces a chordwise velocity at the wing which reduces the relative velocity on the starboard wing and increases it on the port wing.

Analysis of the oscillatory pressure data also revealed an interesting effect. Figure 16 shows a sample of the harmonic analysis of the oscillatory pressures on the wing at $V_s = 300$ knots. The first harmonic frequency is defined as the rotor angular velocity. With a four-bladed rotor, it was expected that the fourth harmonic pressure amplitude would predominate; this is seen to be the case in Figure 16. It was estimated that the random turbulence level in the tunnel was on the order of 0.2 psf, so the fourth harmonic amplitude is the only significant one shown in Figure 16. Figures 17 through 19 present this harmonic as a function of rotor angle of attack at 300 knots for the three wing positions. The data points shown include all values of θ_c , α_f , and flapping trim, but identification of these added nothing to the analysis. Comparison of the port and starboard data at any configuration shows a well defined variation with α_c on the port side but a smaller variation and more scatter on the starboard side. The reason for this phenomenon has not been determined, but the data show a definite variation with wing position. It was also found that this effect could be detected only at $V_s = 300$ knots; at the other speeds, all harmonics of oscillatory pressure remained consistently low. Since C_{LR}/σ increases directly with increasing α_c at 300 knots, the characteristics of the plots in Figures 17 through 19 do not change when C_{LR}/σ is taken as the independent variable.

In Figure 20, the rolling moment measured on the wing balance is plotted as a function of C_{LR}/σ for the medium wing at 120 to 300 knots over a number of rotor operating conditions. It is evident that a large decrease in the sensitivity of the rolling moment to changes in C_{LR}/σ takes place with increased forward speed in line with previous discussion of C_{LR}/σ effect on spanwise normal force coefficient distribution. This effect is summarized in Figure 21 where $\Delta C_{l_W} / \Delta C_{LR}/\sigma$ is plotted as a function of α_f . The decrease in rolling moment sensitivity with forward speed is clearly evident. Also seen is the combined effect of α_f and θ_c which relates to the unsymmetrical loading discussed earlier with reference to

Figure 14.

Pitching moments due to the wing are plotted in Figure 22 for the medium wing at the high position and $V_s = 120$ knots. The moment center is taken at the quarter-chord point of the mid wing position. It is apparent that the overall effect on C_{m_w} is very small, since such effect should be greatest for the configuration and speed considered in Figure 22. Since the wing pitching moment balance accuracy corresponds to a C_{m_w} of 0.05, no further conclusions can be drawn from the data shown in Figure 22.

The qualitative effects of rotor lift on fuselage lift and drag are essentially the same as those discussed for the rotor lift effect on wing lift and drag. This can be seen in Figures 23 and 24, which are plots of C_{L_f} and C_{D_f} as functions of C_{L_R}/σ for two wing-fuselage combinations at $V_s = 120$ and 300 knots. Fuselage frontal area (1.25 square feet) is used for nondimensionalization. The fuselage pitching moments, on the other hand, have their own characteristic variation with C_{L_R}/σ . Figures 25 and 26 present C_{m_f} as a function of C_{L_R}/σ for a number of forward speed configuration combinations. Fuselage frontal area and total fuselage length (9 feet) are used here for nondimensionalization. As with previously discussed rotor effects, the sensitivity of C_{m_f} to changes in rotor lift decreases with forward speed. Also, as in the case of wing lift, C_{m_f} is affected at constant C_{L_R}/σ by a change in θ_c and α_{Tpp} ; while as before, the slope with respect to C_{L_R}/σ remains unaltered. The significant exception to this is when the wing is at the high position at $V_s = 120$ knots. Figure 26 shows that for this condition both the magnitude and the slope are changed by a change in collective pitch at constant C_{L_R}/σ . It is not unreasonable to expect this kind of behavior, since the rotor wake washes directly over the fuselage at nearly every rotor condition shown in Figure 26, and an intimate dependence between fuselage loads and the composition of the rotor wake results. Plotting $\Delta C_{m_f}/\Delta C_{L_R}/\sigma$ as a function of V_s (Figure 27), the effect of forward speed as well as the effect of wing position can be assessed. It should be noted that the position of the wing can have a significant influence on the rotor wake and this contributes to the effect of the rotor on the fuselage.

EFFECT OF WING LIFT, SIZE, AND POSITION ON ROTOR PERFORMANCE

A major portion of this investigation was directed toward establishing the effects of wing geometry and loading on rotor performance and vibratory blade stresses. The model, without wings, was initially tested throughout the speed range over a wide range of rotor operating conditions to obtain basic rotor characteristics. Rotor performance data obtained in this configuration are presented in Appendix II.

The interrelationship of the large number of variables involved in the interference of the wing on rotor behavior is discussed in detail in the following section of the report. It is sufficient to note here that the experimental data necessarily include the effects of all these variables and that in determining the experimental effect of the wing on the rotor it must be appreciated that the data reflect the effect of changes in not only wing lift but rotor control settings, blade flapping, α_f , and μ . Specifically, at a given advance ratio and α_f , the rotor was tested with and without wings and with specified flapping trim values. As a result, the rotor responded to the presence of the wing, the cyclic pitch input required to trim the wing induced rotor blade flapping, and to δ_3 coupled effects of blade coning as described in the following section on theoretical analysis.

Figure 28 illustrates the effect of the large and medium wings on rotor lift and rotor angle of attack at 120 knots. These data represent conditions in which the first harmonic flapping was trimmed to zero degrees with respect to the rotor shaft, so constant values of α_f are equivalent to equal tip path plane angles of attack. With 4 degrees of wing incidence, the wing geometric angle of attack is equal to the fuselage angle of attack plus 4 degrees. It may be seen that even at high wing geometric angles of attack, the wing causes only modest decreases in rotor lift. Figure 29 presents similar data at 200 knots, and it is seen that although the effect of the large wing on rotor lift is somewhat more pronounced, both wings still cause only slight changes in rotor lift. For 300 knots (Figure 30), the interference effect becomes substantial, but the worst condition, $\alpha_f = 4$ degrees and large wing, is of practical importance only during high load factor maneuvers, since the full-scale wing lift at this condition is more than double the gross weight of an aircraft fitted with this rotor system (i.e., 36,000 to 40,000 pounds full-scale).

Although effects resulting from the presence of the wing increase with forward speed, the sensitivity of rotor lift with respect to changes in rotor angle of attack also increases with forward speed. The wing induced loss in rotor lift is easily offset by a small cyclic pitch change. It should also be noted that while the rotor lift interference per degree of wing angle of attack change increases with forward speed, the wing lift increment in pounds per degree of wing angle of attack change also increases rapidly with forward speed. In fact, the rotor lift interference in pounds of rotor lift increment per pound of wing lift increment actually decreases with forward speed. This decrease becomes even more rapid when rotor tip speed is reduced at high forward speeds. This can be deduced from the following relations:

$$\frac{\Delta C_{LR}}{\Delta C_{LW}} = \frac{\Delta L_R}{\pi R^2 \rho (\Omega R)^2} \frac{\frac{1}{2} \rho V^2 S}{\Delta L_W} = \frac{\Delta L_R}{\Delta L_W} f(\text{GEOMETRY}) \left(\frac{V}{\Omega R}\right)^2 \quad (3)$$

$$\frac{\Delta L_R}{\Delta L_W} = \frac{\Delta C_{LR}}{\Delta C_{LW}} \frac{1}{f(\text{GEOMETRY})} \left(\frac{\Omega R}{V}\right)^2 \quad (4)$$

where f is a function of model geometry only.

Figure 31 presents C_{DR}/σ as a function of C_{LR}/σ at 120, 200, and 300 knots. The values obtained with the large wing at the high position can be compared with the no-wing values. An increasing effect of the wing on C_{DR} occurs with increasing forward speed, as was true in the case of C_{LR} . Looking at the 300-knot data, it is seen that for positive α_i the presence of the wing causes an effective angle of attack change on the rotor which results in an increase in drag equivalent to the rotor lift times the sine of the angular rotation of the thrust vector. In the negative rotor lift condition, the increment in drag due to the rotation of the thrust vector is in the opposite direction, so the induced drag is decreased accordingly.

Figure 32 presents C_Q/σ as a function of rotor angle of attack at 120 and 300 knots. No significant change in rotor torque is evident when comparing results measured with and without the wing. These results indicate that the autorotation angle of attack is not affected by the presence of the wing or changes in wing lift.

EFFECTS OF WING SIZE AND POSITION ON ROTOR BLADE VIBRATORY MOMENTS

A potentially significant interference which was investigated is the effect of the wing induced inflow on rotor blade stresses. In Reference 4, a theoretical analysis is discussed in which the local velocities induced by the wing's bound and trailing vortices are added vectorially to a uniform rotor inflow. This analysis indicated that an increase in flapwise vibratory stress will occur and that it may be significant at high speeds.

During the wind tunnel testing, signals from the strain gage bridges on the model rotor blades were recorded as time histories of bending moment for

all rotor operating conditions. The one-half peak-to-peak flapwise bending moment at the 60-percent radial station is shown as a function of C_{LR}/σ in Figures 33 through 35 for the medium wing configurations. At $V_s = 120$ knots (Figure 33), it may be seen that the moment values are similar for the four wing-fuselage combinations when compared at any combination of C_{LR}/σ , α_f , and θ_c . Figure 34 shows similar data at $V_s = 200$ knots and $\alpha_f = -4$ to $+8$ degrees. At this increased speed, there is still no measurable change in the moment amplitude for different configurations. Data taken at 300 knots are shown in Figure 35. At each of three fuselage angles of attack, the data show a higher vibratory moment in the presence of the wing. The measured increment, however, does not appear to depend on the specific vertical location of the wing and does not increase with increasing α_f , i.e., wing lift, as would be expected from basic theoretical considerations.

Data corresponding to those discussed above, but taken in the presence of the large wing, are shown in Figures 36 through 39. Examination of the 120-knot data (Figure 36) reveals that a reduction in vibratory moment occurs at low wing lifts ($\alpha_f = -8$ and 0 degrees). It may be seen that this reduction becomes larger as the wing is raised from the low to the mid and high positions. At $\alpha_f = +8$ degrees, the reduction in moment was not observed, but an increase was measured at low rotor lifts.

Basically similar behavior was observed at 200 and 232 knots, as shown in Figures 37 and 38 respectively. At the latter speed only the wingless and high wing data are shown. Data taken at 300 knots are shown in Figure 39. Due to the considerable reduction in rotor lift associated with the presence of the large wing at this speed, it is not possible to make a direct comparison of the four configurations. However, it may be concluded that no significant stress increase was induced by the wing.

Time histories of the blade bending moments have been examined in order to better define the effect of the wing size and position on vibratory blade moments. Figures 40 through 47 show the azimuthal variation of flapwise, chordwise, and torsional bending moments with the large wing at 200 and 300 knots and at various rotor lifts.

A number of blade instrumentation problems were encountered during the testing, and the serial number of the instrumented blade has been noted on each of the stress plots because of the partial lack of consistency between the data obtained from the different blades. Extreme rotor operating conditions experienced in the wind tunnel, including violent transients caused by a malfunction of the control system, resulted in the loss of several strain gage circuits. Specifically, the circuit leads which were bonded to the trailing edge of the blade spar were broken. Loss of this instrumentation required the use of the reserve instrumented blade,

but during the installation and checkout of this blade, a number of calibration resistors in the data acquisition system were inadvertently set to the wrong values. This is believed to be the cause of the lack of consistency in the data from the two blades. It is suggested that direct quantitative comparisons between results obtained with different blades not be made. The analysis of the effects of the wing on rotor blade moments was made in light of this problem, and the findings discussed below are not affected by it. It should be noted that the zero moment level of the azimuthal variations is based on the measurement of bending moments on the instrumented blade rotating at full rotor speed with zero wind tunnel speed and zero rotor control settings. These values are determined at the start of each data run and vary by an amount equivalent to the repeatability of the bending moment data. As a result, a shift in the mean value of the azimuthal moment variations between different configurations cannot necessarily be attributed to aerodynamic interference effects.

Figure 40 shows the azimuthal variation of flapwise bending moments with the large wing at 200 knots and nearly zero rotor lift. As the wing is brought closer to the rotor, a progressive change in amplitude occurs which is most evident in the vicinity of $\psi = 240$ degrees. The net result of this change is a reduction in the peak-to-peak moment with no significant change in harmonic content. The azimuthal variation of the increment between the wingless and high wing configurations is shown in the lower plot. Similar data for a higher rotor lift and fuselage angle of attack are shown in Figure 41. Although the harmonic content of the basic data differs somewhat from that shown in the previous figure, the incremental variation is similar in form. In this case there is no significant change in the peak-to-peak moment, since the incremental peaks do not coincide with the peaks of the basic moment curve. Additional data are shown in Figure 42 for the large wing at 300 knots. Due to the effect of the wing, C_{LR}/σ is not constant but varies between 0.01 and 0.02. Examination of the moment increment between the wingless and low wing configurations reveals that the effect is similar to that seen at 200 knots (Figure 41). The moment is increased in the vicinity of $\psi = 30$ degrees, at $\psi = 145$ degrees, and again at $\psi = 290$ degrees. At this speed the maximum increments add to the basic moment maximums, causing an increase in the peak-to-peak vibratory moments.

Figure 43 shows a time history of chordwise bending moments for the same configurations and flight conditions as those in Figure 40. It is believed that the mean value shift of the mid wing data does not represent an actual interference effect but is a result of a shift in the zero moment measurement discussed previously. This shift does not affect the vibratory components of the moment. The presence of the wing does not cause any significant effect on the chordwise bending moment. There is a

small change in the peak-to-peak value, but there is no change in the harmonic content. The primary difference between the moments measured with and without the wing is the phase, which changes by approximately 10 degrees. This is reflected in the increment between the wingless and high and low wing configurations, which is also plotted. The low wing is seen to produce the larger effect, although the two increments are very similar in form. It can be concluded from the results that a complex wing circulation-rotor inflow interaction does exist, but the exact nature of this effect could not be determined within the scope of this investigation. At a higher rotor loading (Figure 44), the wing effect is essentially unchanged even though the wing loading is also increased. That is, α_f is increased from -4 degrees to +4 degrees. At $V_s = 300$ knots, (Figure 45), the wing effect is reduced considerably, since both the wing and rotor wake are being washed downstream very rapidly and the maximum velocities induced by them at the rotor disk are correspondingly small.

Figures 46 and 47 present the torsional moment time histories at the same conditions as those seen with the flapwise and chordwise moments. At 200 knots (Figure 46), the presence of the wing has no significant effect on the torsional moment regardless of the rotor lift. However, at 300 knots, Figure 47 shows that the excursion through which the moment passes between $\psi = 270$ degrees and $\psi = 340$ degrees increases as the wing moves closer to the rotor. It is not clear whether this effect stems directly from the presence of the wing or arises from the changes in rotor control settings required to keep the rotor in trim. Some increase also occurs in the vicinity of $\psi = 90$ degrees as the wing is moved toward the rotor, but this is only one-half as large as the increase on the retreating blade.

EFFECTS OF ROTOR AND WING CONDITIONS ON TAIL DOWNWASH ANGLE

The downwash angle at the tail due to the wing at the mid position is shown as a function of α_f in Figure 48. The measured angles for the fuselage alone are also shown. In all four configurations, the rotor blades are removed. The variation of ϵ_f with wing size reflects the increase in wing lift as the wing area is increased; these data were found to be independent of forward speed. Data were not taken in the rotorless configuration with the wing in the high and low positions, and attempts to extrapolate data similar to that of Figure 48 using points with $CL_R/\sigma = 0$ were generally unsuccessful. Even though the contribution of the rotor to ϵ_f could be expected to go to zero as CL_R/σ goes to zero, the mere physical presence of the rotor caused an unacceptable amount of scatter in the $CL_R/\sigma = 0$ data.

In Figure 49, the downwash resulting from the rotor-fuselage configuration is shown at $V_s = 120, 200, \text{ and } 300$ knots as a function of CL_R/σ . The derivative of the downwash with respect to CL_R/σ is seen to vary inversely with forward speed. This is qualitatively in agreement with momentum theory and will be discussed in more detail when the correlation of theory and experiment is considered.

Figure 50 shows the variation of ϵ_f with CL_R/σ , including the effects of the wing at the mid position with $V_s = 120, 200, \text{ and } 300$ knots and $\alpha_f = 4$ degrees. In Figure 50a, the increment added to ϵ_f by the wing is evident, but it can also be seen that this increment is decreasing with increasing CL_R/σ . This effect is particularly noticeable in Figure 50b, where the small wing contribution to the downwash actually goes to zero, in the vicinity of $CL_R/\sigma = 0.06$. The cause of this is the effect of the rotor downwash on the wing wake. As CL_R/σ increases, the wing wake is displaced in a direction which takes it away from the tail; thus its effect at the tail decreases.

In Figure 51, data similar to those of Figure 50 are shown with $\alpha_f = -4$ degrees. It is seen that the conclusion previously reached is not altered by this change in angle of attack.

The cumulative effect of all the downwash contributing factors is shown in Figure 52 for the medium wing in the mid position with $V_s = 200$ knots. The data points represent rotor operating conditions of constant $\alpha_c = 1$ degree. With the flapping trimmed, this yields $\alpha_{Tpp} = \alpha_f$. The superposition line was obtained by adding the individual contributions of the fuselage-rotor and fuselage-wing configurations and subtracting the fuselage-only configuration contribution to negate its inclusion twice. The total downwash line represents the measured value from testing with all components present. In this plot the rotor lift is increasing with α_f ; $CL_R/\sigma = 0.055$ at $\alpha_f = 4$ degrees; and $CL_R/\sigma = -0.023$ at $\alpha_f = -4$ degrees. The lower slope of the total downwash line is what would be expected from consideration of the rotor effect on displacing the wing wake, as previously discussed. It can be concluded then that superposition of the effects of the individual components is in agreement with the total effect for low to moderate values of CL_R/σ , but the rotor-wing interference at high CL_R/σ results in a breakdown of the superposition theory.

WING AERODYNAMIC CHARACTERISTICS

The aerodynamic characteristics of the three wings, based on data taken at the mid position, are presented in Figure 53. The lift and drag coefficients are based on exposed wing area which is 59.4 percent, 74.3

percent, and 82.9 percent of the total areas of the small, medium, and large wings respectively. It can be seen that on this basis the wing lift coefficient is essentially unaffected by wing size, as would be expected from basic aerodynamic considerations. The wing drag coefficient shows a decrease with both increasing size and increasing forward speed, and this also would be expected from consideration of the effect of the parameters on Reynolds numbers which range from 0.3×10^6 for the small wing at 120 knots to 2×10^6 for the large wing at 300 knots.* The scatter of the data at the lowest speed is a result of the fact that the drag values are quite small and border on the balance system accuracy. The pitching moment coefficients exhibit no unusual behavior and are in accord with published values. Rolling moments were found to be consistently insignificant and are not presented.

FUSELAGE AERODYNAMIC CHARACTERISTICS

Fuselage aerodynamic characteristics are based on frontal area and are presented in Figures 54, 55, and 56. The effect of wing size on C_{L_f} for 200 knots and mid position is shown in Figure 54a. By increasing the wing size, the wing lift and lift carry-over to the fuselage increase linearly, thus accounting for the increase in C_{L_f} . C_{D_f} is also shown to vary with wing size. Since the induced component of fuselage drag is proportional to C_{L_f} squared, the increase in C_{D_f} with wing size is primarily a result of the increased lift carry-over seen in the C_{L_f} plots.

Fuselage pitching moments are calculated about the mid wing quarter-chord position. The fuselage has an unstable slope of C_{m_f} versus α_f because the center of pressure is ahead of the reference axis. The addition of a wing as seen above, causes additional lift on the fuselage and as a result, causes the center of pressure to move rearward, thereby decreasing the destabilizing moment.

Rolling moment coefficient is not shown, as it was essentially zero throughout.

Similar results for fuselage aerodynamic characteristics are shown in Figure 54b, for 300 knots and wing in the mid position.

In Figure 55, the fuselage angle of attack is held constant at zero degrees and the medium wing at the mid position is varied through an angle of incidence range of plus and minus 15 degrees. C_{L_f} was found to vary

* These values are based on actual tunnel speeds and model dimensions.

directly with C_{LW} due to wing lift carry-over. The carry-over is not as great, however, as in the preceding figures in which the wing-fuselage combination is varied through the angle of attack range as a unit, i.e., $\Delta i_w = \Delta \alpha_f$. This is qualitatively predicted by Reference 7. C_{Df} and C_{mf} are essentially invariant, as shown.

The effect of vertical wing position, with respect to the fuselage, on C_{Lf} is shown in Figure 56a for the large wing. This increase in C_{Lf} with lower wing position results from the wing's increasing resemblance to a two-dimensional airfoil with a correspondingly higher lift curve slope and therefore greater wing lift carry-over. This is also seen in Figure 56b for the medium-sized wing.

THEORETICAL ANALYSIS AND CORRELATION OF ROTOR-WING-FUSELAGE INTERFERENCE EFFECTS

The experimental results discussed in the preceding section have been correlated with published experimental and theoretical investigations and with theoretical methods described herein. This section includes the evaluation of these correlations with regard to the applicability of the theoretical methods to compound helicopter interference problems.

EFFECTS OF WING LIFT, SIZE, AND POSITION ON ROTOR PERFORMANCE

Description of Theory for the Rotor Inflow Distribution Induced by a Wing

Any parameters which determine the wing circulation distribution and the positioning of the wing and its wake with respect to the rotor blades are significant to the problem of wing induced interference at the rotor. A list of these parameters and their relation to the interference problem is presented in Figure 57.

A method of calculating the wing induced flow through the rotor has recently been developed at United Aircraft Corporation for use in conjunction with several rotor performance and dynamic response computer programs. The analysis calculates the rotor inflow resulting from an assumed wing vortex geometry consisting of a classical lifting line and a series of semi-infinite trailing vortex filaments. With this method, it is possible to account for any desired spanwise wing circulation distribution by varying the vortex geometry and strength. Only the component of induced velocity normal to the rotor tip path plane is considered. In-plane components are neglected on the basis that the tangential velocities are negligible in comparison with the blade rotational velocities.

The mathematical relation used to relate the parameters indicated in Figure 57 as influencing the rotor inflow distribution induced by the wing is the classical Biot-Savart law, which was used to express the induced contribution of each vortex element in terms of the wing circulation and the rotor-wing geometry. The total wing induced velocity at each point in the rotor disk is calculated by superposition of the individual contributions of all the wing bound and trailing vortex elements.

The rotor-wing geometry is shown in Figure 58 for a single horseshoe vortex. Other horseshoe vortices are superimposed to define the wing

circulation distribution more accurately. The normal component of velocity induced by a single trailing and bound wake element respectively is

$$v_{iz_{TRL}} = \left[\frac{1}{4\pi R} \frac{1}{h_{TRL}} (1 + \cos \theta_{TRL}) \cos \sigma_{TRL} \cos(i_{RW}) \right] \Gamma_{TRL}$$

$$v_{iz_{BD}} = \left[\frac{1}{4\pi R} \frac{1}{h_{BD}} (\cos \theta_1 + \cos \theta_2) \cos \sigma_{BD} \right] \Gamma_{BD}$$

(5)

where $h_{TRL} = \sqrt{d_3^2 + (y_{TRL} - r \sin \psi)^2}$

$$h_{BD} = \sqrt{d_1^2 + d_2^2}$$

$$\cos \theta_{TRL} = \frac{d_4}{\sqrt{h_{TRL}^2 + d_4^2}}$$

$$\cos \theta_1 = -\frac{y_1 - r \sin \psi}{\sqrt{h_{BD}^2 + (y_1 - r \sin \psi)^2}}$$

$$\cos \theta_2 = \frac{y_2 - r \sin \psi}{\sqrt{h_{BD}^2 + (y_2 - r \sin \psi)^2}}$$

$$\cos \sigma_{TRL} = \frac{y_{TRL} - r \sin \psi}{h_{TRL}}$$

$$\cos \sigma_{BD} = \frac{d_2}{h_{BD}}$$

$$i_{RW} = \alpha_{iw} - (\alpha_s + \alpha_{ls})$$

$$z_1 = (r - e) \sin \alpha_0 + z_0 \cos \alpha_{ls} + (r \cos \psi \cos \alpha_0 - z_0 \sin \alpha_{ls}) \tan i_{RW}$$

$$d_1 = z_0 \cos \alpha_{ls} + (r - e) \sin \alpha_0$$

$$d_2 = r \cos \psi \cos \alpha_0 - z_0 \sin \alpha_{ls}$$

$$d_3 = z_1 \cos i_{RW}$$

$$d_4 = \frac{r \cos \psi \cos \alpha_0 - z_0 \sin \alpha_{ls}}{\cos i_{RW}} - z_1 \sin i_{RW}$$

A detailed projection of the relevant angles and distances is presented in Figure 59. The final relation for the normal component of induced velocity at the rotor from the above equations and the geometry indicated in Figures 58 and 59 is:

$$\begin{aligned}
 v_{z,r,\psi} = & \sum_{\substack{\text{TRL} \\ \text{WAKE} \\ \text{FILAMENTS}}} \left[\frac{1}{4\pi R} \frac{(y_{\text{TRL}} - r \sin \psi) \cos i_{\text{RW}}}{d_3^2 + (y_{\text{TRL}} - r \sin \psi)^2} \left(1 + \frac{d_4}{\sqrt{d_3^2 + d_4^2 + (y_{\text{TRL}} - r \sin \psi)^2}} \right) \right] \Gamma_{\text{TRL}} \\
 & + \sum_{\substack{\text{BD} \\ \text{WAKE} \\ \text{ELEMENTS}}} \left[\frac{1}{4\pi R} \left(\frac{d_2}{d_1^2 + d_2^2} \right) \left(\frac{y_2 - r \sin \psi}{\sqrt{d_1^2 + d_2^2 + (y_2 - r \sin \psi)^2}} - \frac{y_1 - r \sin \psi}{\sqrt{d_1^2 + d_2^2 + (y_1 - r \sin \psi)^2}} \right) \right] \Gamma_{\text{BD}}
 \end{aligned} \tag{6}$$

The terms within the brackets are referred to as geometric coefficients. All distances are nondimensionalized by the rotor radius.

The parameters neglected in the derivation of these equations are indicated in Figure 57. The equations could be extended to include the parameters which pertain to rotor-wing geometry and are indicated as "neglected in theory". The major state-of-the-art limitations are the representation of the distortions of the vortex sheet shed from the wing due to rotor interference, wake roll-up, and self-induced distortions.

There are many existing methods for determining the spanwise circulation distribution of a wing, including some which are for an isolated wing and some which include provision for a fuselage. For the purposes of the rotor-wing interference method reported herein, the simplest method was found to be sufficient. This semiempirical method, known as Shrenk's method (Reference 5), relates the local spanwise loading to the average loading for an isolated wing by assuming that the loading distribution for a tapered wing is an average between an elliptical loading distribution and the distribution specified by the ratio of the local to mean geometric chord. Mathematically, Shrenk's expression for the local loading ratio is

$$\frac{dL_W/dy}{L_W/b_W} = \frac{1}{2} \left[\frac{c_W}{c_{Wm}} + \frac{4}{\pi} \sqrt{1 - (y/b_W)^2} \right] \tag{7}$$

where $c_W = c_{Wr} \left[\left(\frac{1}{TR} - 1 \right) \left(y/\frac{b_W}{2} \right) + 1 \right]$

This relation does not yield zero loading at the wing tips and thus it must be faired to zero in this region (approximately 3 percent of the span). The loading ratio is related to the bound circulation by the following:

$$\frac{d\ell_w/dy}{L_w/b_w} = \frac{c_\ell/c_w}{C_{L_w}c_{w_m}} = \frac{\rho V \Gamma_{BD}}{L_w/b_w} = \frac{\Gamma_{BD}}{\frac{c_{w_m}}{2} V C_{L_w}}$$

$$\Gamma_{BD} = \left[\frac{d\ell_w/dy}{L_w/b_w} \right] \frac{c_{w_m}}{2} V C_{L_w} \quad (8)$$

From the Helmholtz theorem for the conservation of vorticity, the circulation strengths of the trailing filaments are set equal to the differences of the circulation values of adjoining bound wake elements.

$$\Gamma_{TRL} = \left(\frac{d\Gamma_{BD}}{dy} \right) dy \cong \Delta \Gamma_{BD} \quad (9)$$

Equations (6) through (9) indicate that the theoretical wing induced velocity distribution at the rotor disk is proportional to flight speed and wing lift coefficient and that the constant of proportionality is a function only of the relative positioning of the rotor, the wing, and the wing wake. Thus,

$$v_{iZr,\psi} = \left[f(\text{GEOMETRY}) \right] V C_{L_w} \quad (10)$$

where f is a function of geometry only.

Effect of Wing on Rotor Performance - Linearized Analysis

Superposition of the rotor inflow distribution induced by the wing with the inflow of the isolated rotor in a rotor performance computer program yields the wing effects on rotor performance characteristics. This non-linearized analysis was used for the quantitative results presented in the following sections. However, for the purpose of providing a qualitative understanding of the significant parameters for the effect of wing interference on rotor thrust, linearized performance equations are presented below. A mean effective value of the wing induced inflow at the rotor is used in these linearized equations.

An extension of the classical isolated rotor thrust equation, presented in Reference 6, to include pitch-flap coupling terms and transformed to the shaft axis coordinate system is

$$C_{LR}/\sigma = \frac{\sigma}{2} \left\{ \left(\frac{1}{3} + \frac{\mu^2}{2} \right) \theta_c + \frac{1}{2} \lambda_s - \frac{\mu}{2} B_{1s} + \tan \delta_3 \left[\frac{\mu}{2} b_{1s} - \left(\frac{1}{3} + \frac{\mu^2}{2} \right) a_0 \right] \right\} \quad (11)$$

It is assumed that angles are small and that rotor thrust is equal to rotor lift.

The wing interference effect on integrated rotor thrust is dependent on a radially weighted average of the steady azimuthal wing induced inflow distribution at the rotor. This effective value, \bar{v}_{iZ} , analogous to the local inflow values (equation 10), is linearly proportional to the flight velocity and wing lift coefficient with the proportionality constant a function only of the geometry.

$$\bar{v}_{iZ} = \left[f(\text{GEOMETRY}) \right] V C_{LW} = \left[\frac{\partial \bar{v}_{iZ}}{\partial (V C_{LW})} \right] V C_{LW} \quad (12)$$

When added to the isolated rotor inflow, the total rotor inflow ratio is

$$\lambda_s = \frac{V \sin \alpha_s - v_{iR \text{ MOM}} + \bar{v}_{iZ}}{\Omega R} \quad (13)$$

Relating the momentum inflow to the rotor thrust coefficient, assuming small angles and $\mu \gg \lambda_s$, and substituting equation (12) in (13), we obtain

$$\lambda_s = \mu \alpha_s - \frac{C_{LR}}{2\mu} + \frac{\partial \bar{v}_{iZ}}{\partial (V C_{LW})} \mu C_{LW} \quad (14)$$

Substituting equation (14), and separating the flapping angles into isolated rotor and wing induced components, equation (11) becomes

$$C_{LR}/\sigma = \frac{\sigma}{2} \left\{ \left(\frac{1}{3} + \frac{\mu^2}{2} \right) \theta_c + \frac{\mu}{2} \alpha_s - \frac{1}{4\mu} C_{LR} + \frac{\mu}{2} \left[\frac{\partial \bar{v}_{iZ}}{\partial (V C_{LW})} \right] C_{LW} - \frac{\mu}{2} B_{1s} + \tan \delta_3 \left[(b_{1s0} + b_{1sW}) - \left(\frac{1}{3} + \frac{\mu^2}{2} \right) (a_{00} + a_{0W}) \right] \right\} \quad (15)$$

Previous test results using a rotor and full span wing (no fuselage), as well as the present compound helicopter test results, have confirmed the fact that the wing effect on flapping is linear with wing lift coefficient; thus, the flapping components due to wing interference can be written in transfer function form:

$$a_{0w} = \left(\frac{\partial a_{00}}{\partial C_{LW}} \right) C_{LW}, \quad a_{1sW} = \left(\frac{\partial a_{1s}}{\partial C_{LW}} \right) C_{LW}, \quad b_{1sW} = \left(\frac{\partial b_{1s}}{\partial C_{LW}} \right) C_{LW} \quad (16)$$

where the flapping derivatives vary with advance ratio. Substituting these relations in equation (15) and rearranging, the lift equation including wing interference effects for fixed rotor controls becomes

$$C_{LR}/\sigma = \frac{4\sigma\mu}{8\mu + \sigma} \left\{ \left(\frac{1}{3} + \frac{\mu^2}{2} \right) \theta_c + \frac{\mu}{2} a_s - \frac{\mu}{2} b_{1s} + \tan \delta_3 \left[\frac{\mu}{2} b_{1s0} - \left(\frac{1}{3} + \frac{\mu^2}{2} \right) a_{00} \right] \right. \\ \left. + \left[\frac{\mu}{2} \frac{\partial \bar{v}_{iz}}{\partial \sqrt{C_{LW}}} + \tan \delta_3 \left(\frac{\mu}{2} \right) \left(\frac{\partial b_{1s}}{\partial C_{LW}} \right) - \tan \delta_3 \left(\frac{1}{3} + \frac{\mu^2}{2} \right) \left(\frac{\partial a_{00}}{\partial C_{LW}} \right) \right] C_{LW} \right\} \quad (17)$$

The rate of change of rotor lift with wing lift coefficient for fixed rotor control values (collective and cyclic pitch) and angle of attack is

$$\frac{\partial C_{LR}/\sigma}{\partial C_{LW}} = \frac{4\sigma\mu}{8\mu + \sigma} \left\{ -\frac{1}{2} \tan \delta_3 \left(\frac{\partial a_{00}}{\partial C_{LW}} \right) \mu^2 + \frac{1}{2} \left[\frac{\partial \bar{v}_{iz}}{\partial \sqrt{C_{LW}}} + \tan \delta_3 \left(\frac{\partial b_{1s}}{\partial C_{LW}} \right) \right] \mu \right. \\ \left. - \frac{1}{3} \tan \delta_3 \left(\frac{\partial a_{00}}{\partial C_{LW}} \right) \right\} \quad (18)$$

Thus, theoretically, the presence of a wing in the vicinity of a rotor produces an increment of rotor thrust which (1) may be added to the isolated thrust, (2) is directly proportional to wing lift coefficient, and (3) is a function of rotor advance ratio, rotor-wing geometry, and the wing induced flapping response associated with pitch-flap coupling.

A second set of linearized rotor lift equations can be derived to account for the trimming of wing induced flapping with cyclic pitch. In this case the rotor lift equation is

$$C_{LR}/\sigma = \frac{4a\mu}{8\mu + a\sigma} \left\{ \left(\frac{1}{3} + \frac{\mu^2}{2} \right) \theta_c + \frac{\mu}{2} a_s - \frac{\mu}{2} B_{1s_0} + \tan \delta_3 \left[\frac{\mu}{2} b_{1s_0} - \left(\frac{1}{3} + \frac{\mu^2}{2} \right) a_{s_0} \right] \right. \\ \left. + \left[\frac{\mu}{2} \left(\frac{\partial \bar{V}_{1z}}{\partial \sqrt{C_{LW}}} \right) - \frac{\mu}{2} \left(\frac{\partial B_{1s}}{\partial C_{LW}} \right) - \tan \delta_3 \left(\frac{1}{3} + \frac{\mu^2}{2} \right) \left(\frac{\partial a_0}{\partial C_{LW}} \right) \right] C_{LW} \right\} \quad (19)$$

The wing induced flapping term of equation (17) has been replaced by the cyclic pitch term for flapping trim. The cyclic pitch increments required to trim first harmonic flapping are linear with wing lift coefficient, and thus the longitudinal cyclic pitch increment, $B_{1s_{TRIM}}$, has been expressed in differential transfer function form:

$$B_{1s_{TRIM}} = \left(\frac{\partial B_{1s}}{\partial C_{LW}} \right) C_{LW} \quad (20)$$

The linearity is established by the fact that the cyclic pitch increments are linear functions of the wing induced flapping increments, which, as stated previously (equation 16), are proportional to wing lift coefficient.

From equation (19), the rate of change of rotor lift coefficient-solidity ratio with wing lift coefficient for (1) wing induced flapping trimmed out with cyclic pitch, (2) fixed collective pitch, and (3) fixed angle of attack is

$$\frac{\partial C_{LR}/\sigma}{\partial C_{LW}} = \frac{4a\mu}{8\mu + a\sigma} \left\{ -\frac{1}{2} \tan \delta_3 \left(\frac{\partial a_0}{\partial C_{LW}} \right) \mu^2 + \frac{1}{2} \left[\frac{\partial \bar{V}_{1z}}{\partial \sqrt{C_{LW}}} - \left(\frac{\partial B_{1s}}{\partial C_{LW}} \right) \right] \mu \right. \\ \left. - \frac{1}{3} \tan \delta_3 \left(\frac{\partial a_0}{\partial C_{LW}} \right) \right\} \quad (21)$$

It is of importance to remember that the flapping derivatives are functions of advance ratio. The similarity with equation (18) is evident; the only difference is that the flapping term is replaced by the cyclic pitch term.

The significance of pitch-flap coupling can be shown by eliminating the $\tan \delta_3$ terms from equations (18) and (21). Equation (18), for fixed rotor controls, becomes

$$\frac{\partial C_{LR}/\sigma}{\partial C_{LW}} = \frac{2a\mu^2}{8\mu + a\sigma} \left[\frac{\partial \bar{V}_{1z}}{\partial \sqrt{C_{LW}}} \right] \quad (22)$$

and equation (21), for trimmed wing-induced flapping becomes

$$\frac{\partial C_{LR}/\sigma}{\partial C_{LW}} = \frac{2\sigma\mu^2}{8\mu + \sigma} \left[\frac{\partial \bar{V}_1 z}{\partial (VC_{LW})} - \left(\frac{\partial B_{12}}{\partial C_{LW}} \right) \right] \quad (23)$$

This linearized theory is expected to be most accurate at moderate flight speeds. At high speed conditions (typically $\mu > 0.5$) the effects of flapping sensitivity, blade flexibility, and nonlinearities such as reverse flow become increasingly significant.

Application of Nonlinearized Theory to Test Conditions

The criteria for establishing assumptions and selection of parameters in the analysis of the test conditions were decided upon on the basis of the following factors: range of test parameters, test results, analytical complexity, required accuracy, and cost effectiveness. The choice of test parameters and operating procedures determined the flight condition and the geometric and control parameters. The test results indicated that the interference effects of the wing on local blade stresses could be neglected; this enabled analytical concentration on the integrated performance characteristics. The inclination of the wing's wake to the free stream and to the rotor tip path plane, although included in the theoretical method (irw), was neglected in the induced velocity analysis to minimize the variables. A check of this assumption proved to be justified for the relatively small rotor angles of the test with the flapping trimmed to zero.

The inflow distribution at the rotor induced by the wing was computed for the three wings of varying span length at the three positions on the fuselage (Figure 60). The computations were made by representing the wing vortex pattern by five superimposed horseshoe vortices (Figure 61) and by obtaining wing circulation distributions from Shrenk's method (Reference 5) using the measured value of total wing lift coefficient. The use of the measured lift avoided (1) the requirement for wing airfoil data and (2) inaccuracies in theoretically predicting wing and fuselage lift including the lift carry-over onto the fuselage. The nondimensionalized circulation distribution (loading ratio) from Shrenk's method is presented in Figure 62 for the taper ratio (3:2) and aspect ratio (approximately 6.0) of the tested wings. The downwash and fuselage interference on the shape of the wing circulation distribution was neglected. The effect of this assumption was evaluated and some differences were noted; however, they were not of sufficient magnitude to affect any conclusions of this investigation or to warrant the recomputation of a new distribution for each

point in the analysis. An example of a comparison of Shrenk's distribution with that obtained from the method of Reference 7, which includes the fuselage interference effect, is shown in Figure 63 for the medium-sized wing in the mid position at a wing lift coefficient of 0.7.

The induced velocity distribution due to the wing was used in the Sikorsky rotor performance theory described in Reference 8. This program solves the blade flapping equations and includes stall and reverse flow effects with no small angle assumptions or restrictions on advance ratio.

The program was initially run for the isolated rotor at the five test advance ratios for rotor control parameters (α_f , θ_c , A_{1s} , B_{1s}) set equal to zero. The linearity of wing interference on thrust and flapping with wing lift coefficient was then checked by determining the wing effect at several lift coefficient values for several wing-rotor combinations and advance ratios. The derivatives of rotor lift and flapping with respect to wing lift coefficient were then obtained for all rotor-wing combinations for all advance ratios tested. The rotor operating conditions do not correspond to the test conditions, however, because rotor cyclic pitch controls were not maintained constant during the test. The test procedure consisted of setting the rotor to a specified first harmonic flapping value for the wing-off configuration and then trimming the wing induced flapping for the wing-on configuration back to the wing-off values with cyclic pitch. This introduced rotor lift increments associated with cyclic pitch changes and removed the effect of wing induced flapping on rotor lift.

In order to obtain these cyclic pitch changes required to trim the wing induced flapping, the following linear relations were used in the analysis.

$$\begin{aligned}
 A_{1s\text{TRIM}} &= \left[\frac{1 + \left(\frac{\partial a_{1s}}{\partial B_{1s}} \right) \left(\frac{\partial b_{1s}}{\partial A_{1s}} \right) \Lambda}{\left(\frac{\partial a_{1s}}{\partial A_{1s}} \right)} \right] a_{1sW} + \left[- \left(\frac{\partial a_{1s}}{\partial B_{1s}} \right) \Lambda \right] b_{1sW} \\
 B_{1s\text{TRIM}} &= \left[- \left(\frac{\partial b_{1s}}{\partial A_{1s}} \right) \Lambda \right] a_{1sW} + \left[\left(\frac{\partial a_{1s}}{\partial A_{1s}} \right) \Lambda \right] b_{1sW}
 \end{aligned}
 \tag{24}$$

where the common factor in each term, Λ , is

$$\Lambda = \left[\left(\frac{\partial a_{1s}}{\partial A_{1s}} \right) \left(\frac{\partial b_{1s}}{\partial B_{1s}} \right) - \left(\frac{\partial b_{1s}}{\partial A_{1s}} \right) \left(\frac{\partial a_{1s}}{\partial B_{1s}} \right) \right]^{-1}$$

These relations are simply the cyclic pitch solutions of the simultaneous transfer function equations for flapping:

$$\begin{aligned} a_{1s} &= \left(\frac{\partial a_{1s}}{\partial A_{1s}} \right) A_{1s} + \left(\frac{\partial a_{1s}}{\partial B_{1s}} \right) B_{1s} \\ b_{1s} &= \left(\frac{\partial b_{1s}}{\partial A_{1s}} \right) A_{1s} + \left(\frac{\partial b_{1s}}{\partial B_{1s}} \right) B_{1s} \end{aligned} \quad (25)$$

The derivatives of rotor lift and flapping with respect to wing lift coefficient were then recalculated to reflect the trimming of the wing induced flapping.

In order to indicate the significant effect of the large value of δ_3 (45 degrees) in the test, the analytical method was also applied to the $\delta_3 = 0$ -degree condition for all wings, wing positions, and advance ratios. However, due to the extreme sensitivity of flapping response at high advance ratios without pitch-flap coupling, iterative computer solutions for the trimmed conditions could not be obtained. As a result, the $\delta_3 = 0$ -degree results presented in the next section are for the fixed rotor control condition only.

Theoretical Results

A sample contour plot of the normal component of the velocity field induced by the large high wing is presented in Figure 64 for $\mu = 0.51$. An upward velocity is taken as positive. In general, the wing induces an upflow everywhere upstream from it, due primarily to its bound vorticity, and a downflow in the region immediately downstream from it. It is in the center of the downstream region that the greatest induced velocities occur, for there the effects of the trailing and bound vortex filaments are additive. In the region downstream of the wing lifting line and outboard of the wing tips, the flow may be either positive or negative, depending upon the specific spatial point in question.

The analytical effect of wing induced velocity on blade flapping is presented in Figure 65, which shows that the flapping increment varies linearly with wing lift coefficient. The azimuthal distribution of wing induced flapping presented in Figure 66 is first harmonic when the rotor controls are fixed. A significant increase in the absolute value of the flapping on the advancing side of the rotor disk occurs with increasing wing lift coefficient when there is no pitch-flap coupling incorporated in the rotor control system. This effect may be explained qualitatively by considering the effect of the induced velocity due to the wing (shown in Figure 64), which indicates a large fore-aft variation due to the upwash ahead of, and

the downwash aft of the wing. Such a variation contains a strong first harmonic component, and because of the downwash over the aft portion of the rotor and the 90-degree phase lag of the flapping response to once per revolution forces, this variation results in negative flapping on the advancing blade. The effects of including pitch-flap coupling are a phase shift and a decrease in the peak-to-peak variation relative to the $\delta_3 = 0$ -degree configuration. The trimming of the wing induced first harmonic flapping results in a primarily second harmonic residual flapping motion. This suggests that equation (21) should be extended to include second harmonic flapping.

The variation of the flapping derivative with rotor advance ratio is shown in Figures 67 and 68. The influence of the wing increases with increasing wing size and decreasing rotor-wing separation, and the effect of wing size is more significant than wing position. The inclusion of pitch-flap coupling (Figure 68) decreases the coning and lateral flapping derivatives and reverses the direction of the longitudinal flapping derivative for the large wing. The cyclic pitch requirements to trim out wing induced first harmonic flapping also increased essentially linearly with advance ratio, as shown in Figure 69.

The rotor air load distributions induced by the large high wing at an advance ratio of 0.51, presented in Figure 70, are similar in contour character in that the result of including pitch-flap coupling effects and/or trimming the wing induced flapping is only a shift in the contour locations instead of a major redistribution. The large air load gradient in the first quadrant of the rotor is caused by the gradients of induced velocity and flapping (Figures 64 and 66) in this quadrant which are reflected in the air load distributions through changes in the local angle of attack. Likewise, the air load distributions in the other rotor quadrants can be explained from the same two figures. The similarity of the trimmed and untrimmed distributions indicates that cyclic pitch effect on loading is similar in character to the flapping effect, as would be expected from the equivalence of flapping and feathering.

The linearity of the rotor induced lift with wing lift coefficient obtained from the computer results (nonlinearized analysis) is indicated in Figure 71 for $\mu = 0.51$. This linearity permits the effect of wing lift on the integrated rotor lift to be represented by the derivative $\partial C_{LR}/\sigma / \partial C_{LW}$. The variation of this derivative with advance ratio is presented in Figure 72. The derivative is negative (i.e., positive wing lift reduces rotor thrust). The absolute magnitude of the derivative increases with increasing advance ratio and wing size and decreasing rotor-wing separation values. The sensitivity to wing size is greater than the sensitivity to separation for values characteristic of compound helicopters. The effect of including pitch-flap coupling decreases the magnitude of the

derivative significantly (note scale change in Figure 72b), while trimming the wing induced flapping increases the magnitude of the derivative, as illustrated in Figure 72c.

The influence of the wing on rotor drag and torque characteristics was investigated analytically for the three wing sizes and positions at all test speeds for zero rotor angle of attack and collective pitch setting. No significant change in drag or torque resulted. This result was found to be independent of pitch-flap coupling and wing induced flapping.

A sampling of the quantitative accuracy of the linearized equations (14, 19, 20, and 21, which were only used previously to provide a qualitative understanding of the sensitivity of rotor performance to the wing-rotor parameters) is presented in Figure 73. Since the effective induced velocity required for the linearized equations was unknown, the values of the resultant derivatives $\partial C_{LR}/\sigma/\partial C_{LW}$ of the computer analysis (Figure 72) were used in the linearized equations to compute the effective values shown. These are compared with the radial distribution of the steady azimuthal component of induced velocity from the computer analysis. Considering the greater importance of the blade tip region, the effective values from the linearized equations are found to correlate sufficiently well as representative weighted averages. This suggests the possibility of further developing the linearized theory to include a relation for the effective value (instead of the complete local velocity distribution) and the linear relations of flapping and cyclic pitch to trim flapping with wing lift coefficient. This would thereby enable the application of linearized equations to replace the more costly and complex computer computations to obtain a quantitative approximation of the wing effect on rotor lift at moderate speeds.

Correlation of Theoretical Results With Experiment

A comparison of the theoretical and experimental effect of the wing interference on rotor lift is presented in Figure 74 for the large wing at the high position and the medium wing at the mid position. The experimental points are a result of a statistical average of many data points, and the standard deviation is indicated. The experimental wing lift coefficient, as in the theory, includes the lift carry-over on to the fuselage and is based on total wing area. The theoretical results corresponding to the test points are those for which the wing induced flapping was trimmed with cyclic pitch.

Good correlation is noted for the large high wing throughout the speed range. The correlation of the medium mid wing results is good except at an advance ratio of 1.0 where the theoretical value is outside the range of test values shown. This may be explained, experimentally, by the

increased sensitivity of rotor lift and flapping to small cyclic pitch changes at this high advance ratio, and, theoretically, by the increased influence of the fuselage for the medium wing. Agreement with the theoretical results (Figure 72) as to the increased sensitivity of the interference to wing size relative to wing position was indicated for the other experimental wing configurations, although the standard deviations of the data were greater than those presented in Figure 74.

The insensitivity of the rotor drag and torque characteristics to the wing interference at the zero rotor angle of attack and collective pitch setting investigated for all wing configurations and speeds agrees with the experimental results. Some drag effects were found experimentally at higher collective pitch and angle of attack conditions, but these conditions were not included within the range of variables of the analytical investigation.

In general, the correlation between theory and experiment indicates that the theoretical method can be used to predict interference effects of a wing on rotor performance for compound helicopter design studies.

MUTUAL INTERFERENCE OF WING AND FUSELAGE

The fuselage influences the wing through a change of flow velocity in magnitude and direction at each wing section (i. e., airfoil cross section at a particular spanwise station on the wing). The flow velocity increment decreases with increasing spanwise distance from the fuselage boundary. With the fuselage at an angle of attack, the significant part of this flow is the component normal to the free stream. This is an additive upwash which produces lift on the wing above that resulting from the wing's geometric angle of attack. This flow depends on the shape of the fuselage cross section and on the position of the wing on the fuselage. In addition, the fuselage forms a fixed boundary for all supplementary flows induced at the wing.

For a wing-fuselage combination at incidence, the lift on the wing is carried partially across the body. Also, as mentioned in Reference 9, upstream of the wing, the wing-induced upwash induces a lift force decreasing with distance from the wing. These lift distributions, along with the isolated fuselage distribution, are shown in Figure 75.

The significant parameters for the mutual wing-fuselage interference effects are

1. Ratio of fuselage width to wing span

2. Fuselage cross section shape
3. Fuselage height to width ratio
4. Fuselage fineness ratio, profile, and camber
5. Fuselage angle of attack
6. Wing position on fuselage
7. Wing aspect ratio
8. Wing taper ratio
9. Wing lift curve slope
10. Wing incidence
11. Flight speed
12. Air density

Description of Theory

The method of Reference 7 was used because it combines and extends the theories of References 9 through 15 to calculate the lift distribution on a wing-body combination for a wide range of aspect ratios and fuselage width to wing-span ratios.

The theory assumes a slender body of revolution with an unswept wing placed at the mid-fuselage position operating in subsonic, inviscid flow. The wing position and fuselage fineness ratio, profile, and camber are thus eliminated as variables. The theory is presented for circular and elliptical fuselage cross sections; however, it could be extended to other cross sections and wing positions. The method is applicable to a wide range of planforms (taper ratio), aspect ratios, and fuselage widths. It is assumed that the flow normal to a circular fuselage with a wing in the mid position changes the angle of attack at each spanwise section in proportion to the fuselage angle of attack and in inverse proportion to the square of the spanwise distance from the fuselage.

$$\frac{\Delta a_{wy}}{\Delta a_f} = \frac{1}{(y/R)^2} \quad (26)$$

This is corrected for other cross sections in that the angle of attack increment decreases with increasing fuselage height to width ratio in the region of the fuselage. This relation is used along with the fuselage boundary condition in a conformal transformation to obtain the loading distribution on the wing.

The assumption of inviscid flow leads to an infinite length fuselage with zero total lift on the wingless fuselage for any angle of attack. The interference of the wing in the fuselage region induces a fuselage lift expressed in Reference 7 as

$$L_f = \rho V \int_{\text{WING}} \Gamma_y \left(\frac{\Delta \alpha_{wy}}{\Delta \alpha_f} \right)_y dy \quad (27)$$

where the ratio of angle of attack increments ($\Delta \alpha_{wy} / \Delta \alpha_f$) acts as a weighting factor on the local spanwise circulation, Γ_y . The theory indicates that the total lift of the wing-body combination increases with increasing aspect ratio, decreasing taper ratio, and decreasing cross-sectional axis ratio. Increasing fuselage width to wing-span ratio increases and then decreases total lift for equal fuselage and wing angles of attack, and decreases the total lift for wing angles greater than fuselage angles.

The resulting charts from Reference 7 express the section lift distribution across the fuselage and wing in the form

$$c_l = c_{l_1} + c_{l_2} \quad (28a)$$

in which

$$c_{l_1} = G_1 \frac{2b_W}{57.3 C_W} \alpha_{f_0} \quad c_{l_2} = G_2 \frac{2b_W}{57.3 C_W} (\alpha_{W_0} - \alpha_{f_0}) \quad (28b)$$

The first lift coefficient factor, G_1 , is used to determine the lift of the wing-fuselage combination for the wing at the fuselage angle of attack ($\alpha_{W_0} = \alpha_{f_0}$). The second lift coefficient factor, G_2 , is used to determine the lift increment of the wing-fuselage combination due to the angle of attack increment between the wing and the fuselage reference ($\alpha_{W_0} - \alpha_{f_0}$). The fuselage axis of revolution and the wing zero lift line are the reference axes. These lift coefficient factors are also equivalent to the components of nondimensionalized circulation:

$$G_1 = \frac{\Gamma_y}{V b_W \alpha_{f_0}} (57.3) \quad G_2 = \frac{\Gamma_y}{V b_W (\alpha_{W_0} - \alpha_{f_0})} (57.3) \quad (29)$$

Application of Theory to Test Conditions

The lift distributions were obtained from Reference 7 for the three fuselage width to wing-span ratios of the present test (0.15, 0.22, 0.37). For the aspect ratio of the test configurations (approximately 6), the distributions presented in Reference 7 are available only for a nontapered

wing and circular cross section fuselage. Since the taper ratio of the tested wings is only 1.5, the effect of taper may be neglected (Reference 7). Reference 7 indicates that the differences in interference between an elliptical fuselage cross section having the same height to width ratio as the model fuselage and a circular one are small, but the effects of a rectangular cross section are not defined.

An expression for the local lift coefficient may be derived from equation (28) in terms of the fuselage angle of attack through use of the angle relations detailed in Figure 76:

$$\begin{aligned} a_{fo} &= a_f - i_{fZLL} \\ a_{wo} &= a_w - i_{wZLL} = a_f + i_w - i_{wZLL} \end{aligned} \quad (30)$$

The resulting expression is

$$c_l = \frac{2AR}{57.3} \left[G_1 a_f + (G_2 - G_1) i_{fZLL} + G_2 i_w - G_2 i_{wZLL} \right] \quad (31)$$

Spanwise integration of the local lift coefficient yields a relation for the total lift coefficient of the wing and fuselage:

$$\begin{aligned} C_{Lwf} = \frac{2AR}{57.3} \left[a_f \int_0^1 G_1 d\bar{y} + i_{fZLL} \left(\int_0^1 G_2 d\bar{y} - \int_0^1 G_1 d\bar{y} \right) \right. \\ \left. + i_w \int_0^1 G_2 d\bar{y} - i_{wZLL} \int_0^1 G_2 d\bar{y} \right] \end{aligned} \quad (32)$$

in which y has been nondimensionalized by the wing semispan. For a specific test configuration, C_{Lwf} is a linear function of fuselage angle of attack. Therefore, the lift curve slope of the wing-fuselage combination is

$$\frac{dC_{Lwf}}{da_f} = 2AR \int_0^1 G_1 d\bar{y} \quad (33)$$

Likewise, the fuselage angle of attack for zero lift is

$$\alpha_{fC_L=0} = \frac{i_{fZLL} \left(\int_0^1 G_1 d\bar{y} - \int_0^1 G_2 d\bar{y} \right) - i_W \int_0^1 G_2 d\bar{y} + i_{WZLL} \int_0^1 G_2 d\bar{y}}{\int_0^1 G_1 d\bar{y}} \quad (34)$$

Separate expressions for the fuselage and wing may be obtained by use of the proper limits in equations (32) through (34). Thus, the ratio of the lift carry-over on to the fuselage to the total wing-fuselage lift is

$$\frac{L_f}{L_{Wf}} = \frac{C_{L_f}}{C_{L_{Wf}}} = \frac{\alpha_f \int_0^{\sigma_f} G_1 d\bar{y} + i_{fZLL} \left(\int_0^{\sigma_f} G_2 d\bar{y} - \int_0^{\sigma_f} G_1 d\bar{y} \right) + i_W \int_0^{\sigma_f} G_2 d\bar{y} - i_{WZLL} \int_0^{\sigma_f} G_2 d\bar{y}}{\alpha_f \int_0^1 G_1 d\bar{y} + i_{fZLL} \left(\int_0^1 G_2 d\bar{y} - \int_0^1 G_1 d\bar{y} \right) + i_W \int_0^1 G_2 d\bar{y} - i_{WZLL} \int_0^1 G_2 d\bar{y}} \quad (35)$$

It should be noted that stall effects are neglected. Also, the zero lift line of the fuselage, rather than the fuselage axis from which α_f is measured, has been used as the reference because the test fuselage cross section is not a solid body of revolution. It may be argued that the fuselage axis perpendicular to the shaft may also have been used as the reference axis because it most closely approximates the geometric axis of symmetry. This question as to whether the aerodynamic axis of symmetry (zero lift line) or the axis most closely representing the geometric axis of symmetry should be used led to the inclusion of both in the results to show the effect of the choice of fuselage reference.

Theoretical Results and Correlation With Experiment

The lift coefficient factors (G_1 and G_2) from Reference 7 are presented in Figure 77 as functions of spanwise position for the three wings of the test at the mid fuselage position and for a full-span wing. The term full-span wing refers to an isolated wing (no fuselage). Since the results are presented in nondimensional form the full-span wing size is not specified. The lift coefficient factors were used to obtain the lift coefficient distributions of Figure 78 for the medium wing at the mid position. The distributions of Figure 77 were integrated to obtain the terms of equations (31) through (34). The integrated values are presented in the table on page 39.

INTEGRATED LIFT COEFFICIENT FACTORS TABLE							
	WING AND FUSELAGE		WING		FUSELAGE		
	$\int_0^1 G_1 d\bar{y}$	$\int_0^1 G_2 d\bar{y}$	$\int_{\sigma_q}^1 G_1 d\bar{y}$	$\int_{\sigma_q}^1 G_2 d\bar{y}$	$\int_0^{\sigma_q} G_1 d\bar{y}$	$\int_0^{\sigma_q} G_2 d\bar{y}$	
MID POSITION	LARGE WING	0.388	0.323	0.324	0.274	0.064	0.049
	MEDIUM WING	0.383	0.297	0.303	0.233	0.080	0.064
	SMALL WING	0.356	0.252	0.246	0.176	0.110	0.076
FULL-SPAN WING $\int_0^1 G_1 d\bar{y} = \int_0^1 G_2 d\bar{y} = 0.342$							

Comparisons of the theoretical and experimental lift coefficient variations with fuselage angle of attack for the wing, fuselage, and wing-fuselage combination are presented in Figures 79 through 81 (reference areas are exposed wing area). These results are based on the use of the experimentally determined fuselage zero lift line as the fuselage reference. Summary plots showing the variation, with wing size, of the lift curve slopes and fuselage angle corresponding to zero lift are presented in Figures 82 through 84 for the combined wing-fuselage configuration, the wing, and the fuselage. The influence of the choice of fuselage reference is indicated by the inclusion of the theoretical results based on the use of the fuselage axis as a reference. The lift curve slope, as can be seen from equation (33), is independent of this reference, whereas the angles for zero lift vary by approximately one degree. The theoretical lift curve slope values for the combined wing-fuselage configuration are approximately 10 percent higher than measured, and the error occurs in the predicted wing contribution. The angles of zero lift for the combined configuration become more positive than measured with increasing wing size, and the differences range from 1 to 2 degrees. Greater zero lift angle differences exist for the wing (Figure 83) and the fuselage (Figure 84), and the improved correlation for the combined configuration of Figure 82 is the result of compensating errors.

The application of equation (35) to predict the percent of lift carry-over on to the fuselage indicated an insensitivity to fuselage angle of attack for angles greater than approximately 2 degrees at which the lift first attains appreciable value for all wing sizes. This fact was also found in the test results as demonstrated by the narrow band of Figure 85 which presents the ratio of wing plus fuselage lift to fuselage lift plotted versus the wing span to fuselage width ratio. The characteristic increasing variation with wing size of the theory and test agree; however, the theory predicts magnitudes which are approximately 60 percent lower than the measured values due to the error in zero lift angle (Figure 84). The theoretical lift curve slope and zero lift angles are indicated for a full-span wing (no fuselage) in Figures 82 and 83. The full-span wing values are, in general, in better agreement with the test values than the results of Reference 7 (which include fuselage effects), although the full-span wing values do not, of course, reflect the characteristic trends with fuselage width that the theory of Reference 7 reflects. It thus appears that the added complexity included in Reference 7 does not result in improved predictions of the integrated lift characteristics of compound helicopter wing-fuselage configurations over the classical full-span wing approximation. The exact cause of the discrepancies in the comparison between theory and experiment is unknown. The fuselage shape of the test configuration is not the same as the theoretically assumed slender body of revolution due to the rectangular fuselage cross section, the rotor pylon, and the vertically unsymmetric nose section. Theoretical methods do not

exist for rapidly determining the effects of these departures from the theoretical model for wing-fuselage combinations applicable to compound helicopter configurations.

EFFECT OF WING ON TAIL

The addition of a wing to a helicopter introduces downwash effects at the tail location in addition to those introduced by the rotor and fuselage.

Lifting line theory (References 15 and 16) has been developed for fixed-wing configurations, and satisfactory agreement between predicted and experimental results has been demonstrated.

To determine the effect of the wing interference at the tail, it must be assumed that the rotor interference effects are independent of the wing effects; thus, the correlation is made for the rotor-off configuration.

The passage of the wing wake in close proximity to the tail causes significant tail downwash effects, whose magnitude is dependent on the wake position, as well as the strength and distribution of vorticity in the wake. Thus, the important parameters are:

1. Longitudinal and vertical position of wing and tail
2. Ratio of tail span to wing span
3. Wing geometry: aspect ratio, taper ratio, dihedral, sweepback
4. Wing geometric angle of attack determined by fuselage angle of attack and incidence of wing to fuselage
5. Wing lift coefficient
6. Wing wake displacement and distortions

Description of Theory

The theoretical method of References 15 and 16 employs a classical horseshoe vortex system and lifting line theory to represent the wake of an unswept full-span wing without dihedral. Fuselage effects are not included. The deformation of the wing wake including wake roll-up is neglected. The wake is assumed to be uniformly displaced downward by an amount equal to the displacement of the center of the vortex sheet which is assumed to follow the momentum downflow and is proportional to wing lift coefficients.

The downwash angle at the tail due to the wing is presented in the form of charts in Reference 16 for several wing taper ratio and aspect ratio combinations. The parameters required for these charts, which determine the relative positioning of the wing, wing wake, and tail in the longitudinal plane of symmetry, are shown in Figure 86. The equations for the

longitudinal displacement between the tail and the wing quarter-chord line, x , and the vertical displacement of the wing wake from the tail, $m+h$, referenced to the wing axis are

$$x = \frac{bw}{2} (\eta \cos \alpha_f + \xi \sin \alpha_f) \quad (36)$$

$$m = \frac{bw}{2} (\xi \cos \alpha_f - \eta \sin \alpha_f) + 0.75 c_{w_r} \sin(\alpha_f + i_w) \quad (37)$$

$$h = \left[x - 0.75 c_{w_r} \cos(\alpha_f + i_w) \right] \tan \epsilon_w \quad (38)$$

The vertical displacement of the wing wake from the wing trailing edge at the tail, h , is presented in chart form in which $\cos(\alpha_f + i_w)$ is assumed equal to 1.0 and the wing downwash angle, ϵ_w , is proportional to the wing lift coefficient.

Application of Theory to Test Conditions

The design charts of Reference 16 are limited to longitudinal wing-tail distances of 1.6 wing semispan lengths. The longitudinal wing-tail distances of the small, medium, and large wings of the test are $3.68(b_w/2)$, $2.20(b_w/2)$, and $1.47(b_w/2)$ respectively. Thus the charts are applicable only to the large wing, and this limitation precluded correlations for smaller sized wings for which the limitations of the theory (neglected wake distortion and fuselage effects) may be more critical. Correlations are presented for both the high, $z = 0.290(b_w/2)$ and mid position, $z = 0.415(b_w/2)$, of the large wing on the fuselage.

The charts were interpolated for the aspect ratio (6) and taper ratio (3:2) corresponding to the tested wing. The vertical displacement of the wing wake, h , at the tail longitudinal position, $x = 1.47(b_w/2)$, was found to be $1.4 C_{LW}$ where in all cases the reference area is exposed wing area. The results of the interpolation for the tail downwash angle per unit wing lift coefficient for varying vertical distances between the wing wake and tail are presented in Figure 87. The test parameters required for the theory (wing lift coefficient and wake-tail vertical distance) are indicated in Figure 88 for varying angles of attack. The test values of wing lift coefficient were used, including the lift carry-over on to the fuselage.

Theoretical Results and Correlation With Experiment

The theoretical tail downwash angle for the large wing at the high and mid fuselage positions (obtained from Figures 87 and 88) is presented in Figure 89 along with the test results. It is noted that excellent correlation for both wing positions is obtained if the isolated fuselage test values are removed from the experimental results. This is necessary because the theory is for full-span wing and this does not include provisions for fuselage effects.

It is emphasized that this correlation has been obtained only for a wing which would be considered large and possibly oversized for a typical compound helicopter configuration. Due to limitations of the existing design charts, correlation was not possible for the medium and small wings for which the theory may be less accurate. In smaller wings, the fuselage width is a greater percentage of the span; thus, the fuselage effects are proportionately greater. Also, the smaller span wings place the tip vortices horizontally closer to the tail which could introduce significant effects due to wake distortions and tip vortex roll-up, two factors neglected in the theory. In addition, the downwash variation across the tail span would be greater for these conditions.

The theory was applied only to a rotor-off condition due to limitations in the theory for predicting the effect of the rotor interference on the tail (to be discussed subsequently). The interaction of the rotor wake with that of the wing may distort the wing wake significantly from the mathematical model used in the theory.

EFFECT OF ROTOR ON WING

The rotor flow induces a negative angle of attack increment at the wing which is a function of the rotor lift, loading distribution, advance ratio, and wake skew angle and the relative positioning of the rotor and wing. The wake skew angle is determined by the ratio of the forward speed to the rotor inflow velocity (μ/λ , in nondimensional form), which is dependent on the rotor lift coefficient and angle of attack.

Description of Theory

The incremental angle of attack induced at the wing by the rotor was previously expressed in the description of the experimental results on page 11 as

$$\Delta \alpha_W = k \frac{\sigma}{2\mu^2} \left[C_{LR}/\sigma \right]^{57.3} \quad (39)$$

The ratio of the effective induced velocity at the wing, including a provision for chord variation to the momentum value of the inflow velocity at the rotor, is defined as the effective downwash factor:

$$k = \left(\frac{v_{iW}}{v_{iRMOM}} \frac{c_W}{c_{Wm}} \right)_{MEAN} \quad (40)$$

The downwash factor is related to the wing lift increment induced by the rotor in the following manner:

$$\Delta L = \rho \int_{y_F}^{y_T} \Delta c_l c_W dy \quad (41)$$

where

$$\Delta c_l = \alpha \Delta a_{Wv} \approx \alpha \frac{v_{iW}}{V} \quad (42)$$

from which

$$\Delta L = \alpha \rho A_W \frac{v_{iRMOM}}{V} \left(\frac{v_{iW}}{v_{iRMOM}} \frac{c_W}{c_{Wm}} \right)_{MEAN} \quad (43)$$

or

$$\Delta L = \alpha \rho A_W \frac{v_{iRMOM}}{V} k \quad (44)$$

The theoretical methods of References 17 and 18 were used to obtain the downwash factor values corresponding to the test. This method predicts the time averaged flow field in the vicinity of the rotor based on a wake represented by a series of concentric skewed vortex cylinders of continuously distributed vorticity. The wake skew angle, relative to the tip path plane, is defined by assuming a uniform rotor induced downwash equal to the momentum induced velocity:

$$\chi_{TPP} = \tan^{-1} \left(-\frac{\mu}{\lambda_s} \right) + \alpha_{ls} = \tan^{-1} \left(\frac{V \cos \alpha_s}{V \sin \alpha_s - v_{iRMOM}} \right) + \alpha_{ls} \quad (45)$$

for which

$$v_{iRMOM} = \frac{\Omega R}{2 \mu} C_{LR} \quad (46)$$

The loading distribution is prescribed by the relative circulation strengths assigned to the vortex cylinders.

Thus, the major assumptions in the theory are that (1) wake shape and position are entirely based on the momentum induced velocity, and (2) loading distribution is assumed to be known and is symmetric about the center of the rotor. The first assumption neglects any wake distortions or wake dissipation phenomena, and the second neglects the azimuthal variation of loading which occurs in forward flight.

The advantage of the theoretical method used is that the flow field may be solved analytically and presented in chart form in terms of a limited number of variables; this method was used in Reference 17. Previous comparisons of the theoretical results with experiment (Reference 18) and preliminary applications of the theoretical results in a simplified manner to the wing of an autogyro and compound helicopter (Reference 19) indicated that the method had possible potential for predicting the rotor induced interference of compound helicopters.

Application of Theory to Test Conditions

The wake skew angles corresponding to the test conditions are presented in Figure 90. Since the majority of test points were obtained for the rotor trimmed to zero flapping, the theory will be applied to only these conditions. It is shown in Figure 90 that the test skew angles were limited to the range between 79 and 98 degrees, with respect to the tip path plane. The rotor wake boundaries in relation to the wing positions are presented in Figure 91.

The charts of Reference 17 present the local downwash factor as a function of position relative to the rotor for specific skew angles and rotor loading distributions. The specific wake skew angles (for which the downwash factors are presented) in and near the range of values of the test are 63.4, 76.0, 84.3, and 90.0 degrees, and thus interpolation and extrapolation are required for the test values. Also, the loading distributions presented are termed uniform, triangular, and typical. The typical distribution represents the azimuthally averaged radial load distribution of a lightly loaded rotor with untwisted, untapered blades (similar to the test blades). In order to determine the sensitivity of the effective angle of attack at the wing to rotor loading distribution, all three distributions were used. Calculations were made for the three wing sizes and the three wing positions of the test.

The downwash factor distributions obtained from the charts of Reference 17 were averaged over the exposed area of each wing to obtain a first approximation of the resultant effective downwash at the wing induced by

the rotor (equation 39). The replacement of the distributed downwash pattern by the mean value to approximate the resultant effective downwash neglects three dimensional aspect ratio effects. However, the magnitude of these effects is much smaller than the difference between the theoretical and experimental results, as discussed in the following section. As a result, the conclusions reached herein are not influenced by the mean value approximation.

Theoretical Results

The variation in local downwash factor (expressed as the ratio of averaged local downwash velocity of the wing to rotor momentum induced velocity) with wing spanwise location is presented in Figure 92 for the specific skew angles included in the charts of Reference 17 based on a typical loading distribution. Figure 92 shows that the downwash factor distributions are insensitive to wake skew angle in the skew angle range of the test (greater than 79 degrees). This is explained by the fact that this insensitivity to skew angle exists when the point in question is located outside the wake boundaries. As shown in Figure 91, this occurs for all test conditions and configurations if the rotor flapping is trimmed to zero (a negative value of longitudinal first harmonic flapping could immerse the wing in the rotor wake). The sensitivity of the downwash factor to whether or not the point is immersed in the wake is indicated in Figure 92 for the high wing at a spanwise location of 0.49 for a skew angle of 76 degrees, where a discontinuity in the downwash factor is noted. This location corresponds to the wake boundary for this skew angle. It is noted that the downwash distribution at locations outboard of the wake boundary approaches that of the higher wake skew angles.

Thus, theoretically, wake skew angle may be eliminated as a variable for this test (for the trimmed conditions); in general, it may be eliminated for any wing conditions for which the rotor wake passes completely above the wing.

A summary plot of the wing downwash factor values is presented in Figure 93 as a function of the remaining variables: blade loading distribution, wing size, and wing position. Of special interest is the fact that the theoretical results are not significantly affected by the choice of blade loading distribution for the large wing and are only moderately affected for the medium wing, which means that the theoretical downwash factor results should be satisfactory even though the actual blade loading of the test rotor was not calculated and used in the analysis. The rotor loading distribution for the test model should be most closely represented by the typical loading distribution of Reference 17.

Correlation With Experiment

The experimental downwash factors were obtained by the use of equation (44), the increment in wing lift measured between the rotor-on and rotor-off test configurations, and the experimental lift curve slope.

The experimental downwash factor results presented in Figure 94 are significantly greater in magnitude than the theoretical for both large and medium wings at the three wing positions. For example, the theoretical downwash factor values for the large wing are only approximately 55 percent of the experimental values. These differences could possibly be attributed to these limitations of the theory: (1) in general, the azimuthal loading variation is neglected; and (2) for wing interference in particular, the lateral loading variation, appreciable at the speeds under consideration, is neglected. Also, the momentum criterion for positioning the rotor wake has been shown by use of flow visualization techniques (Reference 20) to be only approximate.

However, a much improved correlation has been obtained from previously unpublished test results obtained at United Aircraft in 1956 (Figure 95). That test differed mainly from the current test in that an isolated wing rather than a wing-fuselage combination was placed under the rotor.

The wing span to rotor diameter ratio was equivalent to that of the large wing of the 1966 test. The wing was rectangular, had an aspect ratio of 5, and was placed at two positions below the rotor ($z_0 = 0.174$ and 0.40), corresponding closely to the 1966 test high and low positions ($z_0 = 0.218$ and 0.408). Tests were conducted at advance ratios up to 0.5 .

Since it appears that the only difference between the two test configurations which could possibly cause the large difference in downwash at the wing is the inclusion of a fuselage; the high downwash values of the compound helicopter test may be attributed to the distortions of the rotor flow by the fuselage.

EFFECT OF ROTOR ON TAIL

Attempts to correlate theoretical average downwash angles at the tail due to rotor interference with measured values were inconclusive. The same charts (Reference 17) used to obtain the rotor downwash effects at the wing were used to obtain the downwash factors for the tail.

The position of the tail pivot was 1.1 rotor radii aft and 0.13 rotor radii below the rotor hub. In order to lie partially within the theoretical rotor

wake, the wake skew angles must fall below 87 degrees. The theoretical skew angles corresponding to the test conditions are all within ± 11 degrees of this critical value. In this range the charts indicate large downwash factor gradients with loading distribution and tail position. Also, any distortions of the rotor wake from the assumed boundaries based on momentum theory can lead to gross inaccuracies. In addition, theoretical downwash velocities in the tail region are only available in the longitudinal plane of symmetry, so finite tail span effects cannot be accounted for.

Thus, due to the proximity of the stabilizer to the rotor wake and the consequent sensitivity of the results to small changes in rotor tip path plane angle, blade loading distribution, and rotor wake boundaries, the method of Reference 17 is not recommended for application to rotor-tail surface interference for compound helicopter designs similar to the test configuration.

EVALUATION OF RESULTS, ROTOR-PROPELLER INTERFERENCE EFFECTS

BASIC PROPELLER CHARACTERISTICS

The peak-to-peak vibratory propeller moments are plotted as functions of geometric angle of attack in Figures 96 through 112 for the isolated propeller and the rotorless model configurations. Edgewise bending moment data were not obtained for the isolated propeller conditions due to instrumentation malfunctions. The propeller speeds corresponding to maximum motor power are given on the isolated propeller plots. These propeller speeds were maintained throughout the testing for each forward speed propeller pitch combination unless noted otherwise. It can be seen that operation at 4200 rpm causes a significant increase in the stress level at the 29-percent radial station. This is a result of the proximity of the first mode flatwise bending frequency to 140 cps or 2 per revolution at 4200 rpm (see Figure 3c). Comparison of Figures 96 through 98 with Figures 99 through 101 reveals that the effect of forward speed on the propeller moments is not as great as the effect of operation near resonance. It is also evident that the propeller set at 41 degrees is more sensitive to changes in angle of attack than the propeller set at 30 degrees. The lateral offset of the isolated propeller data from the zero angle of attack position has not been explained but could be a result of interference induced by the support pylon, even though this structure is one diameter behind the propeller.

Looking at the propeller moment data from the rotorless model configuration, a number of interesting effects appear. For the wing-mounted propeller cases, Figures 102 through 107, the effect of the wing and nacelle on blade bending is evident on comparing these data with the isolated propeller data. It would be expected that the presence of the wing behind the propeller would introduce periodic excitation tending to increase the vibratory moment amplitude, and the data show this to be the case, particularly with the 41-degree propeller at 200 knots (Figures 103 and 106). For purposes of comparison between the isolated propeller moment data and the model mounted propeller moment data, the isolated propeller data should be centered on the minimum moment angle of attack. This will result in a symmetrical distribution with angle of attack and eliminate the offset discussed in the previous paragraph.

Another effect peculiar to the wing mounted propeller is the difference in the starboard and port moments. Figures 102 through 107 show that the 29-percent radius bending moments are consistently higher for the starboard propeller over the low positive angles of attack than for the

port propeller. The reason for this is believed to arise from the fact that since both propellers are turning in the same direction (clockwise, looking forward), the aerodynamic interference with the wing-fuselage structure differs on the two sides of the aircraft. Specifically, for the inboard mounted nacelles, as α_f is increased from zero the propeller blade which has a greater local angle of attack is near the fuselage on the port side and away from the fuselage on the starboard side. Similarly, for the outboard mounted nacelles, the propeller blade assuming the greater local angle of attack is forward of the wing on the port side and outboard of the wing tip on the starboard side. The actual mechanism of the interferences caused in this manner is not understood, but there is no other apparent reason for the indicated difference. The random differences between the starboard and port propeller moments at a specific angle of attack, other than those already discussed, are due to the data acquisition accuracy discussed in the section on model and test facilities.

The notable aspect of the propeller blade edgewise bending moment data is its low sensitivity to changes in angle of attack relative to that of the flatwise bending moments. The variation that does appear in the data results, in part, from coupling with the flatwise moments, since the interaction is not truly corrected when only the peak-to-peak values are dealt with. Only a detailed analysis of the time histories could eliminate this effect, and such an analysis was beyond the scope of this program.

For the pusher propeller configuration, the propeller moments take on a different character. The "V" shape seen in the wing mounted propeller moment data is absent in Figure 108, which presents the pusher propeller bending moments as a function of fuselage angle of attack. The departure of these data from those previously presented is, of course, a result of the placement of the fuselage and wing upstream of the propeller. The overall turbulence in the airstream at the propeller disk is increased by the passage of the flow over the aft end of the fuselage and the pitching strut, and as a result, the propeller blade bending moments are increased by a factor of up to seven over the isolated propeller data in the vicinity of $\alpha_f = 0$ degrees. In addition, the moment is seen to be relatively insensitive to changes in α_f through the low positive values. One qualitative explanation for this arises from the fact that as α_f is increased the downwash from the wing sensed by the propeller acts to moderate the effect of α_f . Decreasing α_f has the effect of decreasing the propeller bending moments. This decrease in propeller bending moments may be the result of two events: (1) since the wing is passing through its zero lift angle of attack, its effect becomes small; in addition, the pitching strut is rotated away from the propeller so that its effect is also being diminished; and (2) the flow is probably entrained along the fuselage, so that the net effect is a relatively cleaner flow for the low negative values of α_f . It would be expected that for larger values of α_f in either the

positive or negative direction, the α_f effect would predominate over all others and an increase in moments would be observed. Whatever phenomena are responsible for the behavior of the pusher propeller moments, it is clear that this propeller is operating in an environment which has an adverse effect on the magnitude of the vibratory moments in comparison with the isolated or the wing mounted tractor propellers.

EFFECT OF ROTOR OPERATION ON PROPELLER BLADE VIBRATORY MOMENTS

The behavior of the vibratory propeller moments discussed in the previous section is complicated by an order of magnitude when the rotor is introduced in the system. Figures 113 through 129 present the vibratory propeller bending moments as functions of rotor lift; first harmonic flapping is trimmed to zero degrees unless otherwise specified. Data at a particular radial station are omitted from a figure when instrumentation malfunctions occurred during the test run in question.

As was the case with the effect of the rotor on the wing characteristics discussed in the section on rotor-wing-fuselage interference, it would be expected that the effect of the rotor on the propeller bending moments would decrease with increasing forward speed due to the increasing rotor wake skew angles, and analysis of the data reveals that this is true. At all speeds, the effect of fuselage attitude dominates the variation of the propeller moments. At $V_s = 120$ knots (Figure 113), the moments on the propellers mounted in the inboard tractor configuration show that the only significant variation with rotor lift occurs at $\alpha_f = -4$ degrees. In this flight condition the rotor wake is in its closest proximity to the propeller, so it might be supposed that the maximum interference would occur; however, if Figure 102 is examined, it is seen that the sensitivity of the propeller moments to changes in α_f is greater for negative values of α_f than for positive values. As a result, a change in the effective angle of attack of the propeller induced by the rotor downwash would cause a larger change in propeller bending moment at a negative α_f than at a positive α_f . In Figure 114, the moments of Figure 113 are reproduced and compared with moments derived by determining an effective angle of attack on the propeller equal to the geometric angle of attack plus the rotor momentum downwash angle, $C_{LR} (57.3/2 \mu^2)$, and using this effective angle to find an empirical blade bending moment from Figure 102. It is apparent that although the rotor wake may be moved closer to or further away from the propeller by changing α_f , the factor which governs the magnitude of the propeller moment is the effective angle of attack described above. The differences that exist between the experimental and empirical data shown in Figure 114 can be attributed to

effects on the order of the accuracy of the data, such as unsteady vibration induced by the rotor wake, but these effects are small relative to the rotor downwash effect.

As far as the edgewise propeller blade moments are concerned, it can be concluded that since these are not sensitive to α_f changes without the rotor, they are likewise insensitive to changes in rotor lift which are equivalent to propeller angle of attack changes. Similar reasoning can be used in the case of the propeller moments shown in Figure 115 where the blade pitch is 30 degrees. Figure 99 shows that this propeller is less sensitive to changes in α_f than the 41-degree propeller, and it is also less sensitive to the rotor lift condition.

At $V_s = 200$ knots (Figure 116), the same general effects are present. It should be noted that analysis of the raw data led to the conclusion that the points at this speed for the inboard tractor configuration when $\alpha_f = 0$ degrees and $\theta_c = 4$ degrees were invalid data points and therefore were discarded.

At $V_s = 300$ knots (Figure 117), the data appear to reflect a high sensitivity to rotor lift changes, but at this speed the rotor lift is changed by angle of attack rather than collective pitch, so the propeller moments are correspondingly changed by angle of attack rather than rotor lift. Again the small variation resulting from collective pitch changes probably stems from unsteady wake effects which are a function of the loading distribution on the rotor rather than the total lift.

The propeller bending moment data for the outboard tractor configuration shown in Figures 118 through 121 exhibit no significant variations with rotor lift at constant fuselage angle of attack at any speed. The only apparent exception is in the case of the starboard edgewise moment at $\alpha_f = 8$ degrees for $V_s = 200$ knots (Figure 120b). The three points shown were the final ones during this particular test run, and on the succeeding run no data were obtained for this bending moment data channel. The validity of these three ($\alpha_f = 8$ degrees) points is therefore felt to be questionable, and the points do not accurately reflect the variation of bending moment with C_{LR}/σ .

The empirical method used to obtain the data in Figure 114, and discussed on page 51, was applied to the case of the outboard propeller configuration at 120 knots. The results are presented in Figure 119. In this case the qualitative agreement is good but the point-to-point correlation of data is not as good as that for the inboard case. This lack of correlation stems from the variation of bending moment with C_{LR}/σ at constant α_f . Because of the "V" shape of the propeller bending moments plotted as a function of α_f for the rotorless configuration, the empirical method will

always yield an increasing moment with increasing C_{LR}/σ for negative values of α_f and a decreasing moment for positive values of α_f . The inboard configuration has the same characteristics and the correlation is good (Figures 113 through 116) but the outboard starboard propeller has the opposite characteristic, that is, a decrease in propeller moments with increasing C_{LR}/σ for negative values of α_f (Figure 119a); thus the correlation begins to break down. For the outboard port propeller, the original trend reappears and the correlation is improved (see Figure 119b).

This experimental-empirical correlation was also used with Figure 102 to assess the effects of rotor tip path plane orientation on the propeller moments, and the results are presented in Figure 122. It is seen as before that the blade bending moments on the tractor propeller are well defined by the effective angle of attack of the propeller, and changes in the orientation of the rotor tip path plane relative to the orientation of the propeller have only a slight effect on the degree of correlation. These results indicate that the relative orientation between the rotor and the propeller has an effect which is an order of magnitude smaller than the effect of the angle of attack seen by the propeller.

The bending moments on the pusher propeller as functions of C_{LR}/σ are presented in Figures 123 through 125. At 120 knots, in the configuration without the tail and tail pylon, the rotor lift has a significant influence on the propeller moment as seen in Figure 123. As rotor lift is increased, the combined effect of an increase in the effective angle of attack on the propeller and the lowering of the rotor wake toward the propeller causes the propeller moment amplitudes to increase as much as 85 percent. Because of the unsteady effect of the rotor wake, the empirical method applied to the tractor configuration is no longer applicable; but the interference effects reflected by the data in Figure 123 can be understood more clearly by plotting the moments three dimensionally, as in Figure 124. This figure shows contours of constant α_f and θ_c as they vary with C_{LR}/σ . If the constant α_f contours are extrapolated with constant curvature to $C_{LR}/\sigma = 0$, it will be found that they approach the rotorless data points shown, as would be expected. These extrapolated contours also exhibit the "V" shape characteristics of the isolated propeller, indicating the influence of rotor lift on the effective propeller angle of attack. Also seen in Figure 124 is the relative insensitivity of the moment to changes in α_f , as discussed earlier with reference to Figures 108 through 112.

The propeller blade edgewise bending moments are less sensitive to changes in rotor lift than the flatwise moments at $V_s = 120$ knots, as seen in Figure 123. The edgewise moment decrease which accompanies a rotor lift increase is probably a reflection of the effect of the principal axis transformation on the measured data. Referring to the interaction

matrix presented on page 8, it is seen that the off-diagonal terms are negative, so a large positive flatwise moment decreases the corresponding edgewise moment.

At 300 knots, only the flatwise propeller moments at the 58-percent radius were obtained; these are shown in Figure 125 at three propeller speeds. The effect of operation of the propeller at 4000 rpm is again evident as the moments are amplified by the proximity of the two-per-revolution resonance, but the effect of the rotor lift change is not well defined. It appears that the rotor lift increases the moments at the low power setting and decreases them at the maximum power setting, but examination of Figure 109, where the moments are plotted for the same configuration but without the rotor, reveals that the moments vary with α_f . Figure 168 of Appendix II shows that C_{LR}/σ is essentially determined by α_f , so the propeller moment variation in Figure 125 is not a direct result of C_{LR}/σ being changed but of α_f being changed. This is consistent with previous results showing the minimum interference by the rotor on the wing at $V_s = 300$ knots.

In Figures 126 through 129, the propeller moments are shown for the pusher configuration with the tail in place, and a significant reduction in the effect of rotor lift takes place, compared to the effect of rotor lift when the tail is absent. The propeller blade moment magnitudes are not altered, but the variations of the moments resulting from changes in rotor lift are on the order of 30 percent at the inboard station compared to 85 percent in the case without the tail. As the speed is increased, the lessening of the effect of rotor lift is again seen (Figures 127 and 128). In this configuration the tail is acting as a shield between the rotor and the propeller, and so the effect of changes in the rotor operating condition is diminished.

The 30-degree propeller data for the pusher configuration with the tail (Figure 129) exhibit a somewhat erratic behavior, but the qualitative effect of the rotor on this propeller is apparently the same as that on the 41-degree propeller. In both of these cases the $\theta_c = 4$ -degree rotor condition tends to cause the highest flapwise moment on the propeller blade at any given angle of attack.

EFFECT OF PROPELLER OPERATION ON ROTOR BLADE VIBRATORY MOMENTS

Figures 130 through 132 show one-half peak-to-peak rotor blade flapwise, chordwise, and torsional bending moments as a function of rotor angle of attack. Data are presented for the various configurations tested at 120, 200, and 300 knots. In general, the characteristic variation of a given

moment with α_f and θ_c is unaffected by changes in the model configuration. Nevertheless, such changes do cause some local variation of the moment amplitudes; these changes will be discussed in the following section. To give a more complete picture of rotor blade moments at $V_s = 300$ knots, some data points obtained during the rotor-wing-fuselage phase of this investigation are included in the following figures. Each of these points was obtained with the same model blade as the rest of the points with which they are plotted, and each is believed to accurately represent the moment levels at the indicated operating conditions.

In all configurations, the flapwise rotor blade bending moment amplitude increases with increasing α_f and θ_c . At 300 knots this moment passes through a minimum in the vicinity of $\alpha_f = 0$ degree and increases as the fuselage is tilted forward or aft while the rotor is kept trimmed. The latter case, increasing α_f , results in a rapid increase in the moment as would be expected because the rotor lift is also increasing while θ_c remains unchanged. At the lower speeds the variation with α_f is more uniform over the range shown, the moment amplitude being lowest at $\alpha_f = -4$ degrees and highest at $\alpha_f = +8$ degrees for any given θ_c value.

The chordwise bending moments (Figure 131) display the same basic characteristics as the flapwise, although they are more sensitive to θ_c changes and less sensitive to α_f changes.

The factor which primarily influences the torsional moments is rotor advance ratio, which is reflected in the changes in forward speed in Figure 132. The effects of θ_c and α_f are significant only under high rotor loading conditions. It is seen in Figure 132 that when $\alpha_f = +8$ degrees and $\theta_c = +8$ degrees the torsional moment amplitude experiences a large increase. The nature of this increase is indicated in Figure 133 where time histories of torsional moment are compared for $\alpha_f = +8$ degrees and $\theta_c = 0$ and 8 degrees at 120 knots. The increase in moment is confined to the retreating side of the rotor disk in the vicinity of $\psi = 270$ degrees. Between these two conditions there is a net change of about 12 degrees in the pitch on the blade at $\psi = 270$ degrees, and the effects of the reverse flow region are beginning to be felt. At 300 knots (Figure 132c), the variation is primarily affected by the pitch on the blade, and the time history of the moment (Figure 134) shows that the retreating side of the disk still contains the large moment cycle, as would be expected. It should be noted that the pitch-flap coupling ($\delta_3 = 45$ degrees) on the rotor may tend to aggravate the torsional moments as high advance ratios are encountered (see Reference 4).

In Figures 135 through 138, data points from Figures 130 through 132 have been superimposed so that the effects of propeller thrust on rotor blade bending moments can be determined. The forces and moments

measured on the wing balances are presented in coefficient form in Appendix III for all test conditions; the reference area is total wing area, and the effects of the propellers and nacelles are included. Note that due to a higher rotational speed (5250 rpm as opposed to 3500 rpm) the 30-degree propeller produces more thrust at $V_s = 120$ knots than the 41-degree propeller. Figure 135 shows that the presence of the propeller tends to increase flapwise bending moments, but only at the higher θ_c settings. In Figure 136 where the flapwise rotor blade bending moments are compared for the inboard and outboard wing mounted configurations, there is evidence of a tendency for the outboard propeller to cause a larger increase than the inboard propeller over the basic moment level. These increases range up to 20 percent for the lower forward speeds and approach 100 percent at 300 knots. Although no data were obtained at 300 knots with the 30-degree propeller, it is known that less thrust will be produced than with the 41-degree propeller, since the propeller speeds are essentially the same (5560 rpm and 5100 rpm); as a result, the data represent a larger increase in rotor blade bending moments than would be experienced with the 30-degree propeller.

The results presented for the effect of the propellers on the flapwise rotor blade bending moments are in agreement with what would be expected from an analysis of the physical situation. The rotor blade periodically passes through the pressure fields induced by the propellers, and the subsequent change in the loading on the rotor blade is reflected in the bending moments and rotor blade flapping. This latter effect can be seen in Figure 139, a time history of the flapping angle for the propellerless and tractor propeller configurations at the same flight condition.

In Figure 137, where flapwise rotor blade bending moments are shown for the pusher propeller configuration, the data show the same effect as that seen in the case of the tractor configuration, although the flapwise moment increases due to the presence of the propeller are generally smaller. This is expected since the rotor no longer passes directly over the propeller. Overall, changing the pusher propeller thrust from the windmill condition (4000 rpm) to the maximum power condition (5000 rpm) has no significant effect on the flapwise rotor blade bending moment at 300 knots.

Figures 140 and 141 show that the chordwise rotor blade bending moments are also increased by the presence of the tractor propellers. As before, the most significant increases occur at the high collective pitch settings. The inboard propeller configuration shows the largest increase with increments up to 55 percent throughout the speed range. It is not clear why this should be so. The basic chordwise rotor blade response is a four-per-revolution bending mode as seen in Figure 144, a time history of chordwise rotor blade bending moment with and without the propellers

at the inboard position; the harmonic content is unchanged in the presence of the propeller, although the vibratory amplitude is increased by 55 percent. A more detailed knowledge of the propeller performance than was obtained in this program would be required to make a cause-effect evaluation of the interference between the propeller and the rotor, but it is significant that the propellers do not induce a high harmonic chordwise response in the rotor blades.

In Figure 142a, the chordwise rotor blade bending moments are compared in the pusher propeller configuration for the 30-degree and 41-degree pitch propellers operating at 5250 rpm and 3500 rpm respectively. A decrease in bending moment at this radial station (60%R) is seen to be the result of the greater propeller thrust of the 30-degree propeller. However, if a comparison is made between chordwise rotor blade bending moments on the rotor alone and on the rotor in the presence of the propeller (Figure 142b), an opposite trend is seen as the moment at the 35-percent radial station increases in the presence of the propeller. Unfortunately, data were not obtained for all three forward speed configuration combinations at the same chordwise radial station, so a firm conclusion cannot be reached as to the effect of the pusher propeller thrust on chordwise rotor blade bending moments. It is felt that comparison of results between two stations on the rotor blade is not justified; however, the pusher propeller does have a significant effect on the chordwise rotor blade moment at 120 knots although the exact nature of the effect is not known.

In Figure 143, chordwise rotor blade bending moments are shown for three values of propeller thrust at 300 knots as indicated by propeller speeds of 5000, 4500, and 4000 rpm. As in the case of the flapwise rotor blade bending moments at the same flight condition (Figure 138), no significant effect is revealed.

In Figures 145 through 147, rotor blade torsional moments are compared for the different model configurations over the forward speed range. The torsional moment amplitudes are unaffected by the presence of the propeller or by changes in propeller thrust.

EFFECT OF FORWARD SPEED ON ROTOR BLADE VIBRATORY MOMENTS

The variation of rotor blade bending moments with forward speed is highly dependent on the specific variation of rotor lift, fuselage angle of attack, and collective pitch that is chosen over the speed range. Since a compound helicopter operates at speeds from zero to 300 knots, all three of these parameters will vary widely, and the actual variation of rotor blade

moments will be determined as much by these parameters as by the actual change in speed. In Figures 148 through 153, plots of rotor blade bending moments as functions of rotor lift are shown at 120, 200, and 300 knots. These plots were taken directly from Figures 130, 131, and 132 for a constant fuselage angle of attack of 4 degrees.

If the rotor lift requirement is specified, the variation of blade bending moment with forward speed can be obtained. In Figures 148 through 153, the lift required at 120 knots was assumed to be $C_{LR}/\sigma = 0.071$. This was reduced to 0.052 at 200 knots and to 0.030 at 300 knots. These conditions are shown as points A, B, and C in the figures, and the corresponding moment amplitudes are plotted in the inserts. A large increase of flapwise moment over the speed range is seen in Figure 148. In Figure 149, the chordwise moments are shown for the same flight conditions. Since the rotor lift at 300 knots is essentially determined by rotor angle of attack rather than collective pitch, the rotor blade moments at this speed are double valued with collective pitch. Point D, in Figure 149, corresponds to high collective pitch setting, and the chordwise rotor blade moments along both operating lines ABC and ABD are plotted in the insert. In the manner just described, the reader can obtain the variation of bending moments with forward speed for any desired flight plan. Figures 150 through 153 present such results for selected model configurations. Figure 154 gives the flapwise rotor blade moments for the inboard tractor configuration at $\alpha_f = 0$ and -4 degrees, indicating the dependence of rotor blade bending moments on collective pitch at the high forward speed rather than on rotor lift.

EFFECTS OF ROTOR AND PROPELLER OPERATION ON TAIL DOWNWASH ANGLE

The downwash at the tail generated by the addition of a propeller is shown in Figures 155 and 156 as a function of C_{LR}/σ . For $\alpha_f = 8$ degrees and $V_s = 200$ knots (Figure 155), the tractor propellers in the outboard position had no significant effect on ϵ_t over the range of rotor lift. This is because the tail is well away from the propeller wake. The inboard tractor configuration, however, reduced ϵ_t by about 1 degree at these operating conditions, compared to operation without the propeller, since the velocity field induced by these propellers adds to the free stream velocity near the tail.

Simplified calculations of the velocity field of the pusher propeller indicated that the flow begins to contract 3 propeller radii ahead of the propeller. Since the tail is about 2 propeller radii above and forward of the propeller, it is near to or immersed in the contracting flow. As a

result, ϵ_i is increased, as shown in Figure 155. This effect is also shown in Figure 156 where $\alpha_i = -4$ degrees and $V_s = 120$ knots. It is seen that decreasing the pitch on the propeller blade to 30 degrees, thus increasing the propeller thrust due to the higher operating rpm, increases ϵ_i over that measured with $\beta_{75} = 41$ degrees.

In Figure 156, the tractor propeller is seen to cause a decrease in ϵ_i similar to that seen in Figure 155.

CONCLUSIONS

ROTOR-WING-FUSELAGE INTERFERENCE EFFECTS, EXPERIMENTAL

The results of the experimental investigation of rotor-wing-fuselage aerodynamic interference effects led to the following principal conclusions.

Rotor Interference on Wing Characteristics

The rotor induced downwash angle at the wing is approximately equal to the momentum downwash angle at the rotor disk. However, wing size and vertical distance from the rotor are important parameters in accurately determining the actual mean downwash value.

In addition to the loss in wing lift caused by the rotor downwash, a small increase in wing drag occurs. The combined result is a decrease in the wing lift-drag ratio at low speeds. However, this interference decreases with forward speed and is not significant when wing performance becomes important.

At pure helicopter speeds, the rotor downwash induces an unsymmetrical spanwise decrease in wing loading at constant wing incidence. The larger reduction in wing lift occurs beneath the advancing rotor blade. This effect increases with decreasing rotor-wing spacing.

Wing Interference on Rotor Characteristics

The effect of increasing wing lift is to decrease rotor lift. The loss in lift is small at low speeds for all conditions. It becomes large only at high speeds, with heavily loaded large wings. However, this interference generally decreases with forward speed when measured on the basis of the pounds of rotor lift decrease per pound of wing lift increase.

The precise nature of the effect of wings on rotor blade stresses is quite complex and could not be defined. However, the presence of a wing caused no significant increase in rotor blade vibratory stresses.

Rotor Interference on Downwash Angle at the Tail

The contribution to the downwash at the tail induced by the wing in the configurations tested decreases as rotor lift is increased, as expected.

ROTOR-WING-FUSELAGE INTERFERENCE EFFECTS, THEORETICAL

The results of the theoretical analysis of the aerodynamic interference between a rotor, a wing, and a fuselage and the correlation of these results with experimental data led to the following principal conclusions.

Wing Interference on Rotor Performance

The rotor inflow distribution induced by a wing consists mainly of downflow in the aft region of the rotor and is linearly proportional to the product of forward speed and wing lift coefficient. The proportionality constant is only a function of the relative positioning of the rotor, the wing, and the wing wake.

The wing interference on flapping increases linearly with wing lift coefficient and increases with advance ratio.

The wing interference induces an increment of rotor lift and is linear with wing lift coefficient. This effect may be represented in derivative form, $\partial C_{LR}/\sigma/\partial C_{LW}$. The derivative is negative and its absolute magnitude increases with increasing advance ratio and wing size and decreasing rotor-wing separation. The sensitivity to wing size is greater than the sensitivity to rotor-wing separation.

The wing-induced effects on rotor lift are sensitive to pitch-flap coupling. The magnitude of the induced flapping and lift derivatives increases with the incorporation of pitch-flap coupling in the control system.

Trimming the first harmonic wing-induced flapping significantly increases the magnitude of the rotor lift derivative, $\partial C_{LR}/\sigma/\partial C_{LW}$, when pitch-flap coupling is present in the control system.

The correlation between the nonlinear theory derived herein and experiment indicates that the theoretical method can be used to accurately predict the interference of a wing on rotor performance. In addition, comparison with the nonlinear theory shows that the linearized equations developed herein are useful for qualitative analysis of wing-induced effects on rotor lift.

Mutual Wing-Fuselage Interference

The angle of attack for zero lift for the tested compound helicopter model configurations is not accurately predicted using the theoretical method of Reference 7.

Lift curve slopes of the wing and of the fuselage are predictable within approximately 10 percent of the experimental values. The characteristic trends of lift curve slope with wing size are also predictable.

Lift carry-over on to the fuselage is greatly overestimated by the theory of Reference 7 due to errors in zero lift angle of attack.

In general, the theory of Reference 7 does not result in improved prediction of the integrated wing-fuselage lift characteristics of compound helicopter configurations over the classical full-span wing approximation.

Wing Interference on the Downwash Angle of the Tail

Increments in the average downwash angle at the tail produced by the addition of a wing (as determined from References 15 and 16) agree well with experiment for the large wing configurations tested herein. The theory is not applicable to the small and medium configurations.

Rotor Interference on Wing Characteristics

Average downwash angles at the wing due to the rotor (determined from the charts of Reference 17) are substantially lower than those derived from the experimental results. The higher experimental values may be the result of fuselage interference, as unpublished data from previous tests of an isolated wing and rotor were found to be in better agreement with theory.

Rotor Interference on Downwash Angle at the Tail

The method of Reference 17 is not satisfactory for application to the rotor-tail surface interference, for compound helicopter designs similar to the tested configurations, due to the close proximity of the tail to the rotor wake and the consequent sensitivity of the downwash angle at the tail to small changes in rotor angle of attack, blade loading distribution, and rotor wake boundaries.

ROTOR-PROPELLER INTERFERENCE EFFECTS, EXPERIMENTAL

The results of the experimental investigation of rotor-propeller aerodynamic interference effects led to the following principal conclusions.

Rotor Interference on Propeller Blade Moments

The primary factors determining the bending moment on wing mounted

tractor propeller blades are the effective angle of attack of the propeller induced by the rotor momentum downwash and the geometric angle of attack of the propeller.

The bending moments on the pusher propeller are larger than the bending moments on the tractor propellers for the same flight conditions, although the pusher propeller is shielded from the rotor by the presence of the empennage, and the propeller moments are insensitive to changes in rotor operating condition. Without the empennage, the pusher propeller blade moments are highly sensitive to changes in rotor operating condition.

Propeller Interference on Rotor Blade Moments

Increasing the thrust of wing mounted tractor propellers increases the flapwise and chordwise rotor blade vibratory bending moments as well as the rotor blade flapping amplitude. Rotor blade torsional moments are insensitive to propeller thrust.

Increasing the thrust of the pusher propeller increases the flapwise rotor blade vibratory moments in the low to moderate forward speed range ($V_s \approx 200$ knots or less). The effect of pusher propeller thrust on chordwise rotor blade vibratory moments could not be defined.

REFERENCES CITED

1. Fradenburgh, Evan A., and Kiely, Edmond F., Development of Dynamic Model Rotor Blades for High Speed Helicopter Research, Symposium on Aeroelastic and Dynamic Modeling Technology, Wright-Patterson Air Force Base, Ohio, September 1963.
2. Rabbott, John P., Jr., Comparison of Theoretical and Experimental Model Helicopter Rotor Performance in Forward Flight, TCREC Technical Report 61-103, U. S. Army Aviation Materiel Laboratories, Fort Eustis, Virginia, July 1961.
3. Bain, Lawrence J., Comparison of Theoretical and Experimental Model Rotor Blade Vibratory Shear Forces, USAAVLABS Technical Report 66-77, U. S. Army Aviation Materiel Laboratories, Fort Eustis, Virginia (to be published).
4. Fradenburgh, Evan A., and Segel, Richard M., Model and Full Scale Compound Helicopter Research, American Helicopter Society Twenty-first Annual National Forum, Washington, D. C., May 1965.
5. Shrenk, O., A Simple Approximation Method for Obtaining the Spanwise Lift Distribution, NACA TM 948, August 1940.
6. Gessow, A., and Myers, G. C., Aerodynamics of the Helicopter, Macmillan Company, New York, 1952.
7. Luckert, H. J., "Lift Distribution of Wings in Combination with Slender Bodies of Revolution," Canadian Aerodynamical Journal, December 1955.
8. Tanner, Watson H., Charts for Estimating Rotary Wing Performance in Hover and at High Forward Speeds, NASA CR-114, November 1964.
9. Weber, J., Kirby, D. A., and Kettle, D. J., An Extension of Multhopp's Method of Calculating the Spanwise Loading of Wing-Fuselage Combinations, Aeronautical Research Council R. & M. No. 2872, 1956.
10. Multhopp, H., Aerodynamics of the Fuselage, NACA TM 1036, 1942.

11. Lennertz, J., "Influence of the Airplane Body on the Wings," Aerodynamic Theory, Volume IV, Division K, Chapter 3, W. I. Durand, Editor, Durand Reprinting Committee, California Institute of Technology, Pasadena, California, 1943.
12. Spreiter, J. R., Aerodynamic Properties of Slender Wing-Body Combinations at Subsonic, Transonic, and Supersonic Speeds, NACA TN 1662, 1948.
13. Low, L., and Stone, H. N., The Subsonic Aerodynamic Characteristics of Wings in Combination With Slender Bodies of Revolution, Cornell Aeronautical Laboratory Report No. CAL/CM - 679, Cornell Aeronautical Laboratory, Buffalo, New York, 1951.
14. Lawrence, H. R., and Flax, A. H., "Wing-Body Interference at Subsonic and Supersonic Speeds Survey and New Developments," Journal of the Aeronautical Sciences, Volume 21, No. 5, 1954, pages 289 - 328.
15. Silverstein, A., Katzoff, S., and Bullivant, K., Downwash and Wake Behind Plain and Flapped Airfoils, NACA TR 651, 1939.
16. Silverstein, A., and Katzoff, S., Design Charts for Predicting Downwash Angles and Wake Characteristics Behind Plain and Flapped Wings, NACA TR 648, 1940.
17. Jewel, J. W., and Heyson, H. H., Charts of the Induced Velocities Near a Lifting Rotor, NASA Memo 4-15-59L, May 1959.
18. Heyson, H. H., and Katzoff, S., Induced Velocities Near a Lifting Rotor With Nonuniform Disk Loading, NACA TR 1319, 1957.
19. Heyson, H. H., Induced Velocity Near a Rotor and its Application to Helicopter Problems, Proceedings of the Fourteenth Annual Forum of the American Helicopter Society, Washington, D. C., April 1958.
20. Tararine, S., Experimental and Theoretical Study of Local Induced Velocities Over a Rotor Disc for Analytical Evaluation of the Primary Loads Acting on Helicopter Rotor Blades, European Research Office Report, No. DE 2012, U. S. Department of the Army, October 1960.

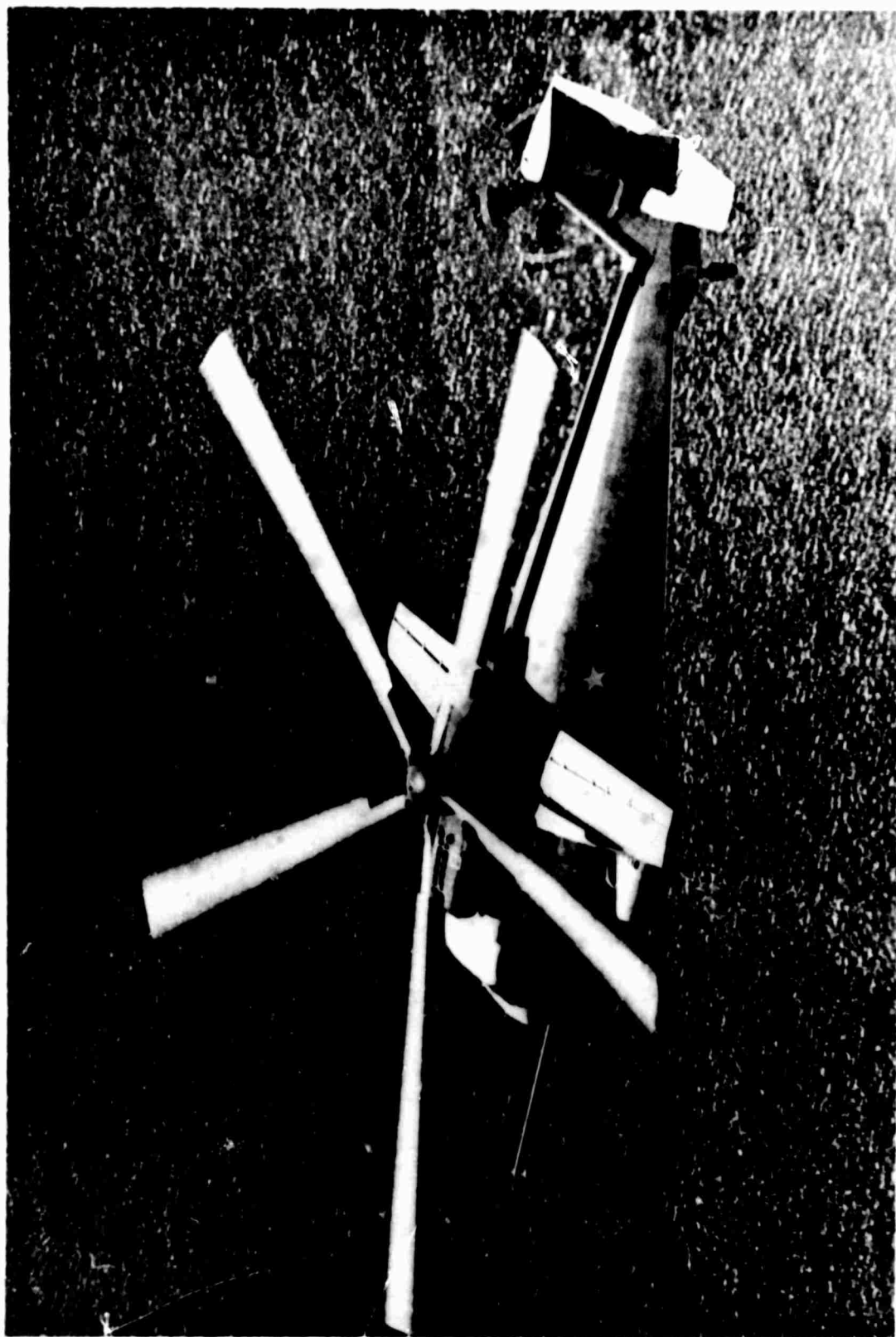
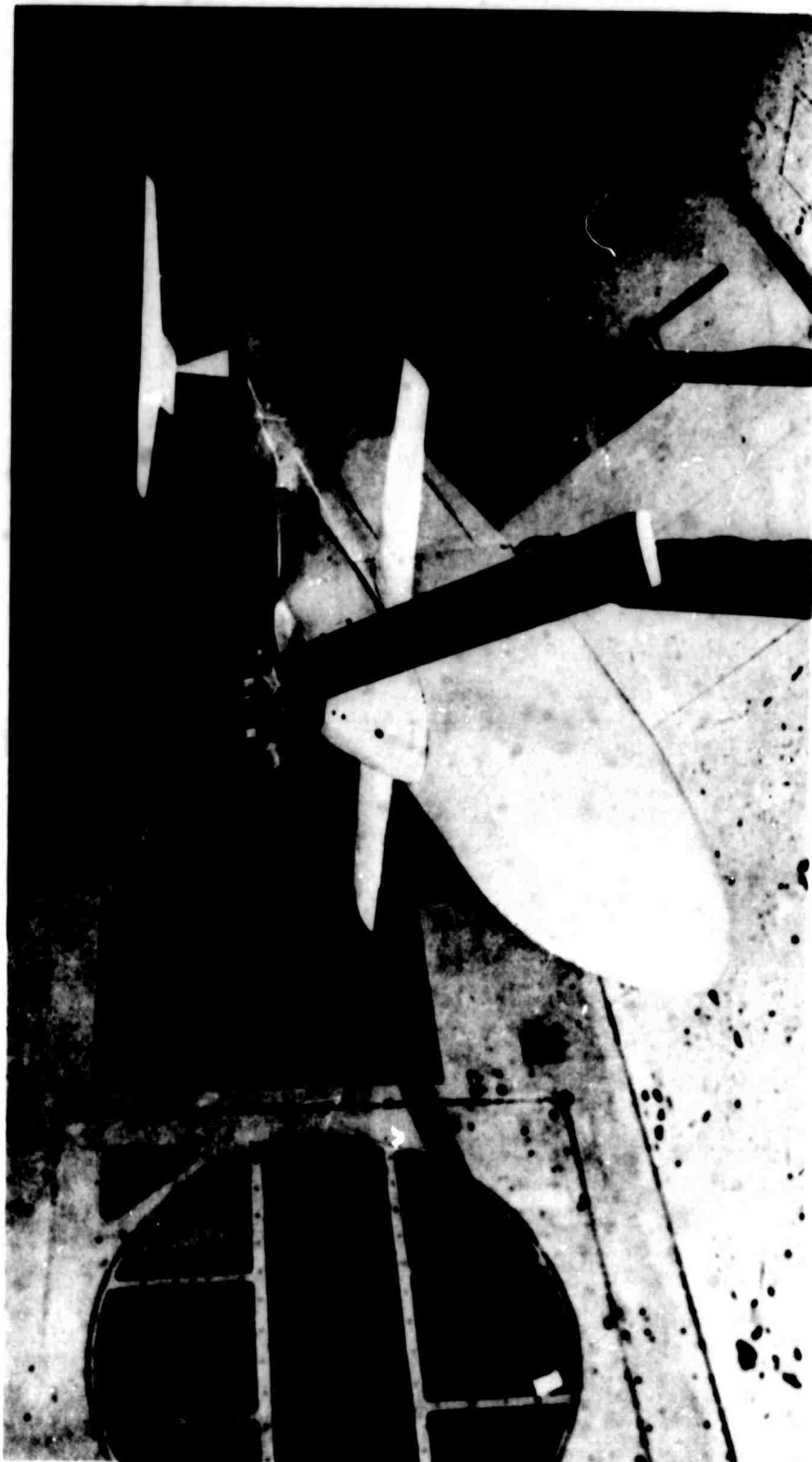
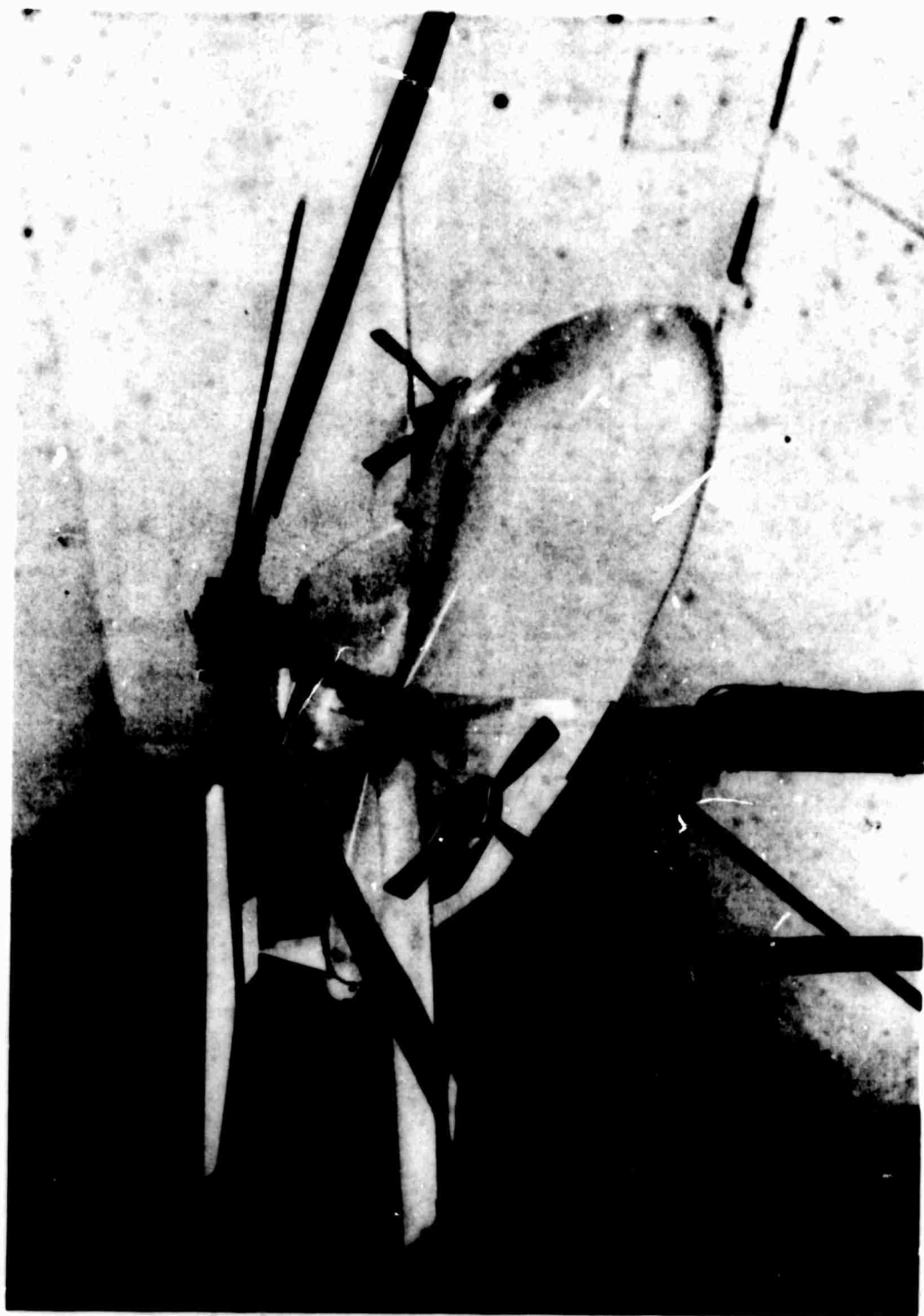


Figure 1. S-61F Research Aircraft.



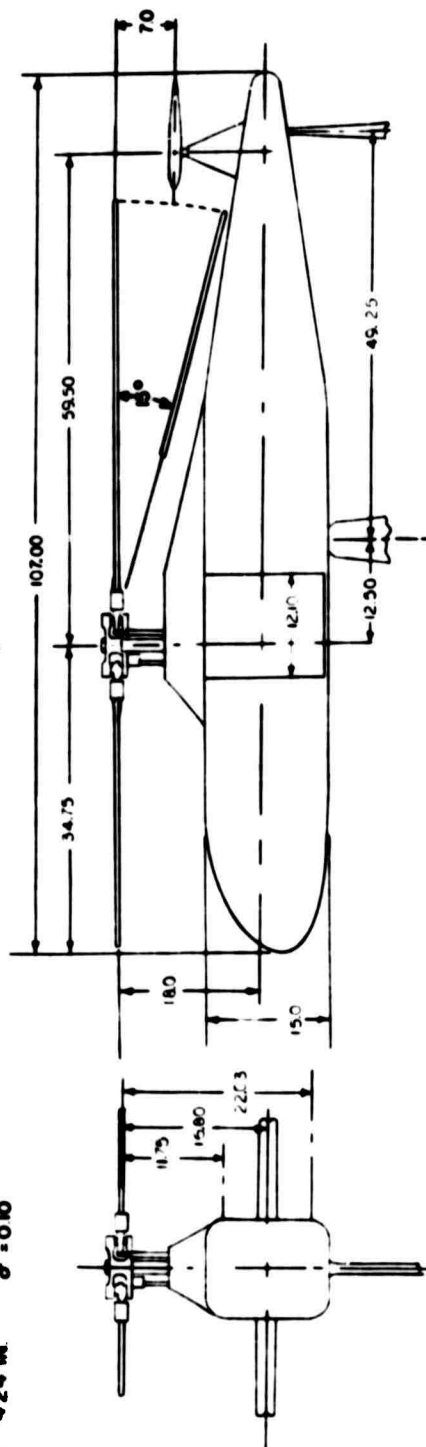
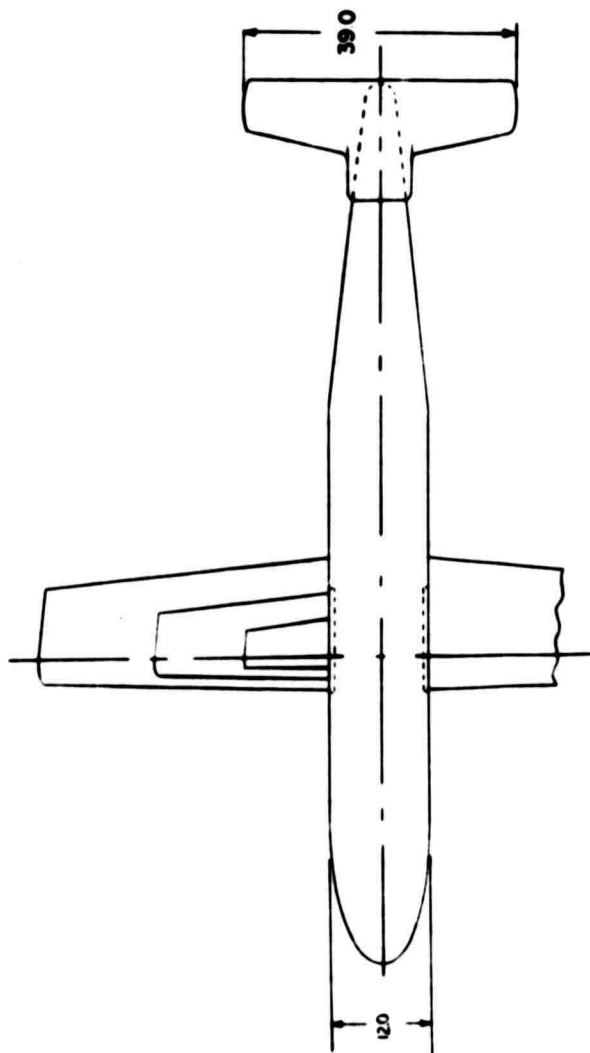
(a) Model in UAC 18-Foot Wind Tunnel

Figure 2. Sikorsky Compound Helicopter Model.



(b) Model With Propellers

Figure 2. Continued.



WING DATA

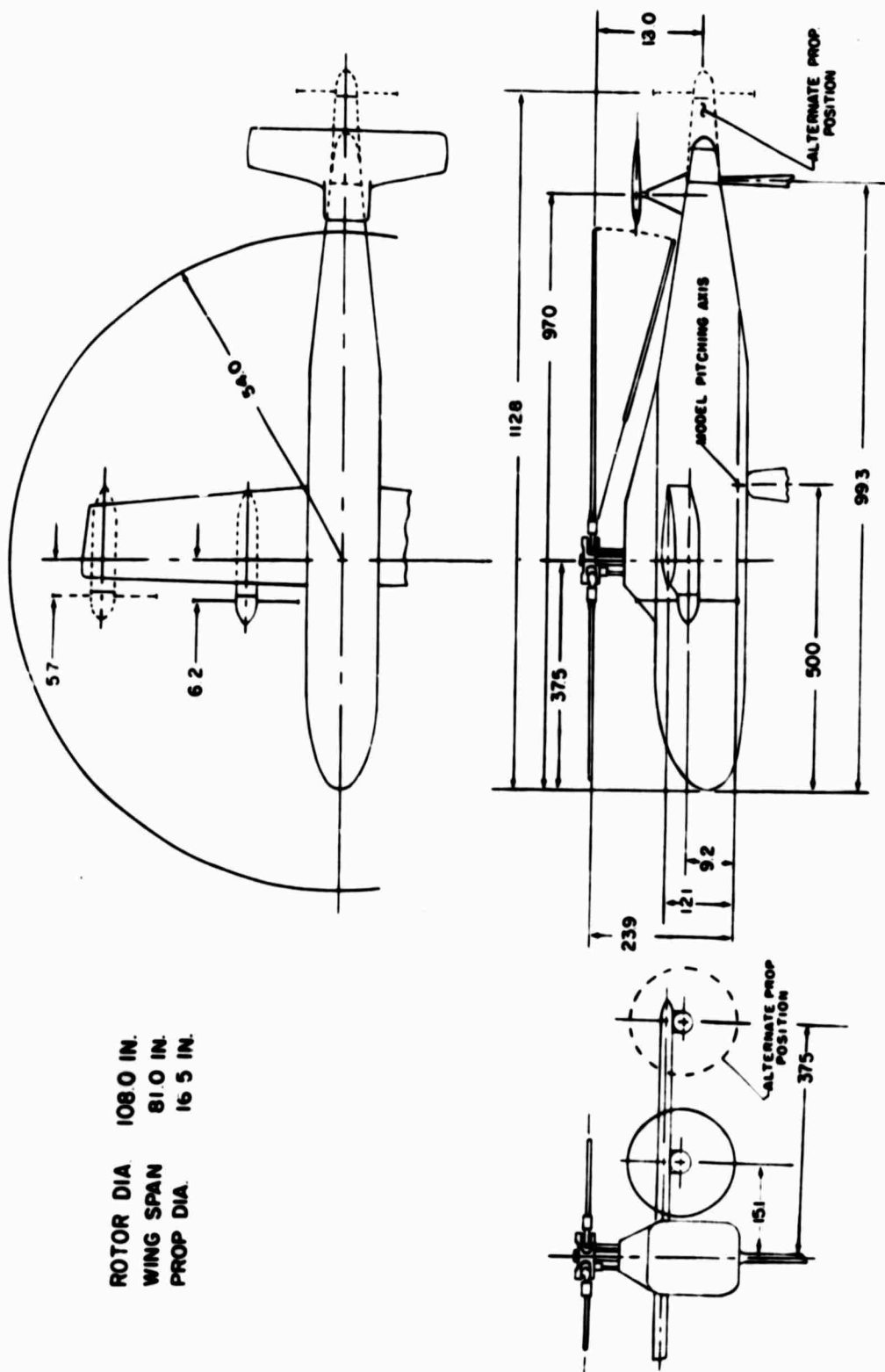
WING	SMALL	MEDIUM	LARGE
SPAN, IN.	32.4	54.0	81.0
b_w/d	0.30	0.50	0.75
AREA, IN ²	175	486	1091
AR	6	6	6
CROOT-IN.	6.48	10.8	16.2
C TIP-IN	4.32	7.20	10.8
TR	3:2	3:2	3:2
AIRFOIL SECTION	NACA 642-415		

ROTOR DATA

RADIUS	54 IN.	NO OF BLADES	4
CHORD	4.24 IN.	σ	0.10

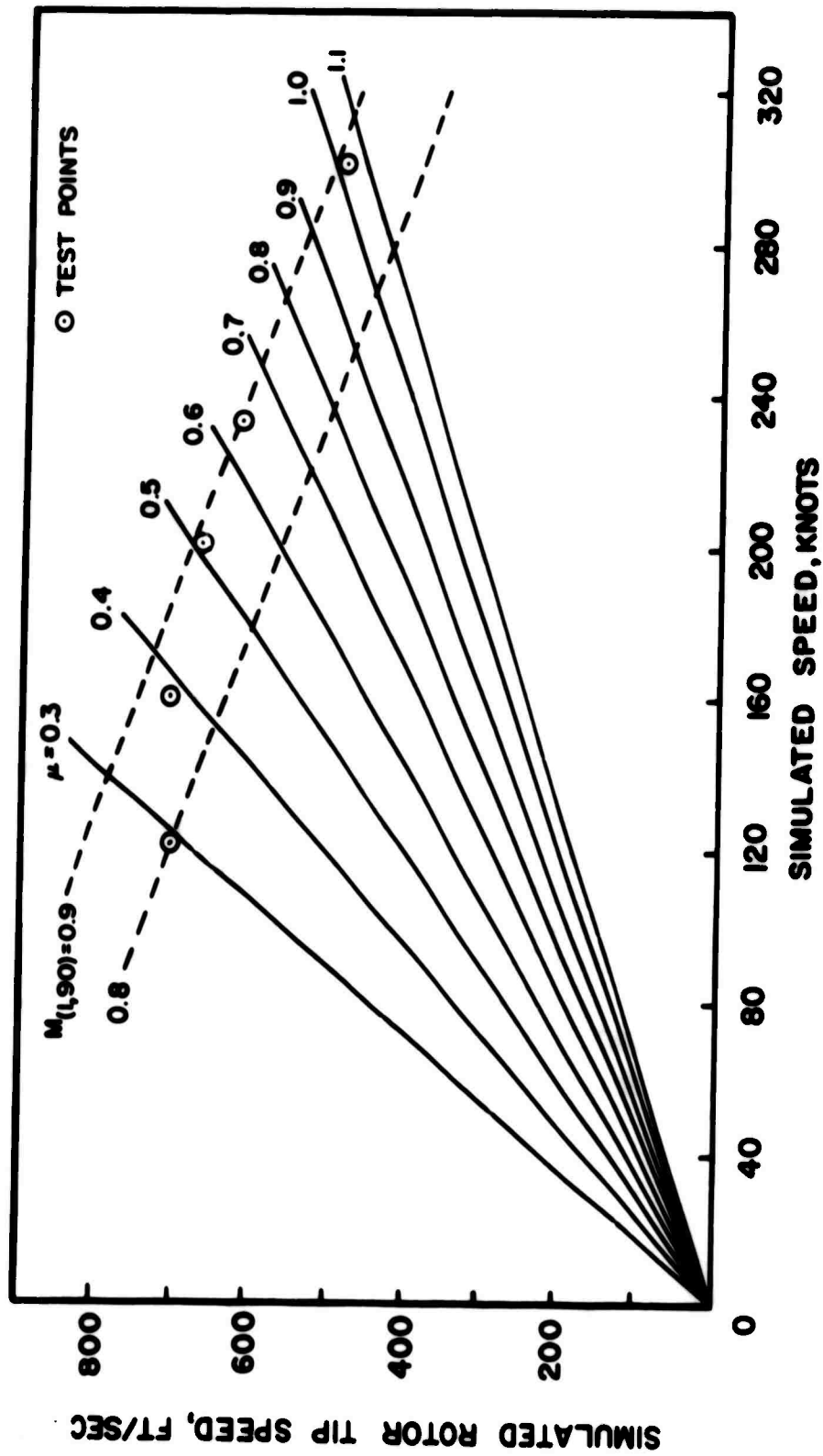
(c) General Arrangement

Figure 2. Continued.



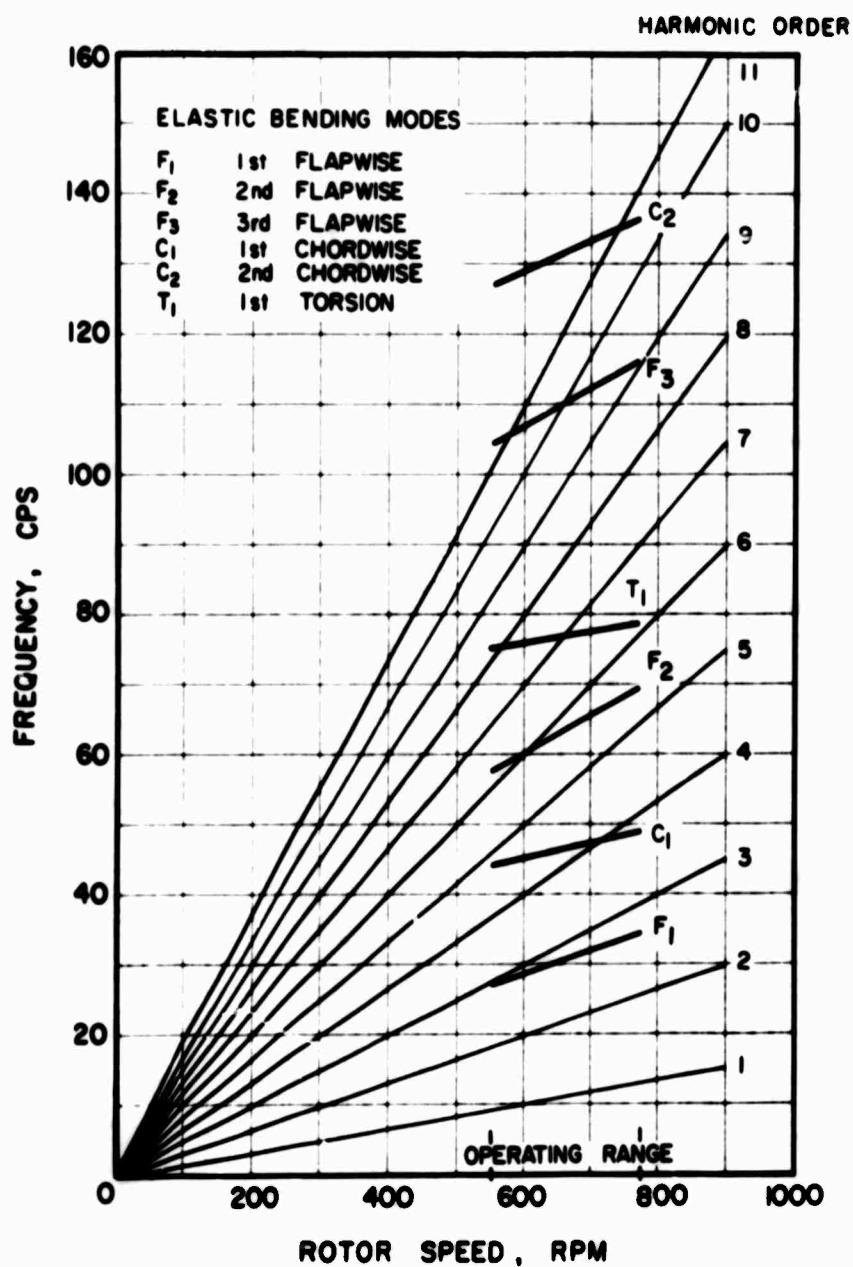
(d) Propeller Arrangement

Figure 2. Concluded.



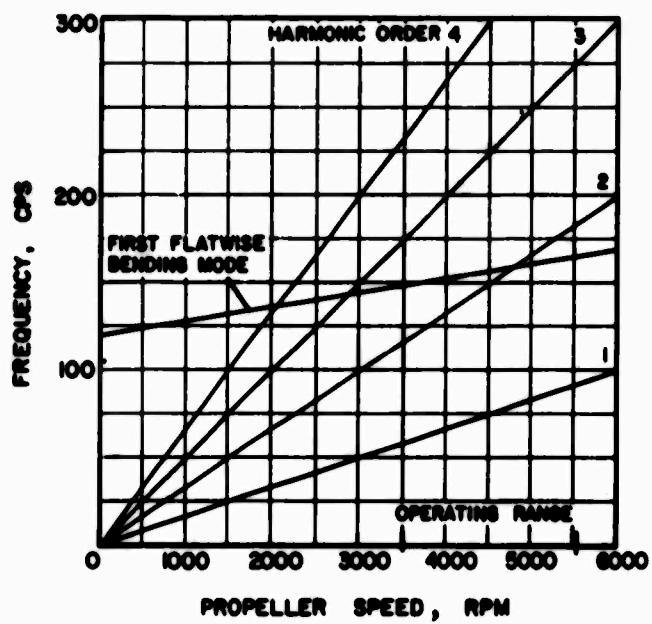
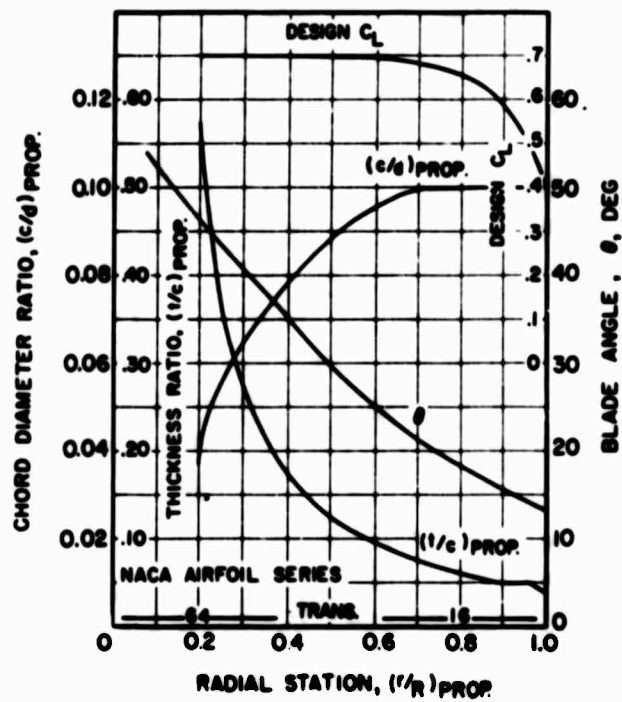
(a) Rotor Test Conditions

Figure 3. Model Operating Characteristics.



(b) Calculated Model Rotor Blade Natural Frequencies

Figure 3. Continued.



(c) Propeller Characteristics

Figure 3. Concluded.

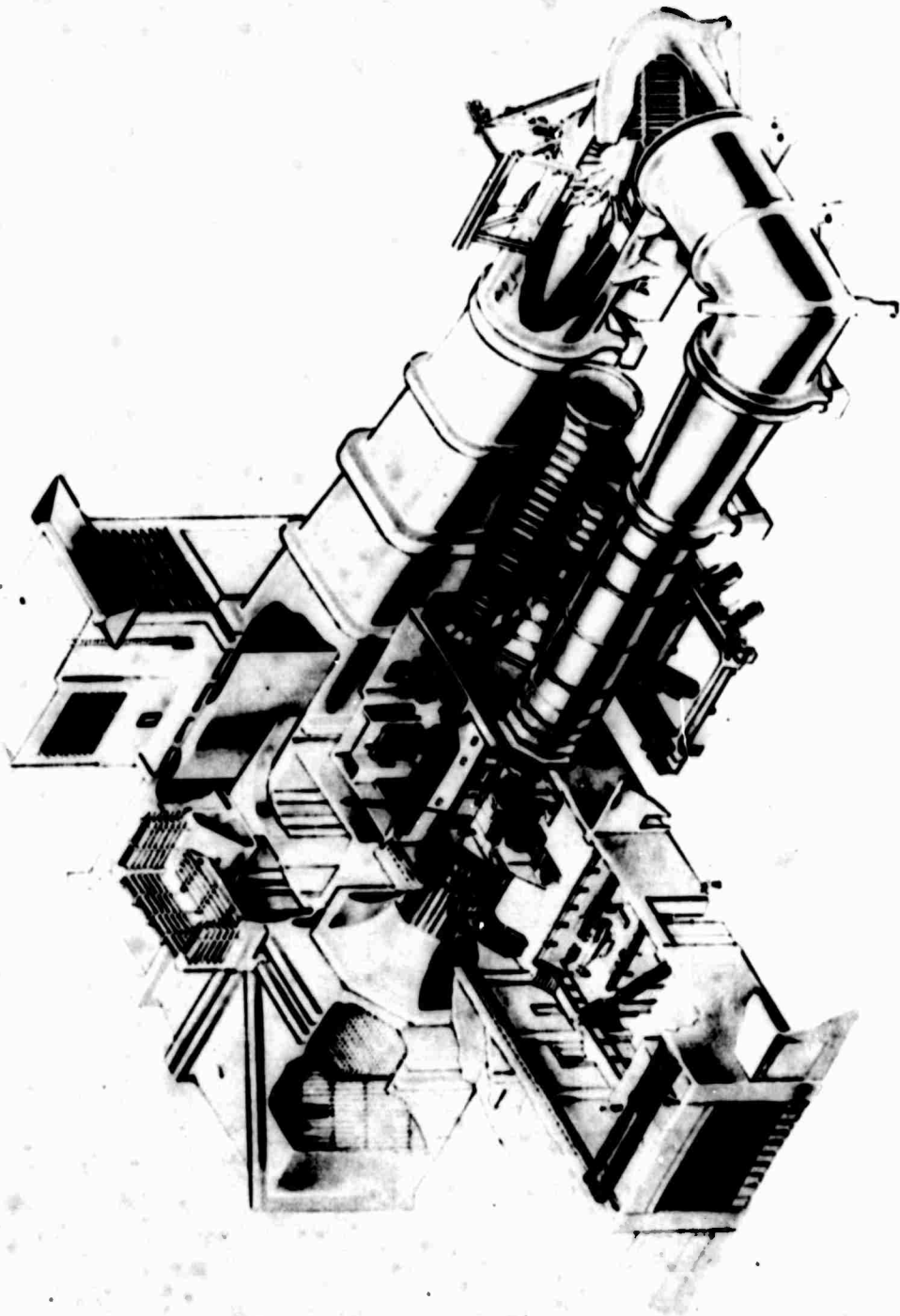
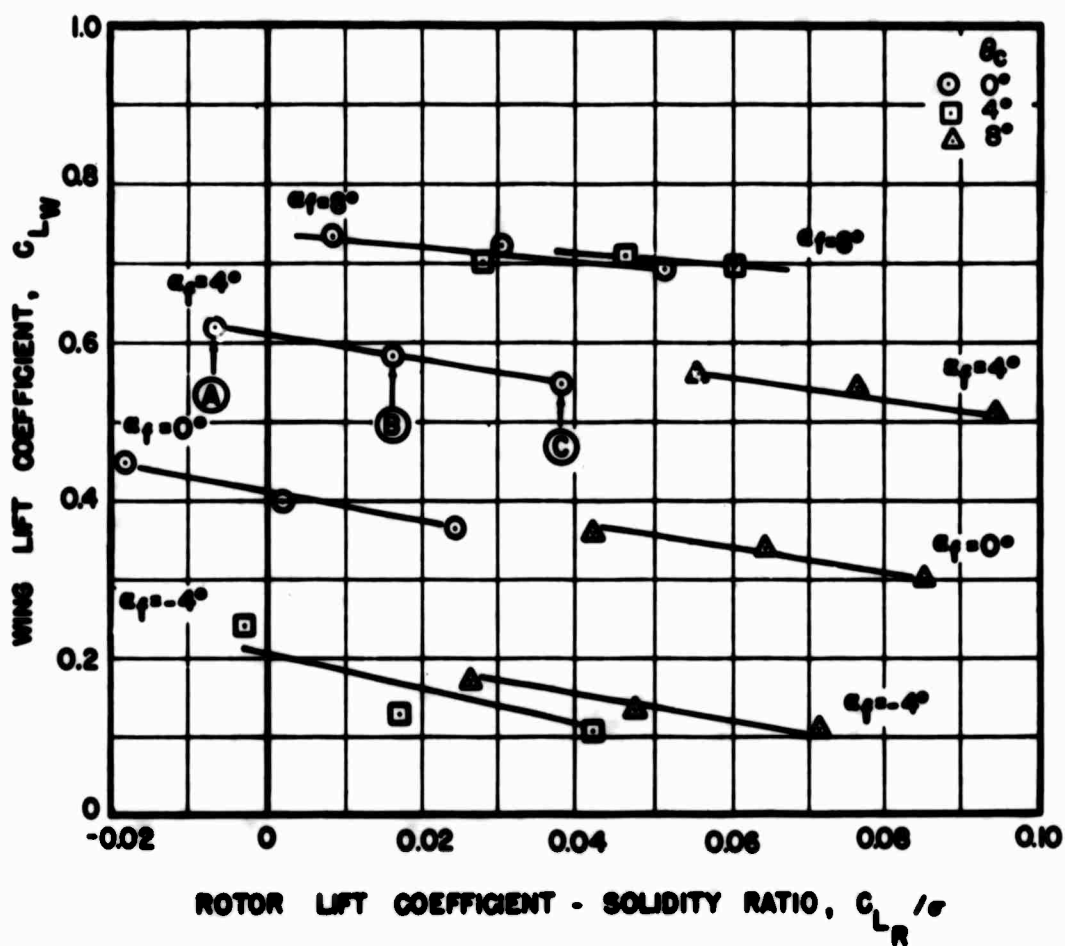


Figure 4. United Aircraft Subsonic Wind Tunnel.

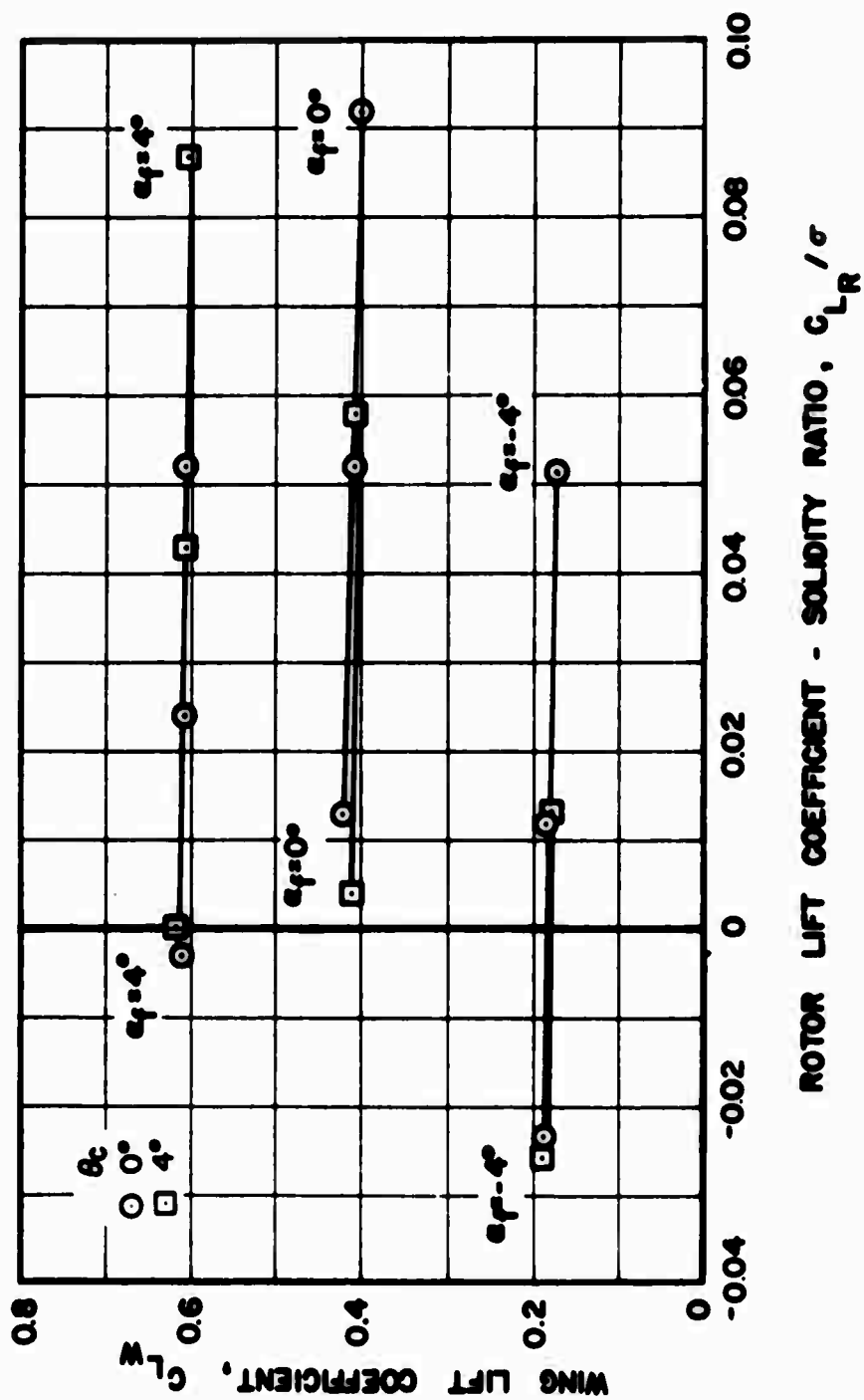


Figure 5. Isolated Propeller Test Fixture.



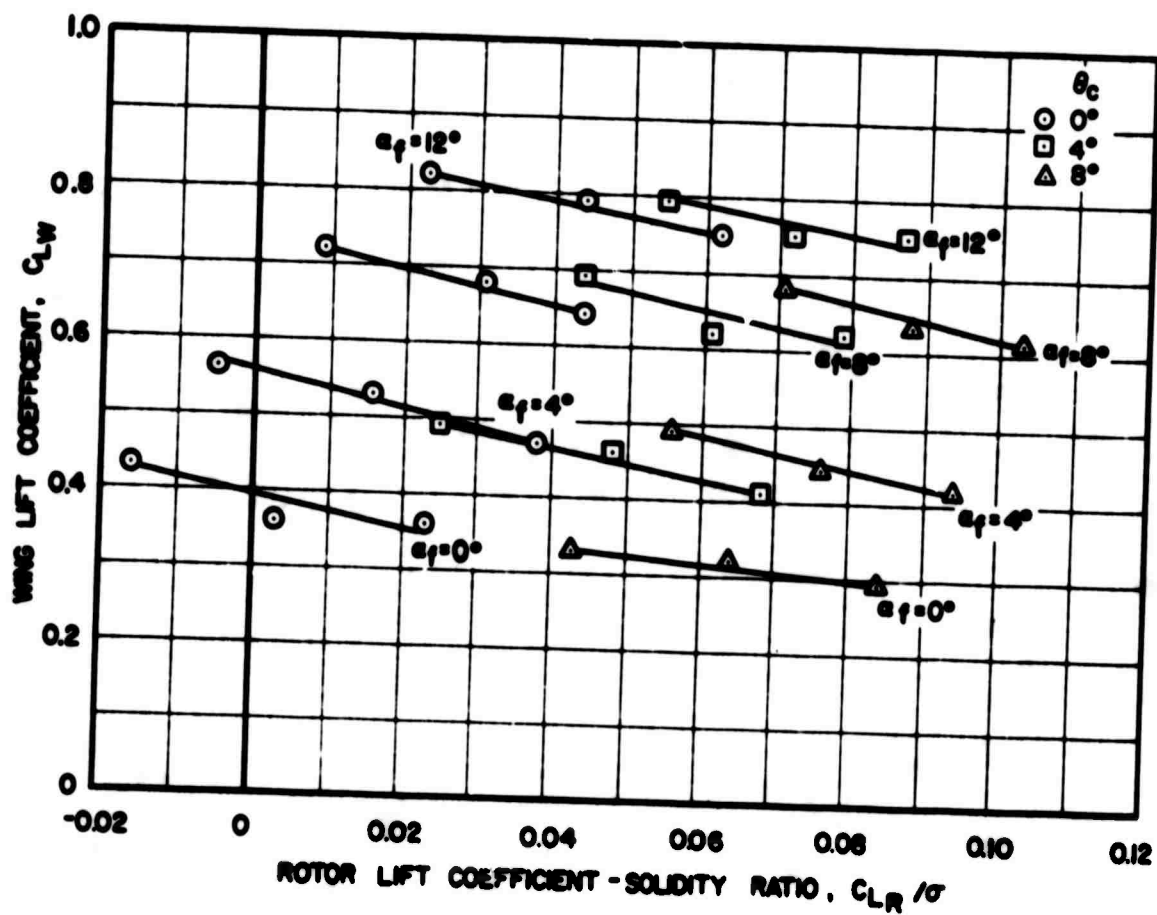
(a) Medium Wing, Mid Position, $V_s = 120$ Knots

Figure 6. Effect of Rotor Lift on Wing Lift for Various Wing Sizes and Positions, Forward Speeds, and Fuselage Angles of Attack.



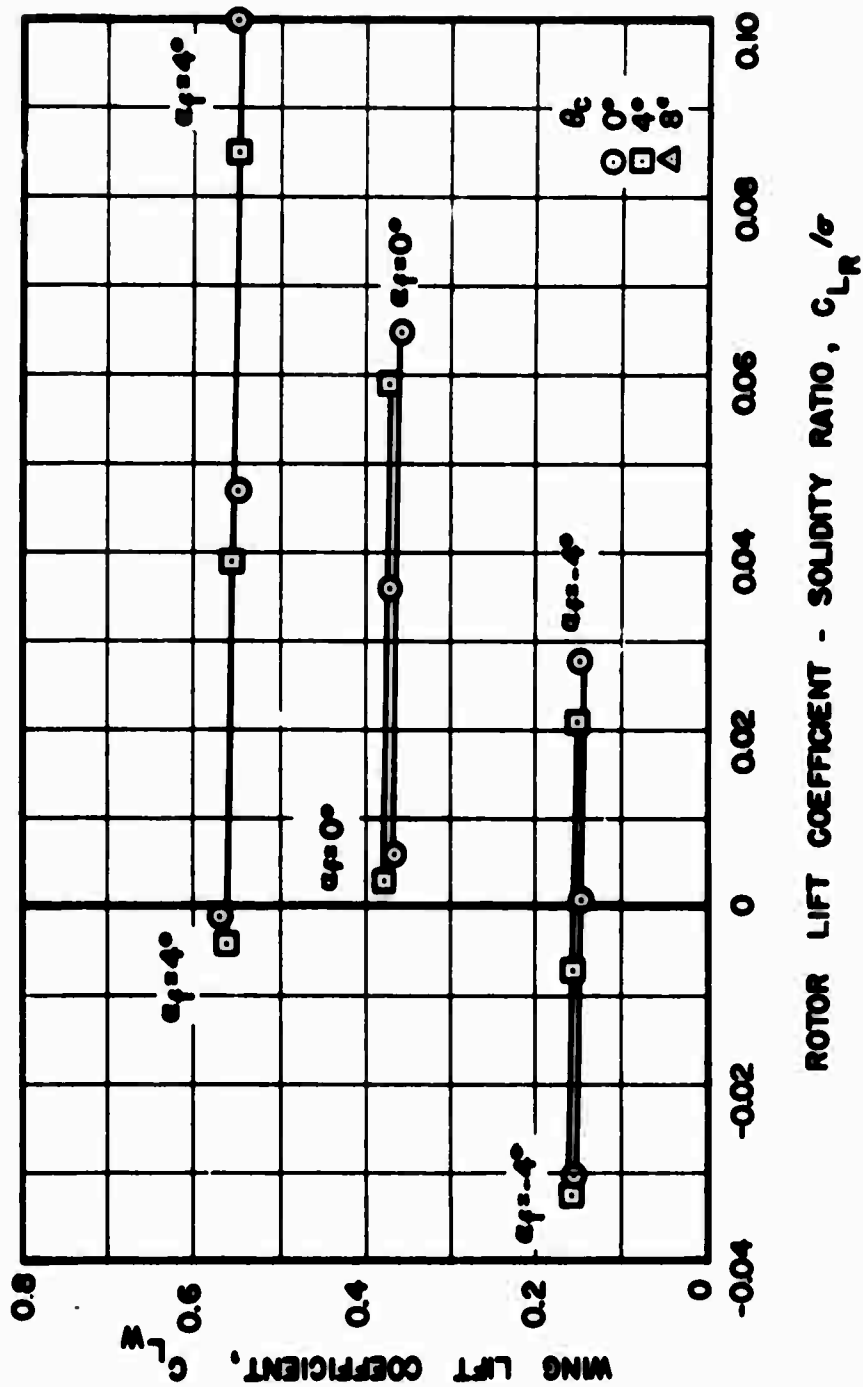
(b) Medium Wing, Mid Position, $V_s = 300$ Knots

Figure 6. Continued.



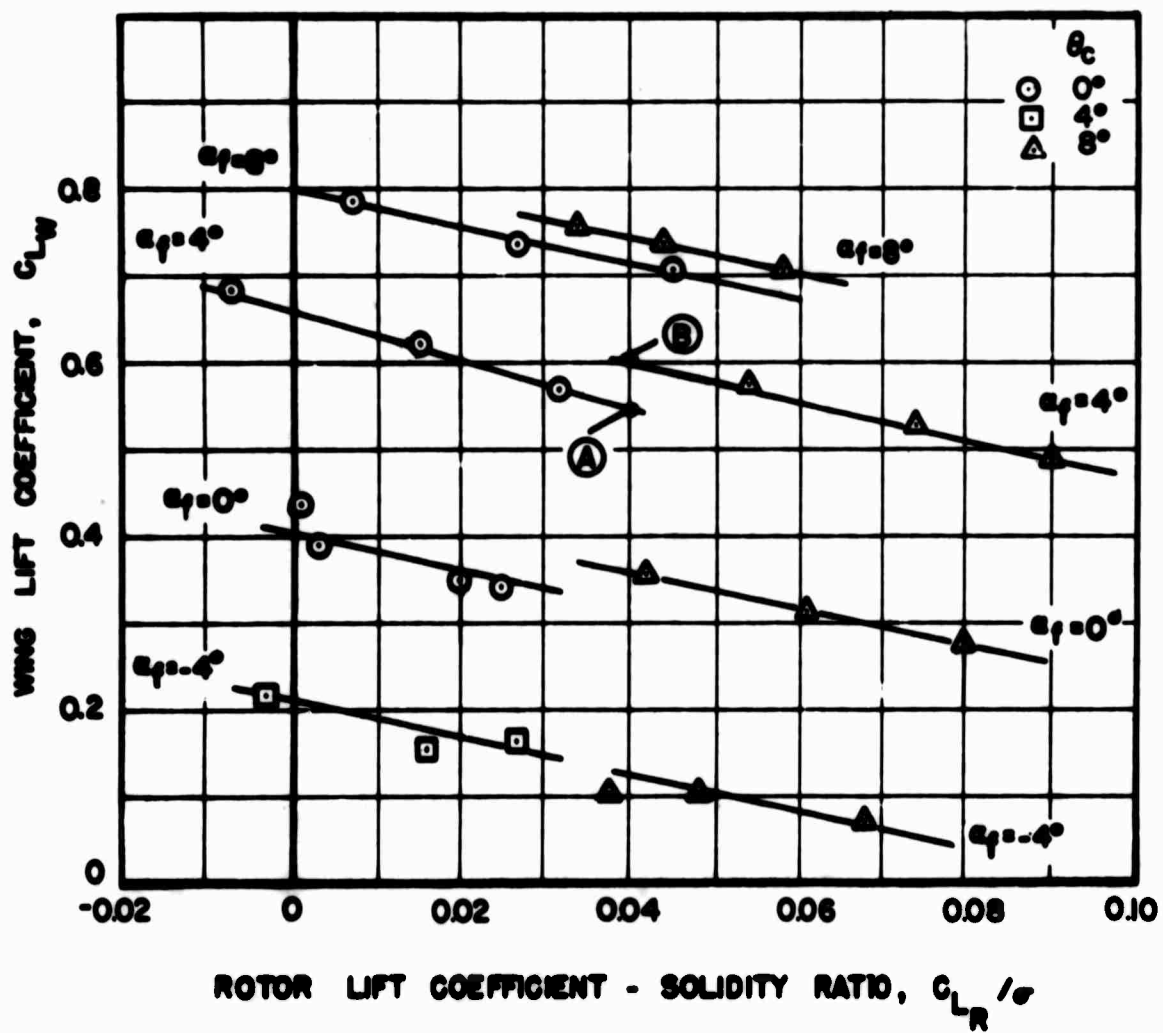
(c) Medium Wing, High Position, $V_s = 120$ Knots

Figure 6. Continued.



(d) Medium Wing, High Position, $V_s = 300$ Knots

Figure 6. Continued.



(e) Large Wing, High Position, $V_s = 120$ Knots

Figure 6. Concluded.

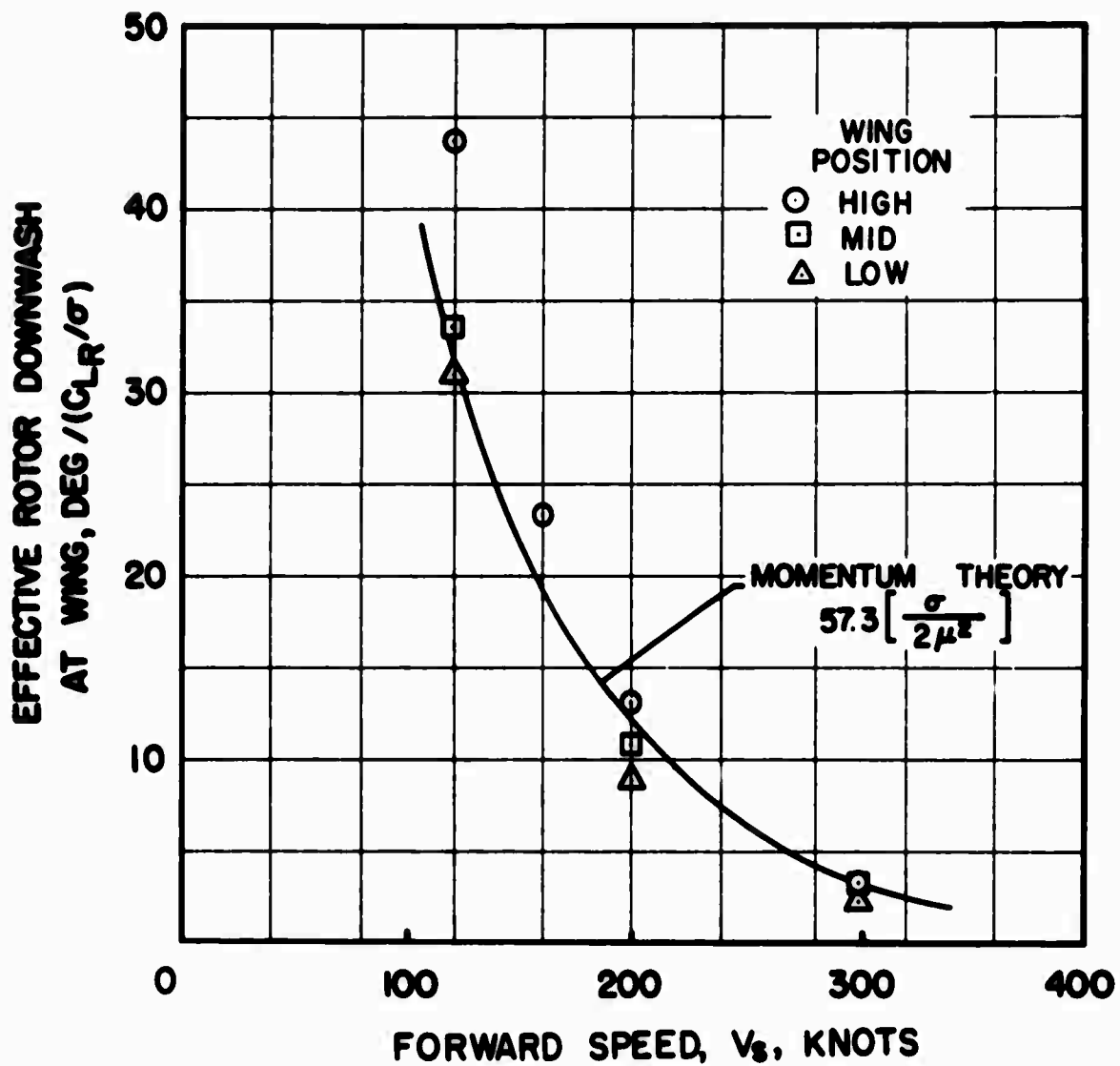


Figure 7. Effect of Forward Speed on Effective Rotor Downwash Angle for the Large Wing at Various Wing Positions.

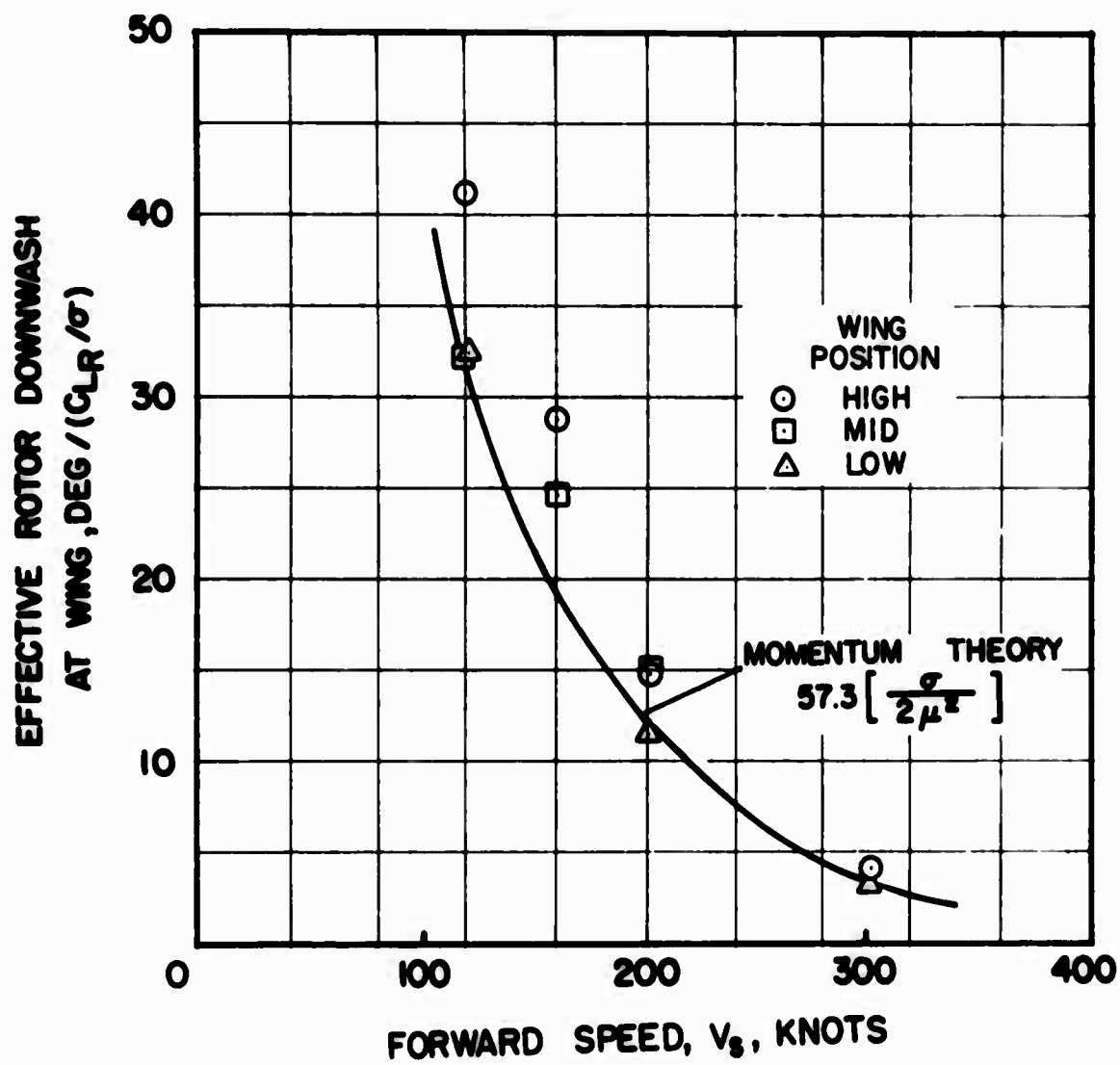


Figure 8. Effect of Forward Speed on Effective Rotor Downwash Angle for the Medium Wing at Various Wing Positions.

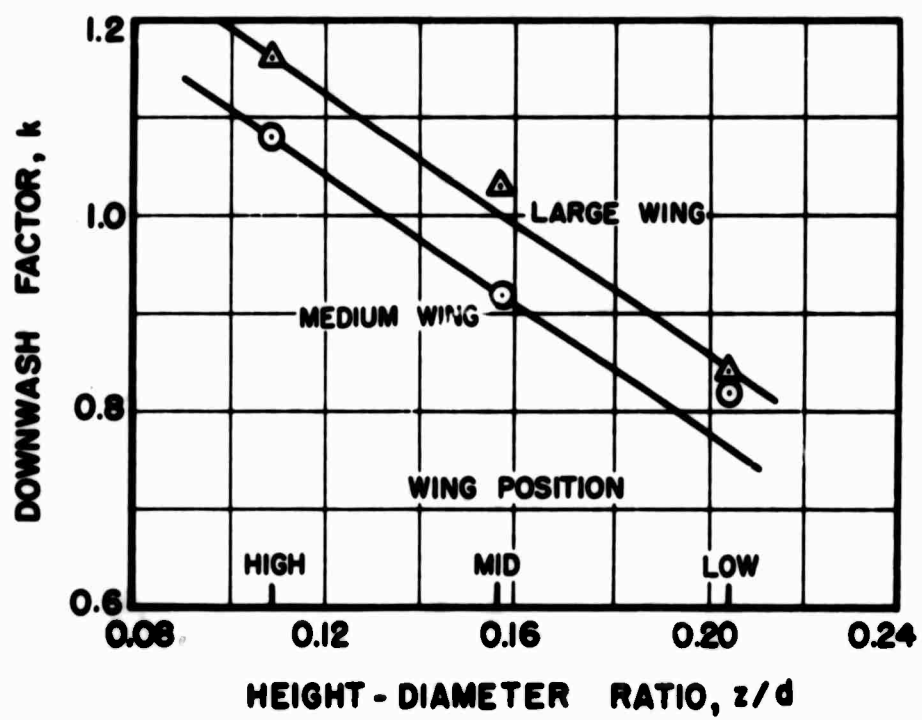
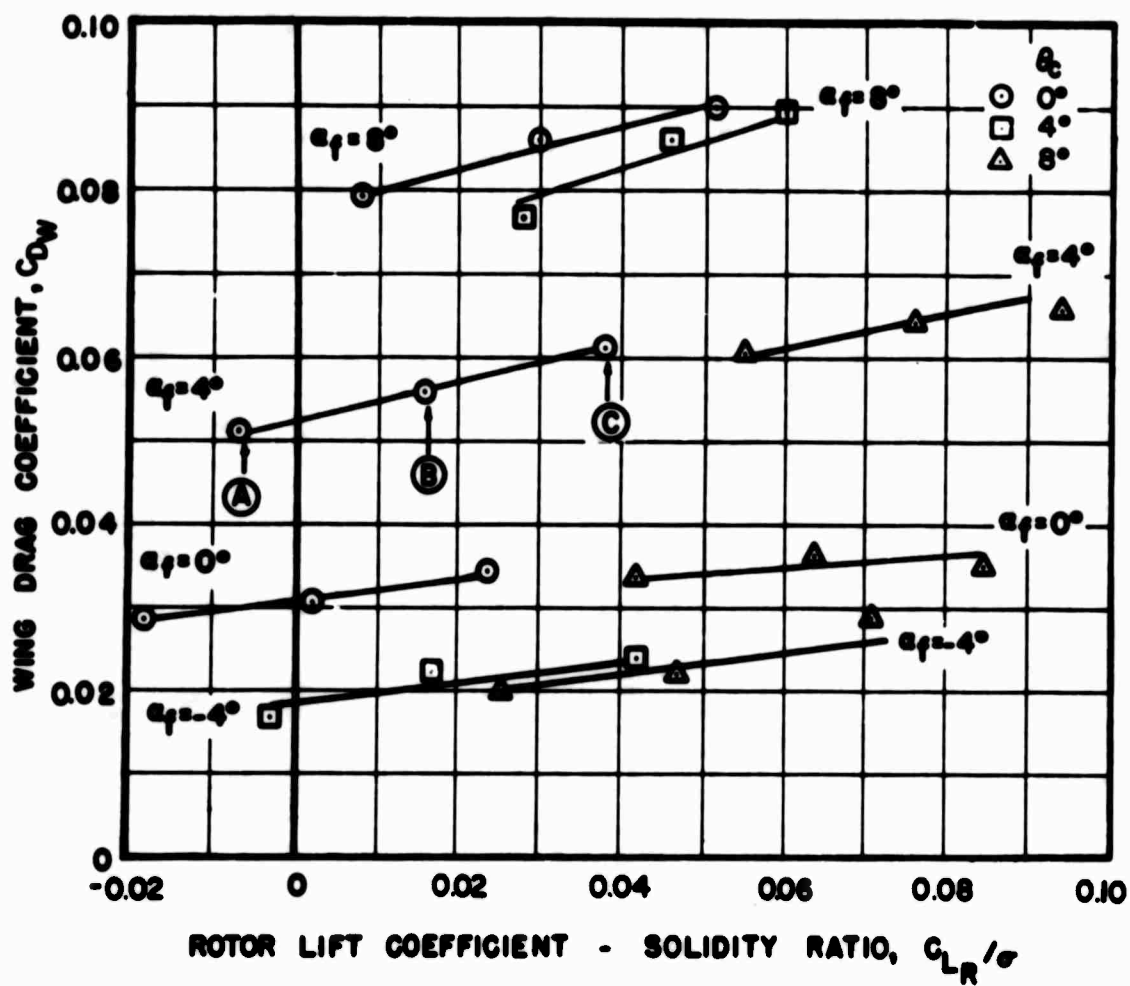
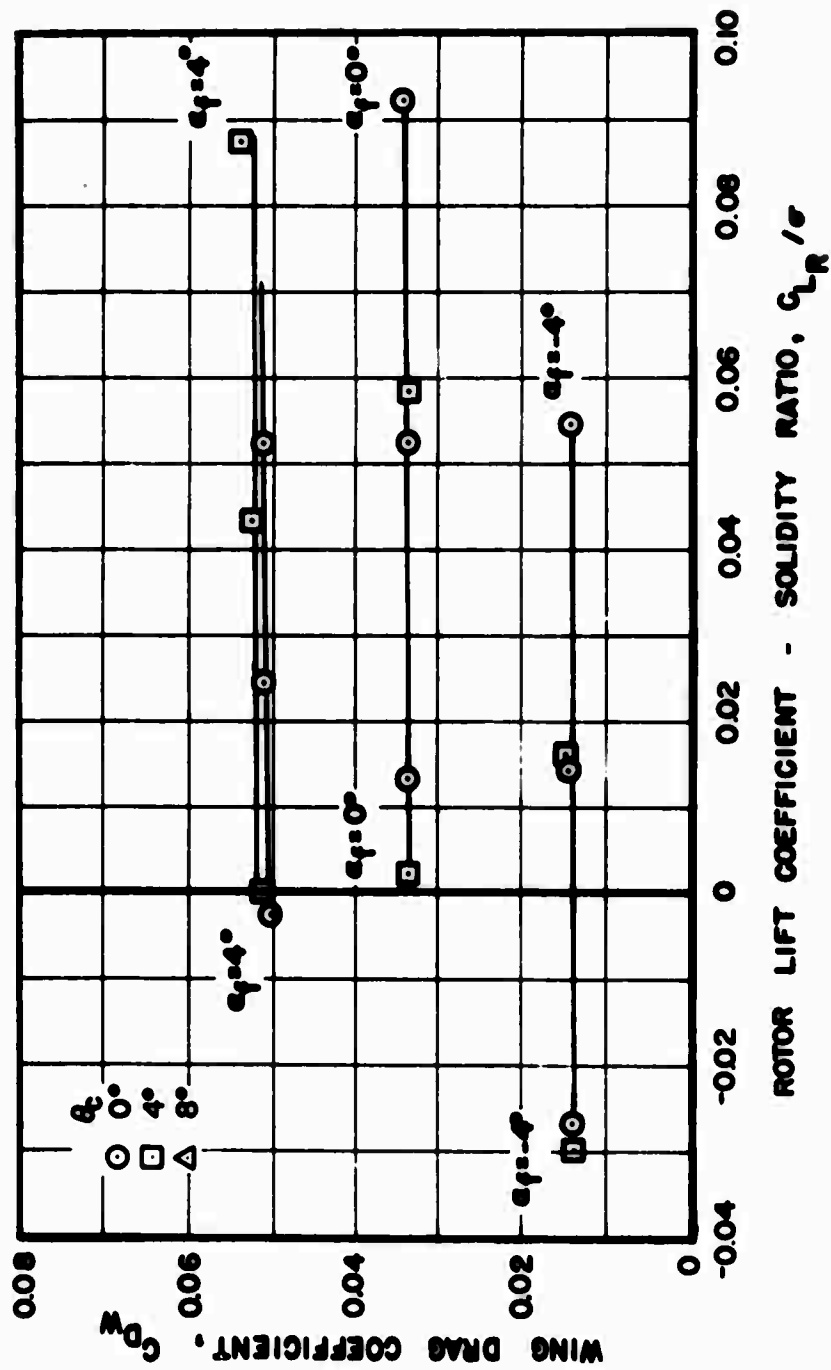


Figure 9. Effect of Wing Position on Downwash Factor for the Large and Medium Wings.



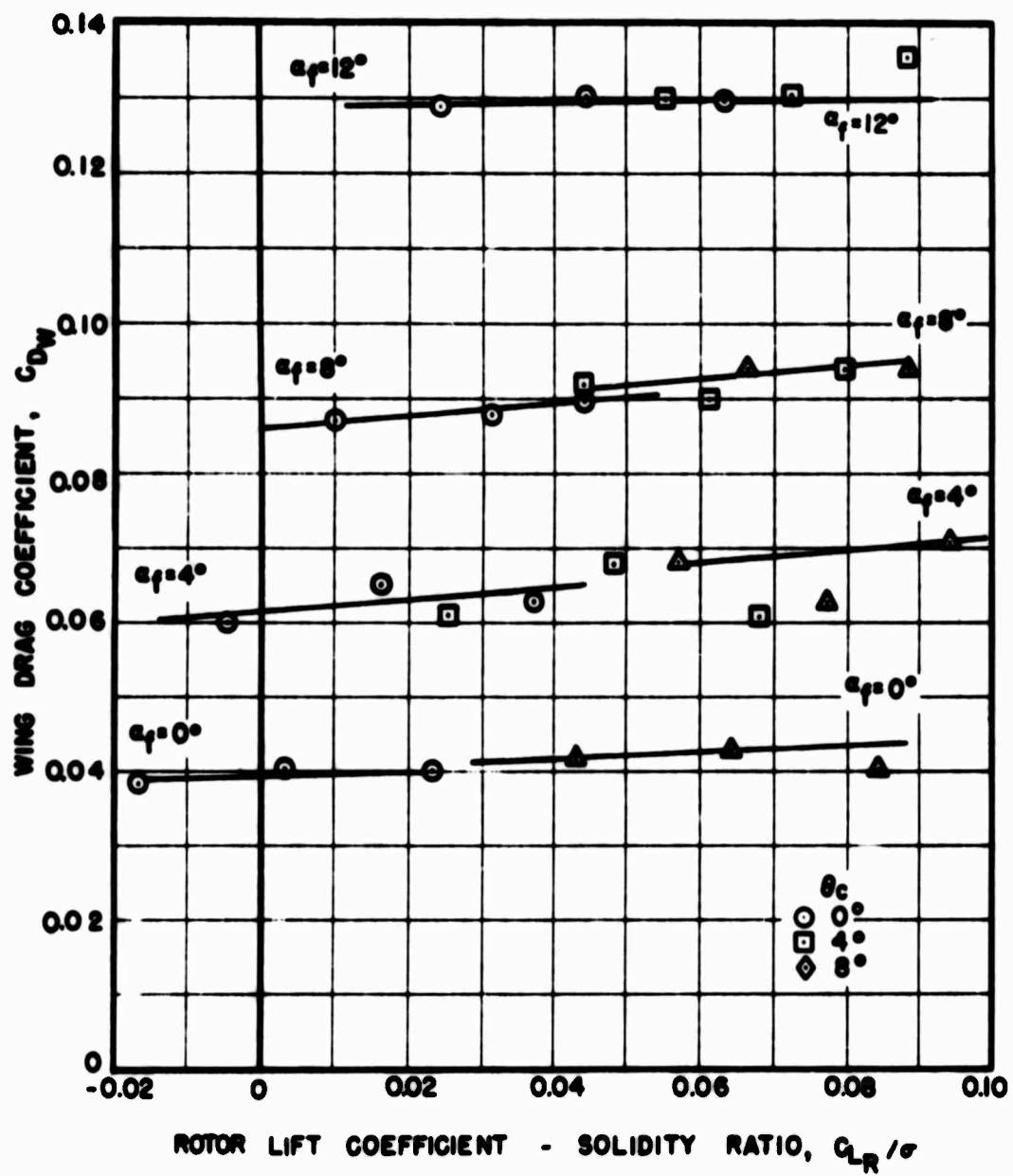
(a) Medium Wing, Mid Position, $V_s = 120$ Knots

Figure 10. Effect of Rotor Lift on Wing Drag for Various Wing Sizes and Positions, Forward Speeds, and Fuselage Angles of Attack.



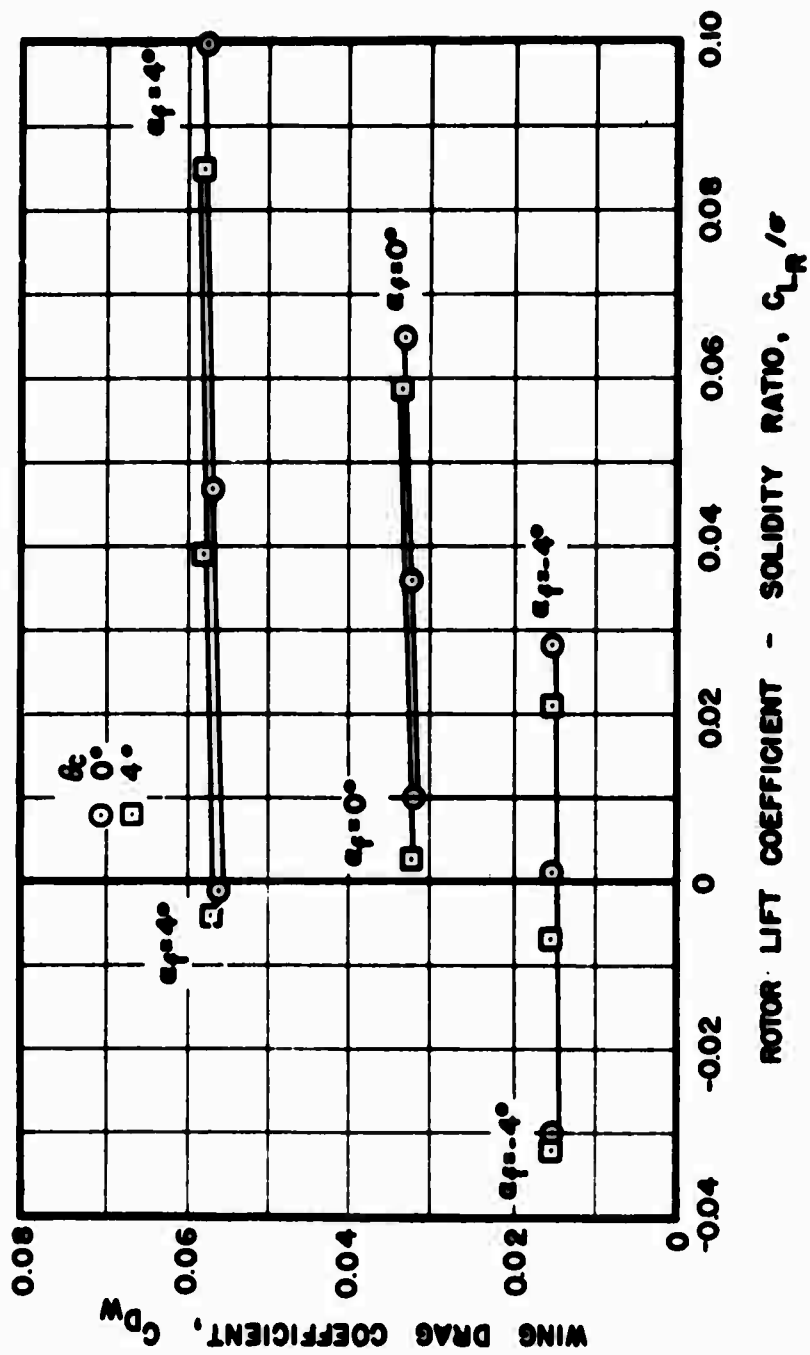
(b) Medium Wing, Mid Position, $V_s = 300$ Knots

Figure 10. Continued.



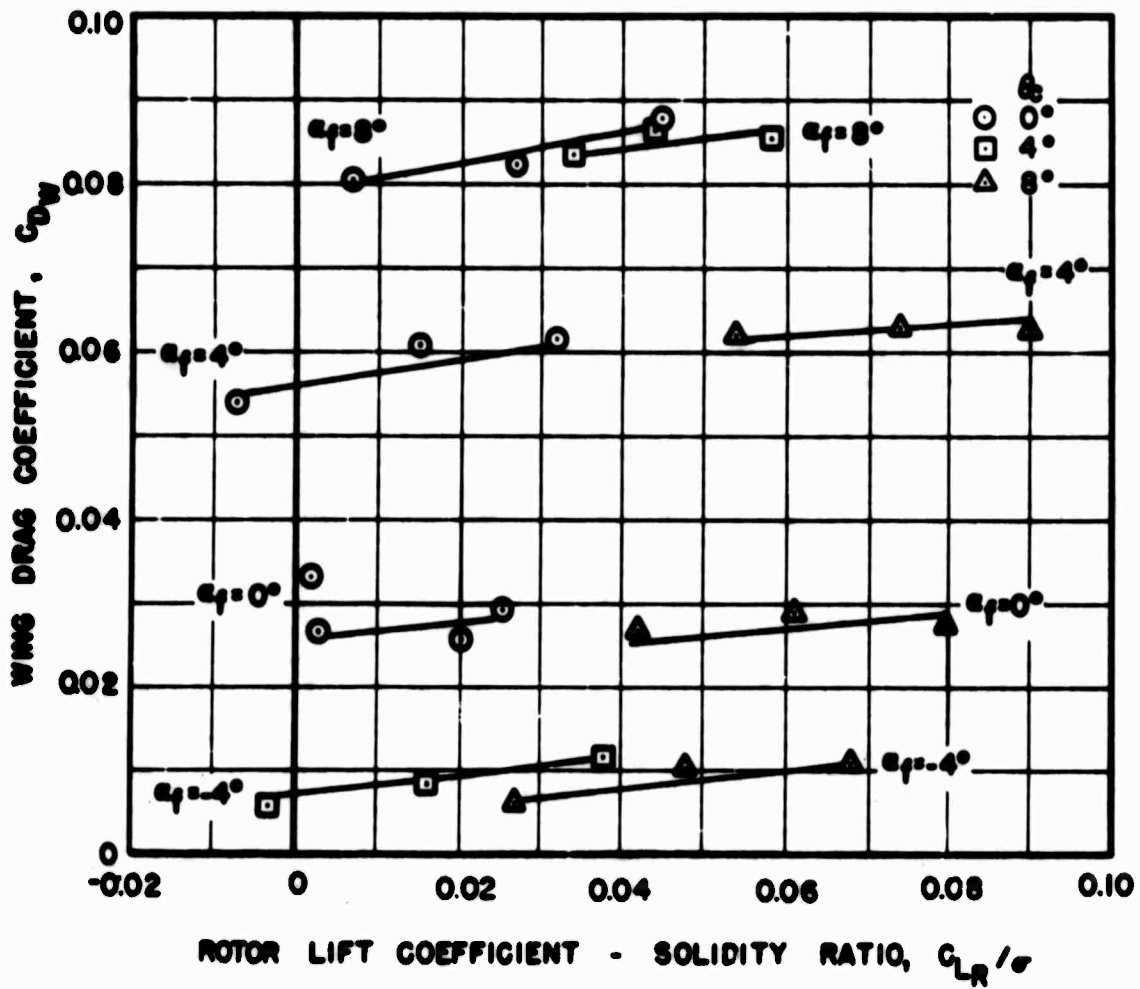
(c) Medium Wing, High Position, $V_s = 120$ Knots

Figure 10. Continued.



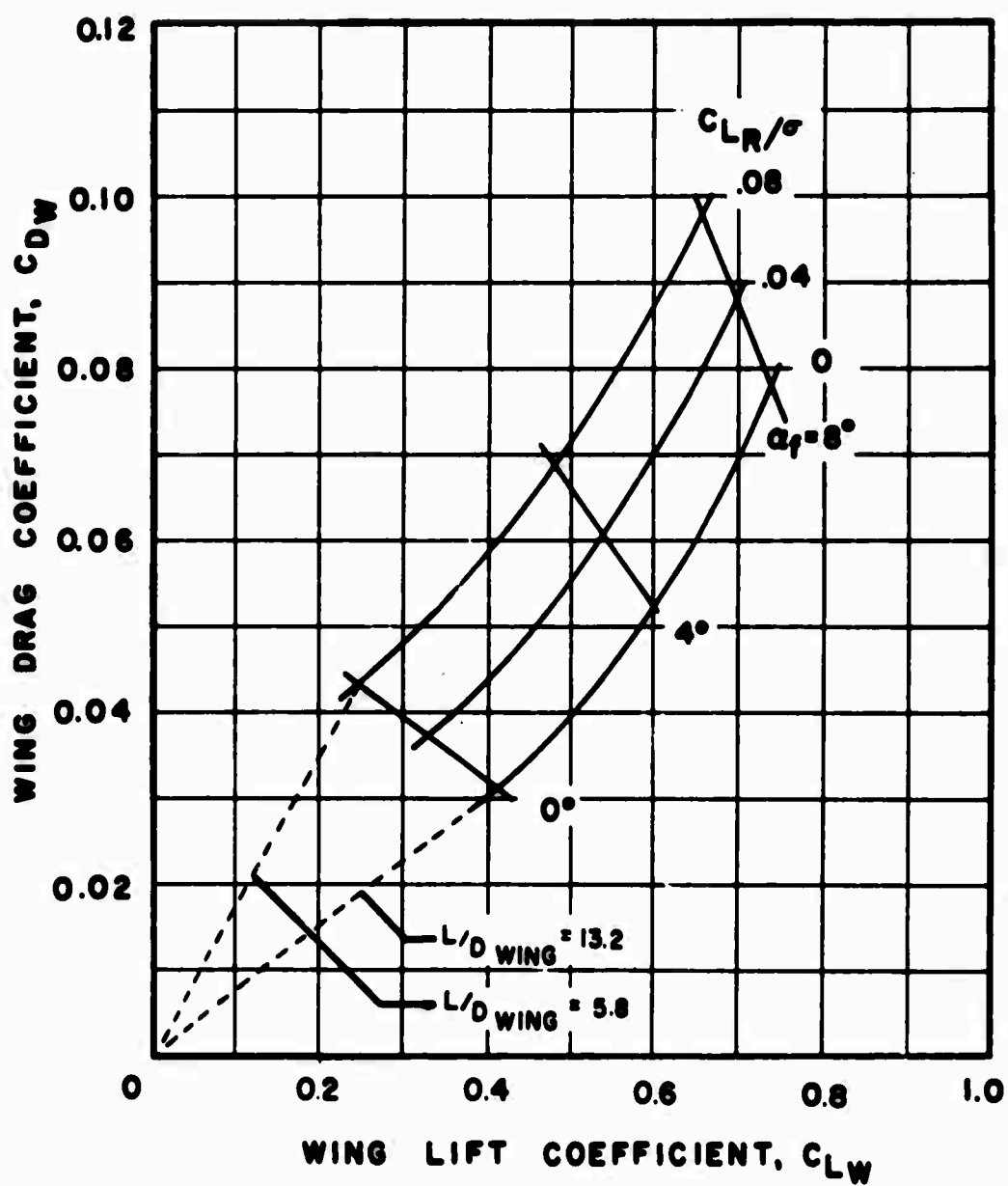
(d) Medium Wing, High Position, $V_s = 300$ Knots

Figure 10. Continued.



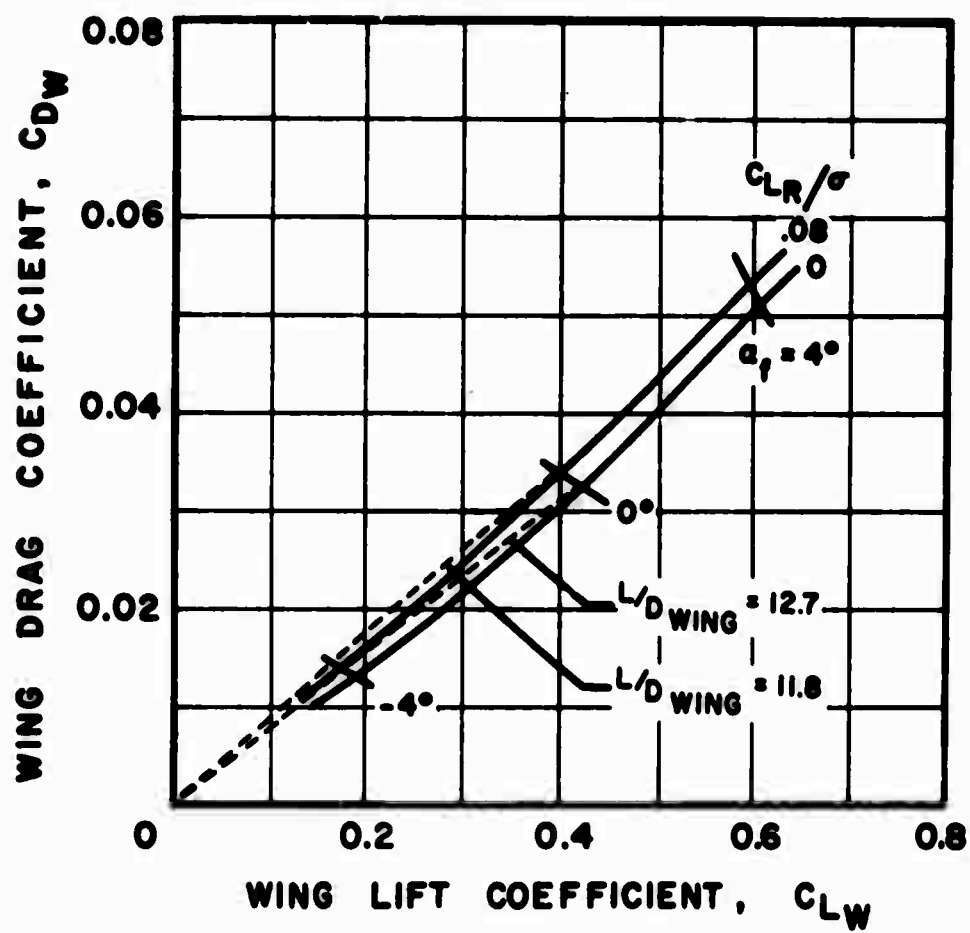
(e) Large Wing, High Position, $V_s = 120$ Knots

Figure 10. Concluded.



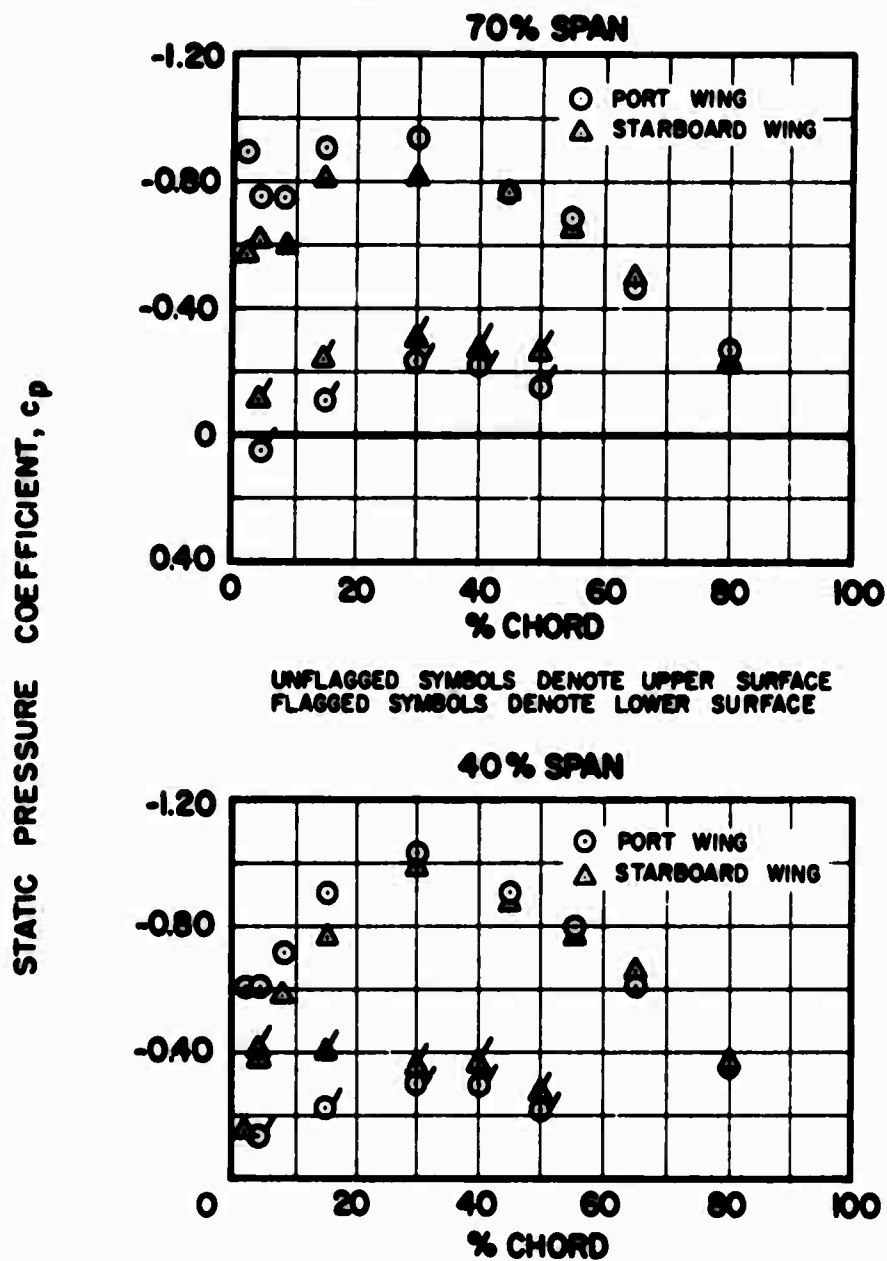
(a) $V_s = 120$ Knots

Figure 11. Effect of Rotor Lift and Fuselage Angle of Attack on Wing Lift and Drag for the Medium Wing, Mid Position at Two Forward Speeds.



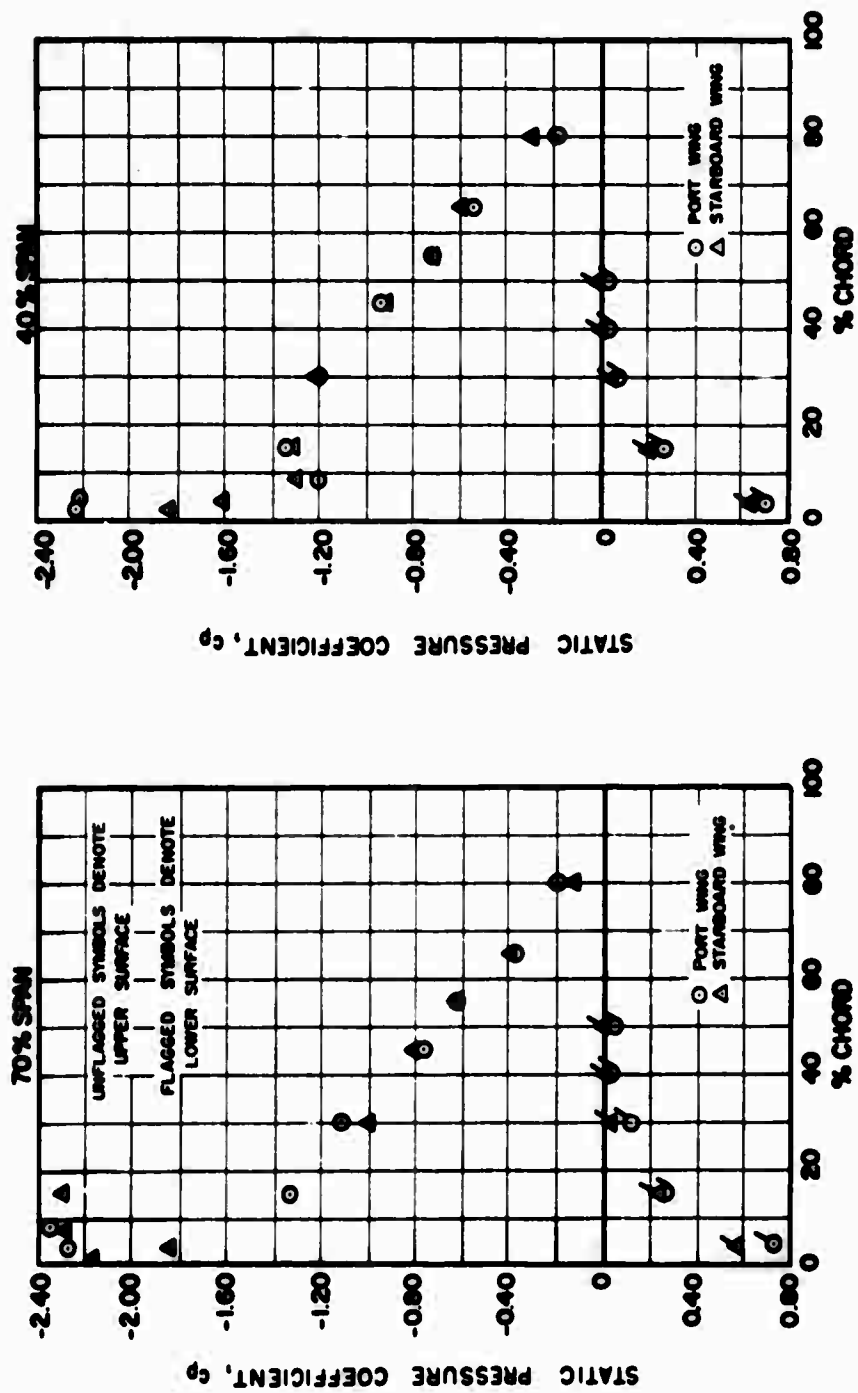
(b) $V_s = 300$ Knots

Figure 11. Concluded.



(a) $\alpha_f = 0^\circ$, $\theta_c = 4^\circ$, $C_{LR}/\sigma = 0.016$

Figure 12. Chordwise Wing Static Pressure Distributions for the Medium Wing, High Position, $V_s = 120$ Knots at Two Spanwise Locations and Two Rotor Lift Conditions.



(b) $\alpha_f = 8^\circ$, $\theta_c = 0^\circ$, $C_{LR}/\sigma = 0.029$

Figure 12. Concluded.

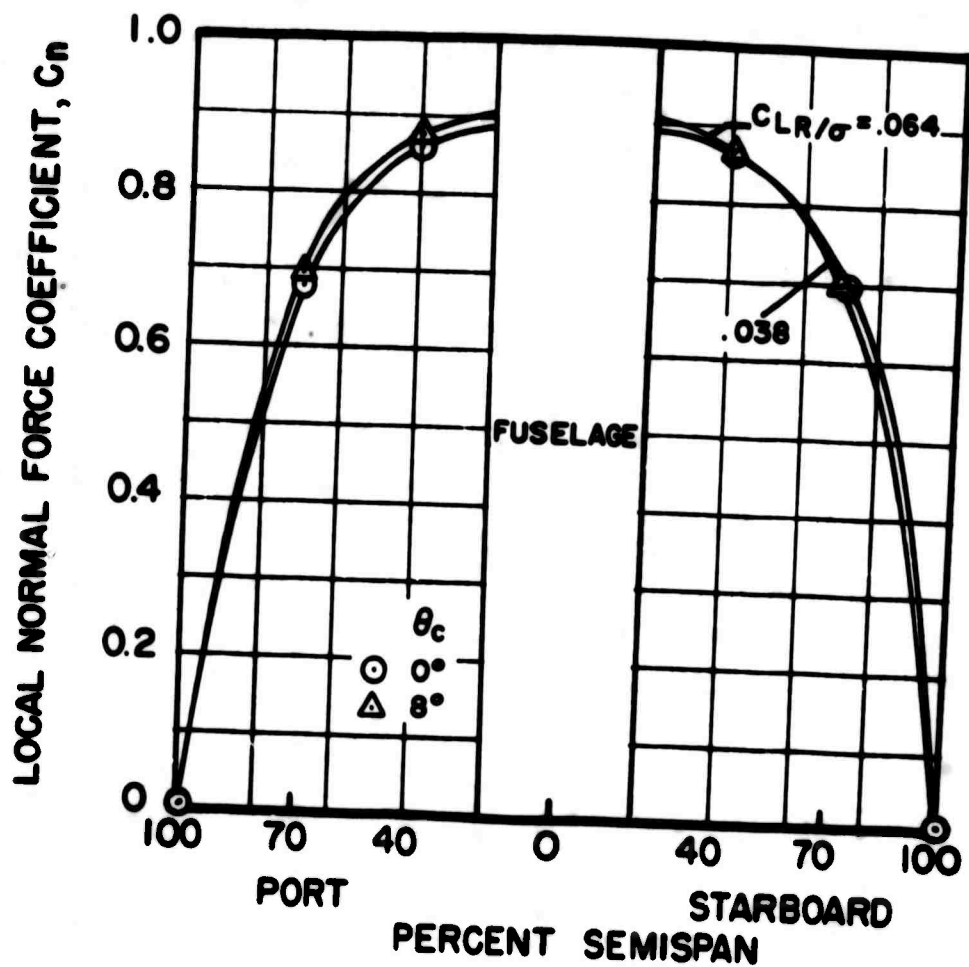


Figure 13. Spanwise Wing Normal Force Coefficient Distributions for the Medium Wing, High Position, $V_s = 200$ Knots, at Two Rotor Lift Conditions and $\alpha_f = 8^\circ$.

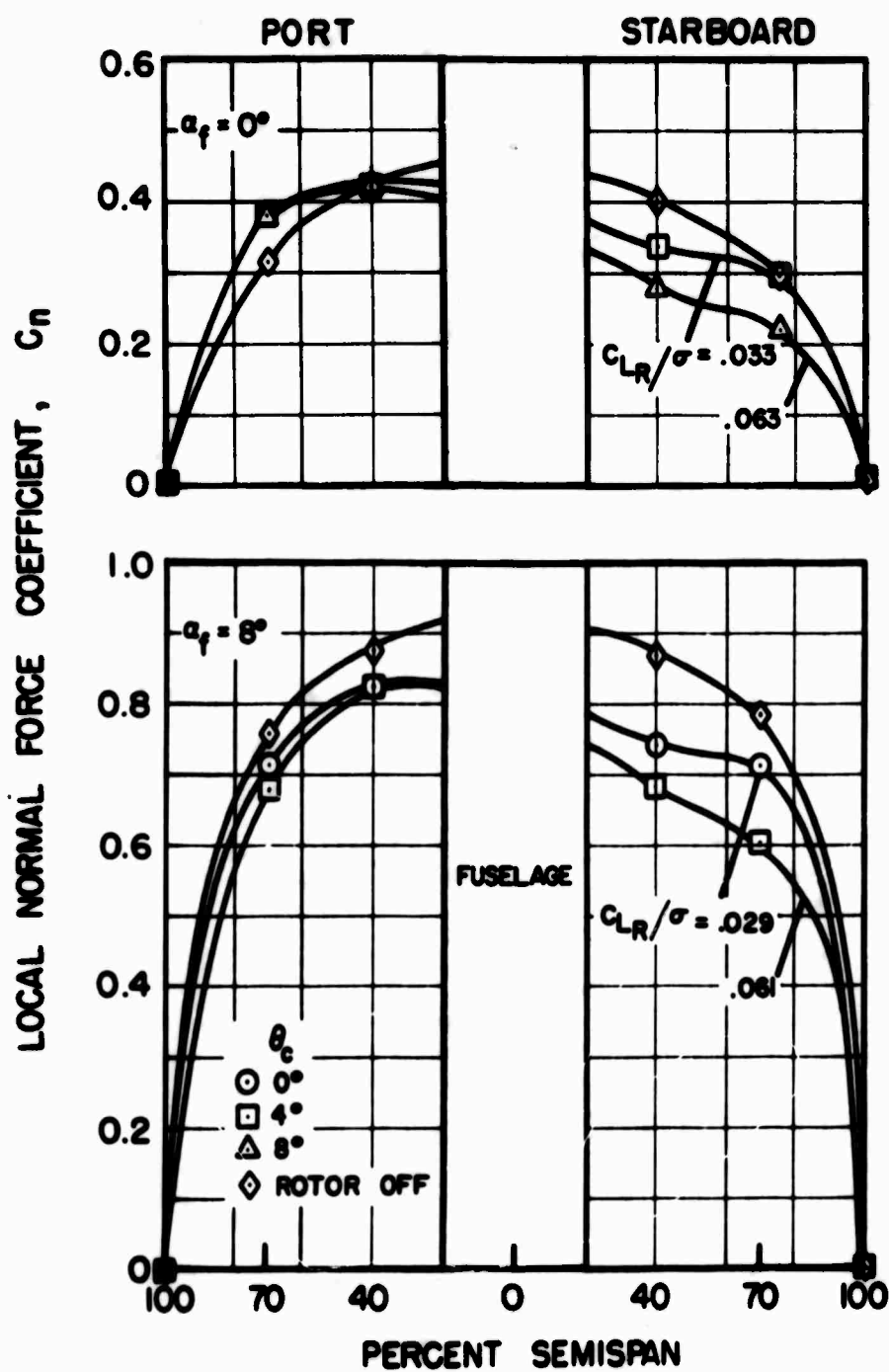


Figure 14. Spanwise Wing Normal Force Coefficient Distributions for the Medium Wing, High Position, $V_s = 120$ Knots, at Two Fuselage Angles of Attack and Various Rotor Lift Conditions.

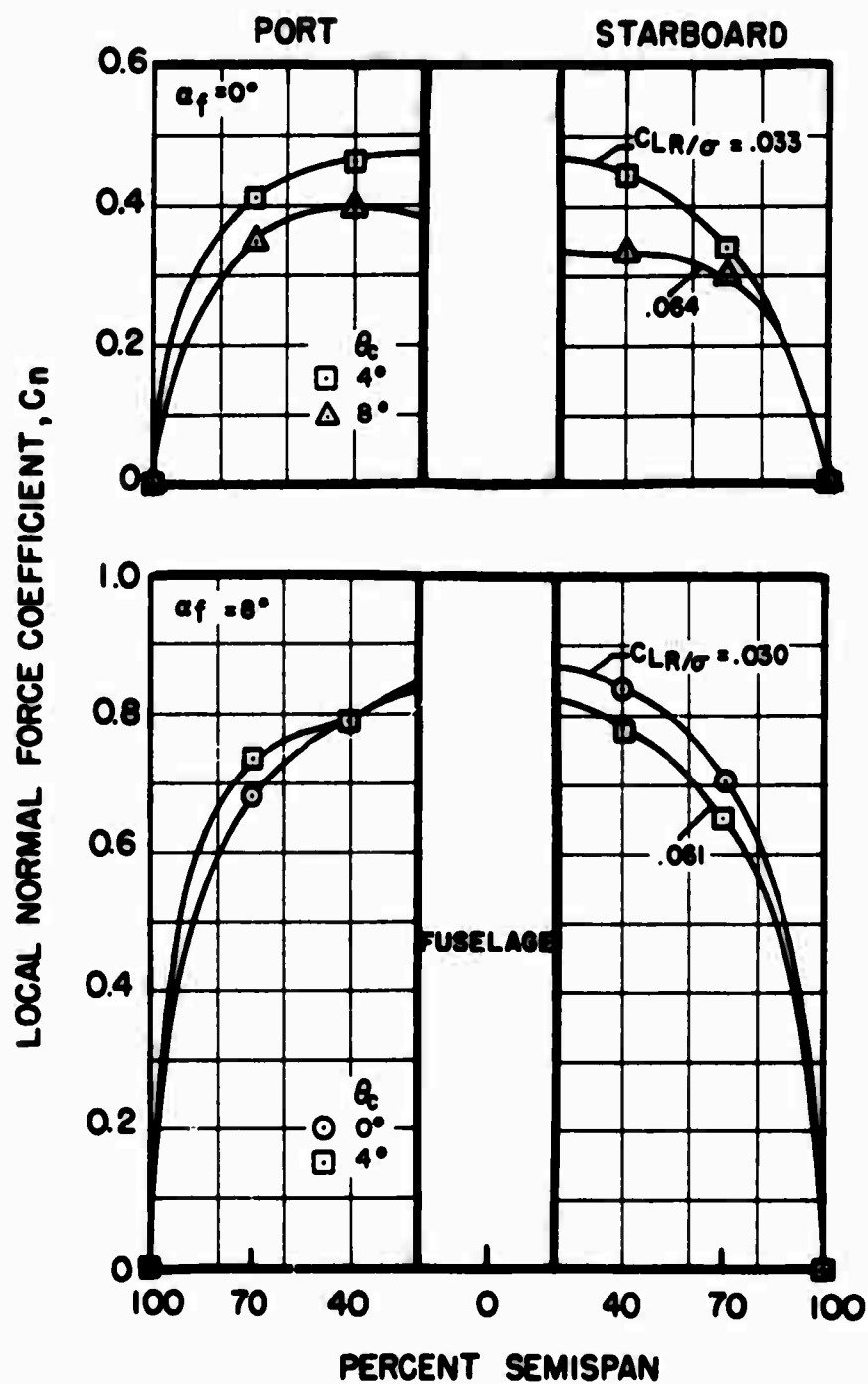


Figure 15. Spanwise Wing Normal Force Coefficient Distributions for the Medium Wing, Mid Position, $V_s = 120$ Knots, at Two Fuselage Angles of Attack and Various Rotor Lift Conditions.

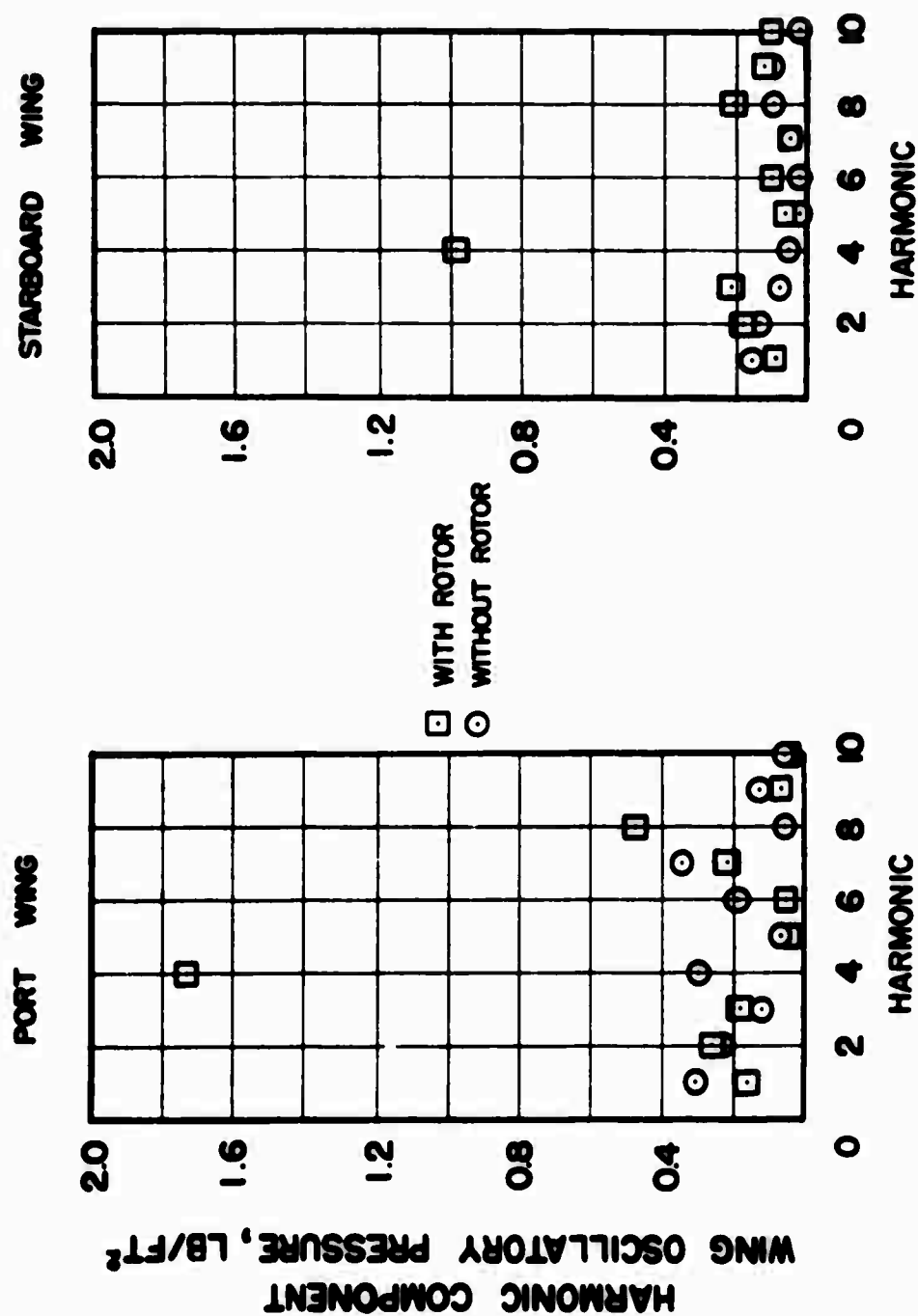
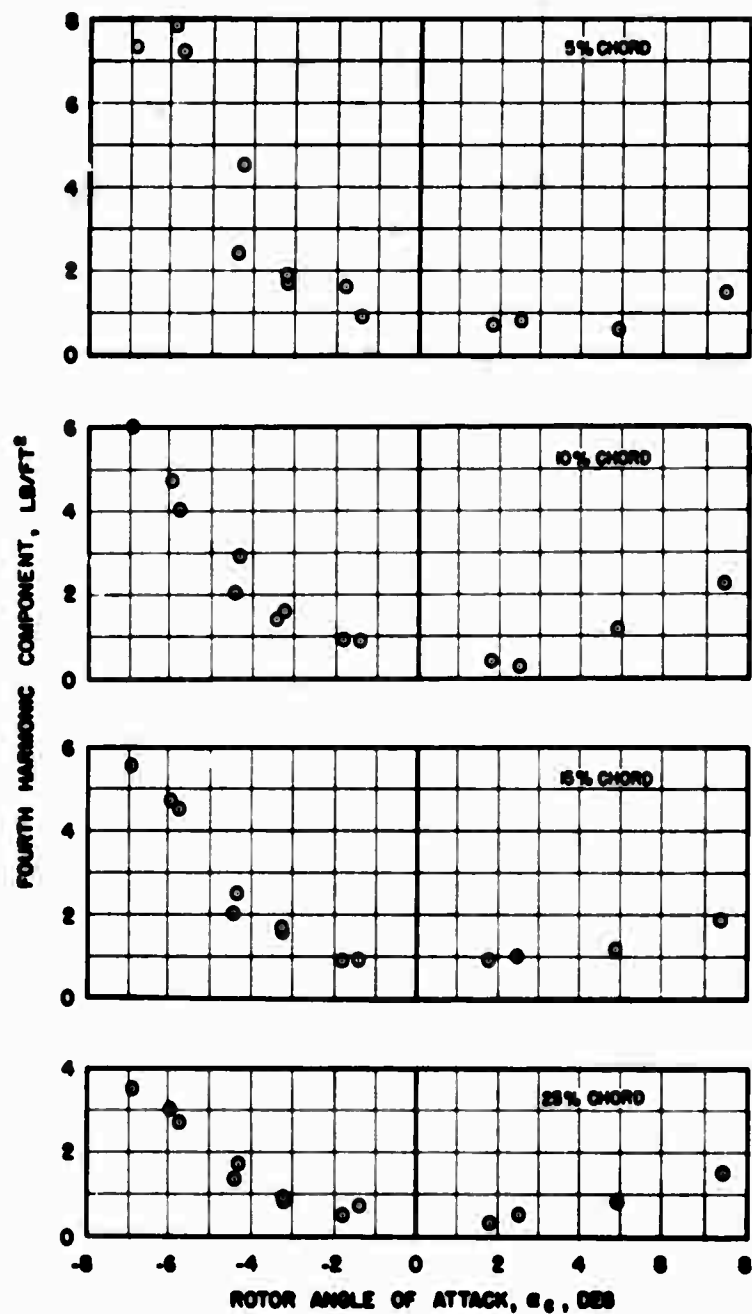
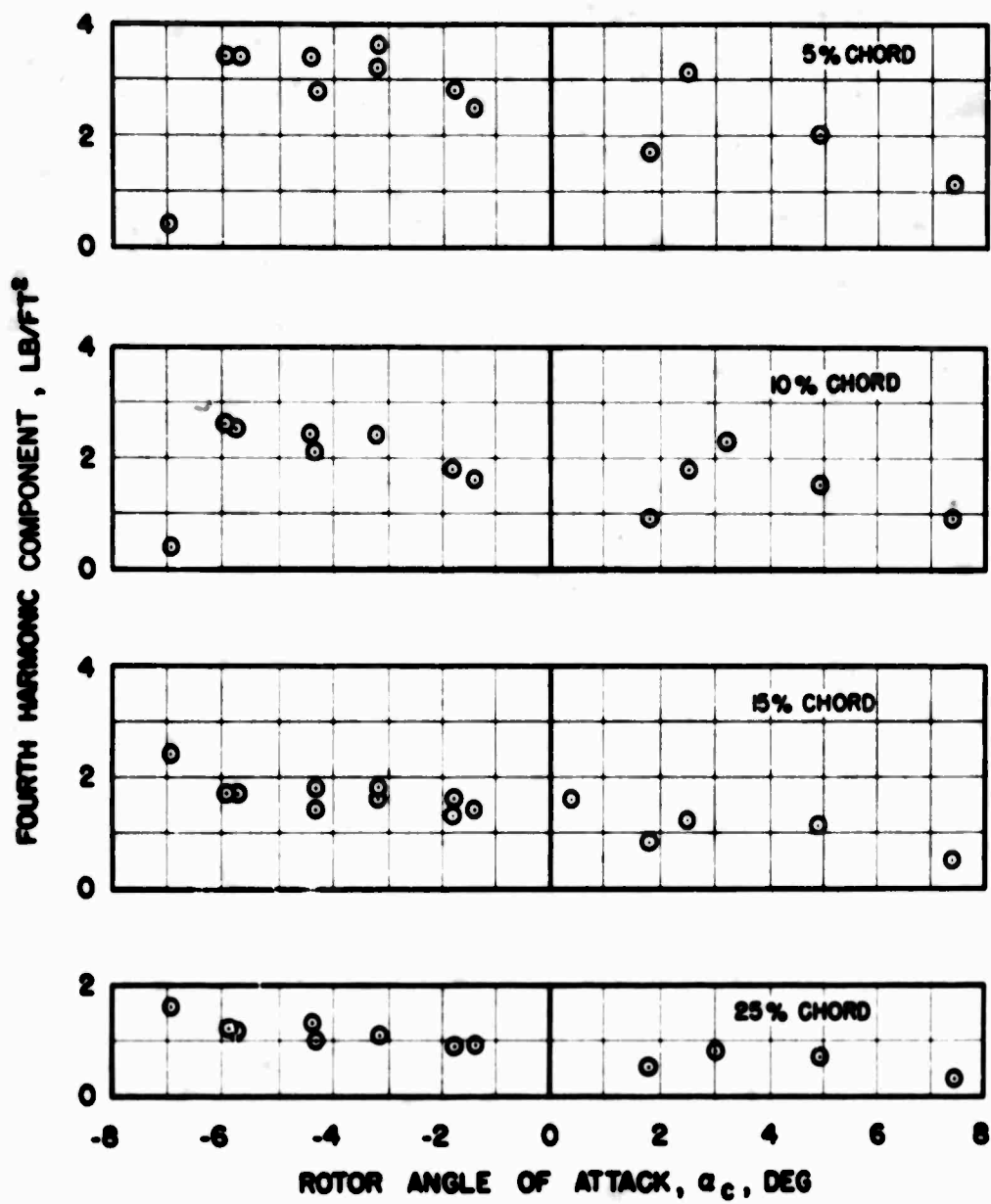


Figure 16. A Sample of Wing Oscillatory Pressure Harmonic Components Taken From Tests With and Without the Rotor on the Medium Wing, High Position, Quarter Chord, $\alpha_f = 0^\circ$, $\theta_c = 4^\circ$, $V_s = 300$ Knots.



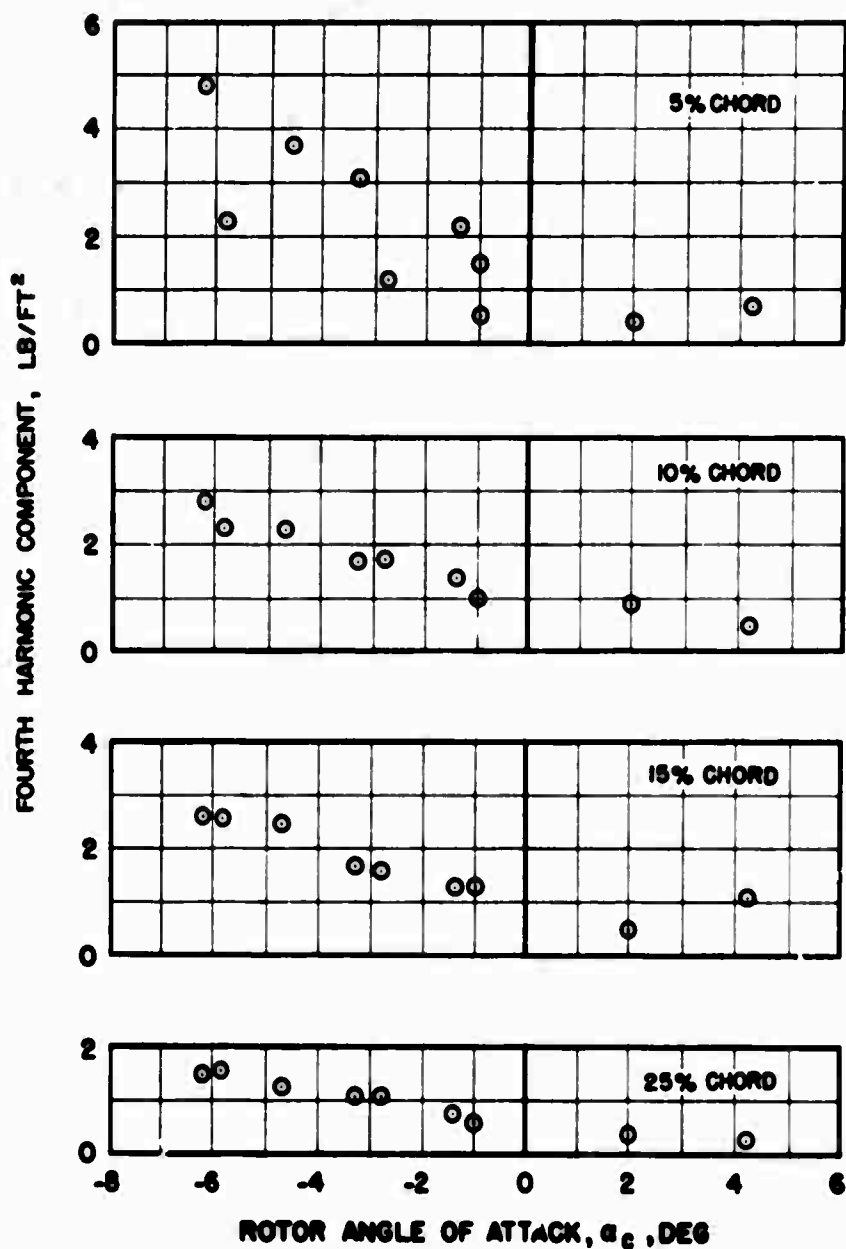
(a) Port

Figure 17. Effect of Rotor Angle of Attack on Fourth Harmonic Oscillatory Wing Pressure at Various Wing Chord Locations for the Medium Wing, High Position, $V_s = 300$ Knots.



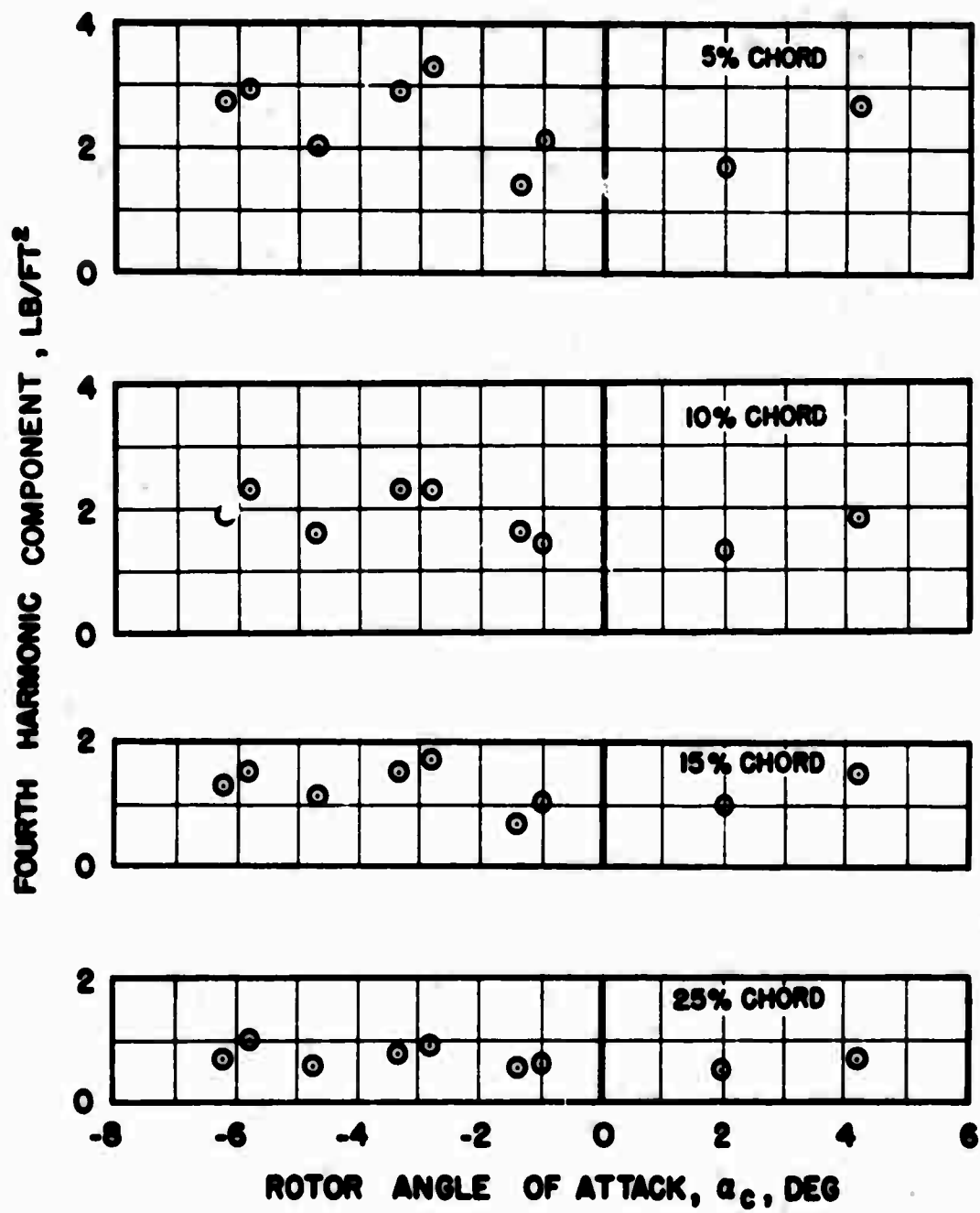
(b) Starboard

Figure 17. Concluded.



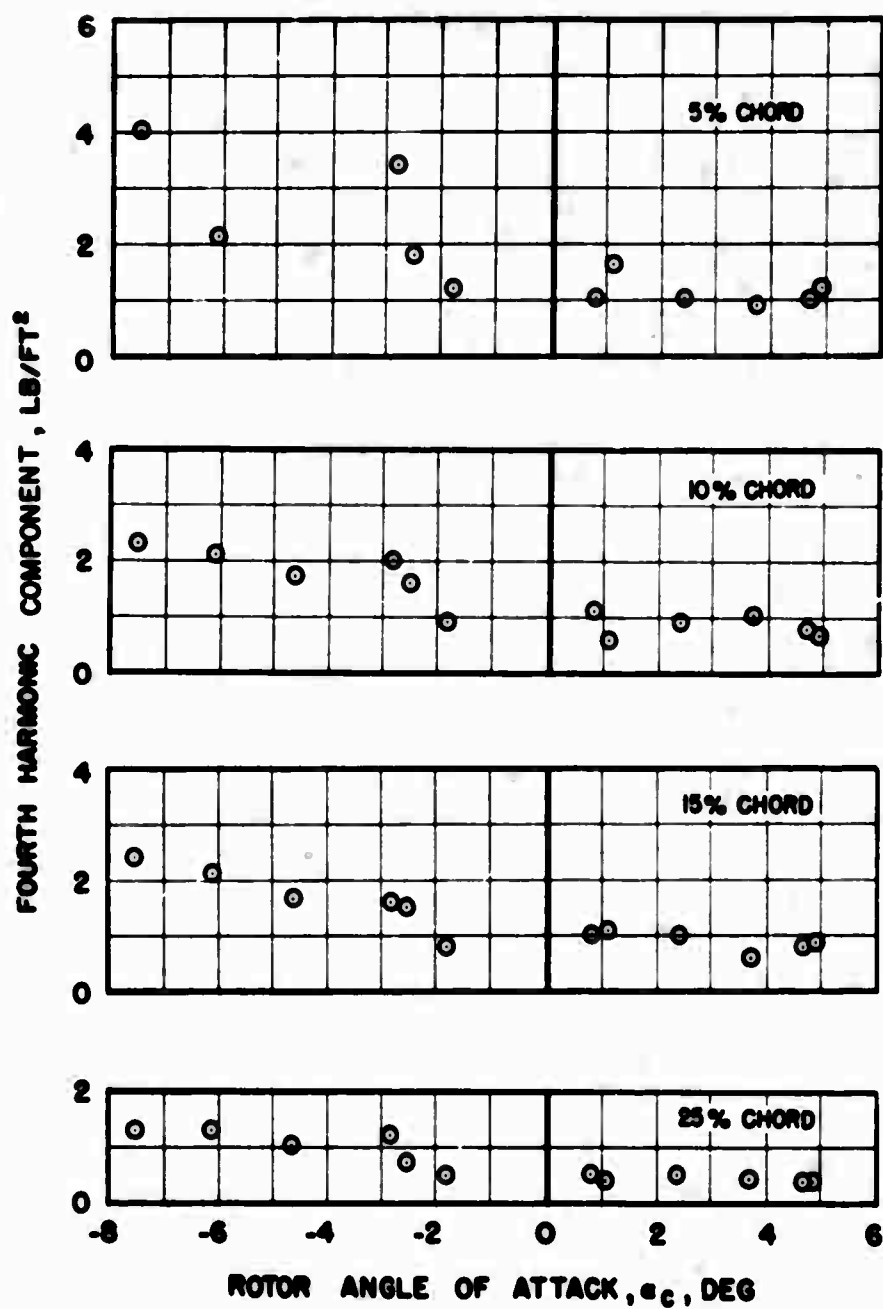
(a) Port

Figure 18. Effect of Rotor Angle of Attack on Fourth Harmonic Oscillatory Wing Pressure at Various Wing Chord Locations for the Medium Wing, Mid Position, $V_5 = 300$ Knots.



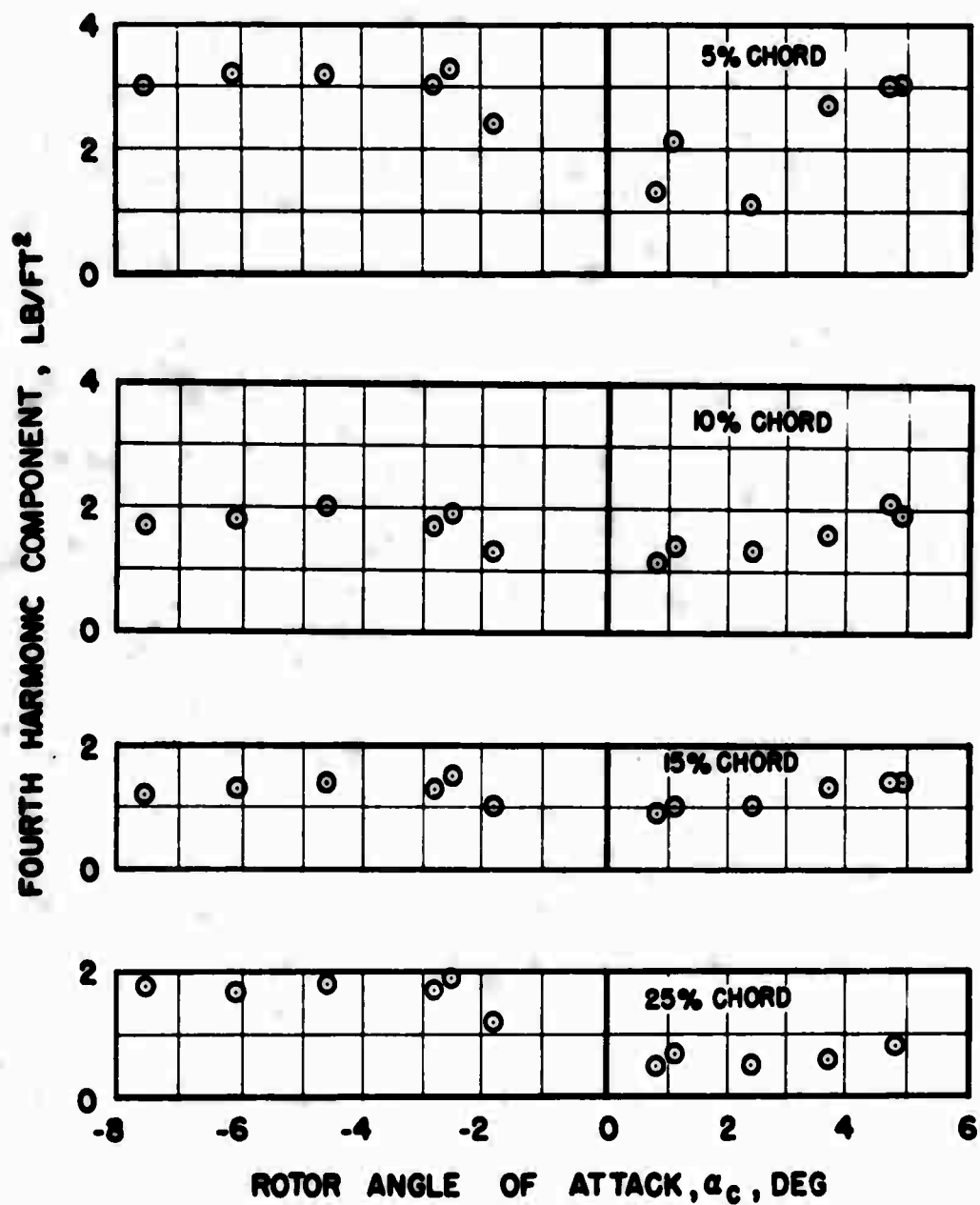
(b) Starboard

Figure 18. Concluded.



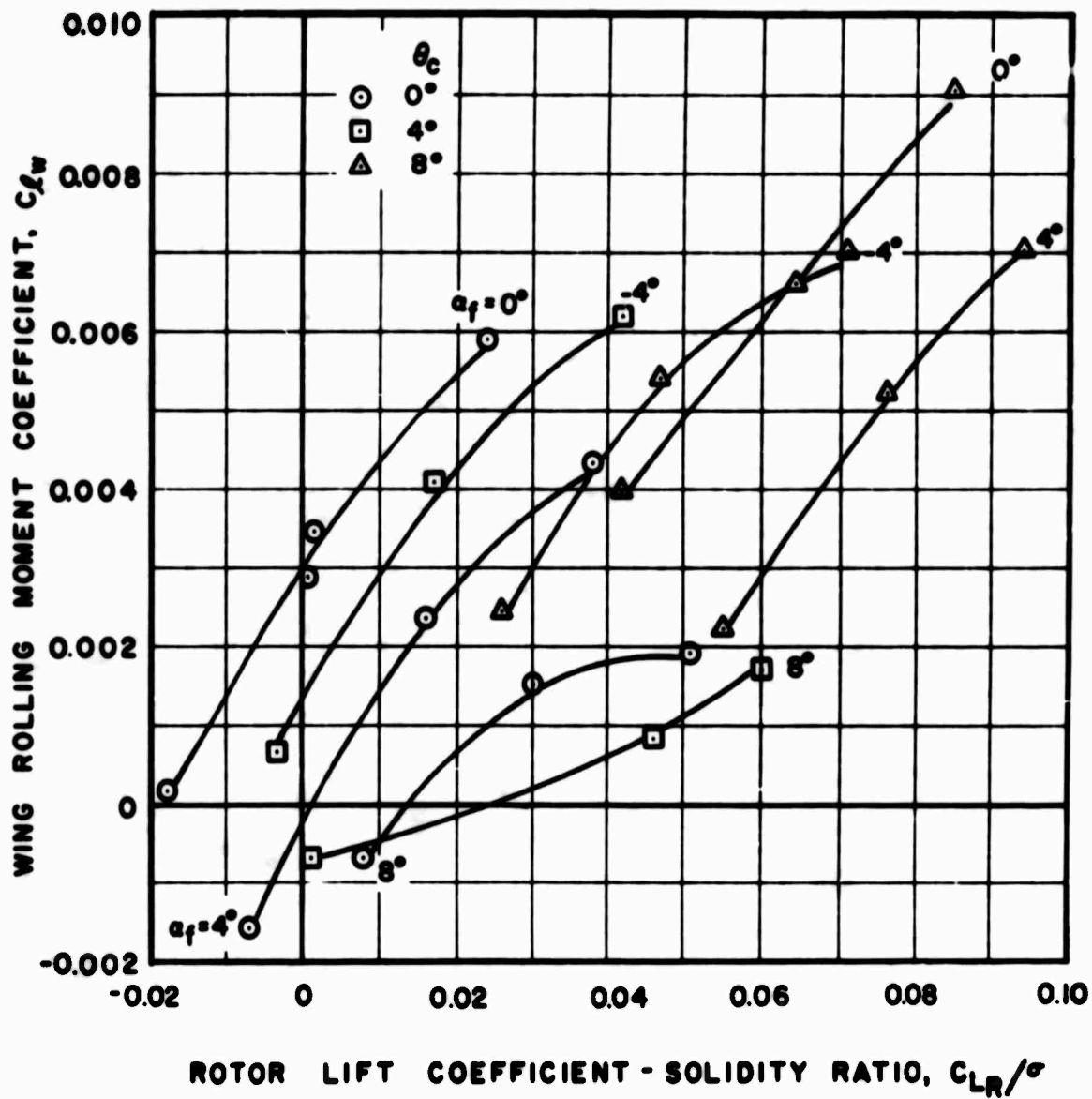
(a) Port

Figure 19. Effect of Rotor Angle of Attack on Fourth Harmonic Oscillatory Wing Pressure at Various Wing Chord Locations for the Medium Wing, Low Position, $V_s = 300$ Knots.



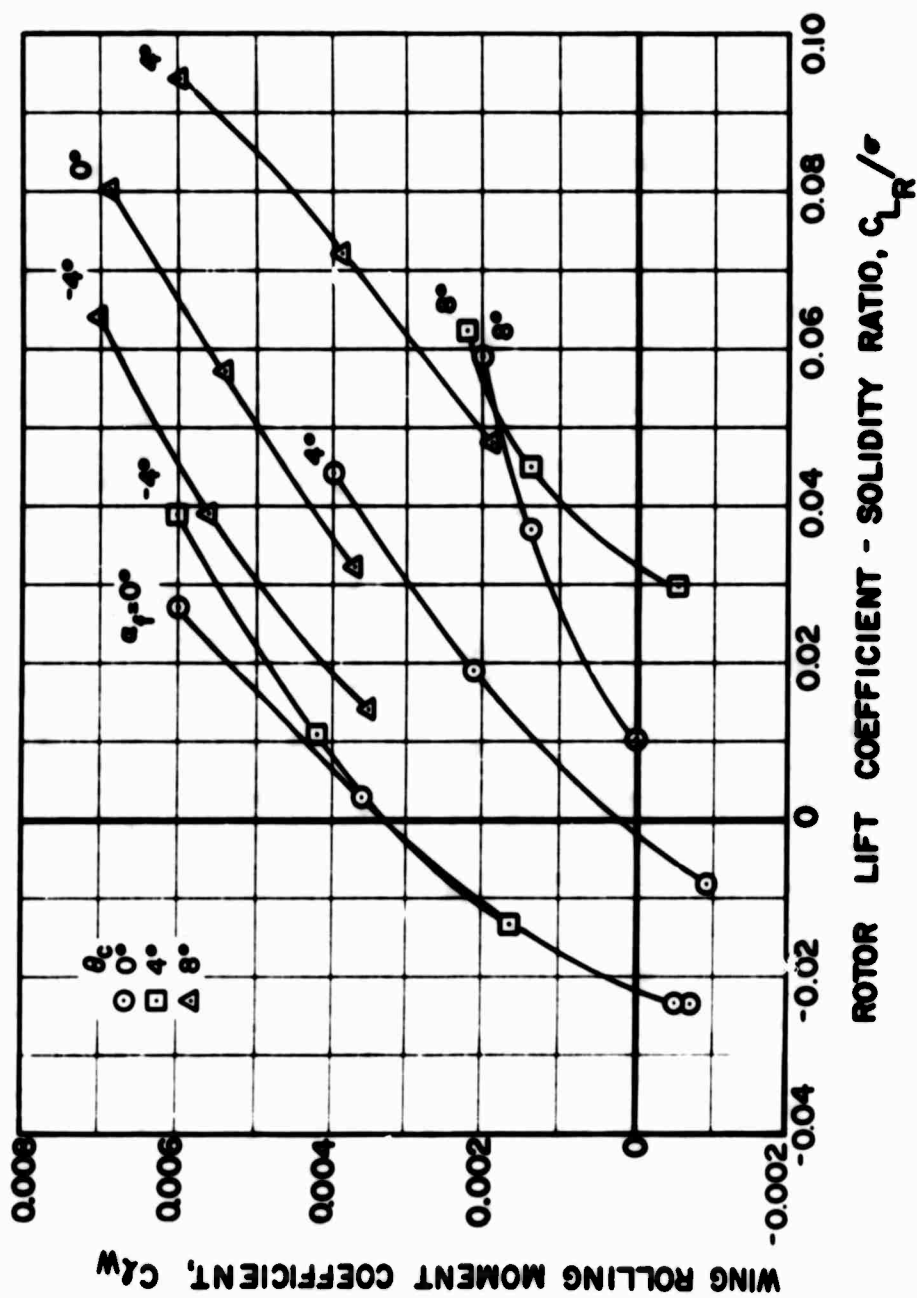
(b) Starboard

Figure 19. Concluded.



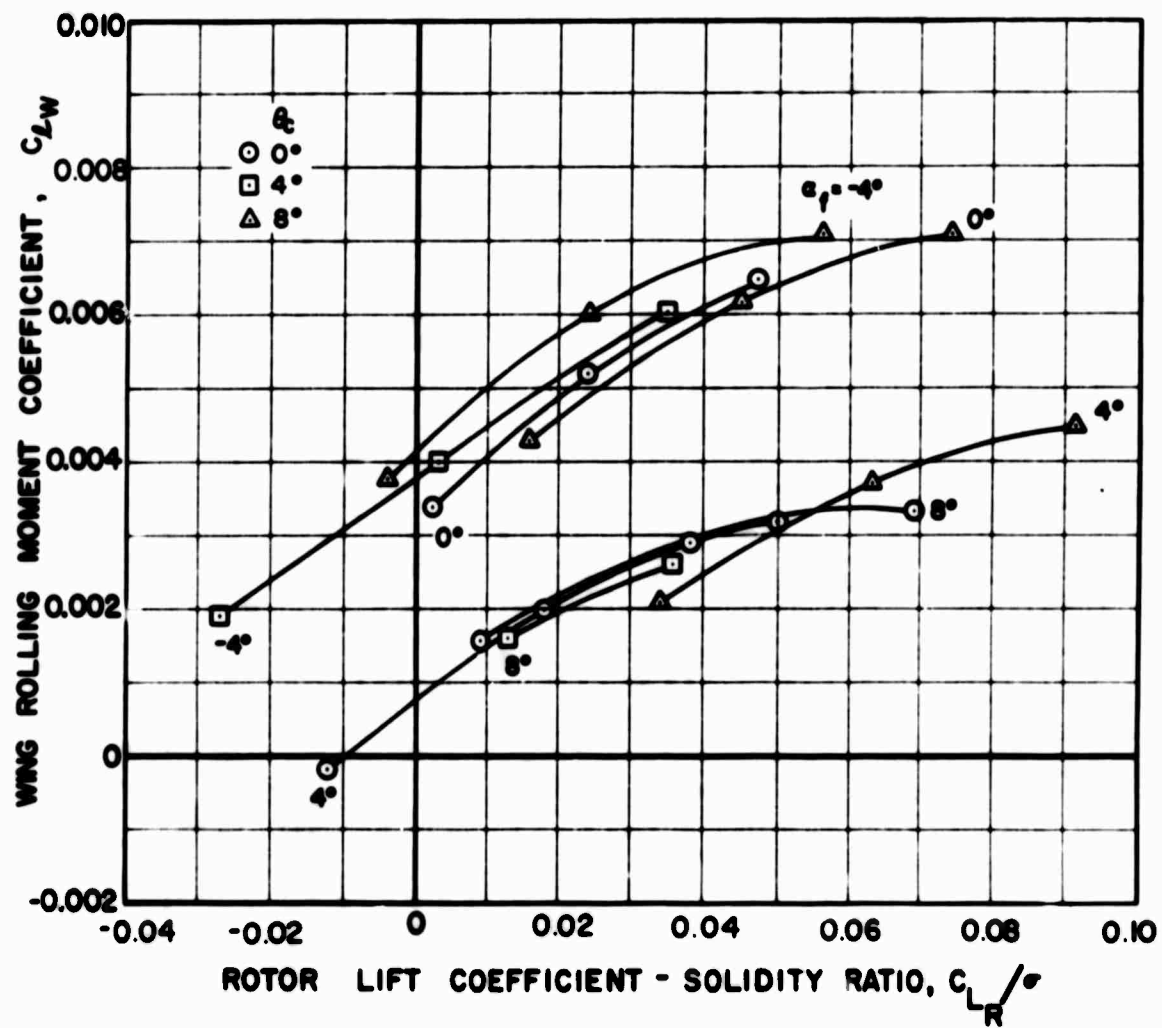
(a) $V_s = 120$ Knots

Figure 20. Effect of Rotor Lift on Wing Rolling Moment for the Medium Wing, Mid Position at Various Forward Speeds and Fuselage Angles of Attack.



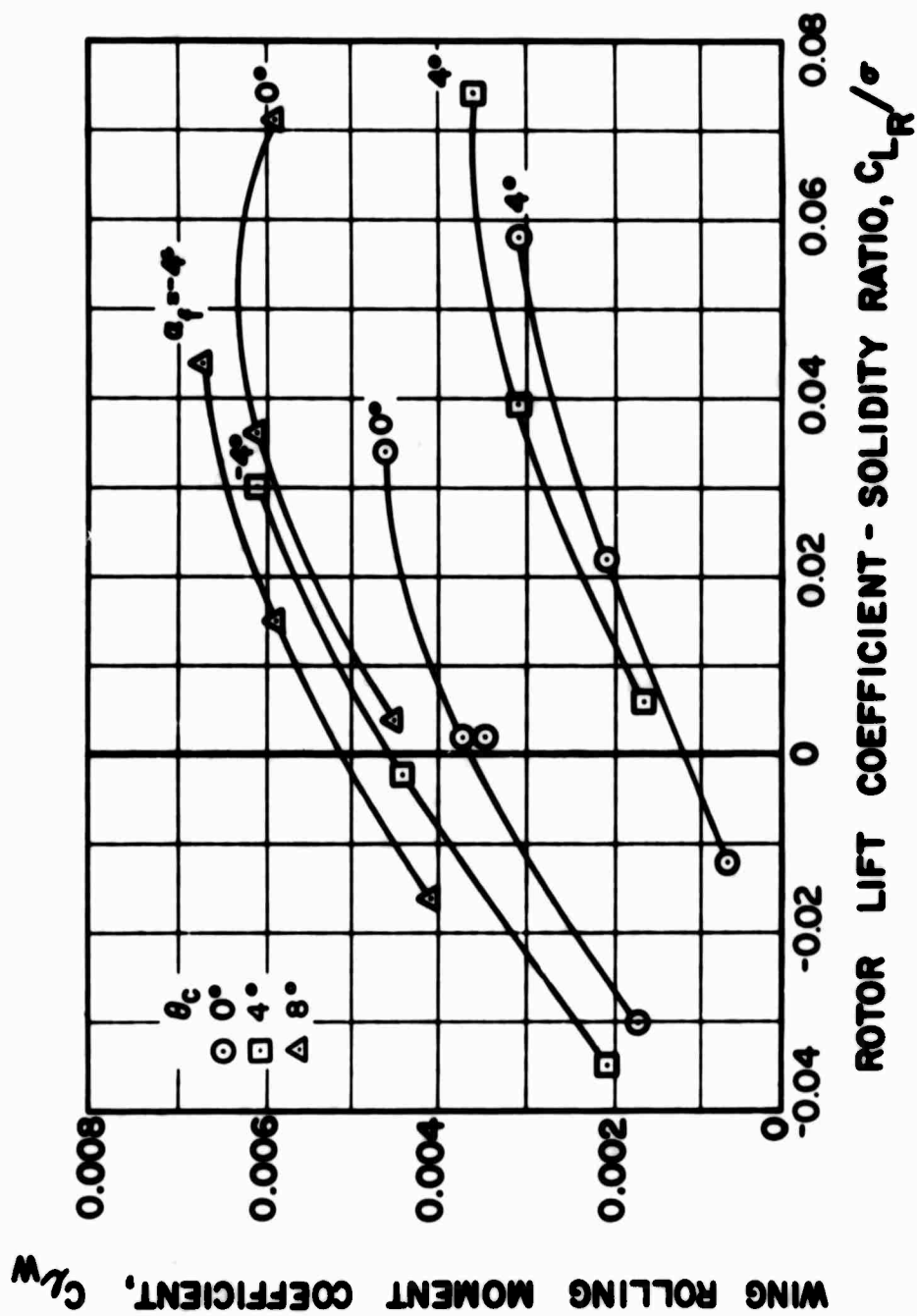
(b) $V_s = 160$ Knots

Figure 20. Continued.



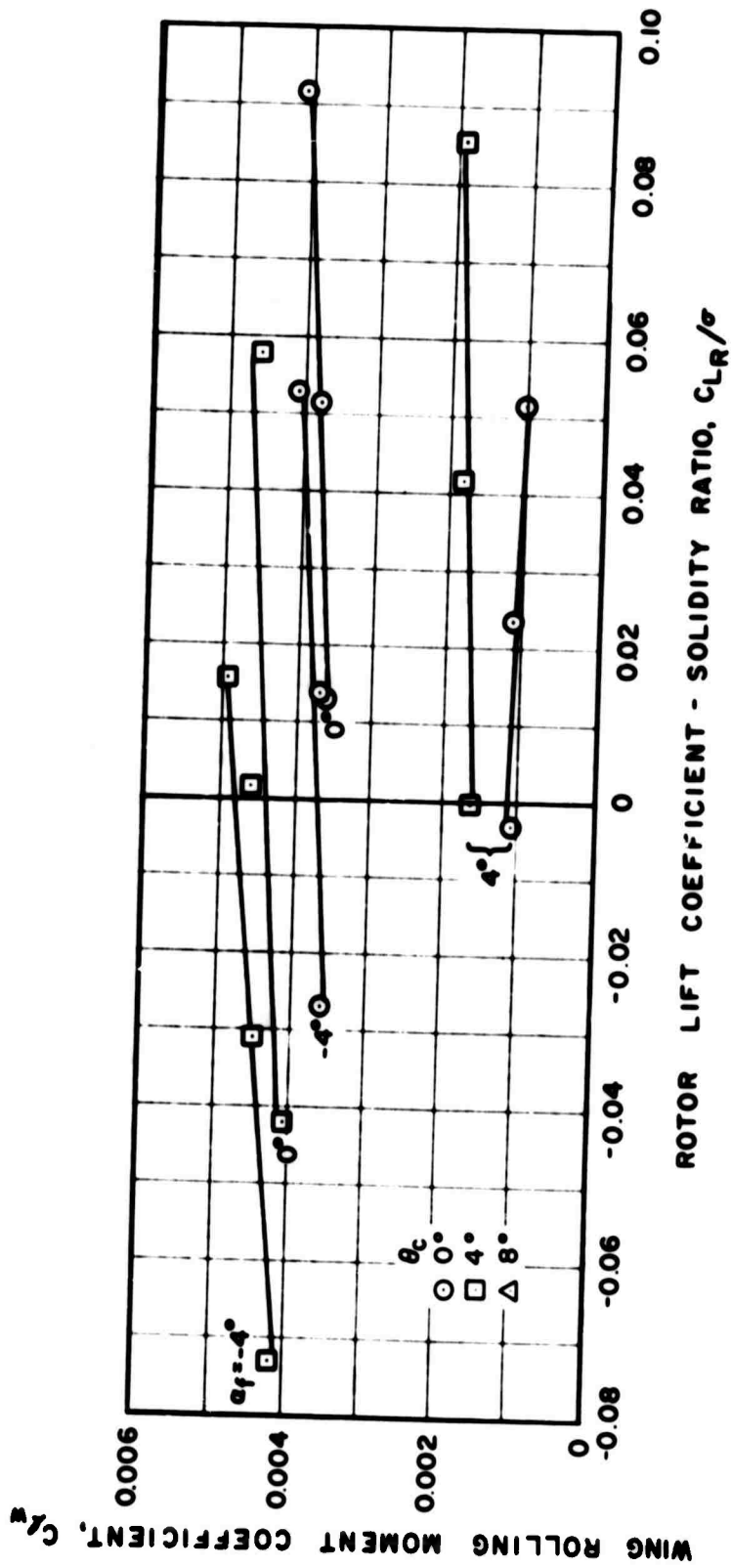
(c) $V_s = 200$ Knots

Figure 20. Continued.



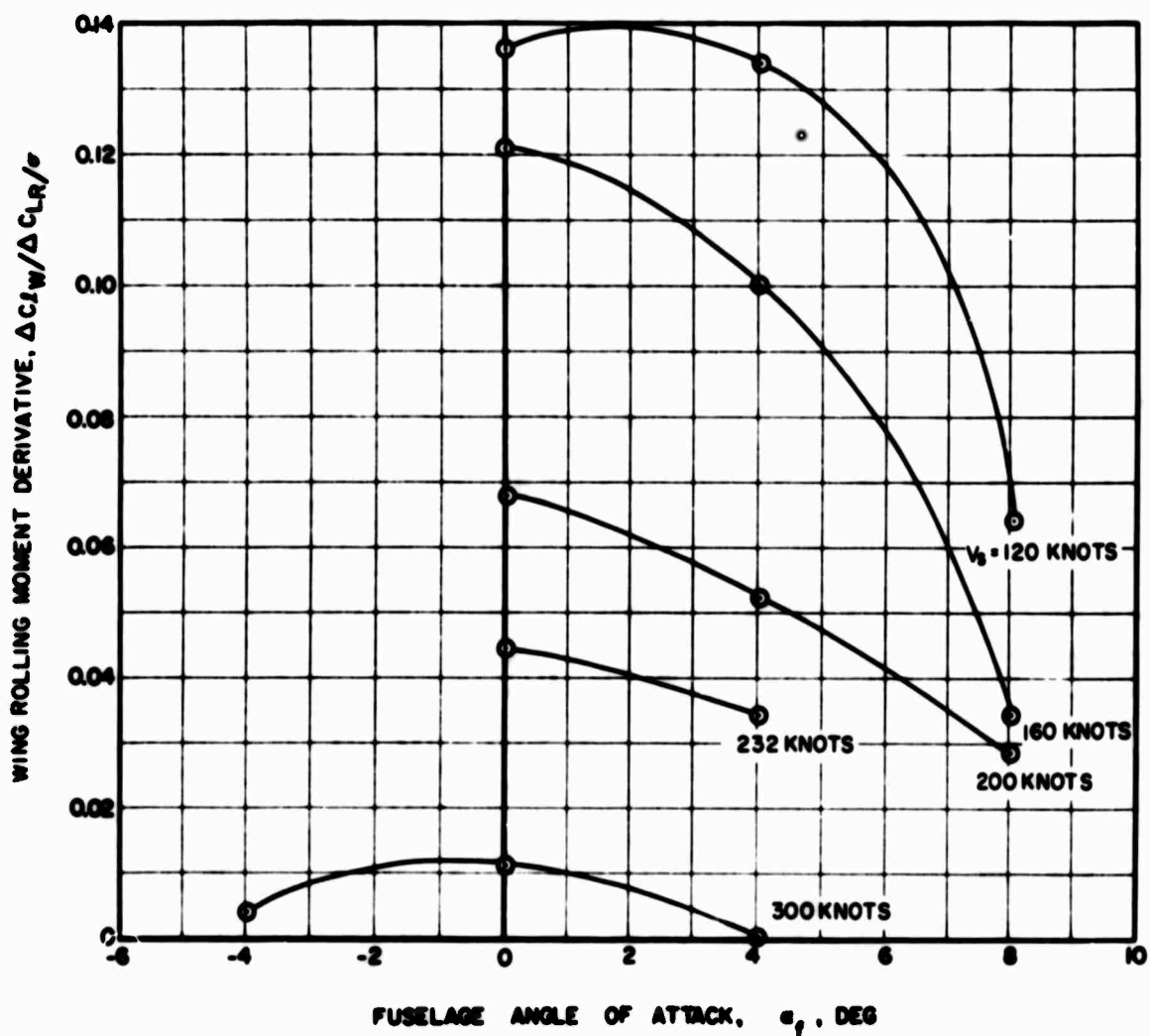
(d) $V_s = 232$ Knots

Figure 20. Continued.



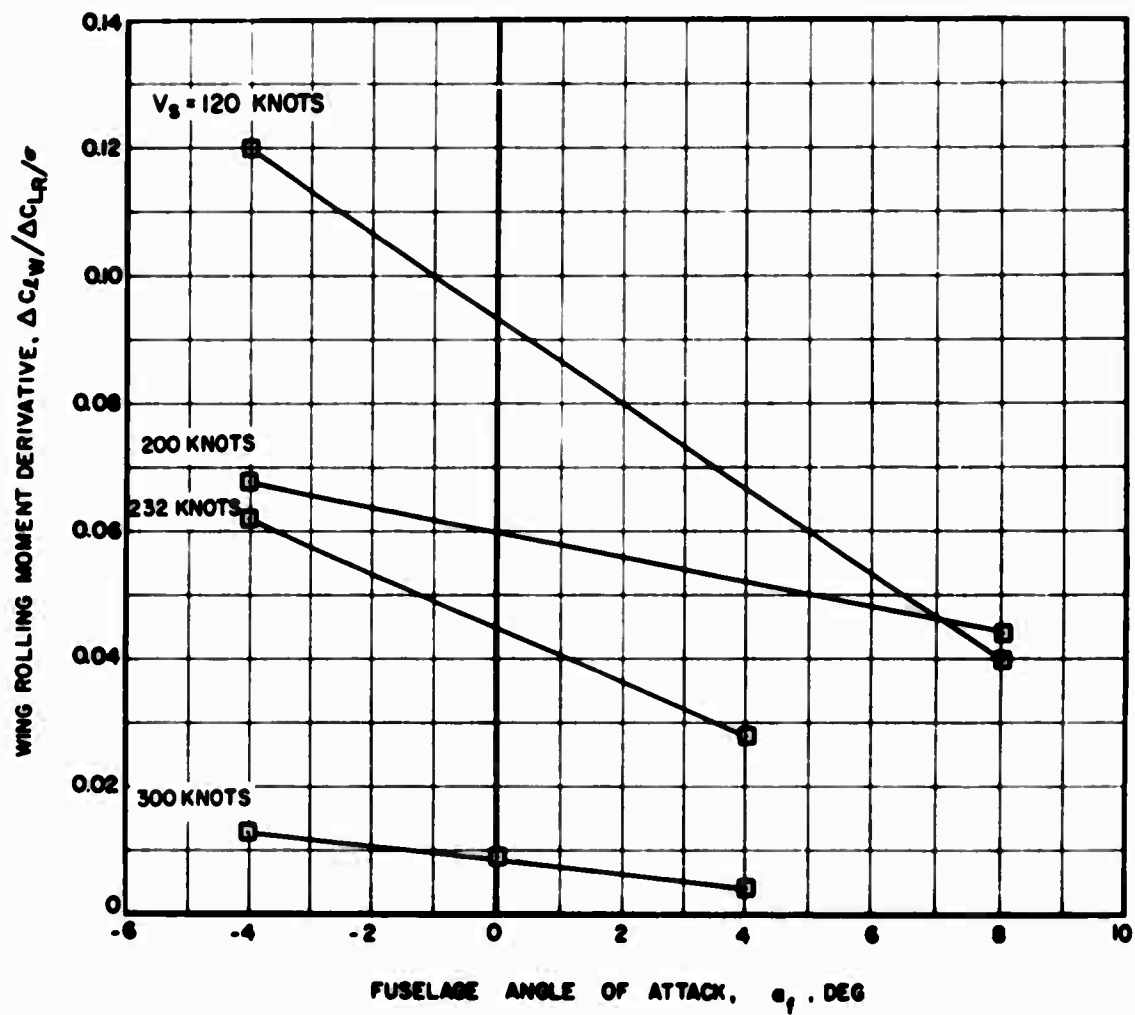
(e) $V_s = 300$ Knots

Figure 20. Concluded.



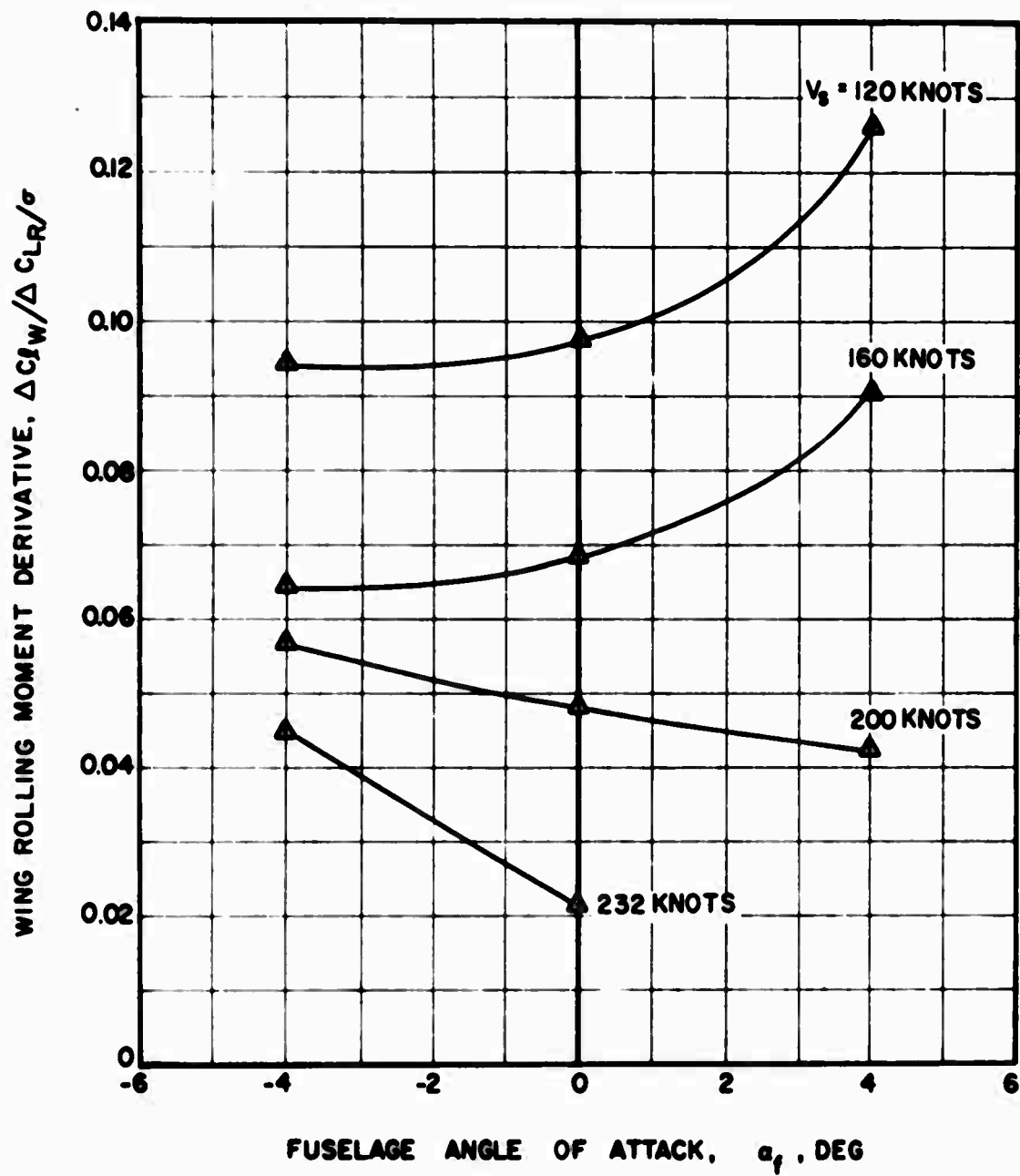
(a) $\theta_c = 0^\circ$

Figure 21. Wing Rolling Moment-Rotor Lift Derivative for the Medium Wing at Various Forward Speeds, Collective Pitch Settings, and Fuselage Angles of Attack.



(b) $\theta_c = 4^\circ$

Figure 21. Continued.



(c) $\theta_c = 8^\circ$

Figure 21. Concluded.

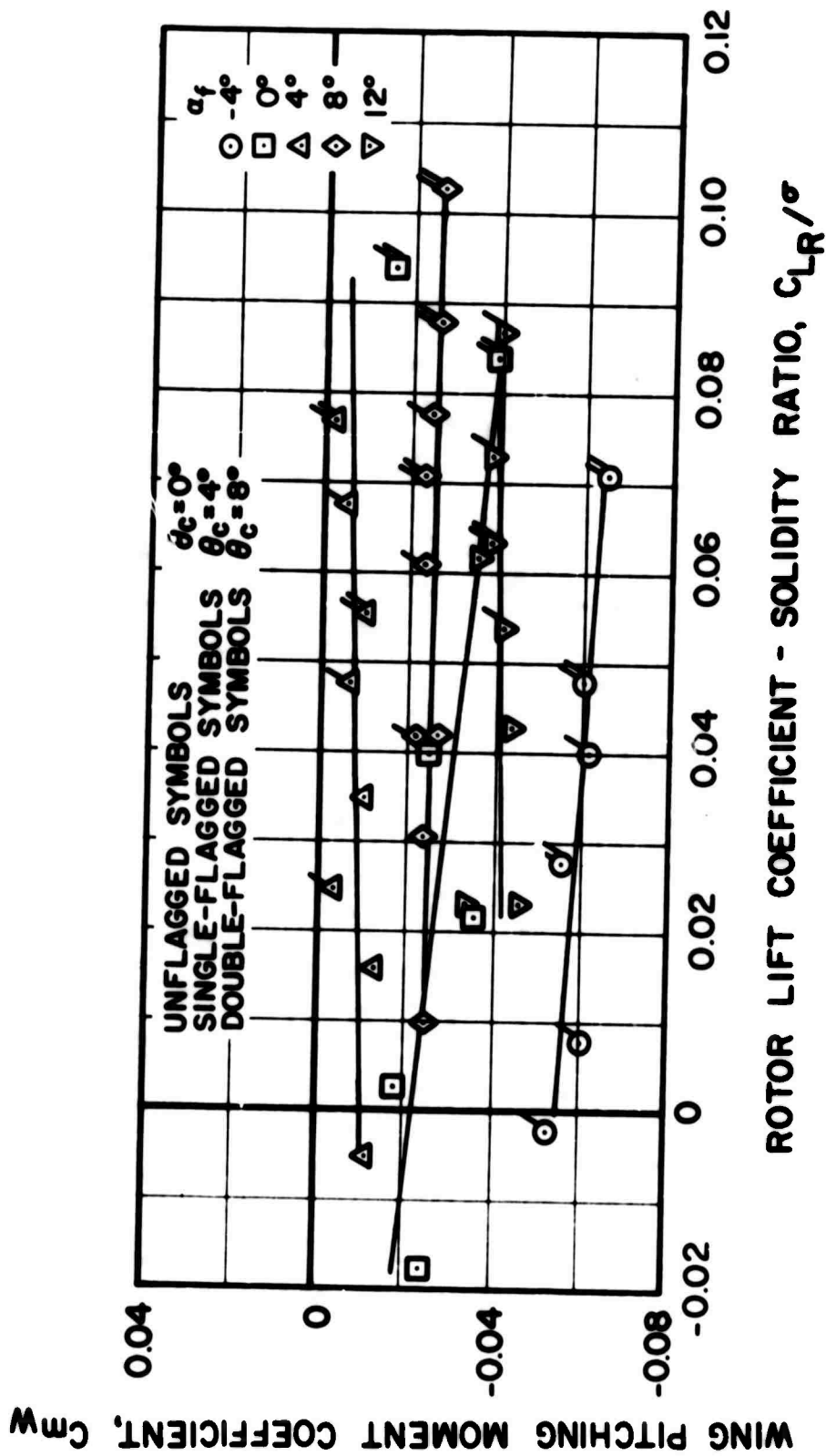
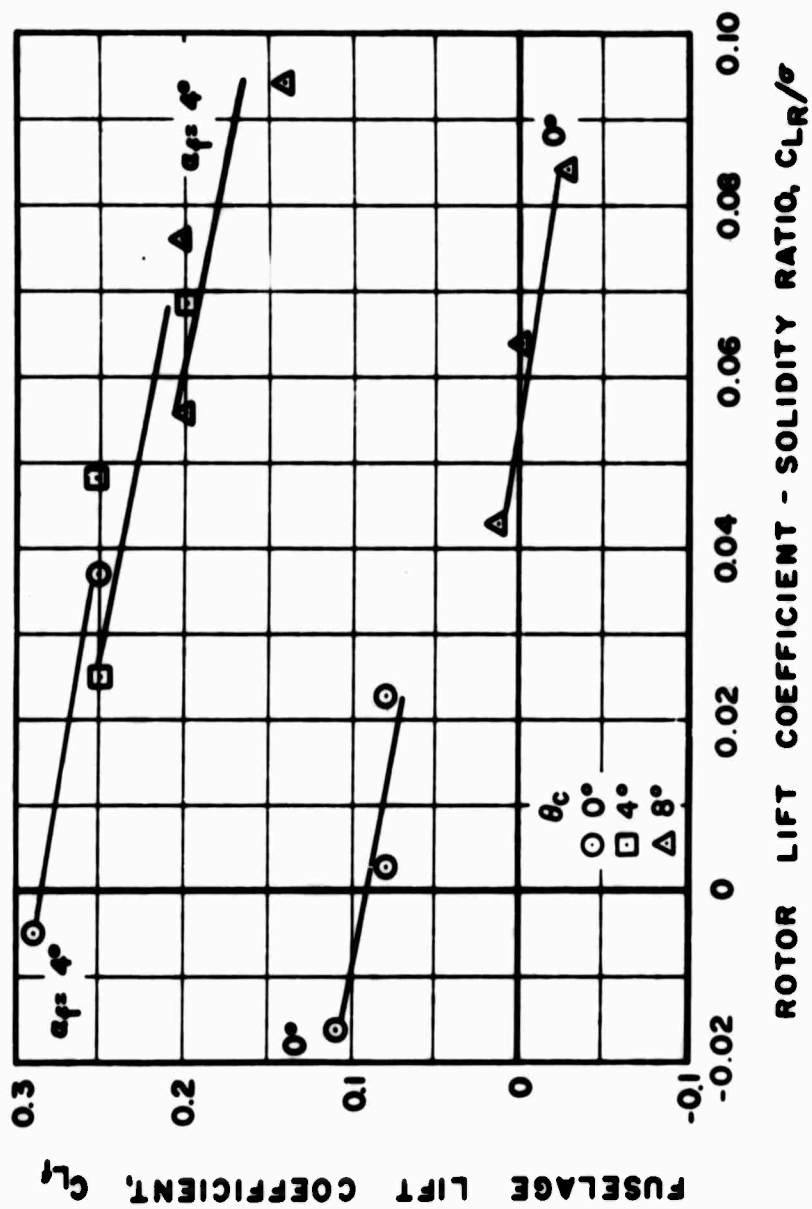
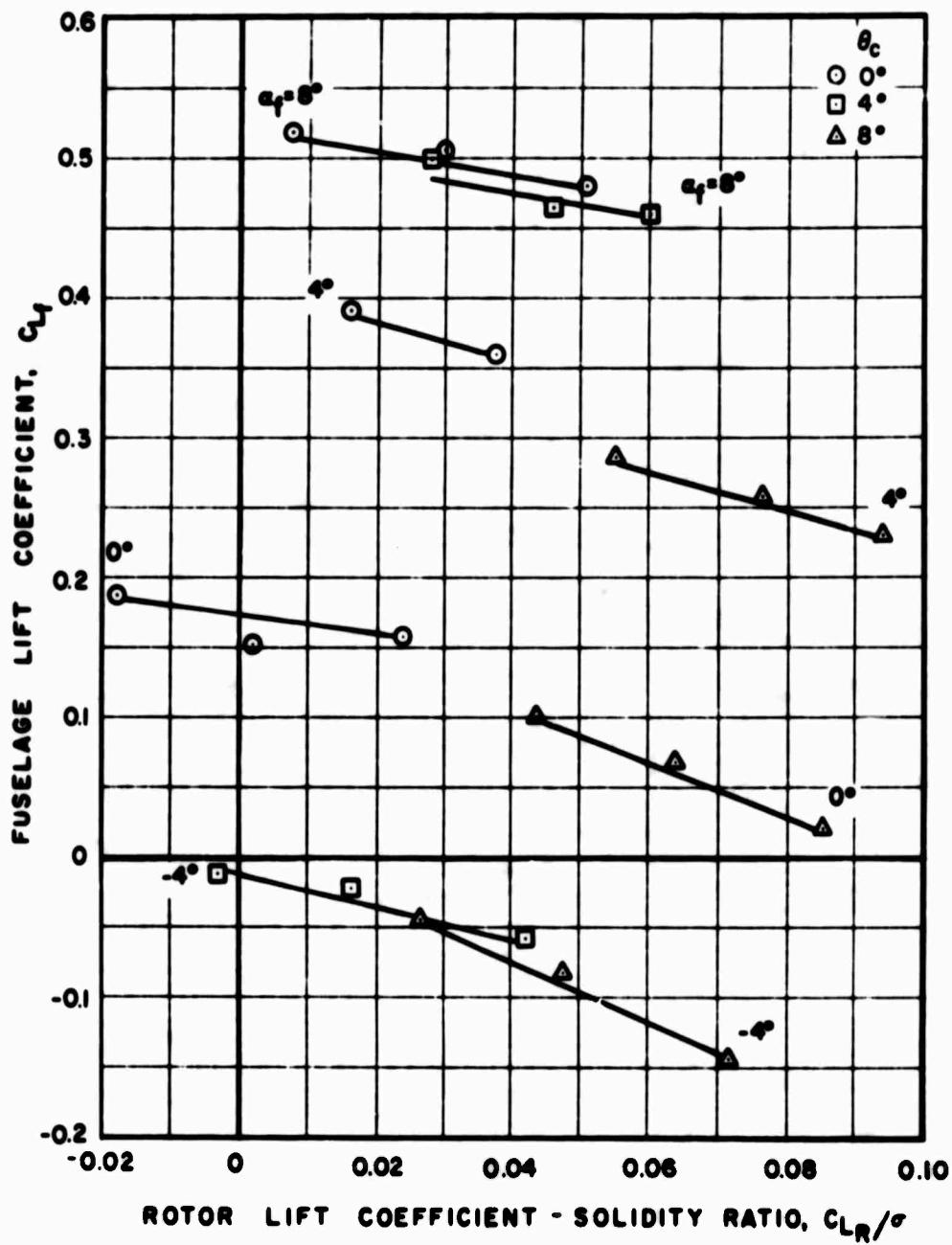


Figure 22. Effect of Rotor Lift on Wing Pitching Moment for the Medium Wing, High Position, $V_s = 120$ Knots, at Various Fuselage Angles of Attack.



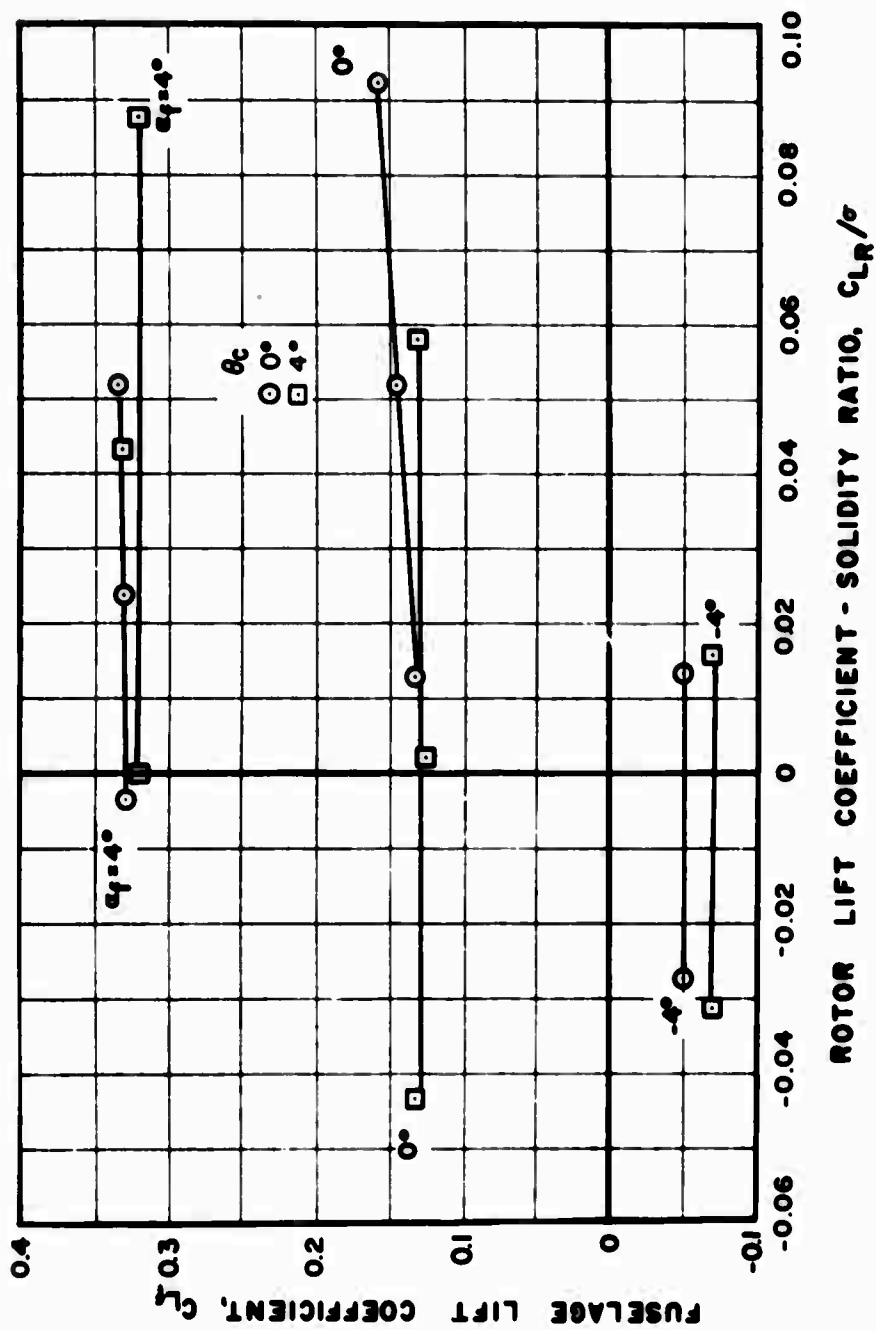
(a) High Position, $V_s = 120$ Knots

Figure 23. Effect of Rotor Lift on Fuselage Lift With the Medium Wing at Two Wing Positions, Two Forward Speeds, and Various Fuselage Angles of Attack.



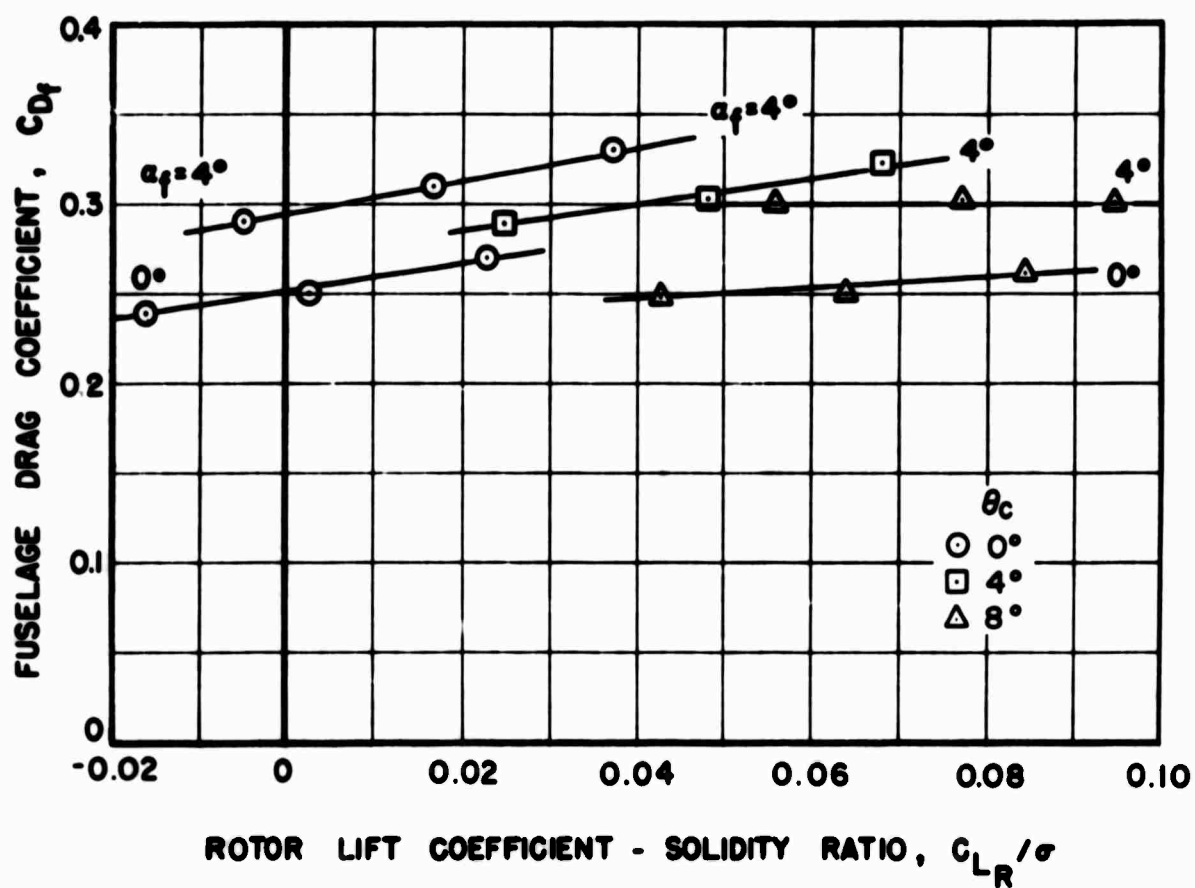
(b) Mid Position, $V_s = 120$ Knots

Figure 23. Continued.



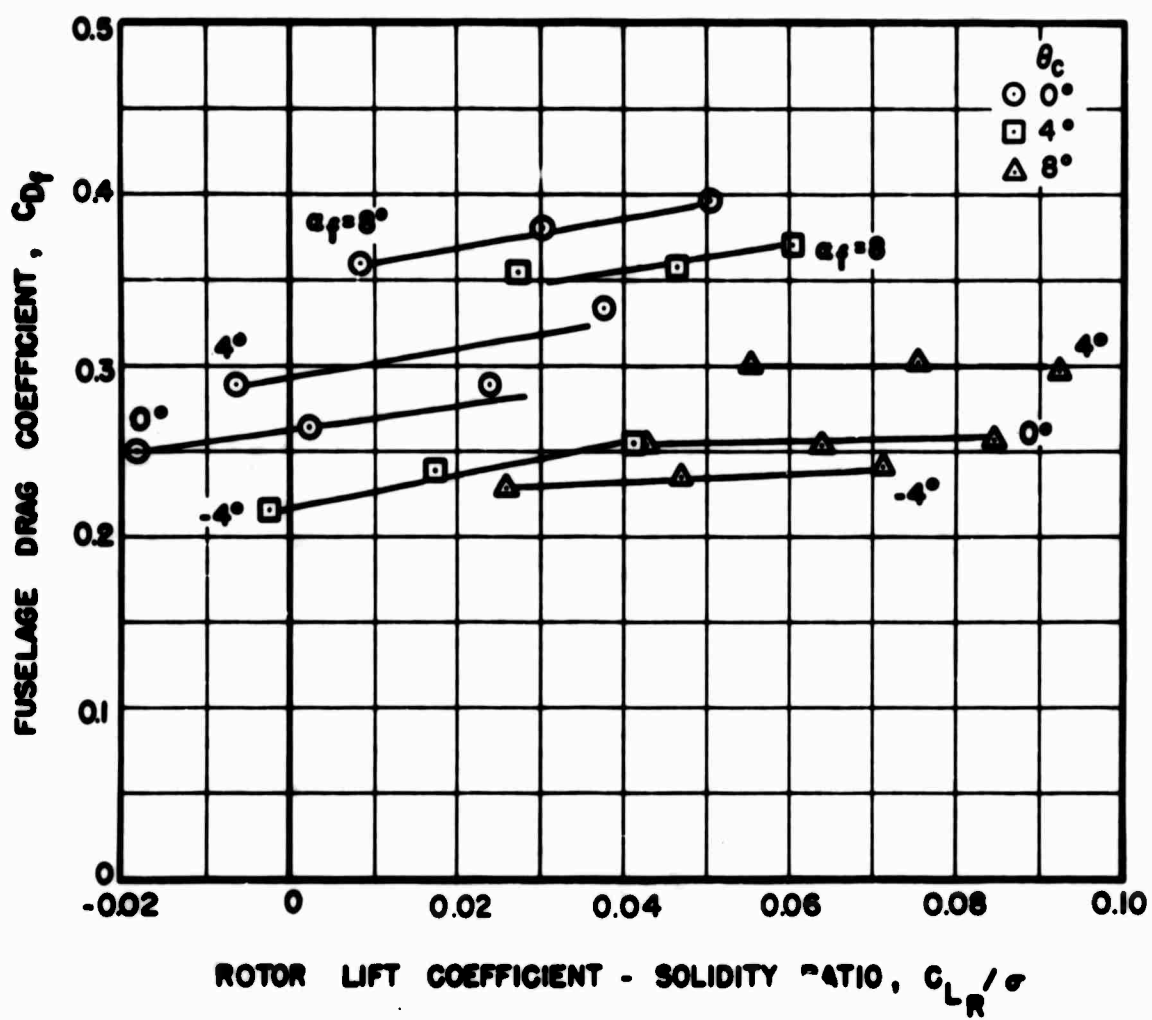
(c) Mid Position, $V_s = 300$ Knots

Figure 23. Concluded.



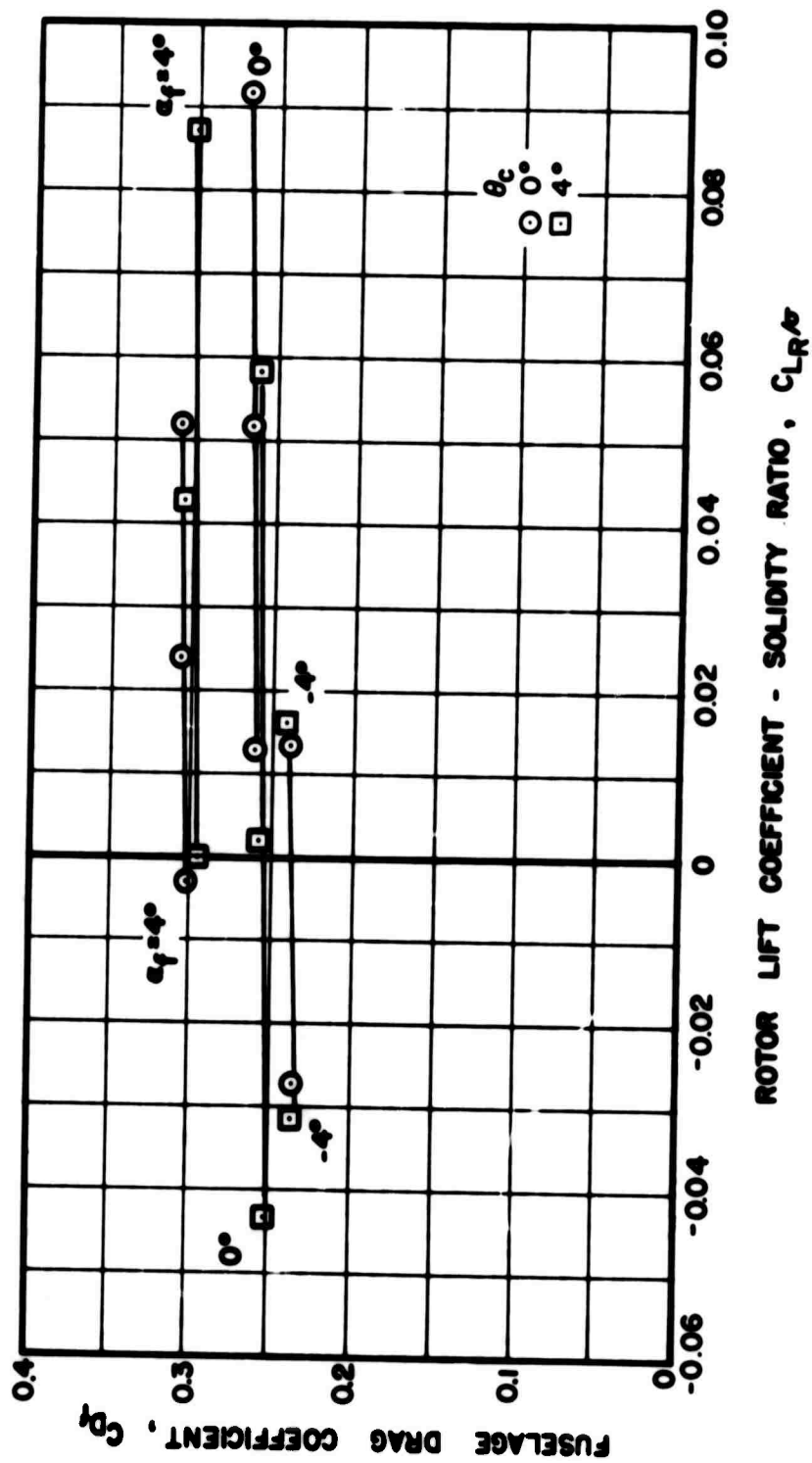
(a) High Position, $V_s = 120$ Knots

Figure 24. Effect of Rotor Lift on Fuselage Drag With the Medium Wing at Two Wing Positions, Two Forward Speeds, and Various Fuselage Angles of Attack.



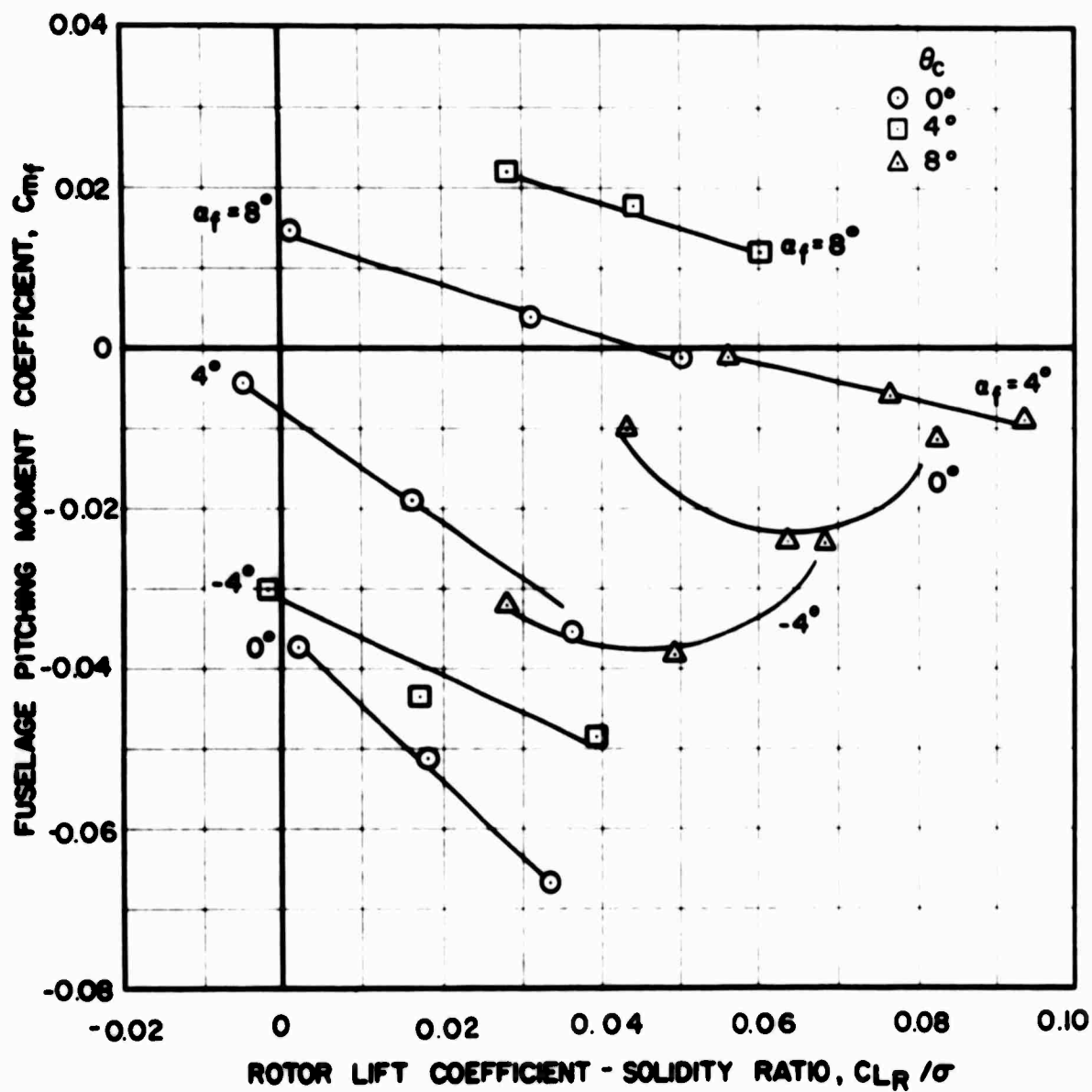
(b) Mid Position, $V_s = 120$ Knots

Figure 24. Continued.



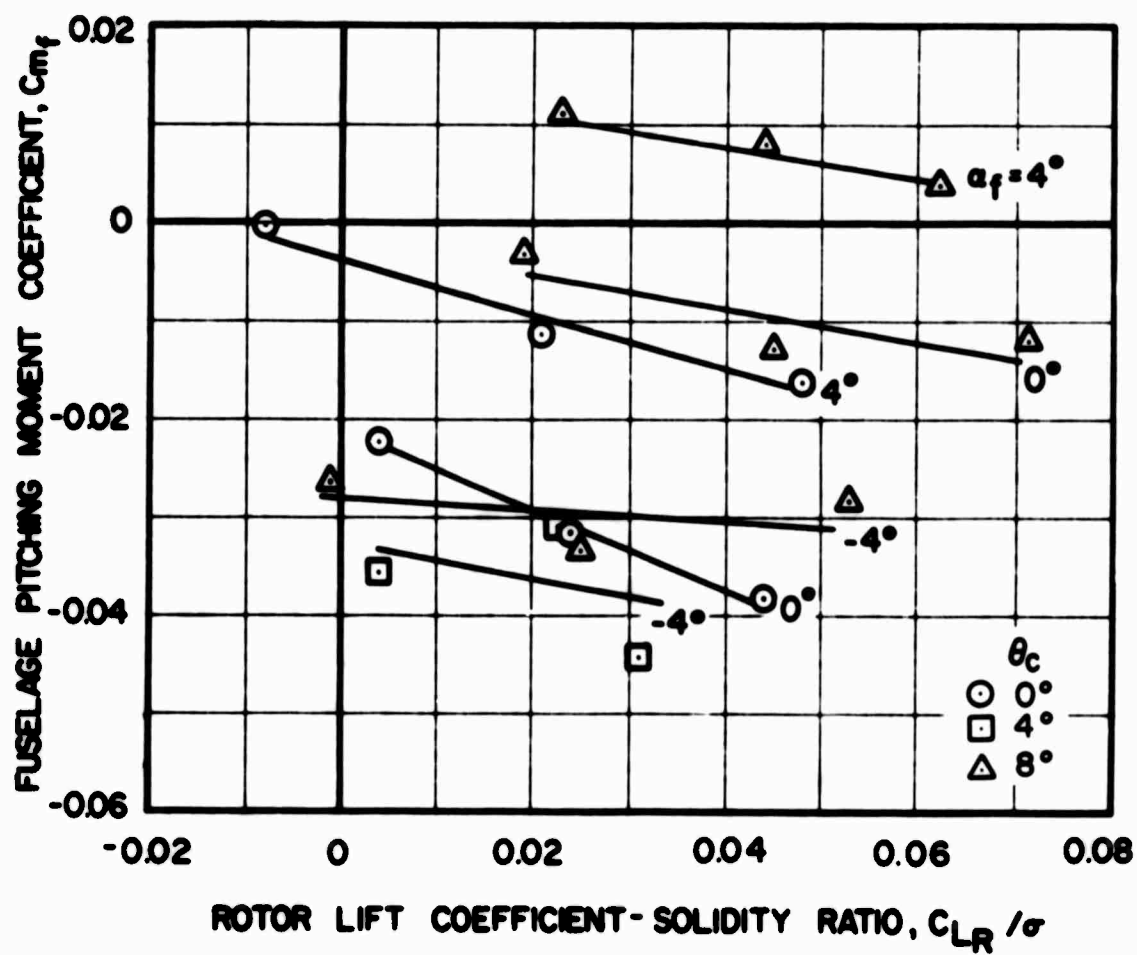
(c) Mid Position, $V_s = 300$ Knots

Figure 24. Concluded.



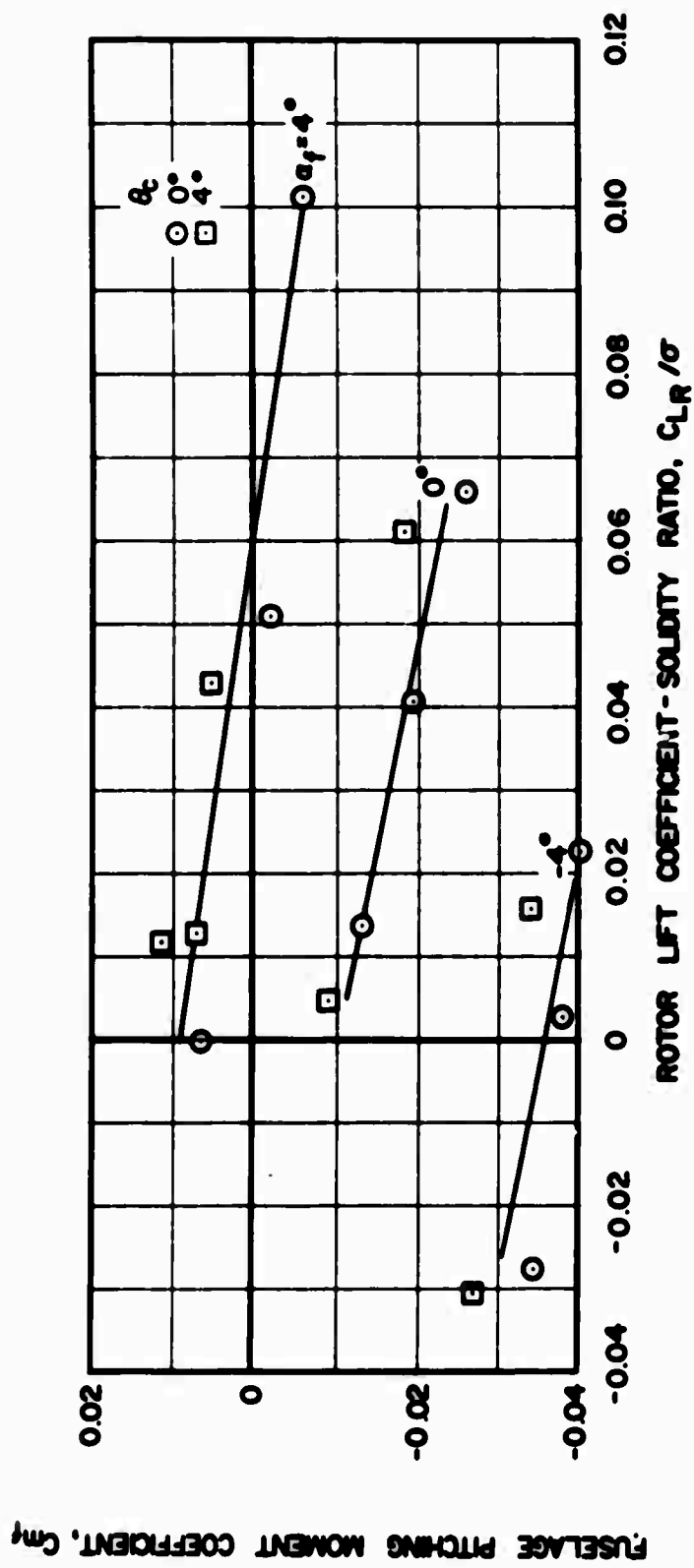
(a) Low Position, $V_s = 120$ Knots

Figure 25. Effect of Rotor Lift on Fuselage Pitching Moment With the Medium Wing at Two Wing Positions and Various Forward Speeds and Fuselage Angles of Attack.



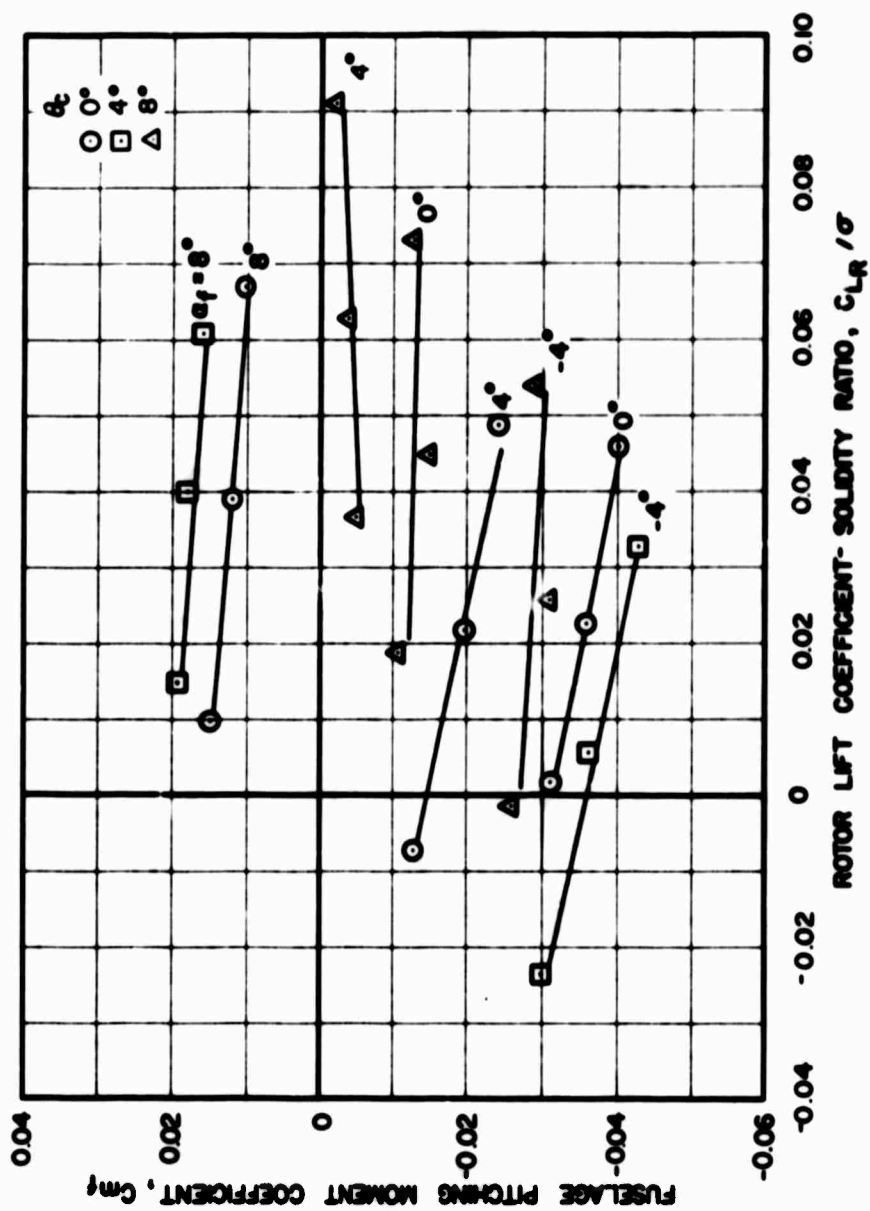
(b) Low Position, $V_s = 200$ Knots

Figure 25. Continued.



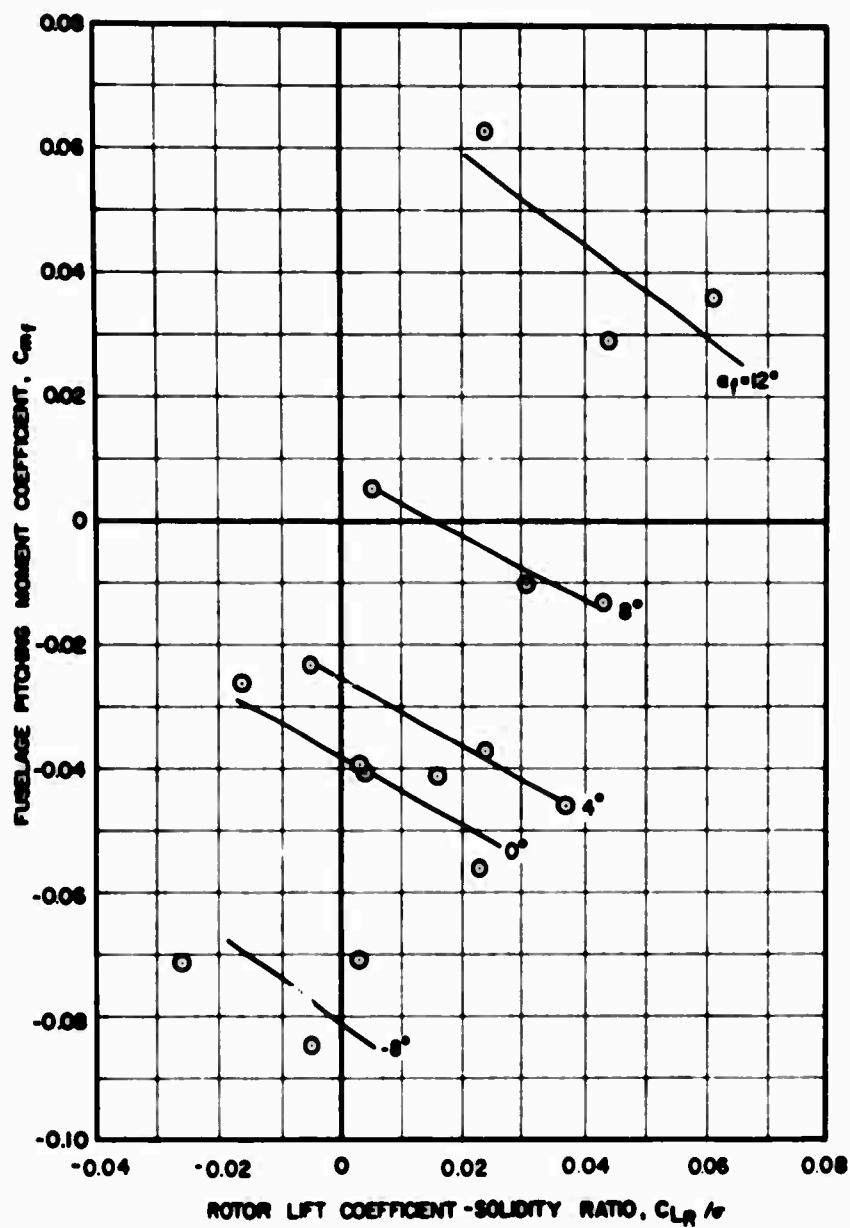
(c) Low Position, $V_s = 300$ Knots

Figure 25. Continued.



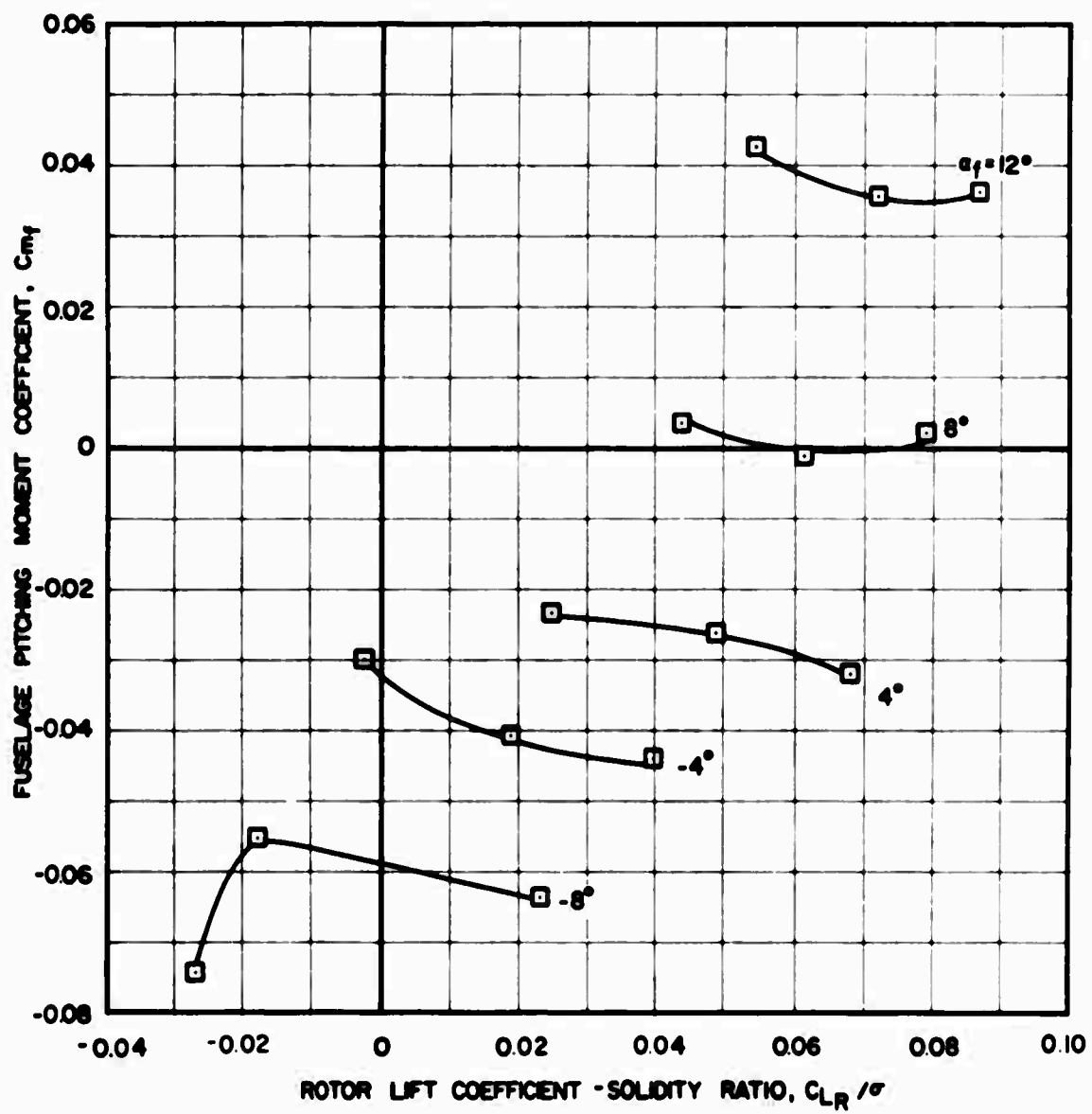
(d) High Position, $V_s = 200$ Knots

Figure 25. Concluded.



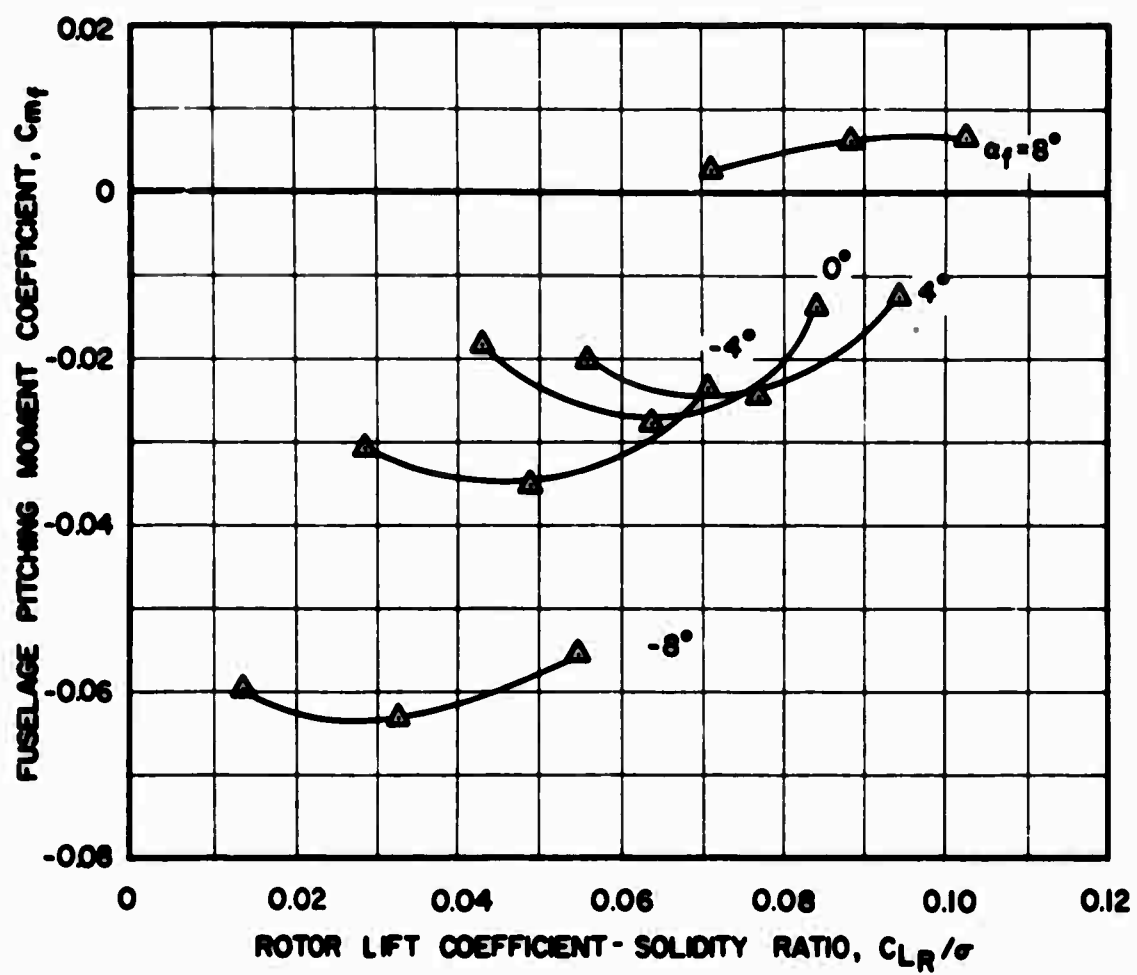
(a) $\theta_c = 0^\circ$

Figure 26. Effect of Rotor Lift on Fuselage Pitching Moment With the Medium Wing, High Position, $V_s = 120$ Knots, at Various Collective Pitch Settings and Fuselage Angles of Attack.



(b) $\theta_c = 4^\circ$

Figure 26. Continued.



(c) $\theta_c = 8^\circ$

Figure 26. Concluded.

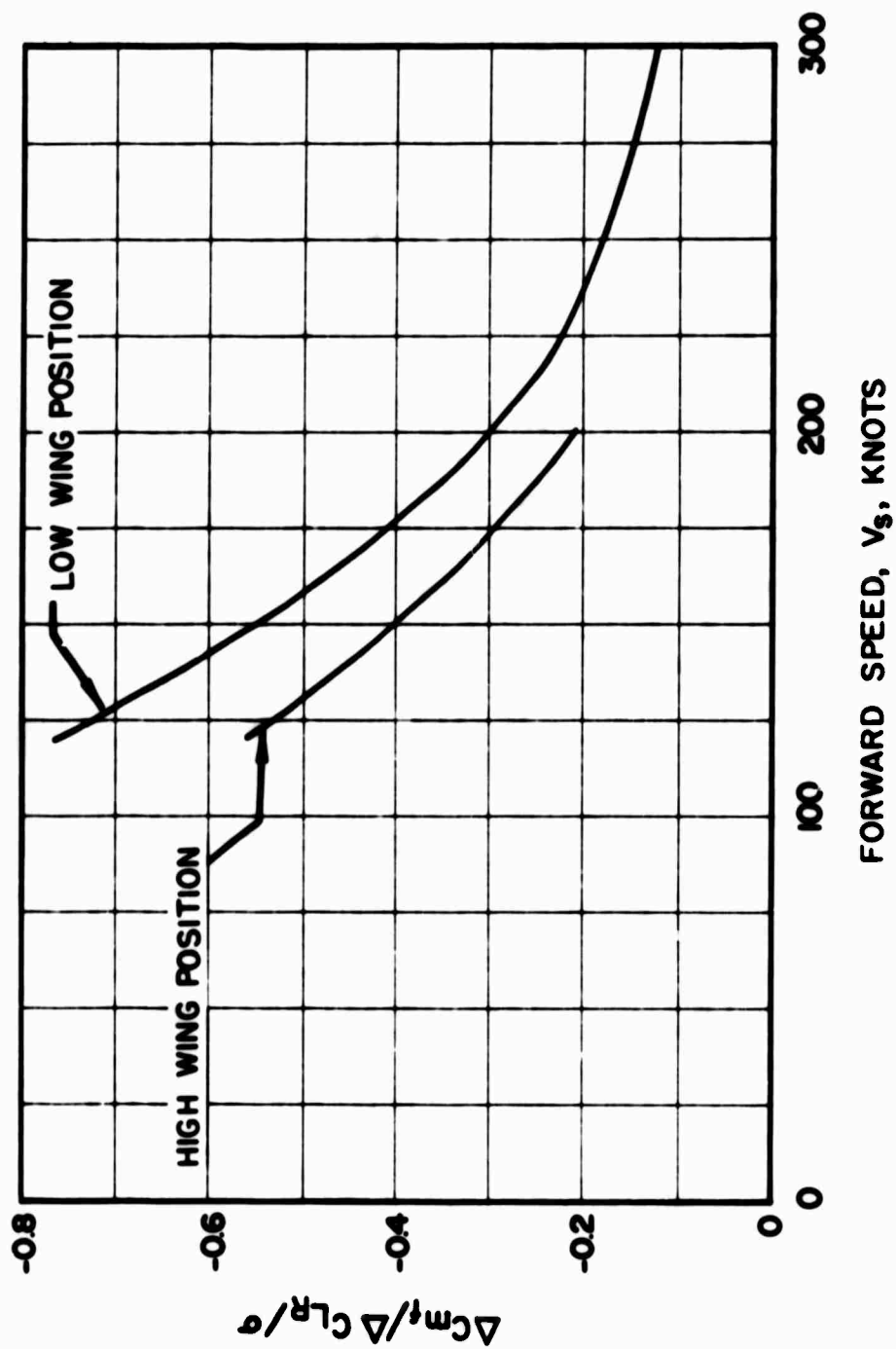
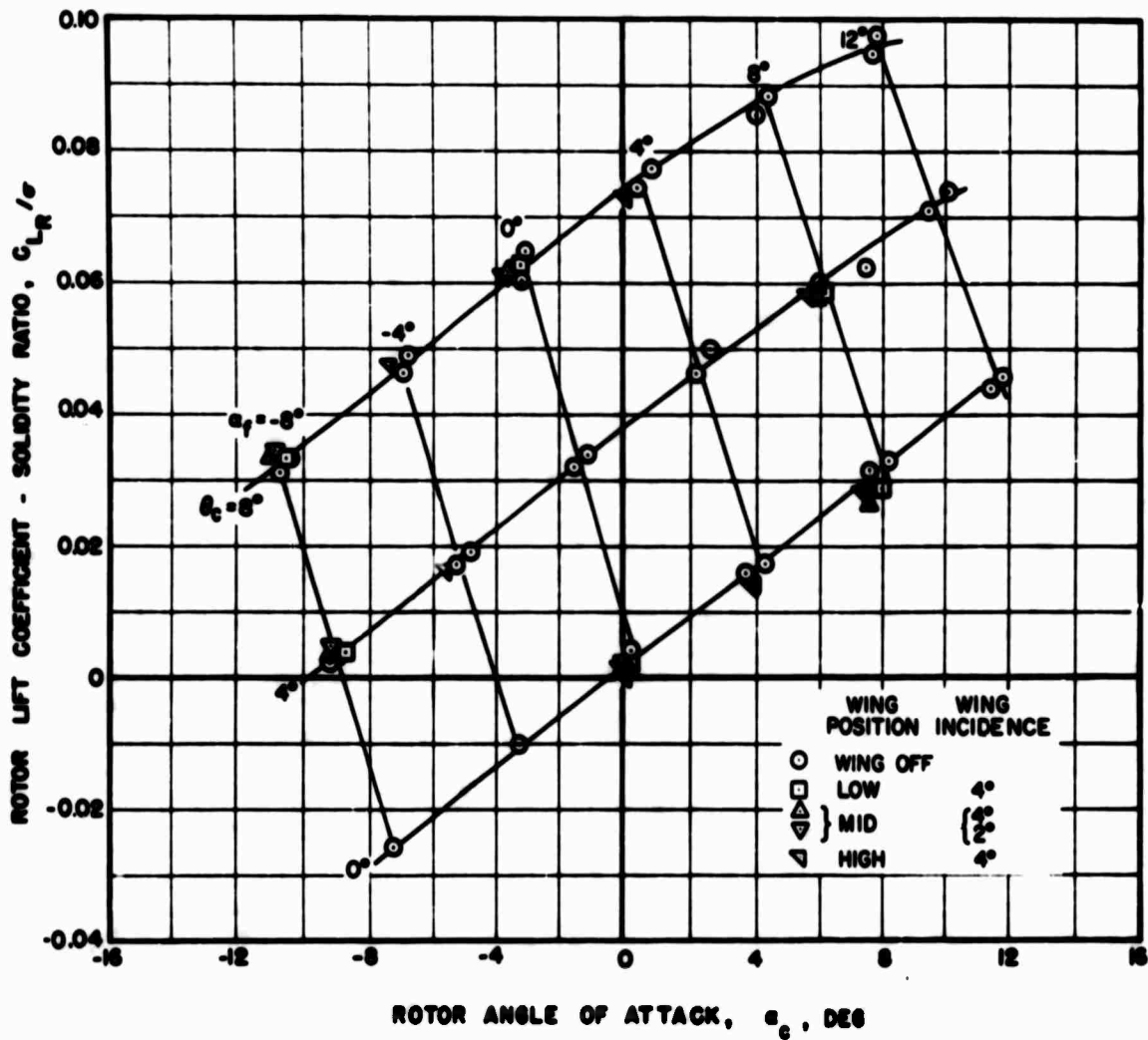
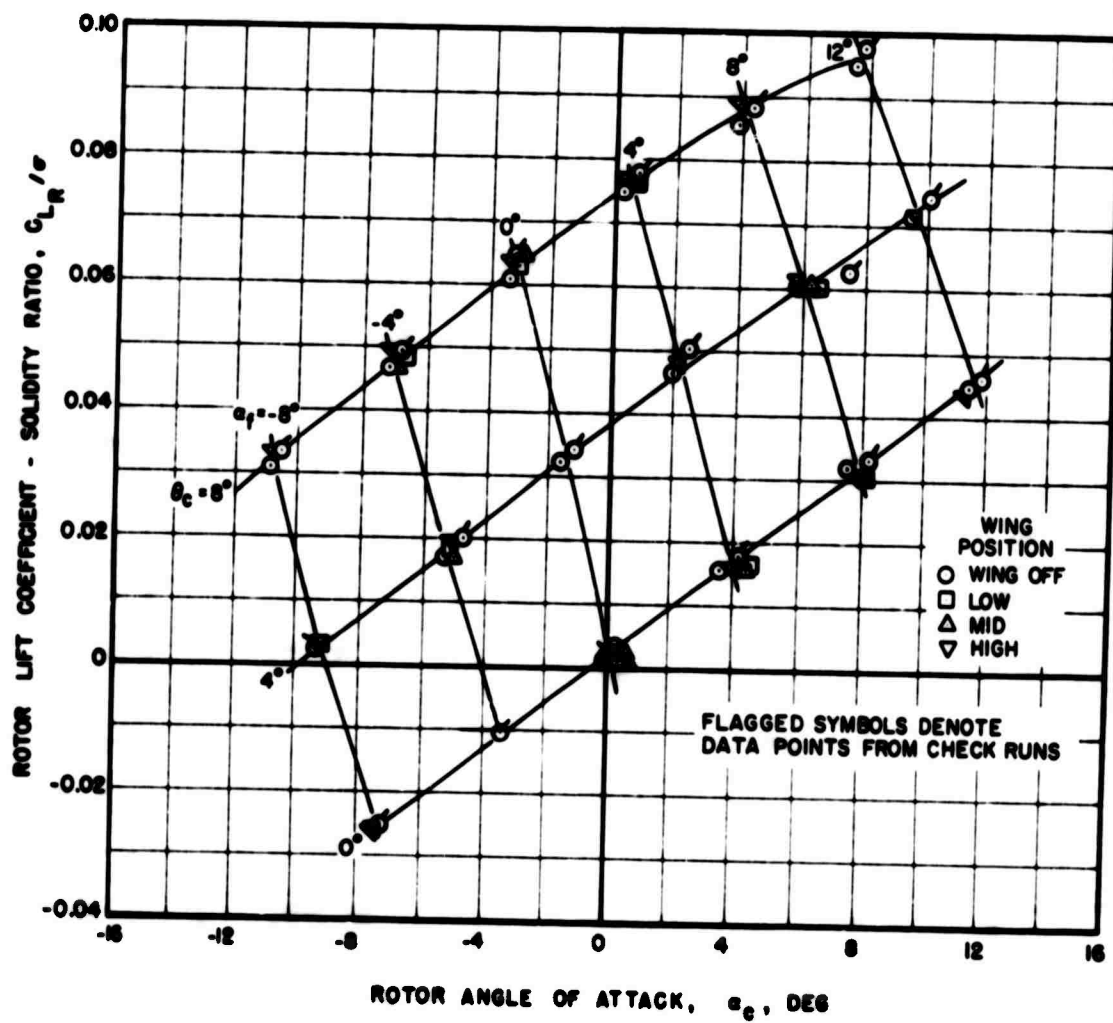


Figure 27. Effect of Forward Speed on Fuselage Pitching Moment Per Unit Change in $C_{L/R}$ With the Medium Wing at Two Wing Positions and $\alpha_f = 4^\circ$.



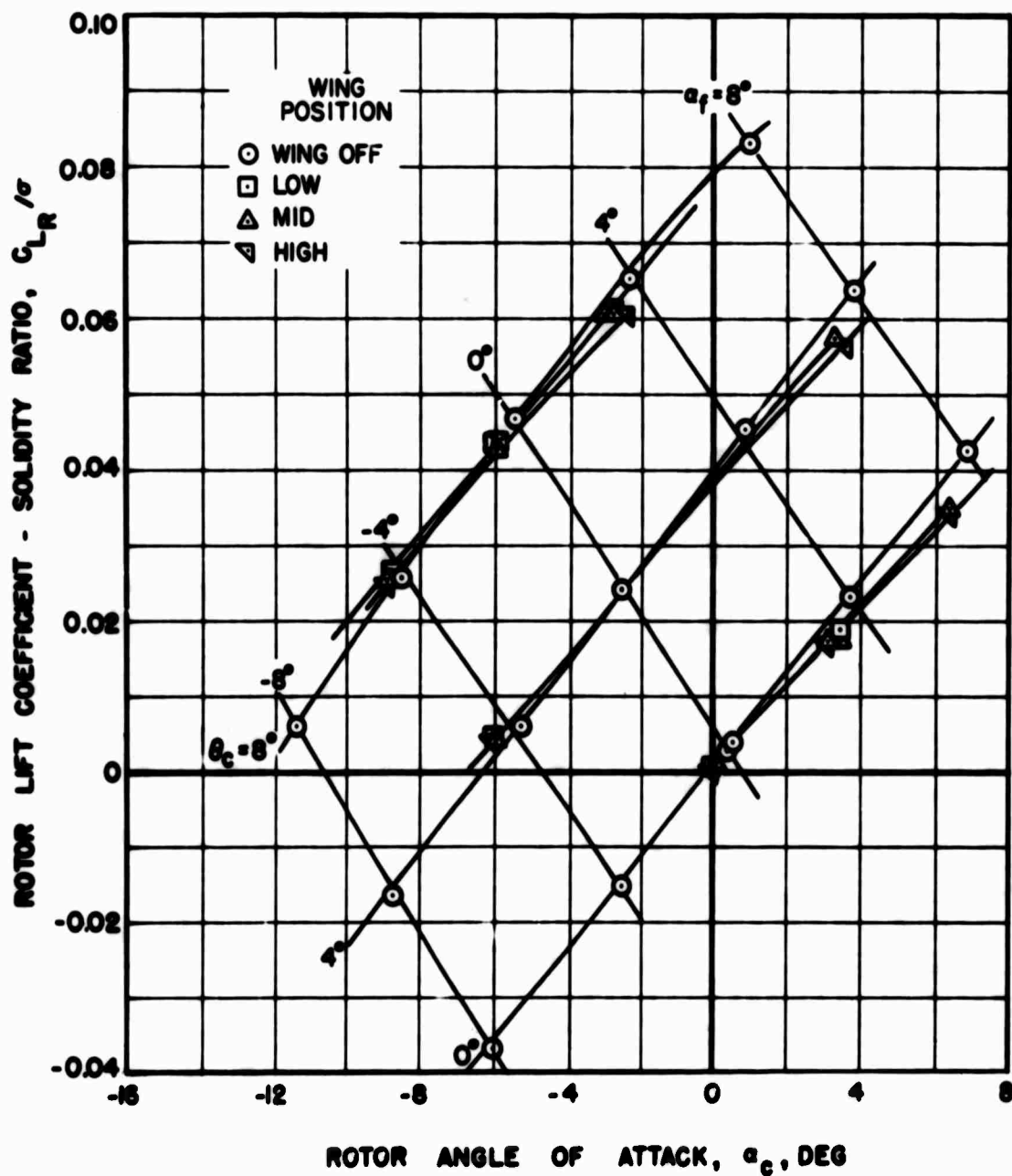
(a) Large Wing

Figure 28. Effect of Wing Size and Position on Rotor Lift and Angle of Attack at Various Fuselage Angles of Attack and $V_s = 120$ Knots.



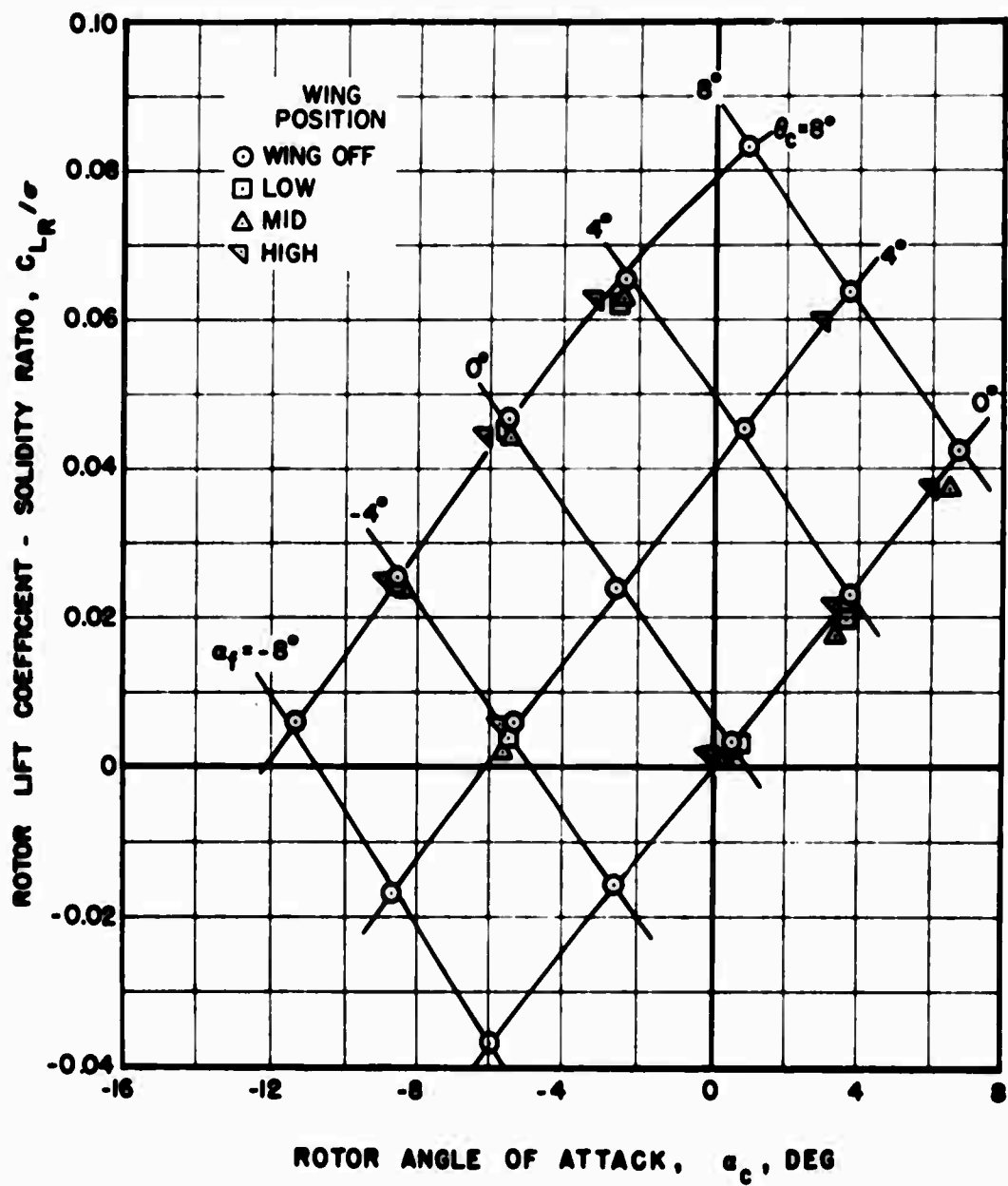
(b) Medium Wing

Figure 28. Concluded.



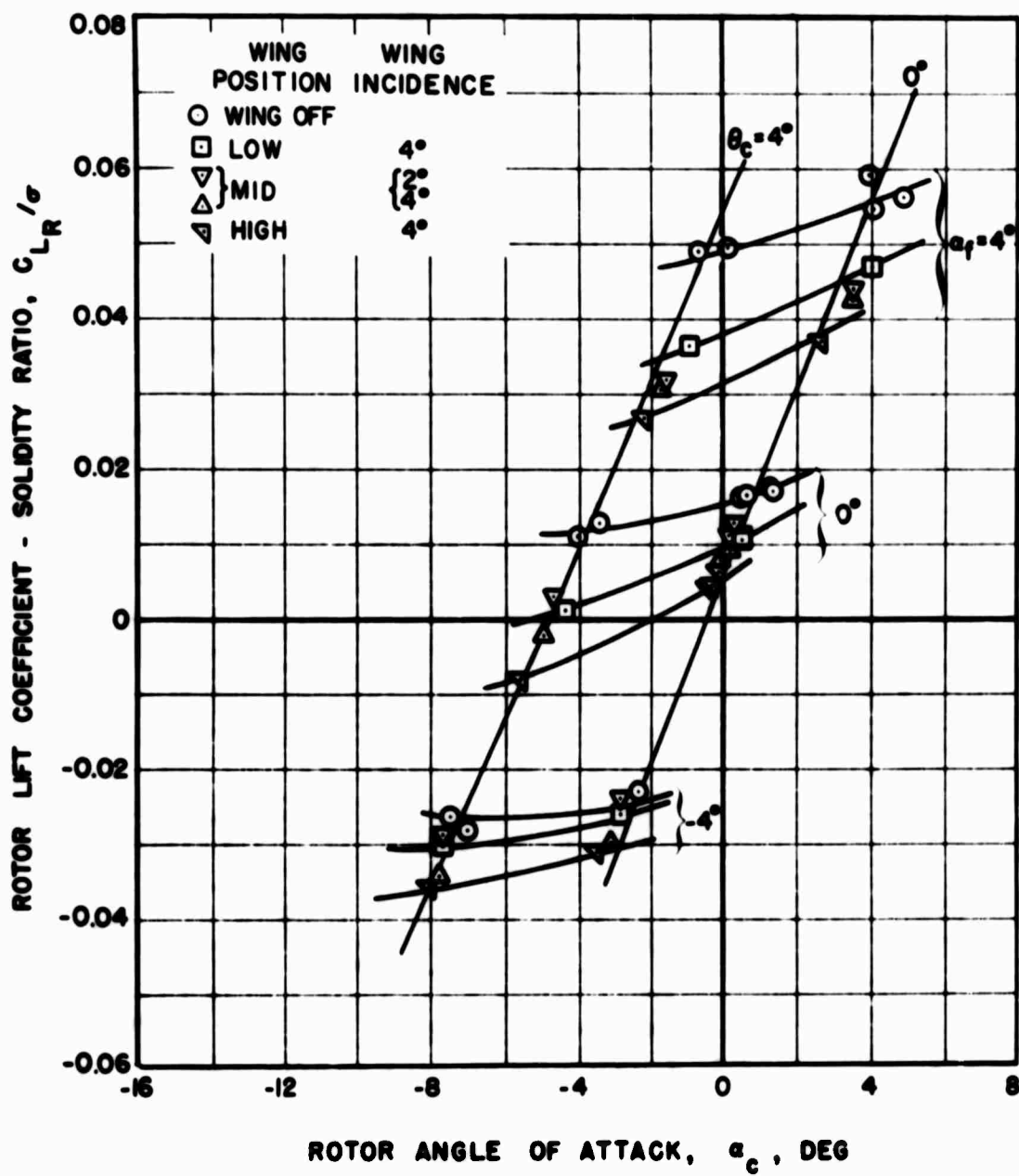
(a) Large Wing

Figure 29. Effect of Wing Size and Position on Rotor Lift and Angle of Attack at Various Fuselage Angles of Attack and $V_s=200$ Knots.



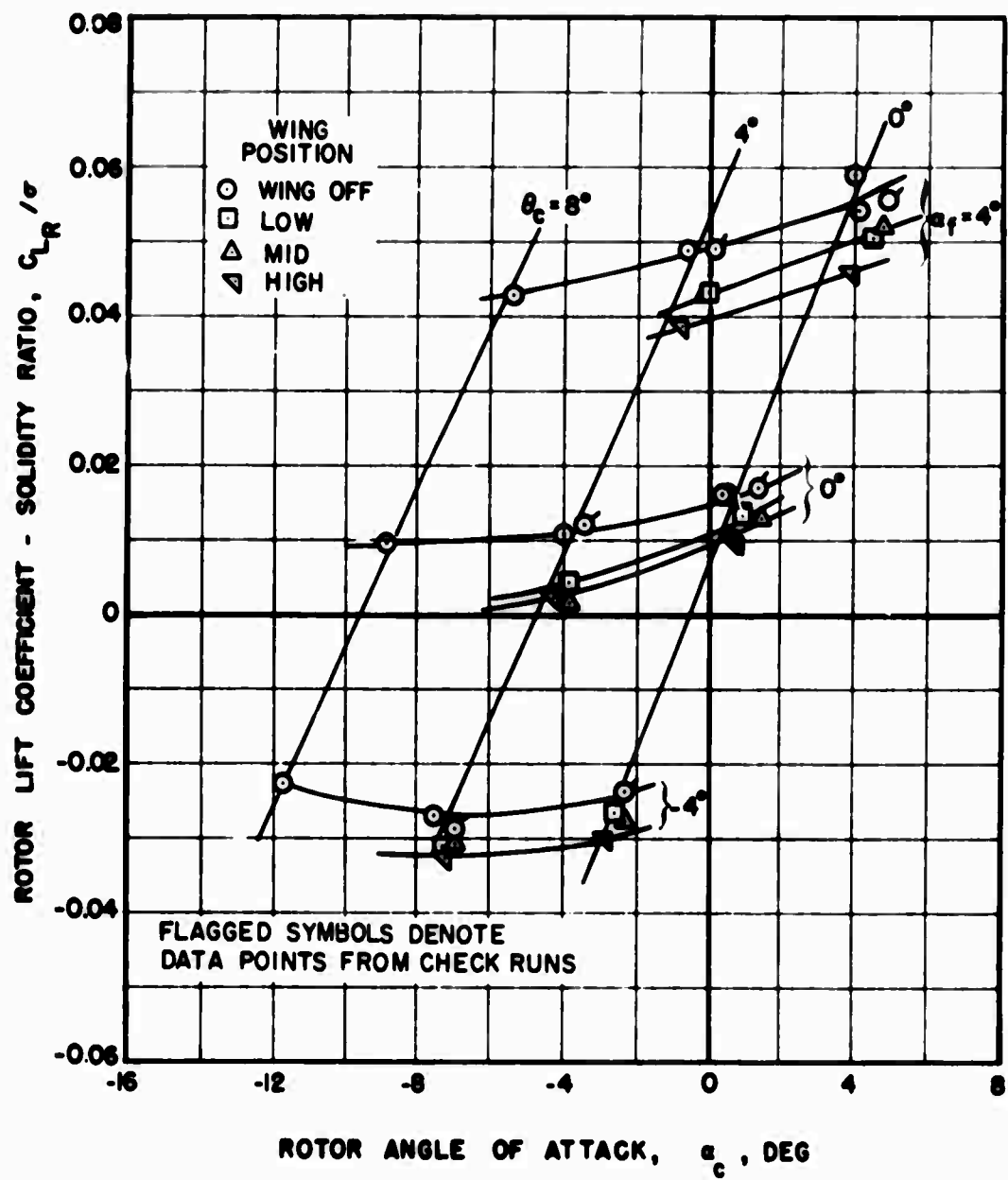
(b) Medium Wing

Figure 29. Concluded.



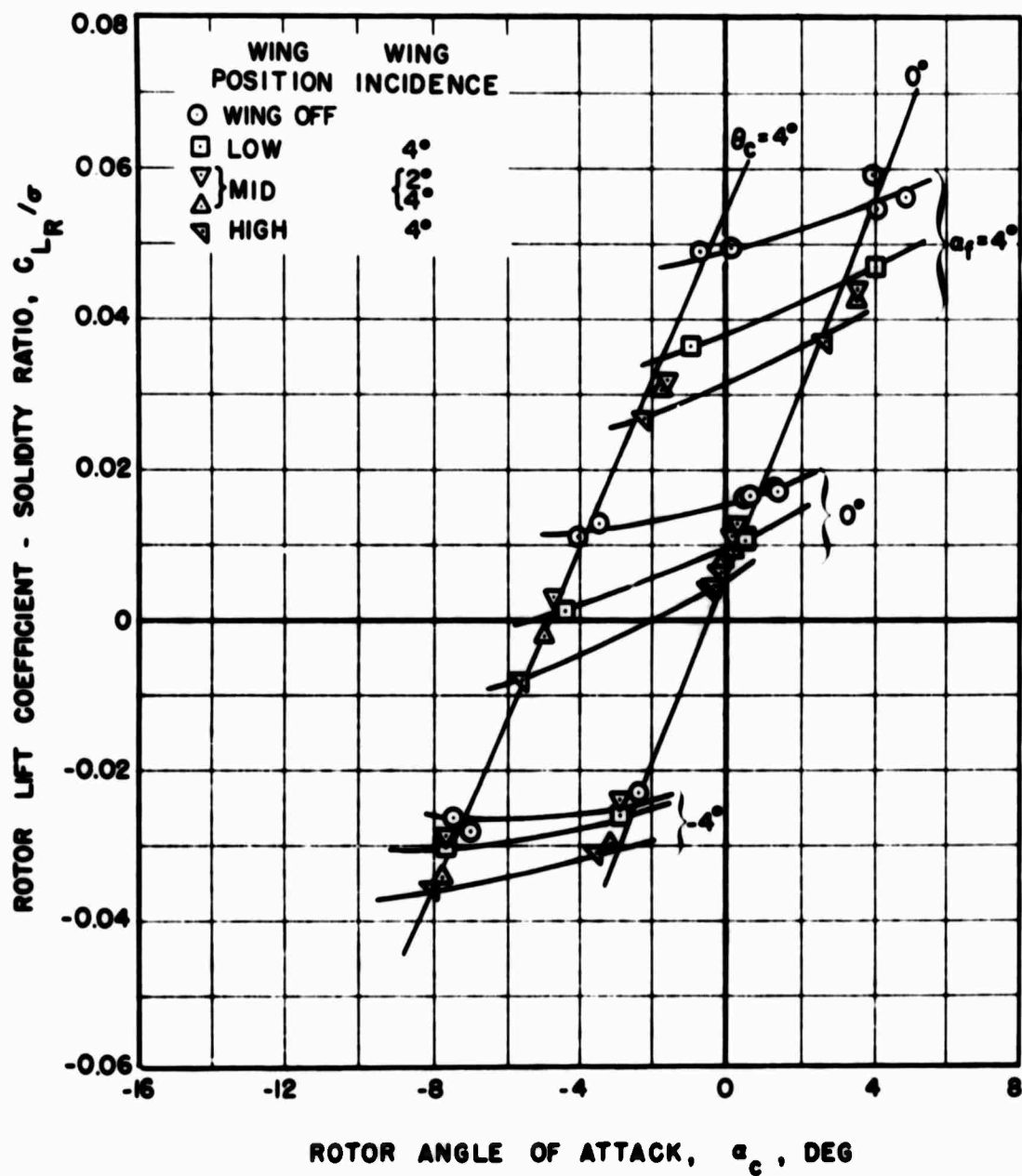
(a) Large Wing

Figure 30. Effect of Wing Size and Position on Rotor Lift and Angle of Attack for Various Fuselage Angles of Attack and $V_s = 300$ Knots.



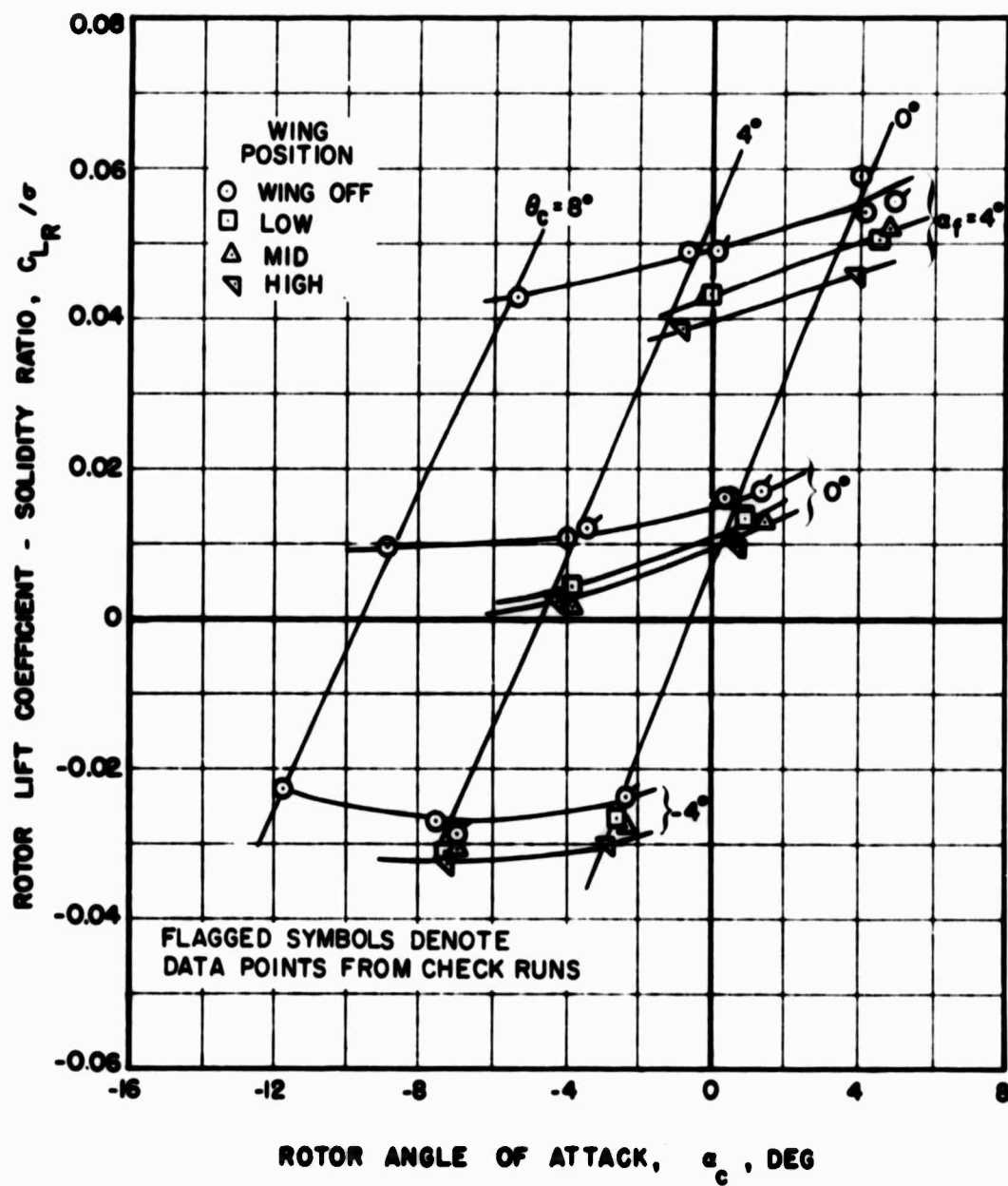
(b) Medium Wing

Figure 30. Concluded.



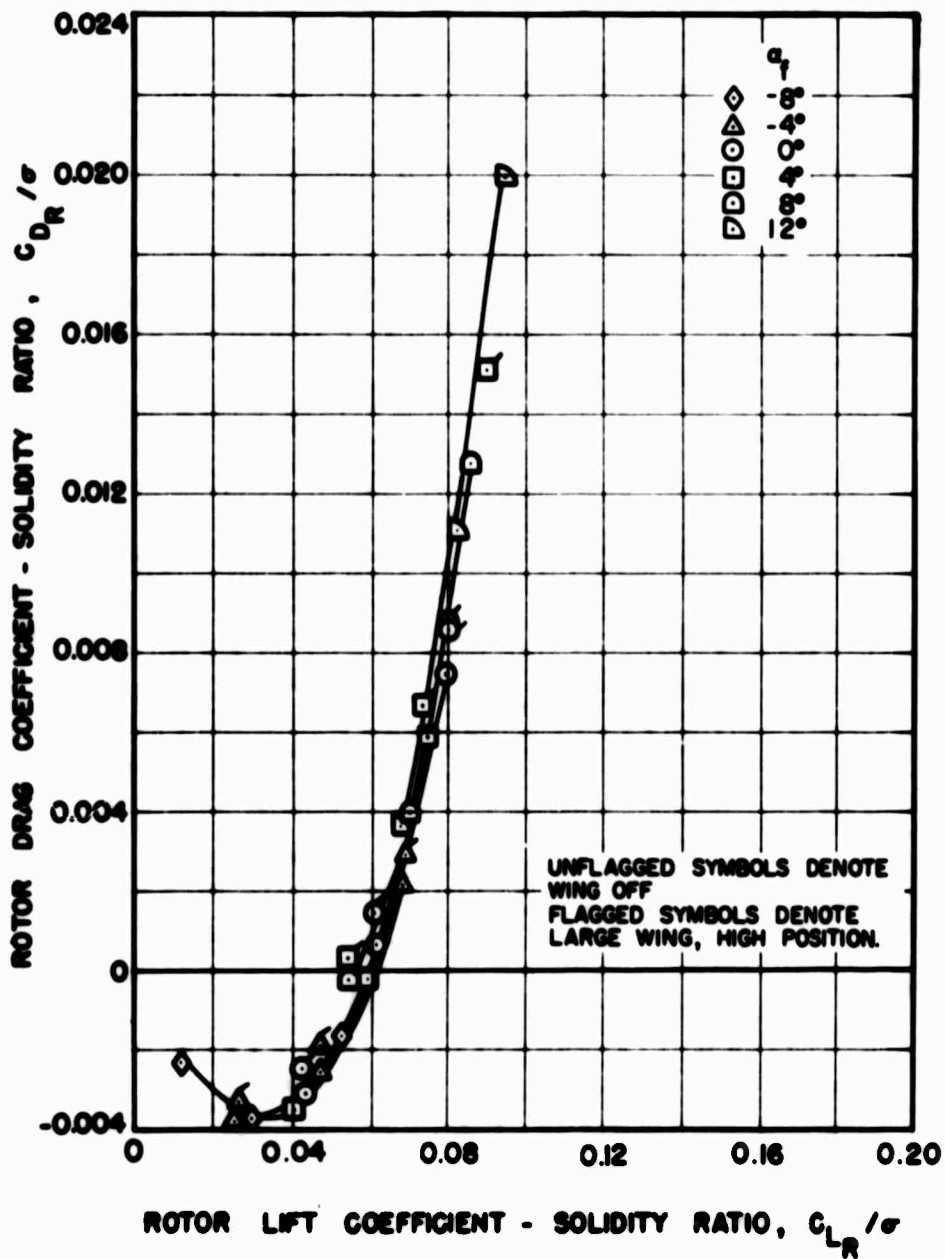
(a) Large Wing

Figure 30. Effect of Wing Size and Position on Rotor Lift and Angle of Attack for Various Fuselage Angles of Attack and $V_s = 300$ Knots.



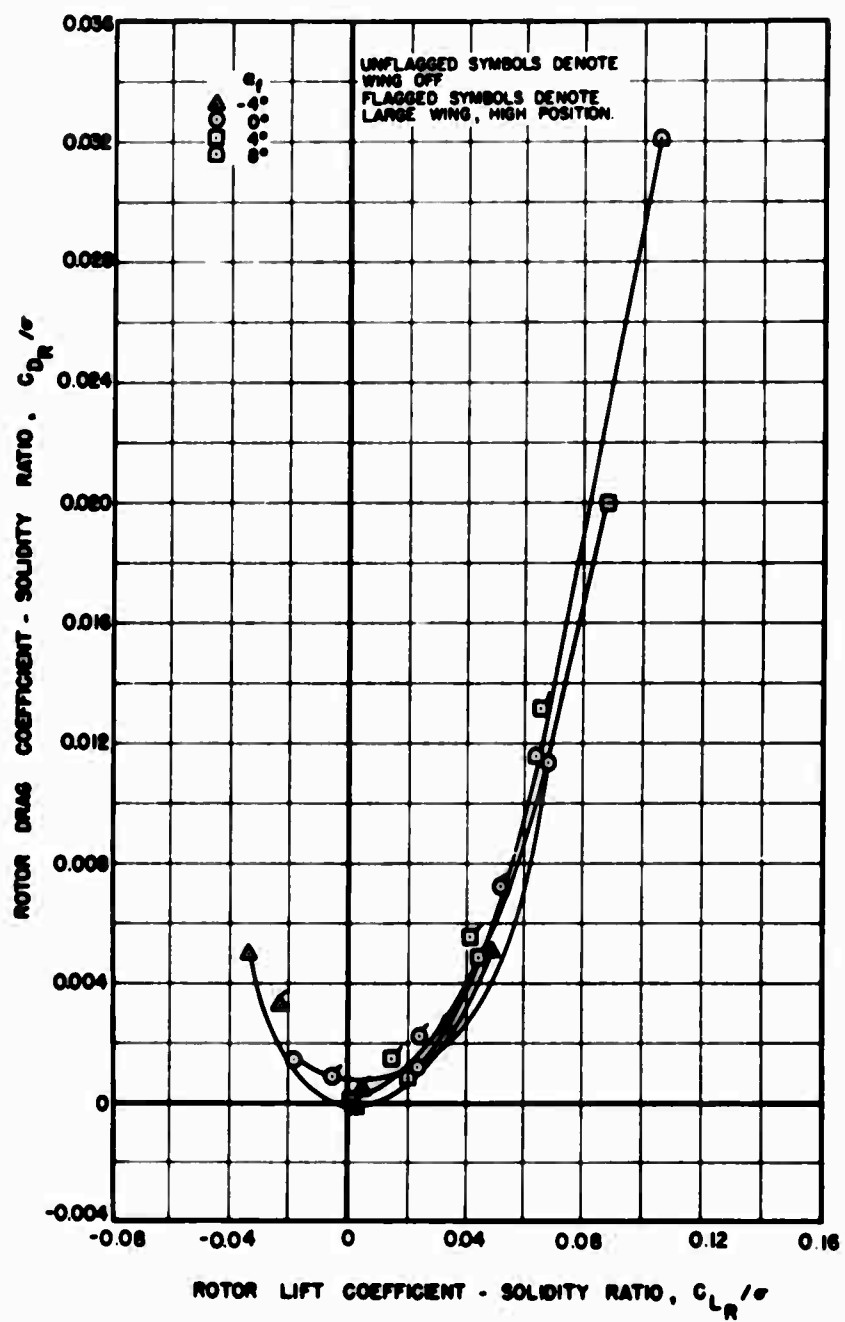
(b) Medium Wing

Figure 30. Concluded.



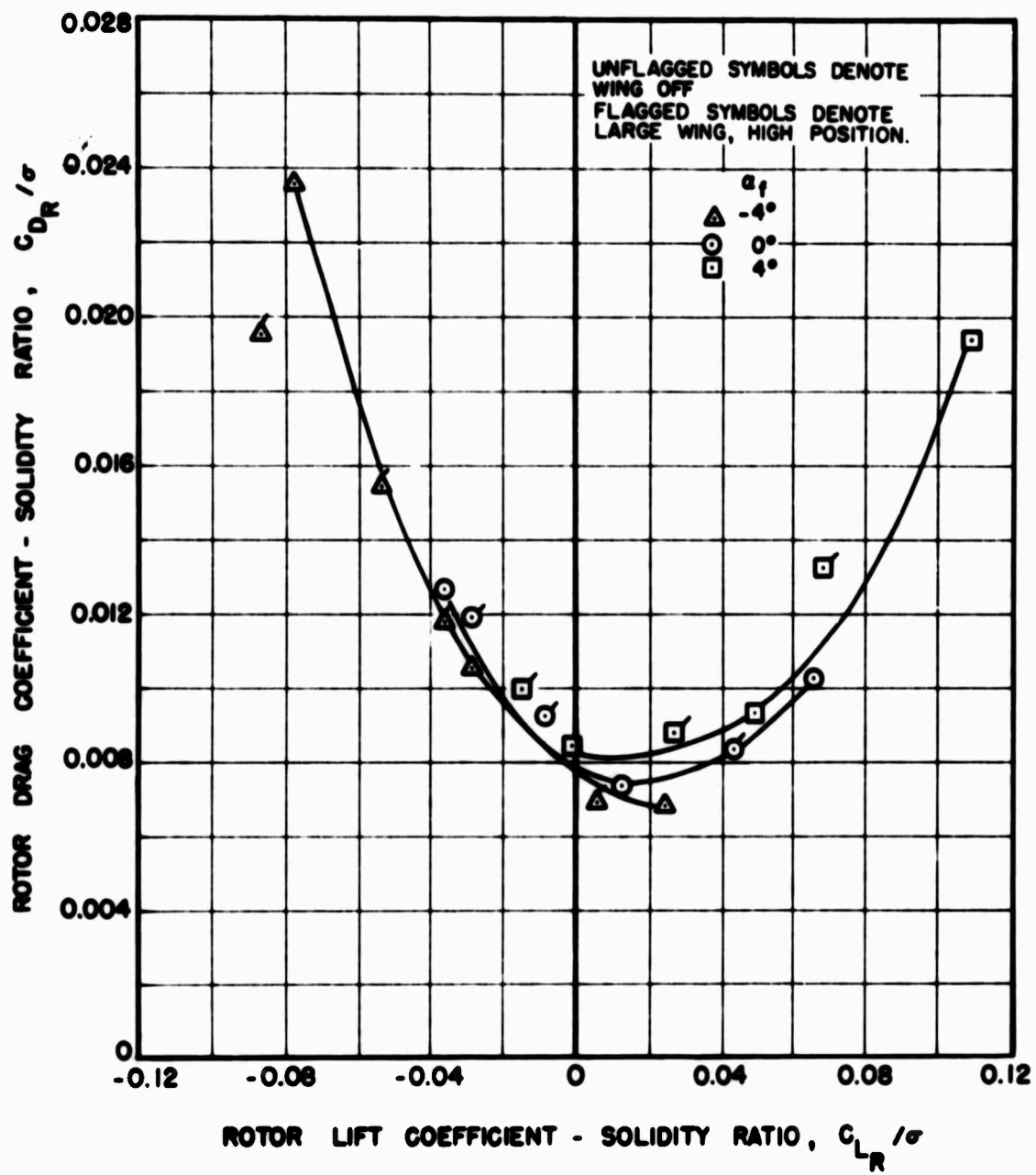
(a) $V_s = 120$ Knots, $\theta_c = 8^\circ$

Figure 31. Effect of the Large Wing, High Position on Rotor Lift and Drag for Various Fuselage Angles of Attack and Forward Speeds.



(b) $V_s = 200$ Knots, $\theta_c = 8^\circ$

Figure 31. Continued.



(c) $V_s = 300$ Knots, $\theta_c = 4^\circ$

Figure 31. Concluded.

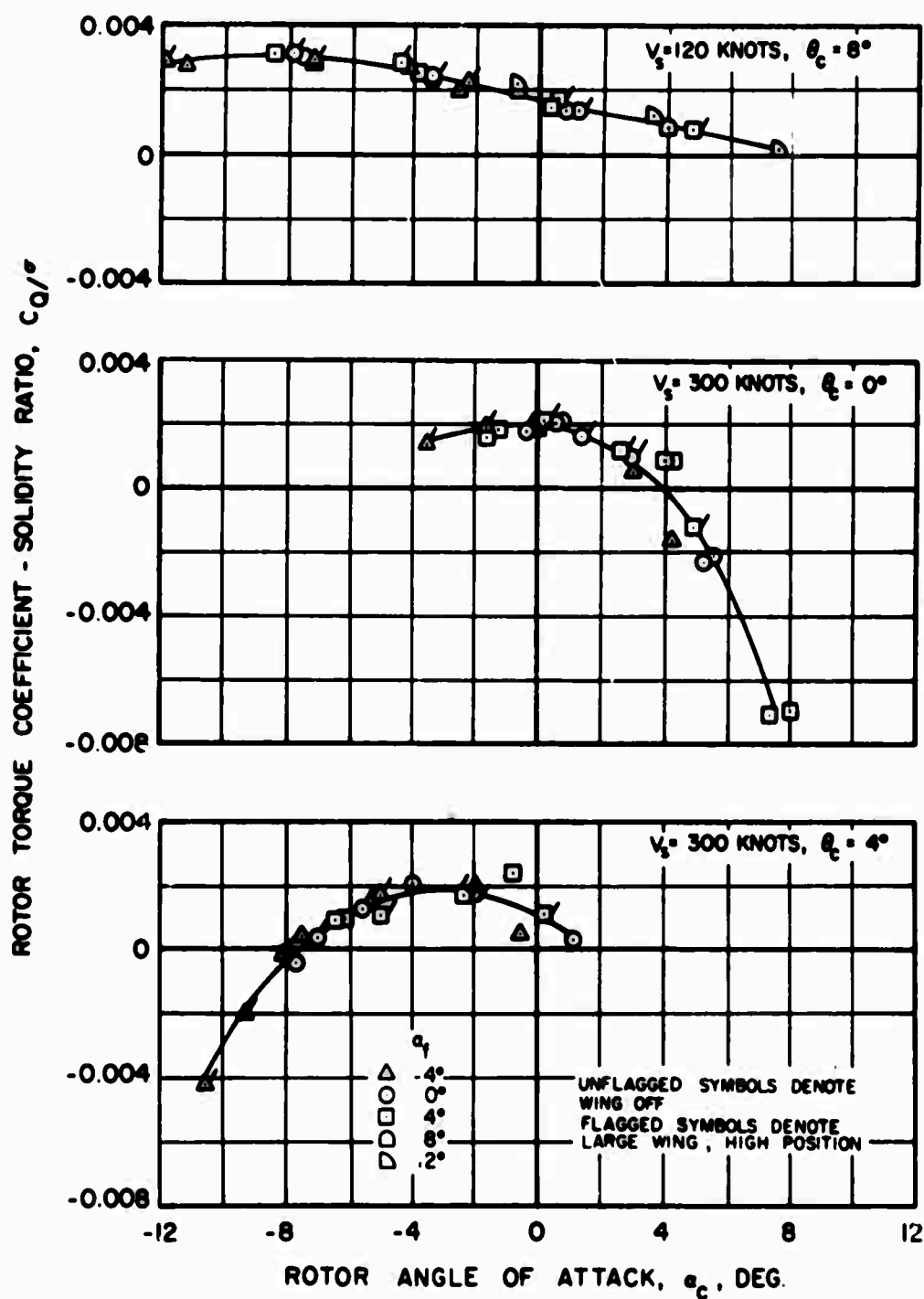


Figure 32. Effect of the Large Wing, High Position on Rotor Torque for Two Forward Speeds and Various Fuselage Angles of Attack.

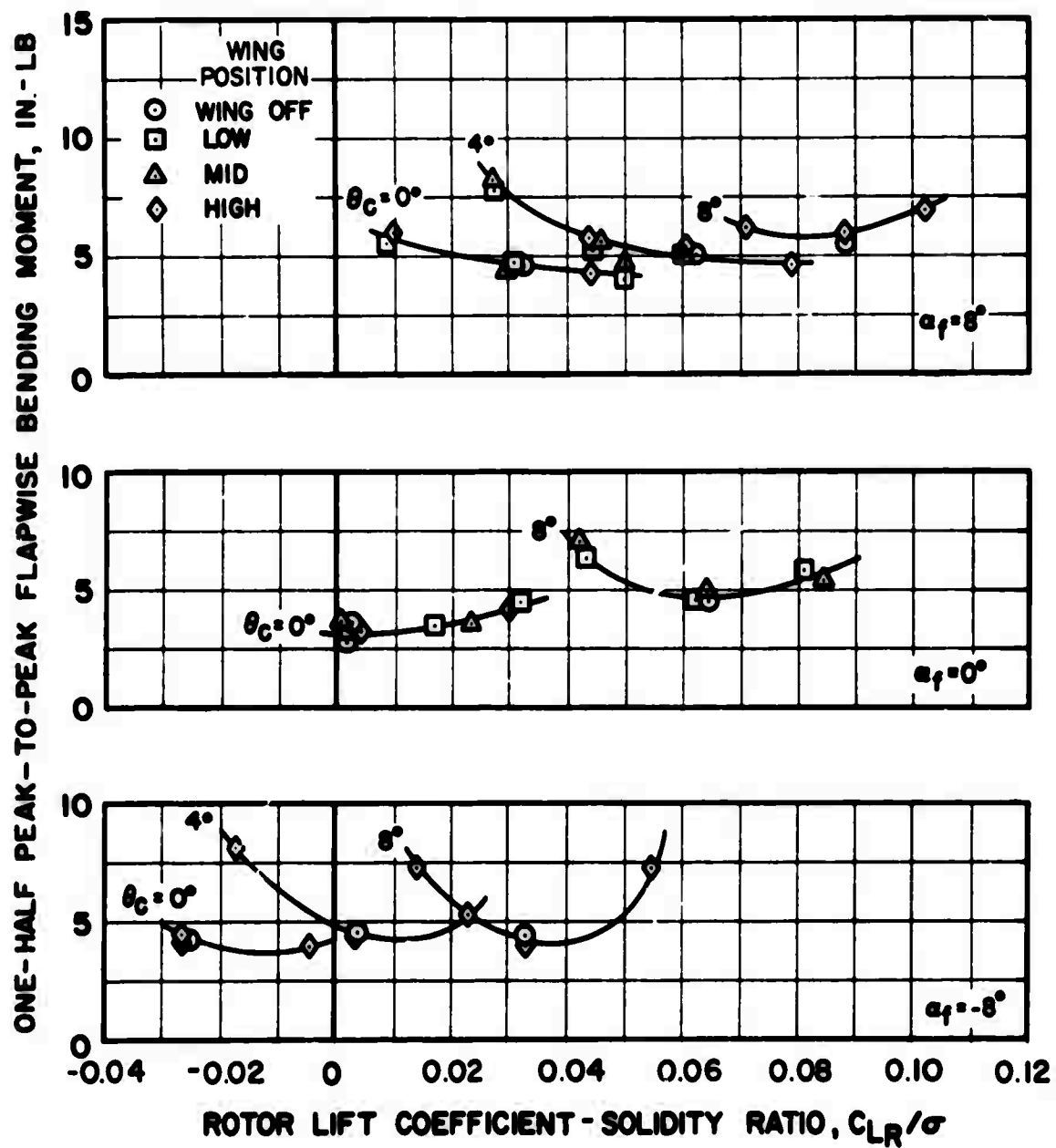


Figure 33. Effect of Rotor Lift, Wing Position, and Fuselage Angle of Attack on Rotor Blade Flapwise Vibratory Moments at $V_s = 120$ Knots, Medium Wing, Blade #1, 60%R.

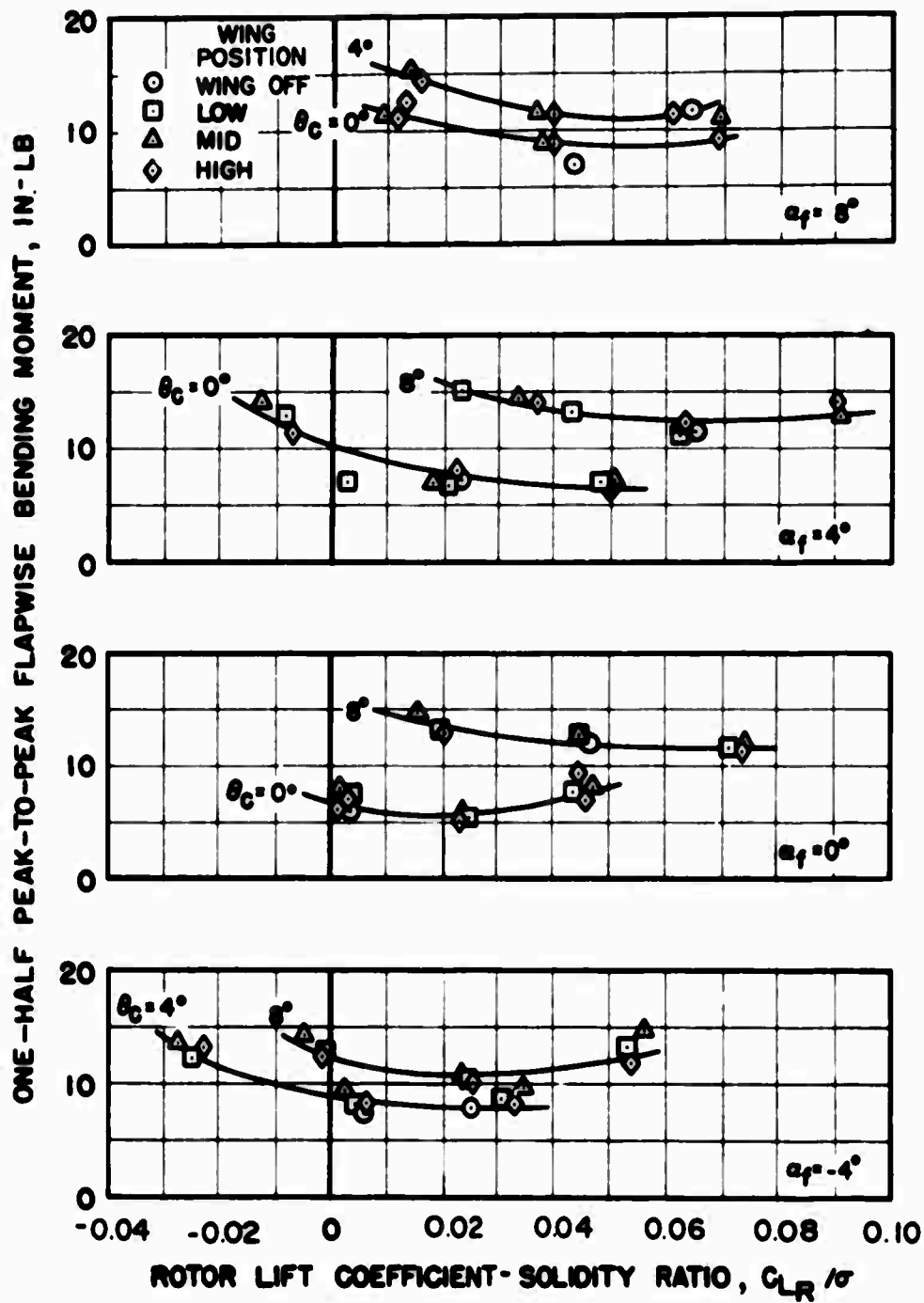


Figure 34. Effect of Rotor Lift, Wing Position, and Fuselage Angle of Attack on Rotor Blade Flapwise Vibratory Moments at $V_s = 200$ Knots, Medium Wing, Blade #1, 60%R.

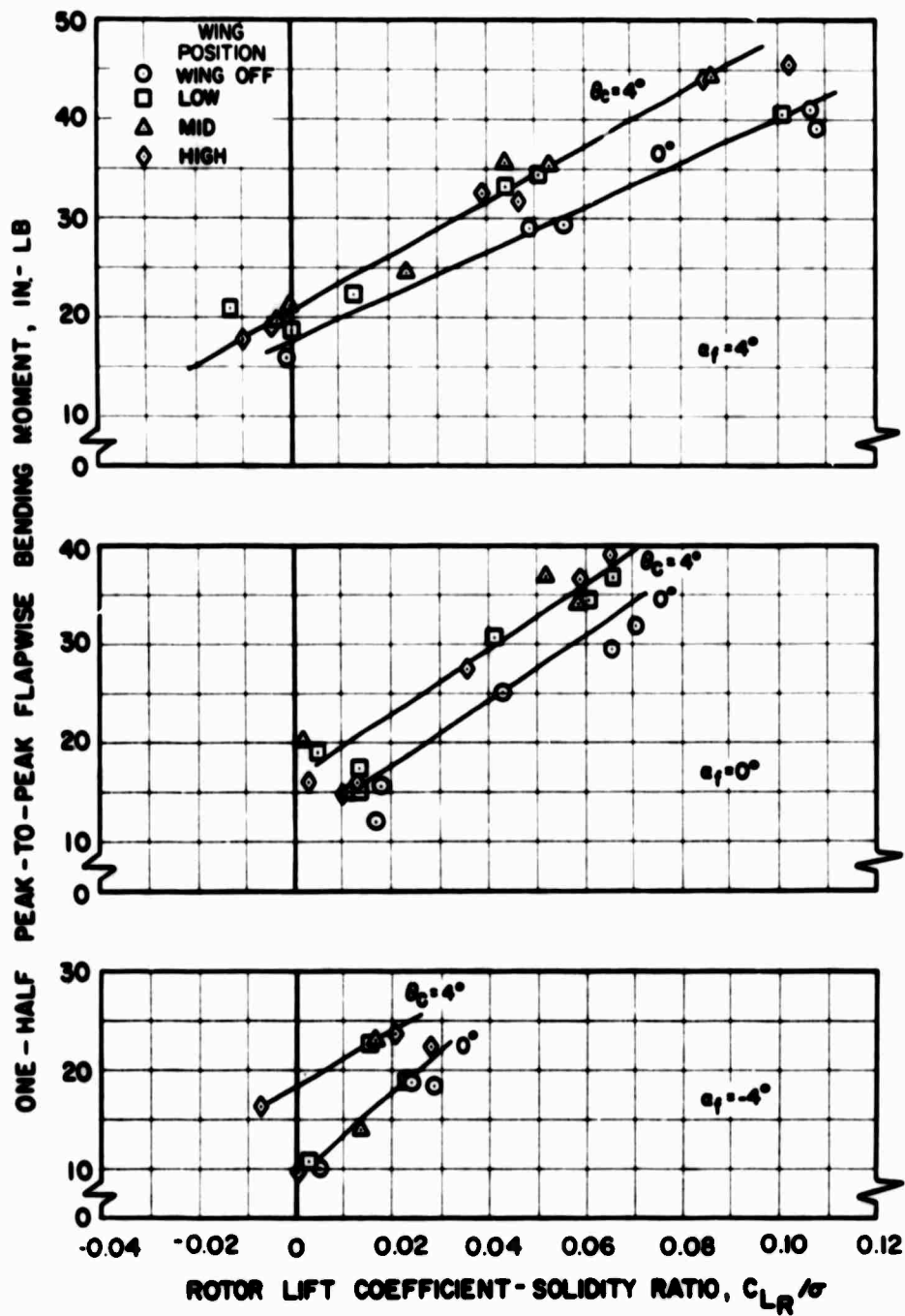


Figure 35. Effect of Rotor Lift, Wing Position, and Fuselage Angle of Attack on Rotor Blade Flapwise Vibratory Moments at $V_s = 300$ Knots, Medium Wing, Blade #1, 60%R.

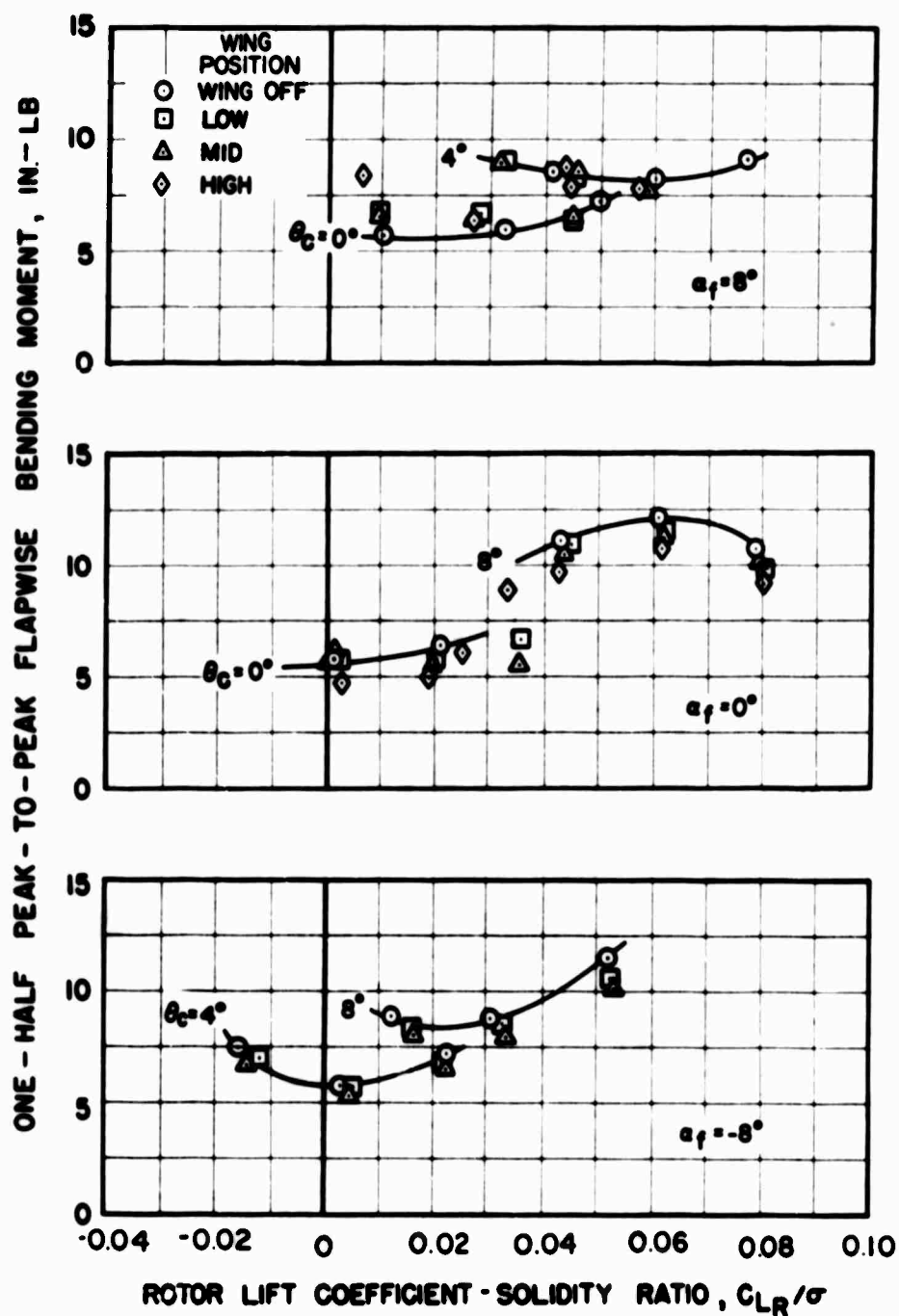


Figure 36. Effect of Rotor Lift, Wing Position, and Fuselage Angle of Attack on Rotor Blade Flapwise Vibratory Moments at $V_s = 120$ Knots, Large Wing, Blade #2, 60%R.

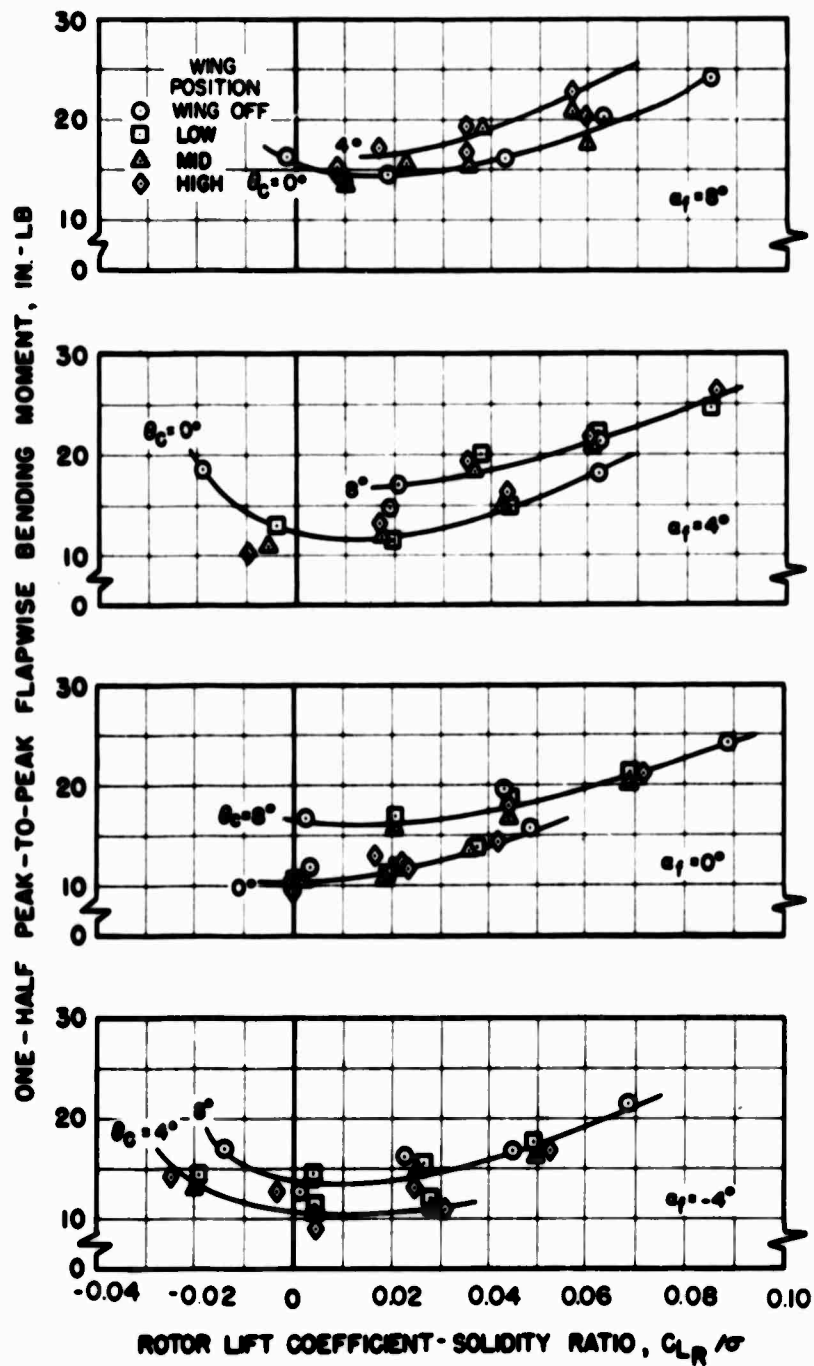


Figure 37. Effect of Rotor Lift, Wing Position, and Fuselage Angle of Attack on Rotor Blade Flapwise Vibratory Moments at $V_s = 200$ Knots, Large Wing, Blade #2, 60%R.

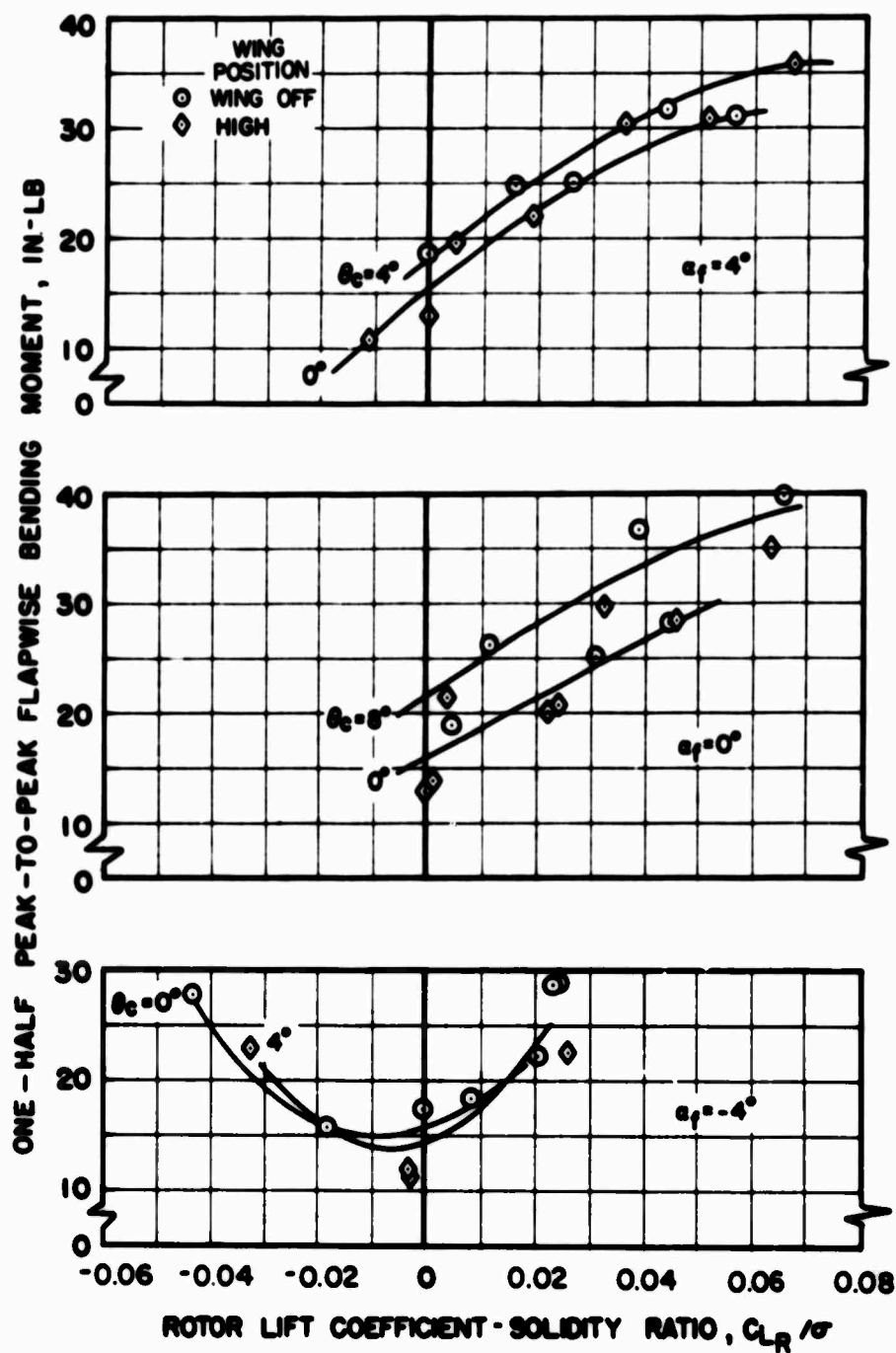


Figure 38. Effect of Rotor Lift, Wing Position, and Fuselage Angle of Attack on Rotor Blade Flapwise Vibratory Moments at $V_s = 232$ Knots, Large Wing, Blade #2, 60%R.

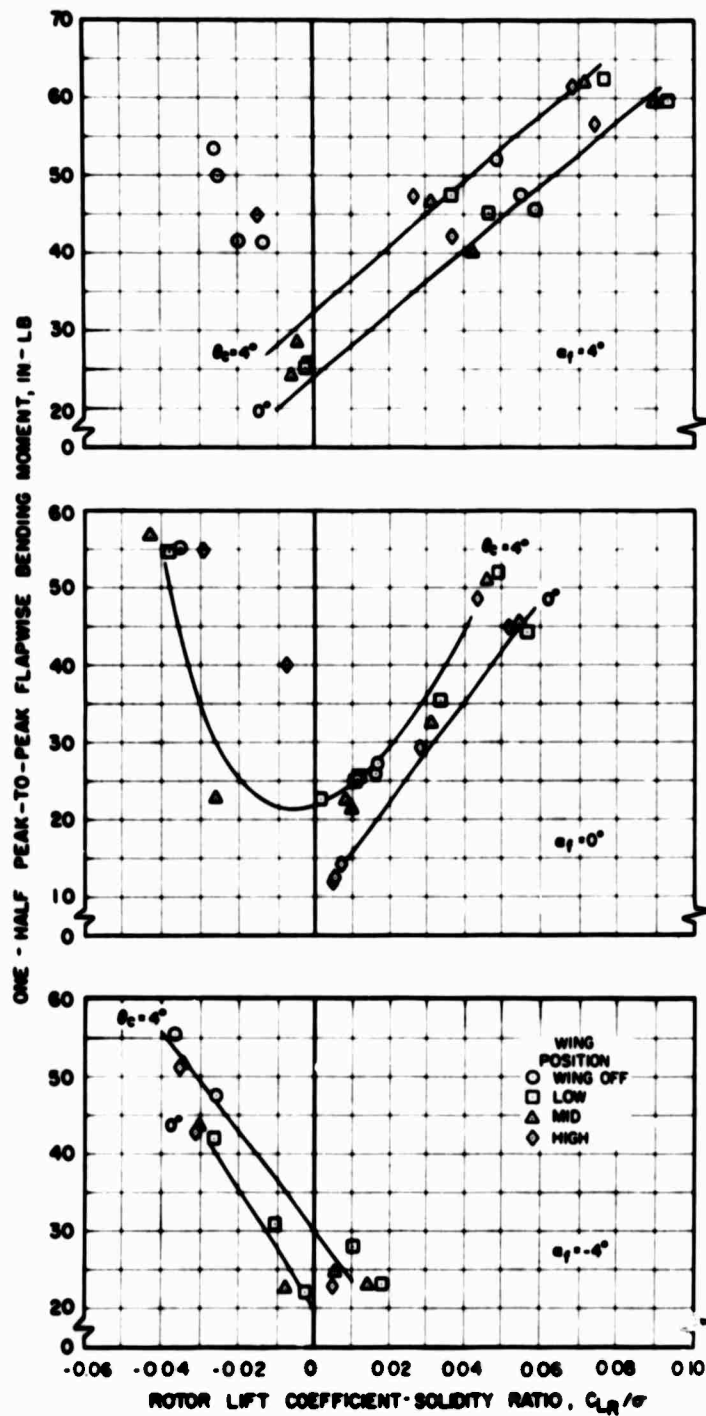


Figure 39. Effect of Rotor Lift, Wing Position, and Fuselage Angle of Attack on Rotor Blade Flapwise Vibratory Moments at $V_s = 300$ Knots, Large Wing, Blade #2, 60%R.

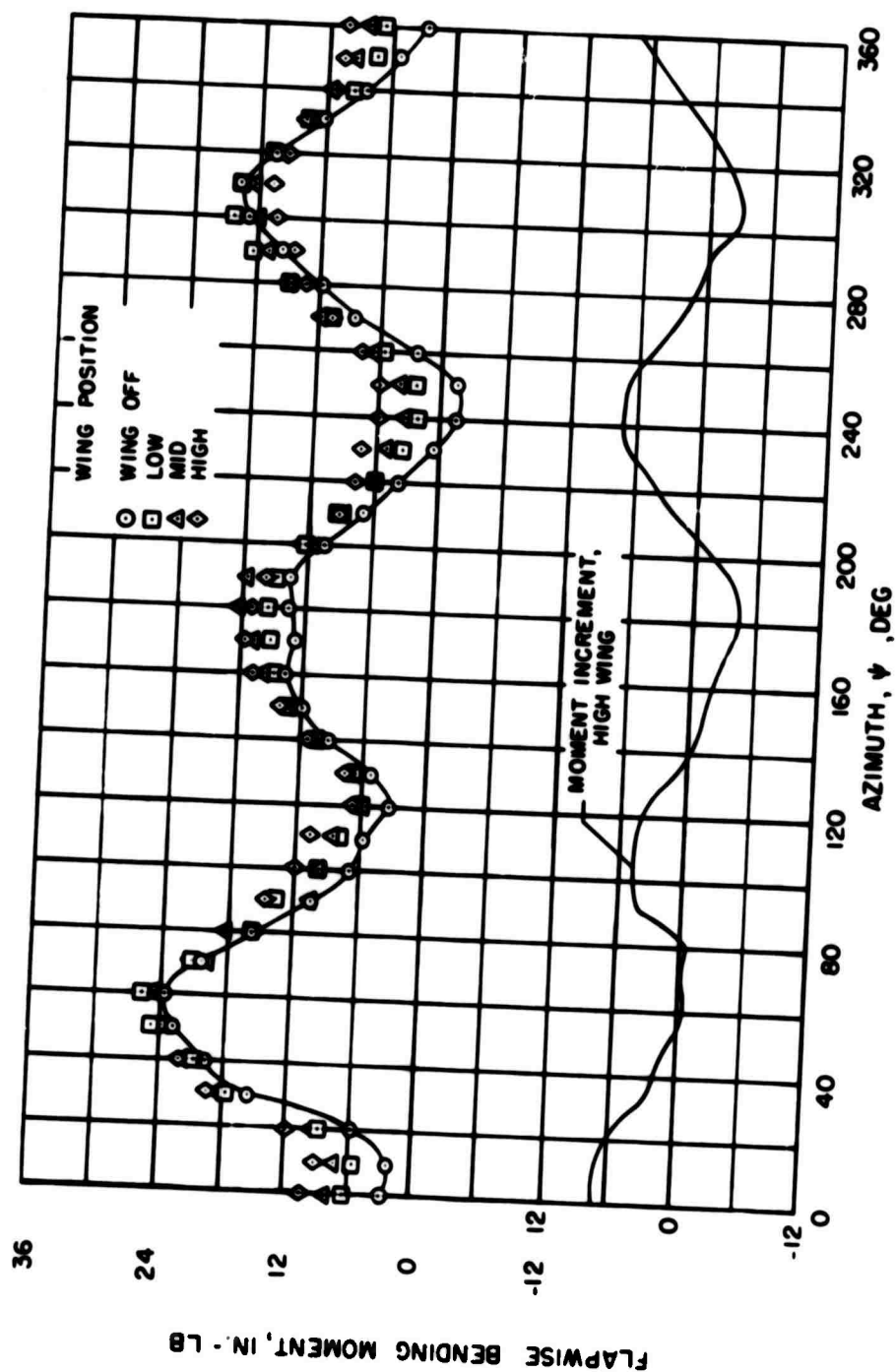


Figure 40. Effect of Wing Position on Rotor Blade Flapwise Moment Azimuthal Variation for the Large Wing at $V_s = 200$ Knots, $\alpha_f = -4^\circ$, $\theta_c = 4^\circ$, $C_{LR}/\sigma = 0.005$, Blade #2, 60%R.

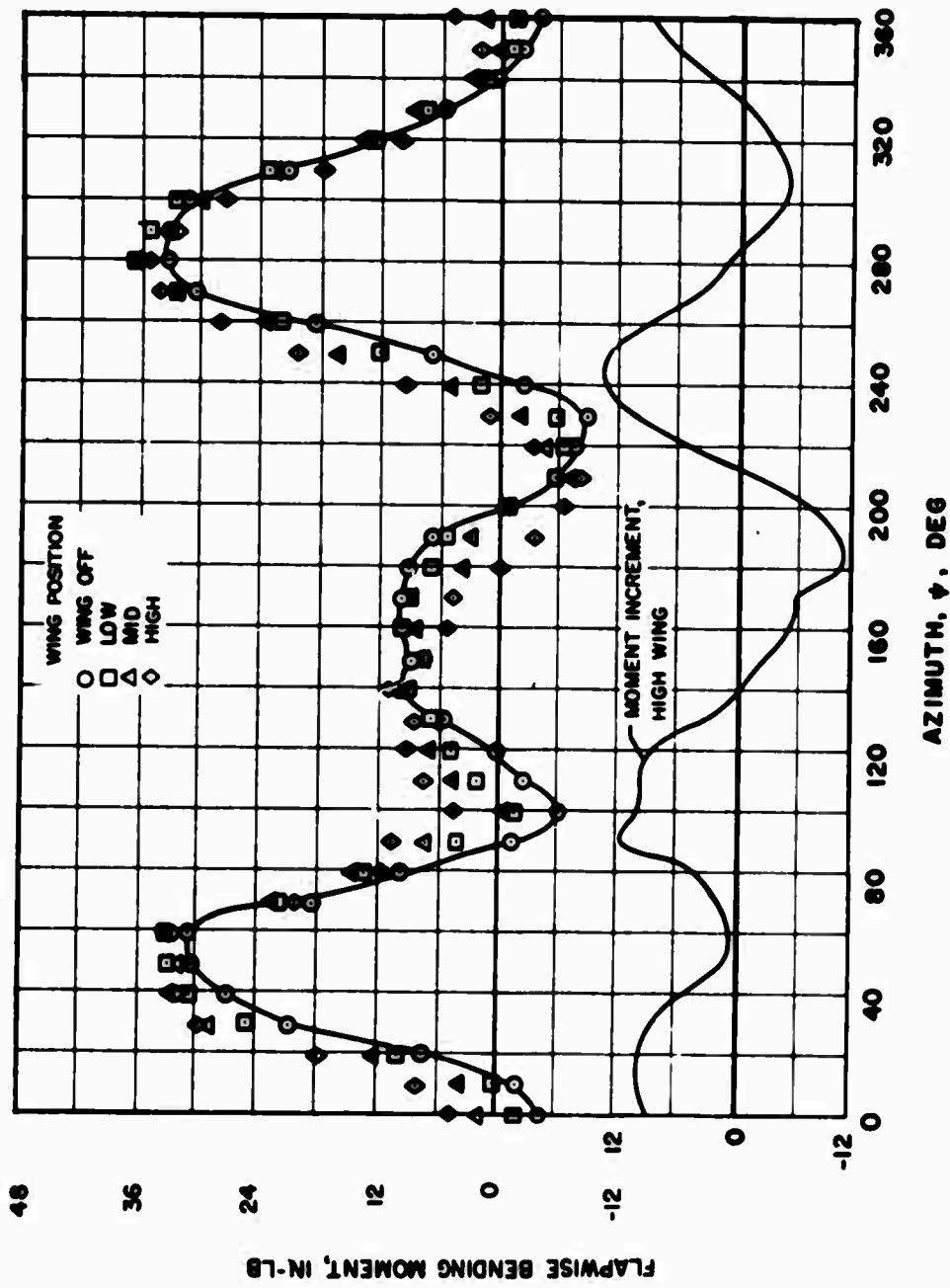


Figure 41. Effect of Wing Position on Rotor Blade Flapwise Moment Azimuthal Variation for the Large Wing at $V_s = 200$ Knots, $\alpha_f = 4^\circ$, $\theta_c = 8^\circ$, $C_{L_R}/\sigma = 0.065$, Blade #2, 60%R.

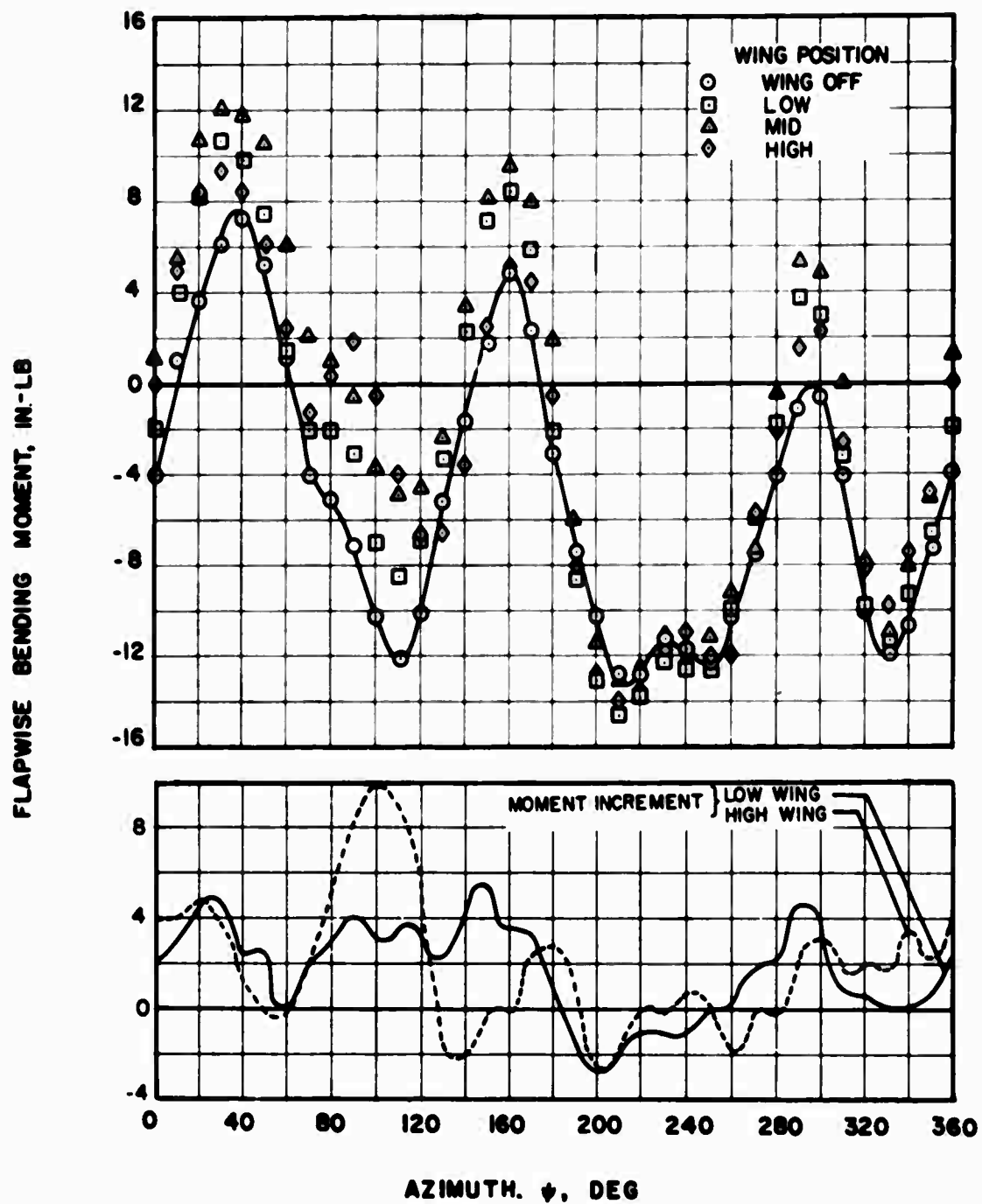


Figure 42. Effect of Wing Position on Rotor Blade Flapwise Moment Azimuthal Variation for the Large Wing at $V_s = 300$ Knots, $\alpha_f = 0^\circ$, $\theta_c = 0^\circ$, $C_{LR}/\sigma \approx 0.020$, Blade #1, 60%R.

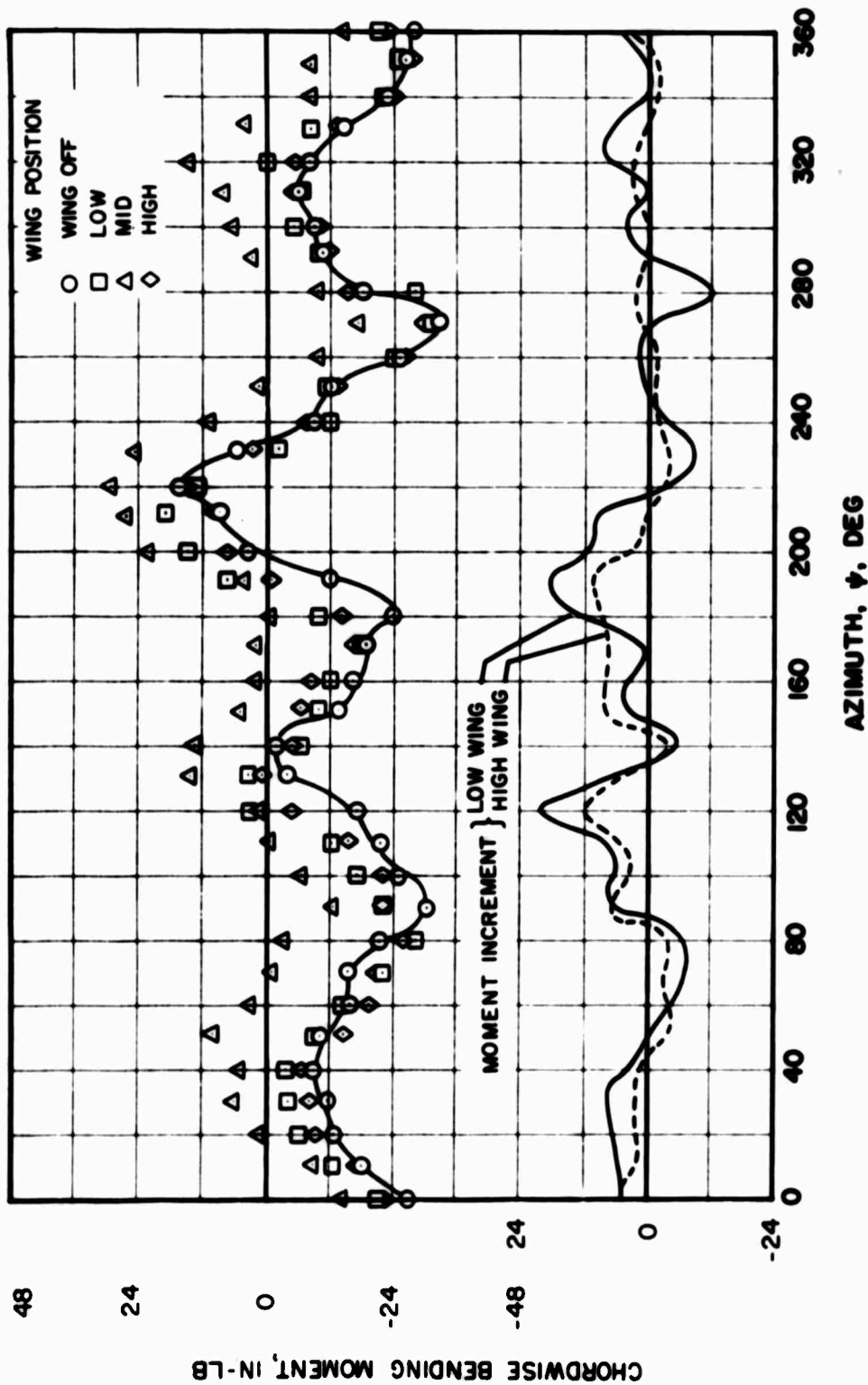


Figure 43. Effect of Wing Position on Rotor Blade Chordwise Moment Azimuthal Variation for the Large Wing at $V_s = 200$ Knots, $\alpha_f = -4^\circ$, $\theta_c = 4^\circ$, $C_{L_R}/\sigma = 0.005$, Blade #2, 20%R.

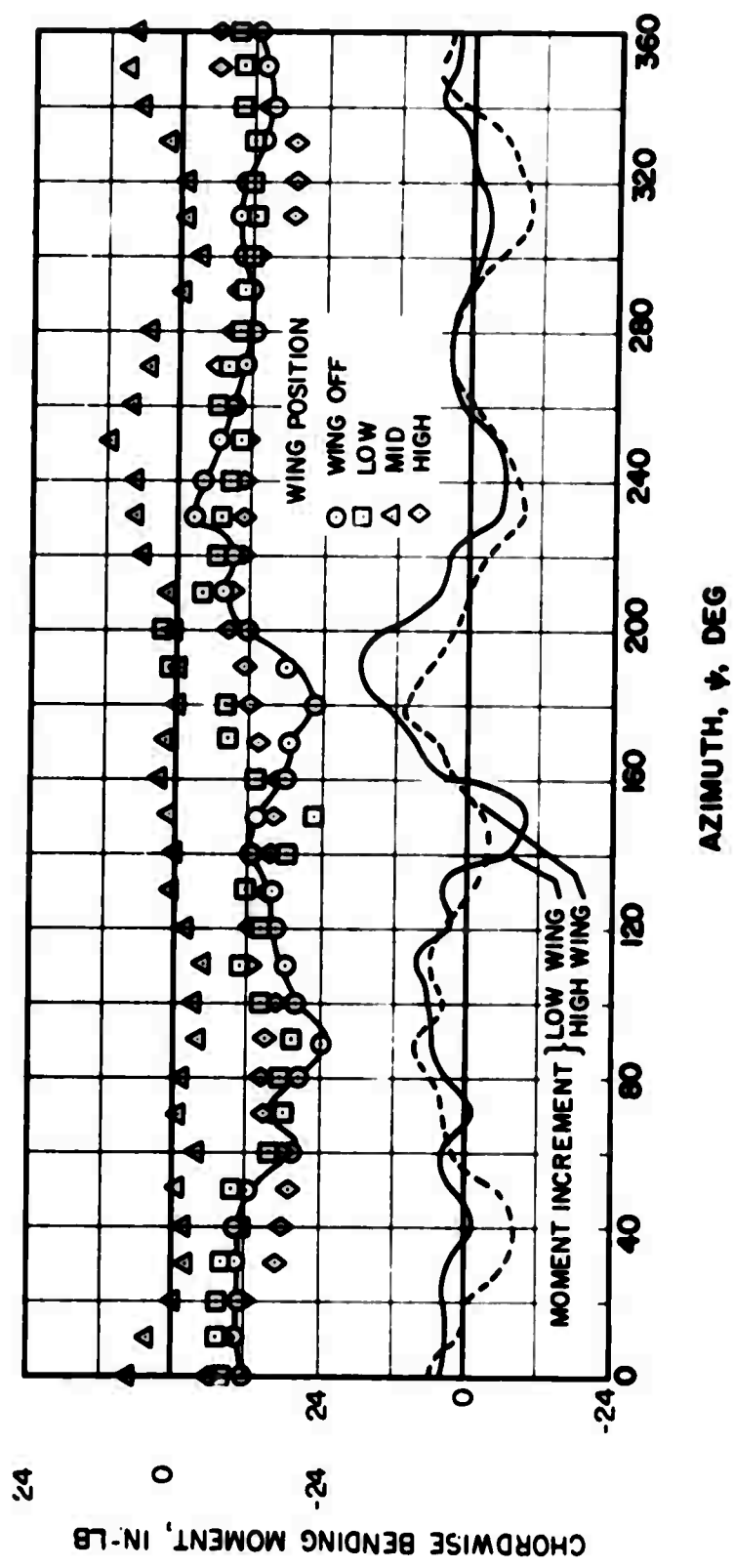


Figure 44. Effect of Wing Position on Rotor Blade Chordwise Moment Azimuthal Variation for the Large Wing at $V_s = 200$ Knots, $\alpha_f = 4^\circ$, $\theta_c = 8^\circ$, $C_{LR}/\sigma = 0.065$, Blade #2, 20%R.

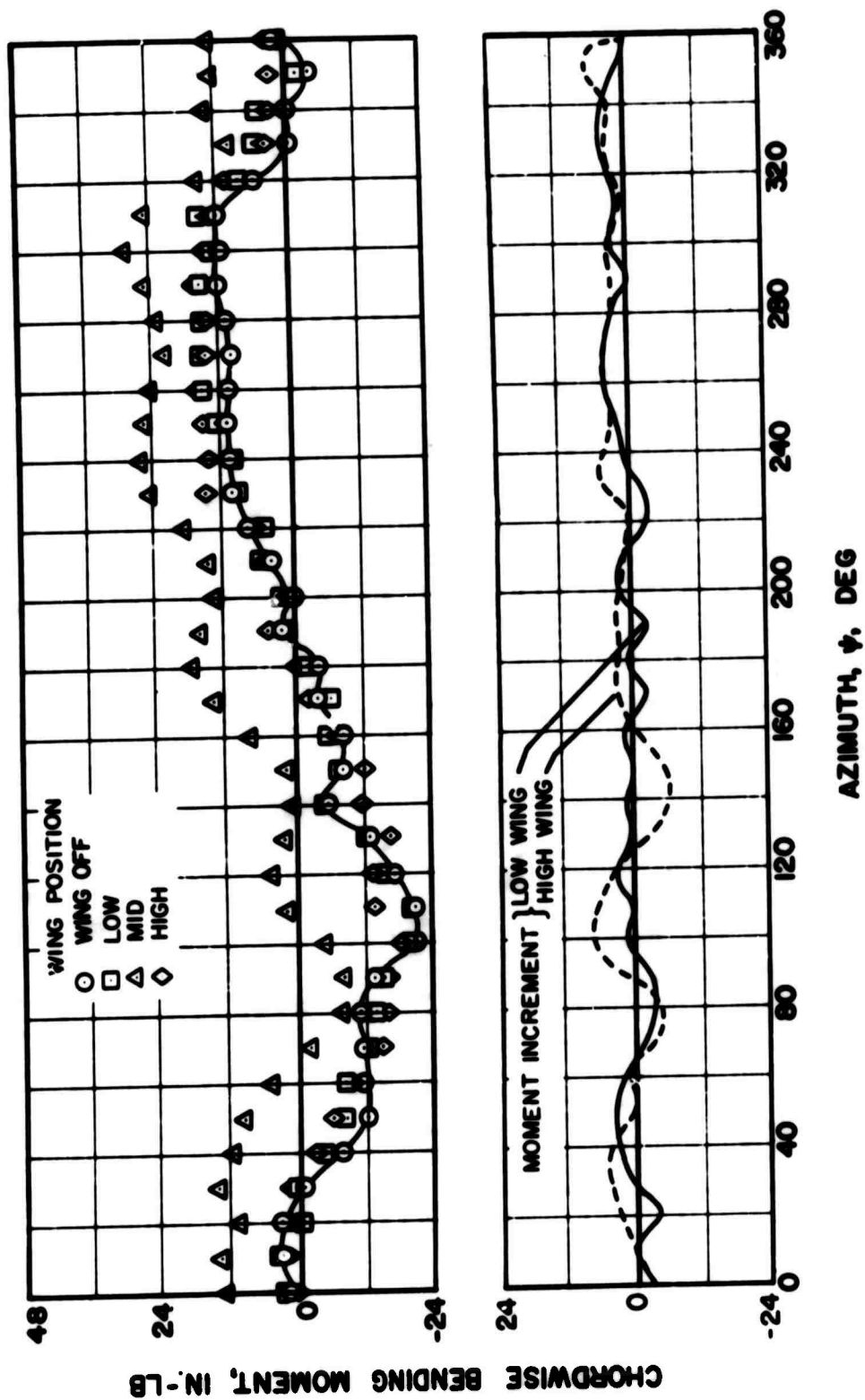


Figure 45. Effect of Wing Position on Rotor Blade Chordwise Moment Azimuthal Variation for the Large Wing at $V_s = 300$ Knots, $\alpha_t = 0^\circ$, $\theta_c = 0^\circ$, $CL_R/\sigma \approx 0.020$, Blade #1, 20%R.

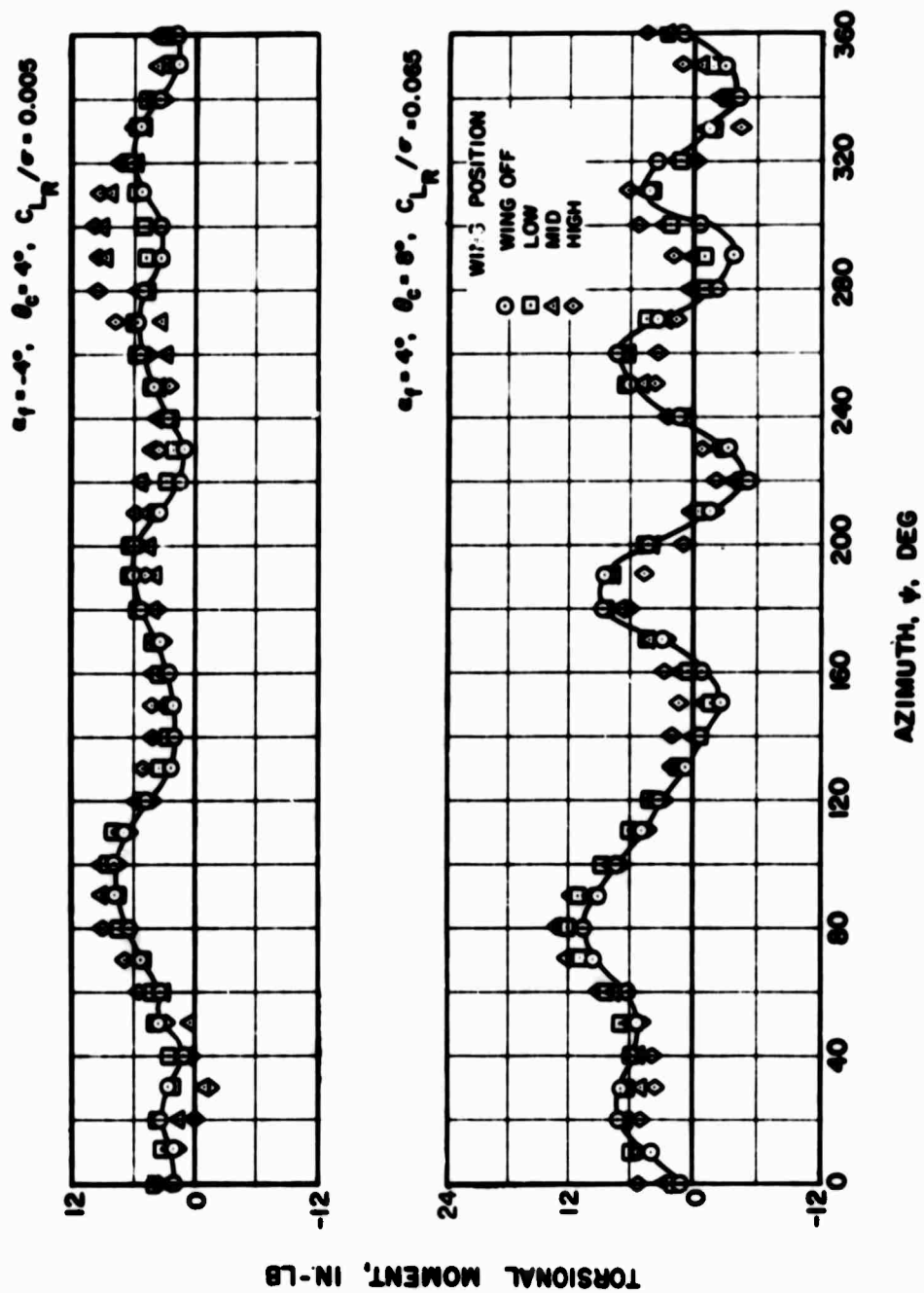


Figure 46. Effect of Wing Position on Rotor Blade Torsional Moment Azimuthal Variation for the Large Wing at $V_s = 200$ Knots and Two Rotor Operating Conditions, Blade #2, 18%R.

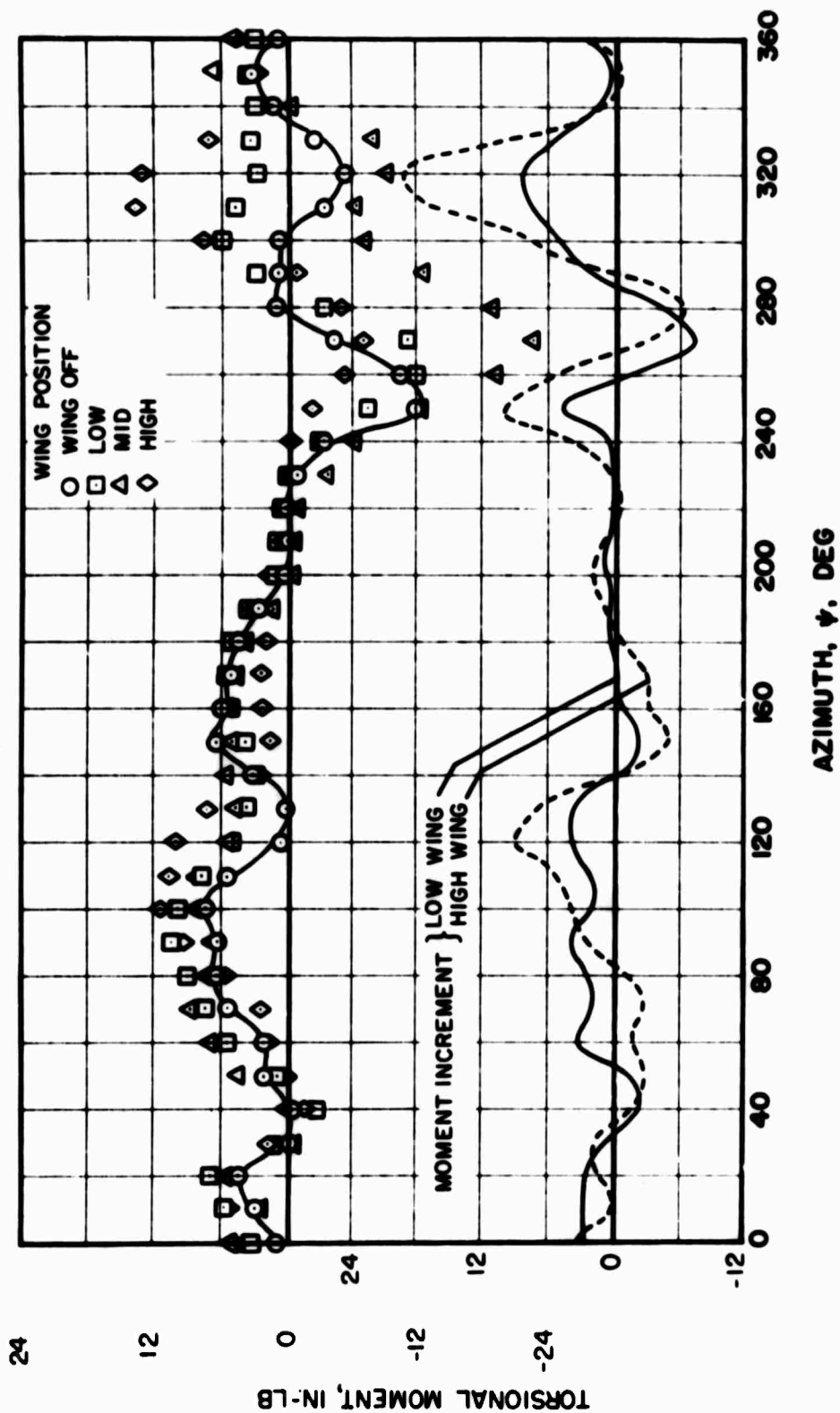


Figure 47. Effect of Wing Position on Rotor Blade Torsional Moment Azimuthal Variation for the Large Wing at $V_s = 300$ Knots, $\alpha_f = 0^\circ$, $\theta_c = 0^\circ$, $CL_R/\sigma \approx 0.020$, Blade #1, 18%R.

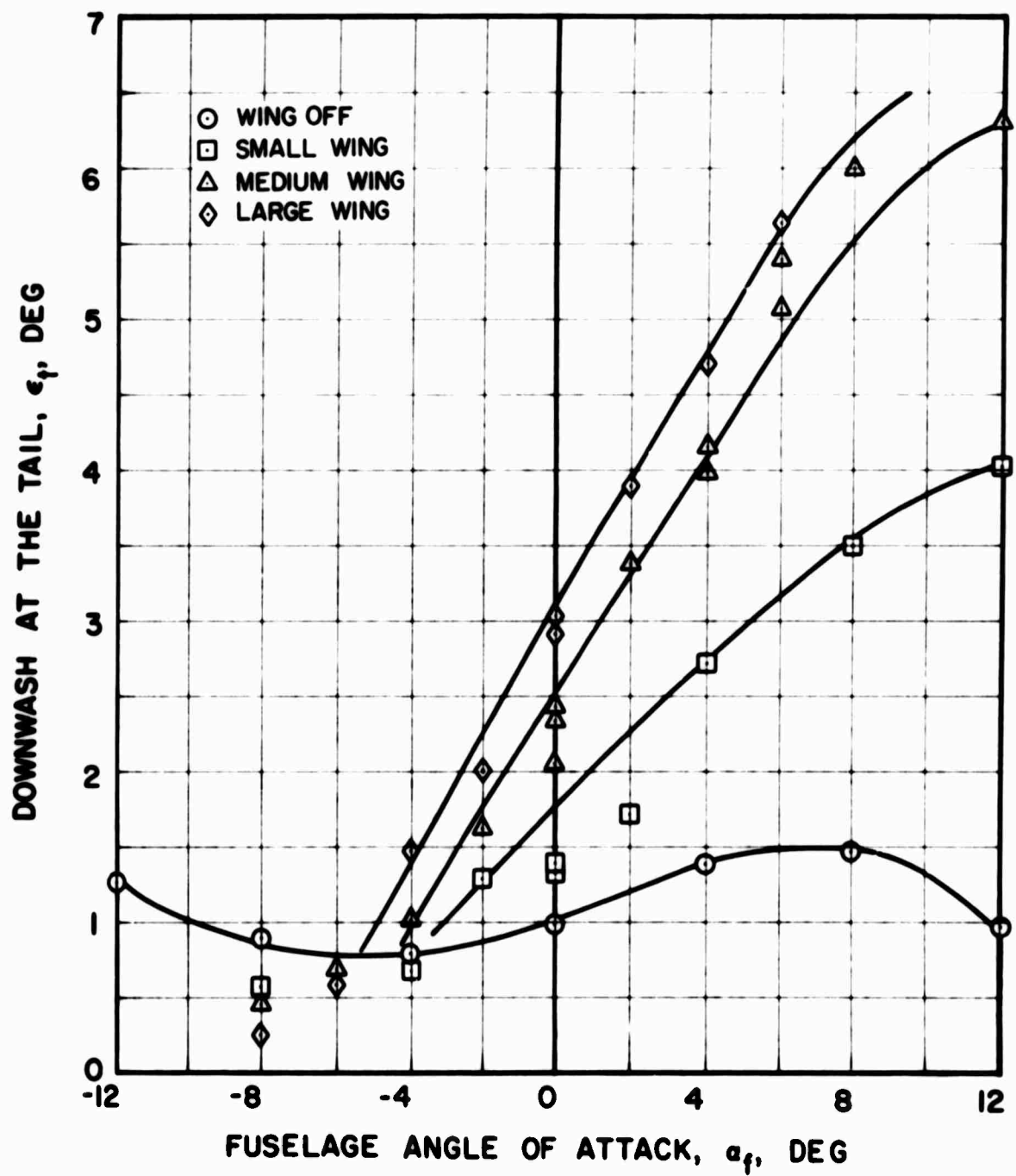


Figure 48. Effect of Fuselage Angle of Attack on Downwash Angle at the Tail for Various Size Wings at the Mid Position, Without Rotor.

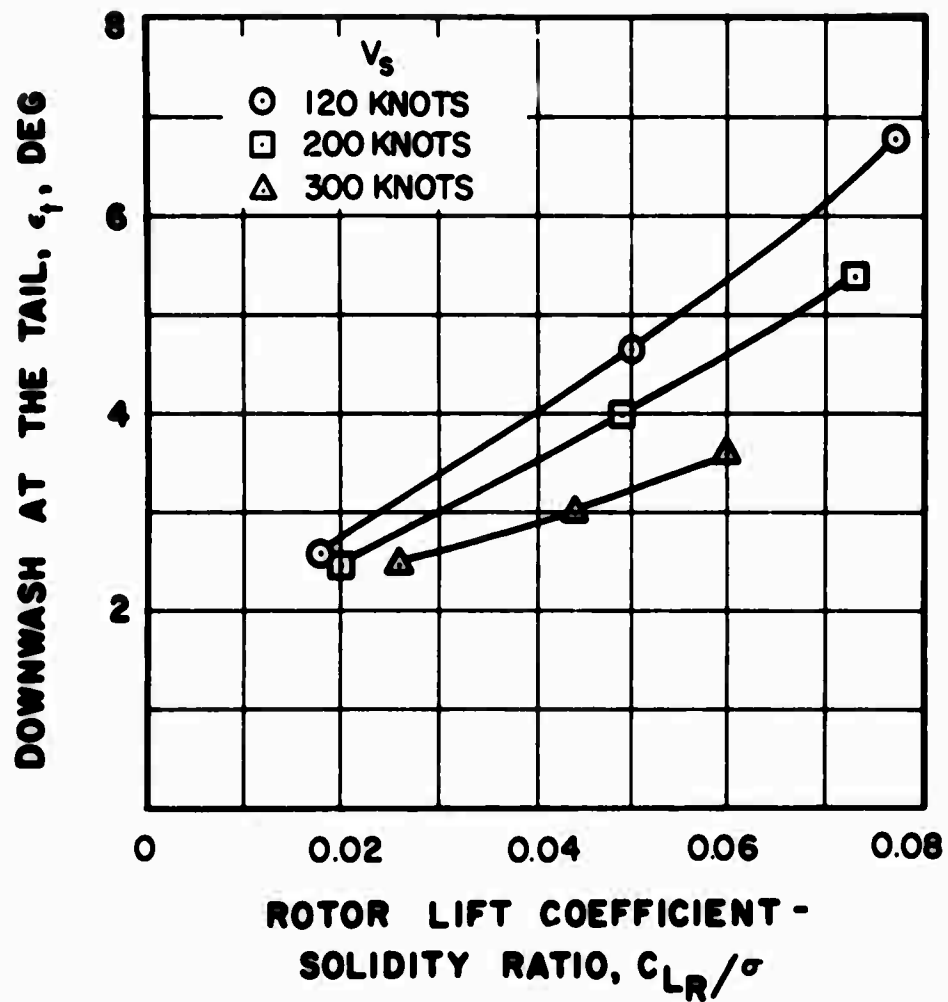
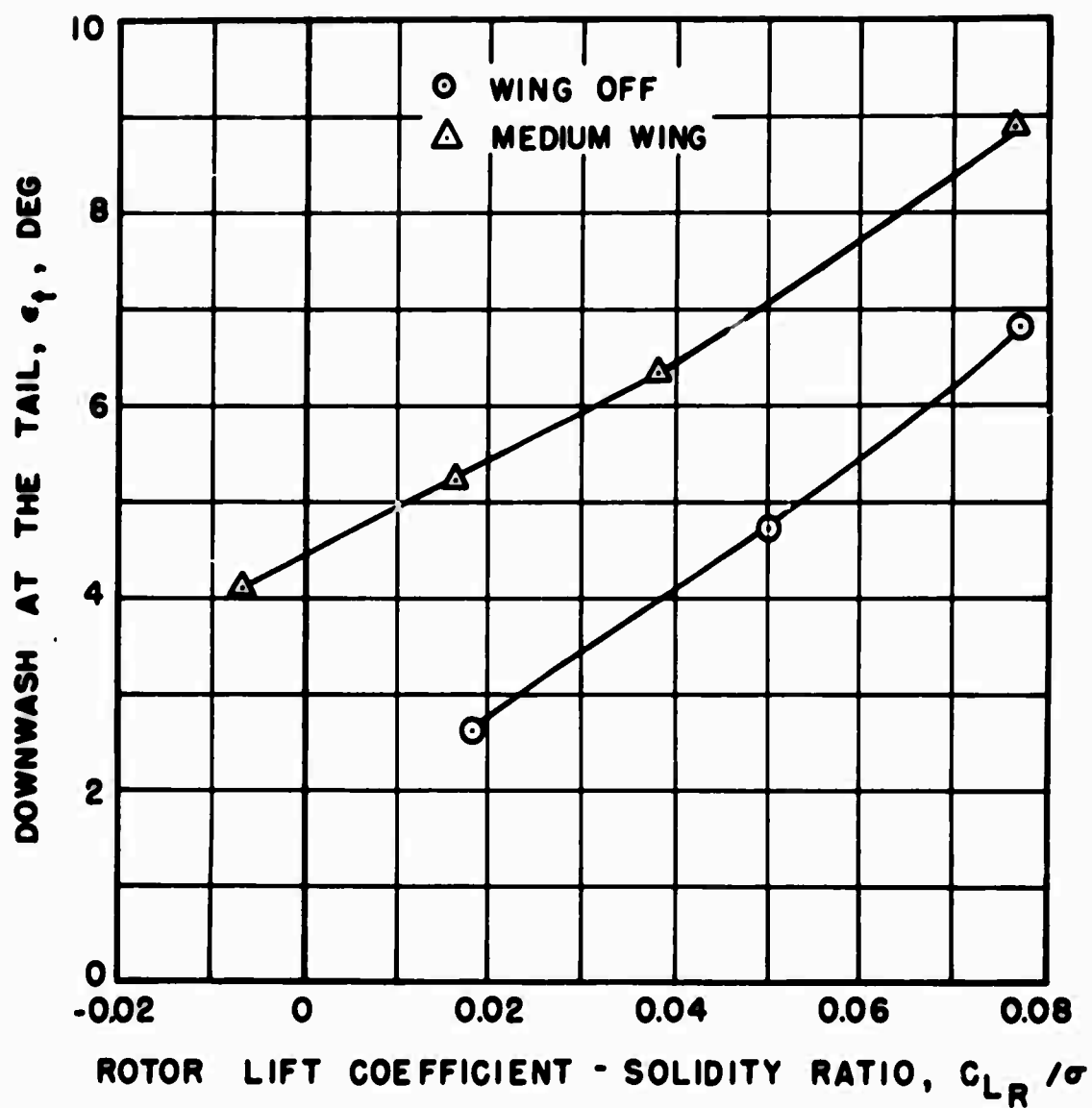
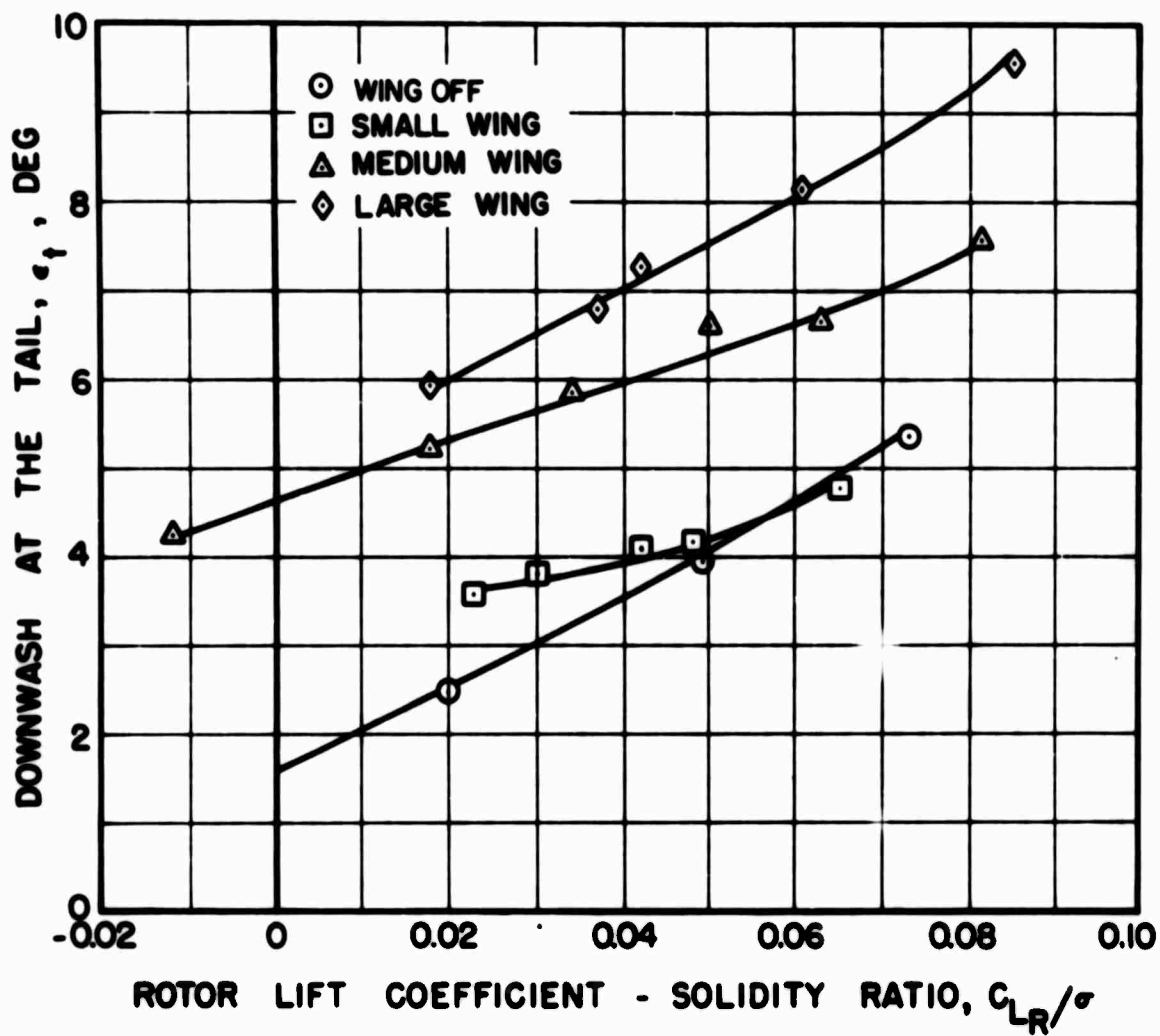


Figure 49. Effect of Rotor Lift on Downwash Angle at the Tail at Various Forward Speeds and $\alpha_f = 4^\circ$, Wing Off.



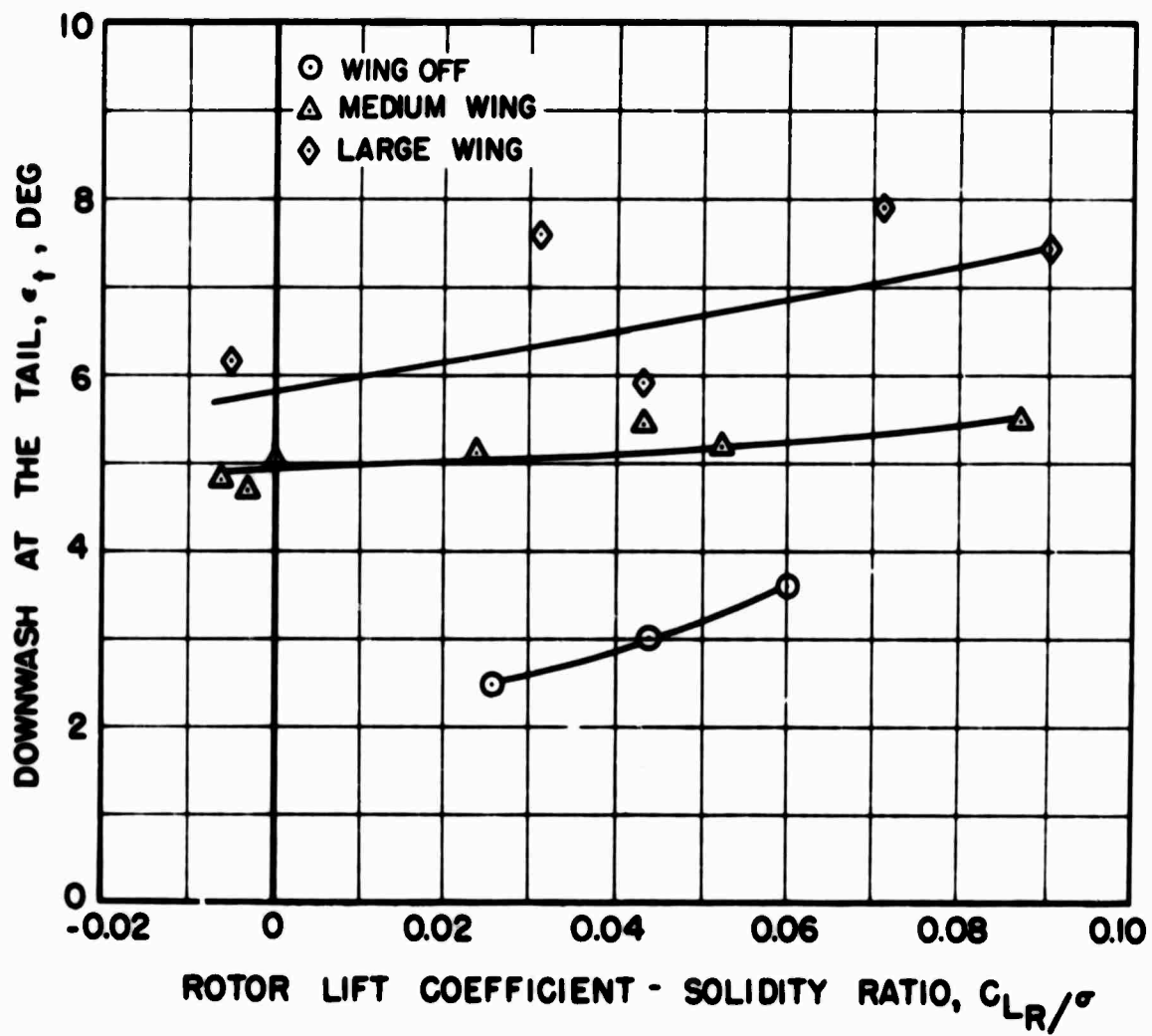
(a) $V_s = 120$ Knots

Figure 50. Effect of Rotor Lift on Downwash Angle at the Tail for Various Size Wings at the Mid Position, Various Forward Speeds, and $\alpha_f = 4^\circ$.



(b) $V_s = 200$ Knots

Figure 50. Continued.



(c) $V_s = 300$ Knots

Figure 50. Concluded.

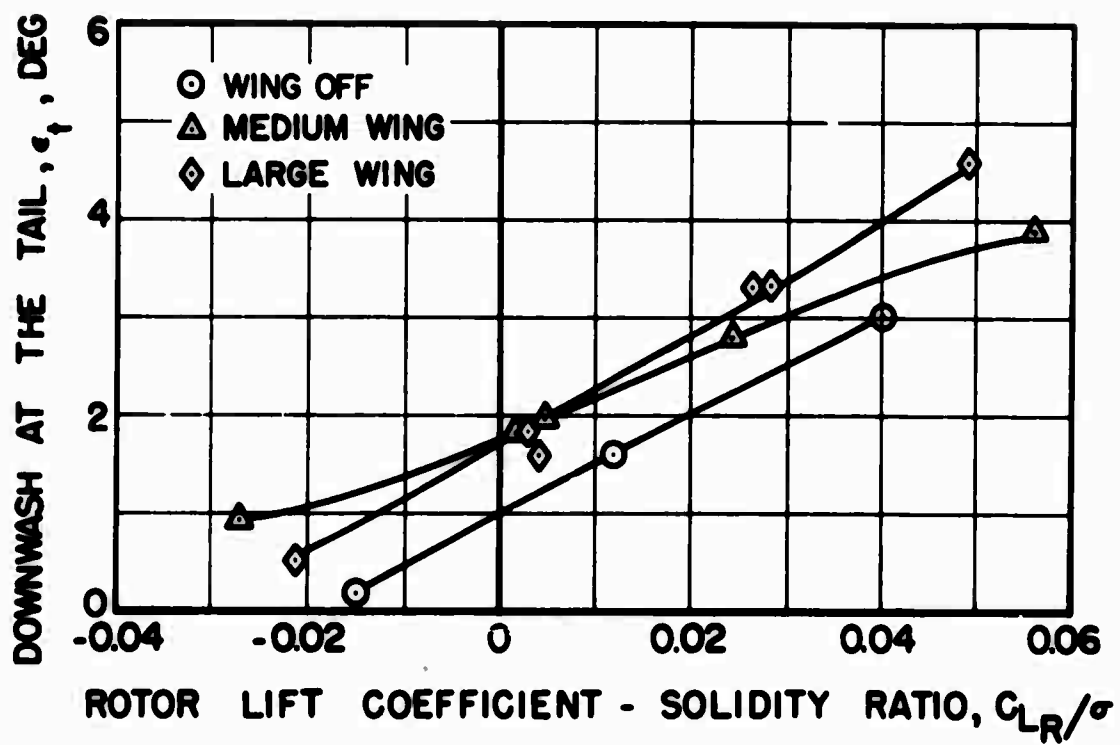


Figure 51. Effect of Rotor Lift on Downwash Angle at the Tail for the Medium and Large Wings at the Mid Position, $V_s = 200$ Knots, and $\alpha_f = -4^\circ$.

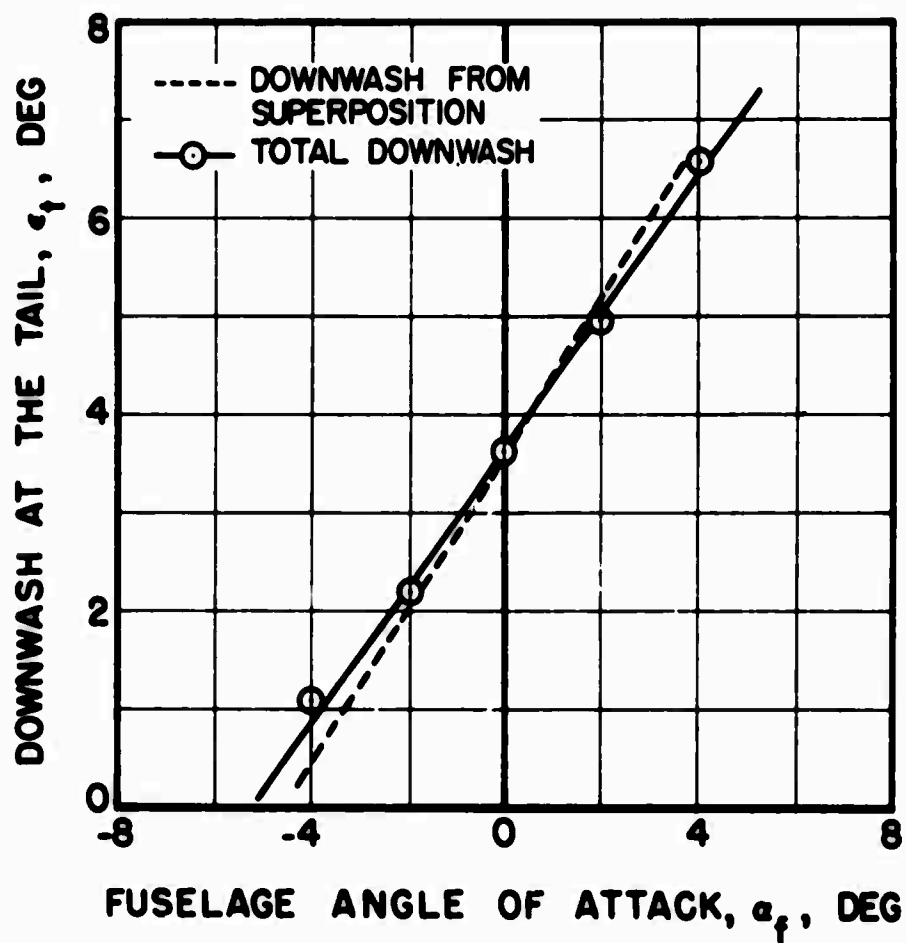
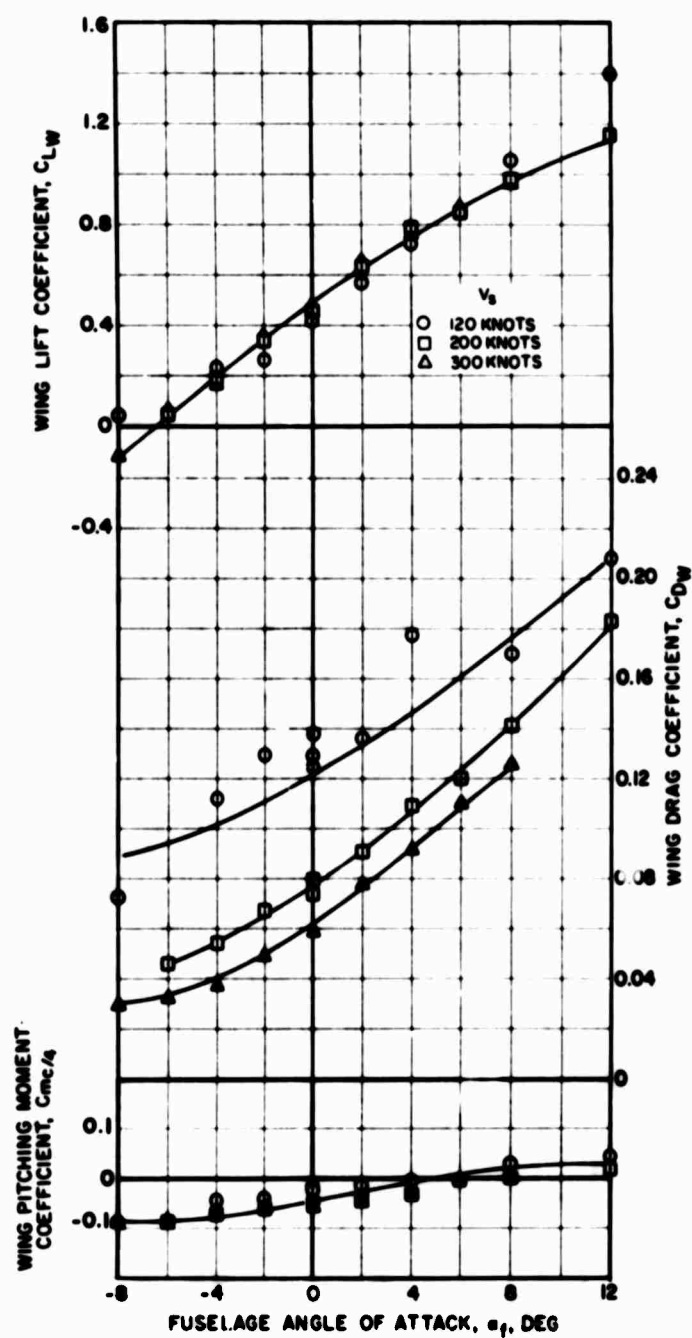
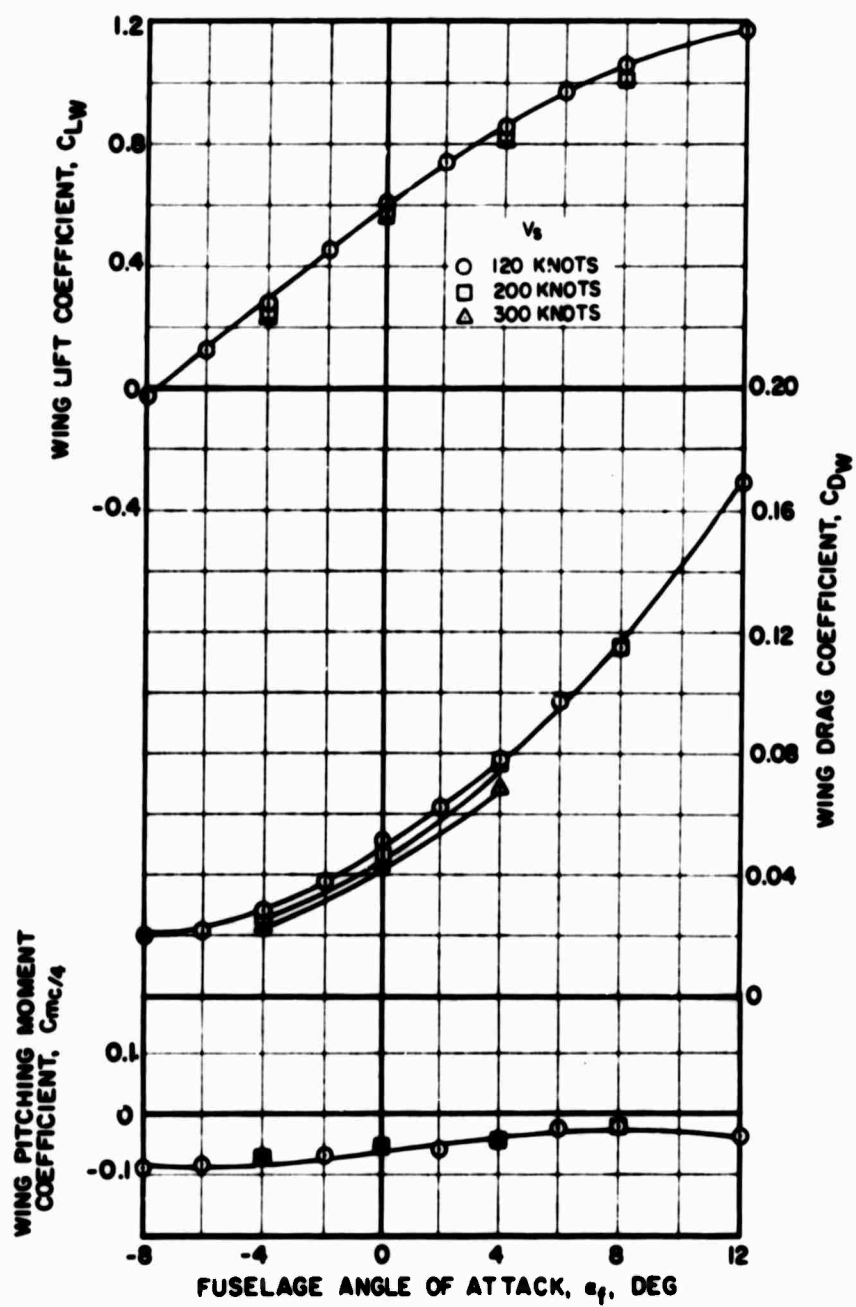


Figure 52. Comparison of the Effect of Fuselage Angle of Attack on Measured Downwash and Downwash Obtained by Superposition for the Medium Wing, Mid Position, $V_s = 200$ Knots.



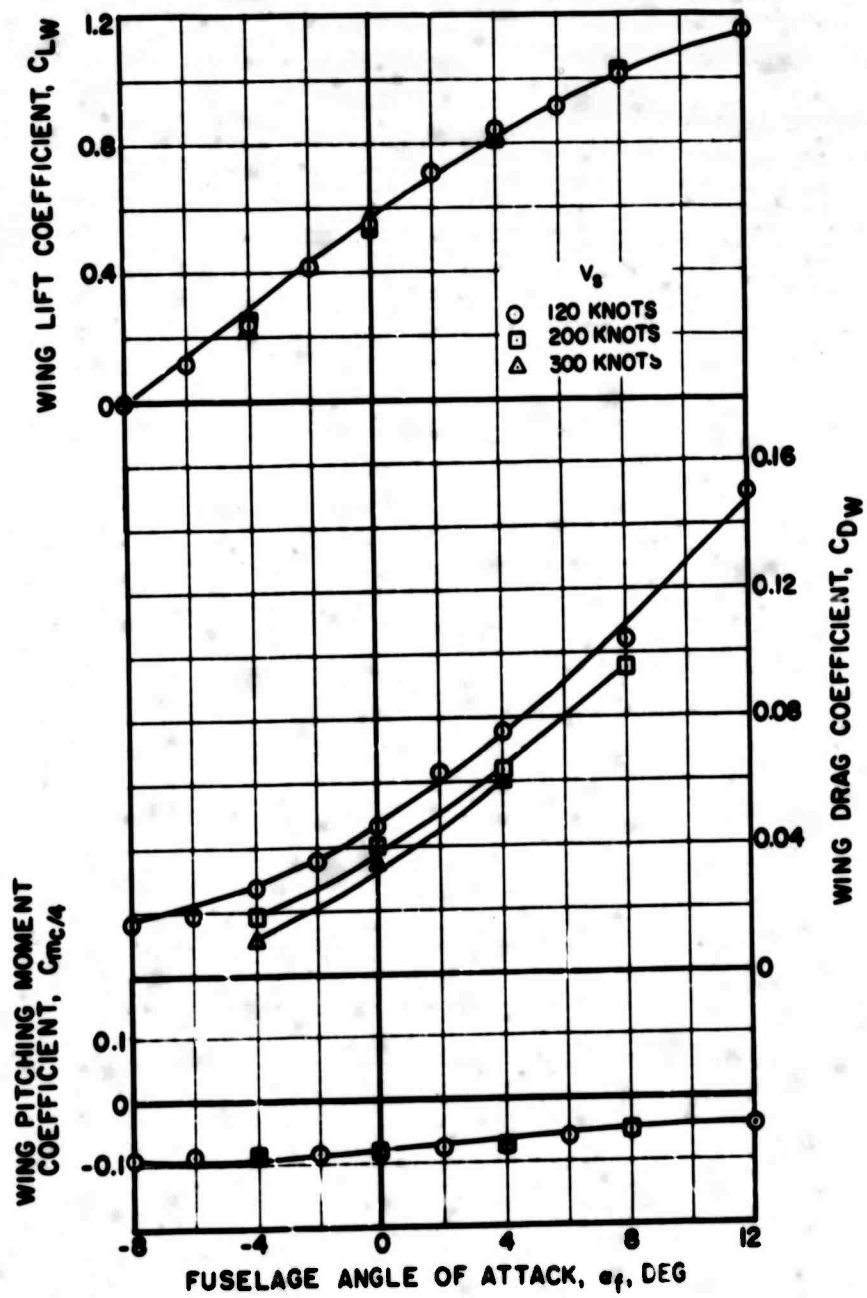
(a) Small Wing

Figure 53. Aerodynamic Characteristics of the Small, Medium, and Large Wings at the Mid Position for Various Forward Speeds.



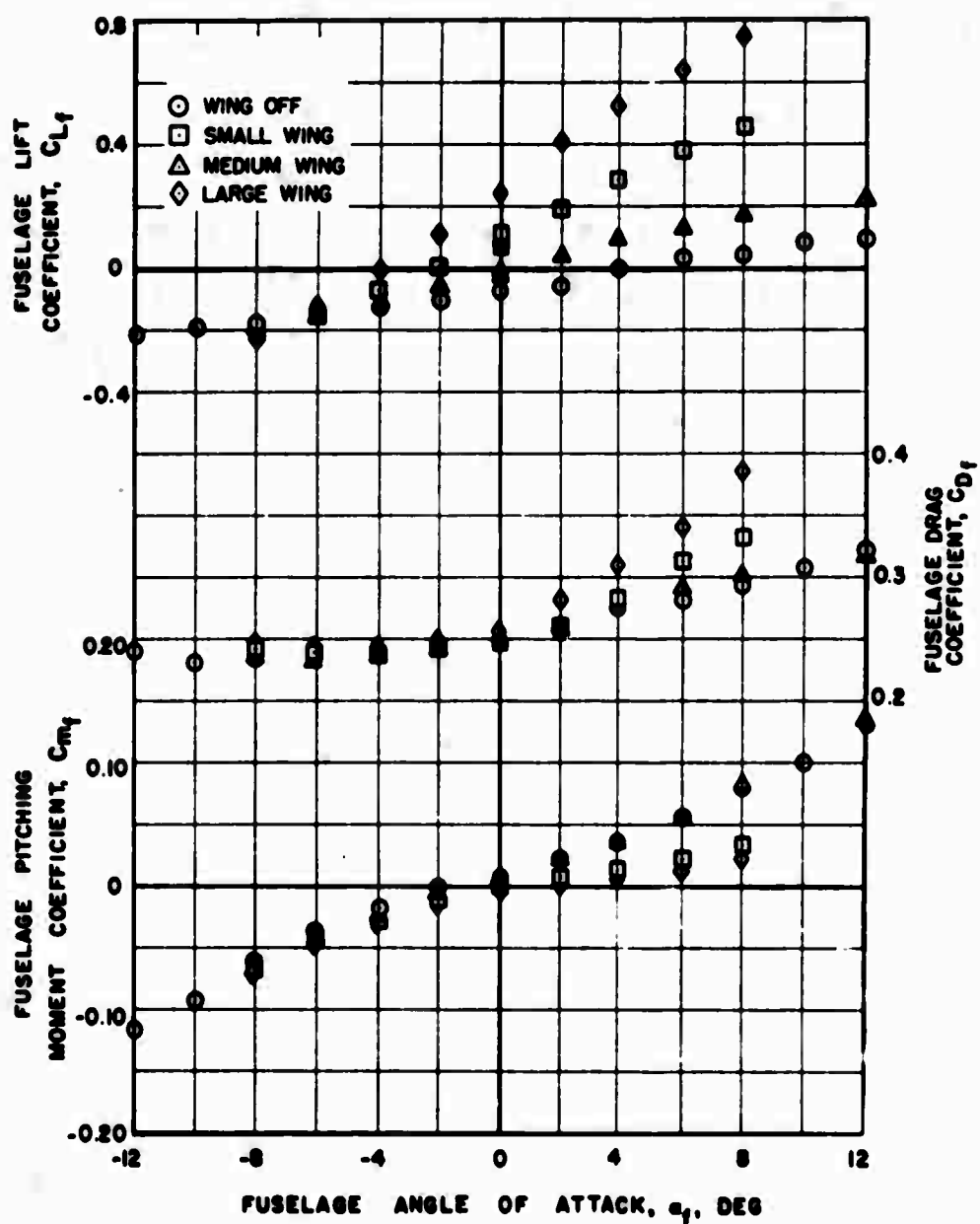
(b) Medium Wing

Figure 53. Continued.



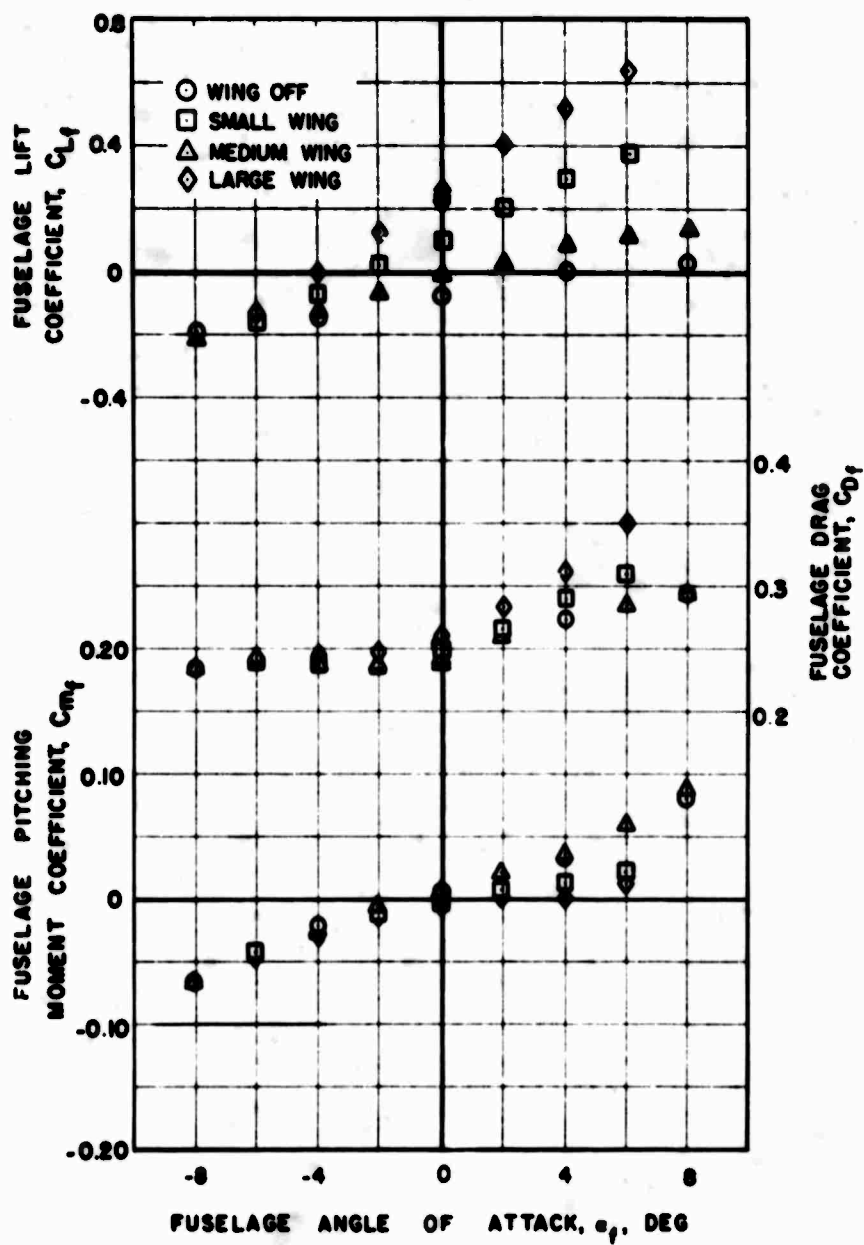
(c) Large Wing

Figure 53. Concluded.



(a) $V_s = 200$ Knots

Figure 54. Fuselage Aerodynamic Characteristics With the Small, Medium, and Large Wings at the Mid Position for Various Forward Speeds.



(b) $V_s = 300$ Knots

Figure 54. Concluded.

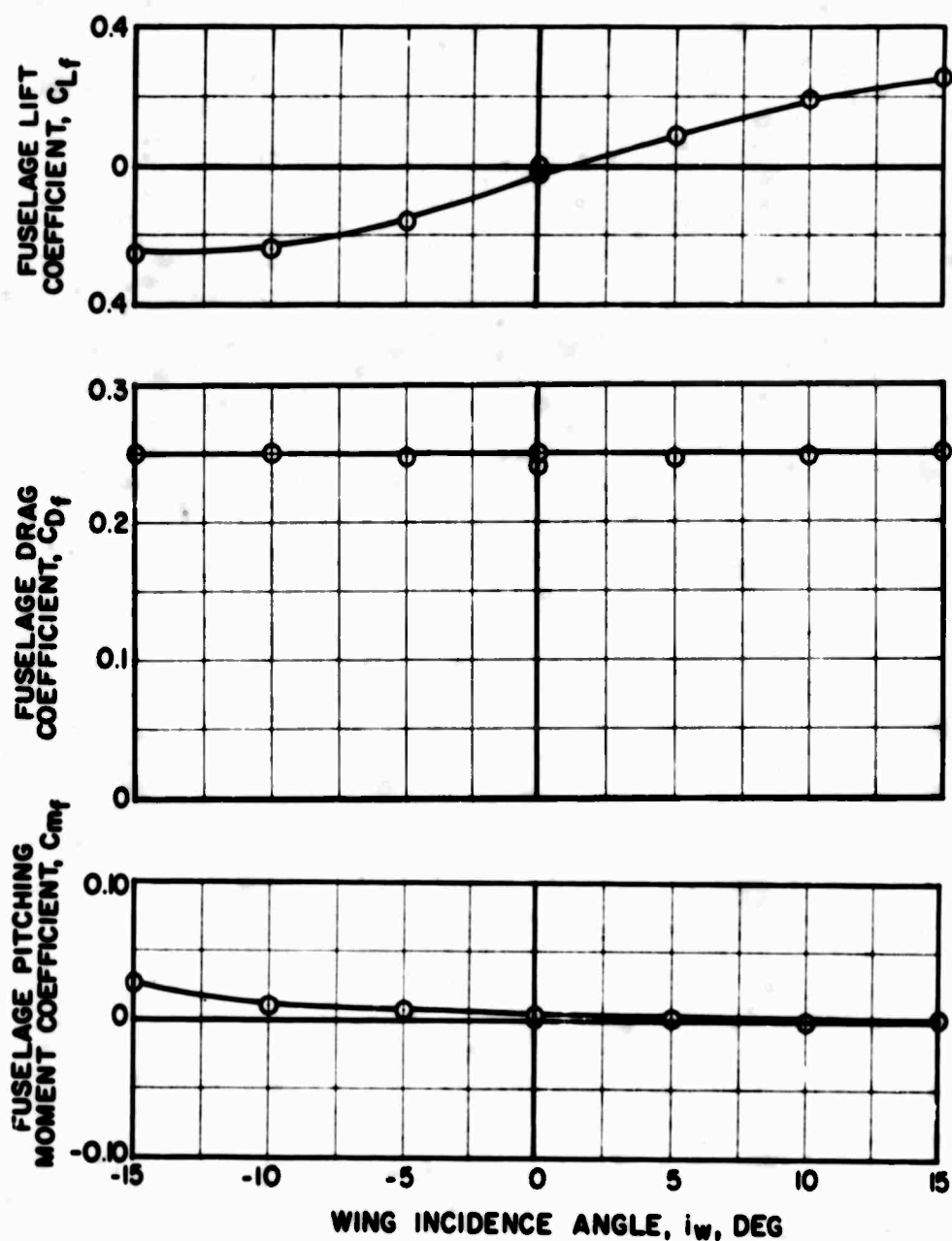
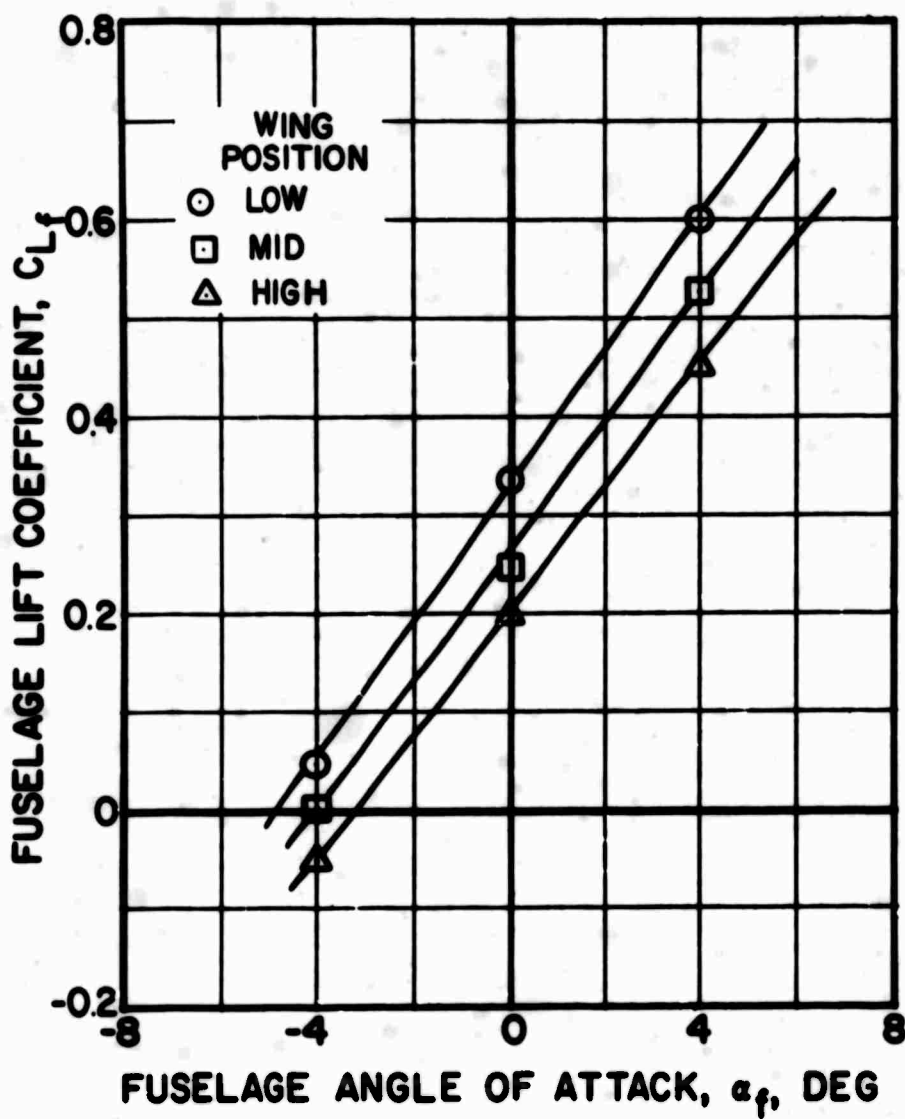
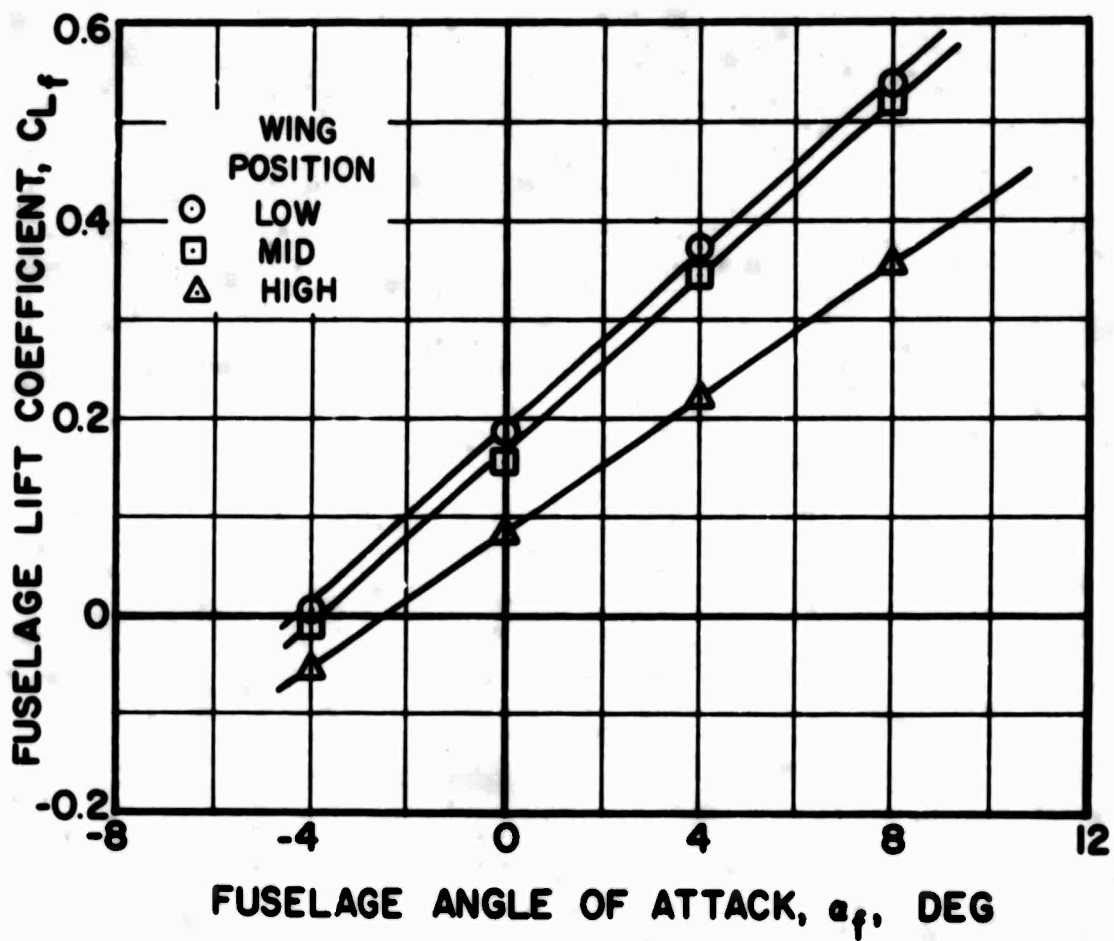


Figure 55. Fuselage Aerodynamic Characteristics With the Medium Wing at the Mid Position for Various Wing Incidence Angles, $V_s = 200$ Knots, and $\alpha_f = 0^\circ$.



(a) Large Wing

Figure 56. Effect of Wing Position on Fuselage Lift for the Large and Medium Wings and Various Fuselage Angles of Attack.



(b) Medium Wing

Figure 56. Concluded.

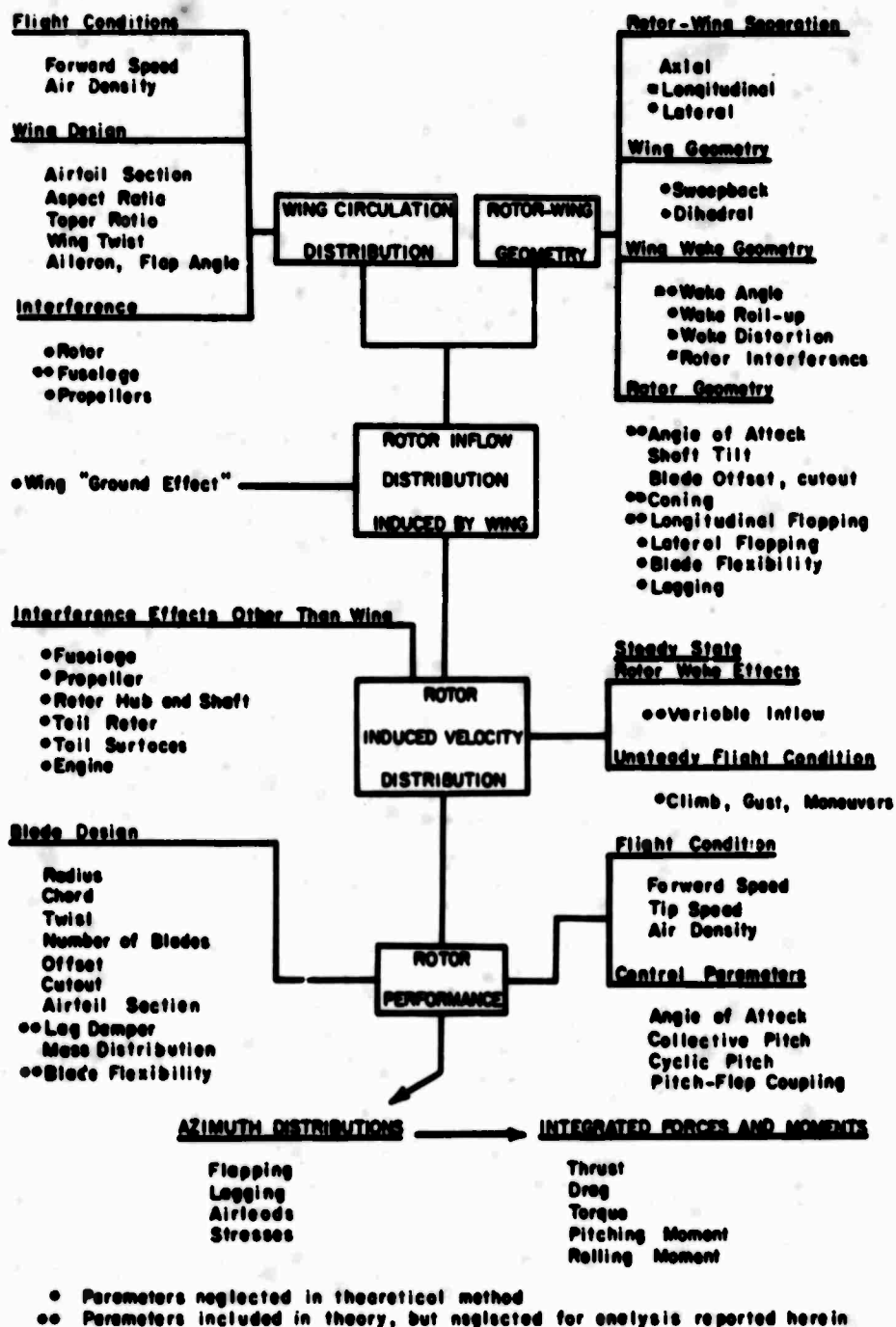


Figure 57. Parameters for the Effect of Wing Interference on Rotor Performance.

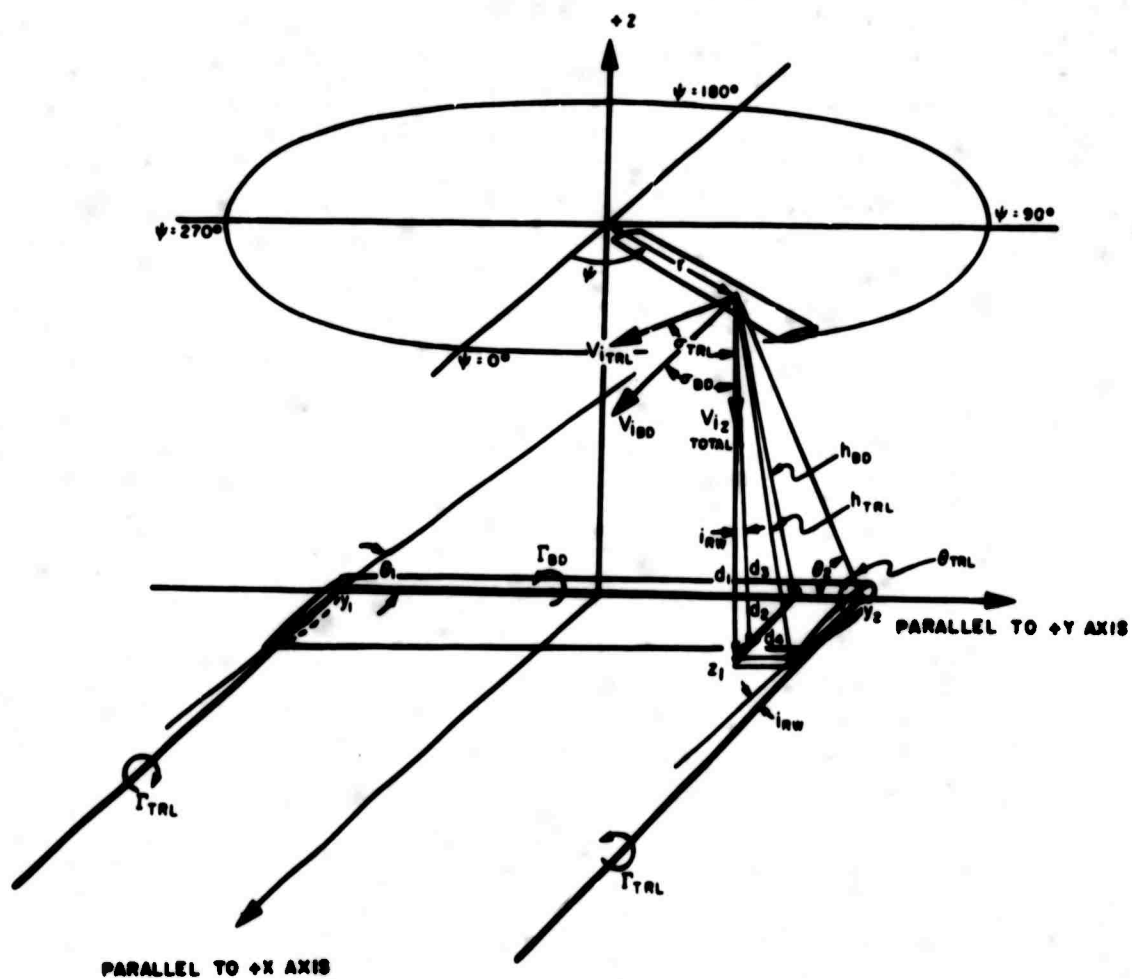


Figure 58. Rotor-Wing-Wing Wake Geometry.

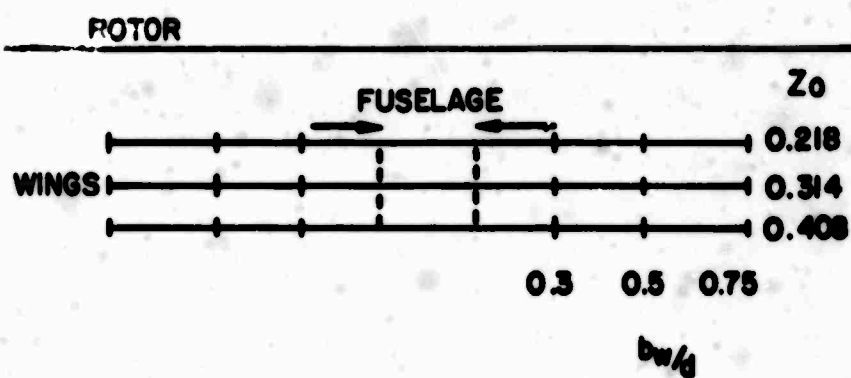
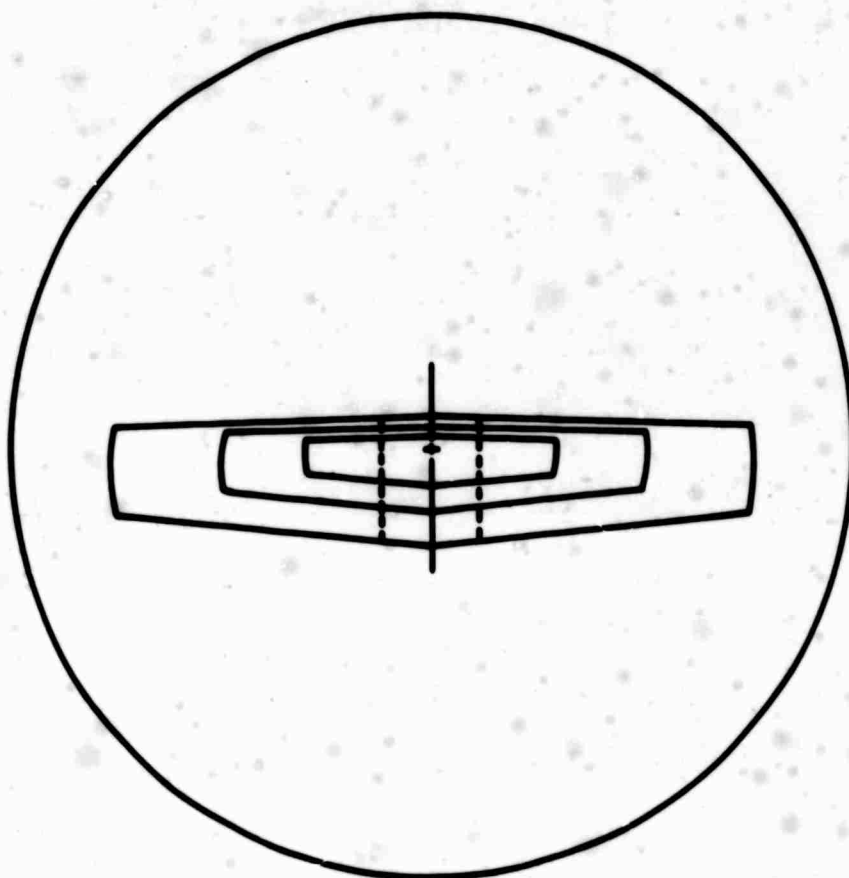


Figure 60. Rotor-Wing Configurations.

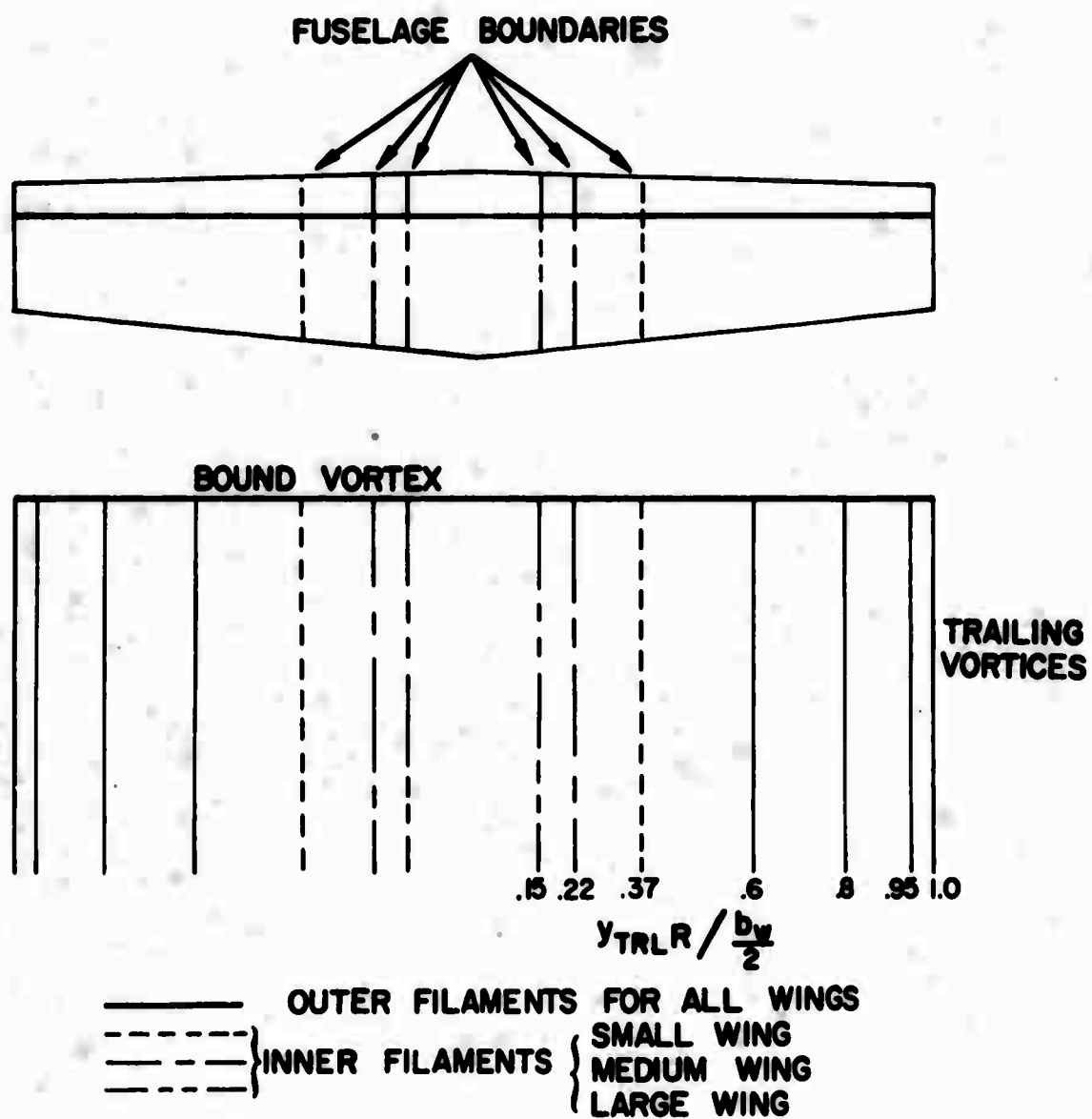


Figure 61. Vortex Representation of Wing Wake.

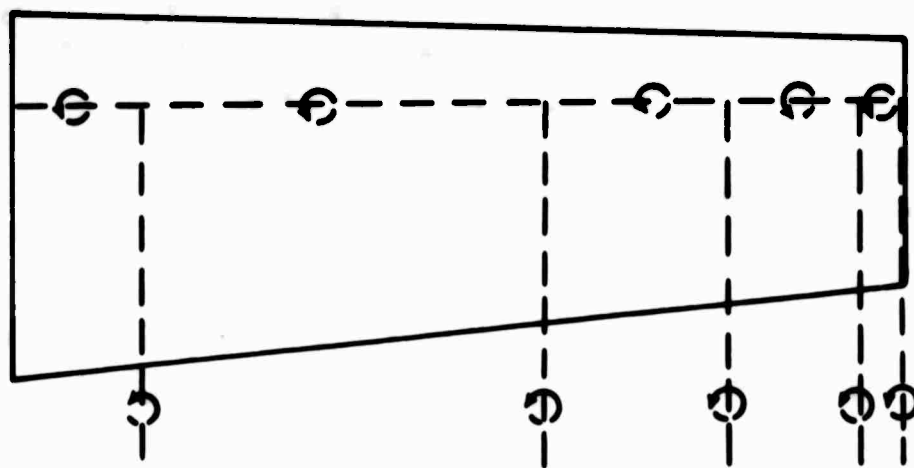
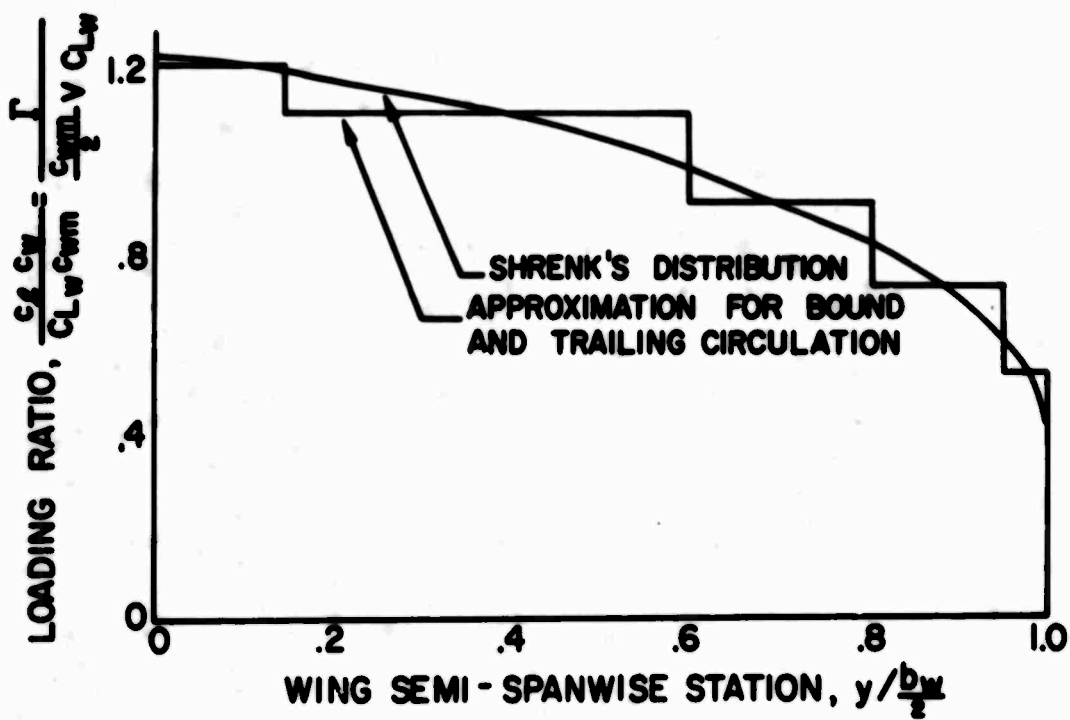


Figure 62. Wing Circulation Distribution, Large Wing.

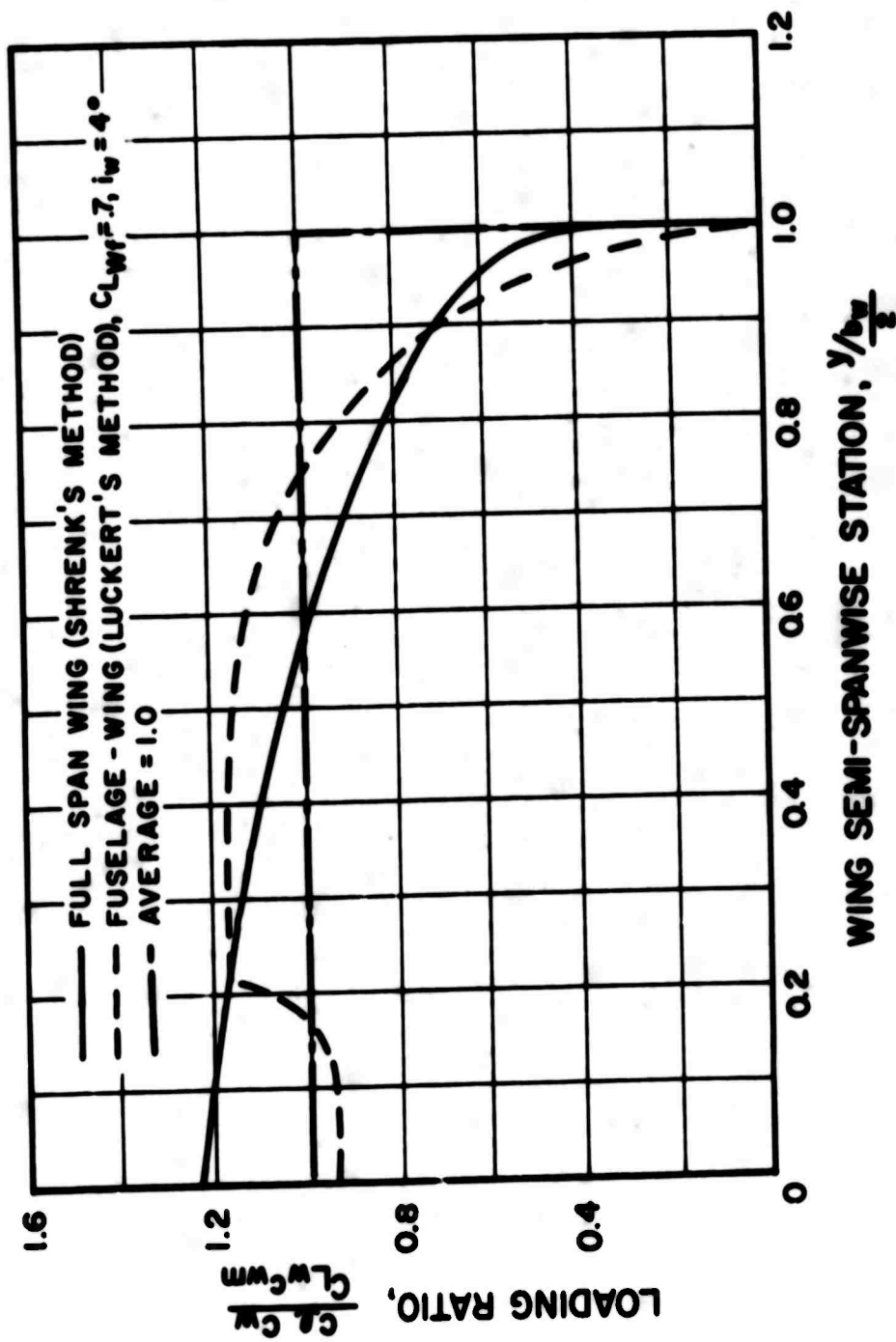


Figure 63. Comparison of Loading Distributions Between Full Span Wing and Wing-Fuselage Configuration, Medium Wing, Mid Position.

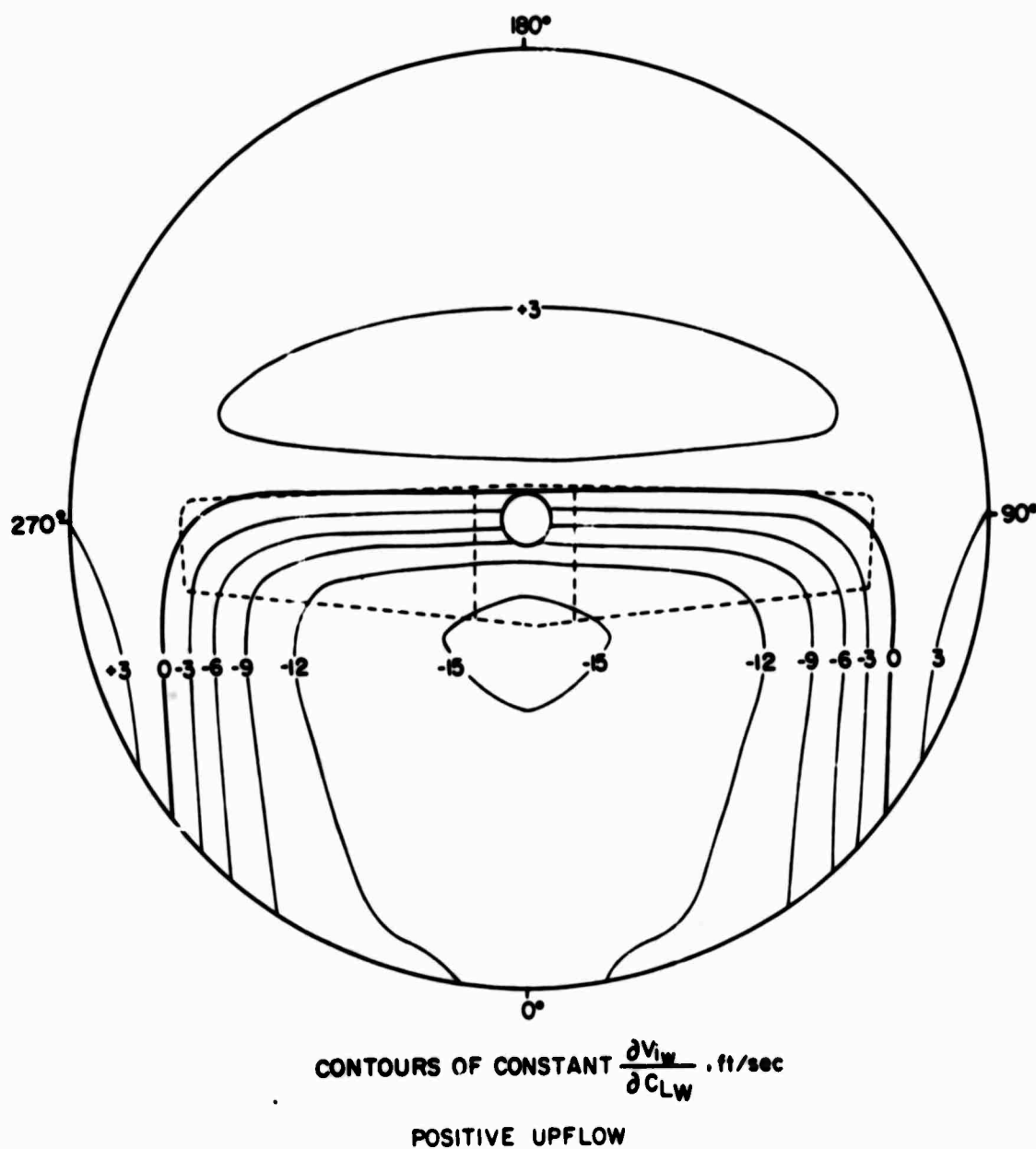


Figure 64. Theoretical Wing Induced Velocity Normal to Rotor Plane, Large Wing, High Position, $V_s = 200$ Knots.

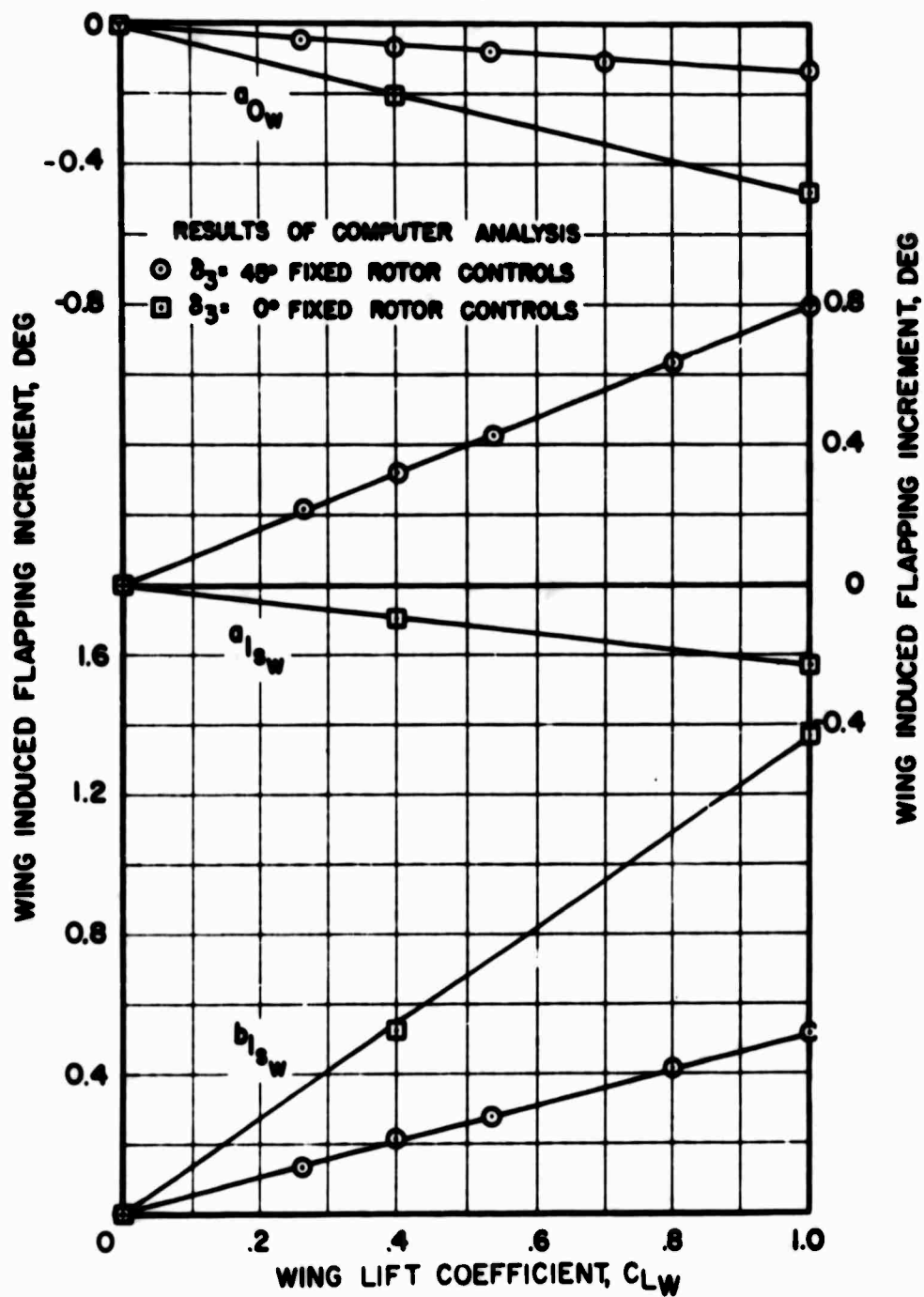


Figure 65. Theoretical Linearity of Wing Induced Flapping With Wing Lift Coefficient for Fixed Rotor Controls and Two Values of Pitch-Flap Coupling.

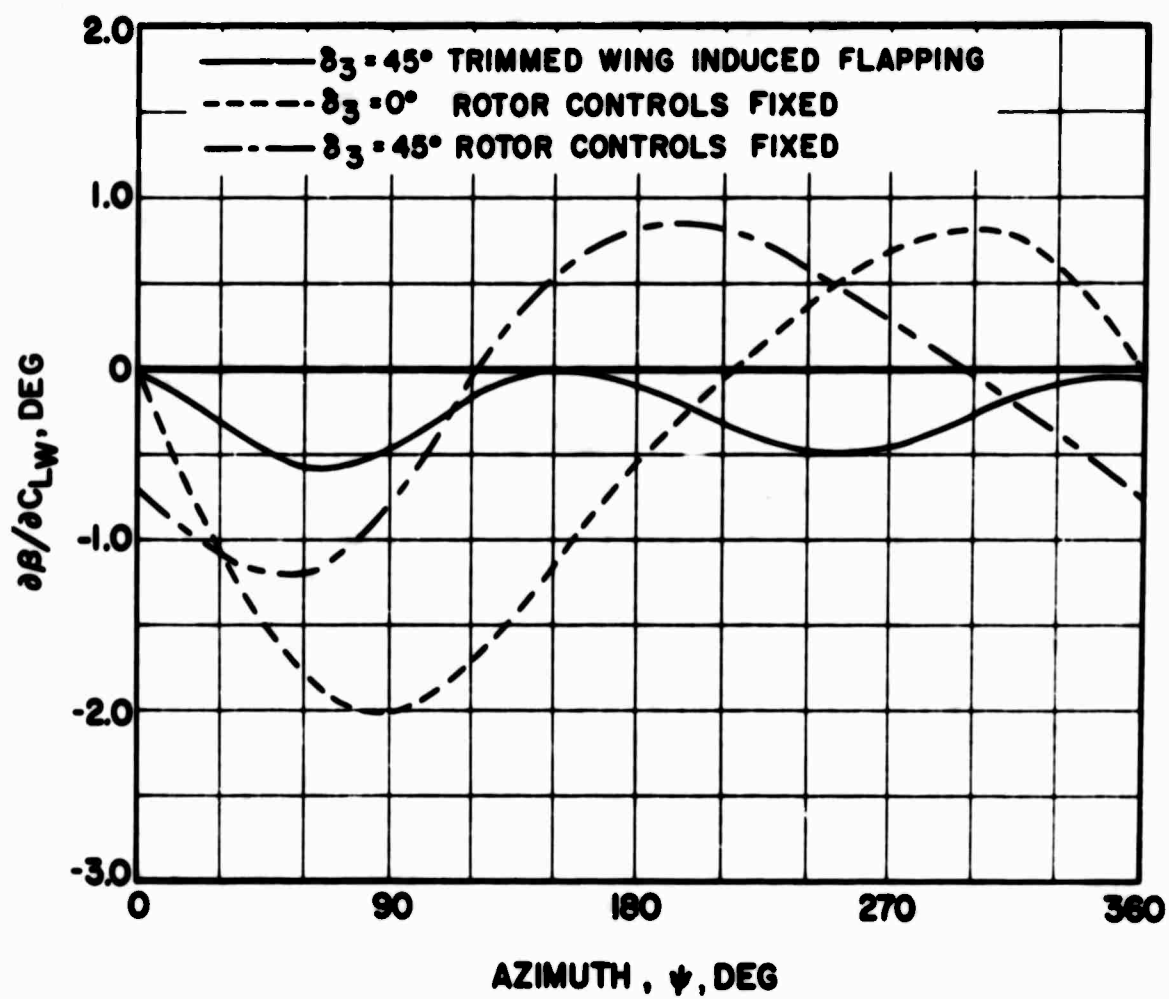
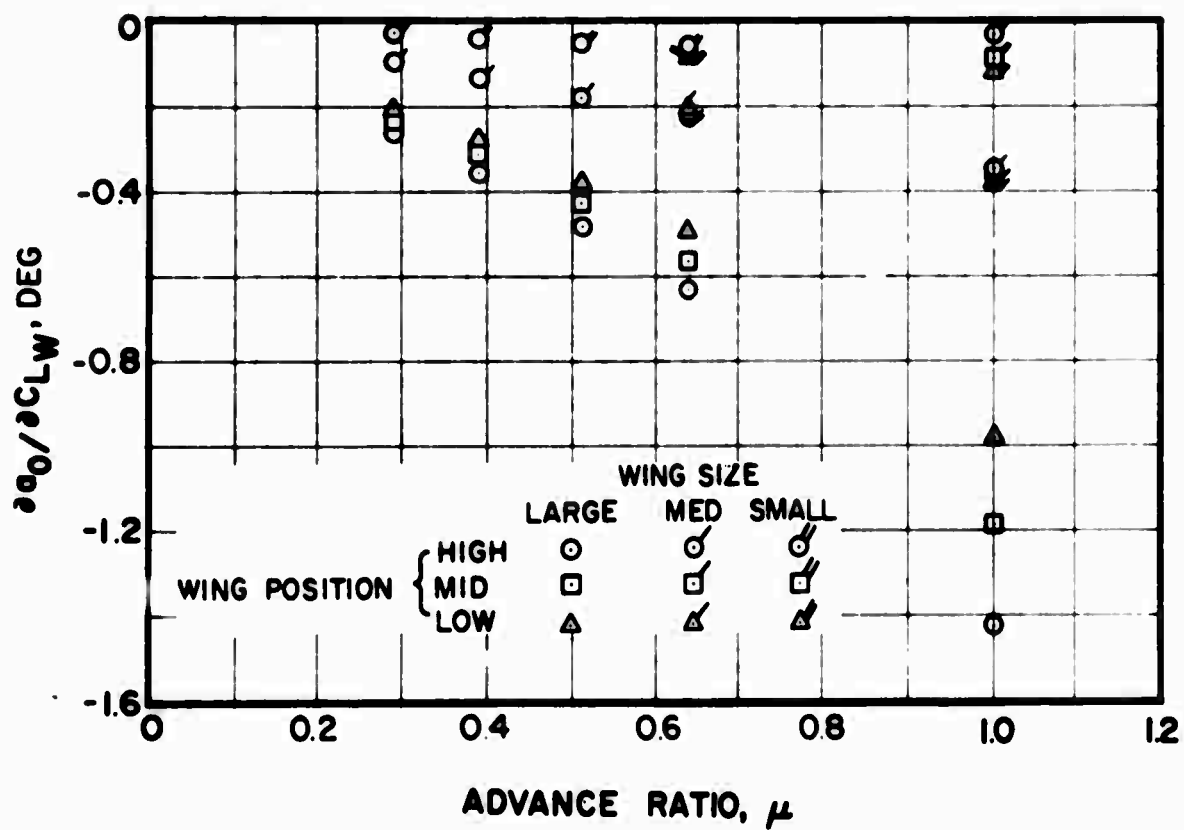
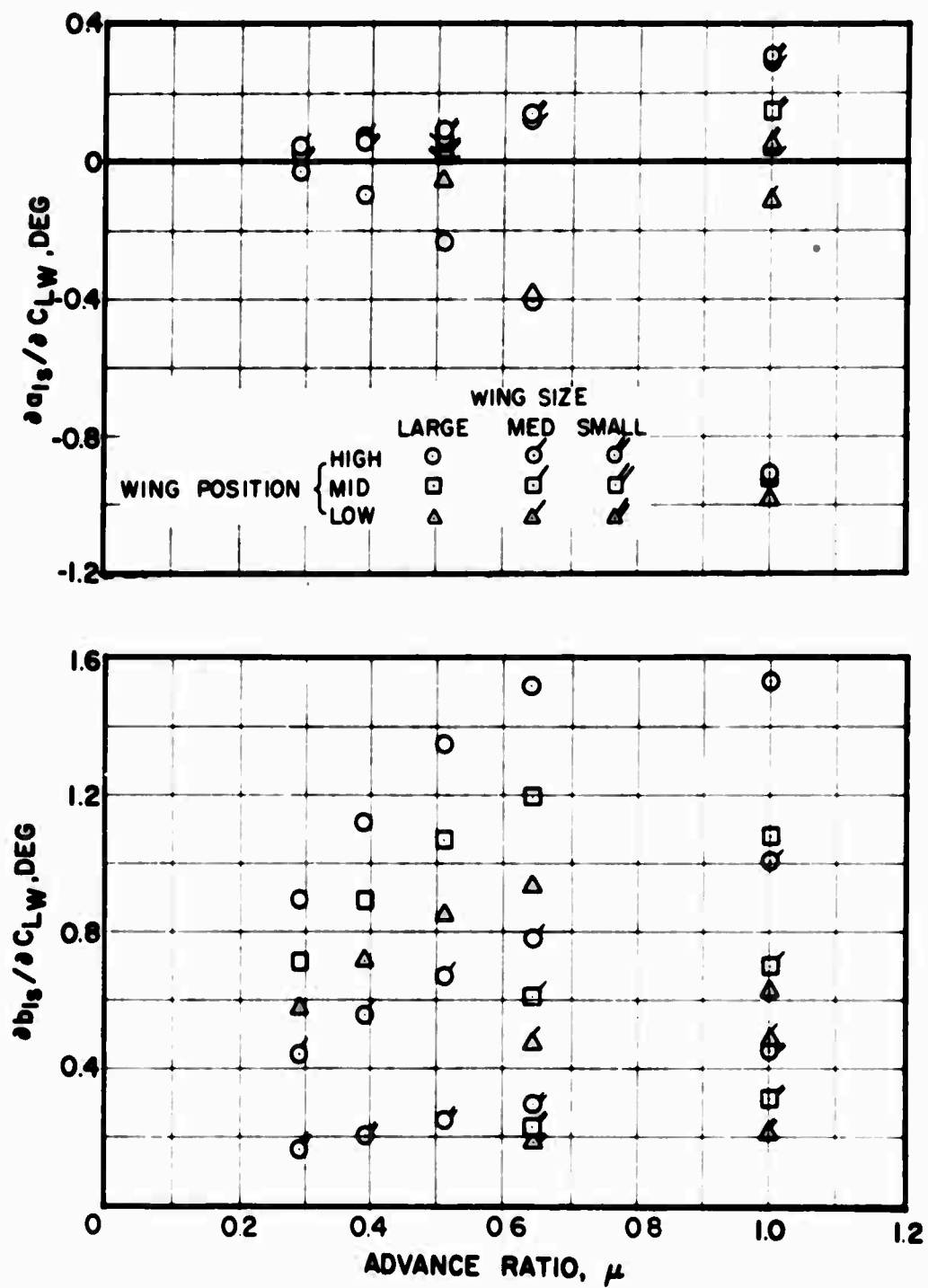


Figure 66. Azimuth Distribution of Wing Effect on Rotor Blade Flapping, Large Wing, High Position, $\mu = 0.51$.



(a) Coning Angle Derivative

Figure 67. Theoretical Effect of Wing Size and Position on Rotor Blade Flapping, $\delta_3 = 0^\circ$, Fixed Rotor Controls.



(b) Flapping Angle Derivatives

Figure 67. Concluded.

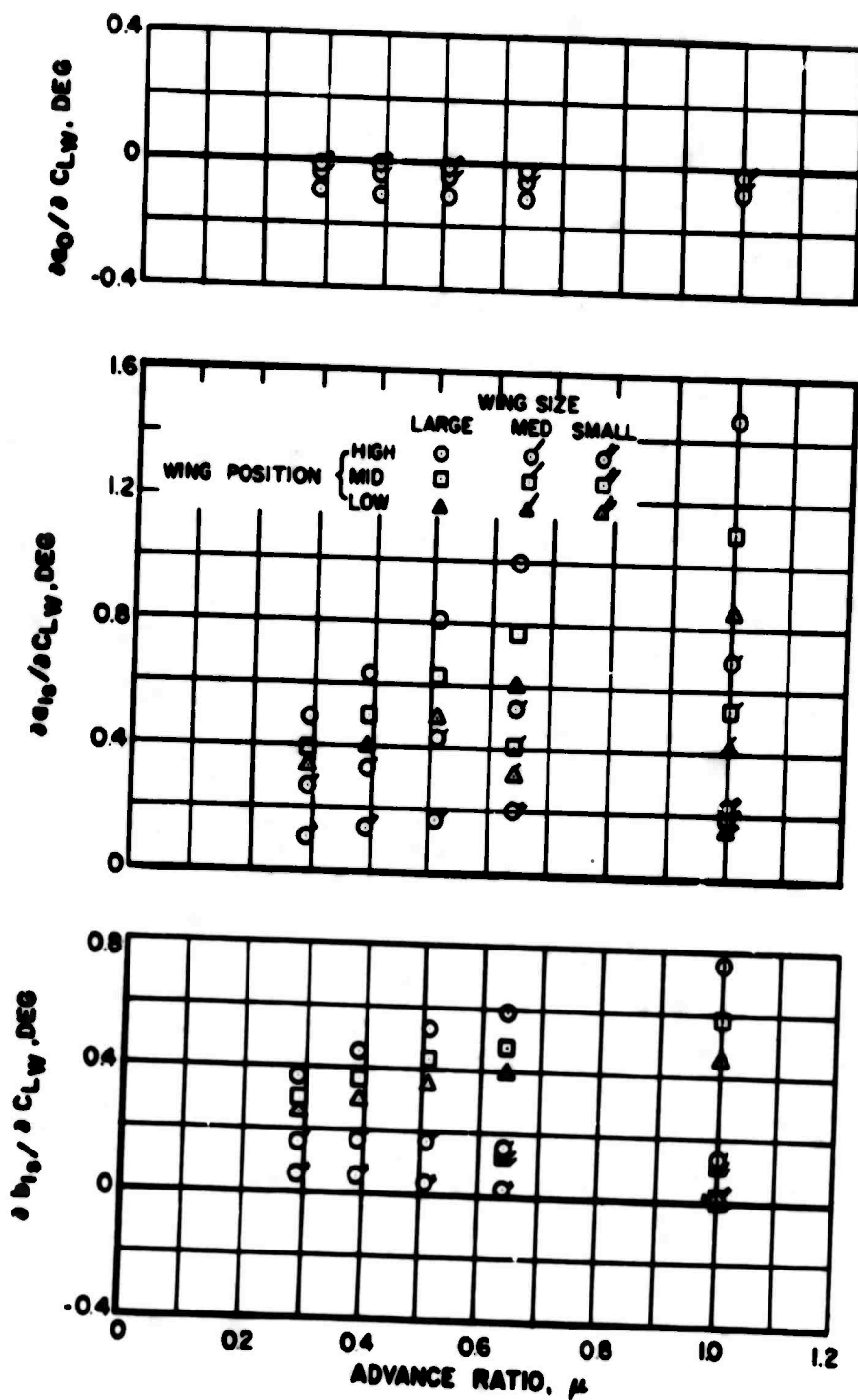


Figure 68. Theoretical Effect of Wing Size and Position on Rotor Blade Flapping. $\delta_3 = 45^\circ$. Fixed Rotor Controls.

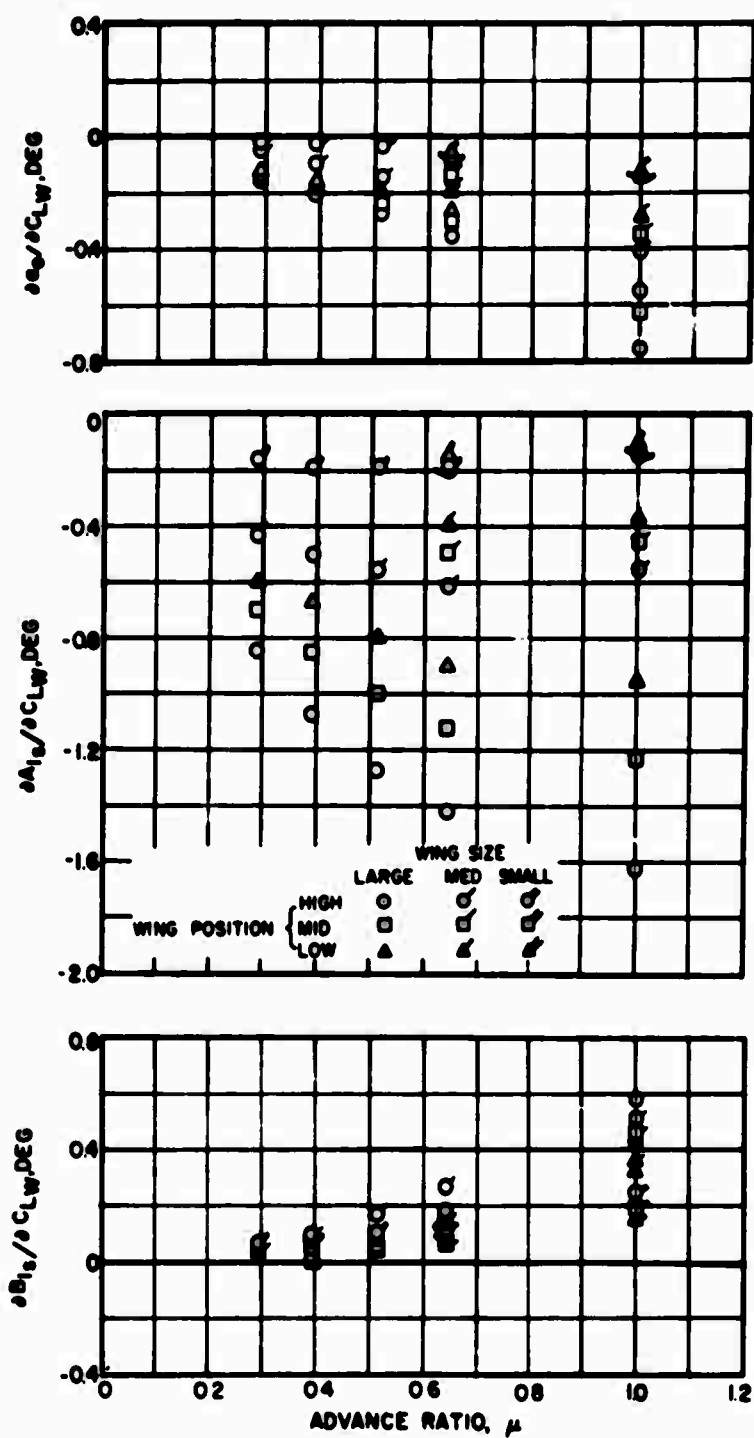
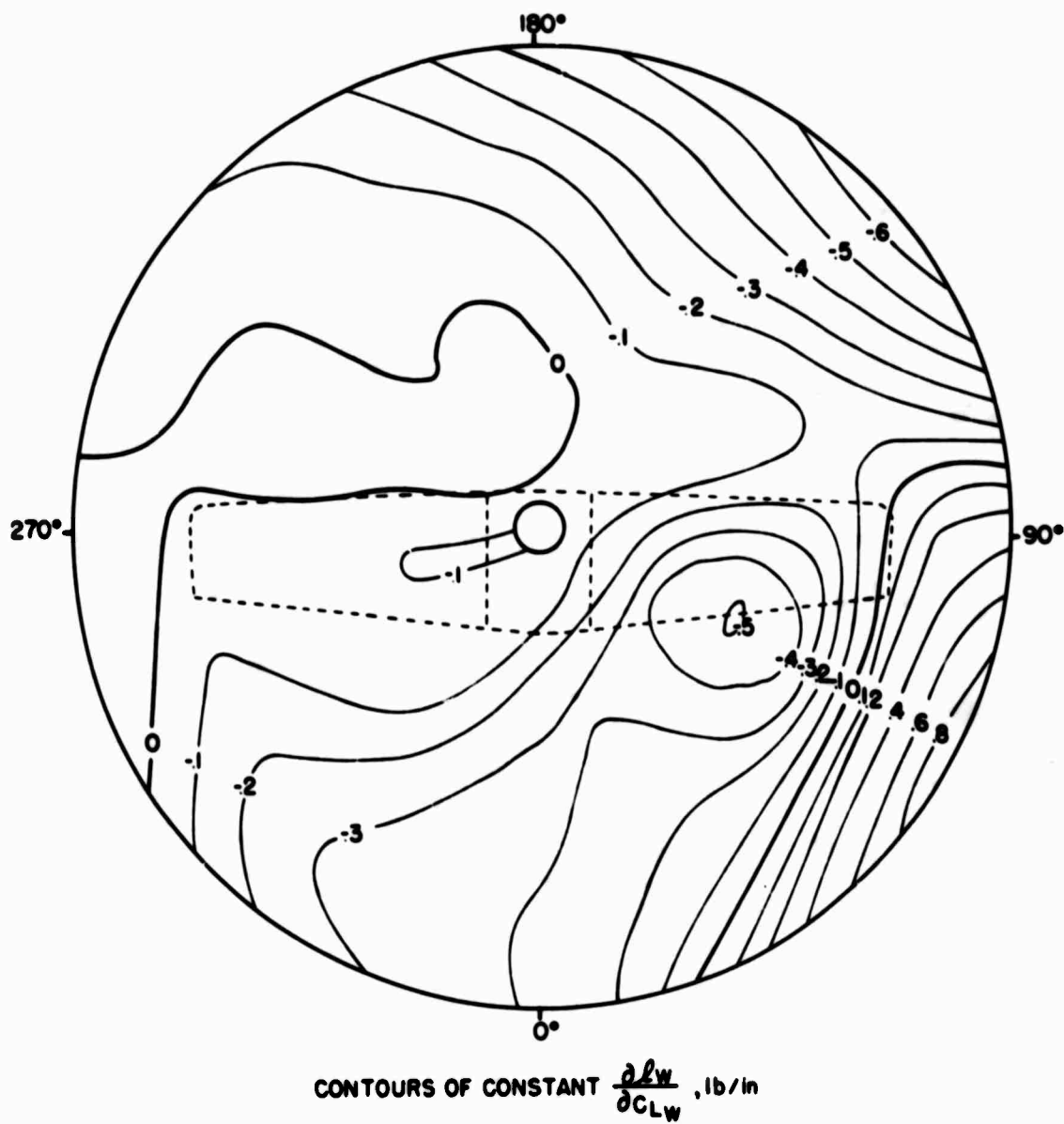
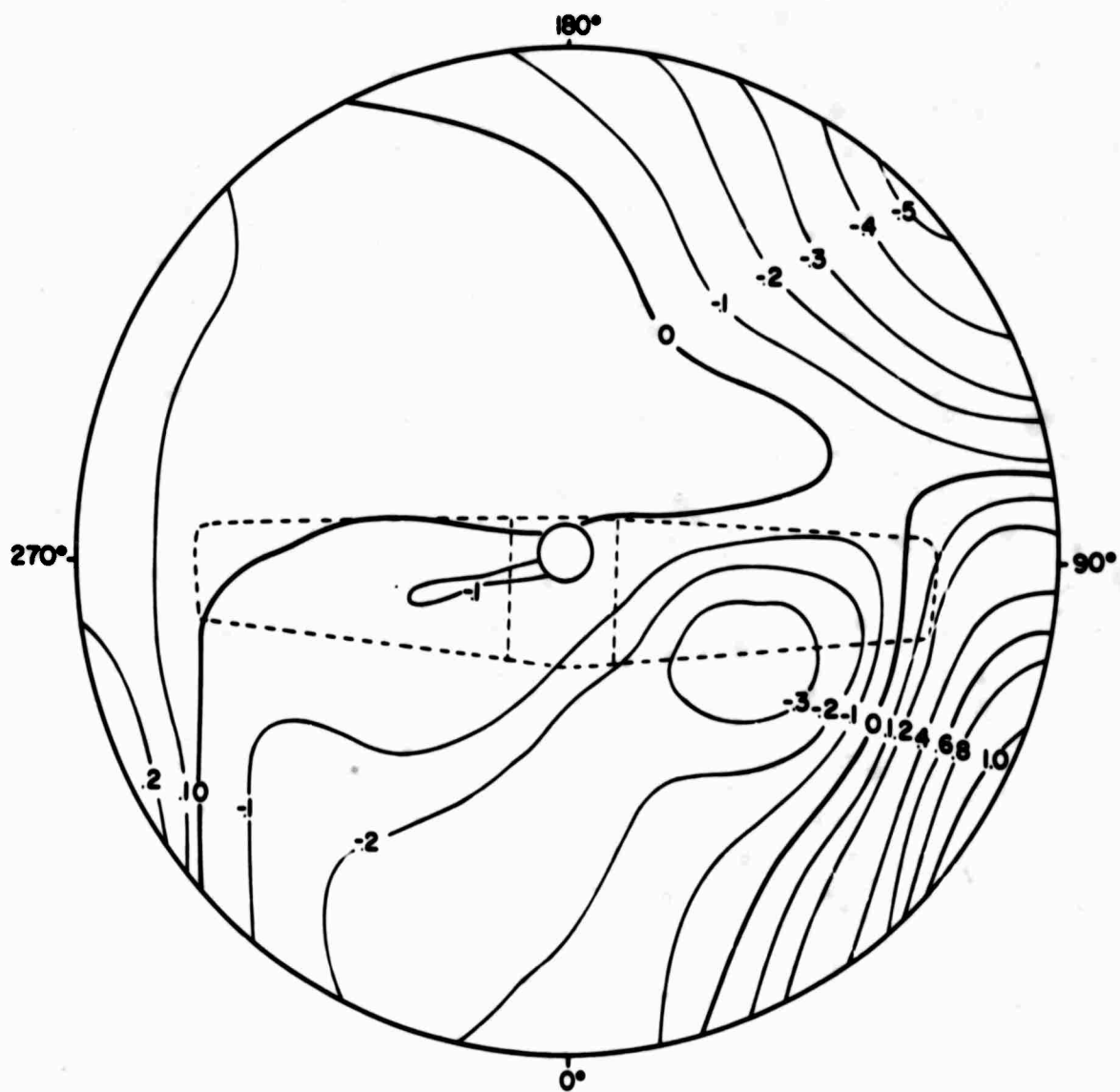


Figure 69. Theoretical Effect of Wing Size and Position on Coning and Cyclic Pitch Required to Trim Out Wing Induced First Harmonic Flapping, $\delta_3 = 45^\circ$.



(a) $\delta_3 = 0^\circ$, Fixed Rotor Controls

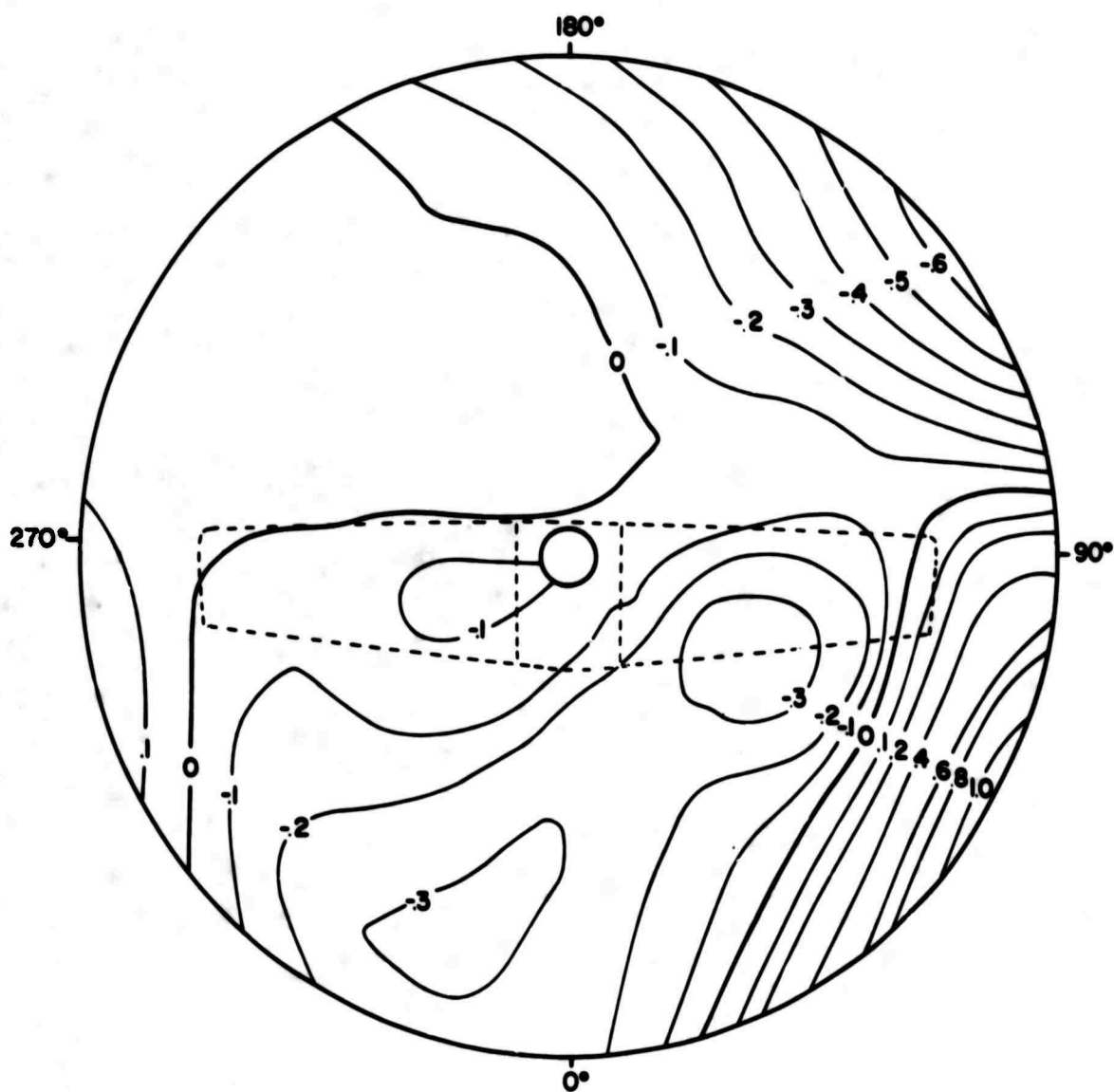
Figure 70. Theoretical Rotor Air Load Distribution Induced by the Large Wing at the High Position, $\mu = 0.51$.



CONTOURS OF CONSTANT $\frac{\partial C_L}{\partial x_{LE}}$, lb/in

(b) $\delta_3 = 45^\circ$, Fixed Rotor Controls

Figure 70. Continued.



CONTOURS OF CONSTANT $\frac{\partial C_L}{\partial A_{LP}}$, lb/in

(c) $\delta_3 = 45^\circ$, Trimmed Wing Induced Flapping

Figure 70. Concluded.

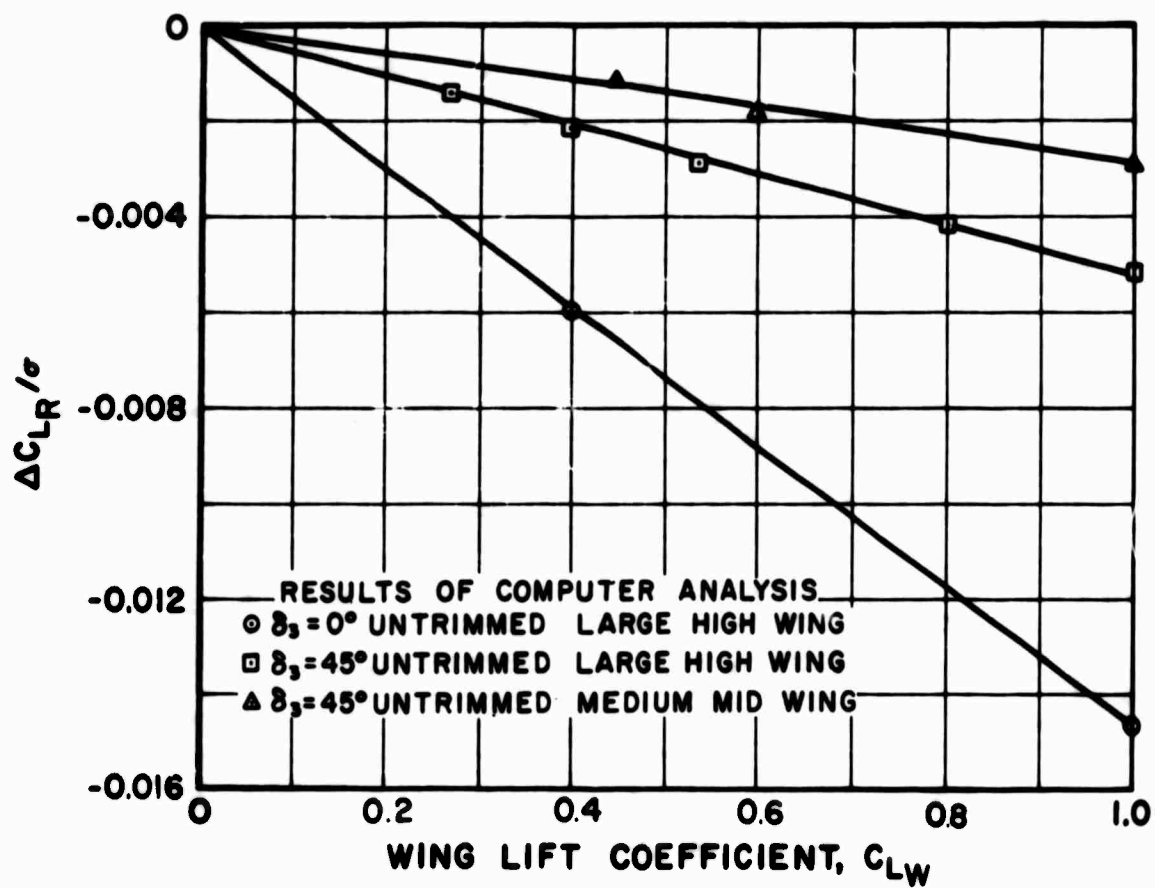
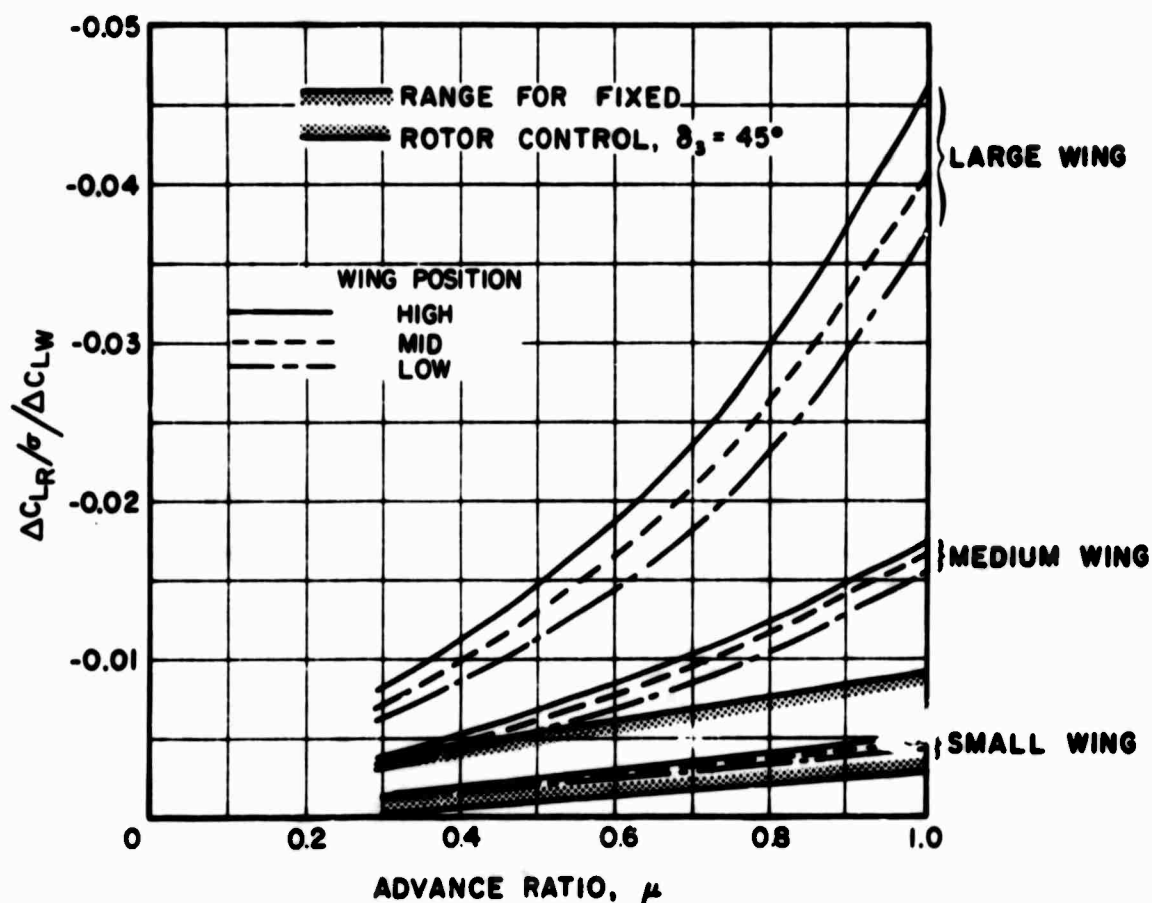
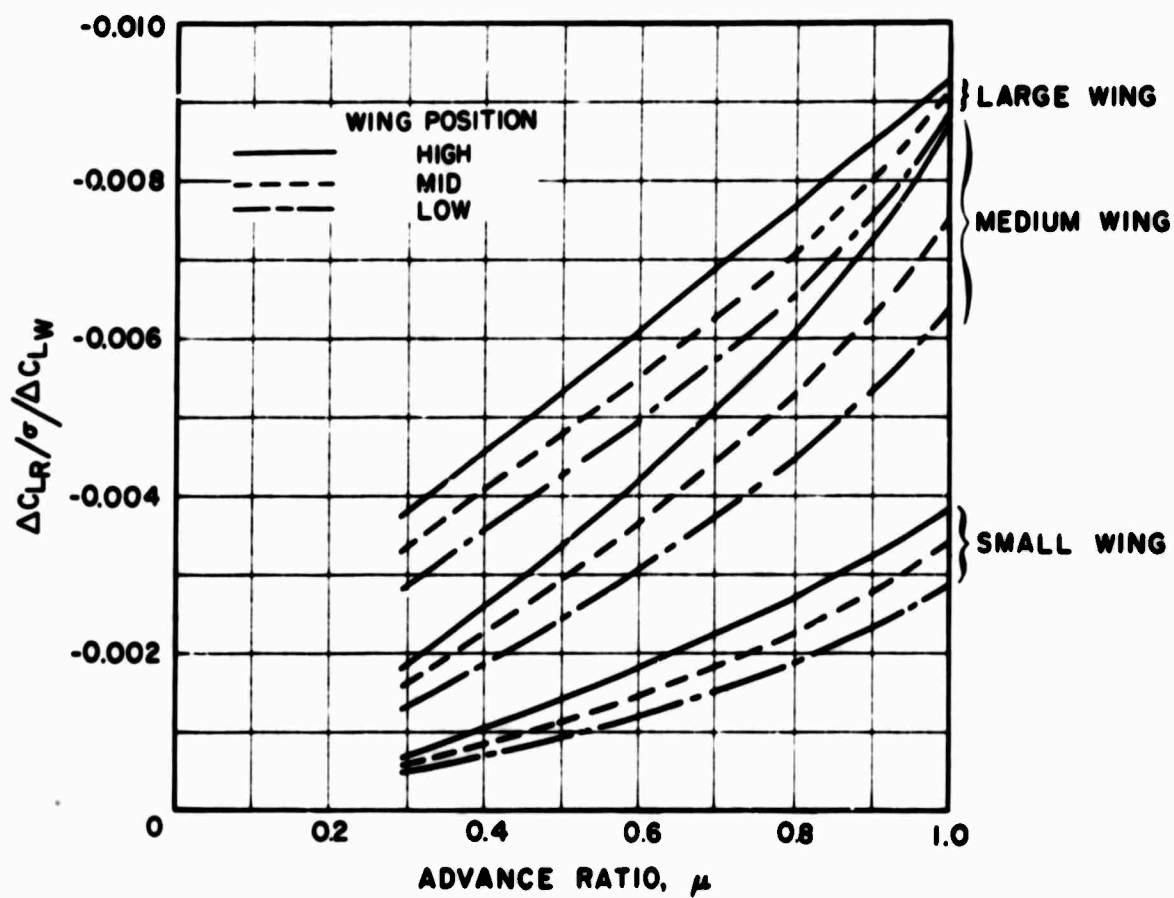


Figure 71. Linearity of Wing Induced Rotor Lift With Wing Lift Coefficient, $\mu = 0.51$.



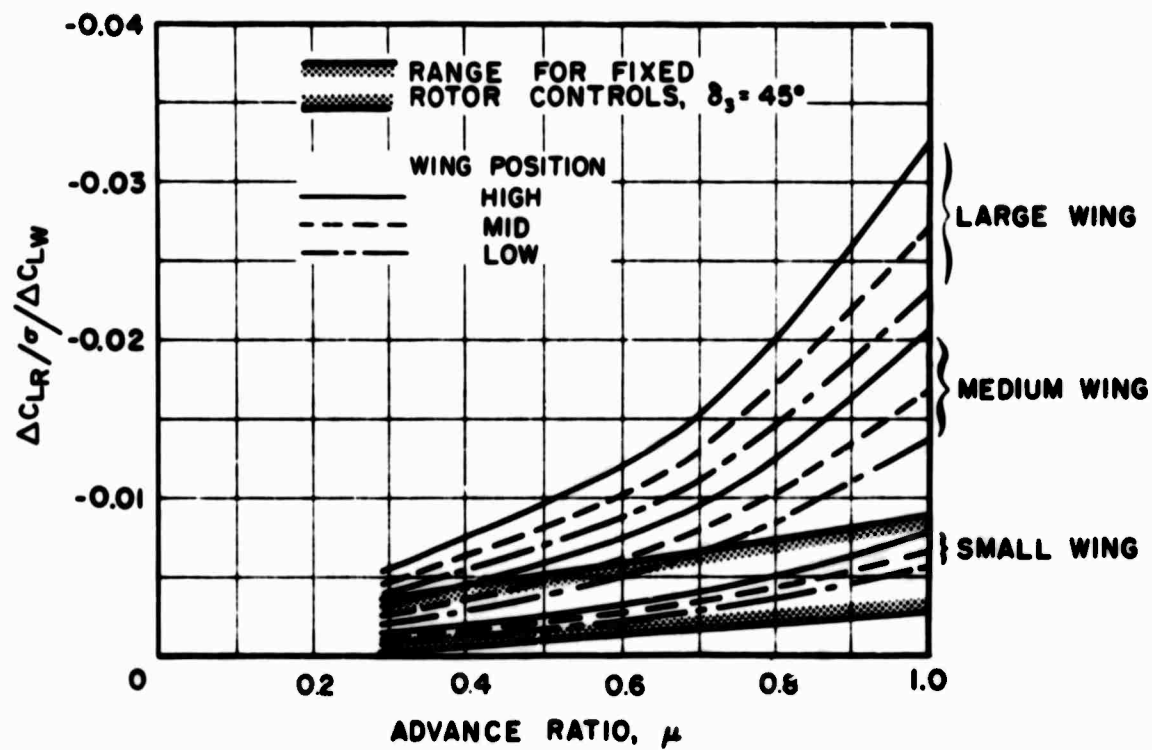
(a) $\delta_3 = 0^\circ$, Fixed Rotor Controls

Figure 72. Theoretical Effect of Wing Size and Position on Rotor Lift at Various Advance Ratios, Two Values of Pitch-Flap Coupling, and With Trimmed and Untrimmed Rotor Blade Flapping.



(b) $\delta_3 = 45^\circ$, Fixed Rotor Controls

Figure 72. Continued.



(c) $\delta_3 = 45^\circ$, Trimmed Wing Induced Flapping

Figure 72. Concluded.

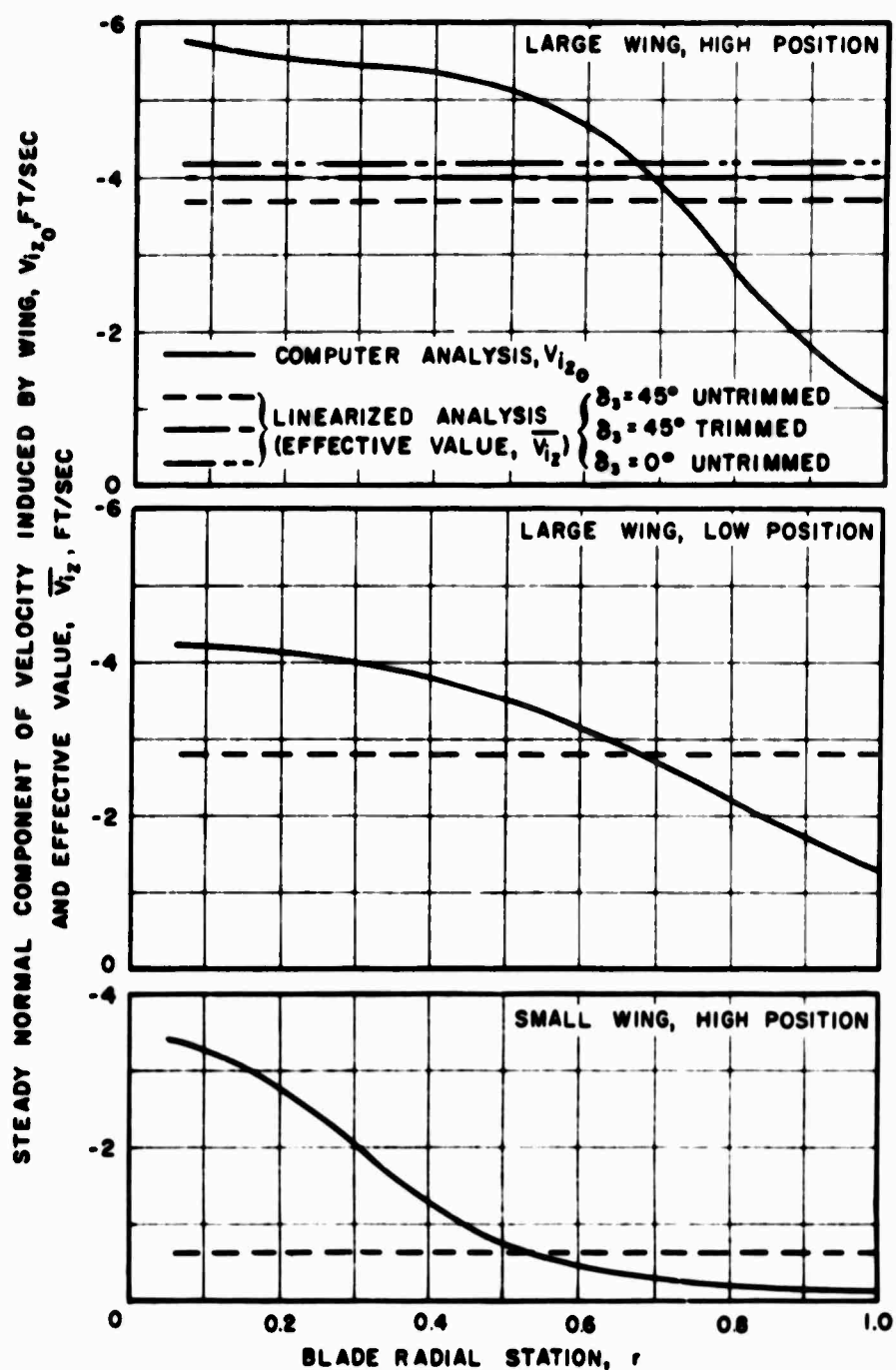
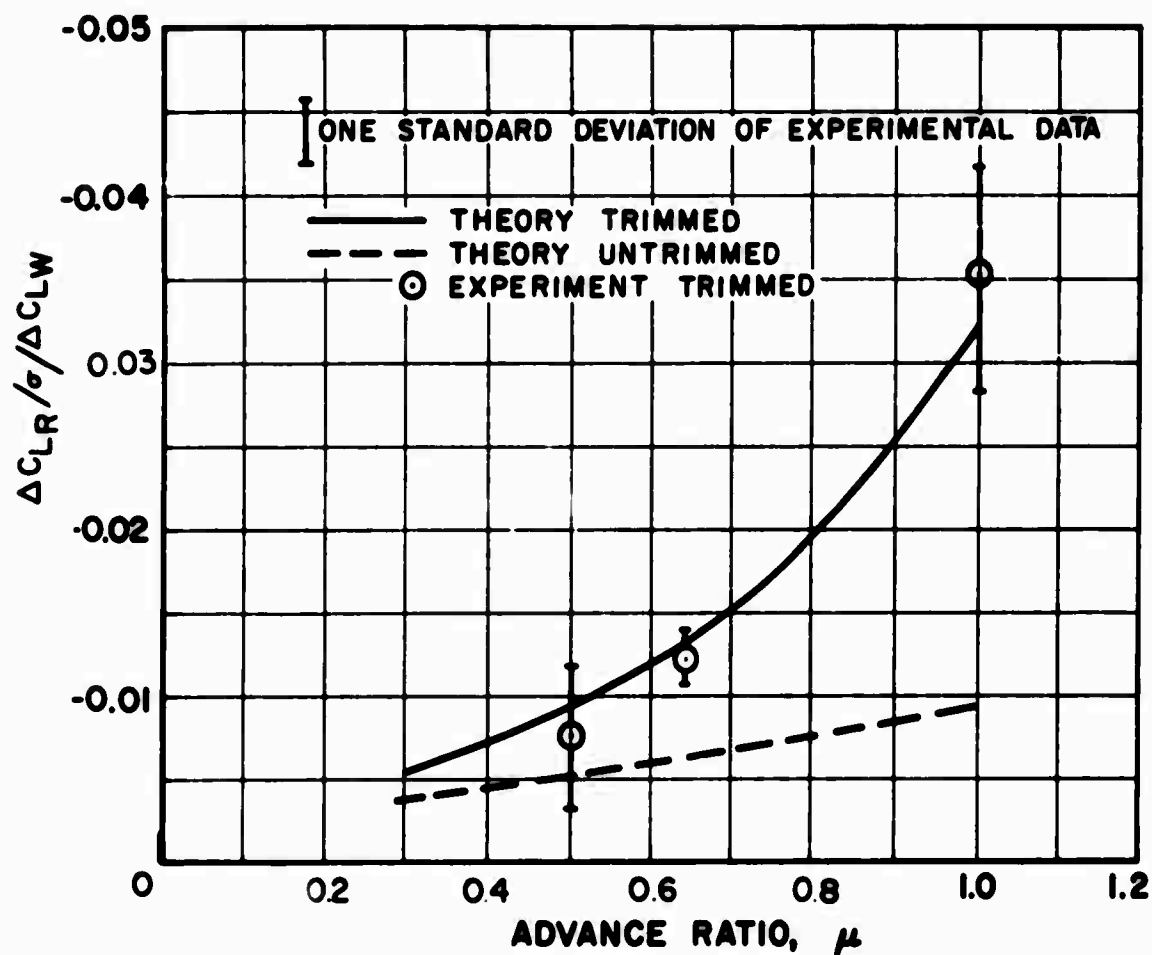
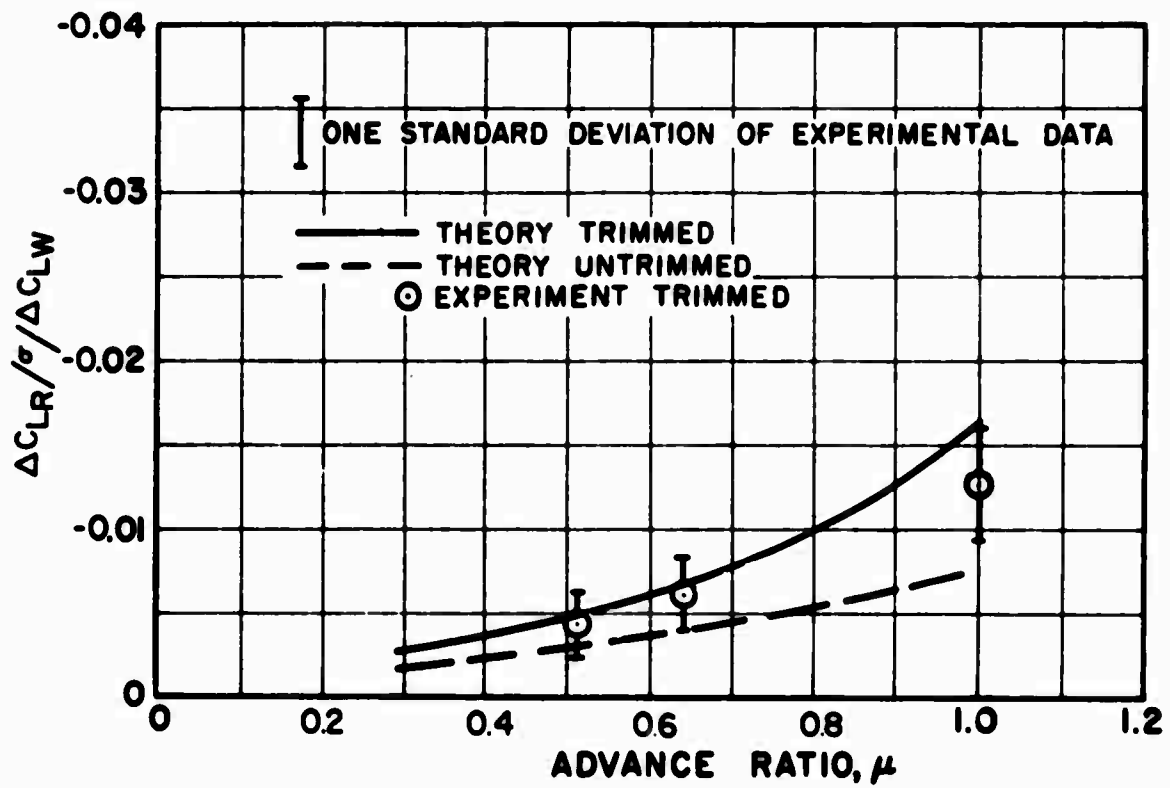


Figure 73. Comparison of Sample Results of Linearized Equations With Computer Results.



(a) Large Wing, High Position

Figure 74. Comparison of Theoretical and Experimental Effect of Wing Interference on Rotor Lift Versus Advance Ratio.



(b) Medium Wing, Mid Position

Figure 74. Concluded.

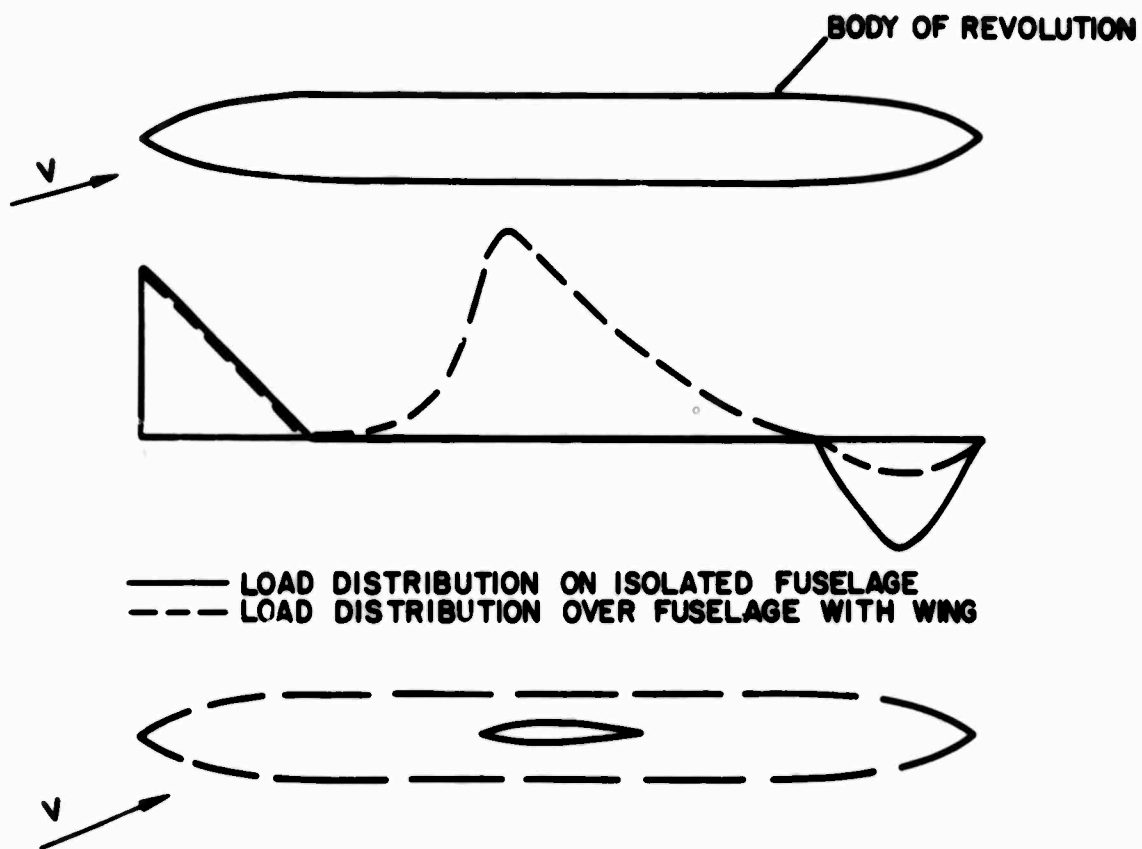


Figure 75. Fuselage Load Distribution.

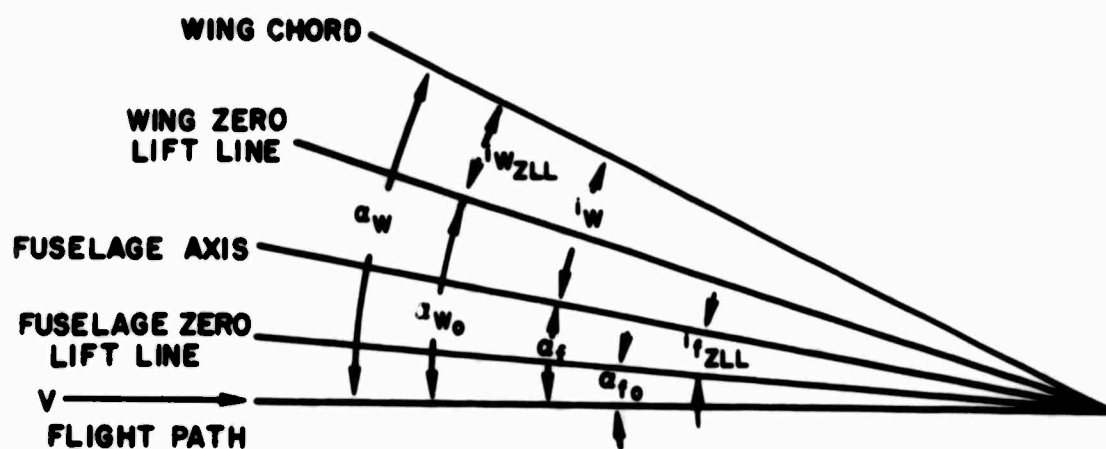


Figure 76. Wing-Fuselage Angles.

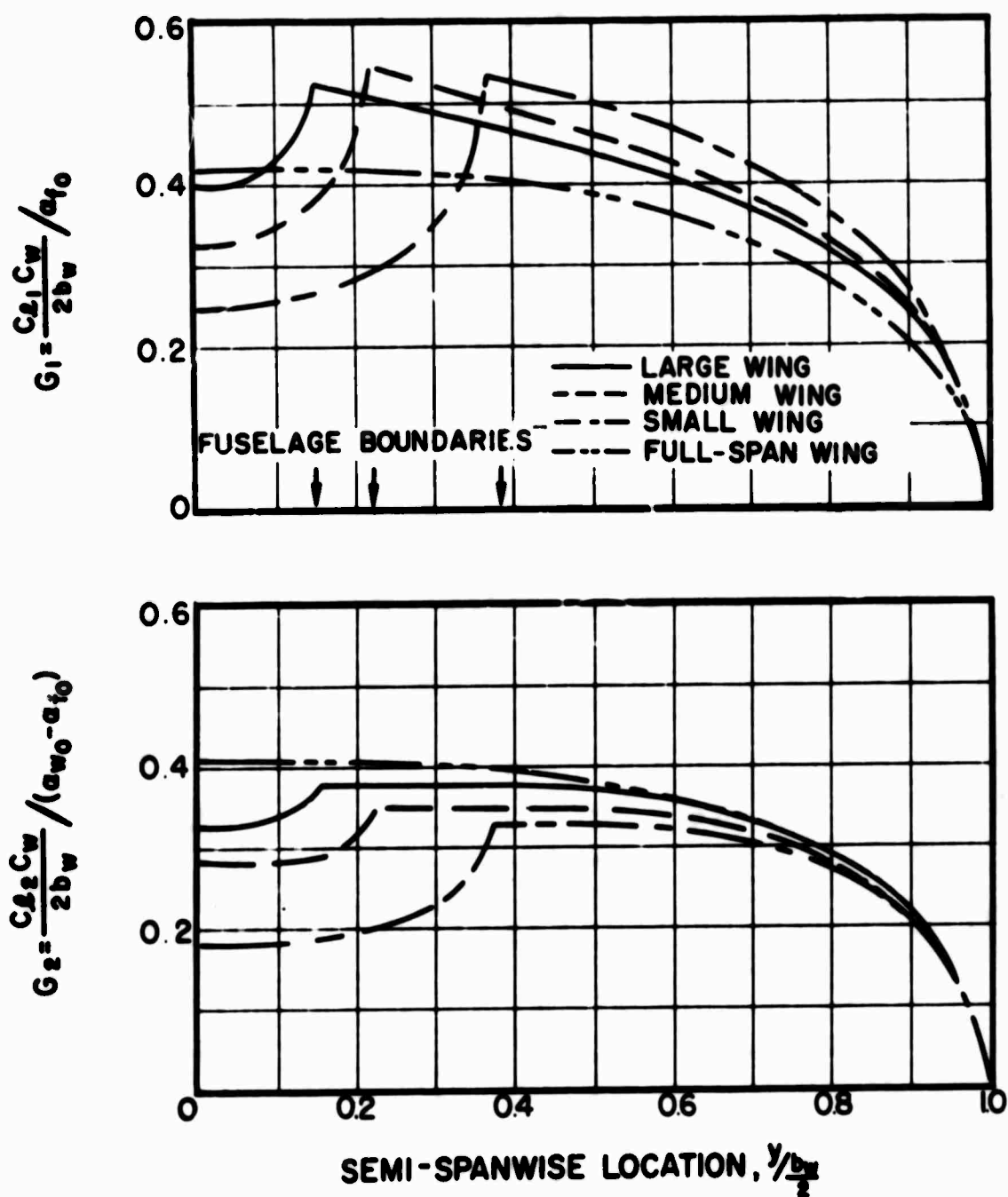


Figure 77. Components of Lift Distribution on Wing Alone and on Wing-Body Combinations at the Mid Wing Position.

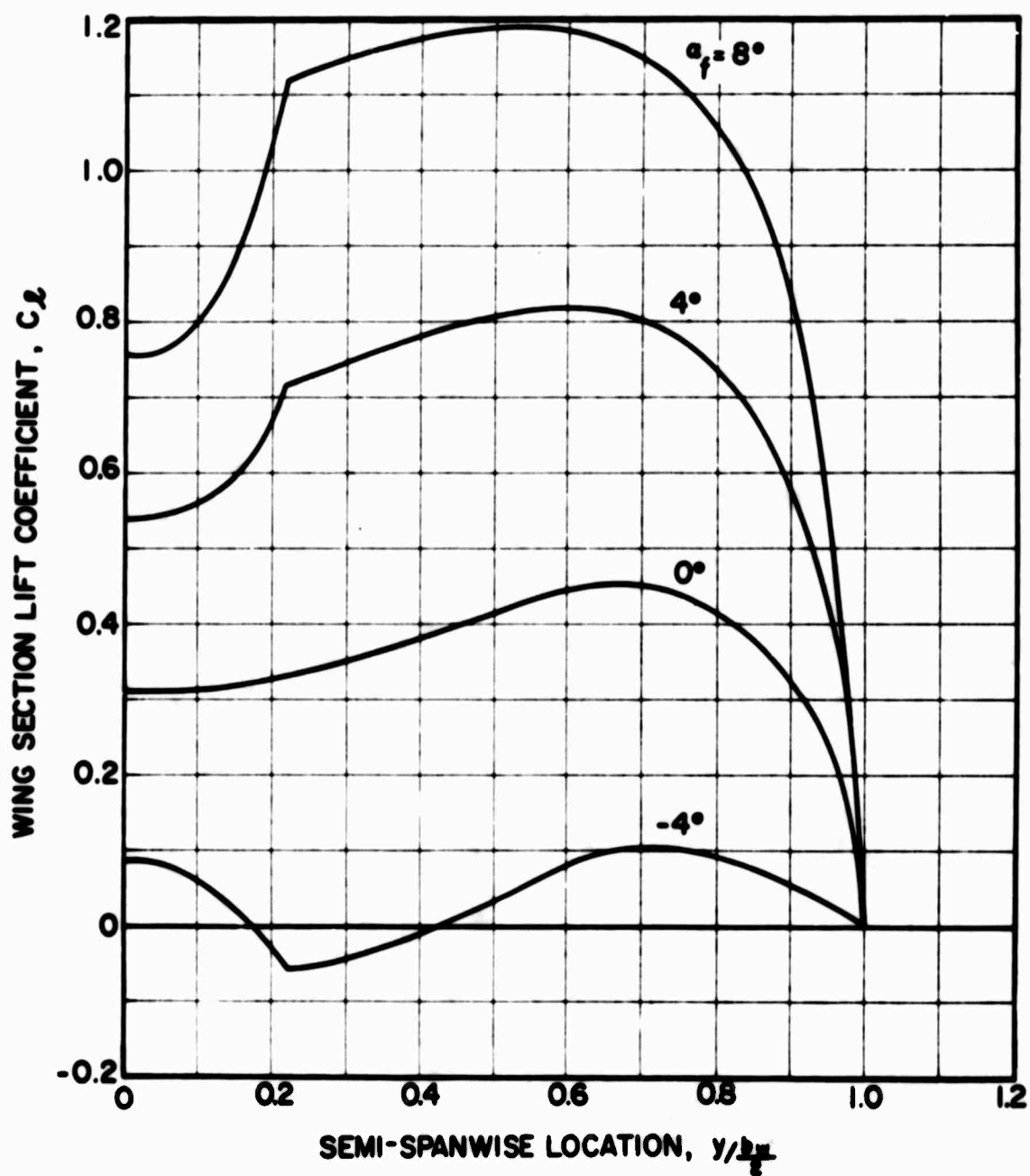


Figure 78. Theoretical Lift Coefficients on the Medium Wing, Mid Position at Various Fuselage Angles of Attack.

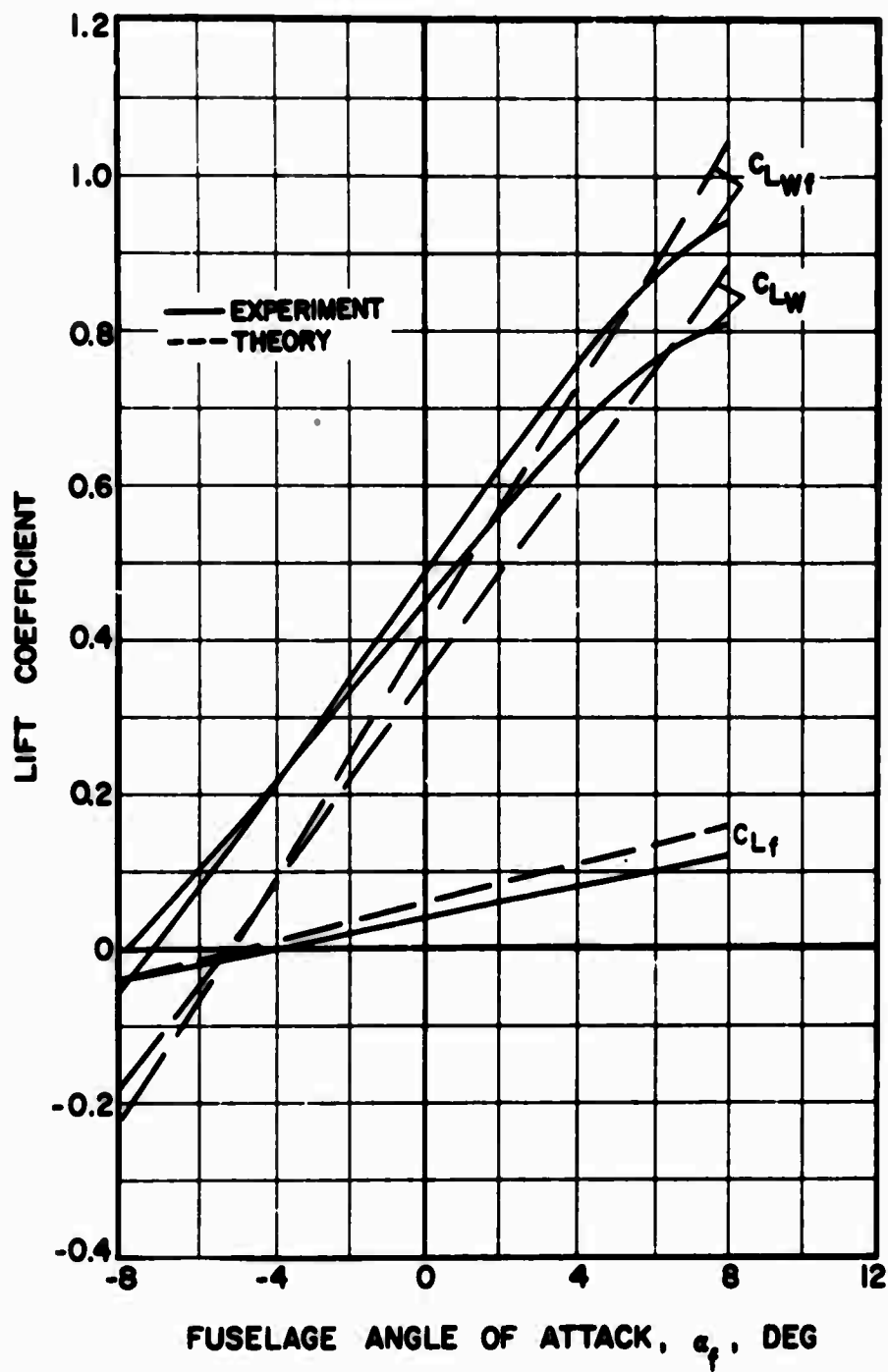


Figure 79. Comparison of Theoretical and Experimental Lift Characteristics of the Fuselage and Large Wing at the Mid Position for Various Angles of Attack, Without Rotor.

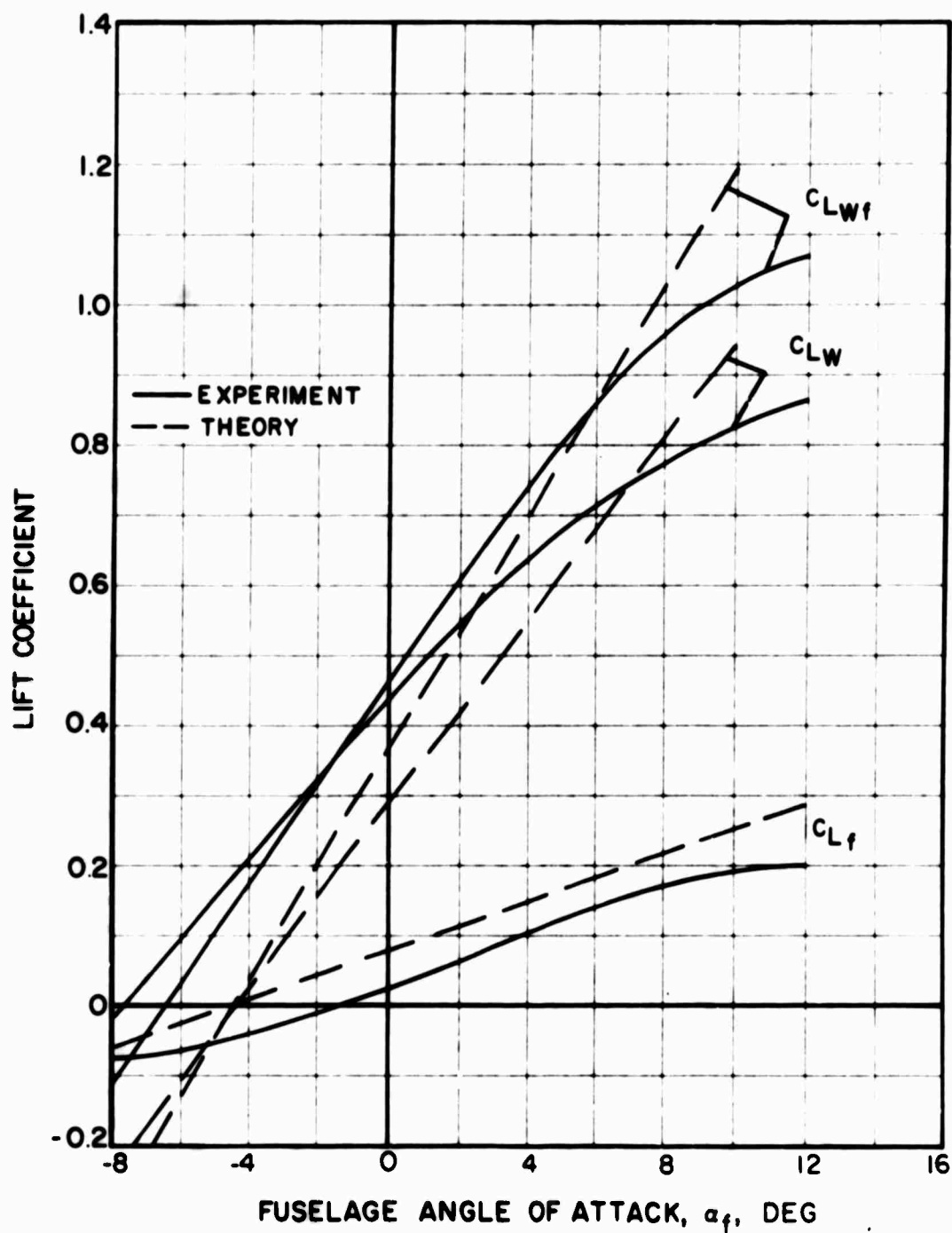


Figure 80. Comparison of Theoretical and Experimental Lift Characteristics of the Fuselage and Medium Wing at the Mid Position for Various Fuselage Angles of Attack, Without Rotor.

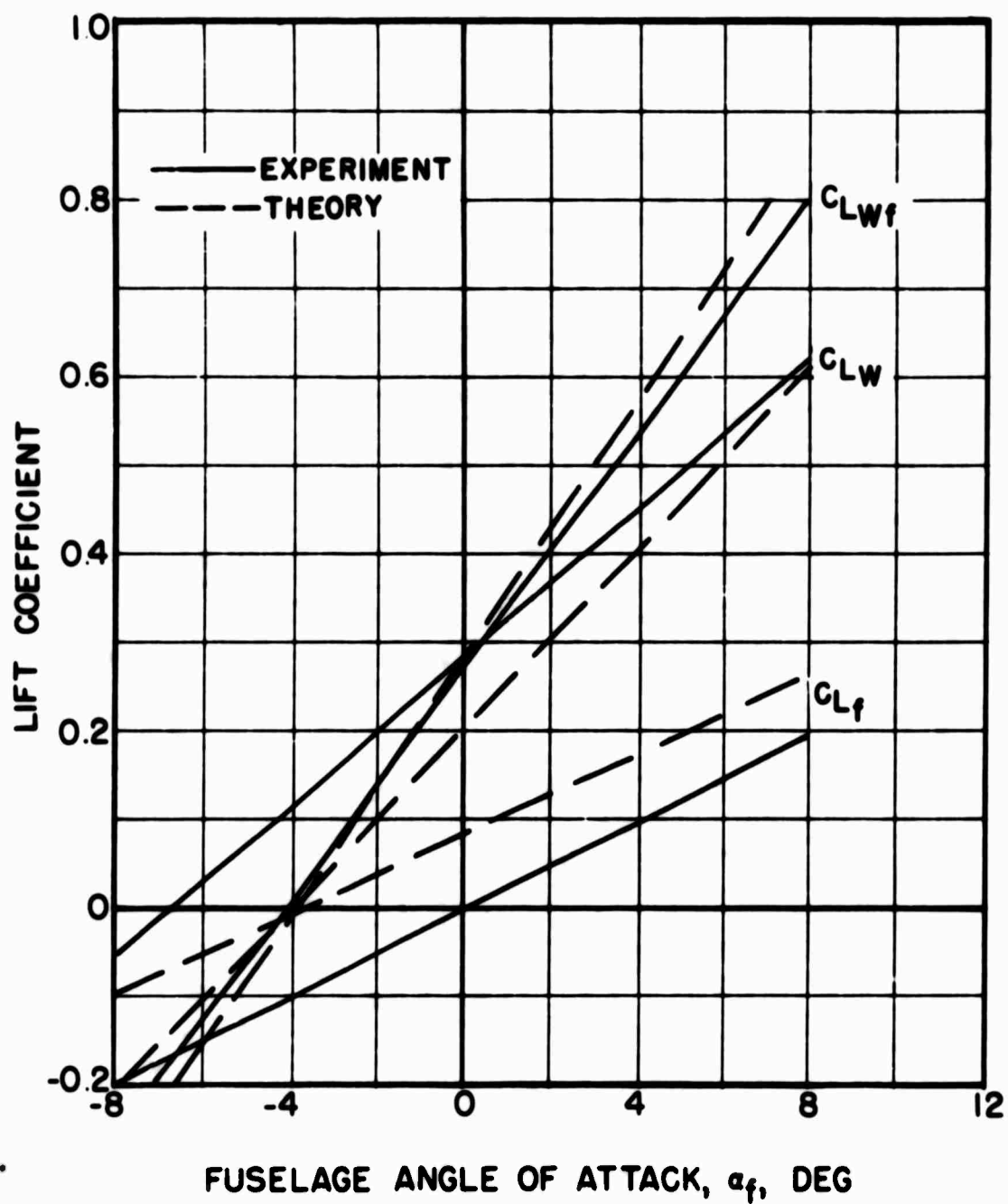


Figure 81. Comparison of Theoretical and Experimental Lift Characteristics of the Fuselage and Small Wing at the Mid Position for Various Fuselage Angles of Attack, Without Rotor.

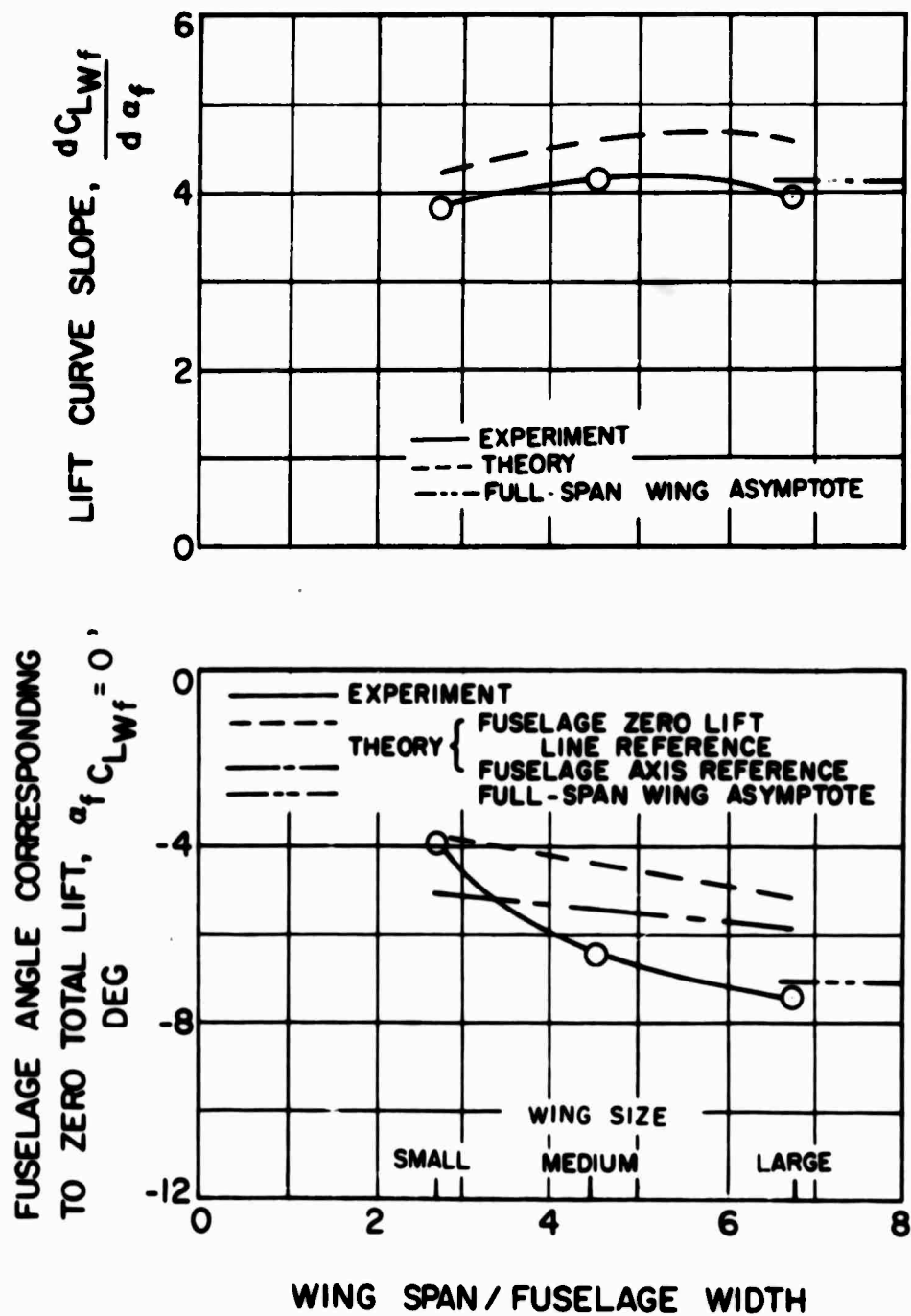


Figure 82. Comparison of Experimental and Theoretical Combined Wing-Fuselage Lift Characteristics for Various Wing Sizes.

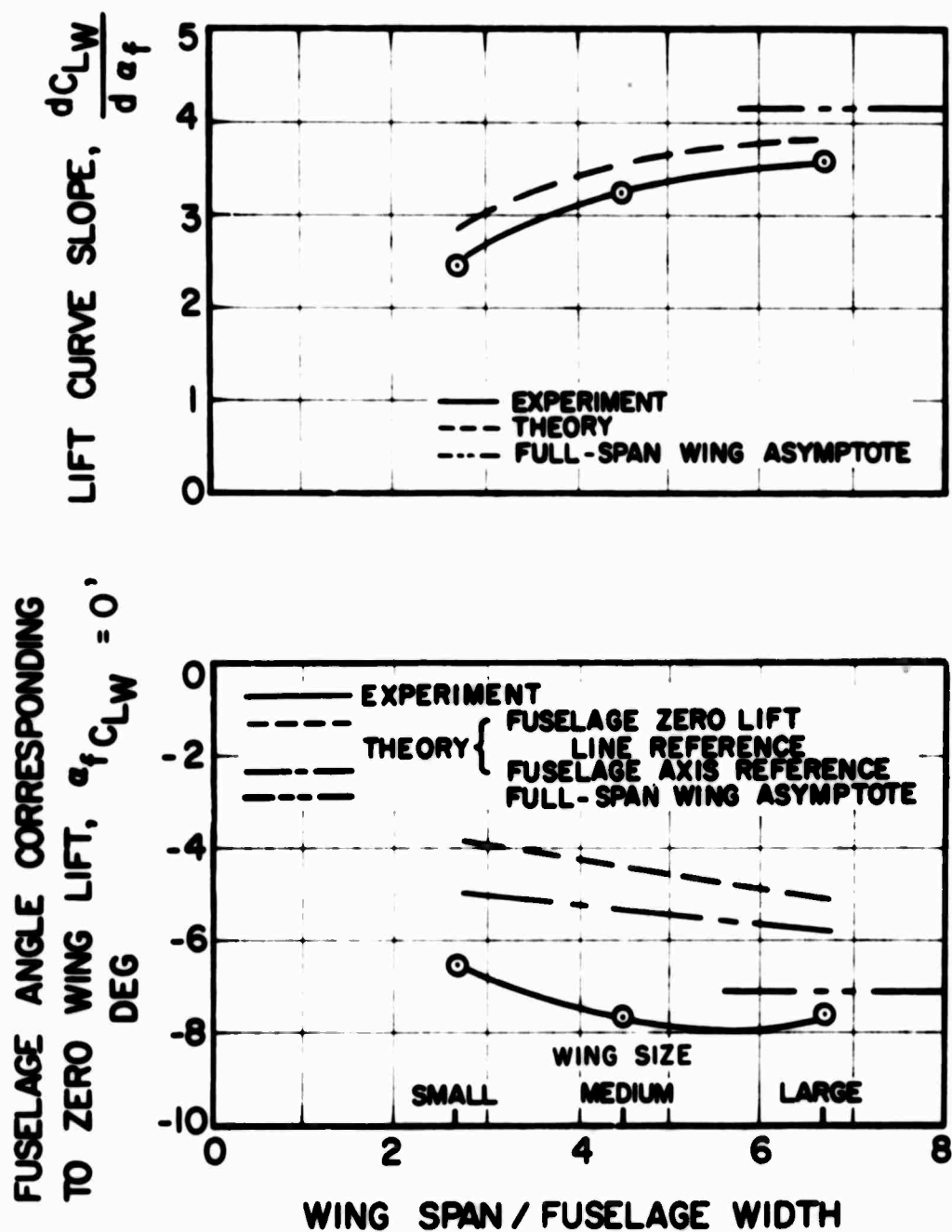


Figure 83. Comparison of Experimental and Theoretical Wing Lift Characteristics for Various Wing Sizes.

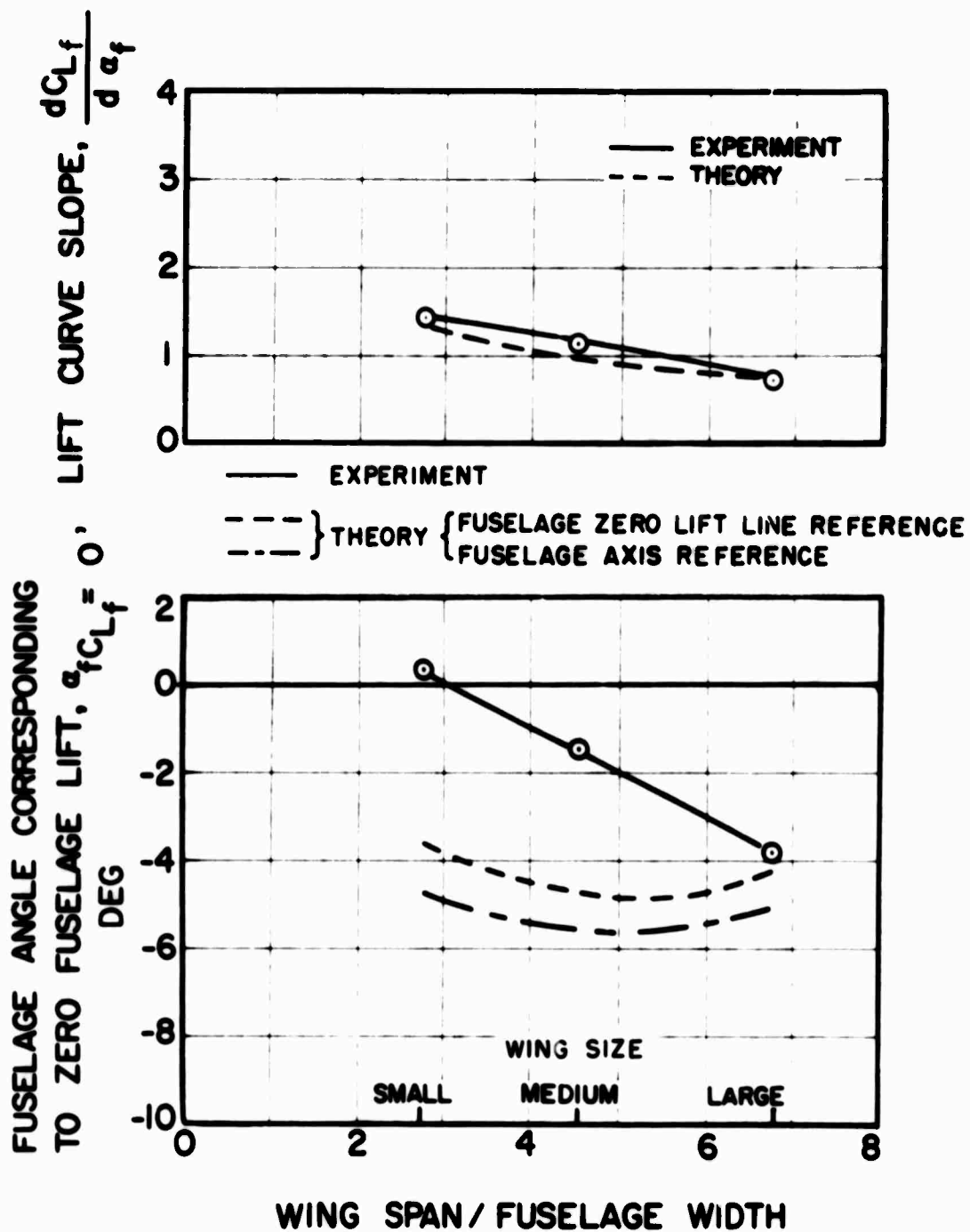


Figure 84. Comparison of Experimental and Theoretical Fuselage Lift Characteristics for Various Wing Sizes.

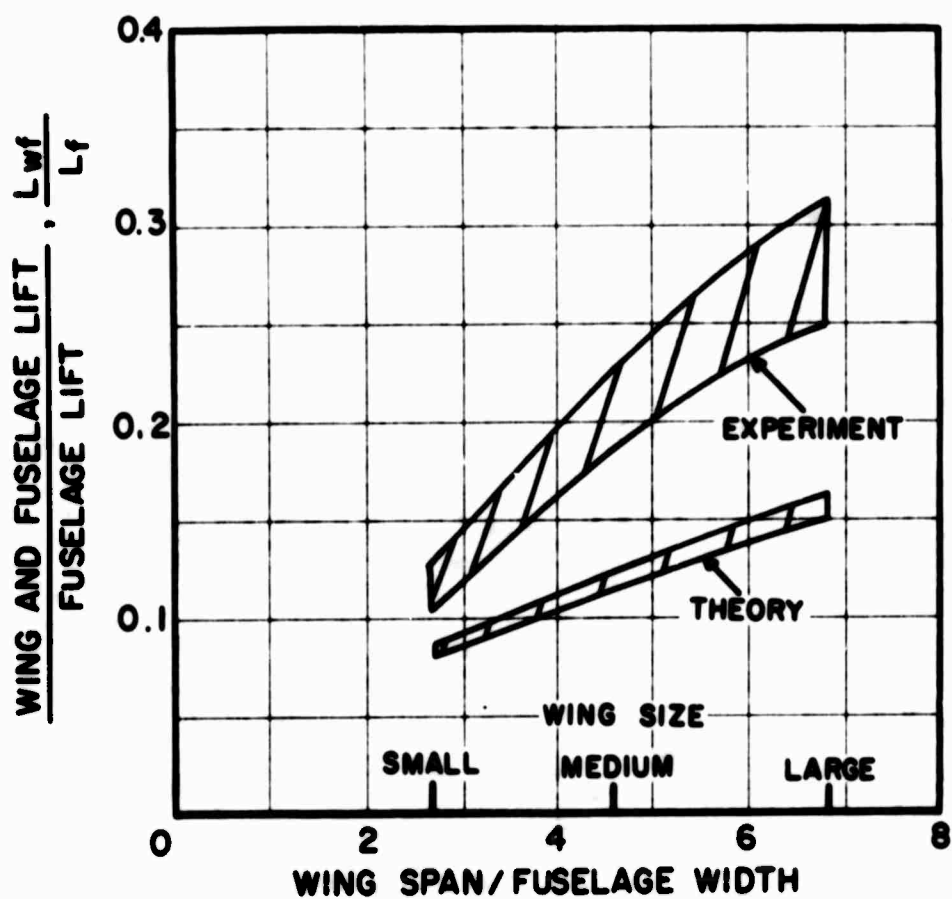


Figure 85. Comparison of Experimental and Theoretical Lift Carry-Over on Fuselage for Various Wing Sizes.

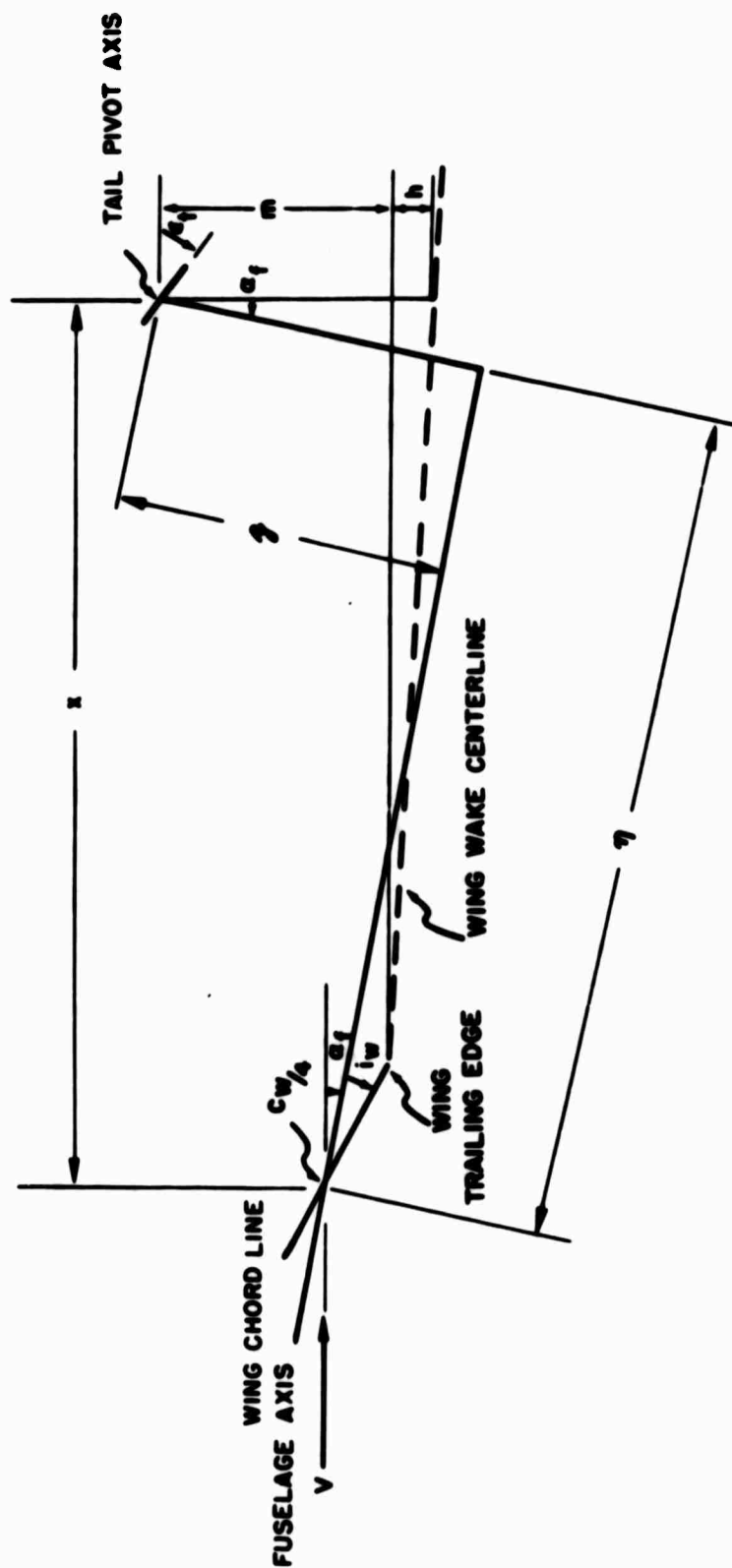


Figure 86. Wing-Tail Geometry for Reference 16 Theory.

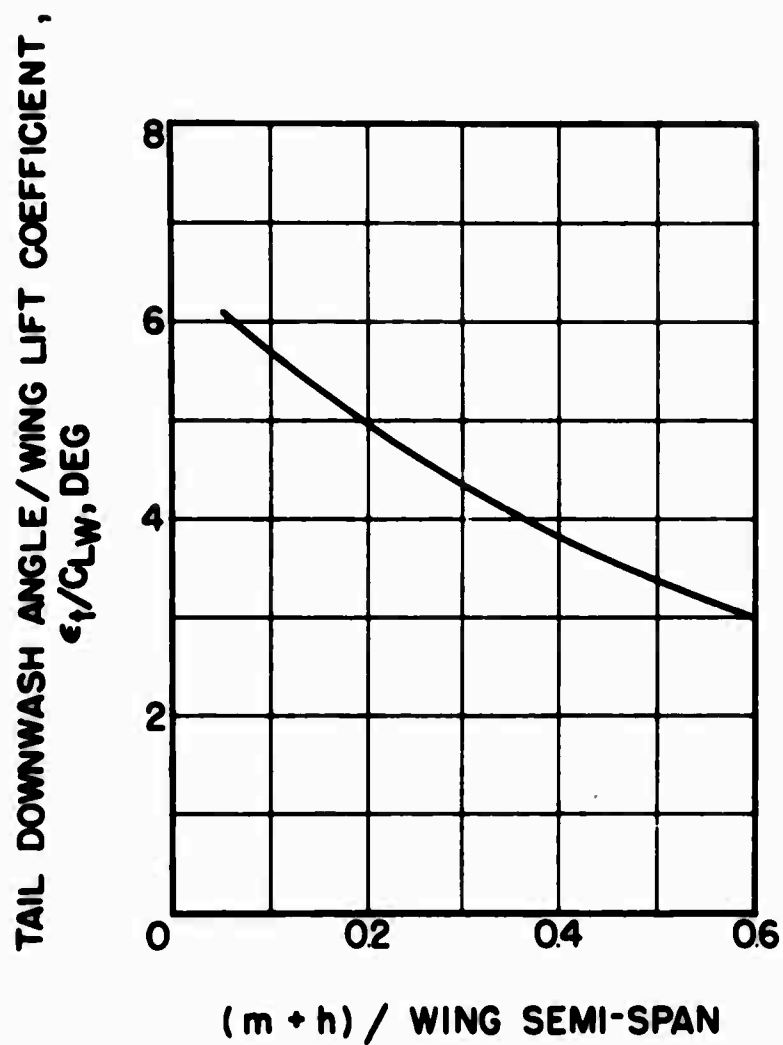


Figure 87. Theoretical Effect of Vertical Distance Between Wing Wake Centerline and Tail Pivot on Tail Downwash Angle Per Unit CL_W , Large Wing.

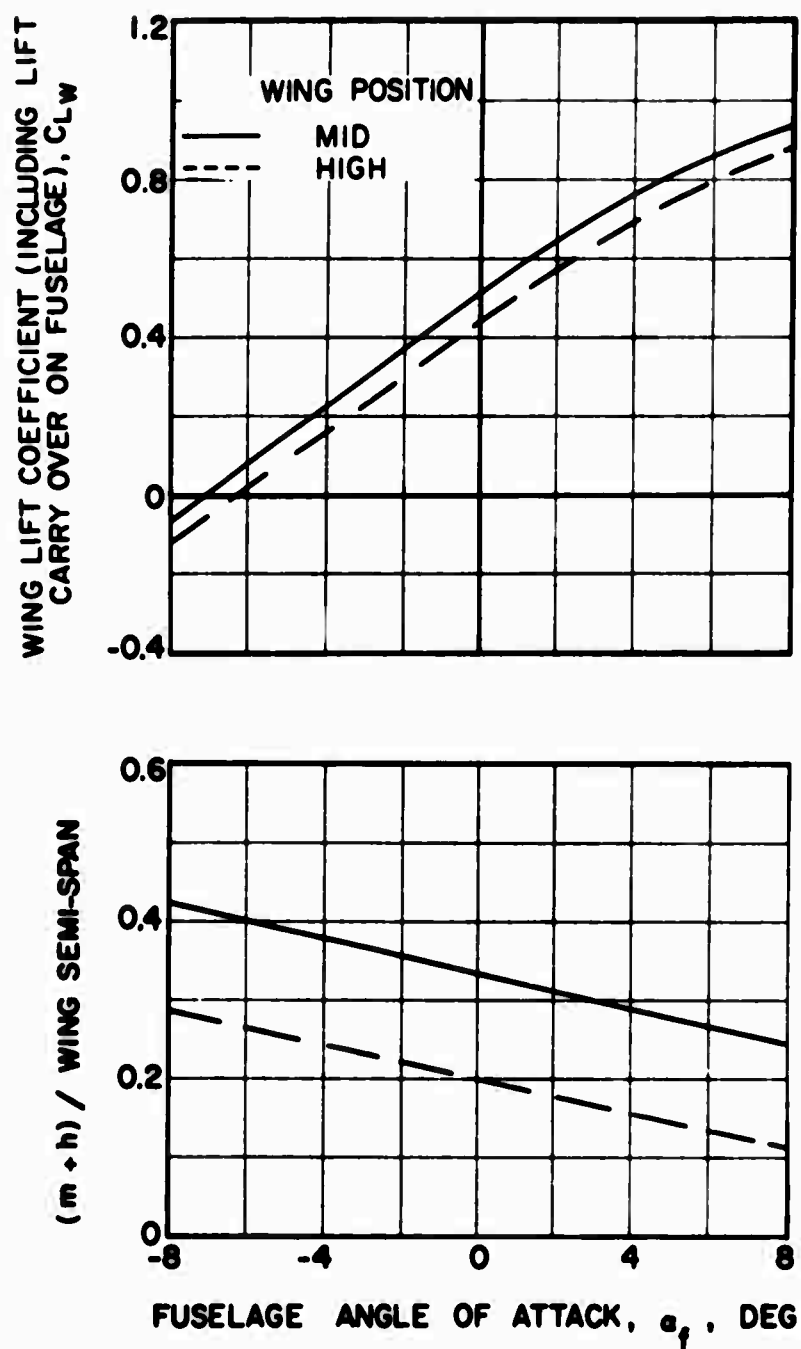


Figure 88. Experimental Wing Lift Coefficient and Vertical Distance Between Wing Wake Centerline and Tail Pivot Versus Fuselage Angle of Attack; Large Wing at Two Positions.

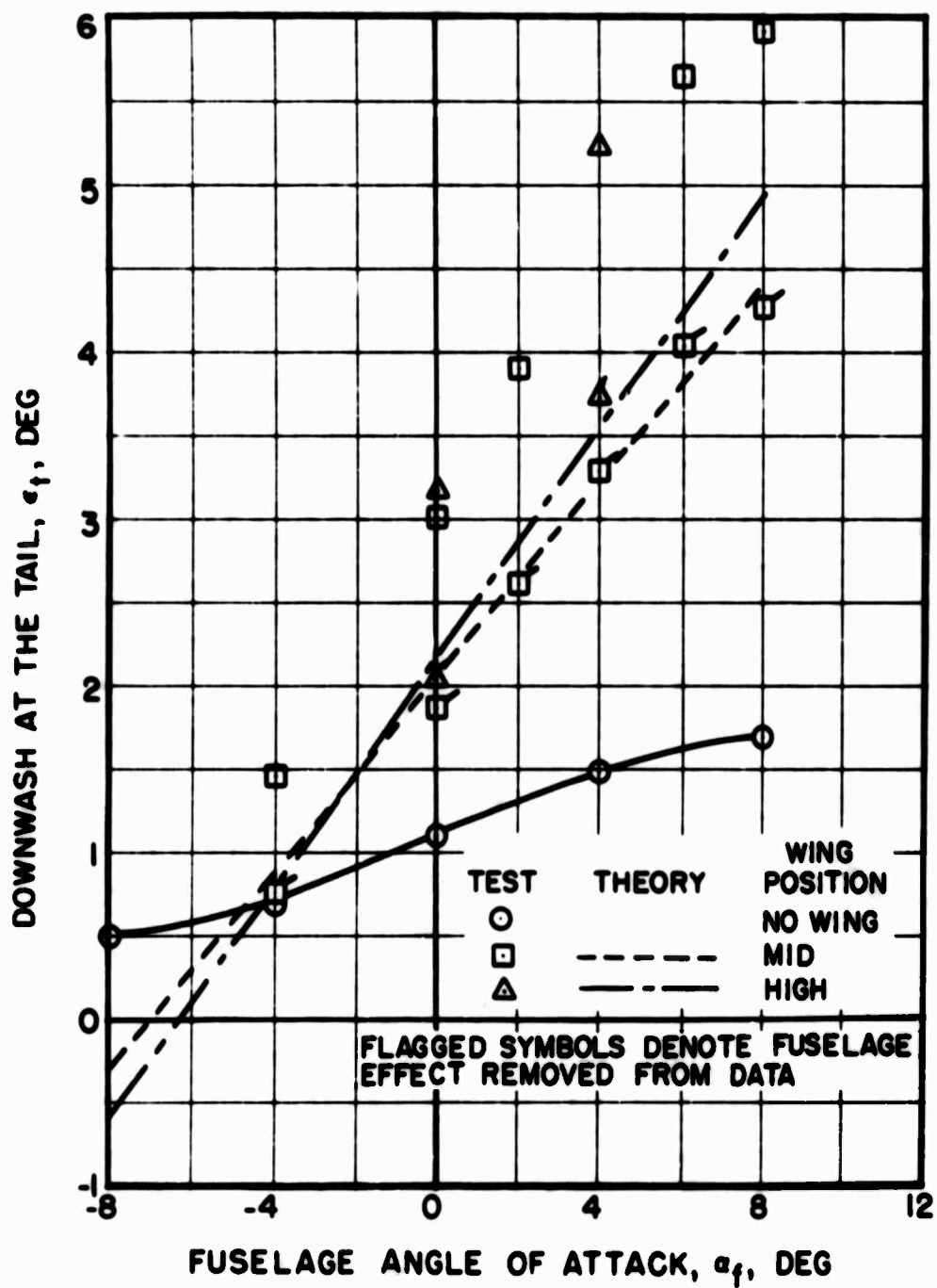


Figure 89. Comparison of Theoretical and Experimental Tail Downwash Angles for the Large Wing at Various Fuselage Angles of Attack.

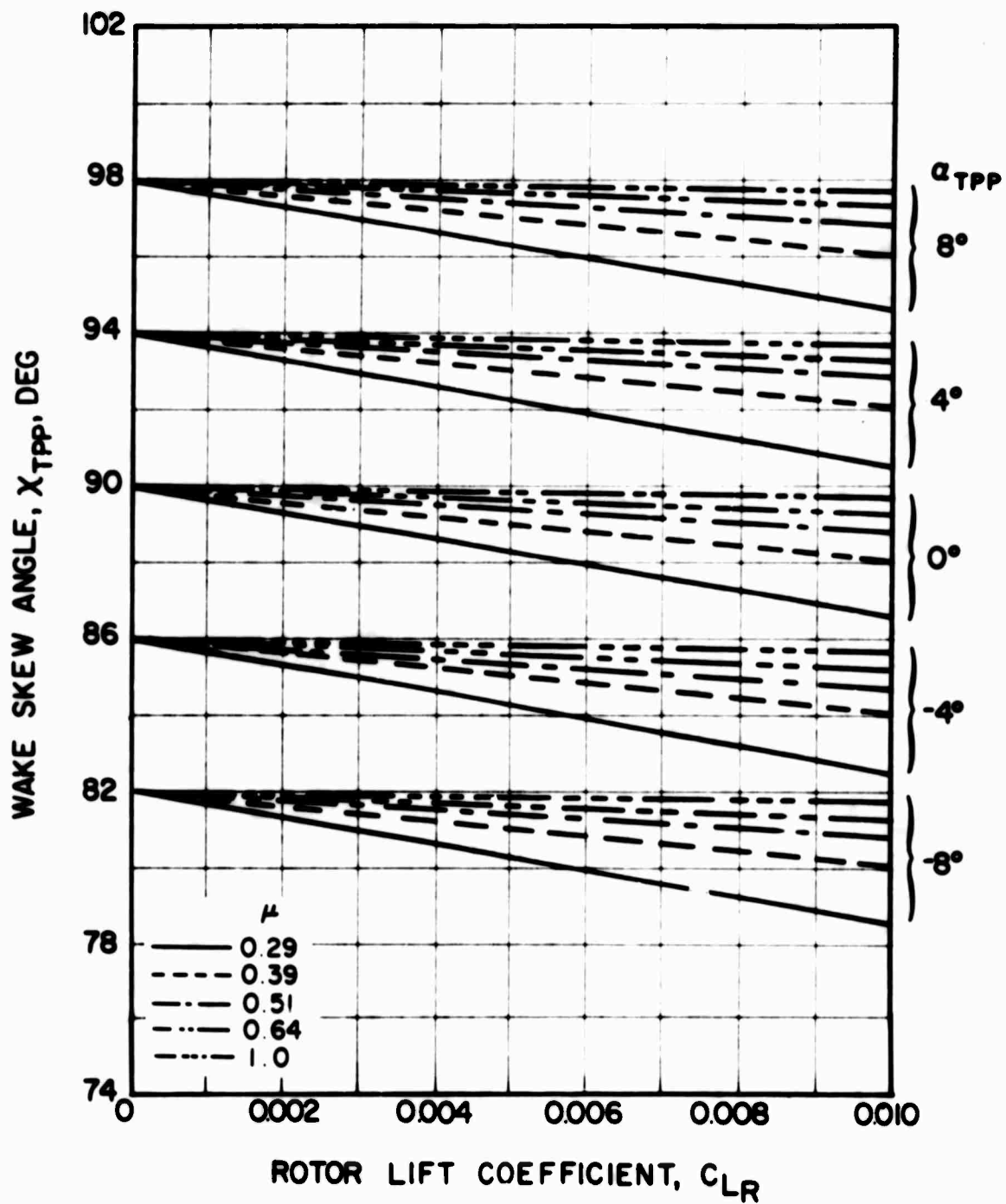


Figure 90. Effect of Rotor Lift and Angle of Attack on Rotor Wake Skew Angle for Several Advance Ratios.

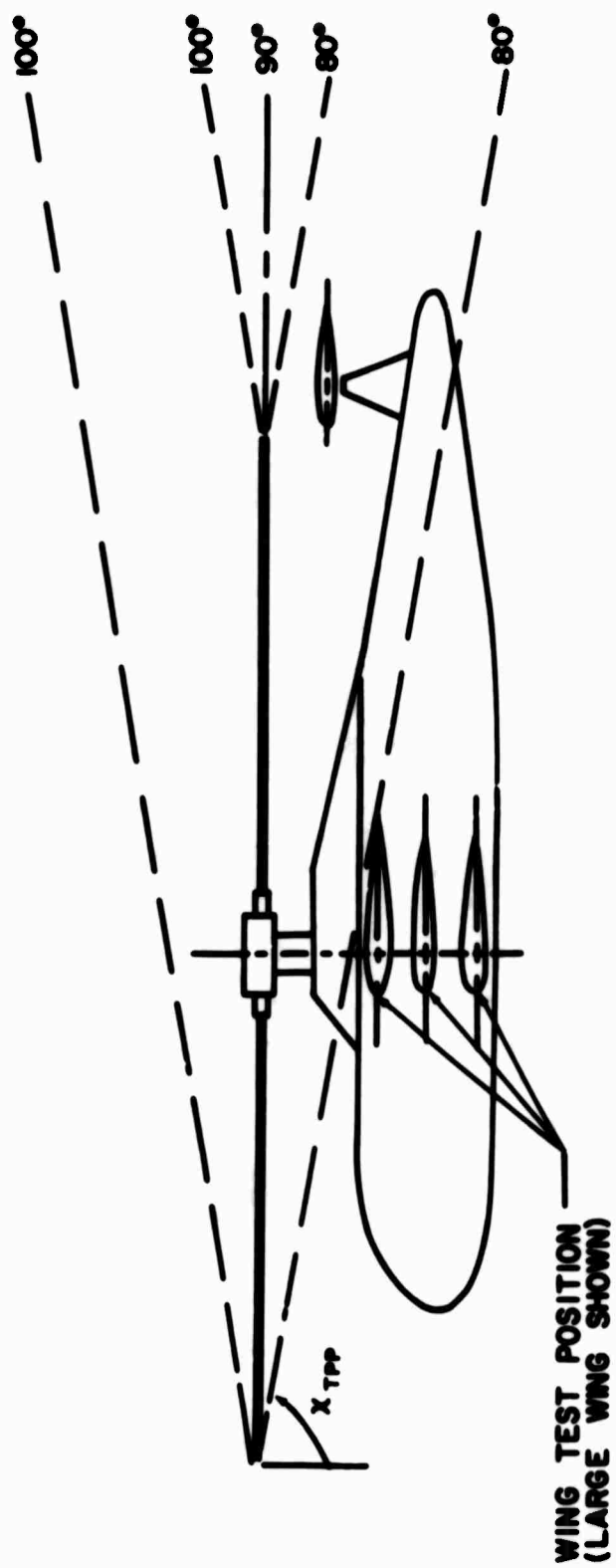


Figure 91. Rotor Wake Skew Angle Boundaries for Zero Rotor Blade Flapping.

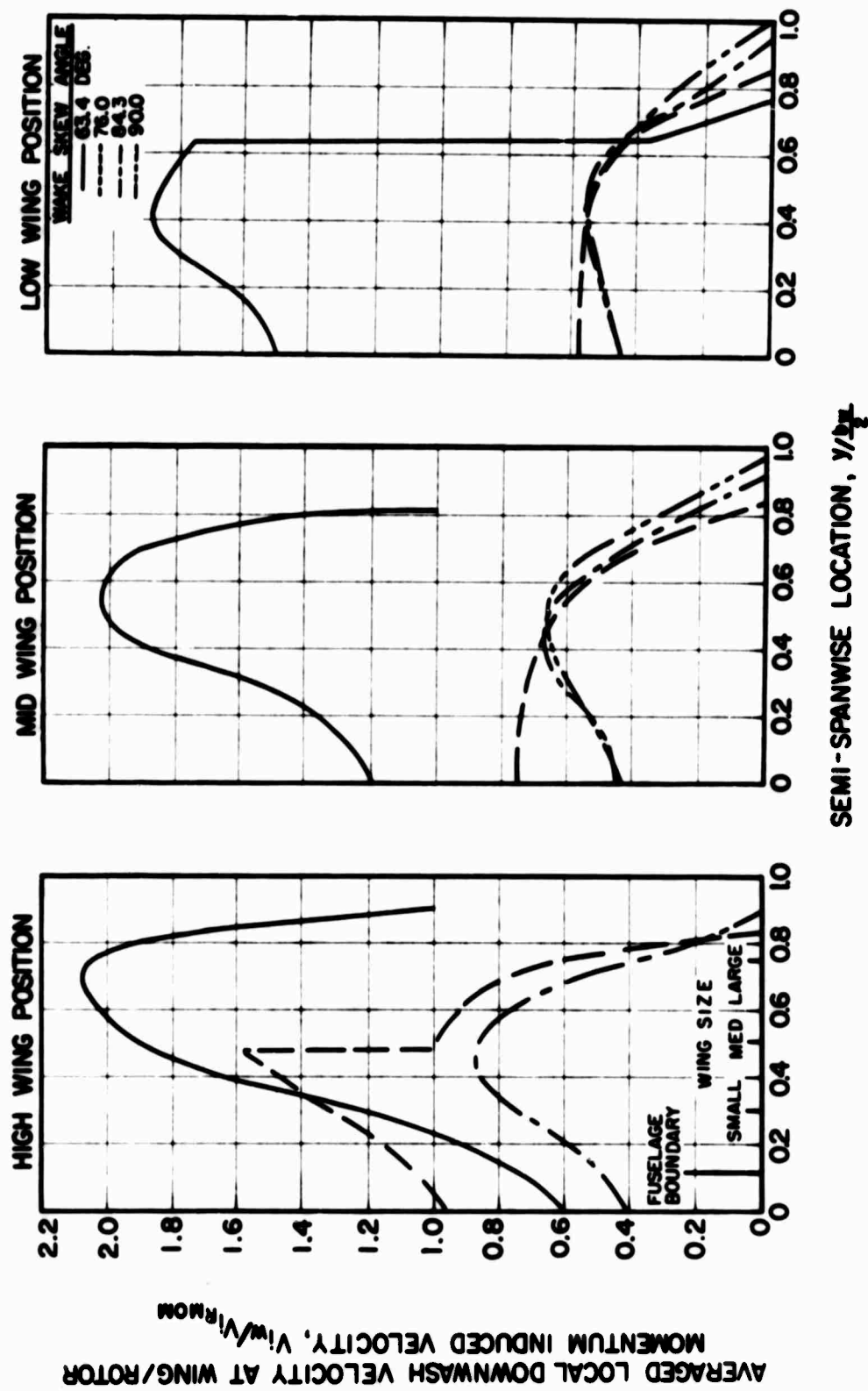


Figure 92. Local Downwash Factor Distributions for Skew Angles of Reference 17.

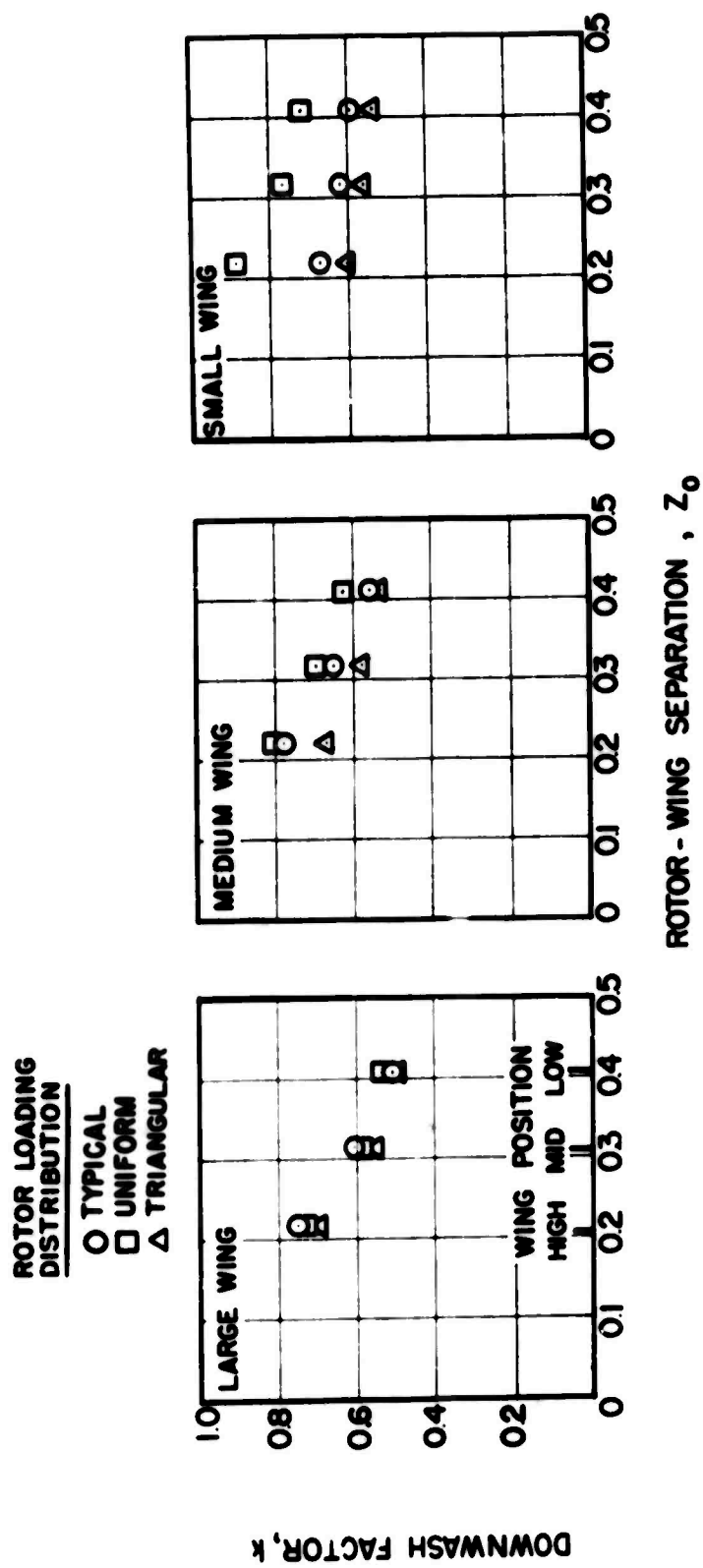


Figure 93. Theoretical Effect of Rotor Loading Distribution on Downwash Factor for Various Wing Sizes and Positions.

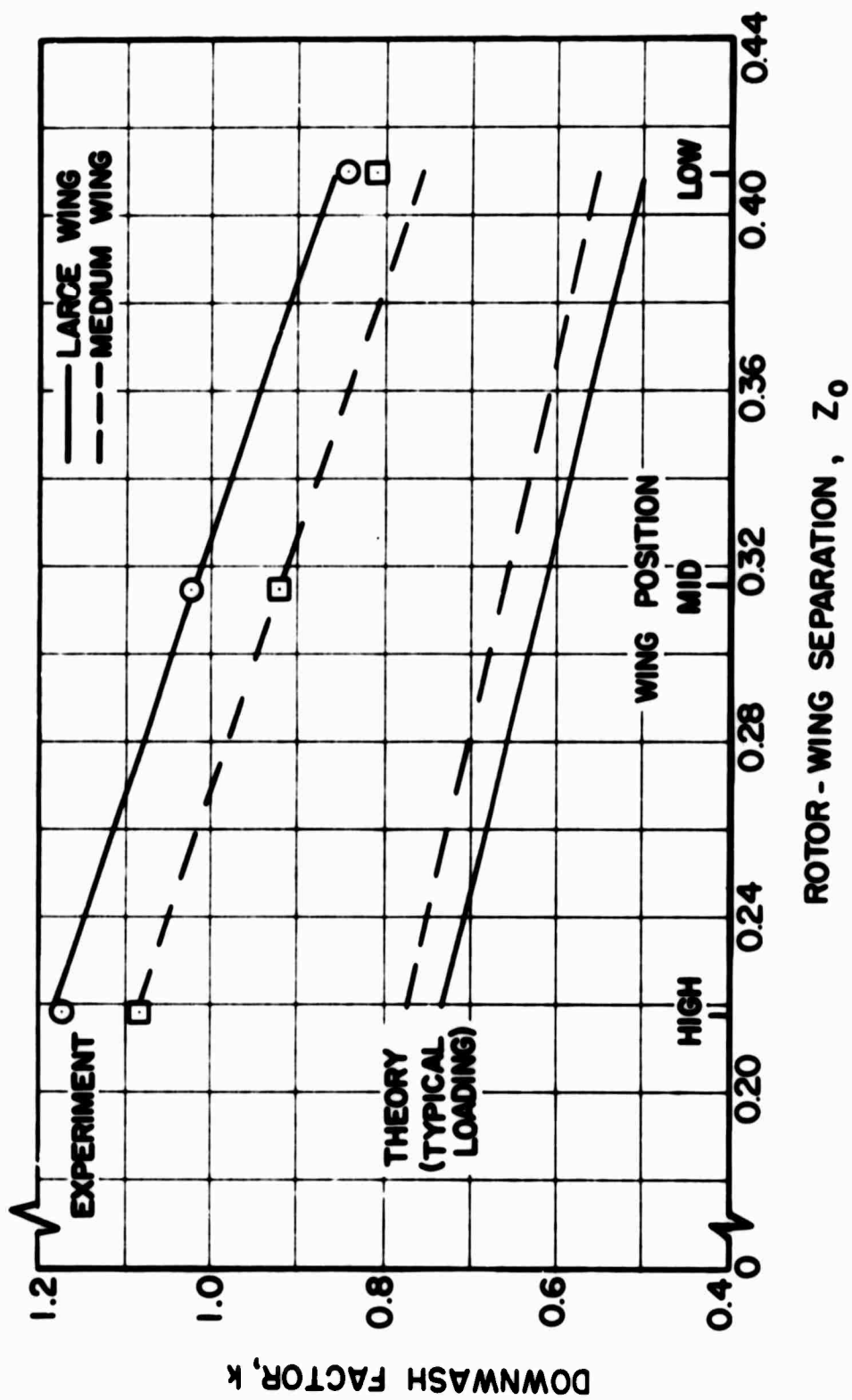


Figure 94. Comparison of Theoretical and Experimental Effects of Wing Position on Downwash Factor for the Large and Medium Wings.

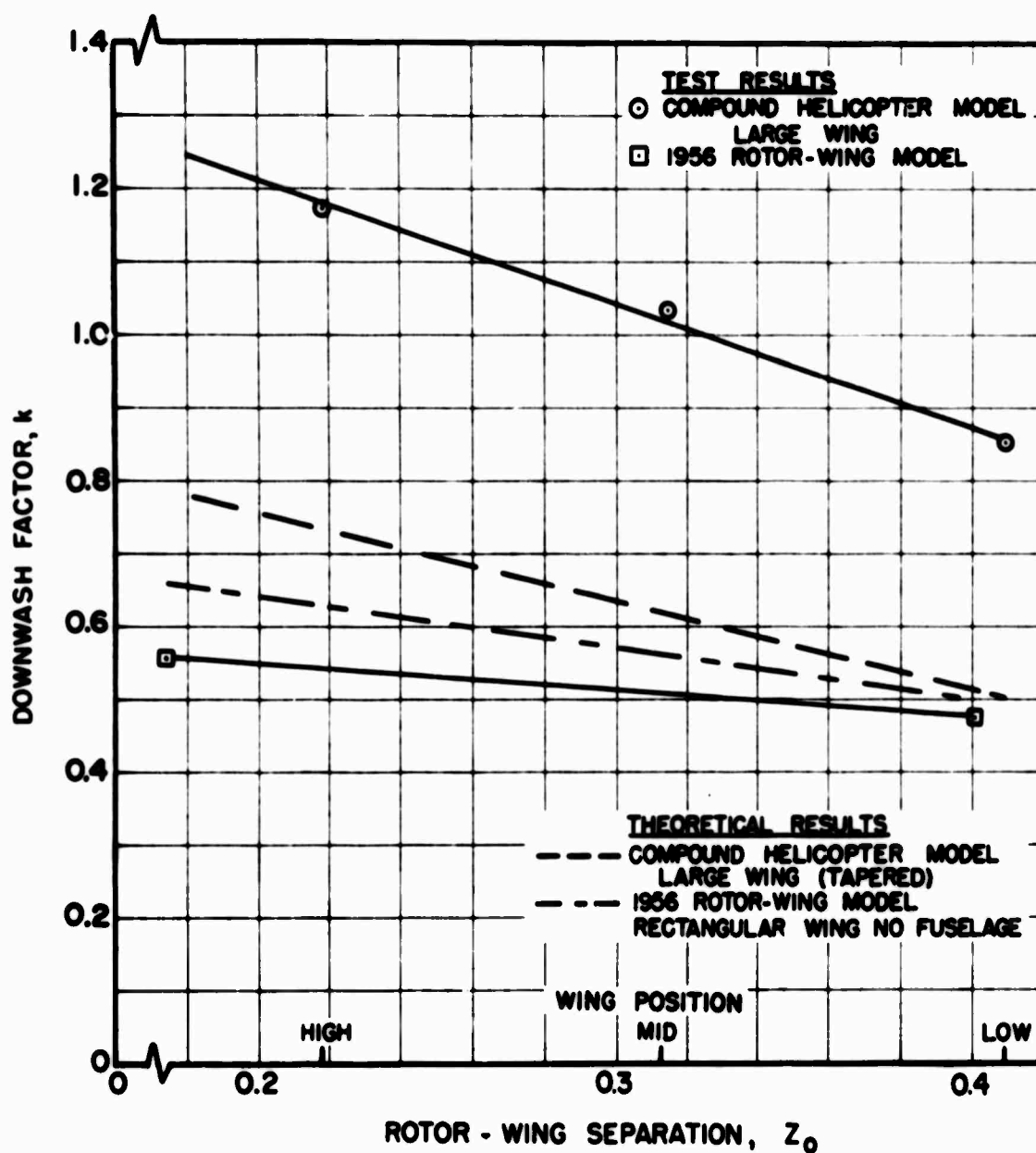


Figure 95. Comparison of Previous Experimental Results With Theoretical and Experimental Effects of Wing Position on Downwash Factor for the Large Wing.

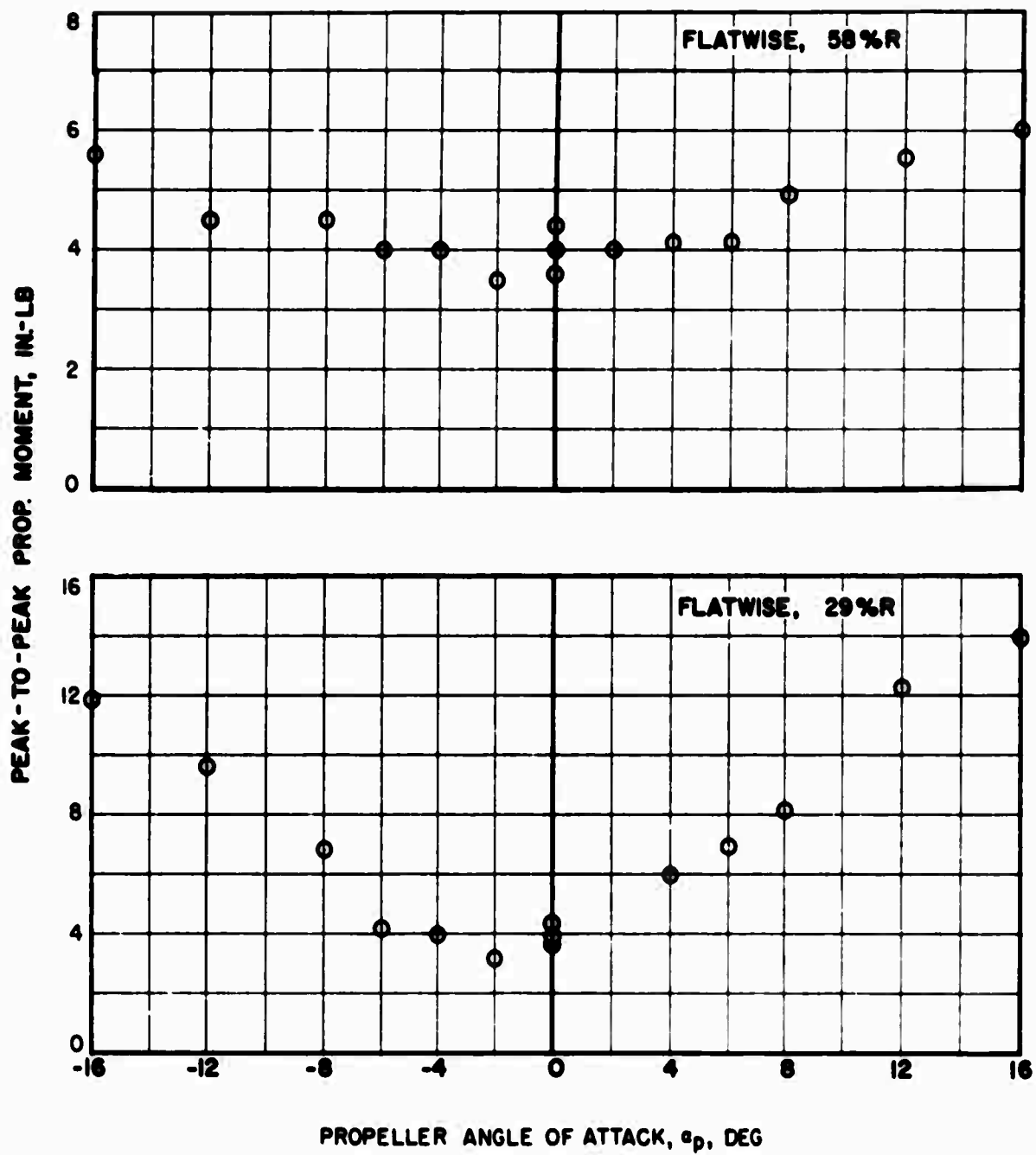


Figure 96. Isolated Propeller Blade Vibratory Moment Characteristics at Various Propeller Angles of Attack, $N_{PROP} = 3500$ rpm, $V_s = 120$ Knots, $\beta_{75} = 41^\circ$.

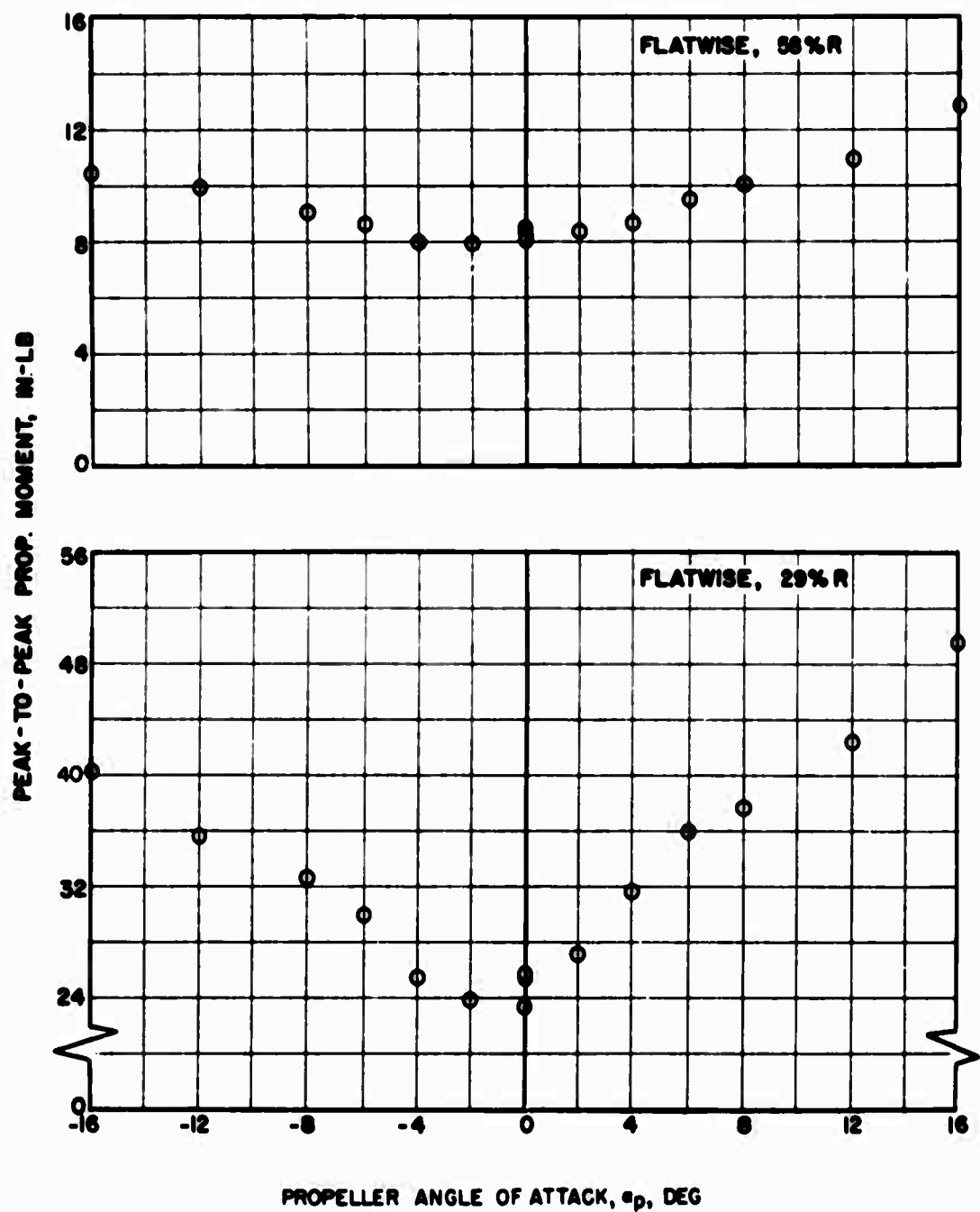


Figure 97. Isolated Propeller Blade Vibratory Moment Characteristics at Various Propeller Angles of Attack, $N_{PROP} = 4200$ rpm, $V_S = 200$ Knots, $\beta_{.75} = 41^\circ$.

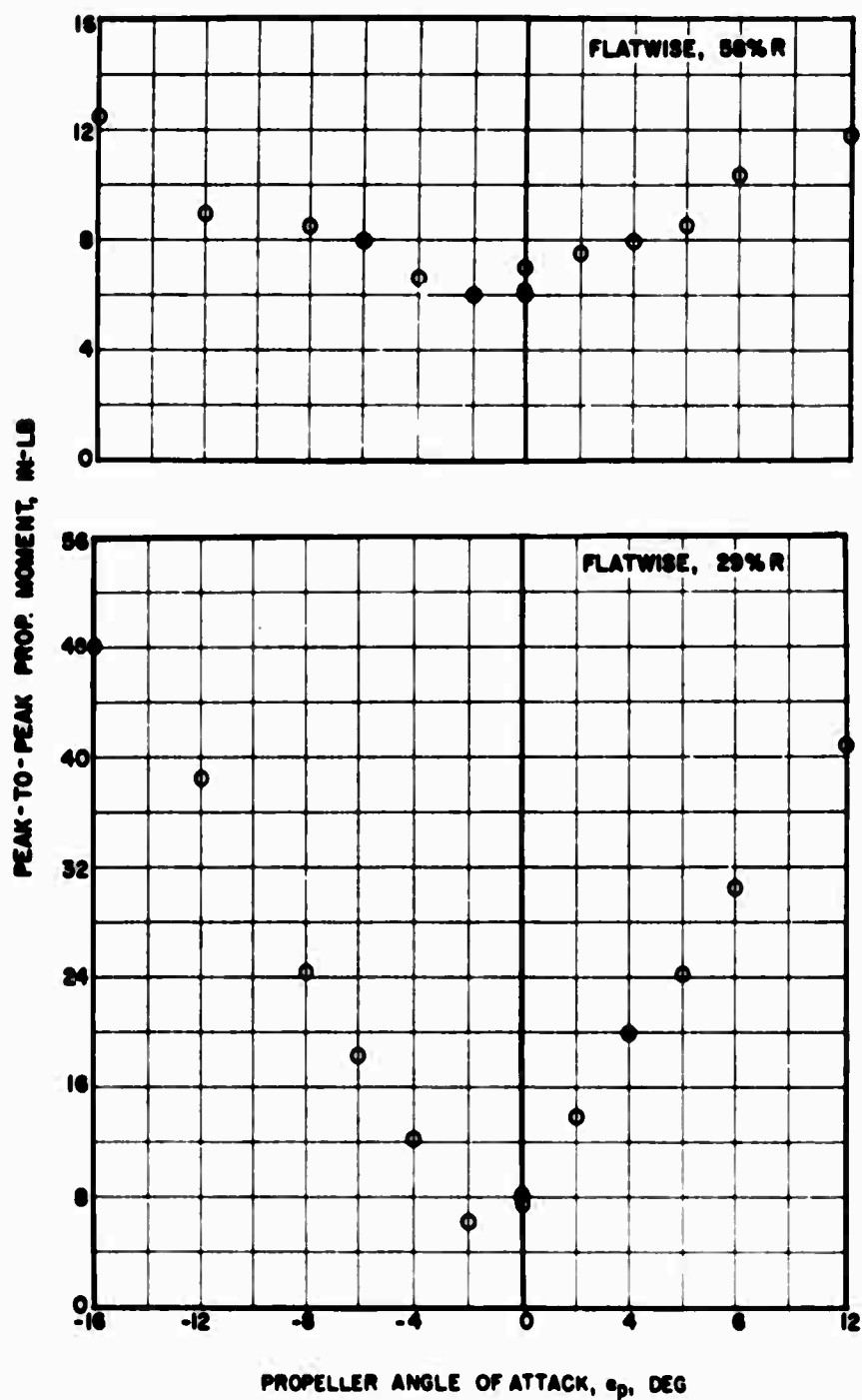


Figure 98. Isolated Propeller Blade Vibratory Moment Characteristics at Various Propeller Angles of Attack, $N_{PROP} = 5100$ rpm, $V_S = 300$ Knots, $\beta_{.75} = 41^\circ$.

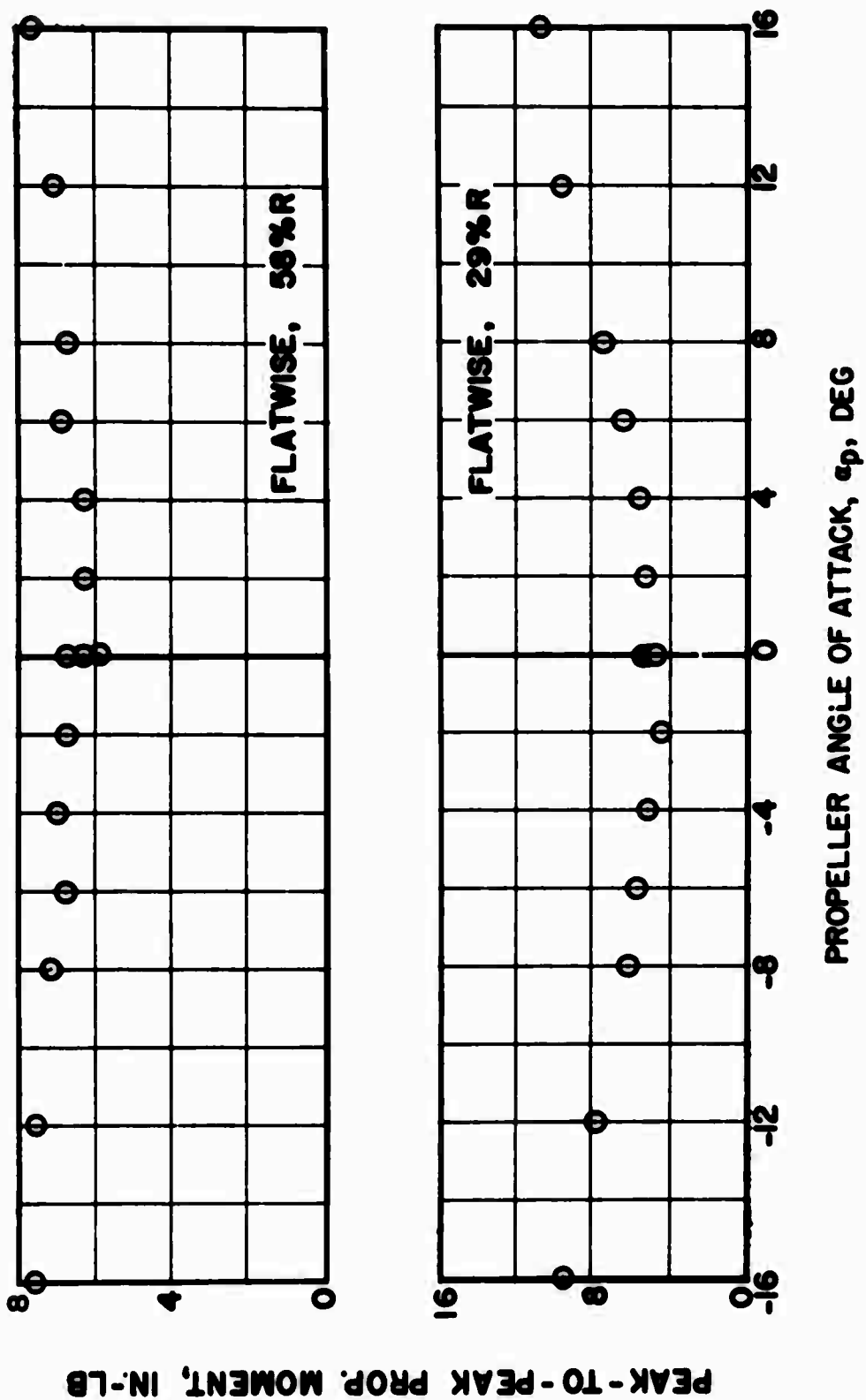


Figure 99. Isolated Propeller Blade Vibratory Moment Characteristics at Various Propeller Angles of Attack, $N_{PROP} = 5250$ rpm, $V_S = 120$ Knots, $\beta_{75} = 30^\circ$.

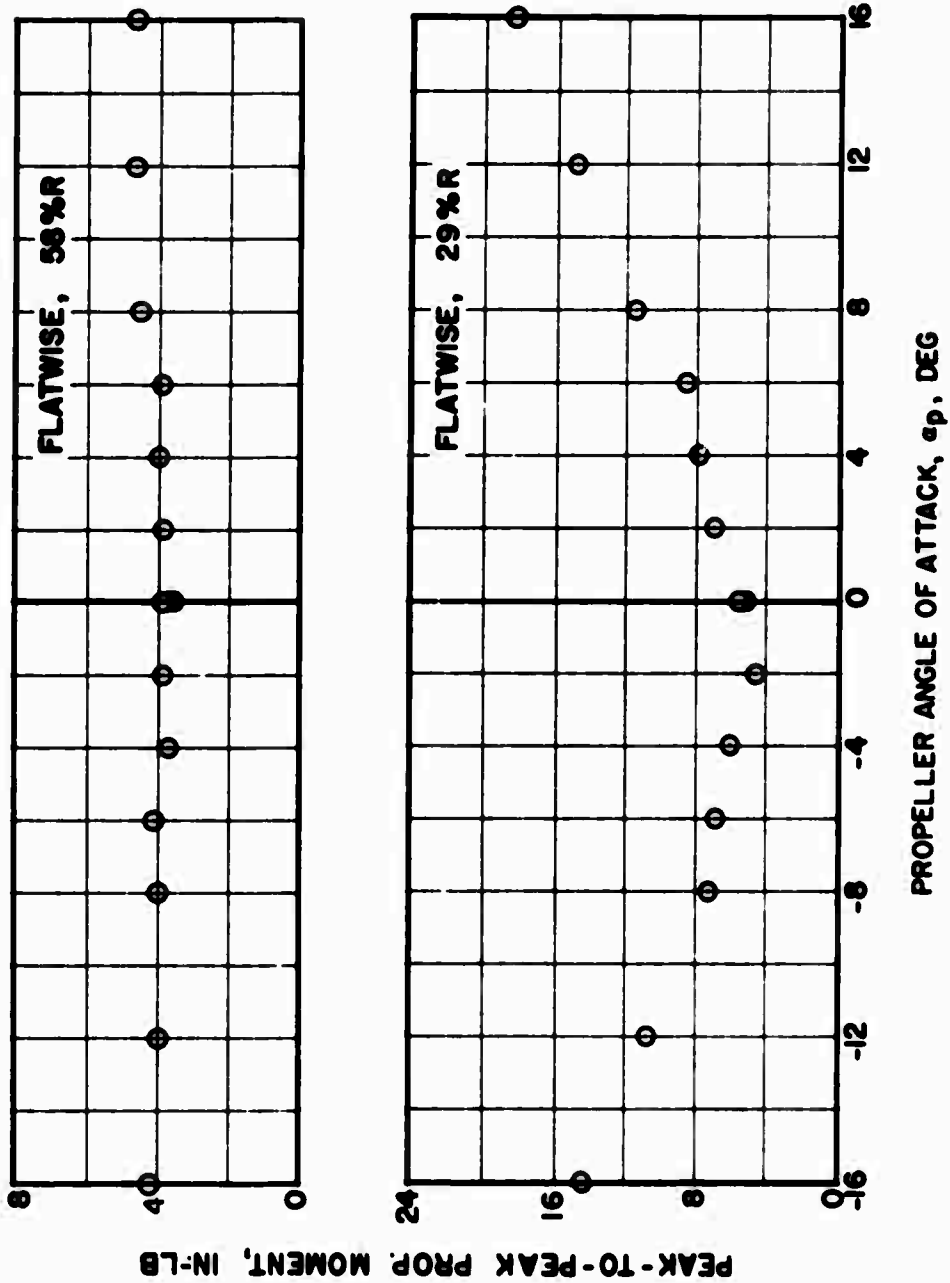


Figure 100. Isolated Propeller Blade Vibratory Moment Characteristics at Various Propeller Angles of Attack, $N_{PROP} = 5560$ rpm, $V_S = 200$ Knots, $\beta_{75} = 30^\circ$.

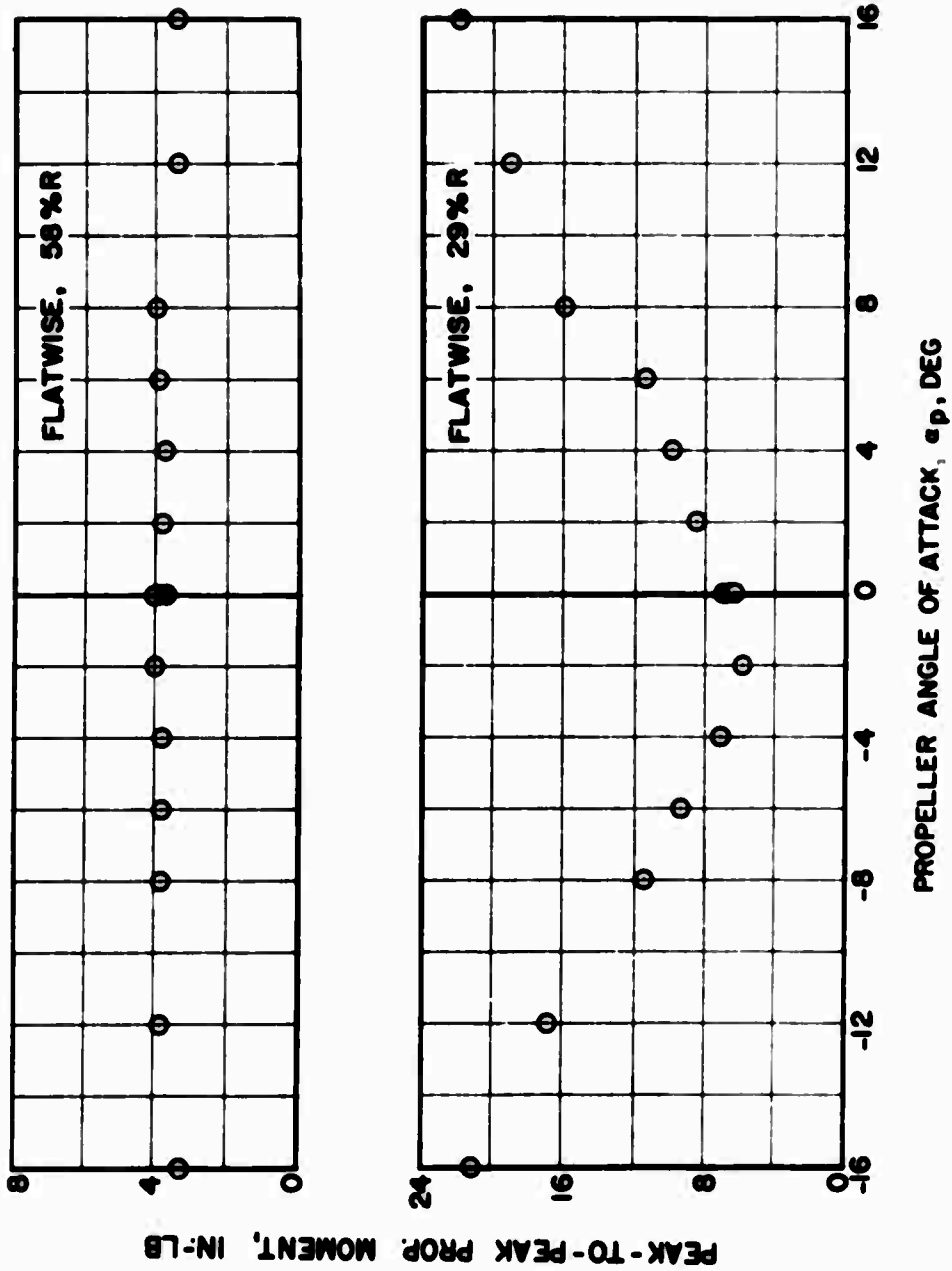


Figure 101. Isolated Propeller Blade Vibratory Moment Characteristics at Various Propeller Angles of Attack, $N_{PROP} = 5560$ rpm, $V_s = 300$ Knots, $\beta_{75} = 30^\circ$.

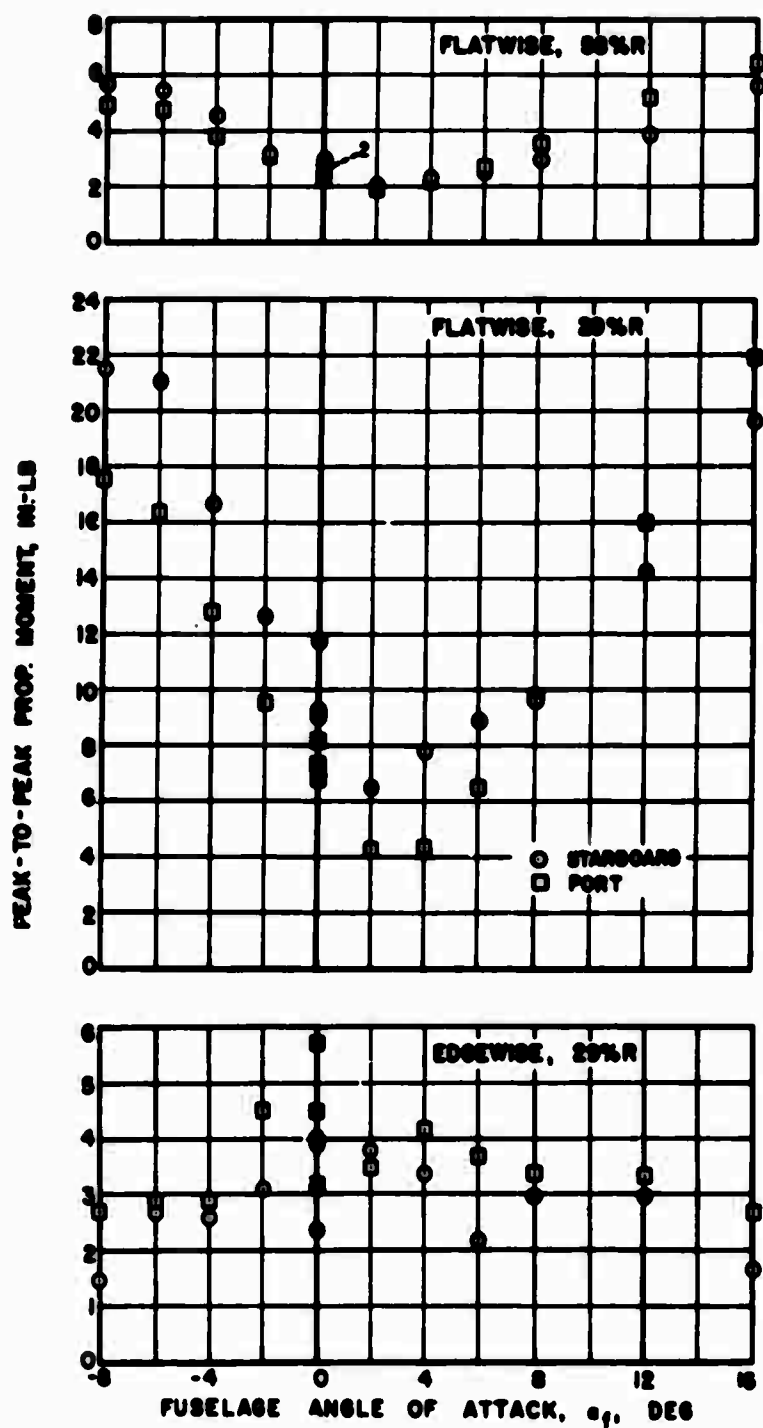
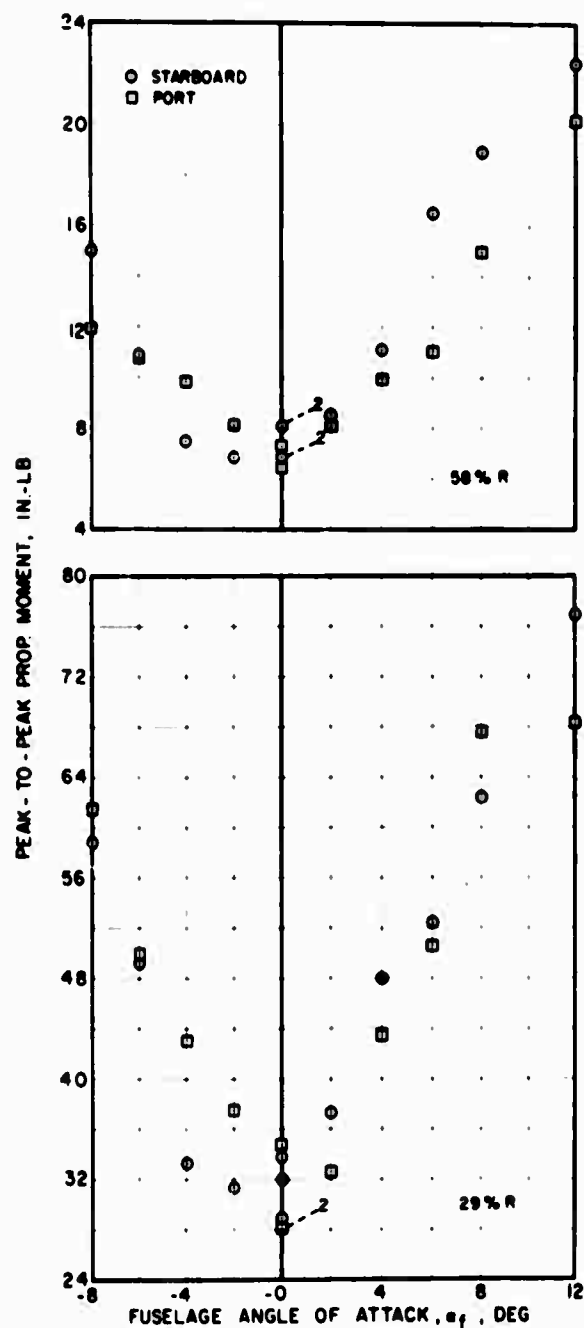
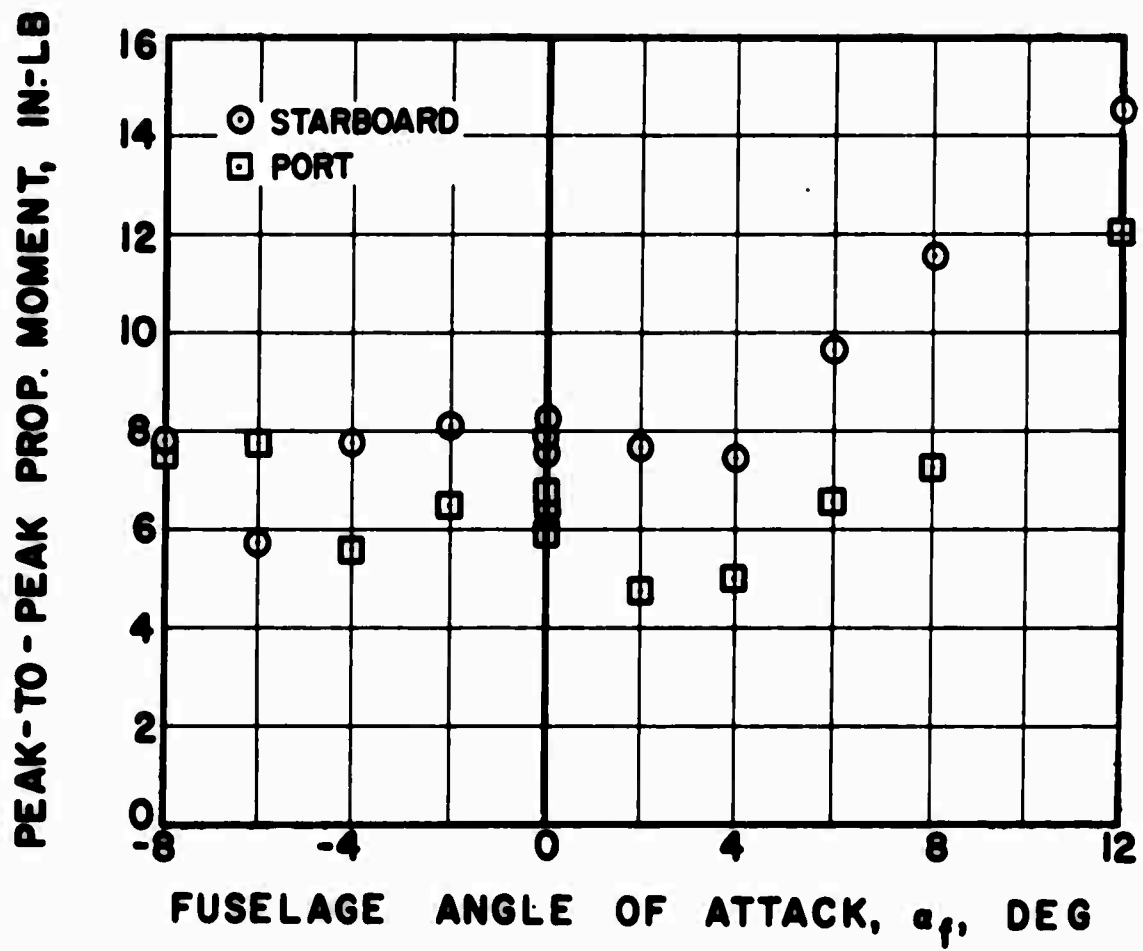


Figure 102. Effect of Fuselage Angle of Attack on Inboard Tractor Propeller Blade Vibratory Moments. Without Rotor, $V_s = 120$ Knots, $\beta_{.75} = 41^\circ$.



(a) Flatwise

Figure 103. Effect of Fuselage Angle of Attack on Inboard Tractor Propeller Blade Vibratory Moments, Without Rotor, $V_s = 200$ Knots, $\beta_{75} = 41^\circ$.



(b) Edgewise, 29%R

Figure 103. Concluded.

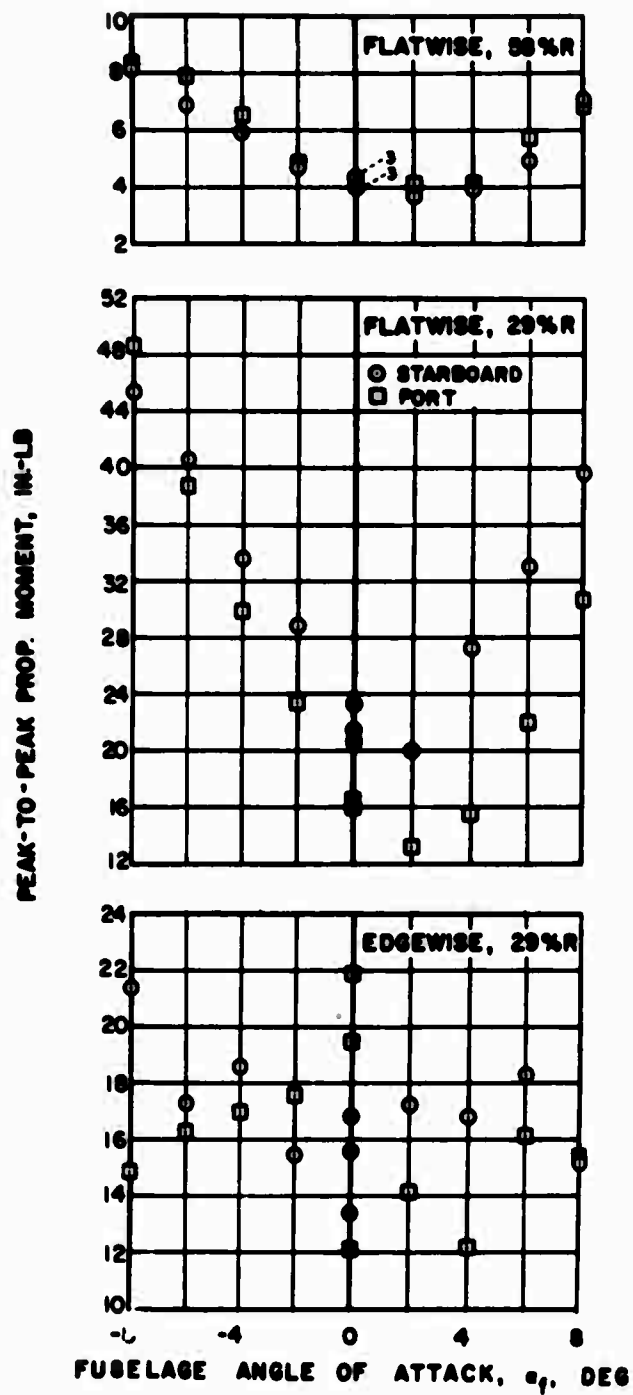


Figure 104. Effect of Fuselage Angle of Attack on Inboard Tractor Propeller Blade Vibratory Moments, Without Rotor, $V_s = 300$ Knots, $\beta_{.75} = 41^\circ$.

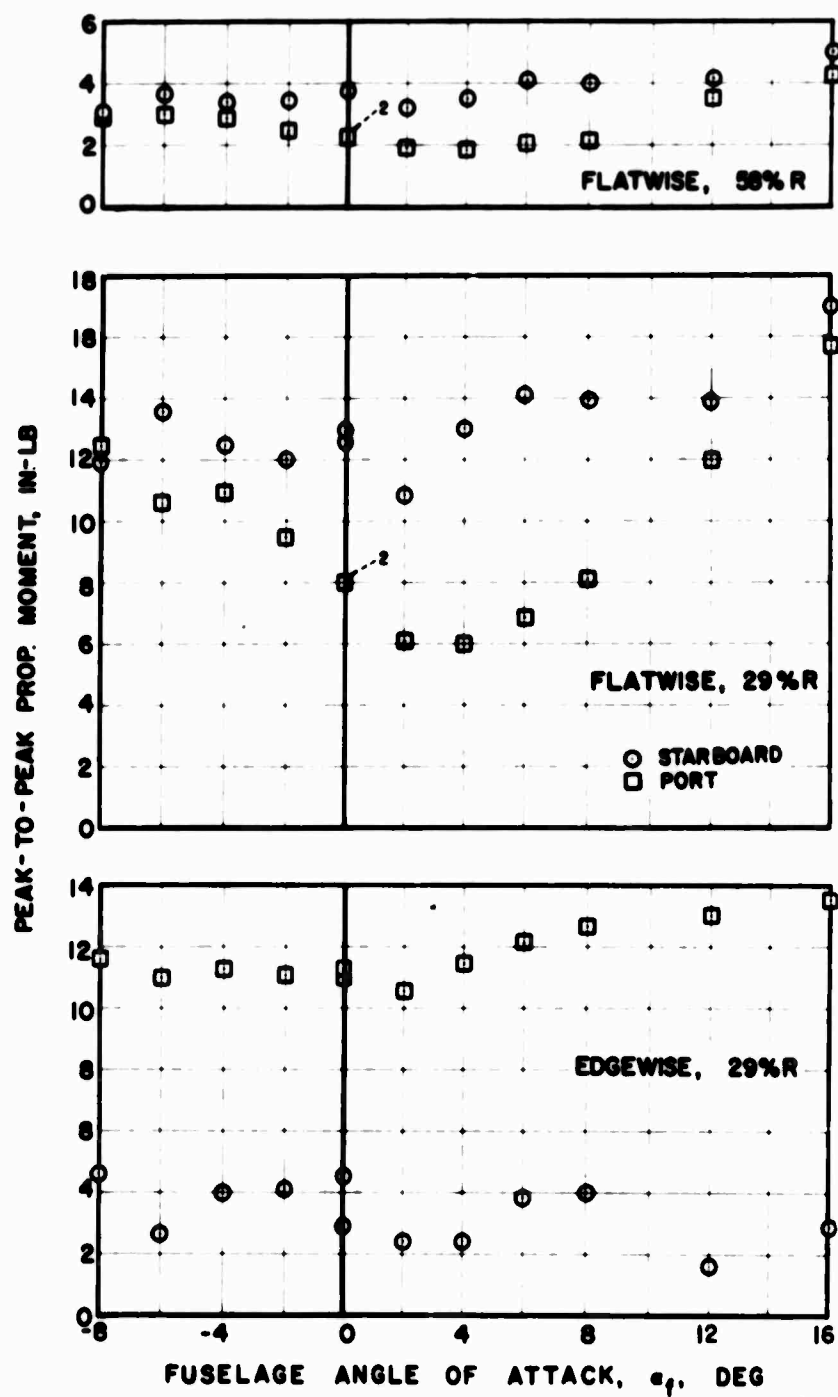
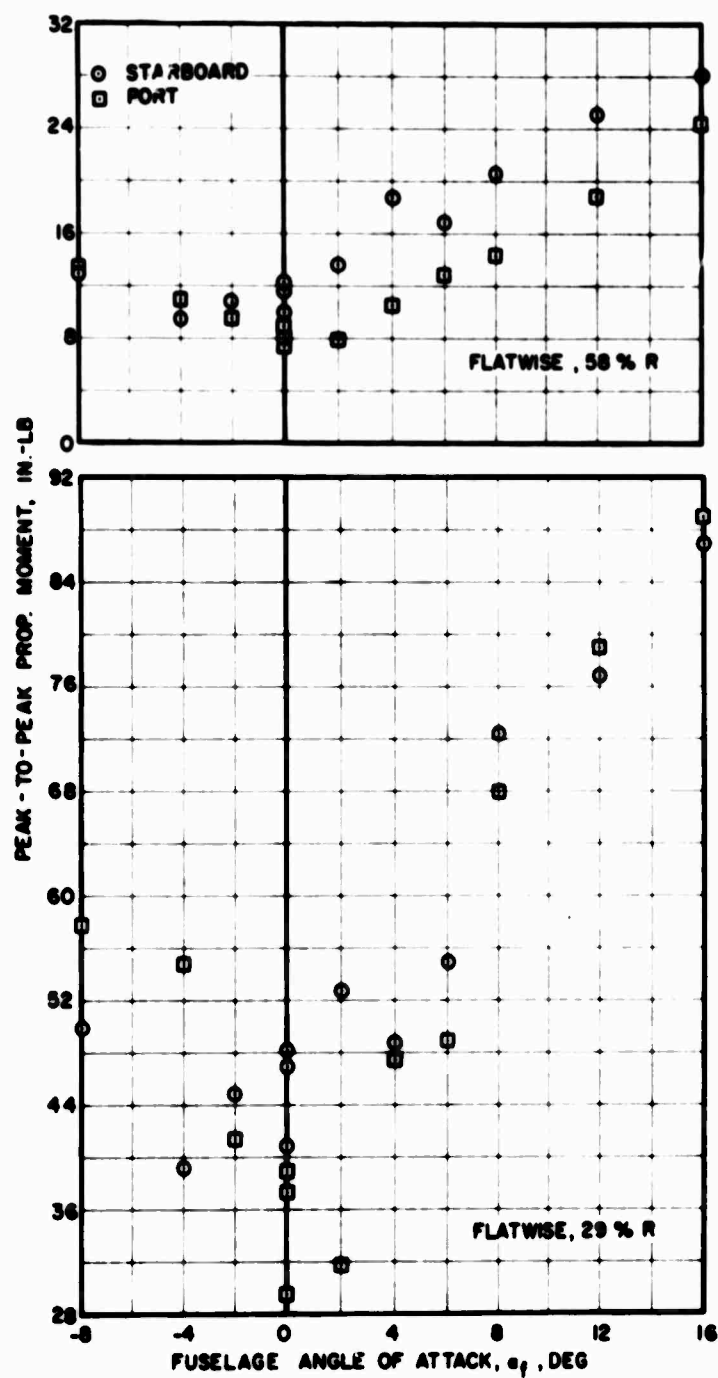
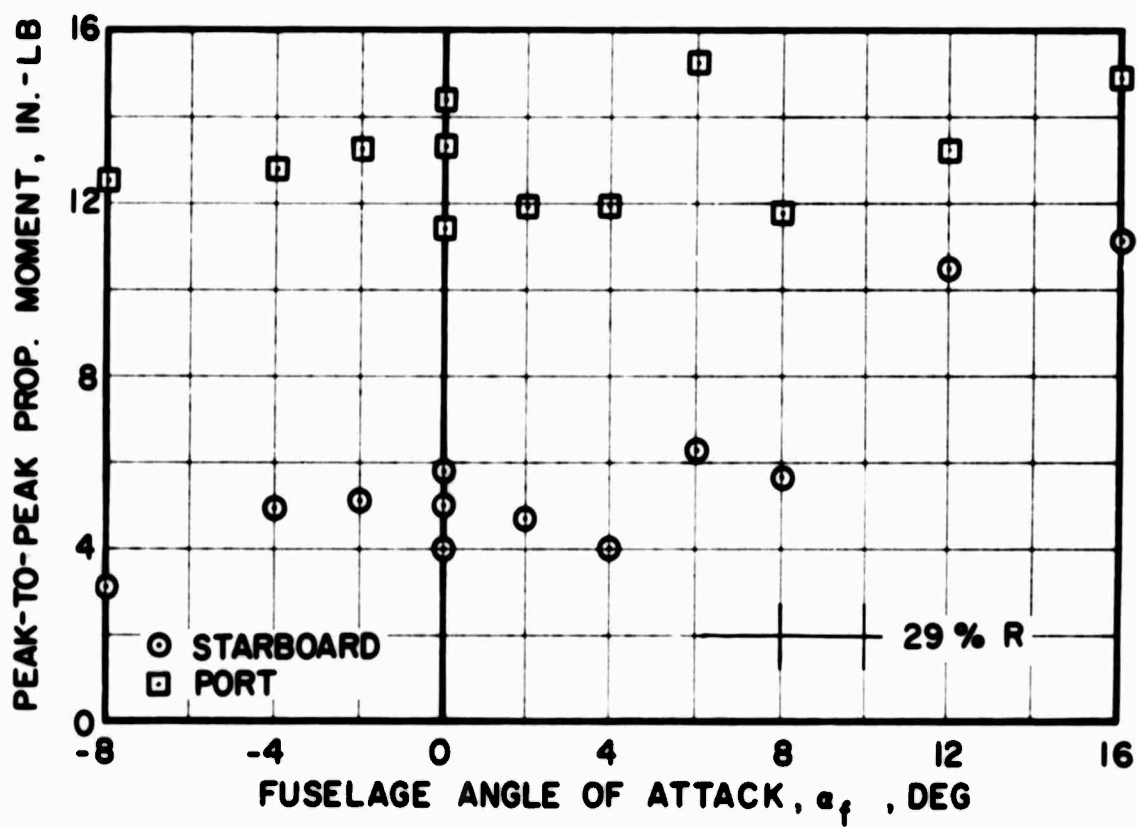


Figure 105. Effect of Fuselage Angle of Attack on Outboard Tractor Propeller Blade Vibratory Moments, Without Rotor, $V_S = 120$ Knots, $\beta_{75} = 41^\circ$.



(a) Flatwise

Figure 106. Effect of Fuselage Angle of Attack on Outboard Tractor Propeller Blade Vibratory Moments, Without Rotor, $V_s = 200$ Knots, $\beta_{.75} = 41^\circ$.



(b) Edgewise

Figure 106. Concluded.

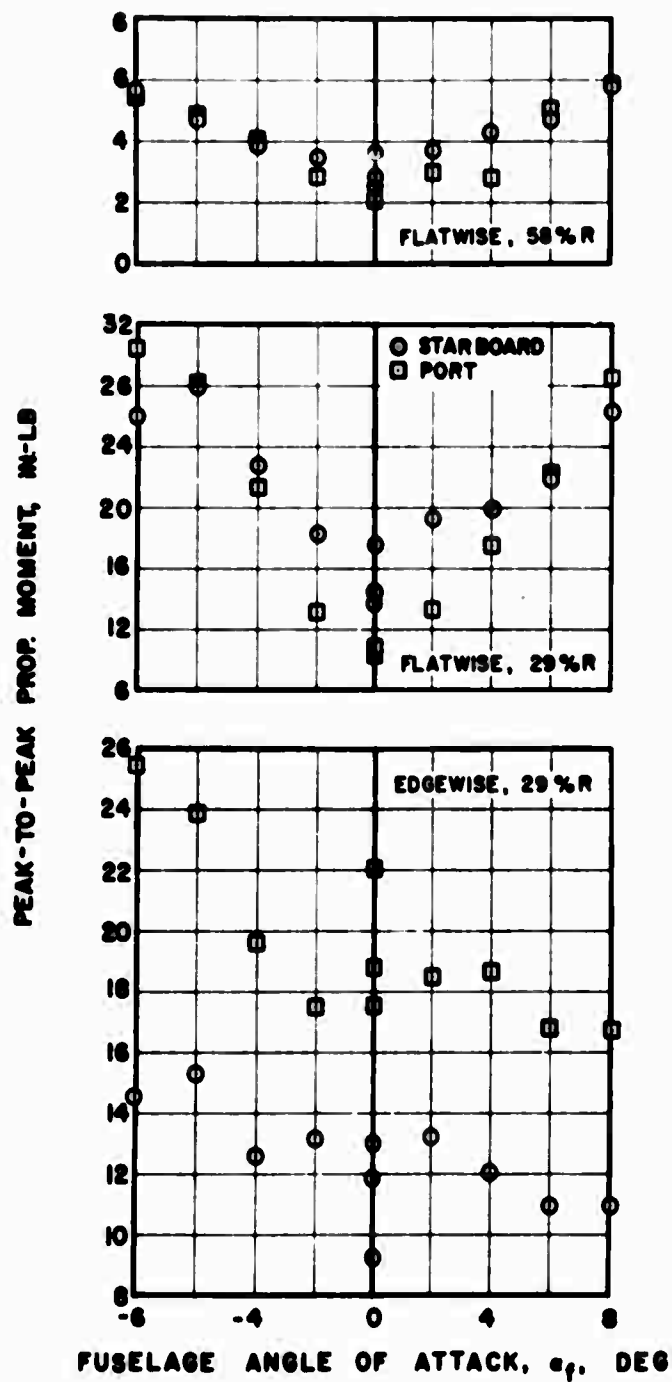


Figure 107. Effect of Fuselage Angle of Attack on Outboard Tractor Propeller Blade Vibratory Moments, Without Rotor, $V_s = 300$ Knots, $\beta_{75} = 41^\circ$.

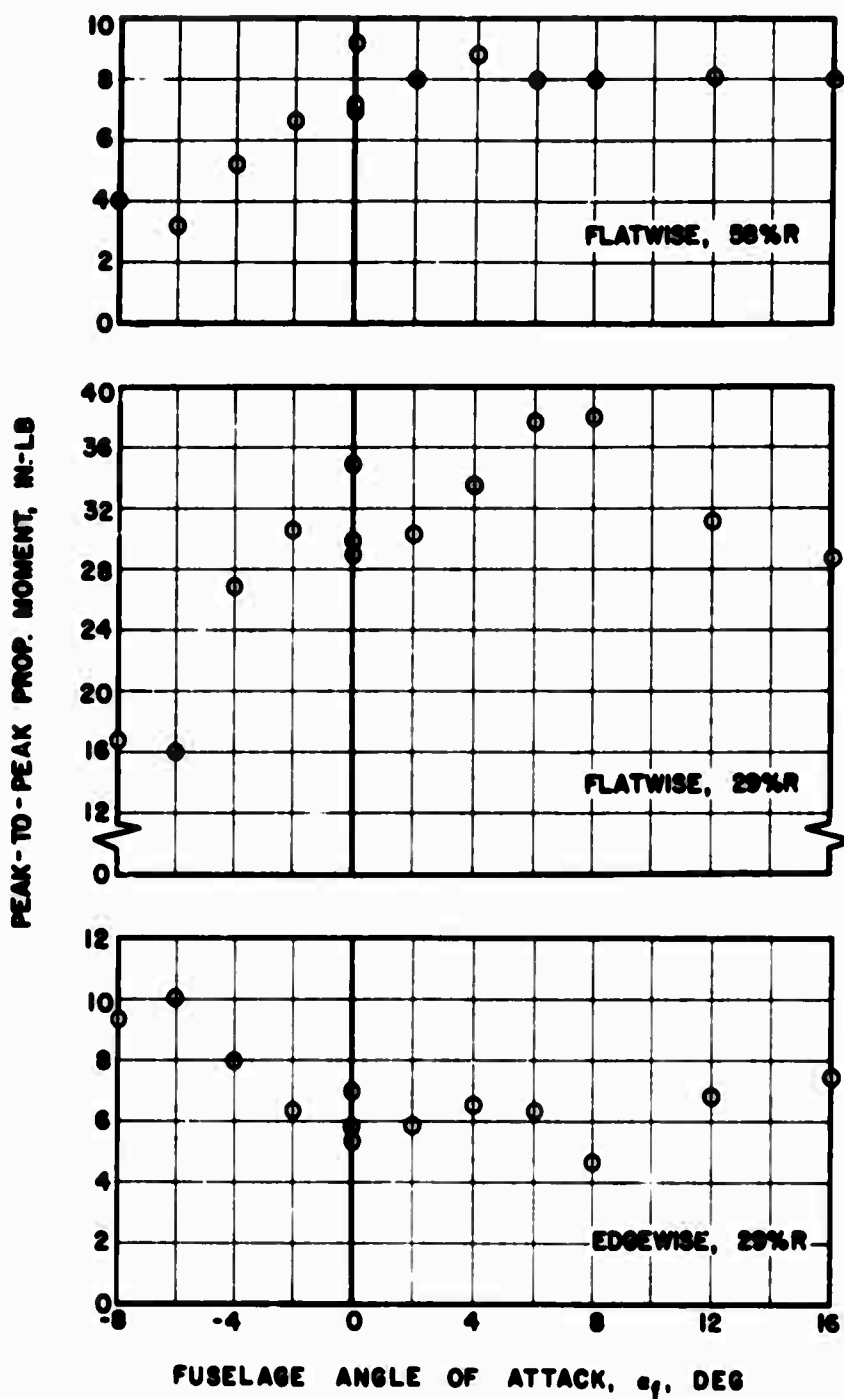


Figure 108. Effect of Fuselage Angle of Attack on Pusher Propeller Blade Vibratory Moments, Without Empennage or Rotor, $V_s = 120$ Knots, $\beta_{.75} = 41^\circ$.

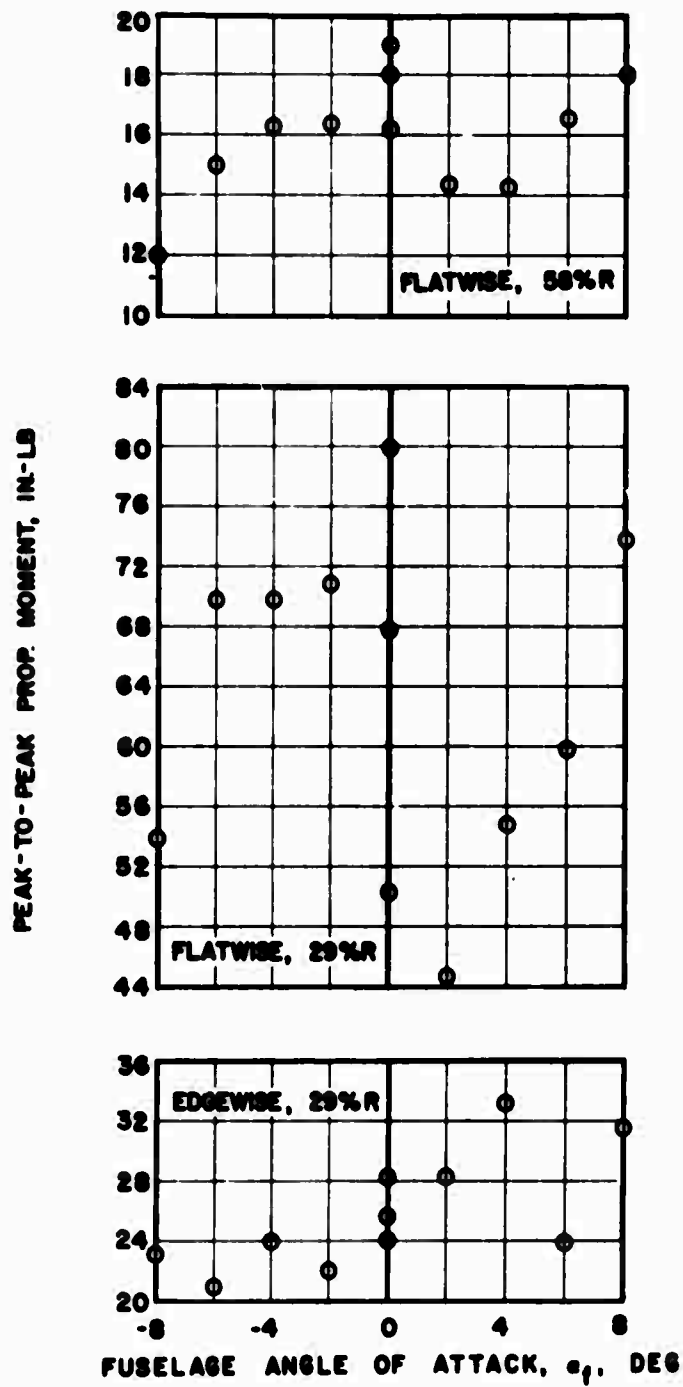


Figure 109. Effect of Fuselage Angle of Attack on Pusher Propeller Blade Vibratory Moments, Without Empennage or Rotor, $V_S = 300$ Knots, $\beta_{.75} = 41^\circ$.

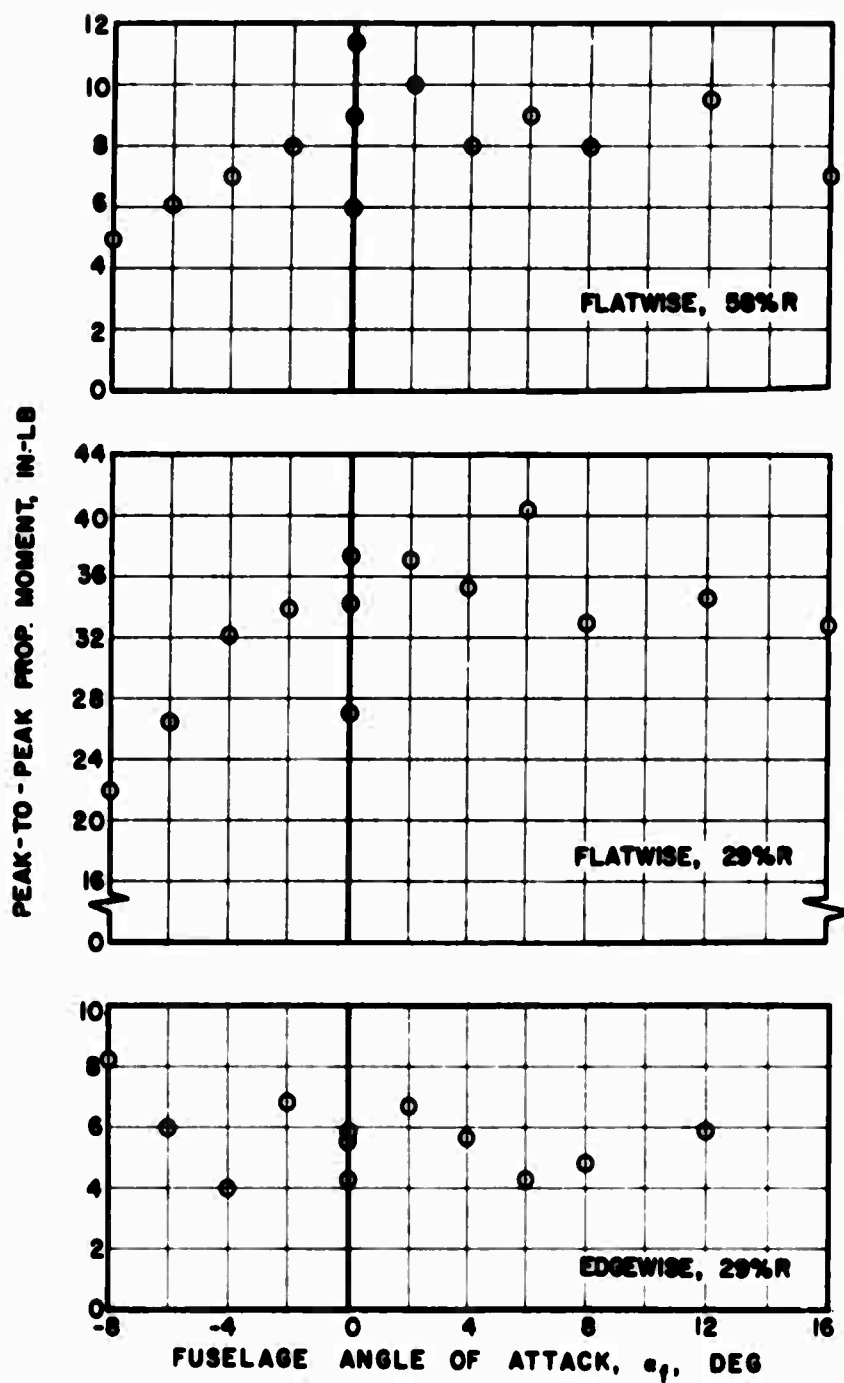
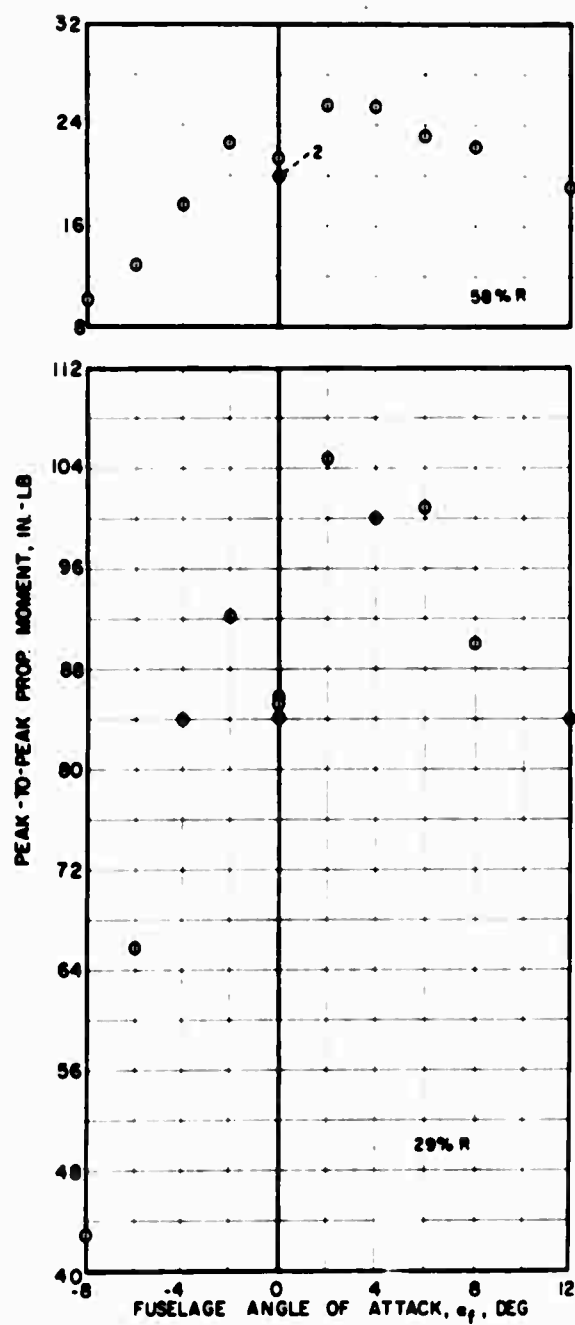
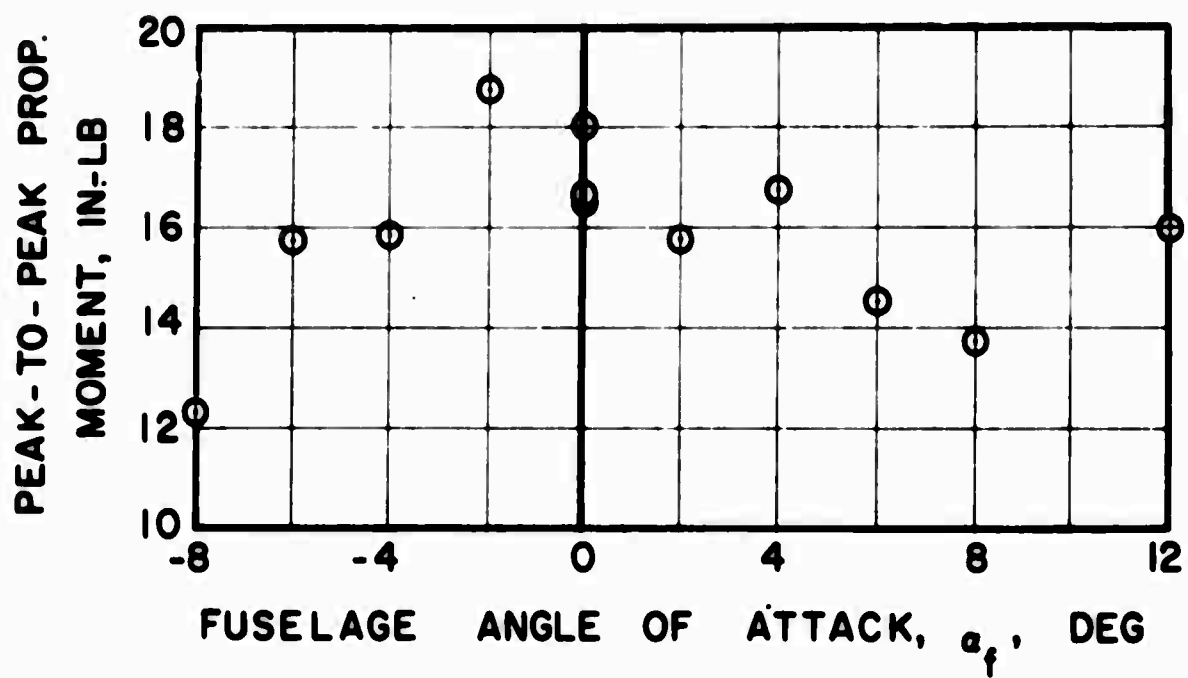


Figure 110. Effect of Fuselage Angle of Attack on Pusher Propeller Blade Vibratory Moments With Empennage, Without Rotor, $V_s = 120$ Knots, $\beta_{75} = 41^\circ$.



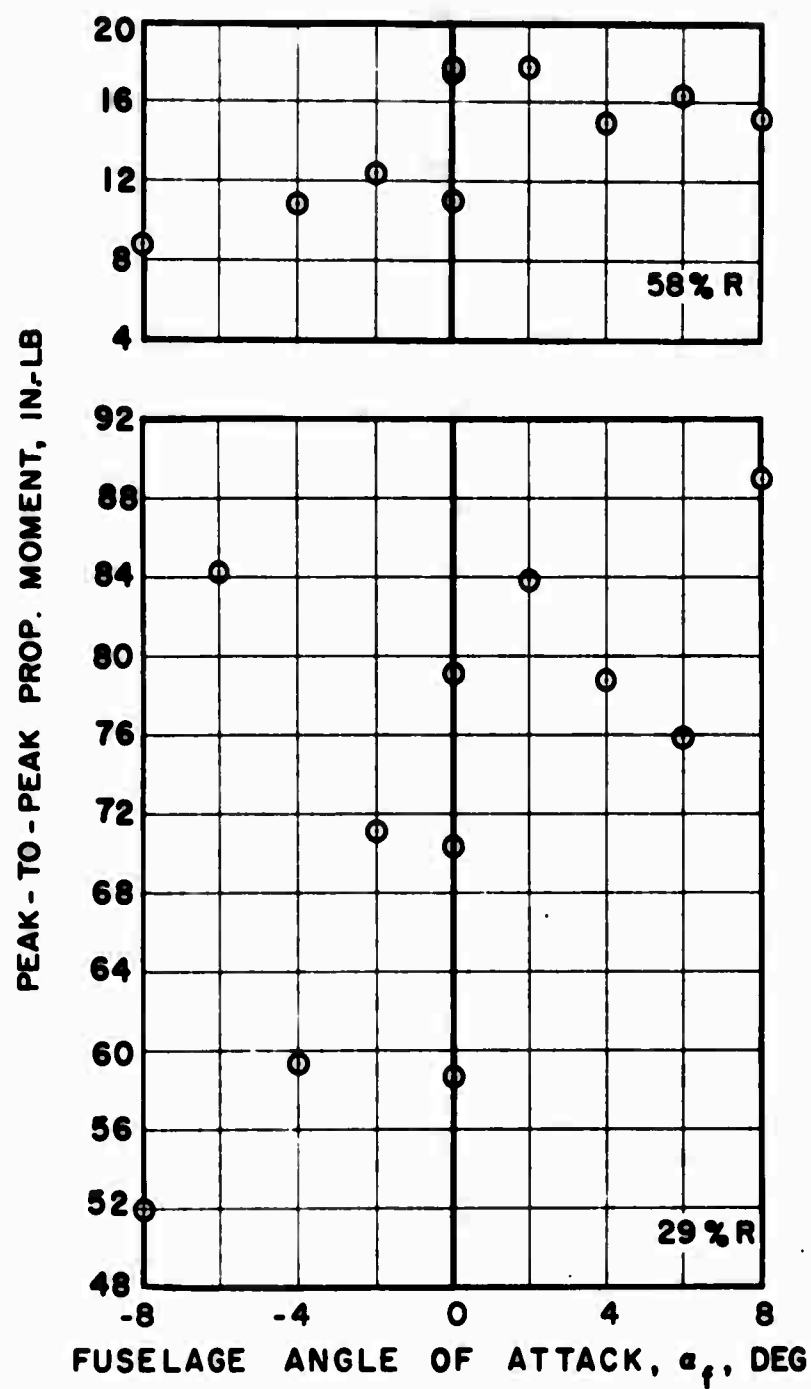
(a) Flatwise

Figure 111. Effect of Fuselage Angle of Attack on Pusher Propeller Blade Vibratory Moments With Empennage, Without Rotor, $V_s = 200$ Knots, $\beta_{75} = 41^\circ$.



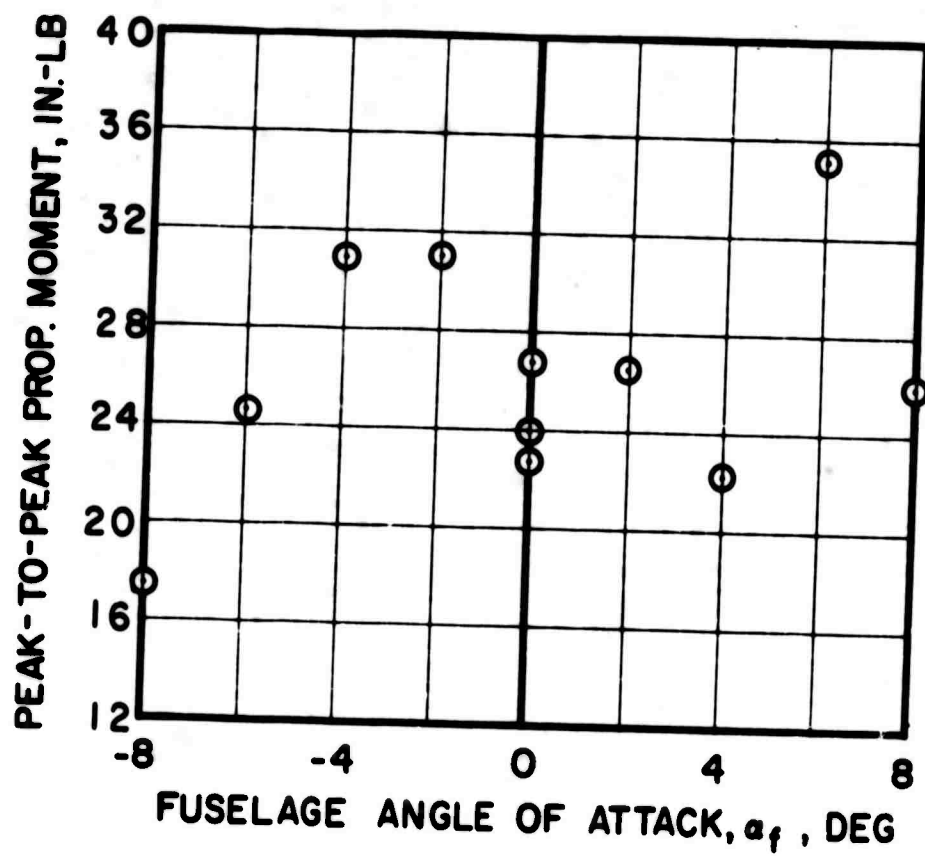
(b) Edgewise, 29%R

Figure 111. Concluded.



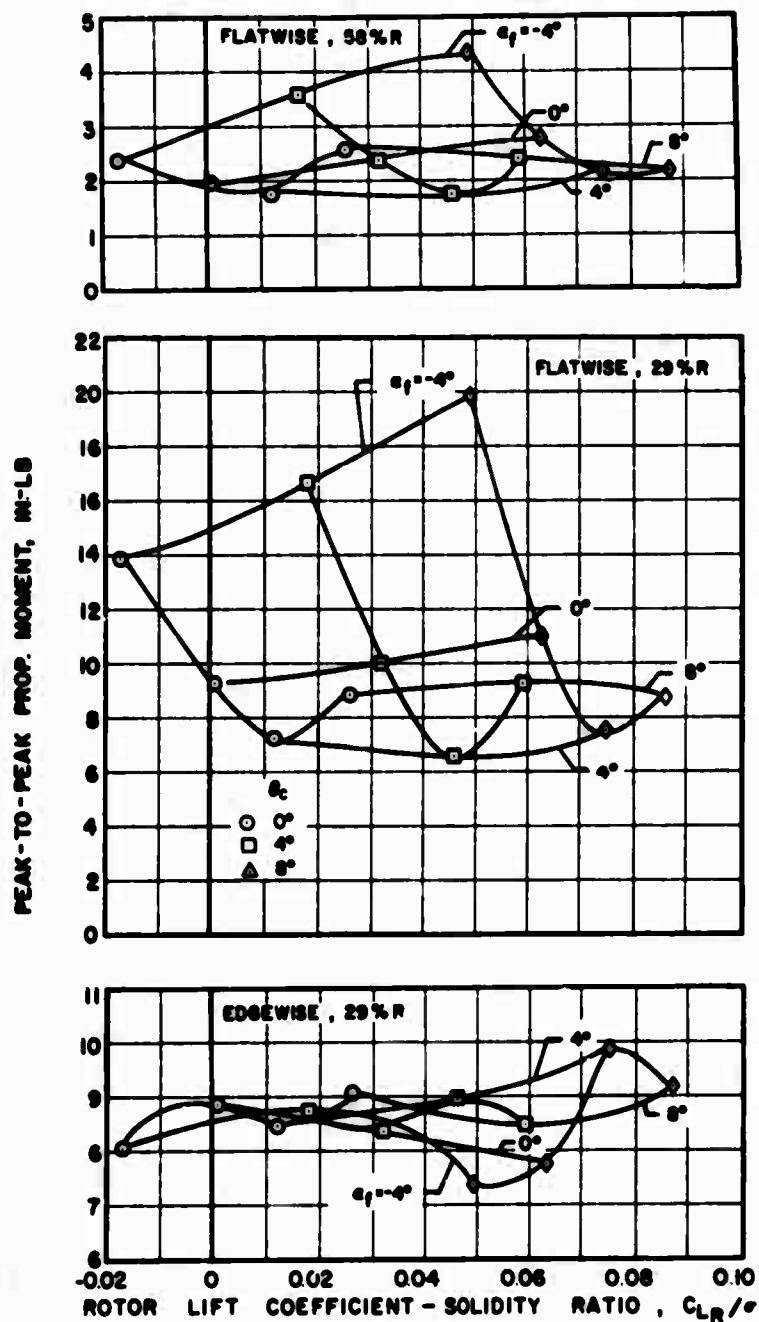
(a) Flatwise

Figure 112. Effect of Fuselage Angle of Attack on Pusher Propeller Blade Vibratory Moments With Empennage, Without Rotor, $V_s = 300$ Knots, $\beta_{75} = 41^\circ$.



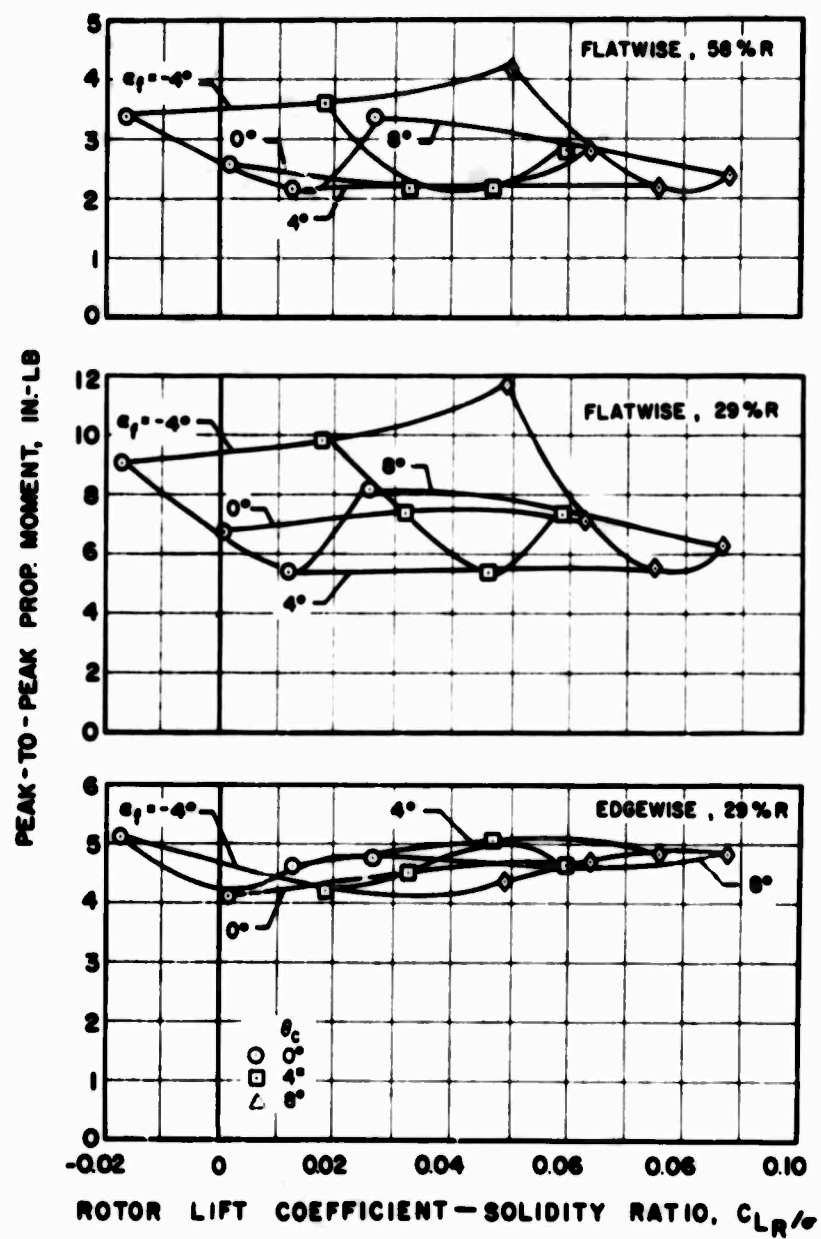
(b) Edgewise, 29%R

Figure 112. Concluded.



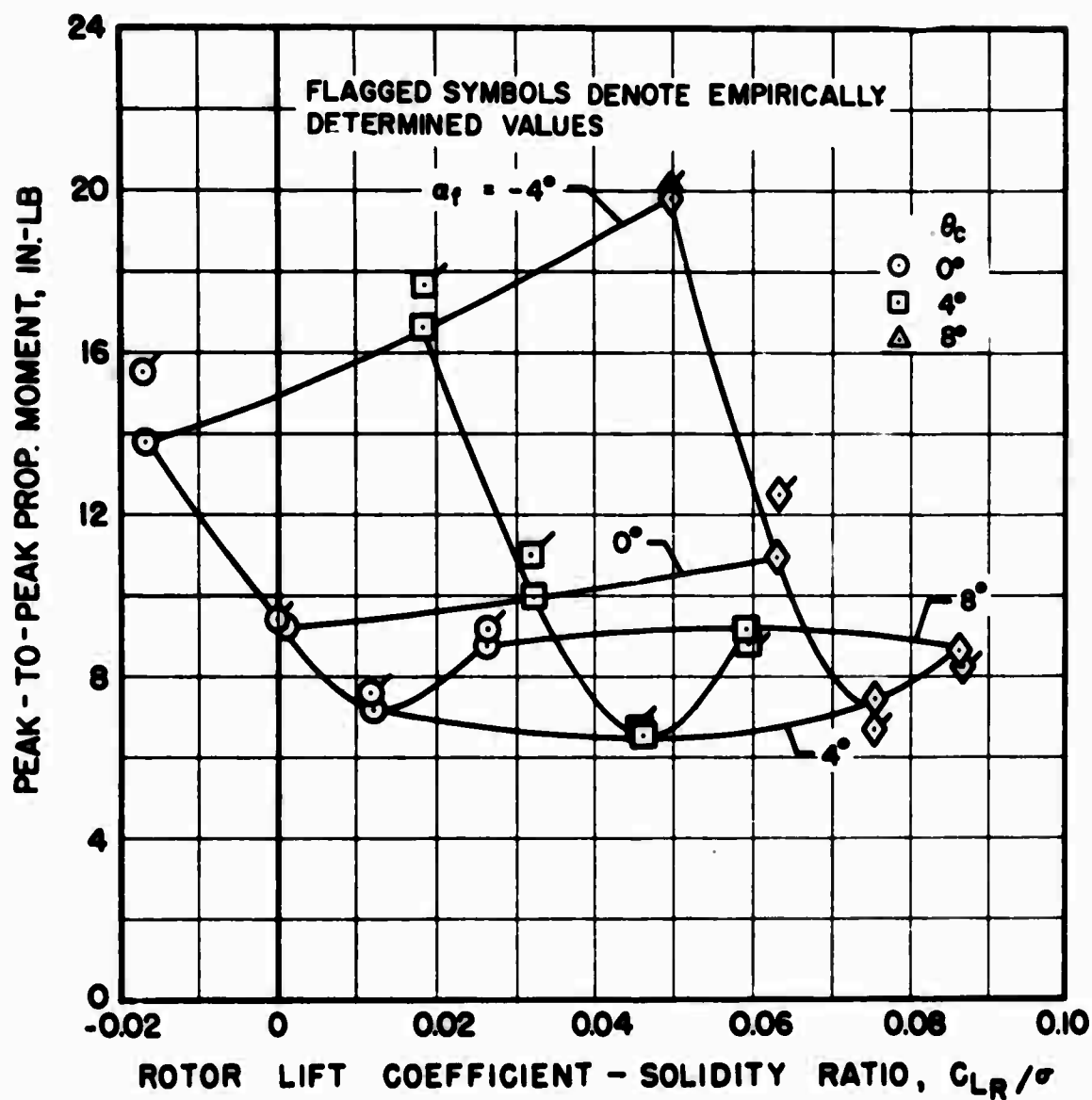
(a) Starboard

Figure 113. Effect of Rotor Lift on Inboard Tractor Propeller Blade Vibratory Moments for Various Fuselage Angles of Attack, and Collective Pitch Settings, $V_s = 120$ Knots, $\beta_{75} = 41^\circ$.



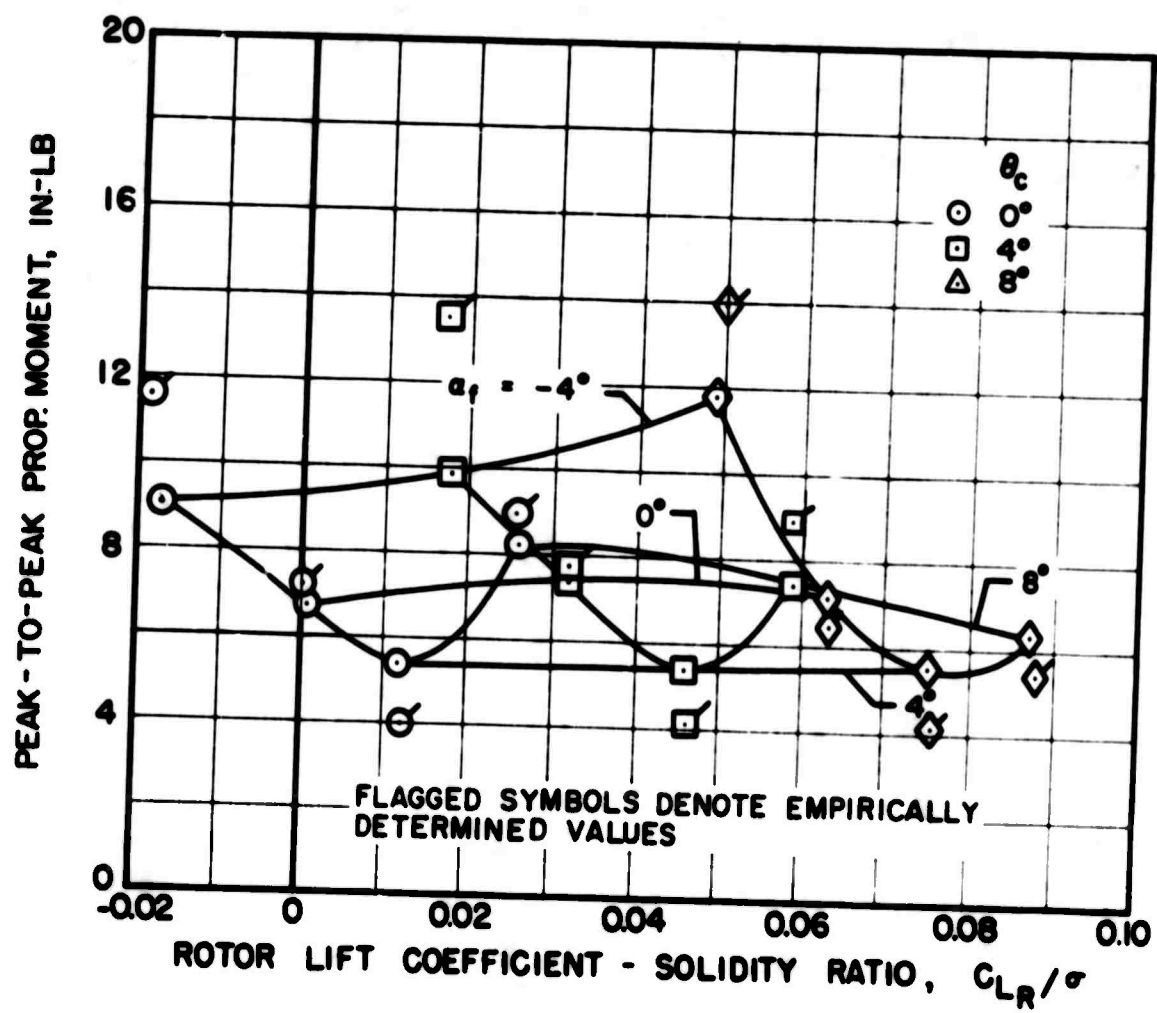
(b) Port

Figure 113. Concluded.



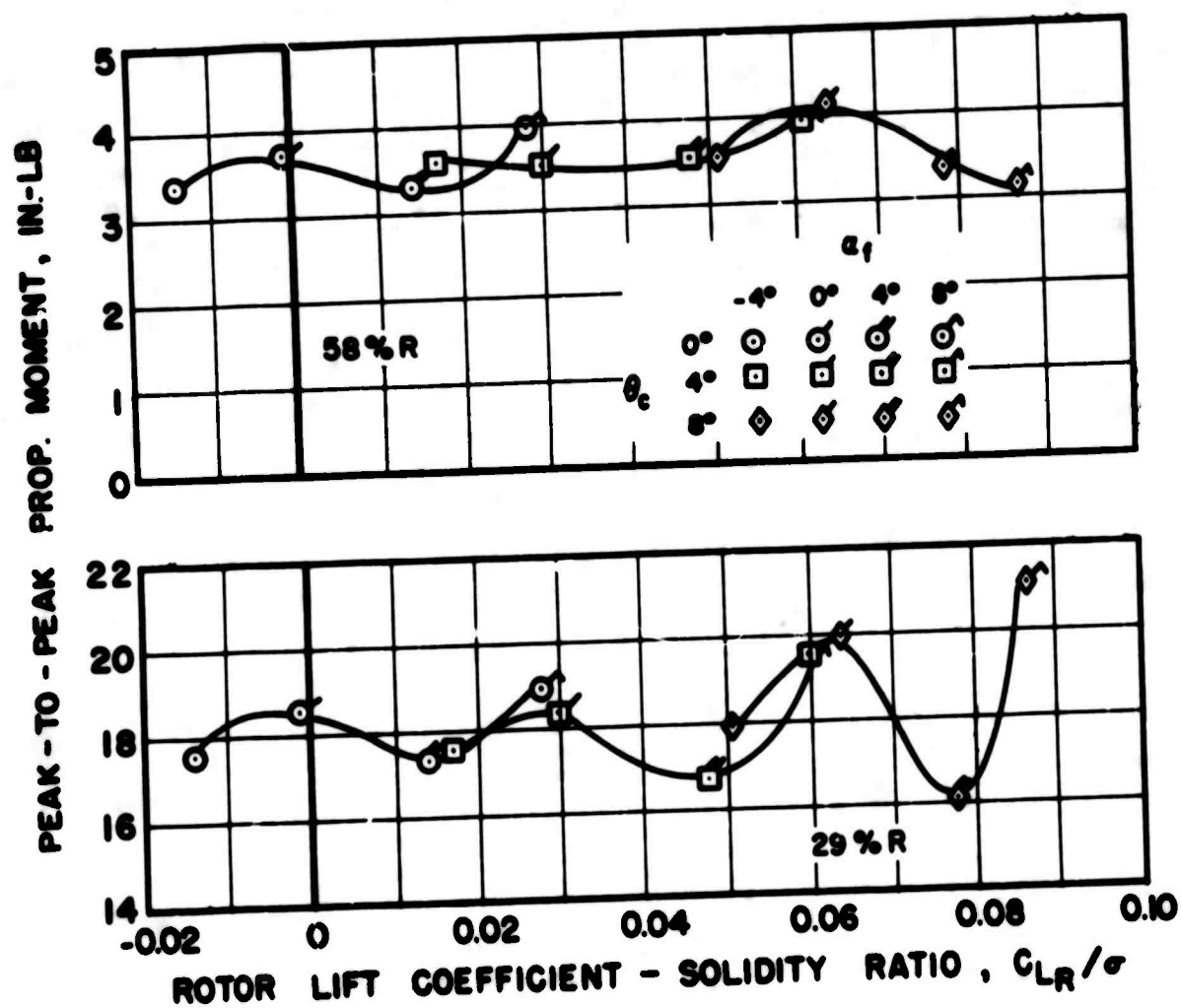
(a) Starboard

Figure 114. Comparison of Experimental and Empirical Effects of Rotor Lift on Inboard Tractor Propeller Blade Flatwise Vibratory Moments for Various Fuselage Angles of Attack and Collective Pitch Settings, $V_s = 120$ Knots, $\beta_{75} = 41^\circ$, 29%R.



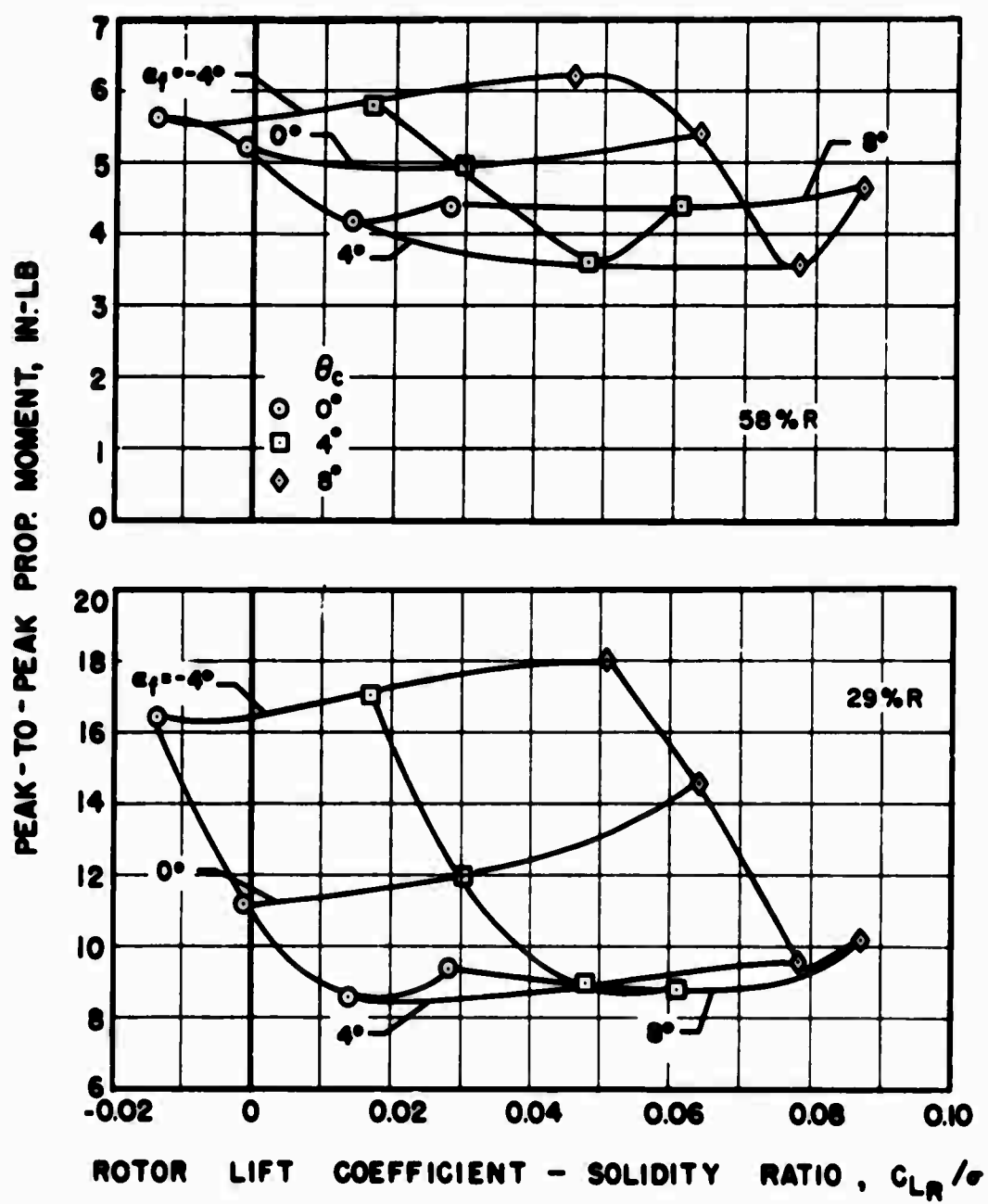
(b) Port

Figure 114. Concluded.



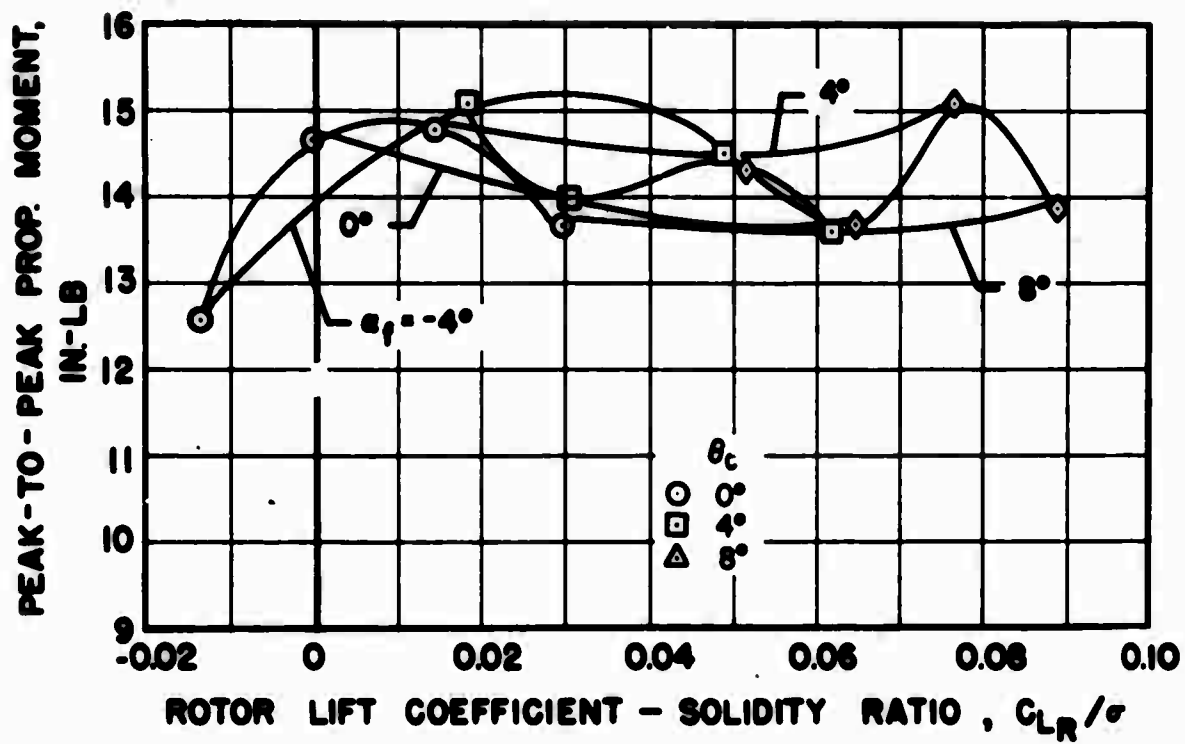
(a) Starboard, Flatwise

Figure 115. Effect of Rotor Lift on Inboard Tractor Propeller Blade Vibratory Moments for Various Fuselage Angles of Attack and Collective Pitch Settings, $V_s = 120$ Knots, $\beta_{.75} = 30^\circ$.



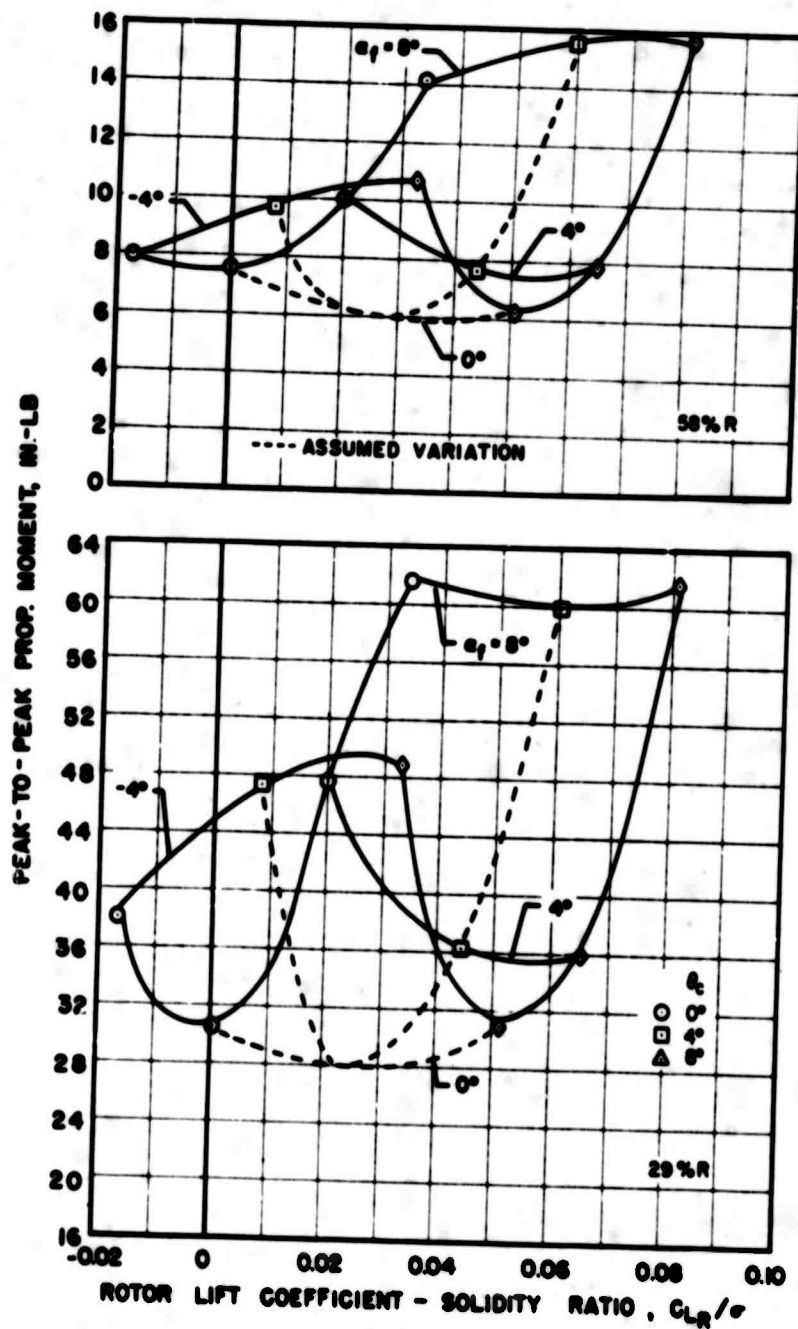
(b) Port, Flatwise

Figure 115. Continued.



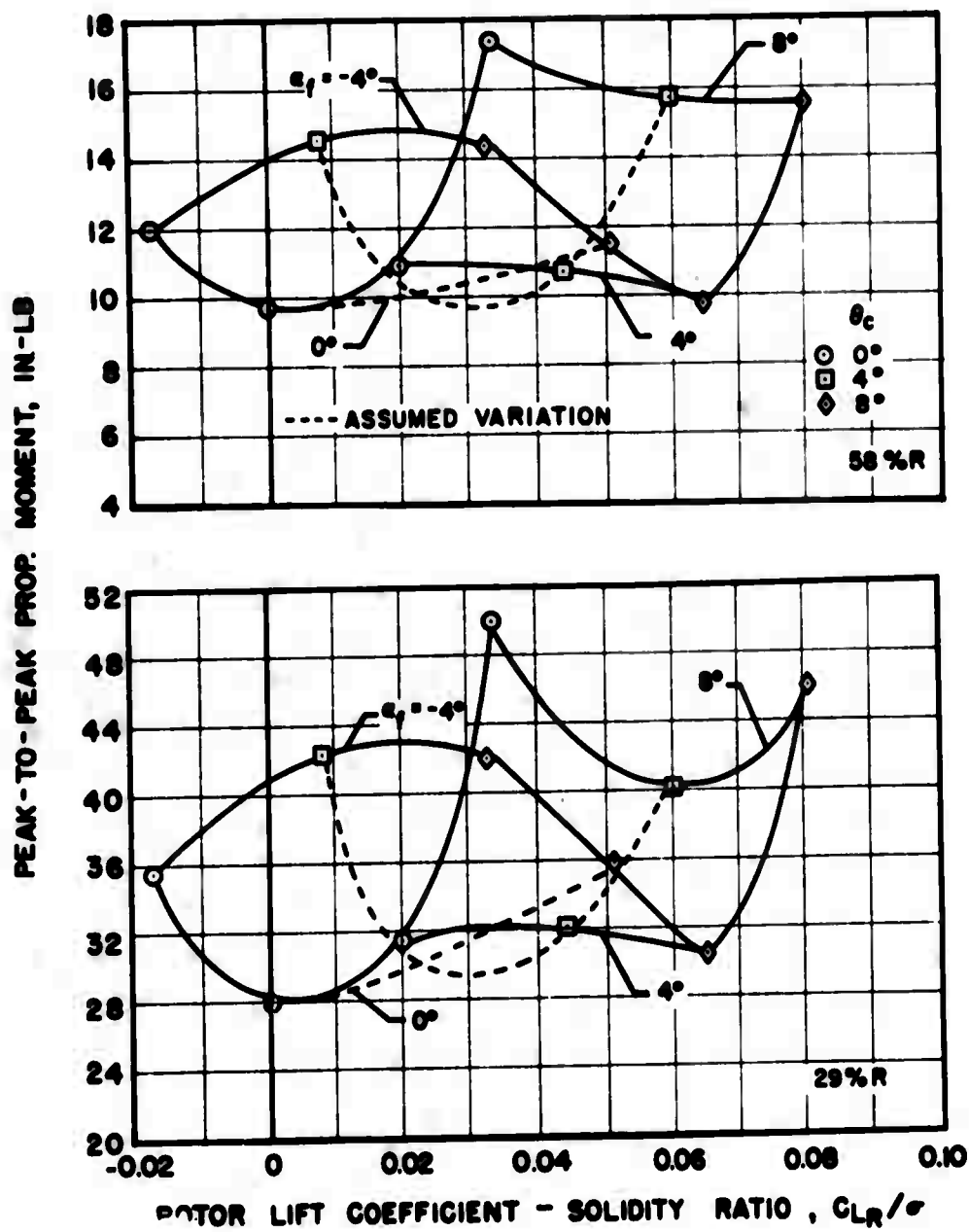
(c) Port, Edgewise, 29%R

Figure 115. Concluded.



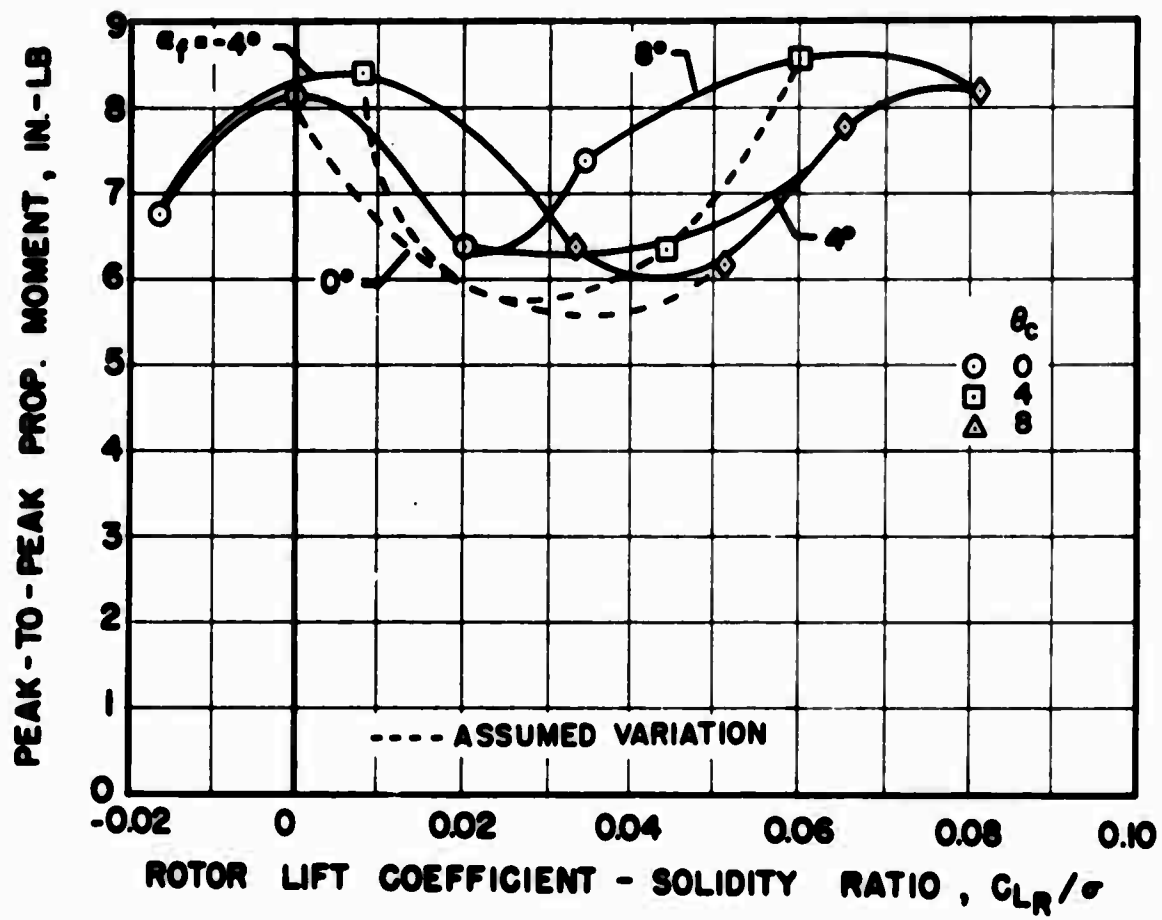
(a) Starboard, Flatwise

Figure 116. Effect of Rotor Lift on Inboard Tractor Propeller Blade Vibratory Moments for Various Fuselage Angles of Attack and Collective Pitch Settings, $V_s = 200$ Knots, $\beta_{.75} = 41^\circ$.



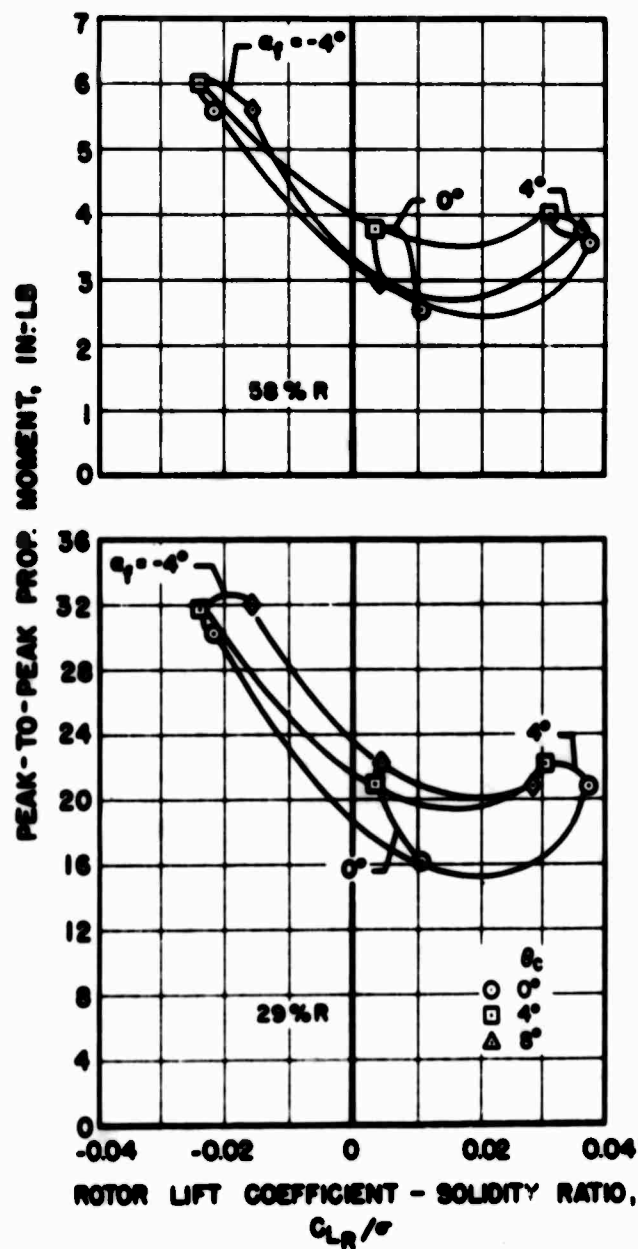
(b) Port, Flatwise

Figure 116. Continued.



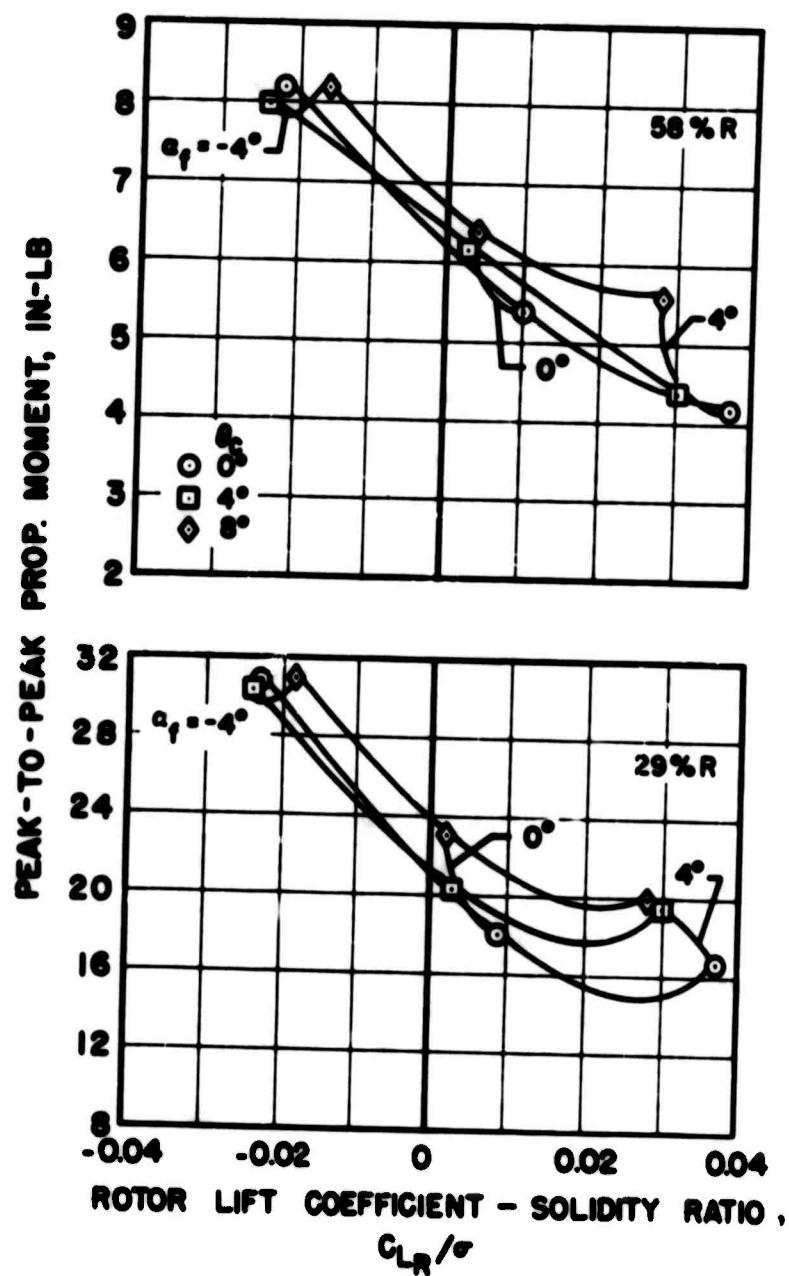
(c) Port, Edgewise, 29%R

Figure 116. Concluded.



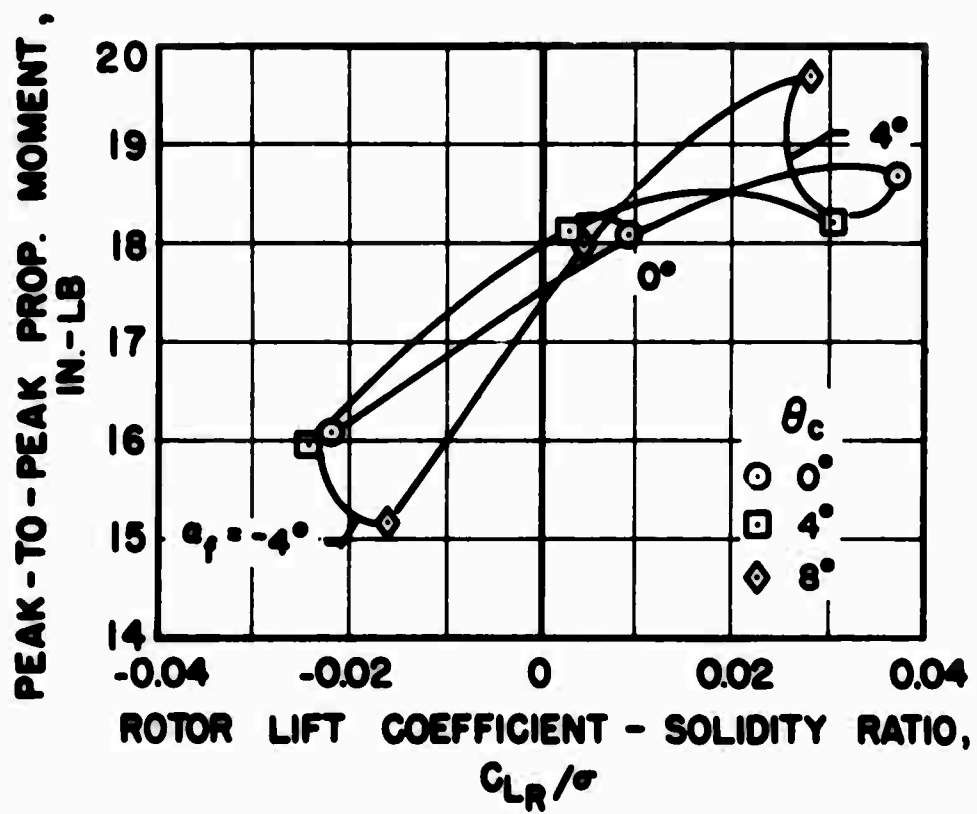
(a) Starboard, Flatwise

Figure 117. Effect of Rotor Lift on Inboard Tractor Propeller Blade Vibratory Moments for Various Fuselage Angles of Attack and Collective Pitch Settings, $V_s = 300$ Knots, $\beta_{.75} = 41^\circ$.



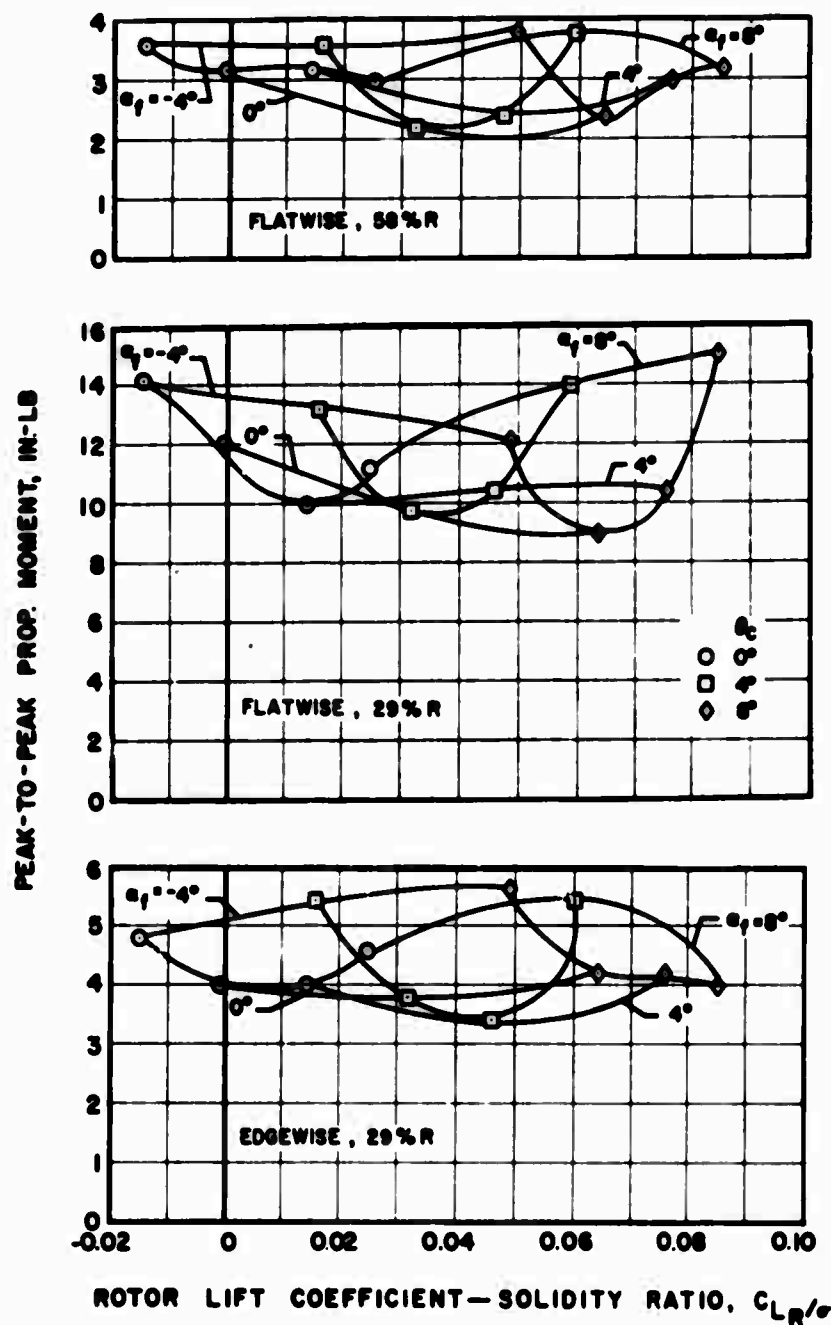
(b) Port, Flatwise

Figure 117. Continued.



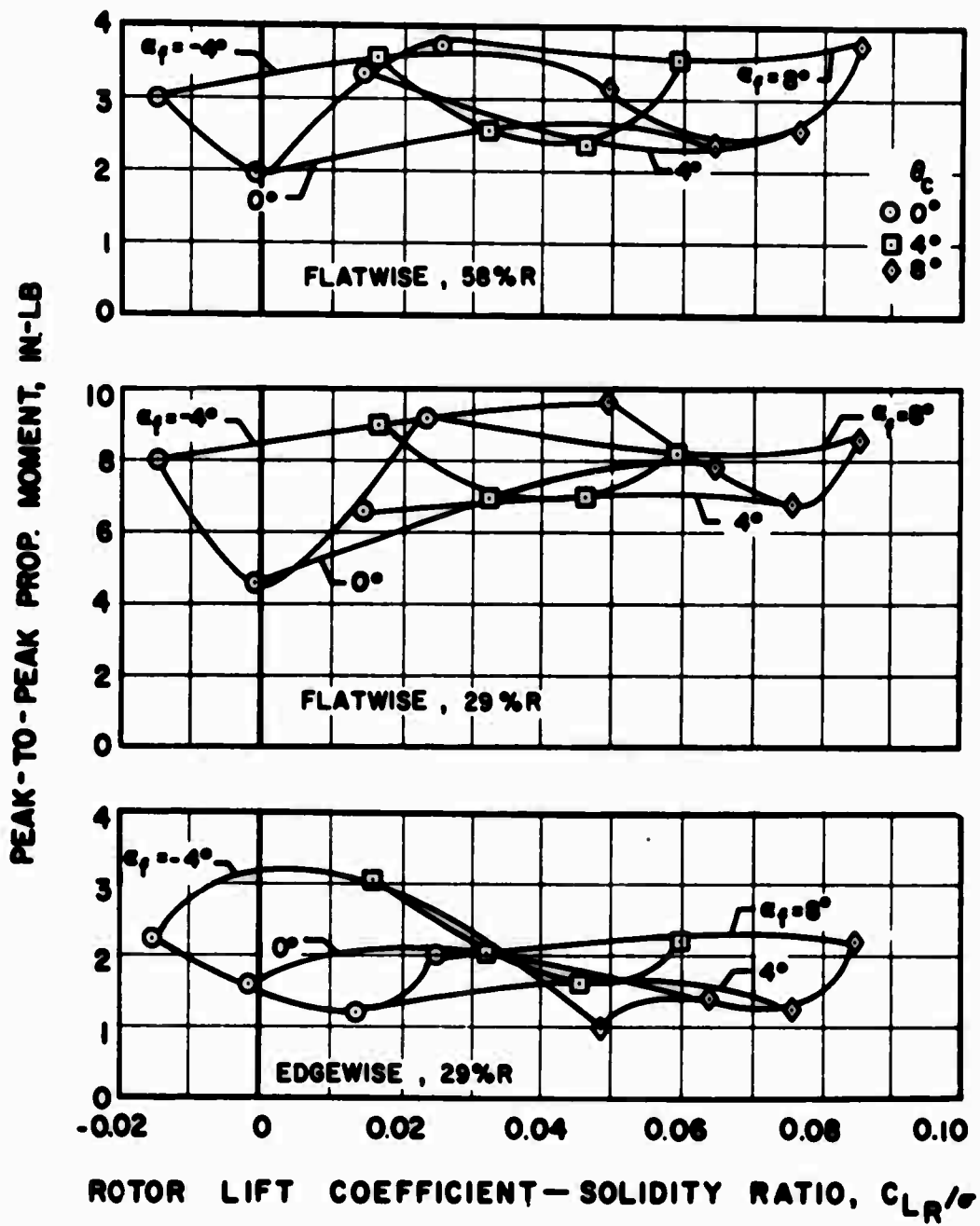
(c) Port, Edgewise, 29%R

Figure 117. Concluded.



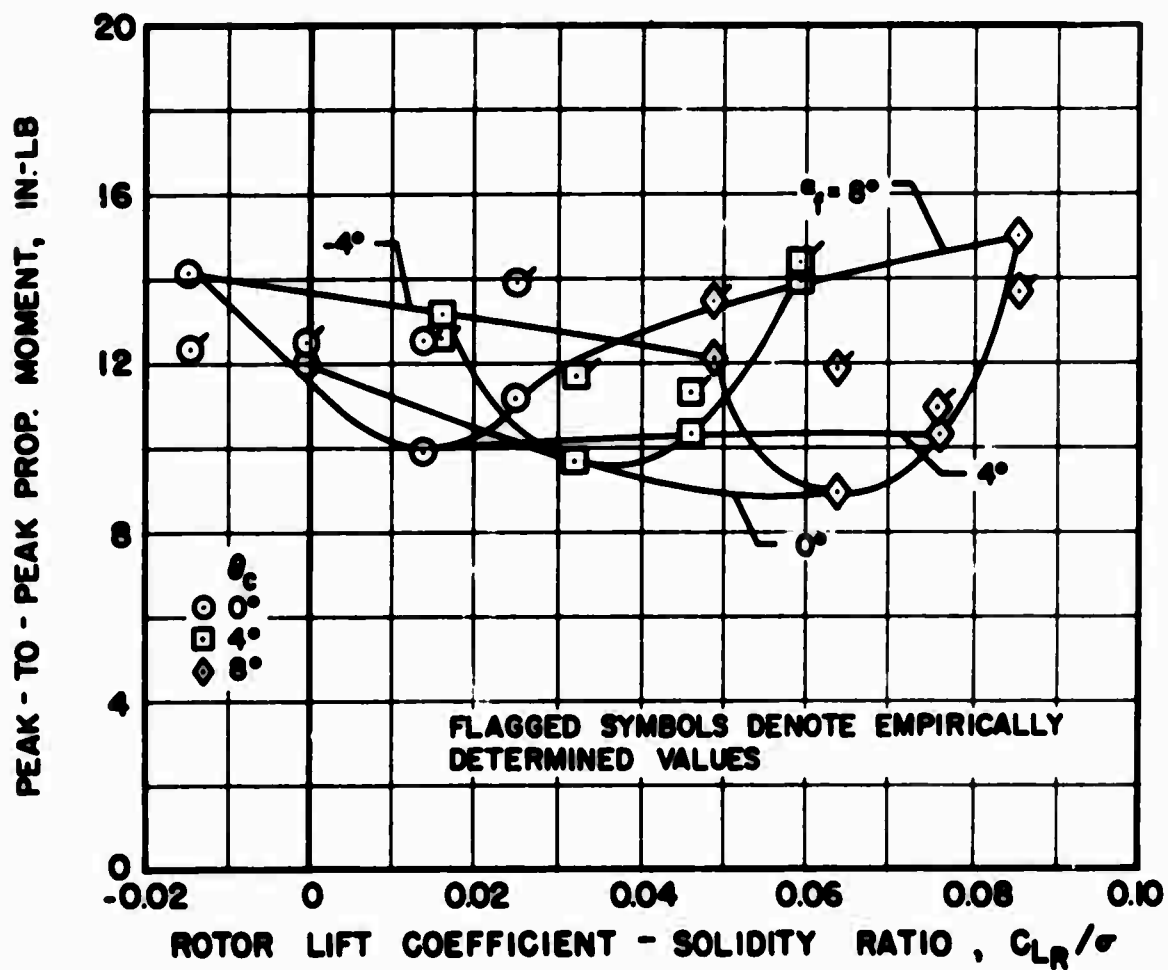
(a) Starboard

Figure 118. Effect of Rotor Lift on Outboard Tractor Propeller Blade Vibratory Moments for Various Fuselage Angles of Attack and Collective Pitch Settings, $V_S = 120$ Knots, $\beta_{75} = 41^\circ$.



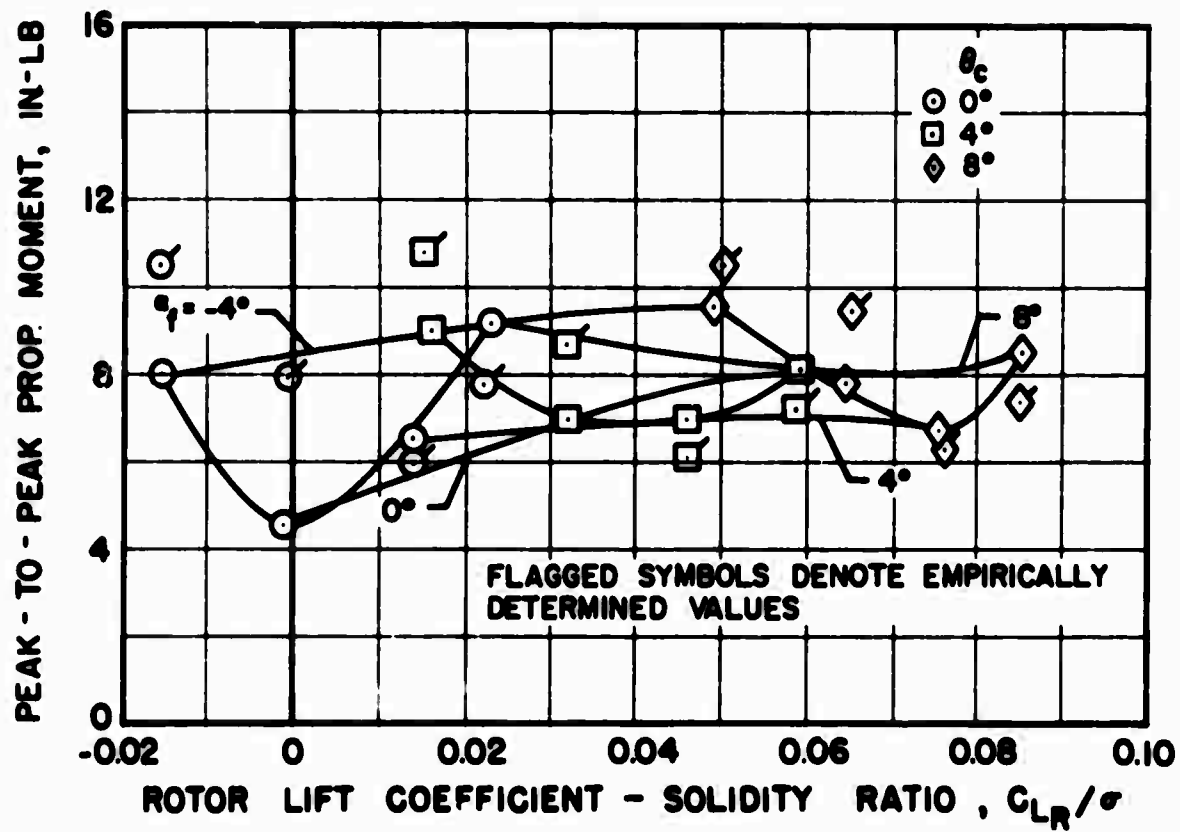
(b) Port

Figure 118. Concluded.



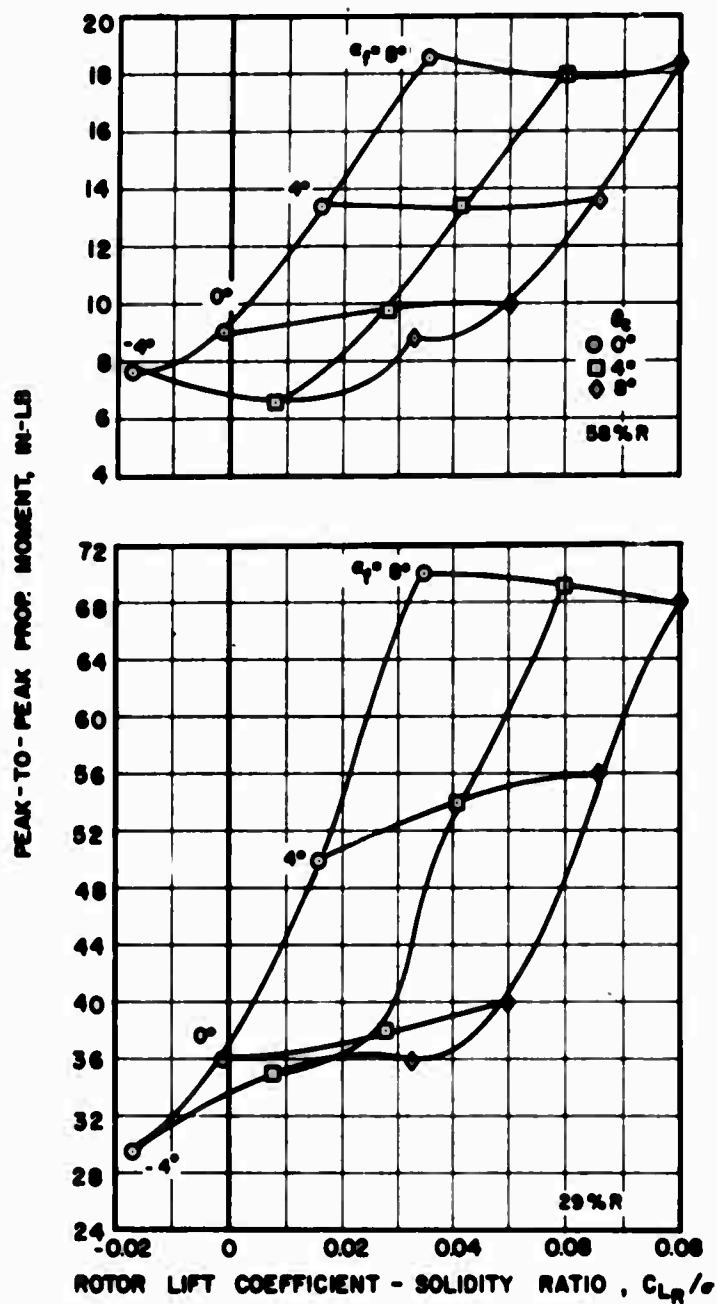
(a) Starboard

Figure 119. Comparison of Experimental and Empirical Effects of Rotor Lift on Outboard Tractor Propeller Blade Flatwise Vibratory Moments for Various Fuselage Angles of Attack and Collective Pitch Settings, $V_s = 120$ Knots, $\beta_{75} = 41^\circ$, 29%R.



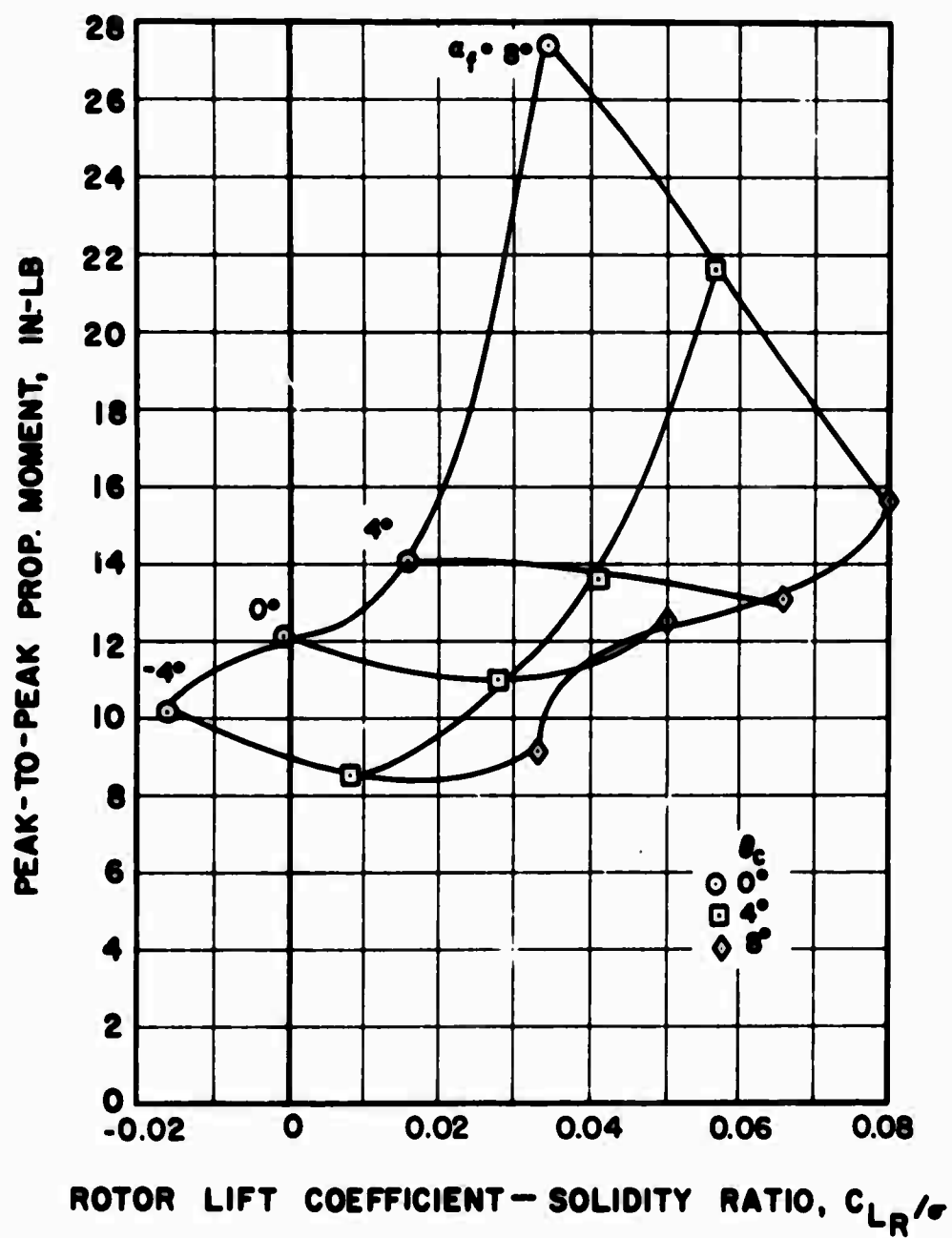
(b) Port

Figure 119. Concluded.



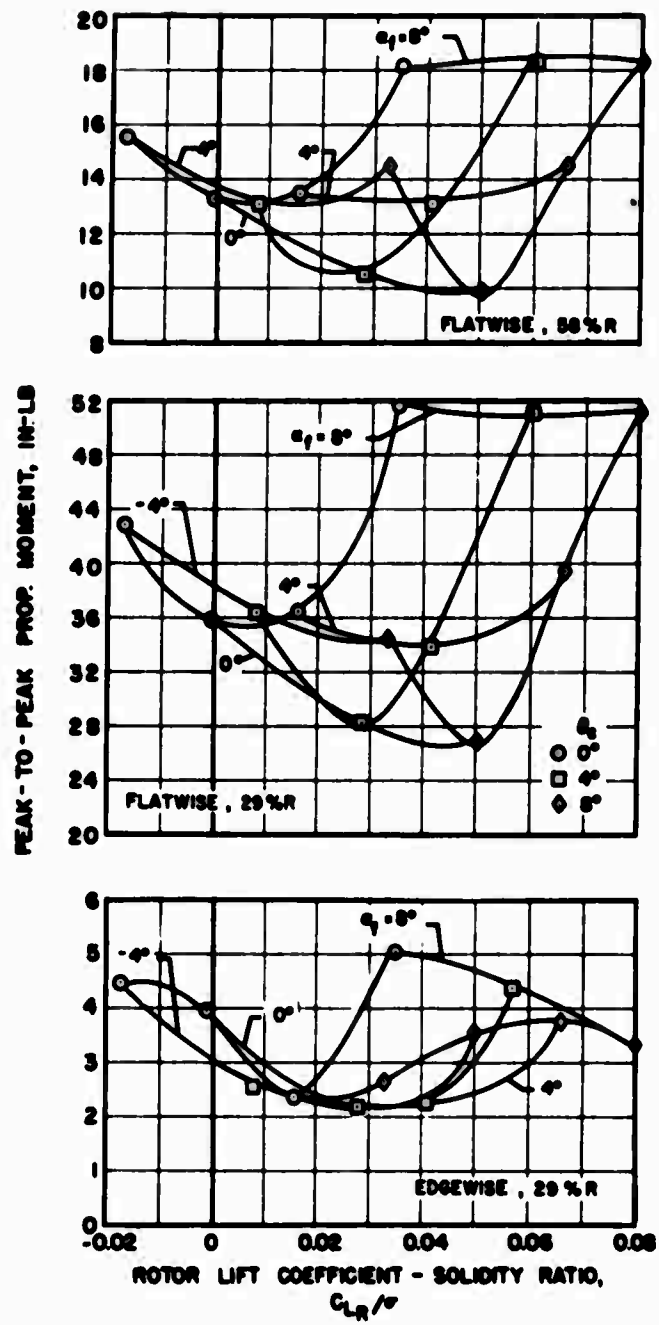
(a) Starboard, Flatwise

Figure 120. Effect of Rotor Lift on Outboard Tractor Propeller Blade Vibratory Moments for Various Fuselage Angles of Attack and Collective Pitch Settings, $V_S = 200$ Knots, $\beta_{75} = 41^\circ$.



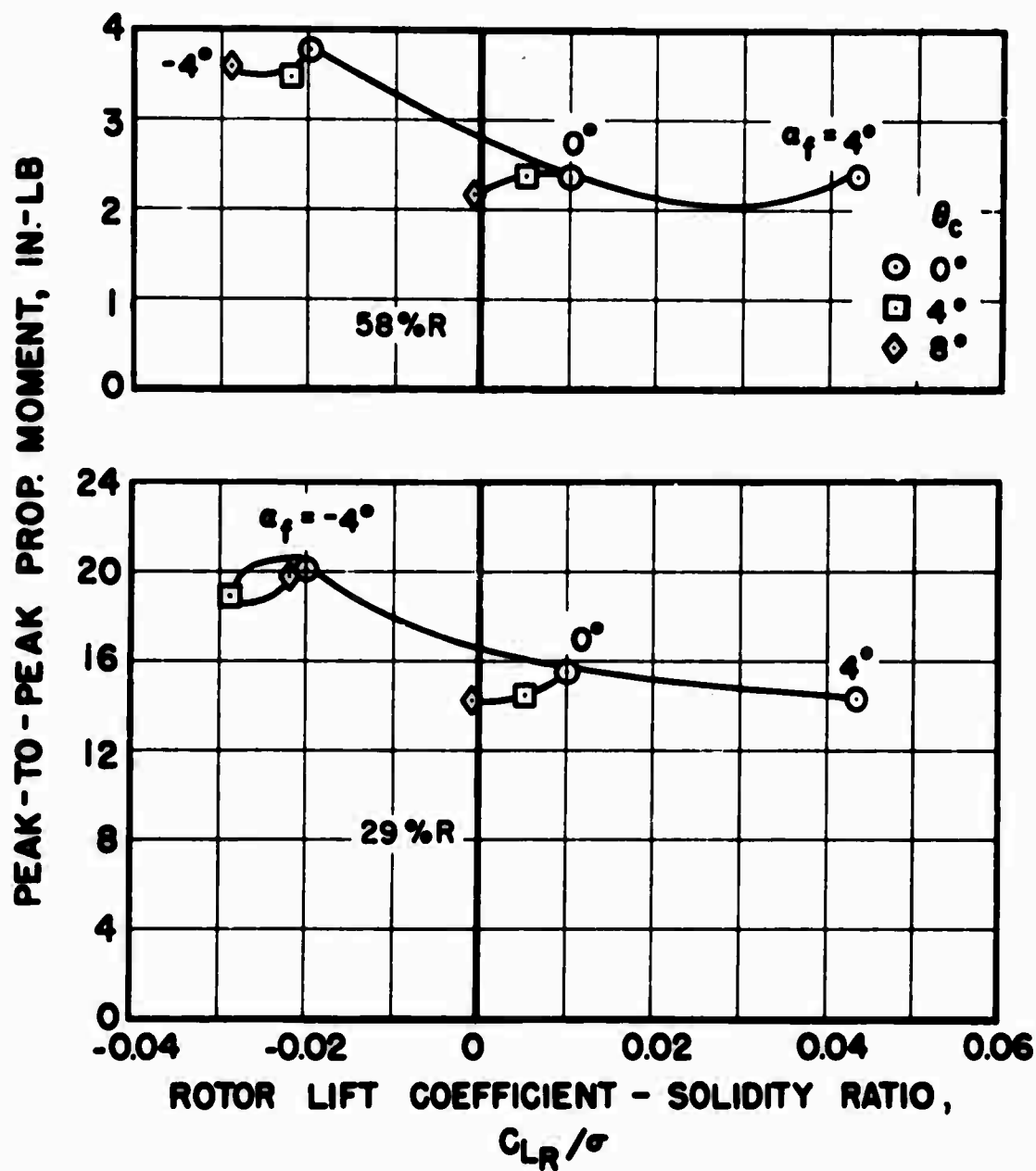
(b) Starboard, Edgewise, 29%R

Figure 120. Continued.



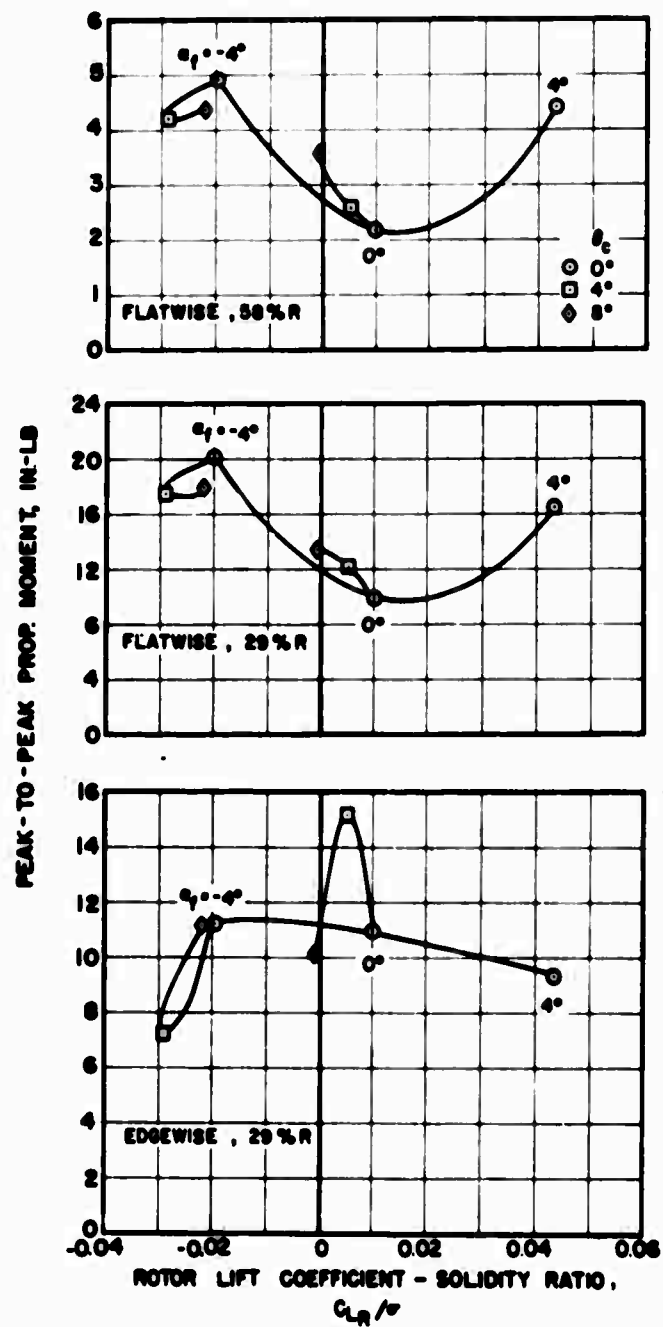
(c) Port

Figure 120. Concluded.



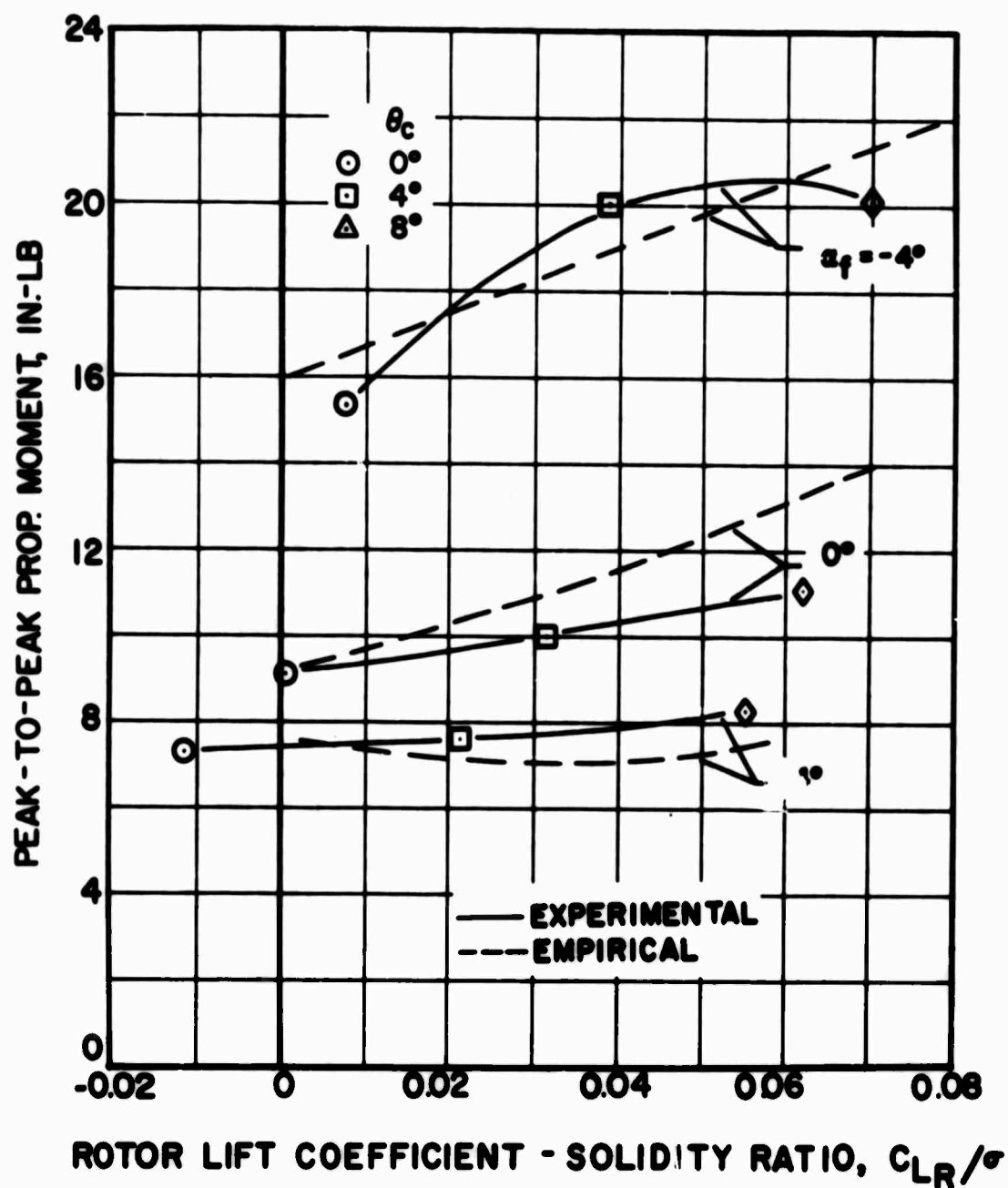
(a) Starboard, Flatwise

Figure 121. Effect of Rotor Lift on Outboard Tractor Propeller Blade Vibratory Moments for Various Fuselage Angles of Attack and Collective Pitch Settings, $V_s = 300$ Knots, $\beta_{75} = 41^\circ$.



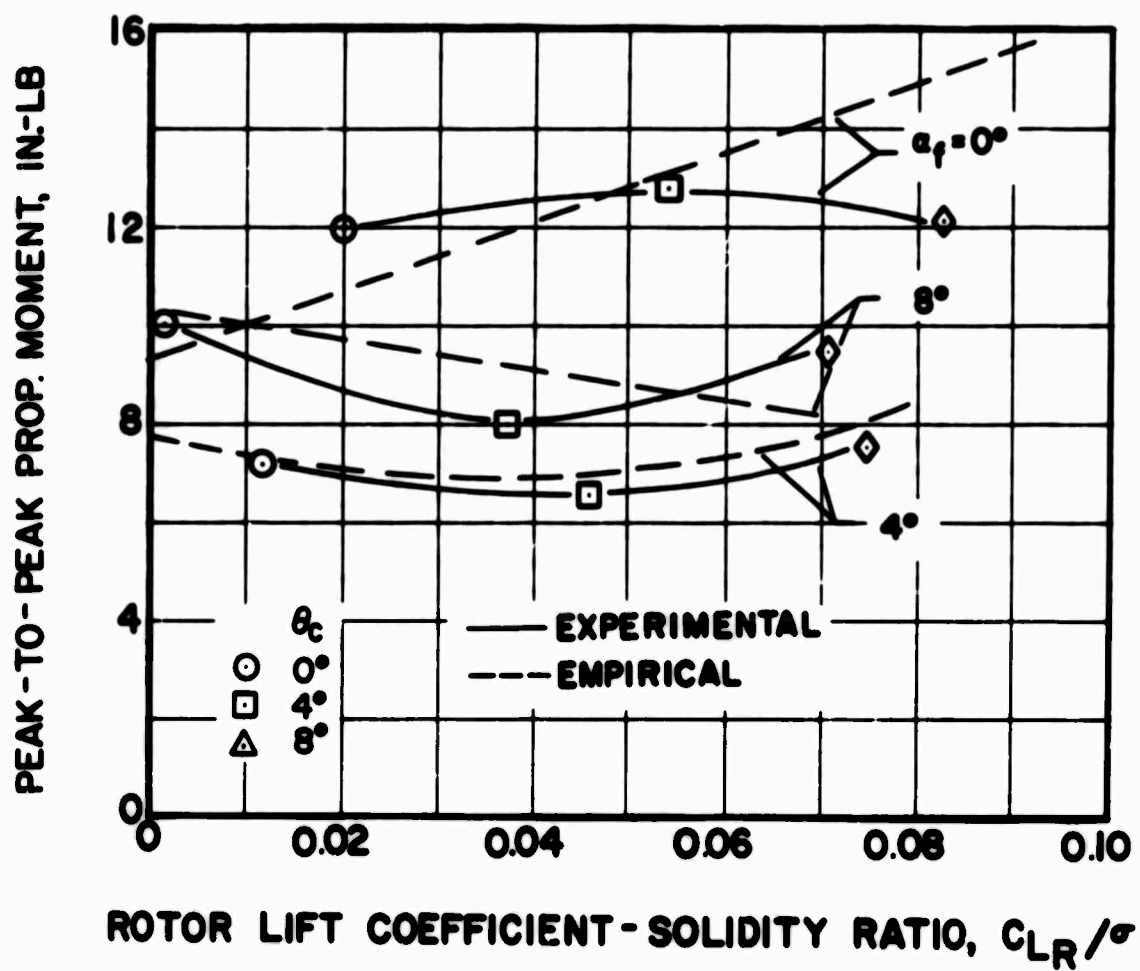
(b) Port

Figure 121. Concluded.



(a) $\alpha_{TPP} = 0^\circ$

Figure 122. Comparison of Experimental and Empirical Effects of Rotor Lift on Inboard Tractor Propeller Blade Flatwise Vibratory Moments at Two Rotor Tip Path Plane Angles of Attack, $V_s = 120$ Knots, $\beta_{.75} = 41^\circ$, Starboard, 29%R.



(b) $\alpha_{TPP} = 4^\circ$

Figure 122. Concluded.

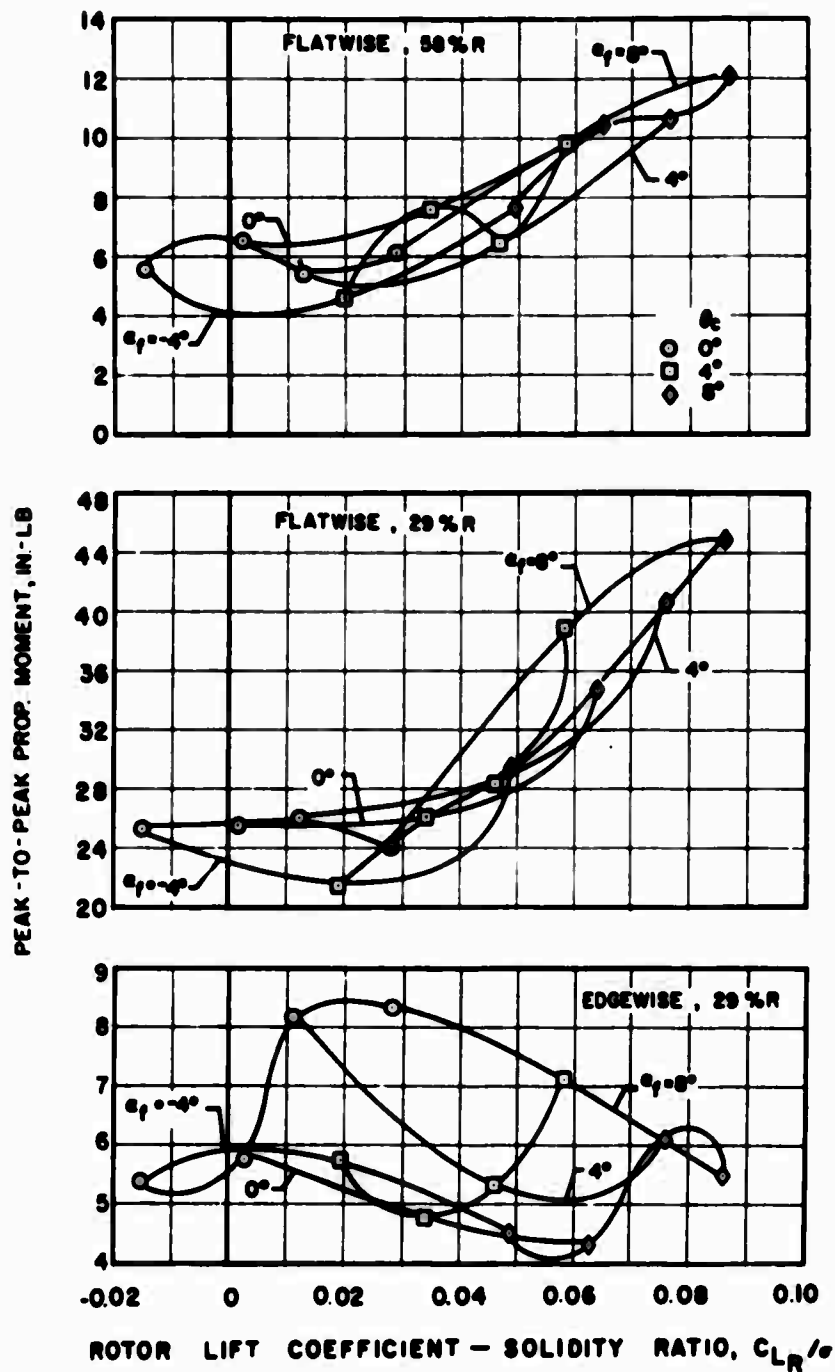


Figure 123. Effect of Rotor Lift on Pusher Propeller Blade Vibratory Moments for Various Fuselage Angles of Attack and Collective Pitch Settings, Without Empennage, $V_s = 120$ Knots, $\beta_{.75} = 41^\circ$.

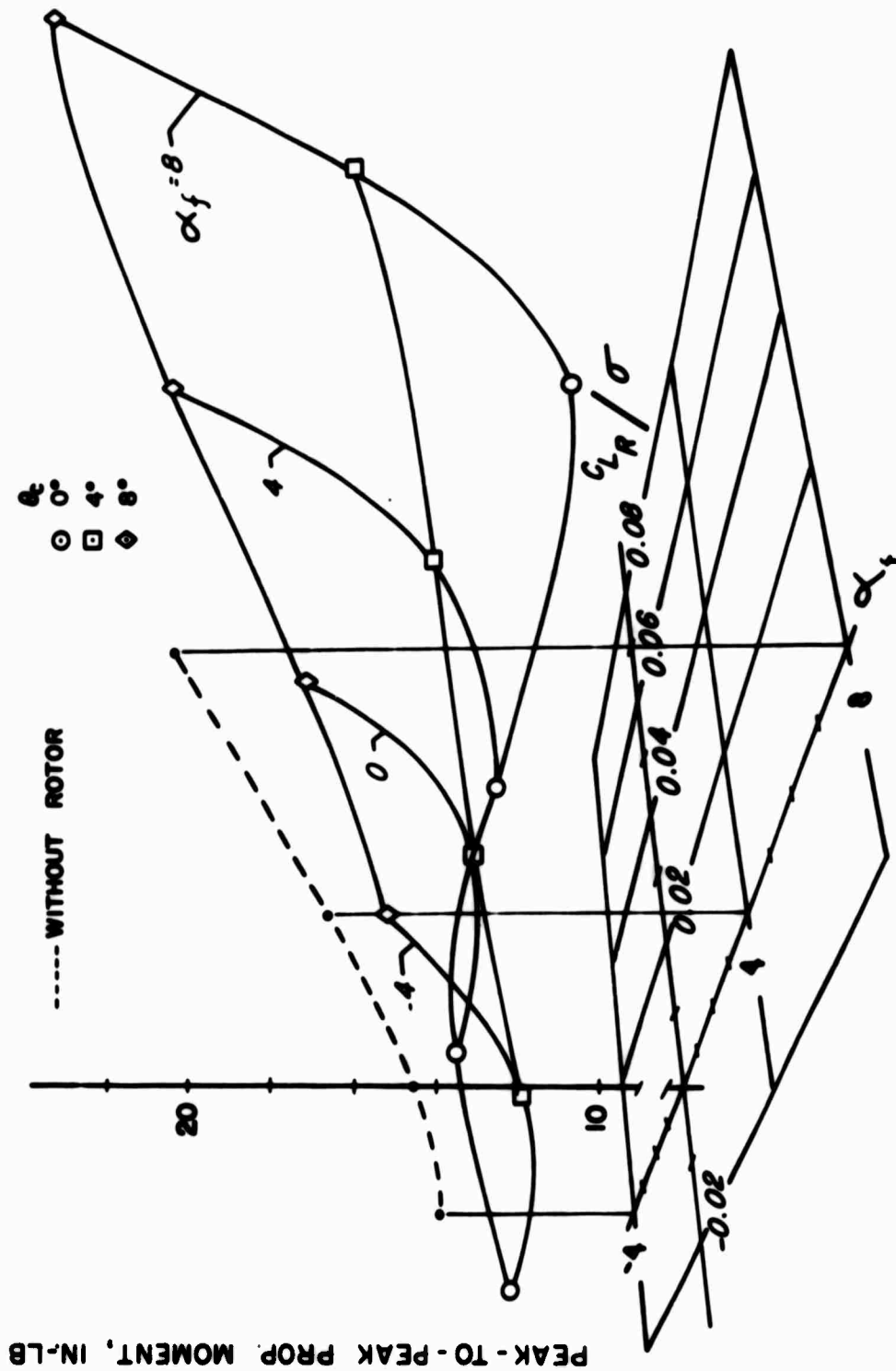


Figure 124. Effect of Rotor Lift and Fuselage Angle of Attack on Pusher Propeller Blade Flatwise Vibratory Moments, Without Empennage, $V_s = 120$ Knots, $\beta_{75} = 41^\circ$, 29%R.

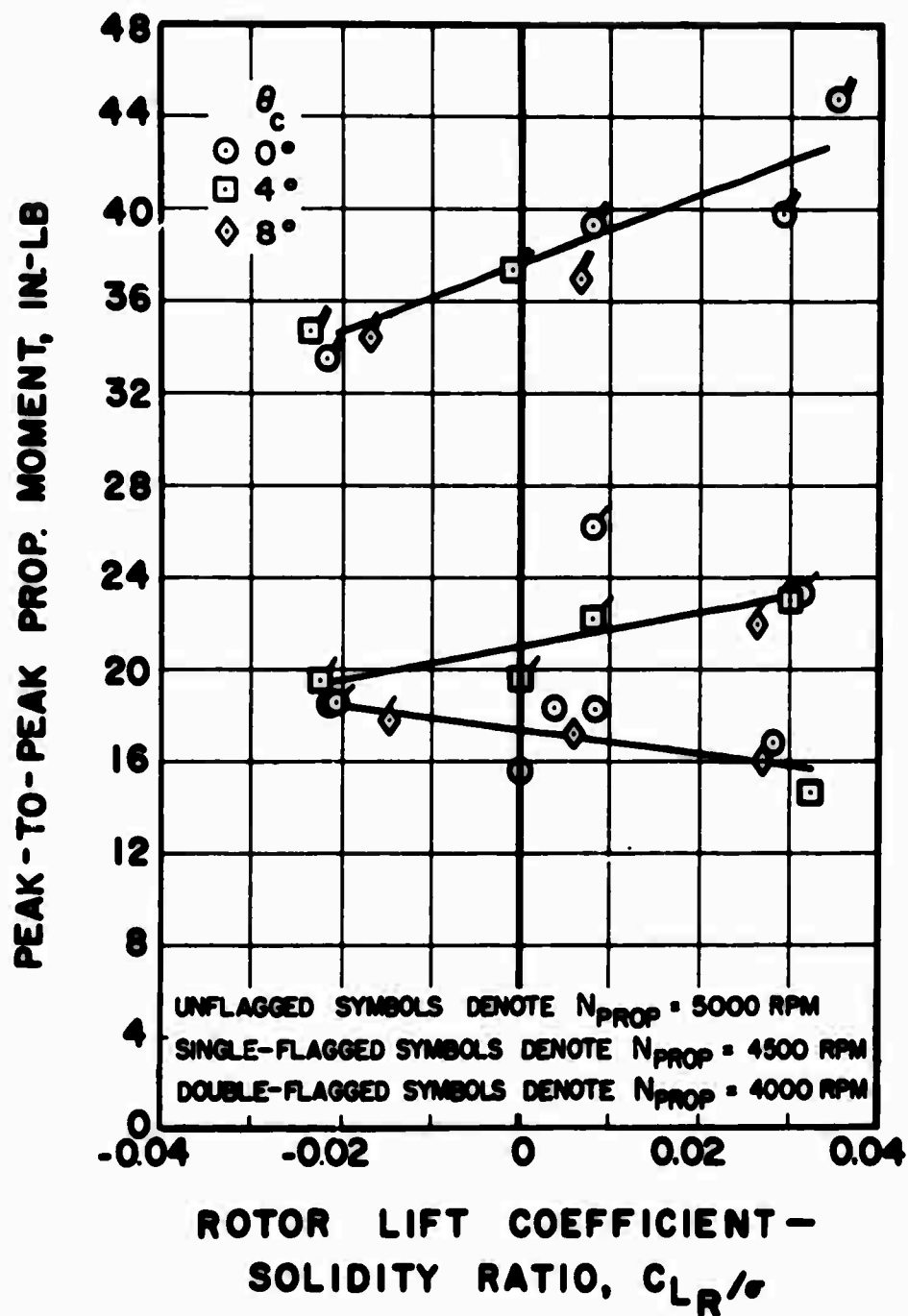


Figure 125. Effect of Rotor Lift on Pusher Propeller Blade Flatwise Vibratory Moments for Three Collective Pitch Settings and Propeller Speeds, Without Empennage, $V_s = 300$ Knots, $\beta_{75} = 41^\circ$, 58%R.

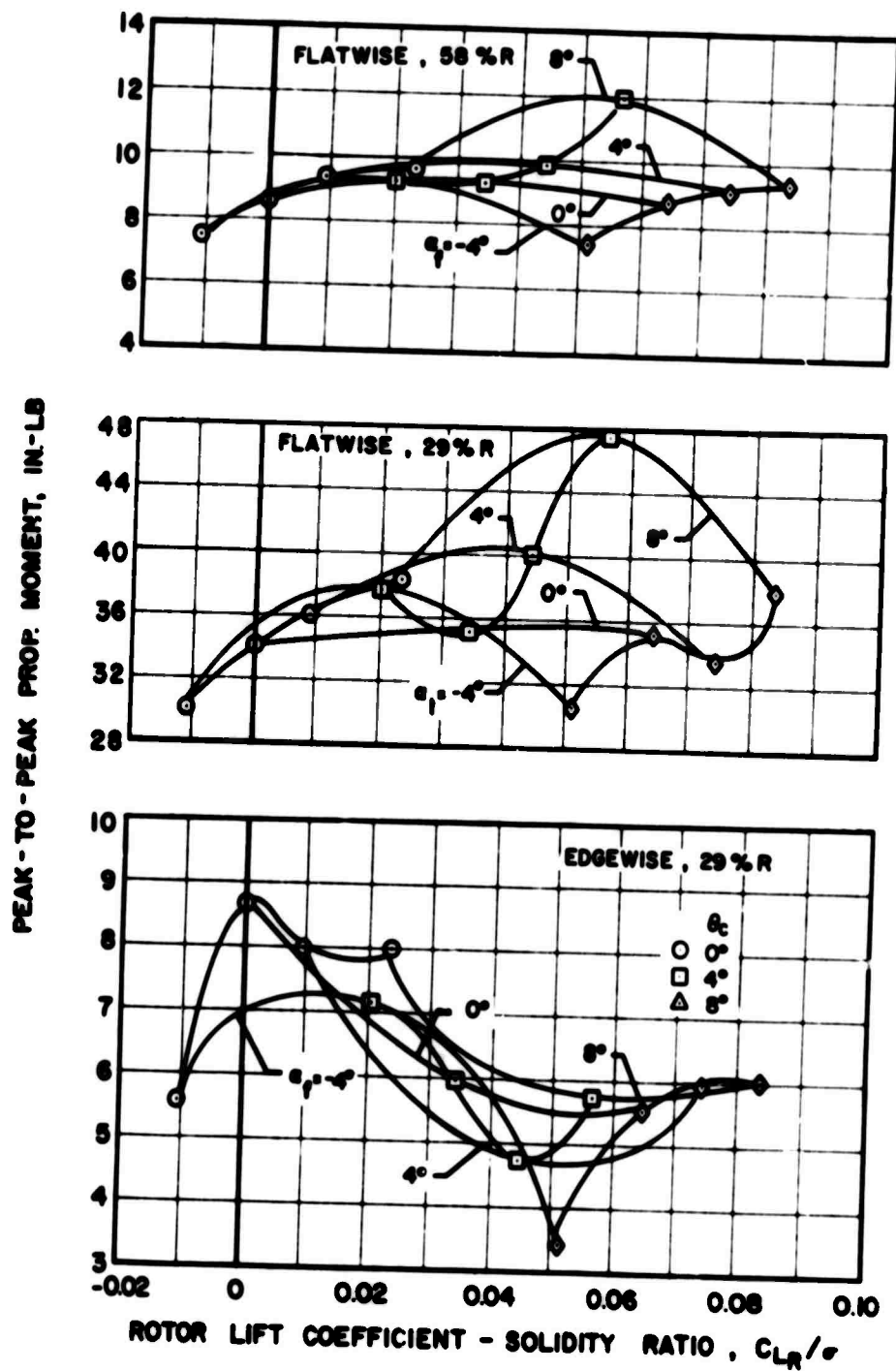


Figure 126. Effect of Rotor Lift on Pusher Propeller Blade Vibratory Moments for Various Fuselage Angles of Attack and Collective Pitch Settings, With Empennage, $V_s = 120$ Knots, $\beta_{75} = 41^\circ$.

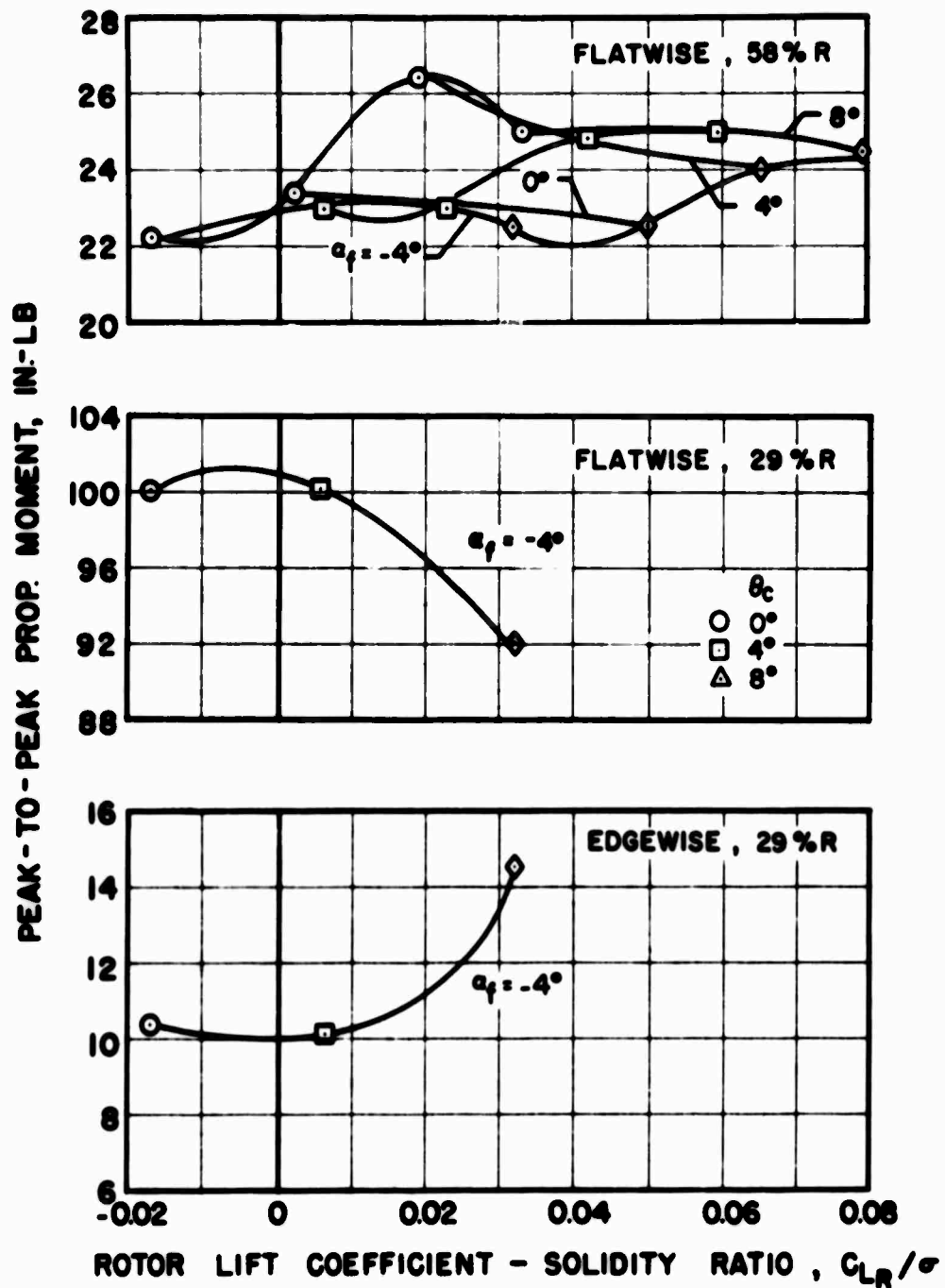


Figure 127. Effect of Rotor Lift on Pusher Propeller Blade Vibratory Moments for Various Fuselage Angles of Attack and Collective Pitch Settings, With Empennage, $V_s = 200$ Knots, $\beta_{.75} = 41^\circ$.

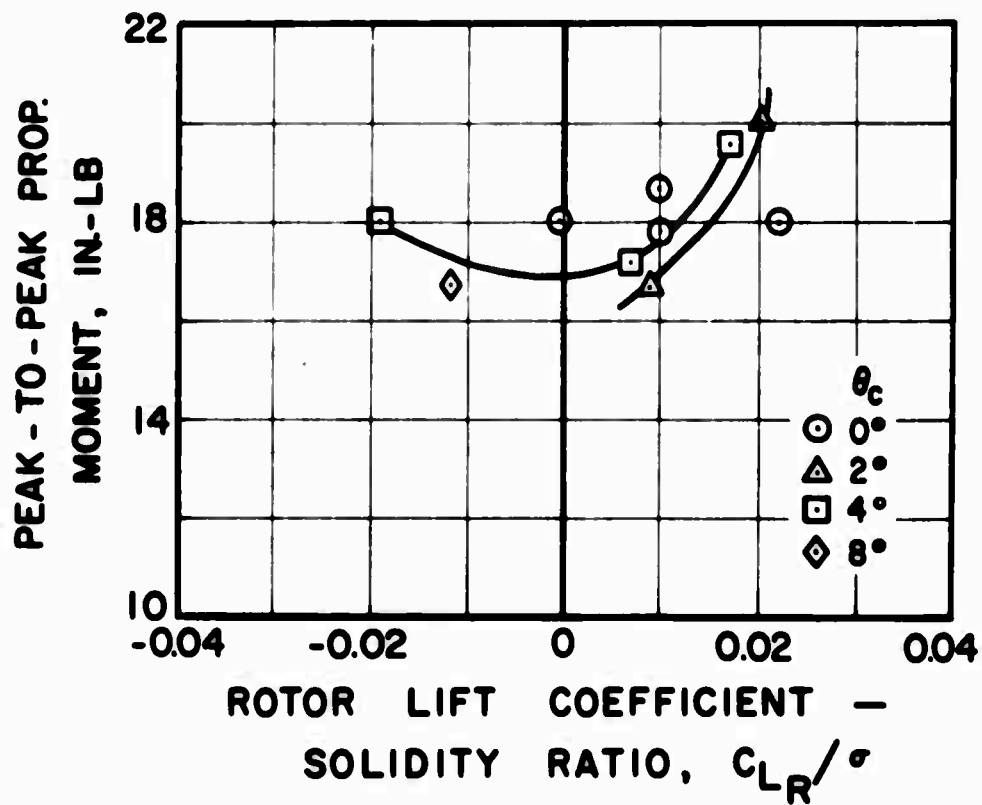


Figure 128. Effect of Rotor Lift on Pusher Propeller Blade Flatwise Vibratory Moments for Various Collective Pitch Settings, With Empennage, $V_s = 300$ Knots, $\beta_{75} = 41^\circ$, 58%R.

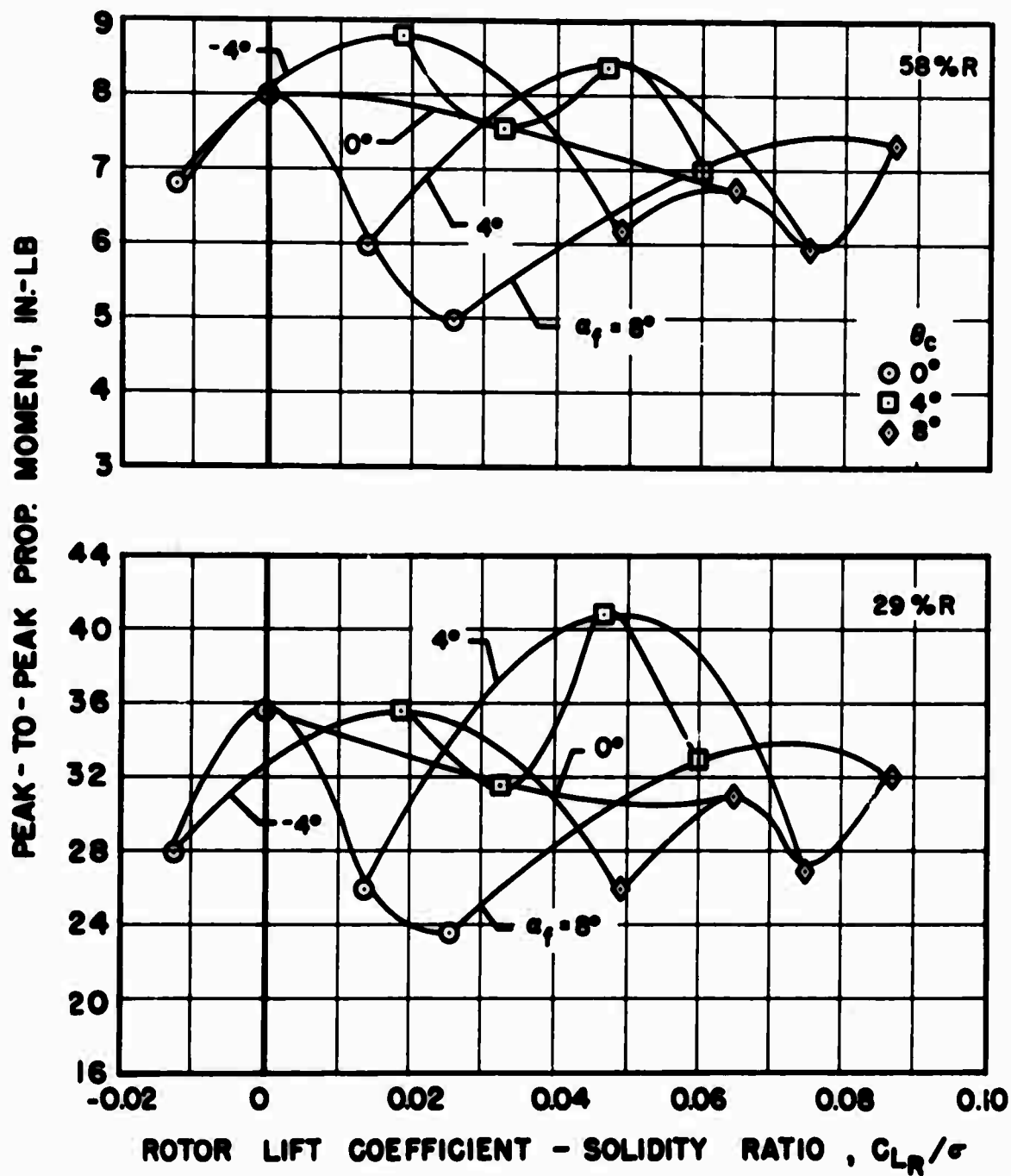
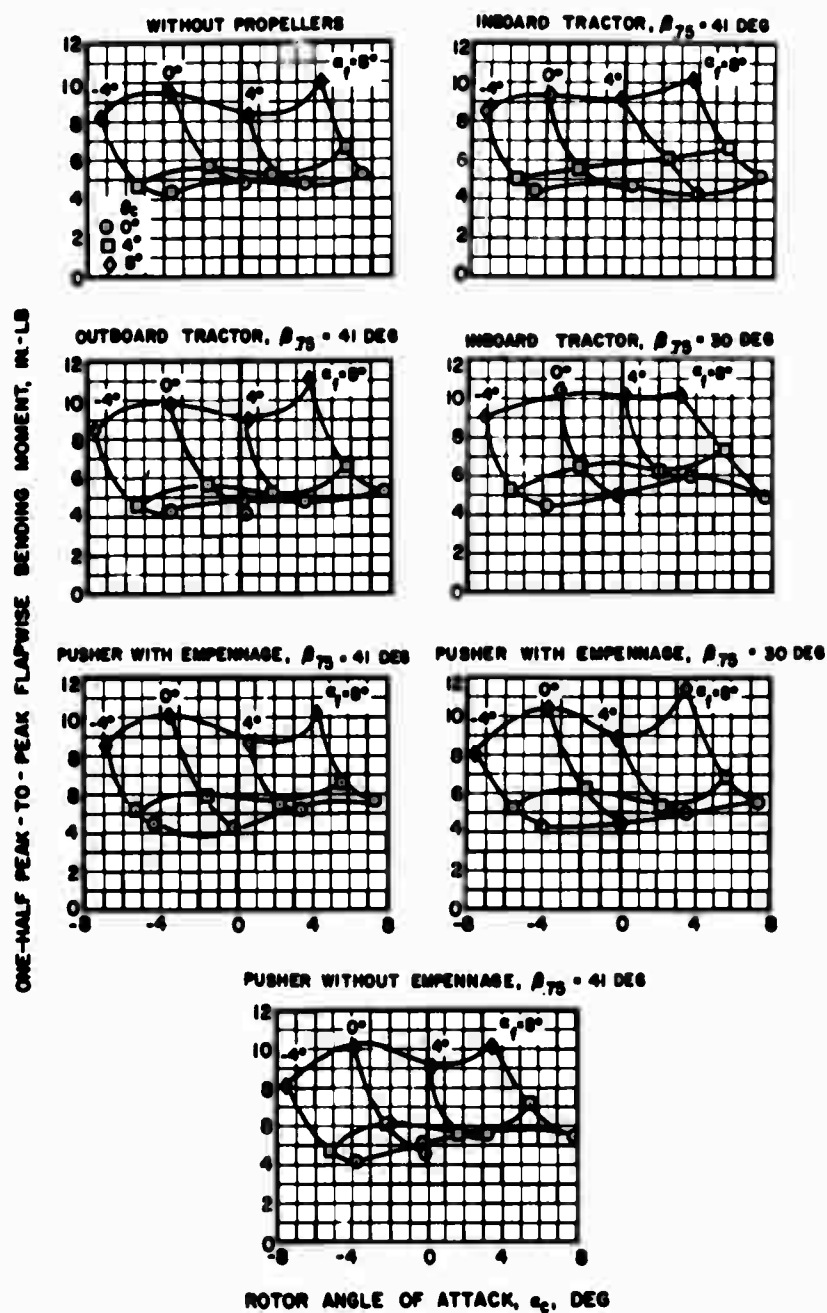


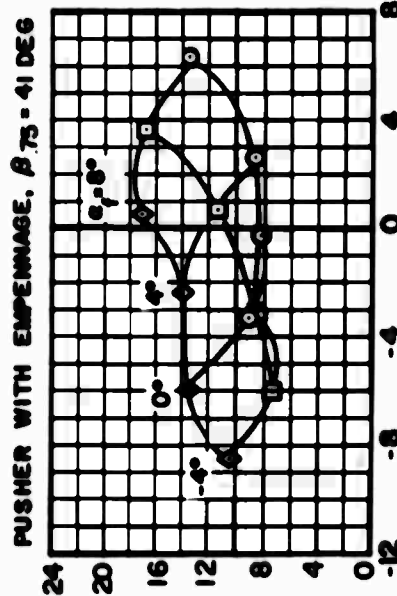
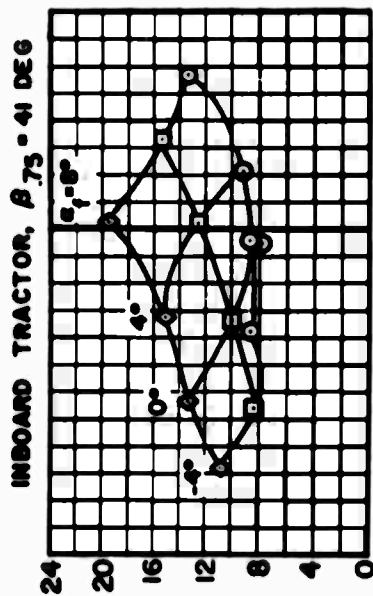
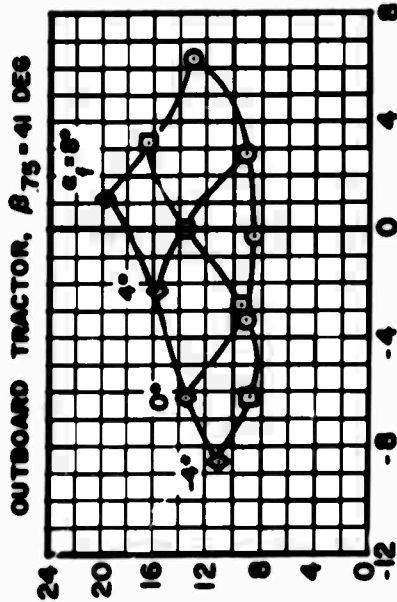
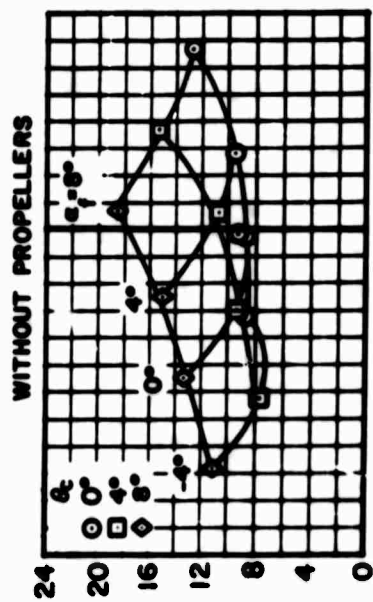
Figure 129. Effect of Rotor Lift on Pusher Propeller Blade Flatwise Vibratory Moments for Various Fuselage Angles of Attack and Collective Pitch Settings, With Empennage, $V_s = 120$ Knots, $\beta_{.75} = 30^\circ$.



(a) $V_s = 120$ Knots

Figure 130. Effect of Propeller Configuration on Rotor Blade Flapwise Vibratory Moment Amplitudes for Various Fuselage Angles of Attack, Collective Pitch Settings, and Forward Speeds, 60%R.

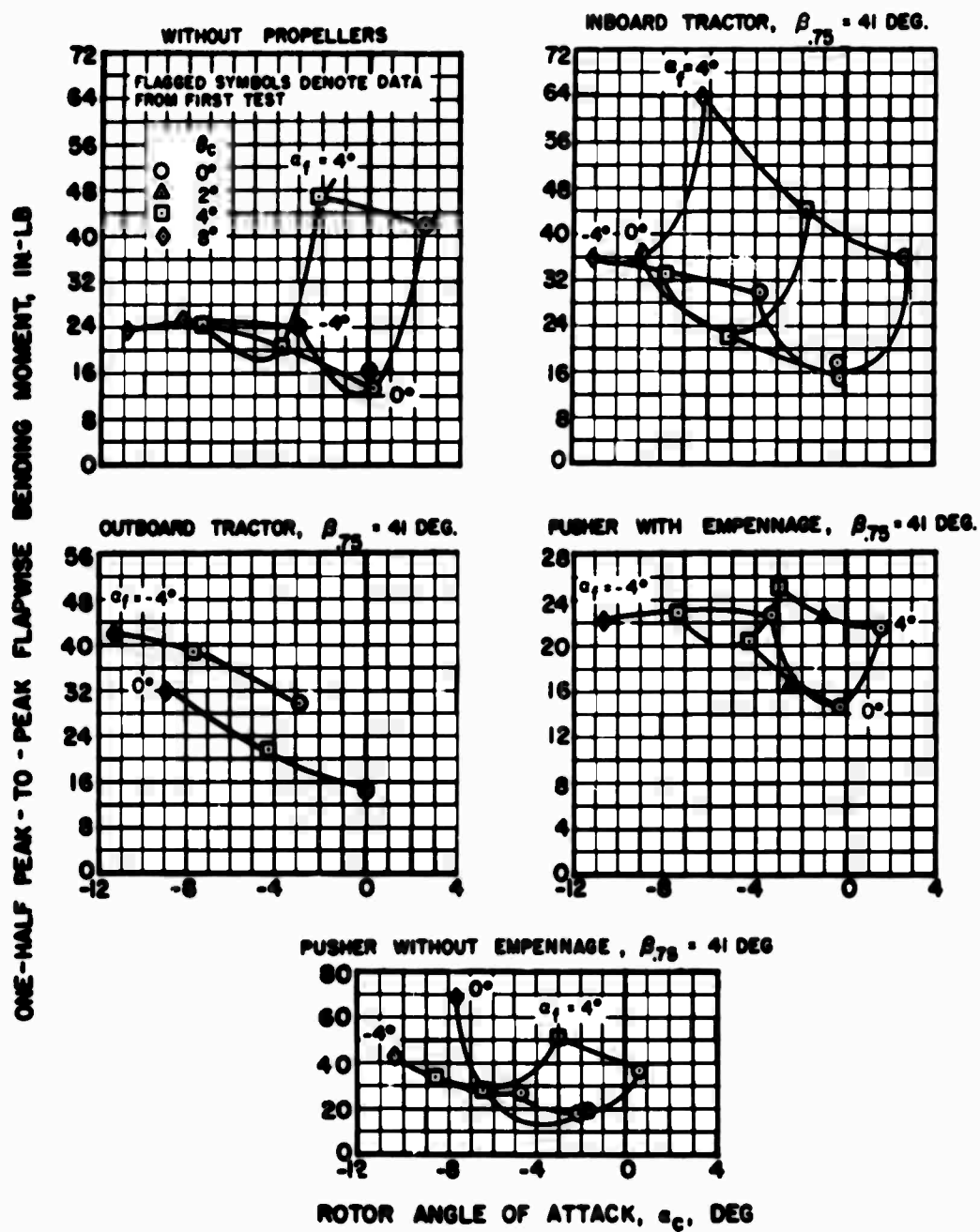
ONE-HALF PEAK-TO-PEAK FLAPWISE BENDING MOMENT, IN-LB



ROTOR ANGLE OF ATTACK, α_c , DEG

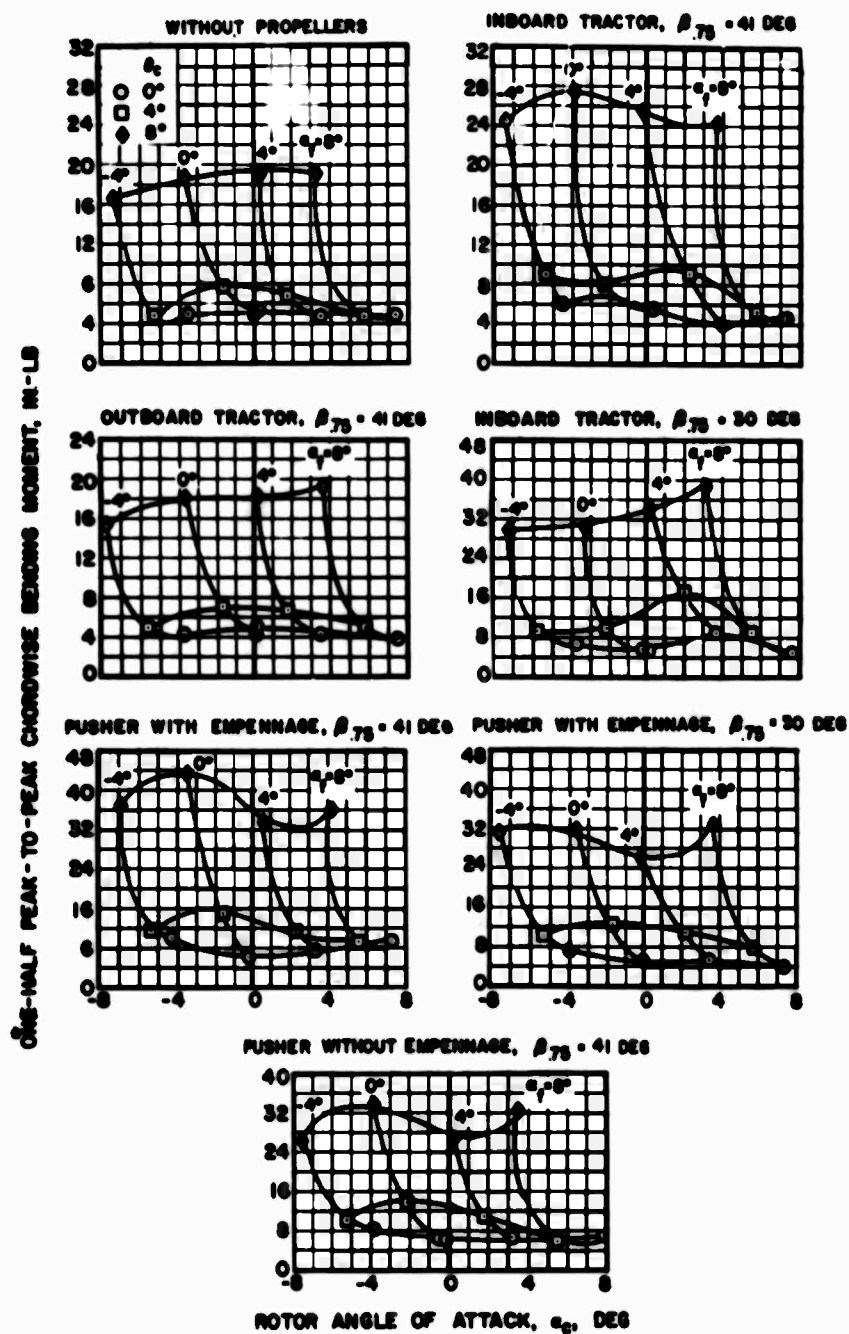
(b) $V_s = 200$ Knots

Figure 130. Continued.



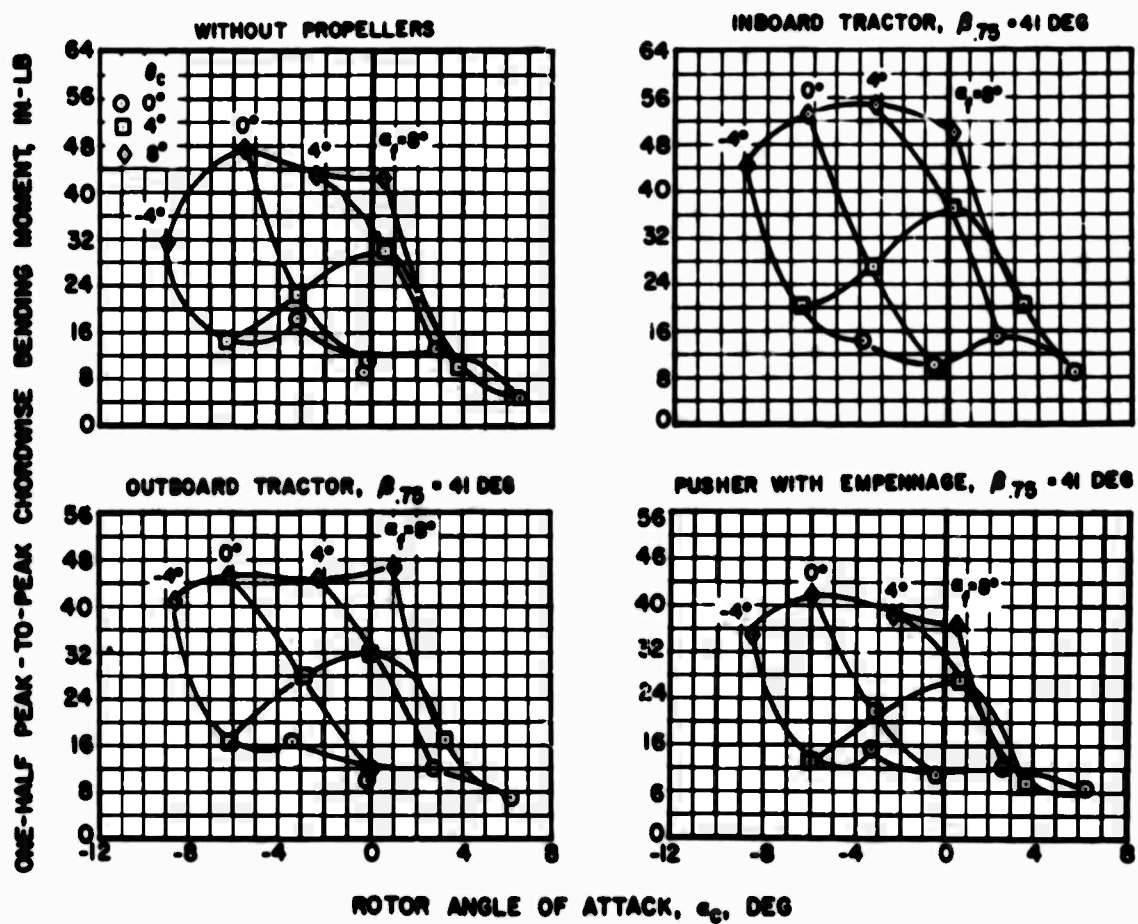
(c) $V_5 = 300$ Knots

Figure 130. Concluded.



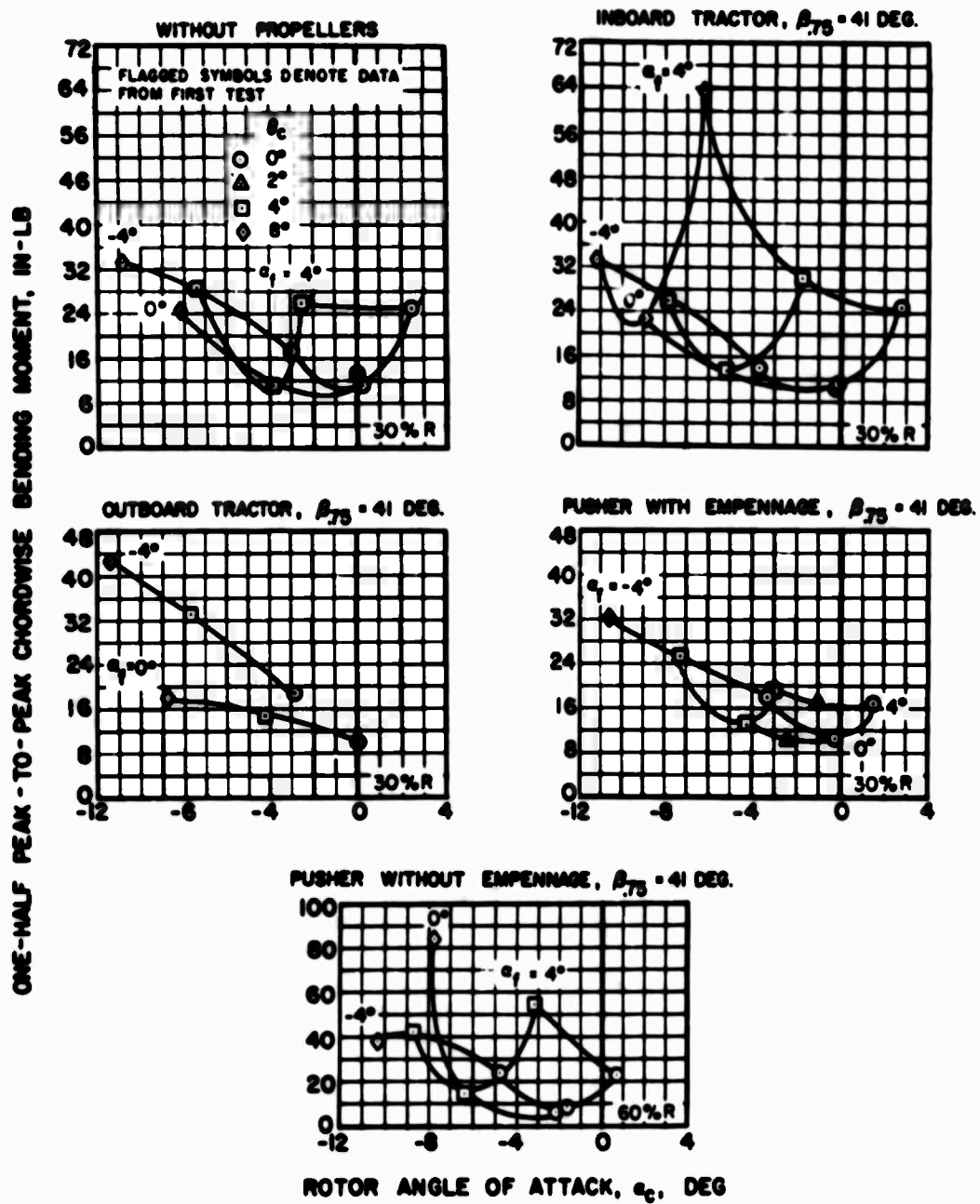
(a) $V_s = 120 \text{ Knots, } 30\%R$

Figure 131. Effect of Propeller Configuration on Rotor Blade Chordwise Vibratory Moment Amplitudes for Various Fuselage Angles of Attack, Collective Pitch Settings, and Forward Speeds.



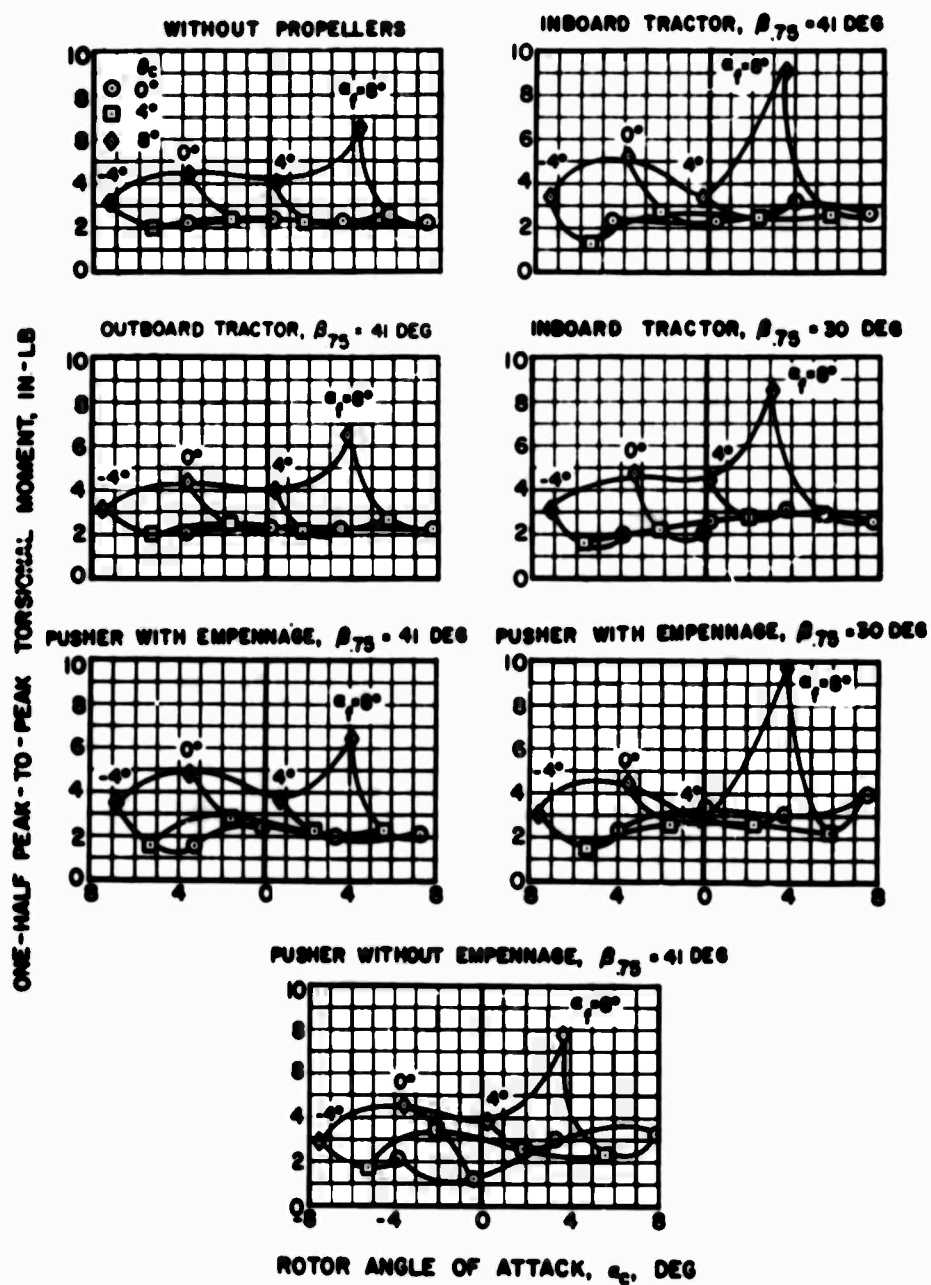
(b) $V_s = 200$ Knots, 30%R

Figure 131. Continued.



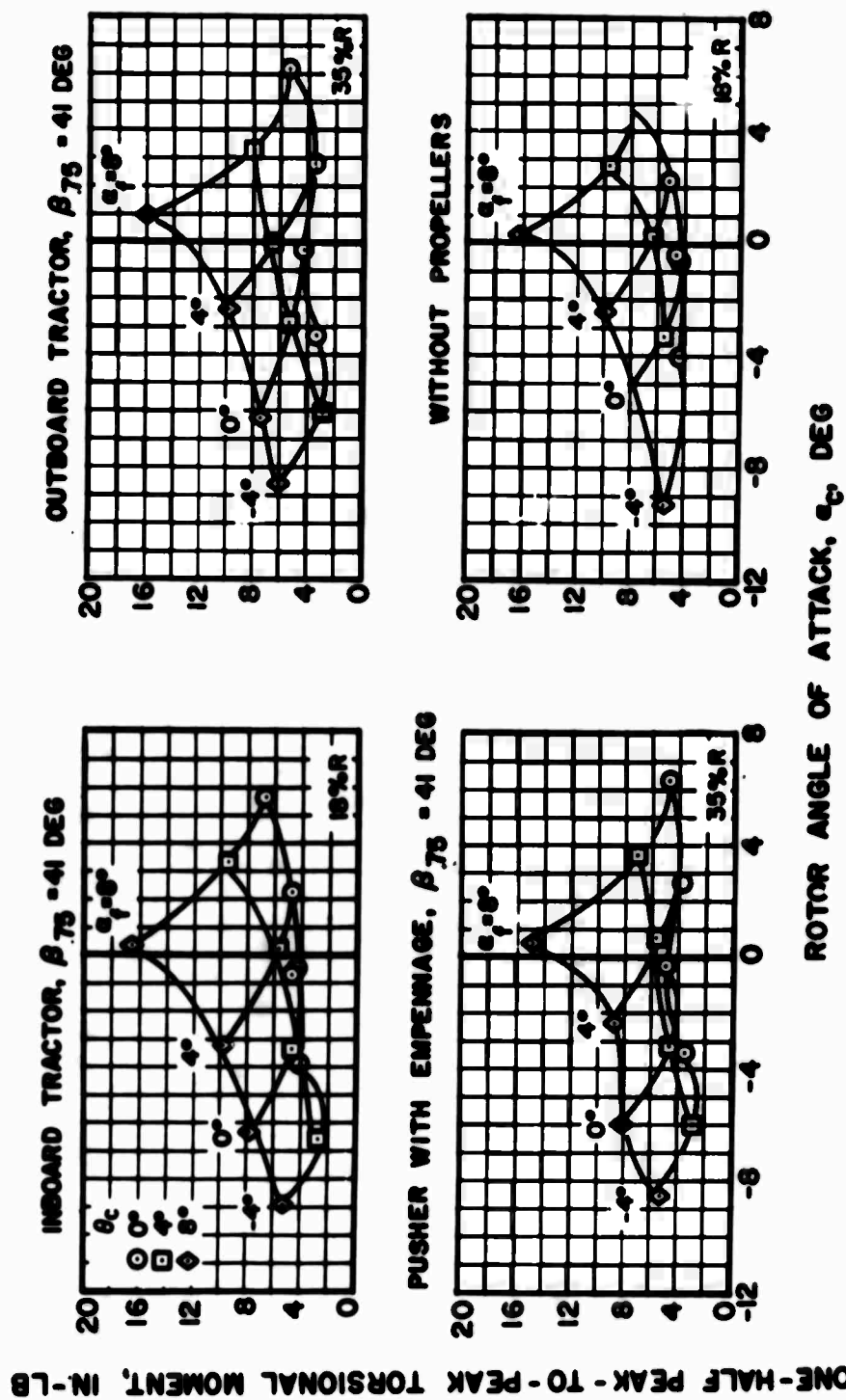
(c) $V_s = 300$ Knots

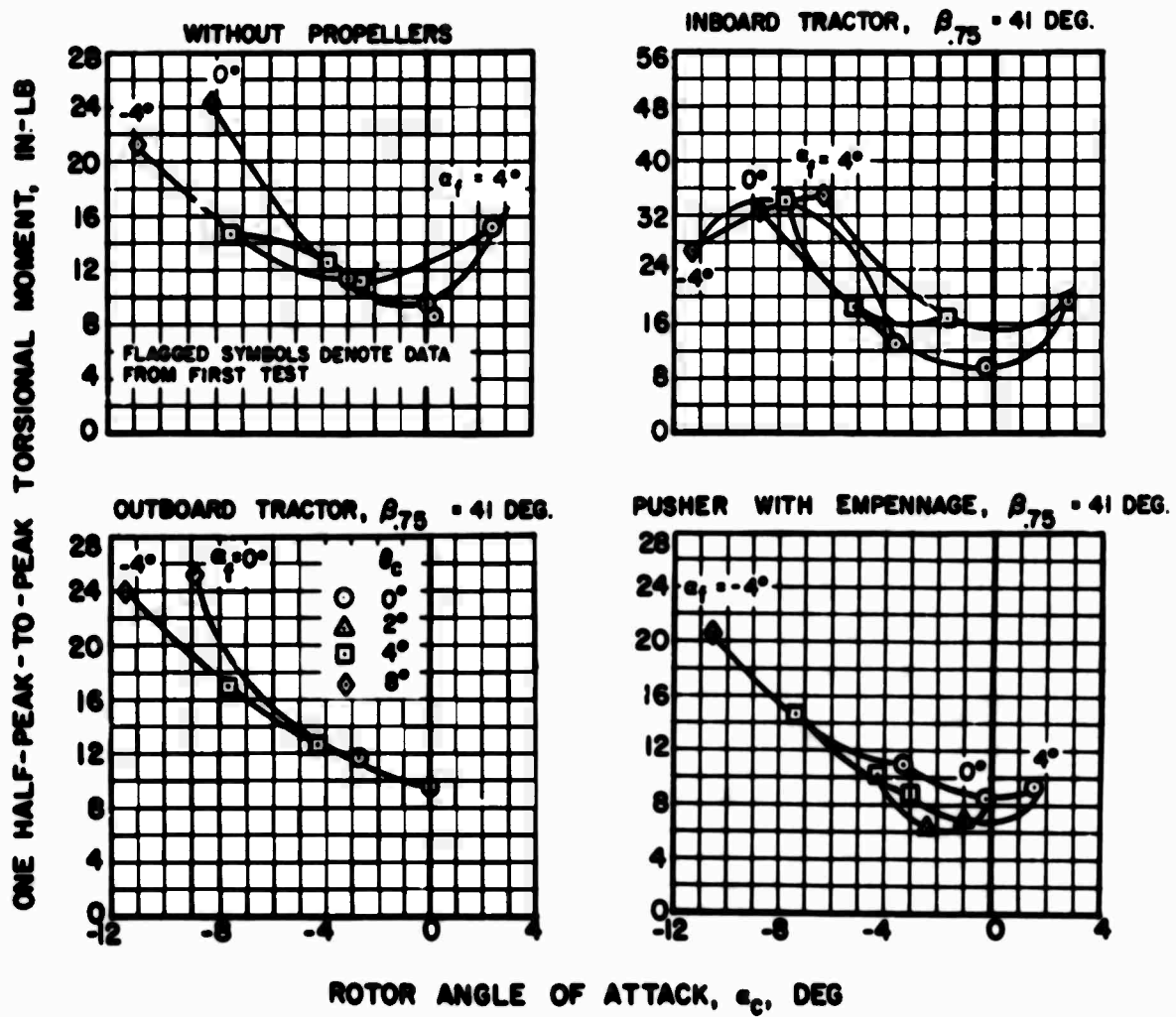
Figure 131. Concluded.



(a) $V_S = 120$ Knots, 18%R

Figure 132. Effect of Propeller Configuration on Rotor Blade Torsional Vibratory Moment Amplitudes for Various Fuselage Angles of Attack, Collective Pitch Settings, and Forward Speeds.





(c) $V_s = 300$ Knots, 35%R

Figure 132. Concluded.

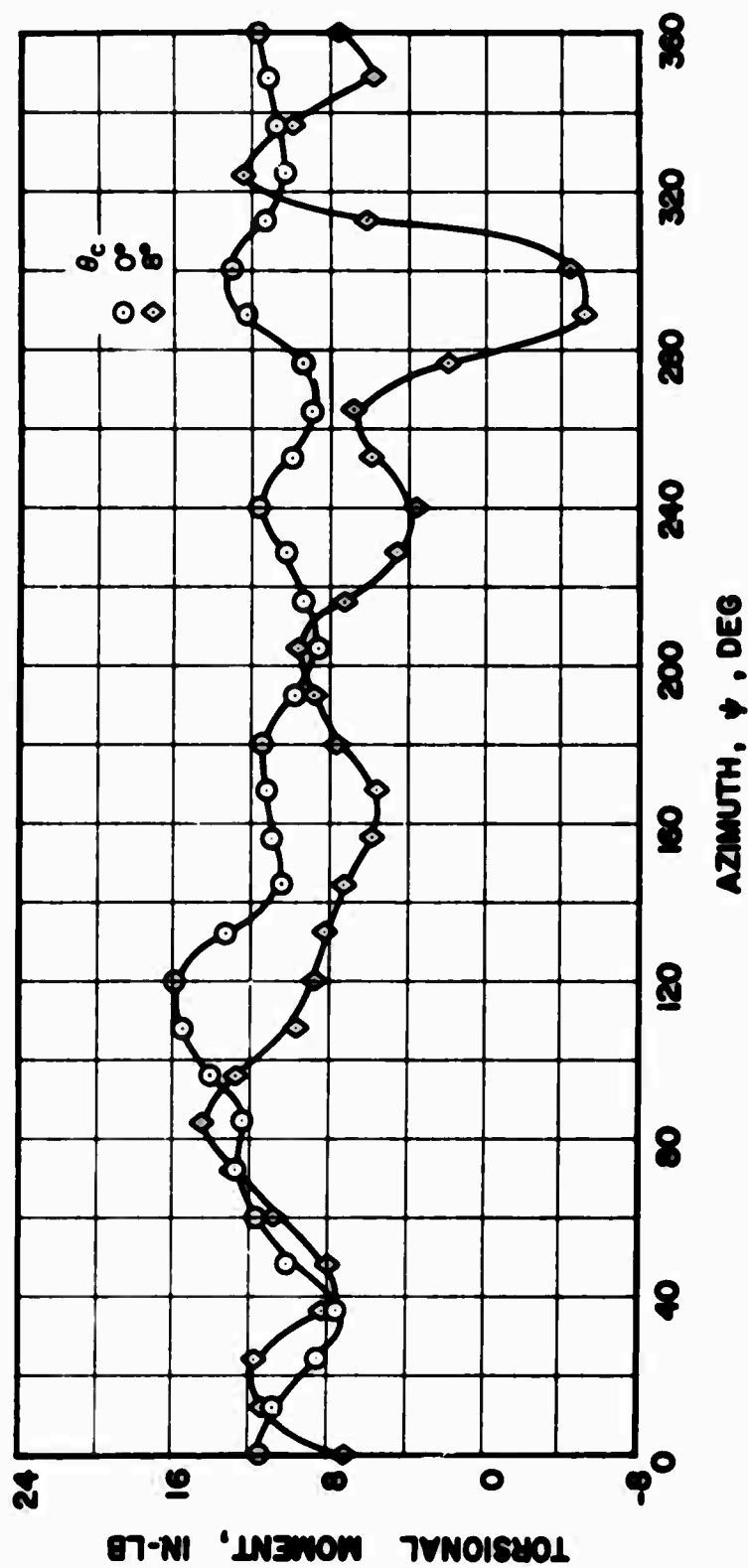


Figure 133. Effect of Collective Pitch Setting on Rotor Blade Torsional Moment Azimuthal Variation, With Pusher Propeller and Empennage, $\beta_{75} = 30^\circ$, $V_s = 120$ knots, $\alpha_f = 8^\circ$, $18\%R$.

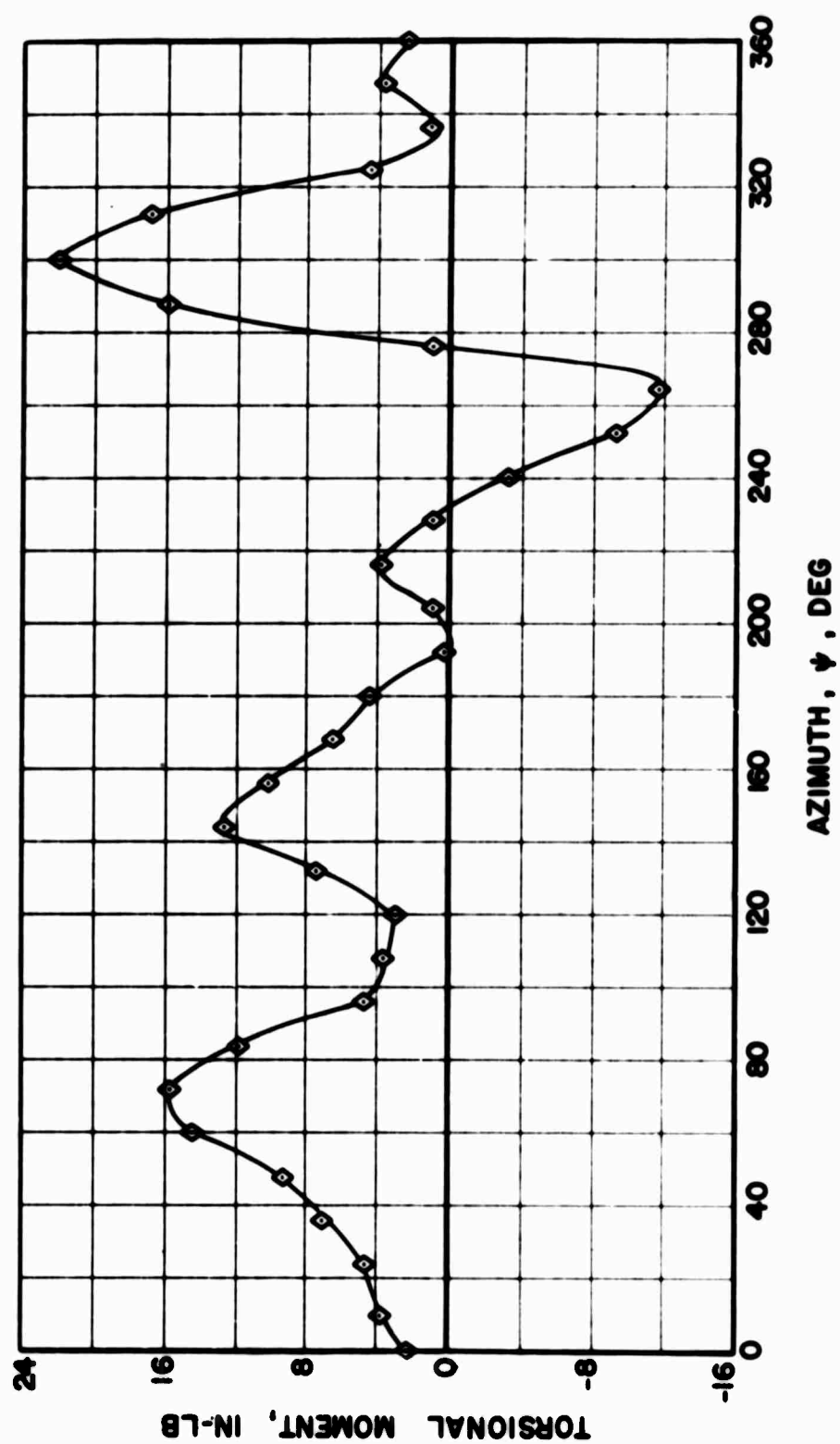


Figure 134. Rotor Blade Torsional Moment Azimuthal Variation With Outboard Tractor Propellers, $\beta_{75} = 41^\circ$, $V_s = 300$ Knots, $\alpha_f = 4^\circ$, $\theta_c = 4^\circ$, $35\%R$.

ONE-HALF PEAK - TO - PEAK FLAPWISE

BENDING MOMENT, IN.-LB

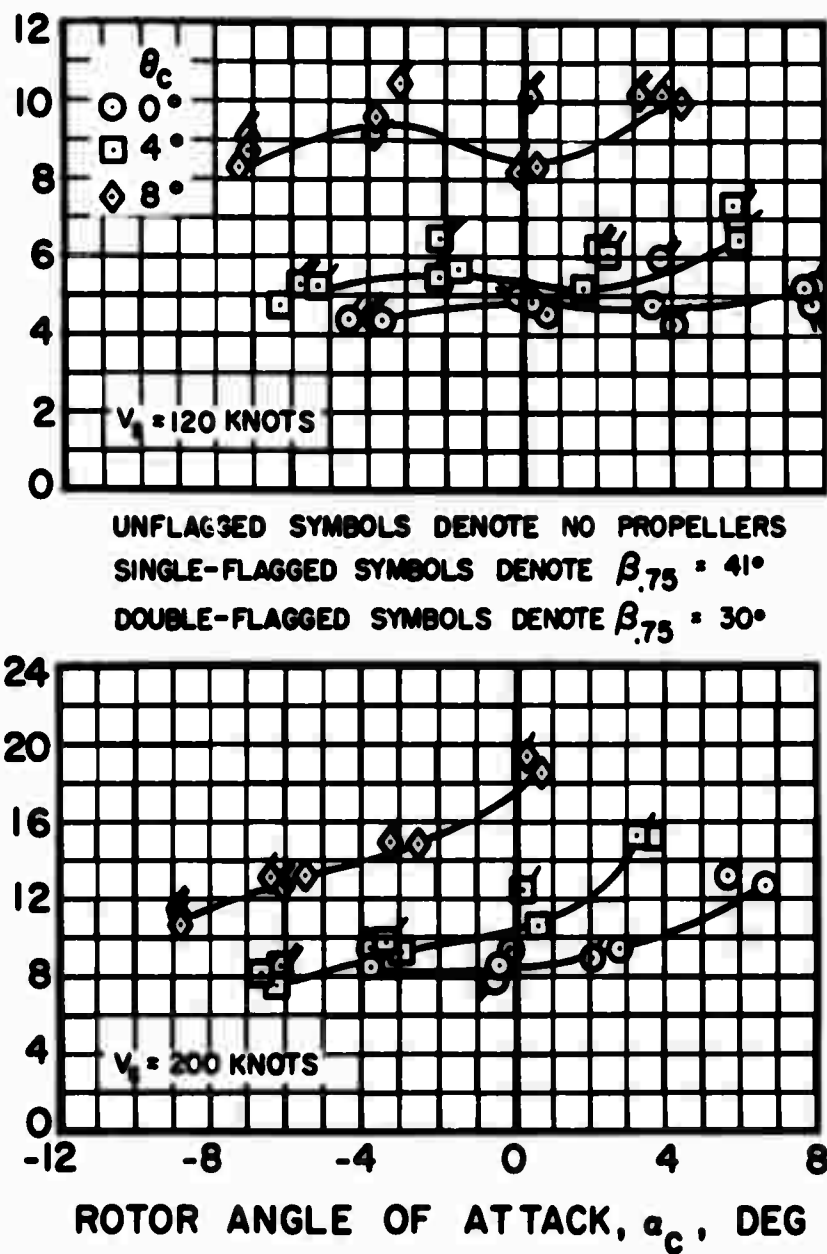


Figure 135. Effect of Inboard Tractor Propeller Thrust on Rotor Blade Flapwise Vibratory Moment Amplitudes at Various Rotor Angles of Attack and Collective Pitch Settings and Two Forward Speeds, 60%R.

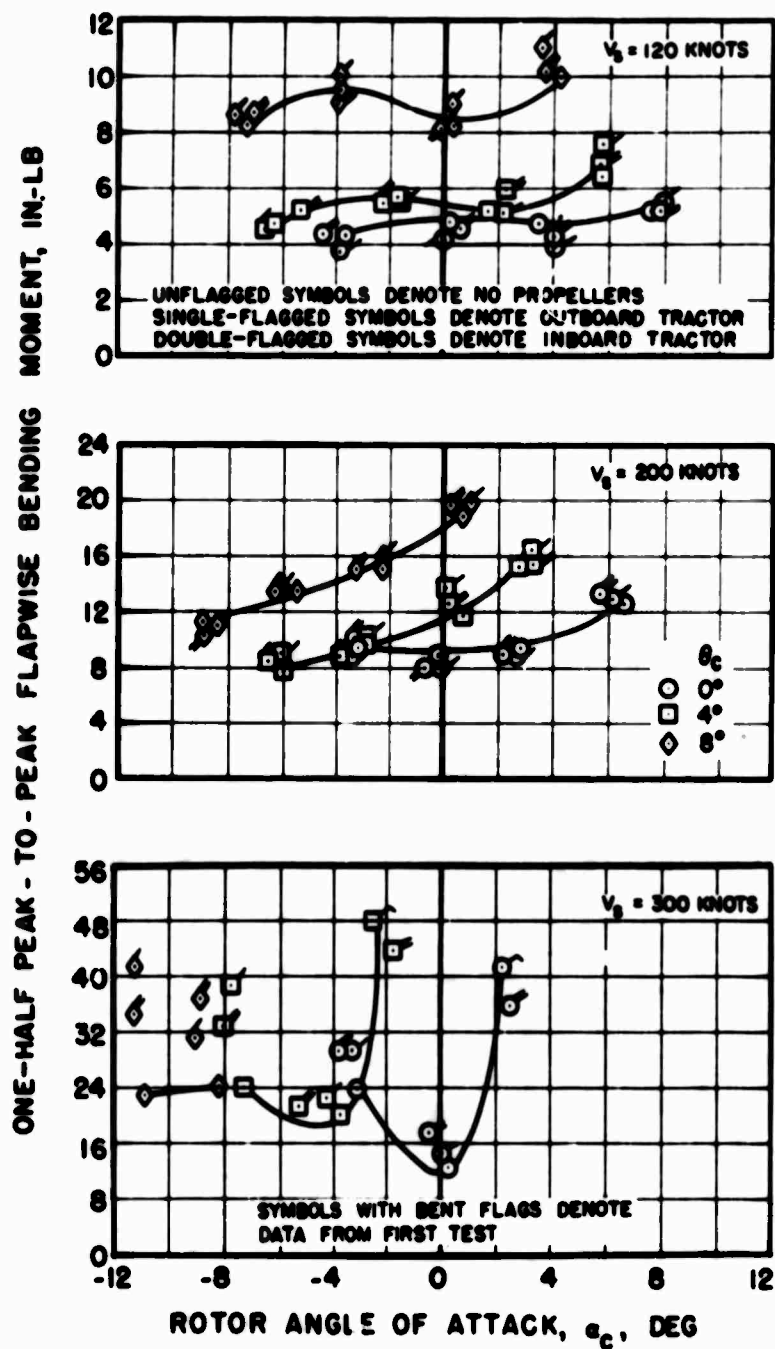


Figure 136. Effect of Tractor Propeller Location on Rotor Blade Flapwise Vibratory Moment Amplitudes at Various Rotor Angles of Attack, Collective Pitch Settings, and Forward Speeds, 60%R, $\beta_{.75} = 41^\circ$.

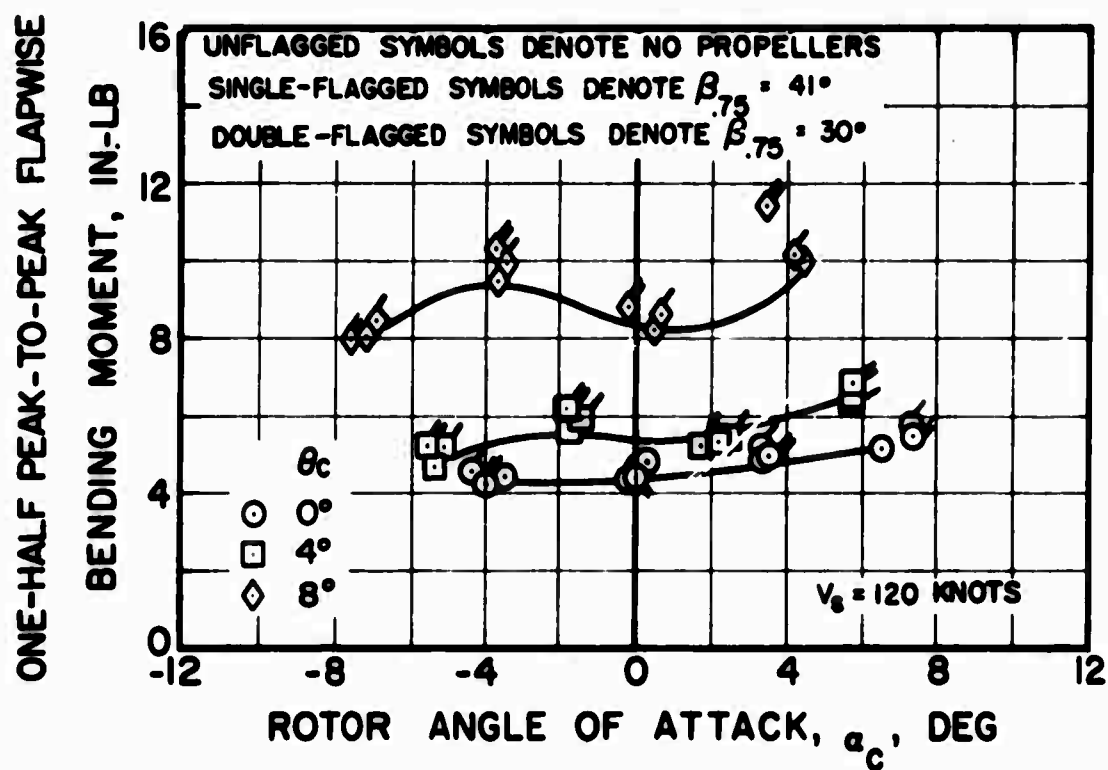


Figure 137. Effect of Pusher Propeller Thrust on Rotor Blade Flapwise Vibratory Moment Amplitudes at Various Rotor Angles of Attack and Collective Pitch Settings, With Empennage, $V_s = 120$ Knots, 60%R.

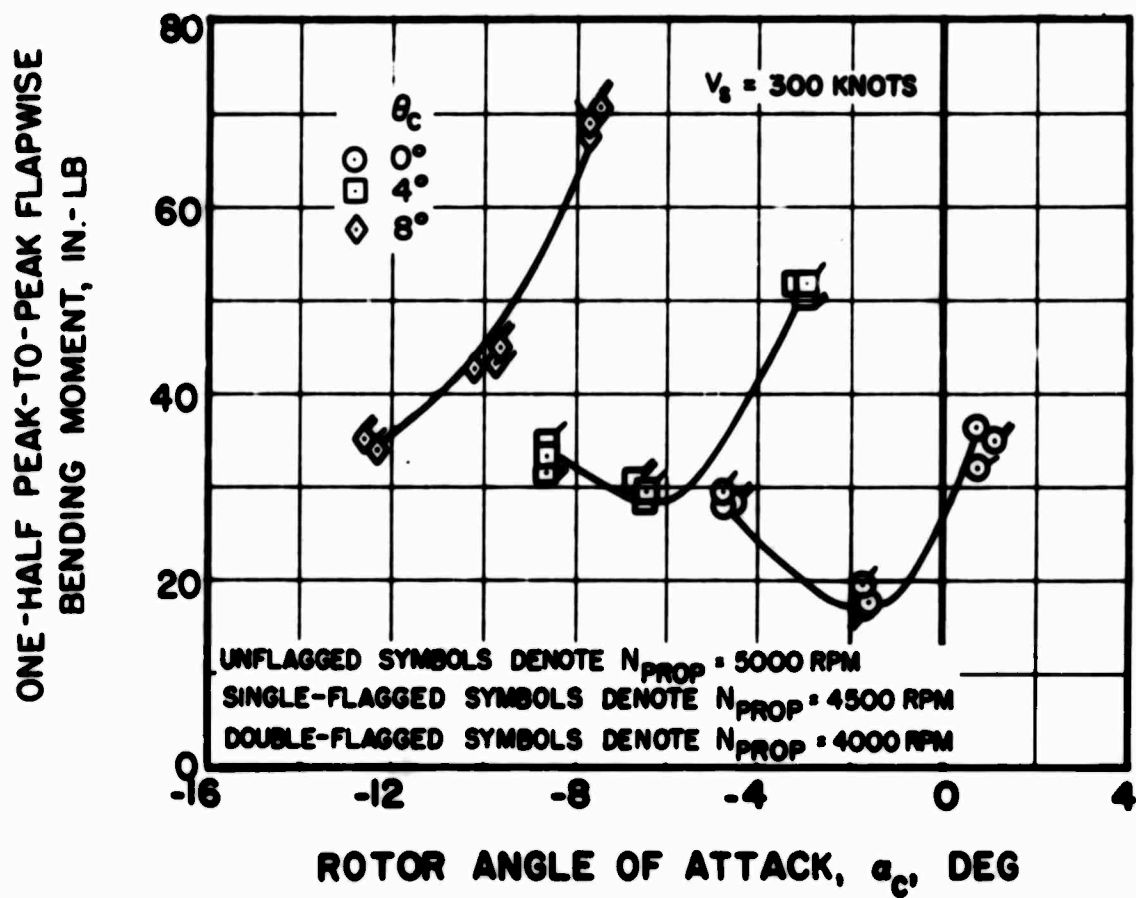


Figure 138. Effect of Pusher Propeller Thrust on Rotor Blade Flapwise Vibratory Moment Amplitudes at Various Rotor Angles of Attack and Collective Pitch Settings, Without Empennage, $V_s = 300$ Knots, 60%R.

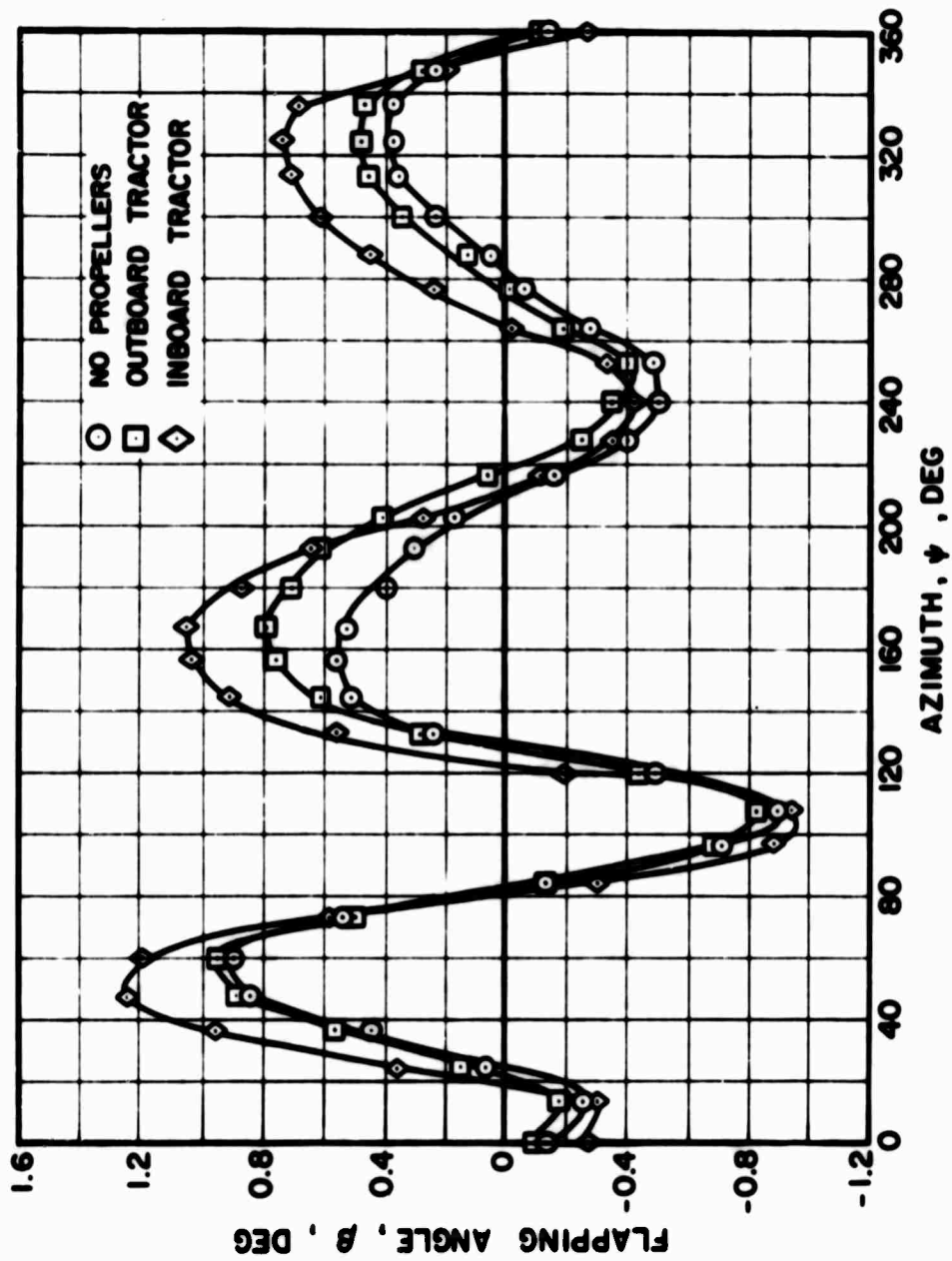


Figure 139. Effect of Tractor Propeller Location on Rotor Blade Flapping at $V_s = 300$ Knots, $\alpha_f = 4^\circ$, $\theta_c = 8^\circ$, $\beta_{75} = 41^\circ$.

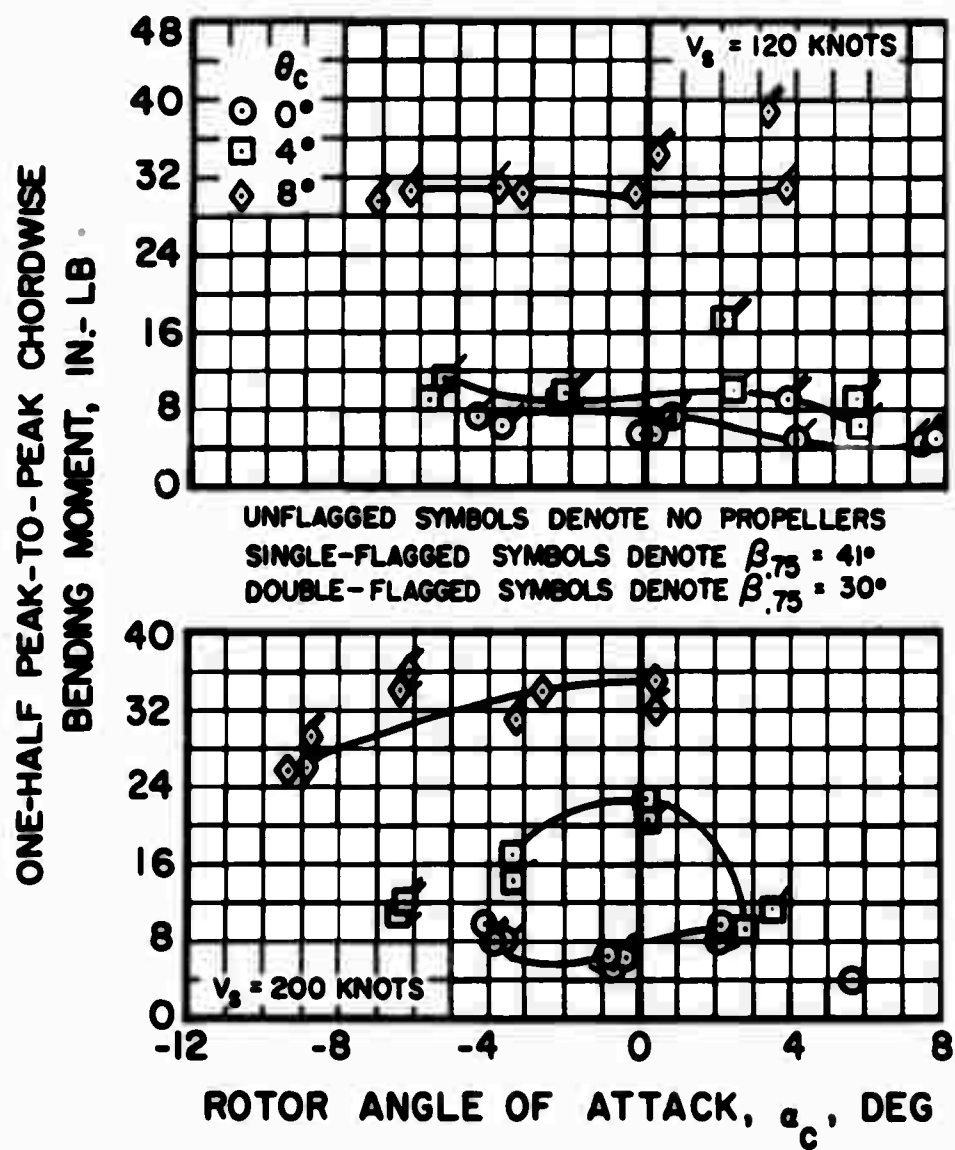


Figure 140. Effect of Inboard Tractor Propeller Thrust on Rotor Blade Chordwise Vibratory Moment Amplitudes at Various Rotor Angles of Attack and Collective Pitch Settings and Two Forward Speeds, 60%R.

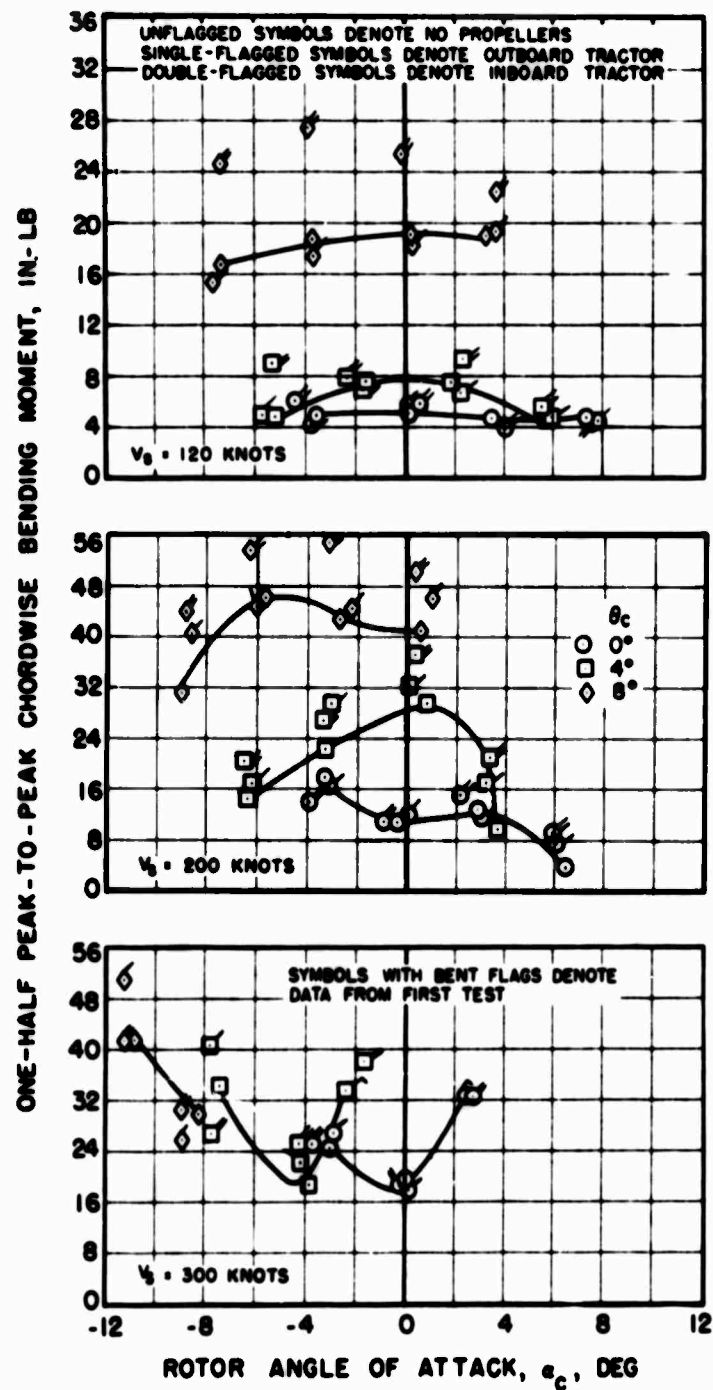


Figure 141. Effect of Tractor Propeller Location on Rotor Blade Chordwise Vibratory Moment Amplitudes at Various Rotor Angles of Attack, Collective Pitch Settings and Forward Speeds, 30%R, $\beta_{75} = 41^\circ$.

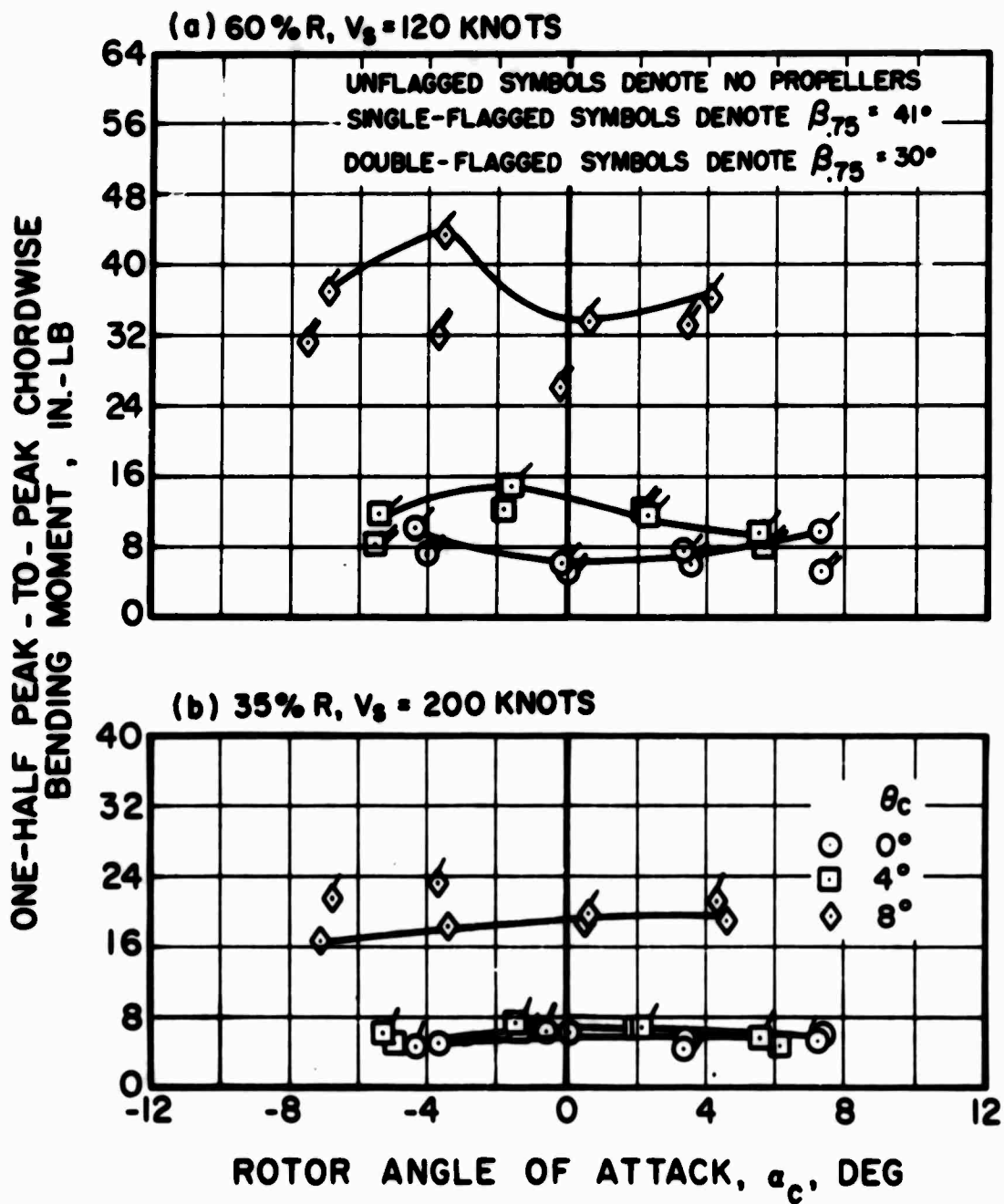


Figure 142. Effect of Pusher Propeller Thrust on Rotor Blade Chordwise Vibratory Moment Amplitudes at Various Rotor Angles of Attack and Collective Pitch Settings and Two Forward Speeds, With Empennage.

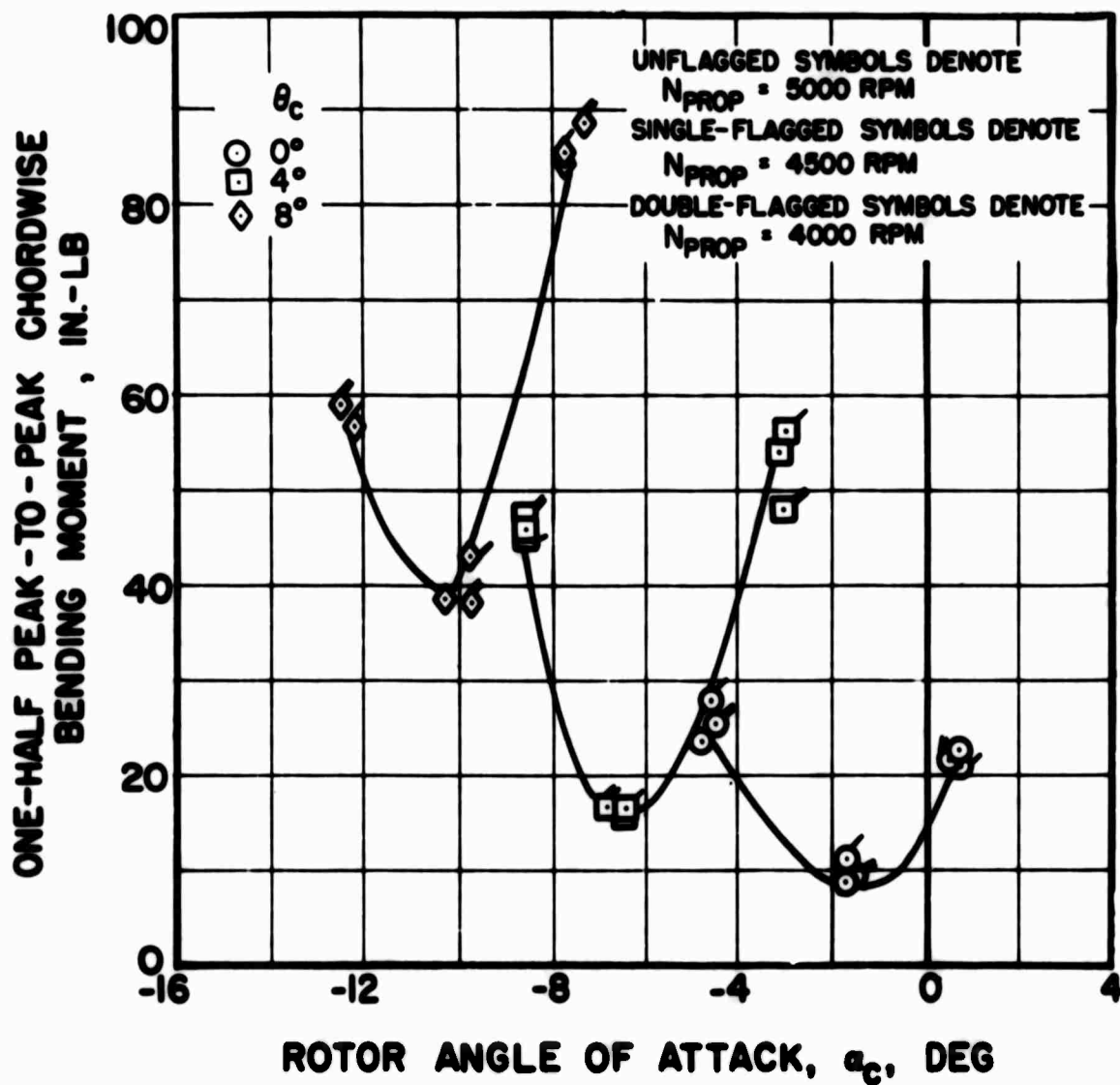


Figure 143. Effect of Pusher Propeller Thrust on Rotor Blade Chordwise Vibratory Moment Amplitudes at Various Rotor Angles of Attack and Collective Pitch Settings, Without Empennage, $V_s = 300$ Knots, $\beta_{.75} = 41^\circ$.

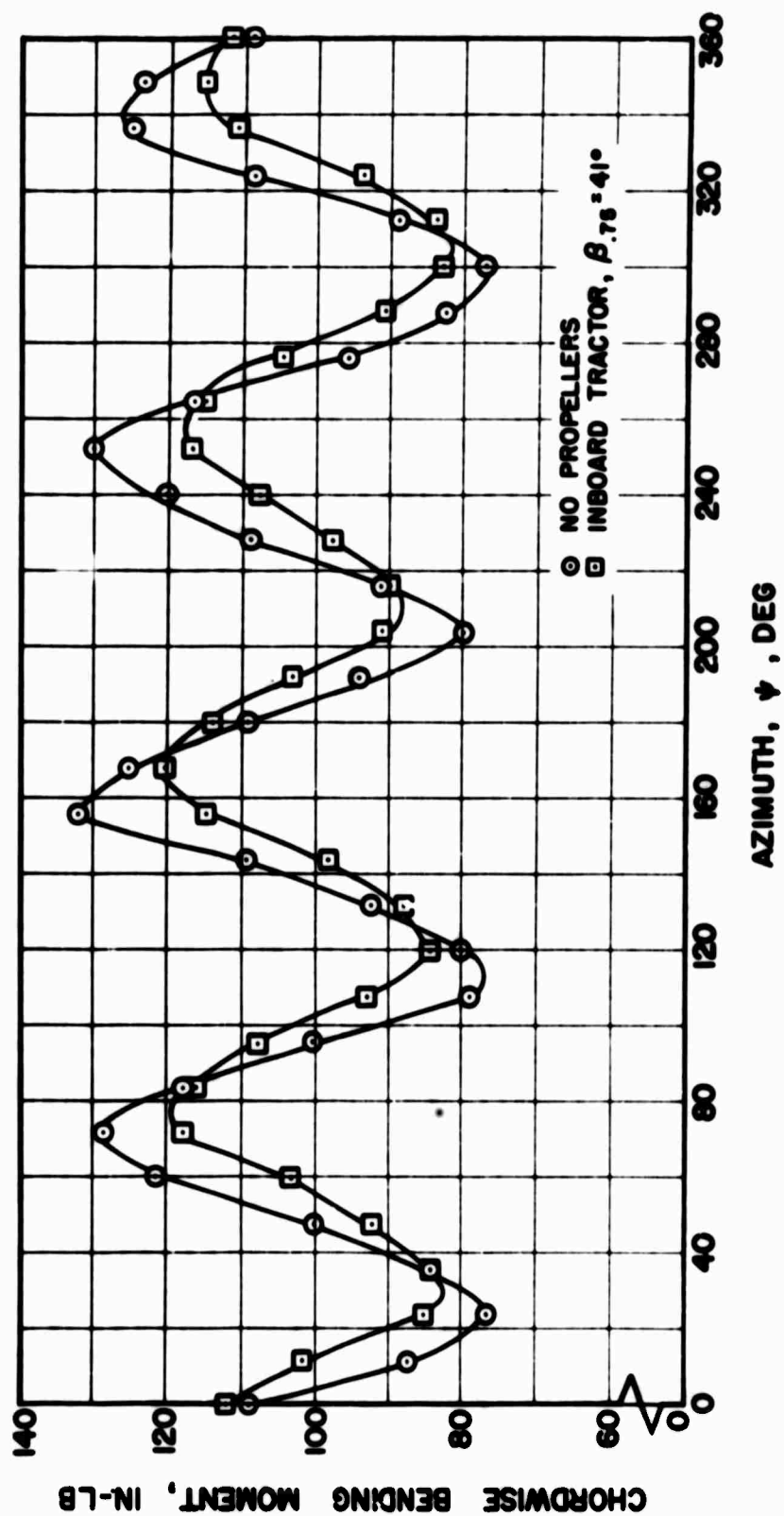


Figure 144. Effect of Inboard Tractor Propeller Thrust on Azimuthal Variation of Rotor Blade Chordwise Moment at $V_s = 120$ Knots, $\alpha_f = 0^\circ$, $\theta_c = 8^\circ$, $30\%R$, $\beta_{75} = 41^\circ$.

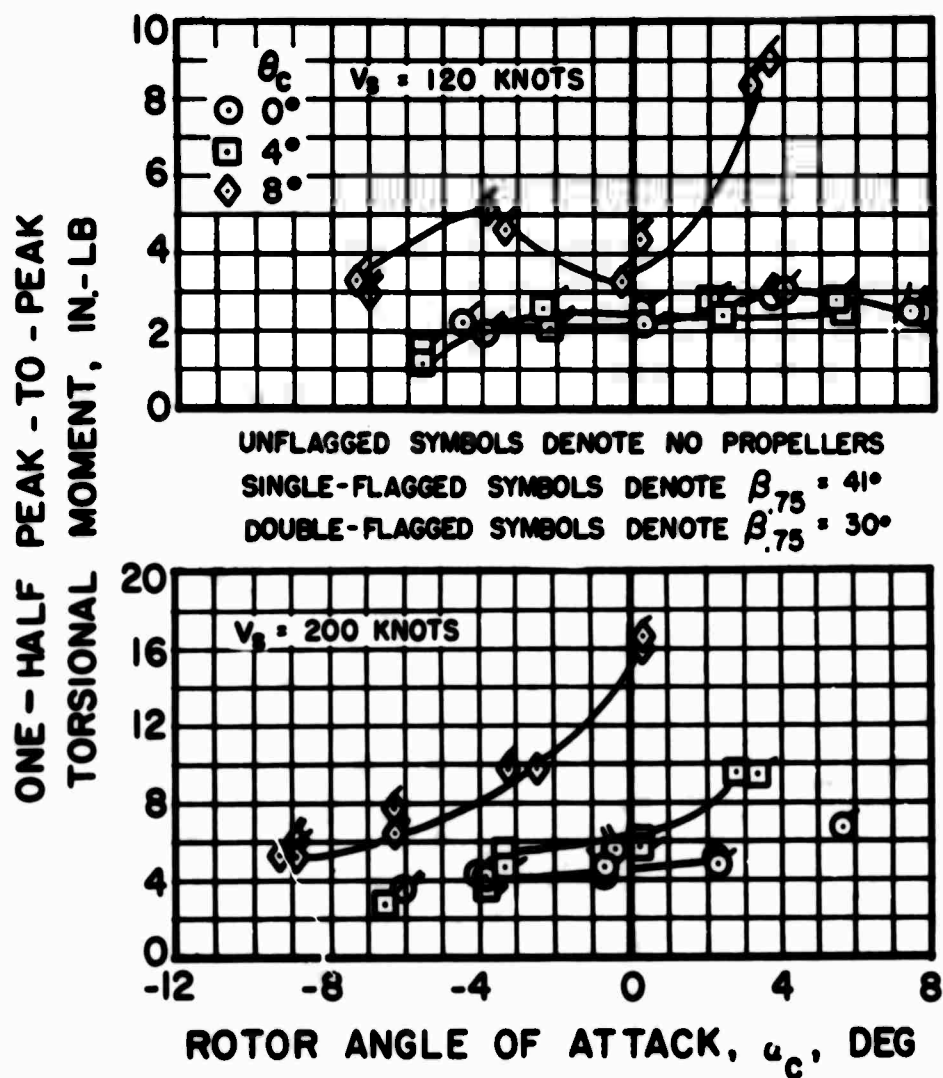


Figure 145. Effect of Inboard Tractor Propeller Thrust on Rotor Blade Torsional Vibratory Moment Amplitudes at Various Rotor Angles of Attack and Collective Pitch Settings and Two Forward Speeds, 18%R.

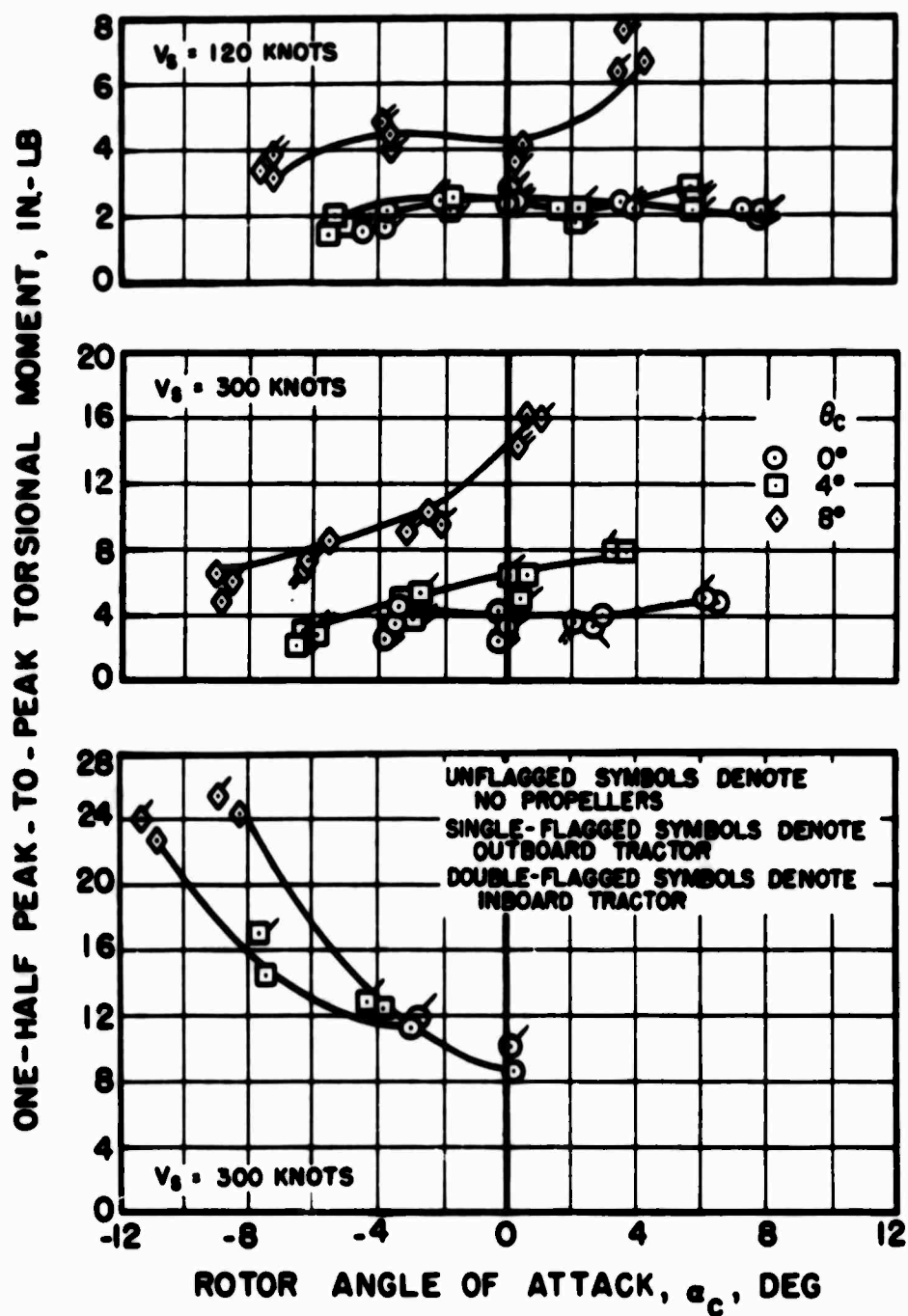


Figure 146. Effect of Tractor Propeller Location on Rotor Blade Torsional Vibratory Moment Amplitudes at Various Rotor Angles of Attack, Collective Pitch Settings, and Forward Speeds, 35%R, $\beta_{.75} = 41^\circ$.

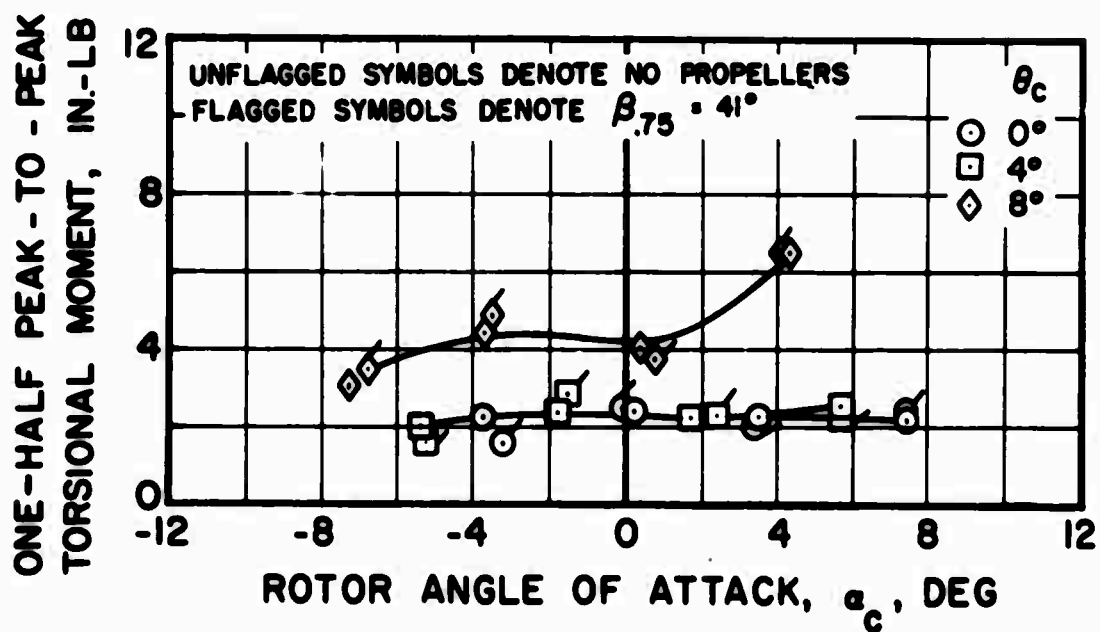


Figure 147. Effect of Pusher Propeller Thrust on Rotor Blade Torsional Vibratory Moment Amplitudes at Various Rotor Angles of Attack and Collective Pitch Settings, With Empennage, $V_s = 120$ Knots, 35%R.

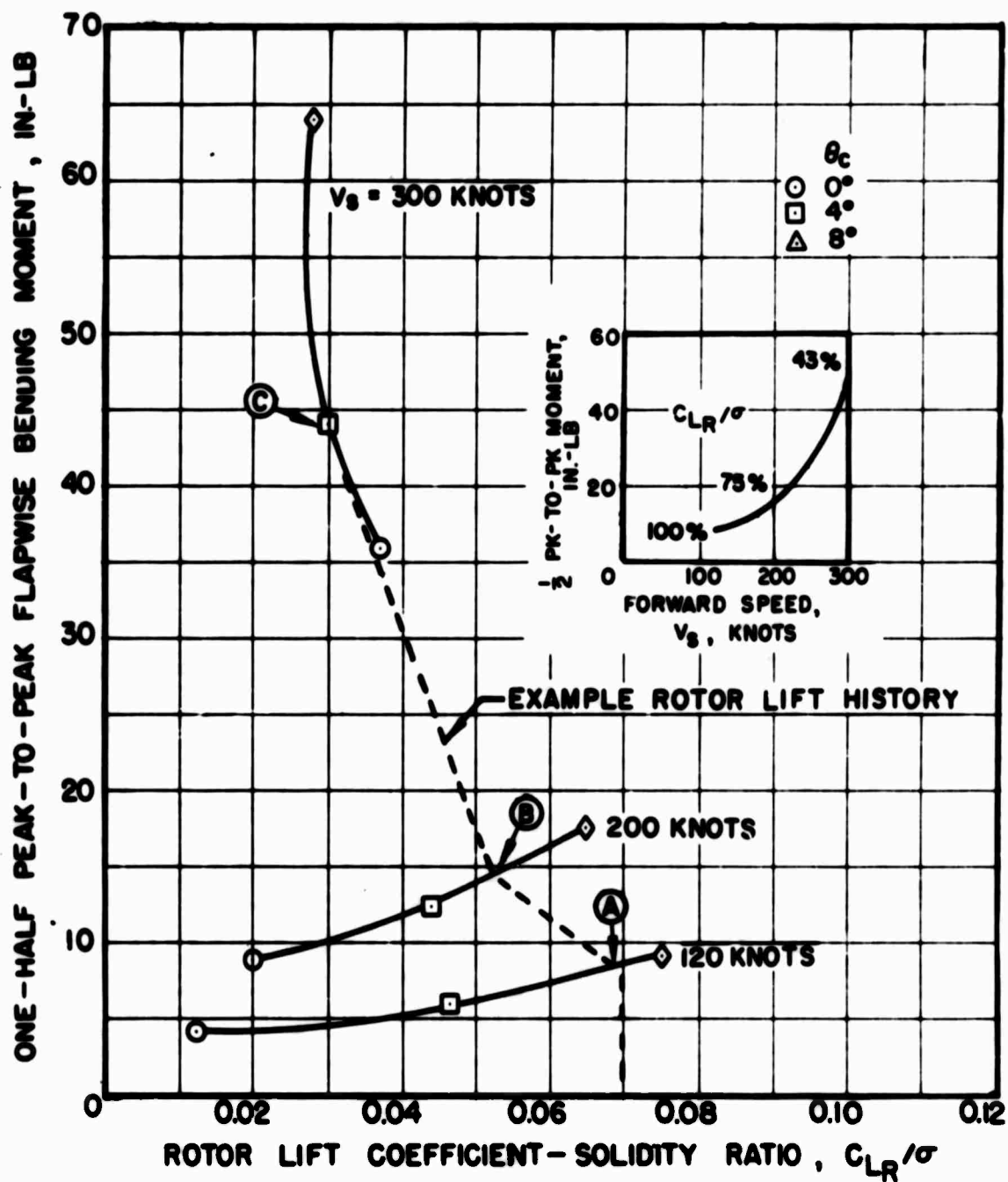


Figure 148. Effect of Forward Speed, Rotor Lift, and Collective Pitch Setting on Rotor Blade Flapwise Vibratory Moment Amplitudes With the Inboard Tractor Propellers, $\beta_{75} = 41^\circ$, $\alpha_f = 4^\circ$, 60%R.

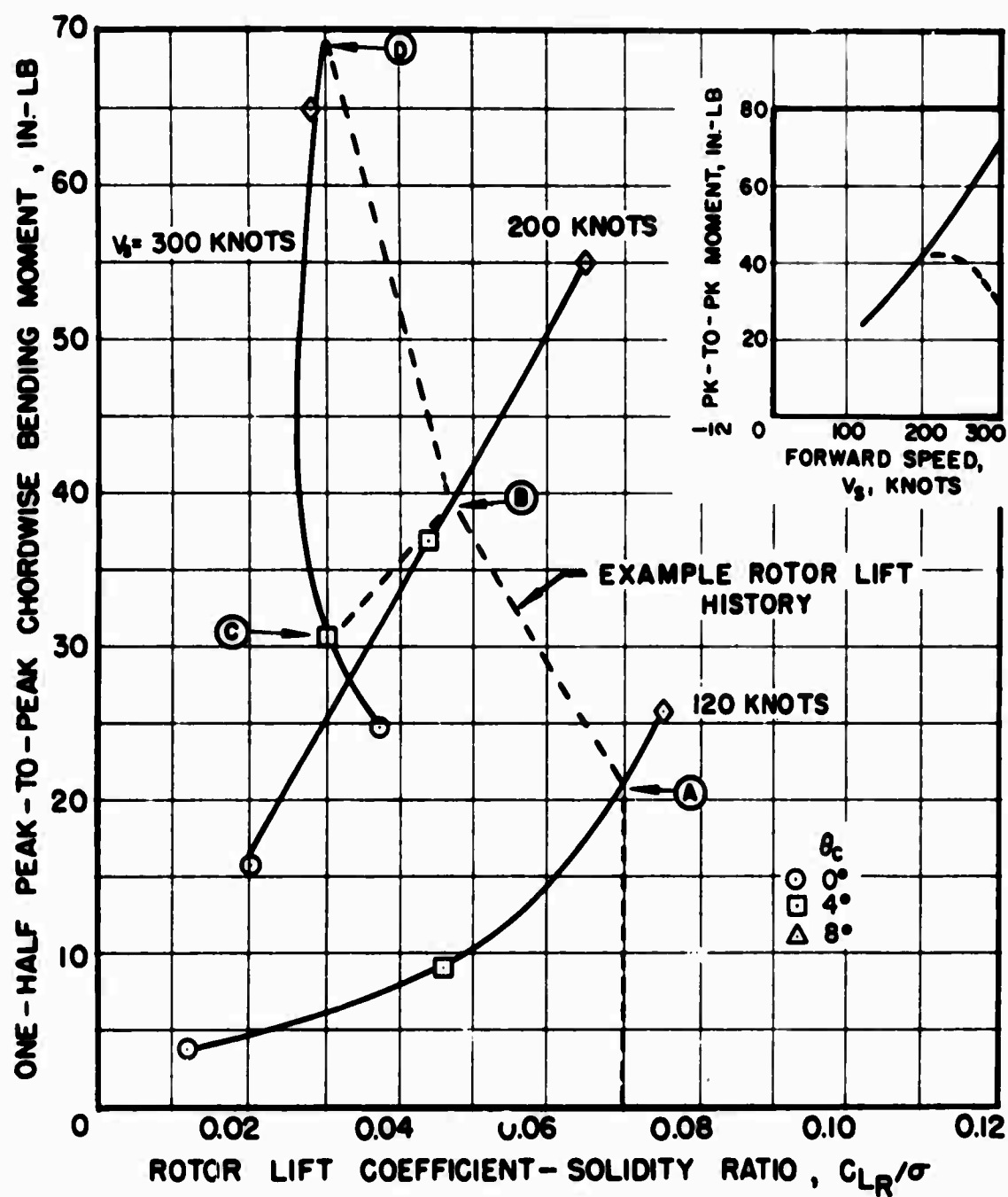


Figure 149. Effect of Forward Speed, Rotor Lift, and Collective Pitch Setting on Rotor Blade Chordwise Vibratory Moment Amplitudes With the Inboard Tractor Propellers, $\beta_{75} = 41^\circ$, $\alpha_f = 4^\circ$, 30%R.

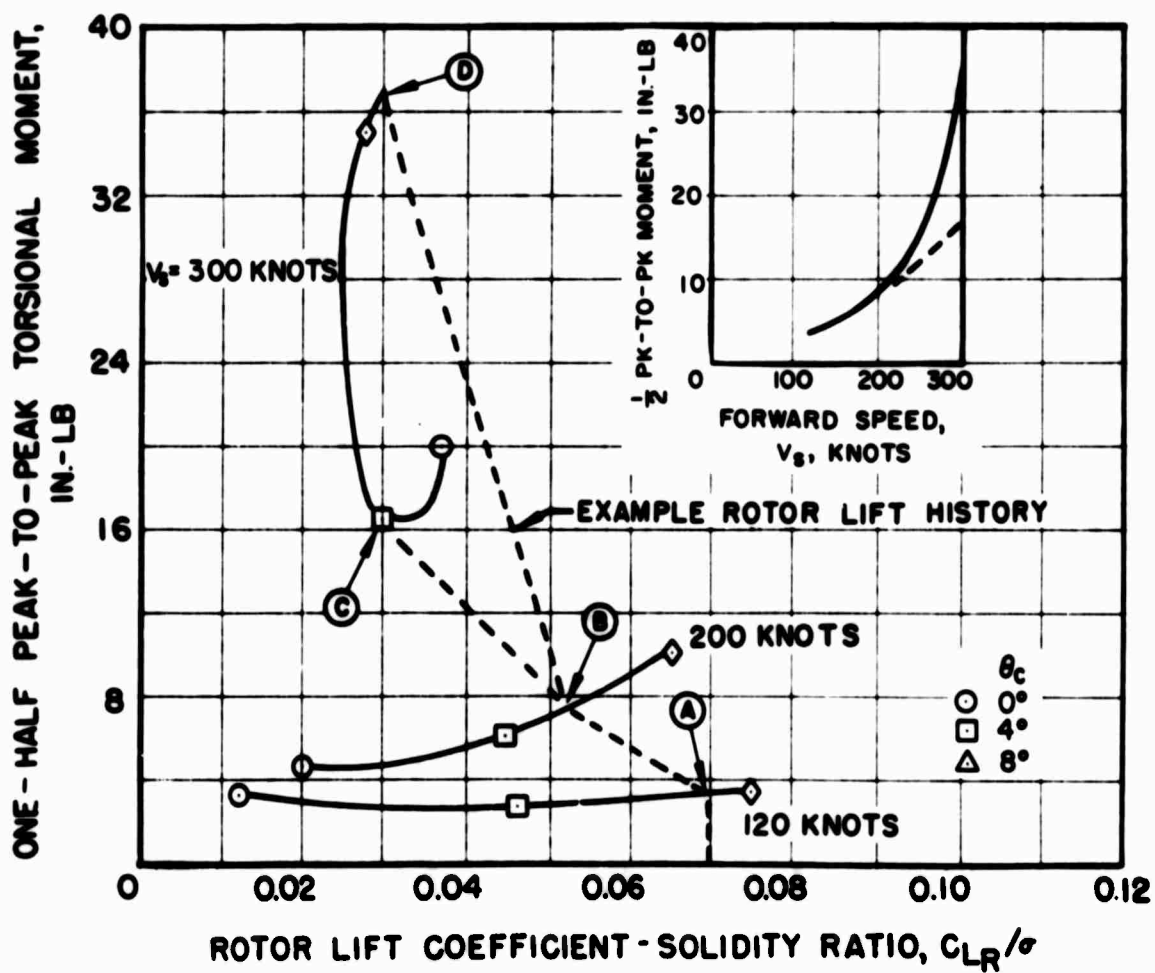


Figure 150. Effect of Forward Speed, Rotor Lift, and Collective Pitch Setting on Rotor Blade Torsional Vibratory Moment Amplitudes With the Inboard Tractor Propellers, $\beta_{.75} = 41^\circ$, $\alpha_f = 4^\circ$, 18%R.

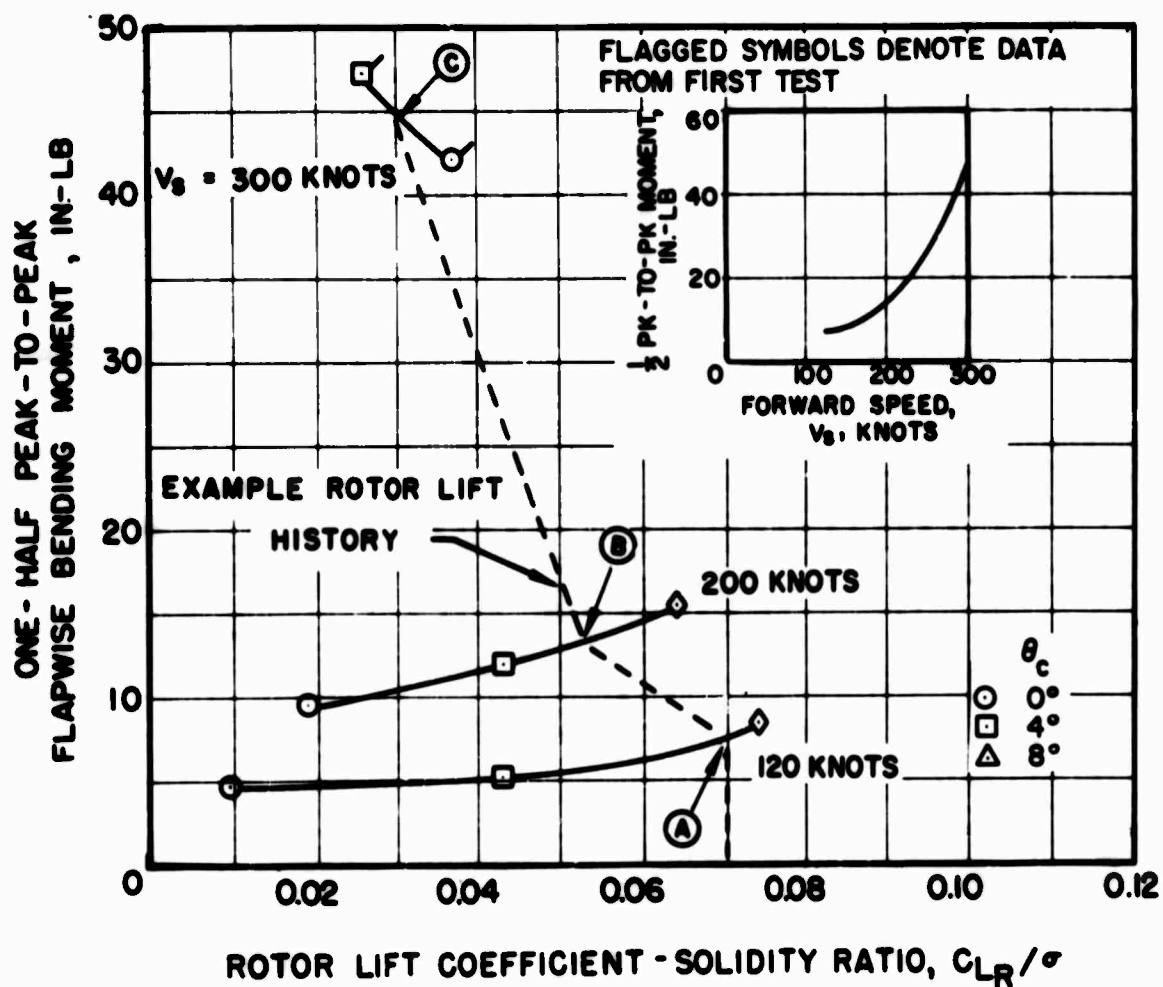


Figure 151. Effect of Forward Speed, Rotor Lift, and Collective Pitch Setting on Rotor Blade Flapwise Vibratory Moment Amplitudes Without Propellers, $\alpha_f = 4^\circ$, 60%R.

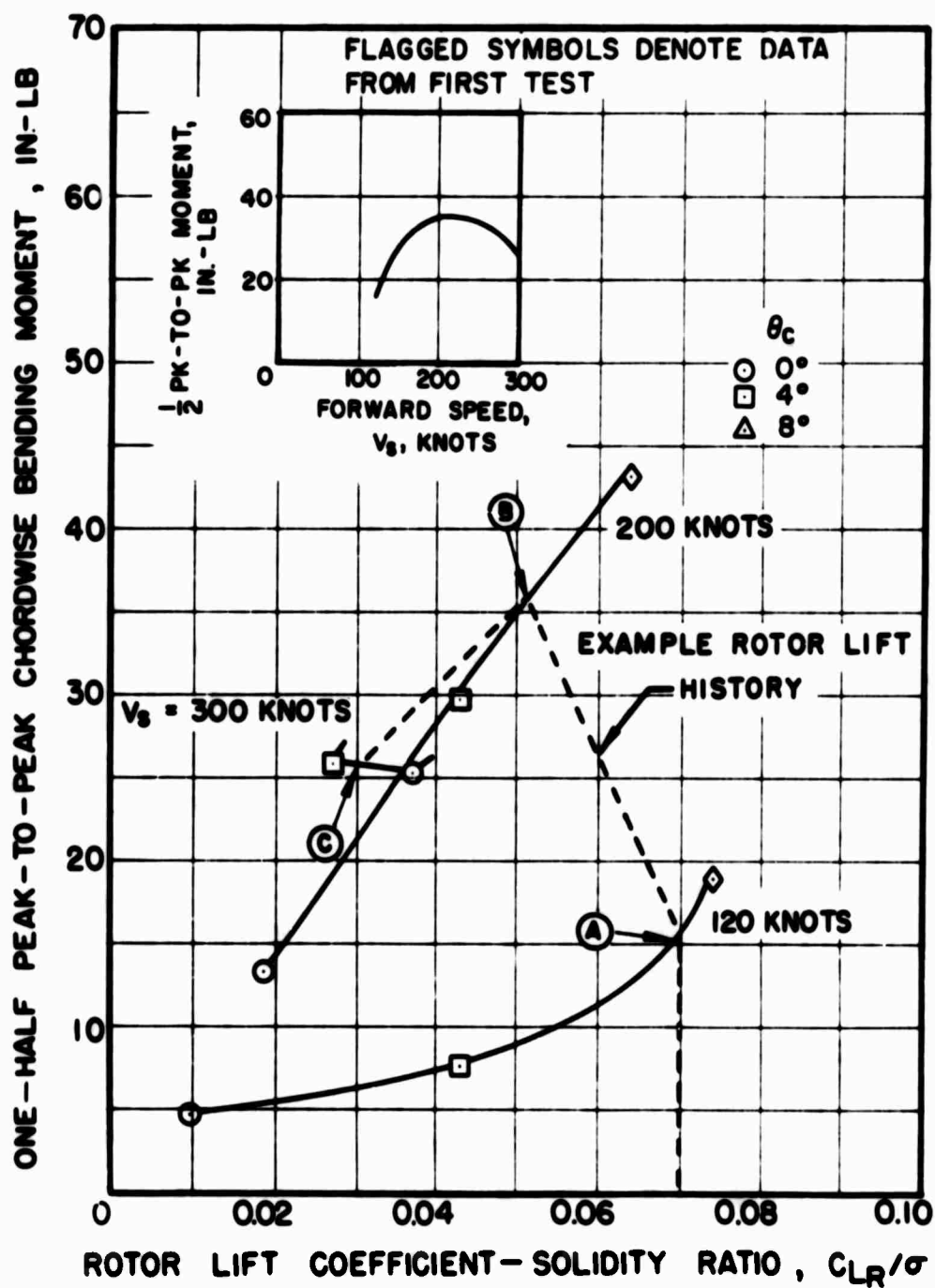


Figure 152. Effect of Forward Speed, Rotor Lift, and Collective Pitch Setting on Rotor Blade Chordwise Vibratory Moment Amplitudes Without Propellers, $\alpha_f = 4^\circ$, 30%R.

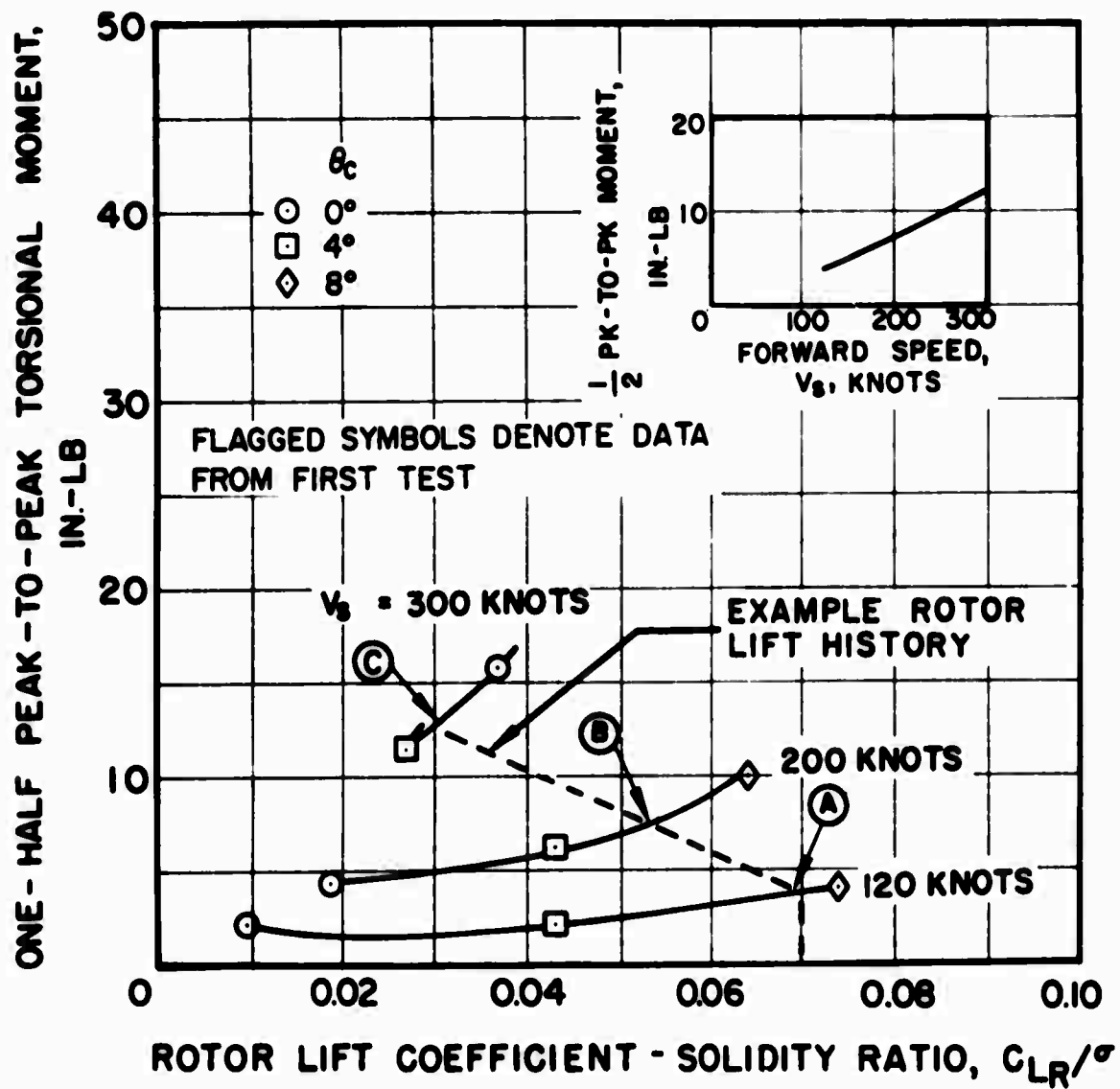
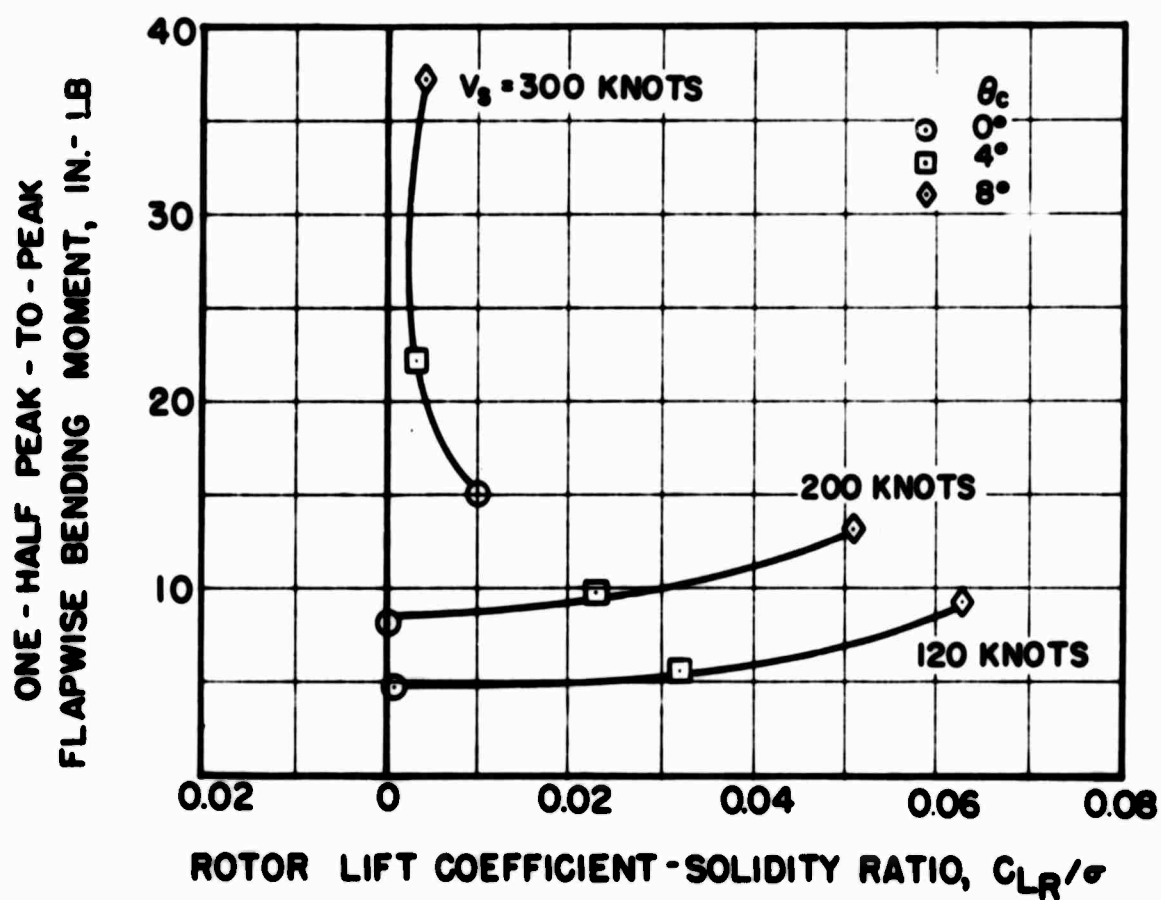
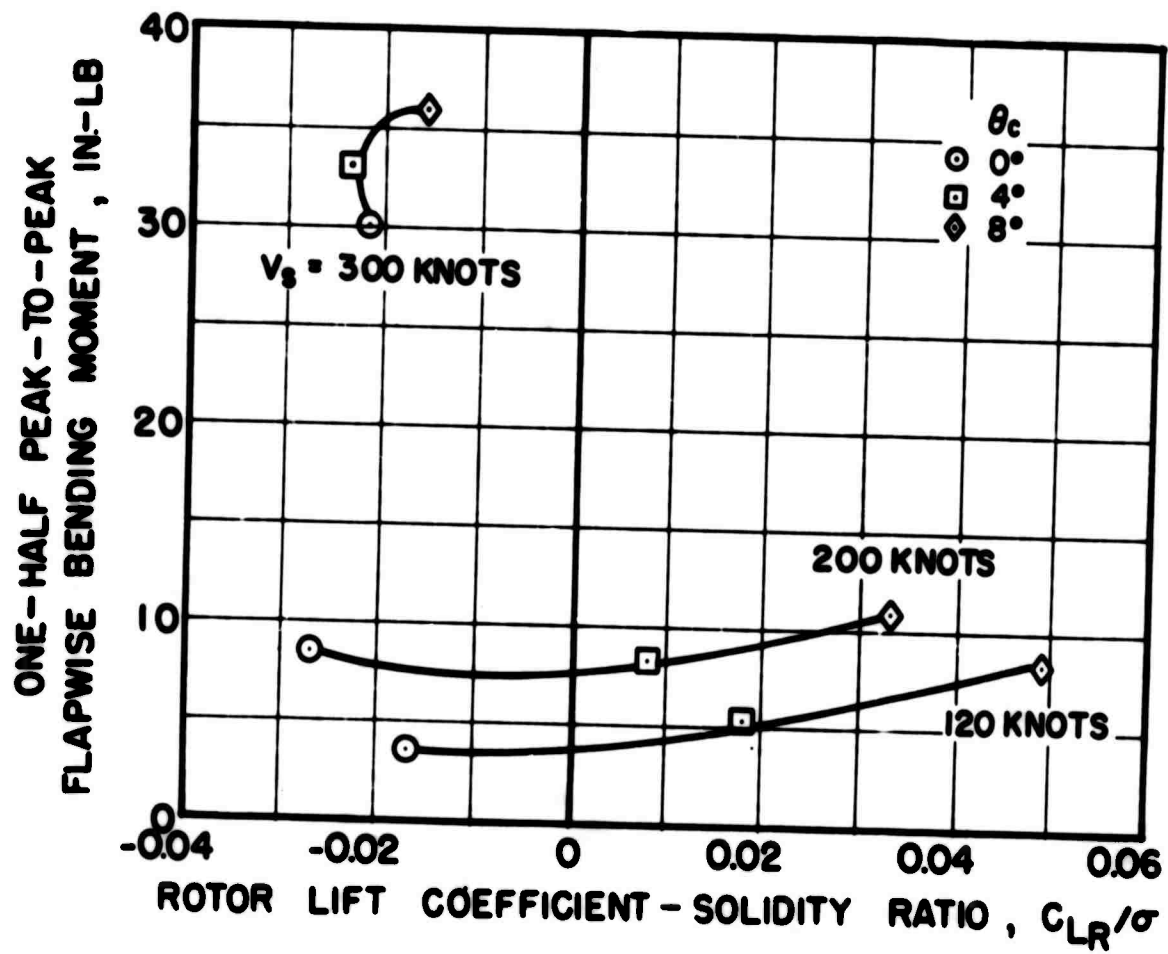


Figure 153. Effect of Forward Speed, Rotor Lift, and Collective Pitch Setting on Rotor Blade Torsional Moment Amplitudes Without Propellers, $\alpha_f = 4^\circ$, 35%R.



(a) $\alpha_f = 0^\circ$

Figure 154. Effect of Forward Speed, Rotor Lift, Collective Pitch Setting, and Fuselage Angle of Attack on Rotor Blade Flapwise Vibratory Moment Amplitudes With Inboard Tractor Propellers, $\beta_{75} = 41^\circ$, 60%R.



(b) $\alpha_f = -4^\circ$

Figure 154. Concluded.

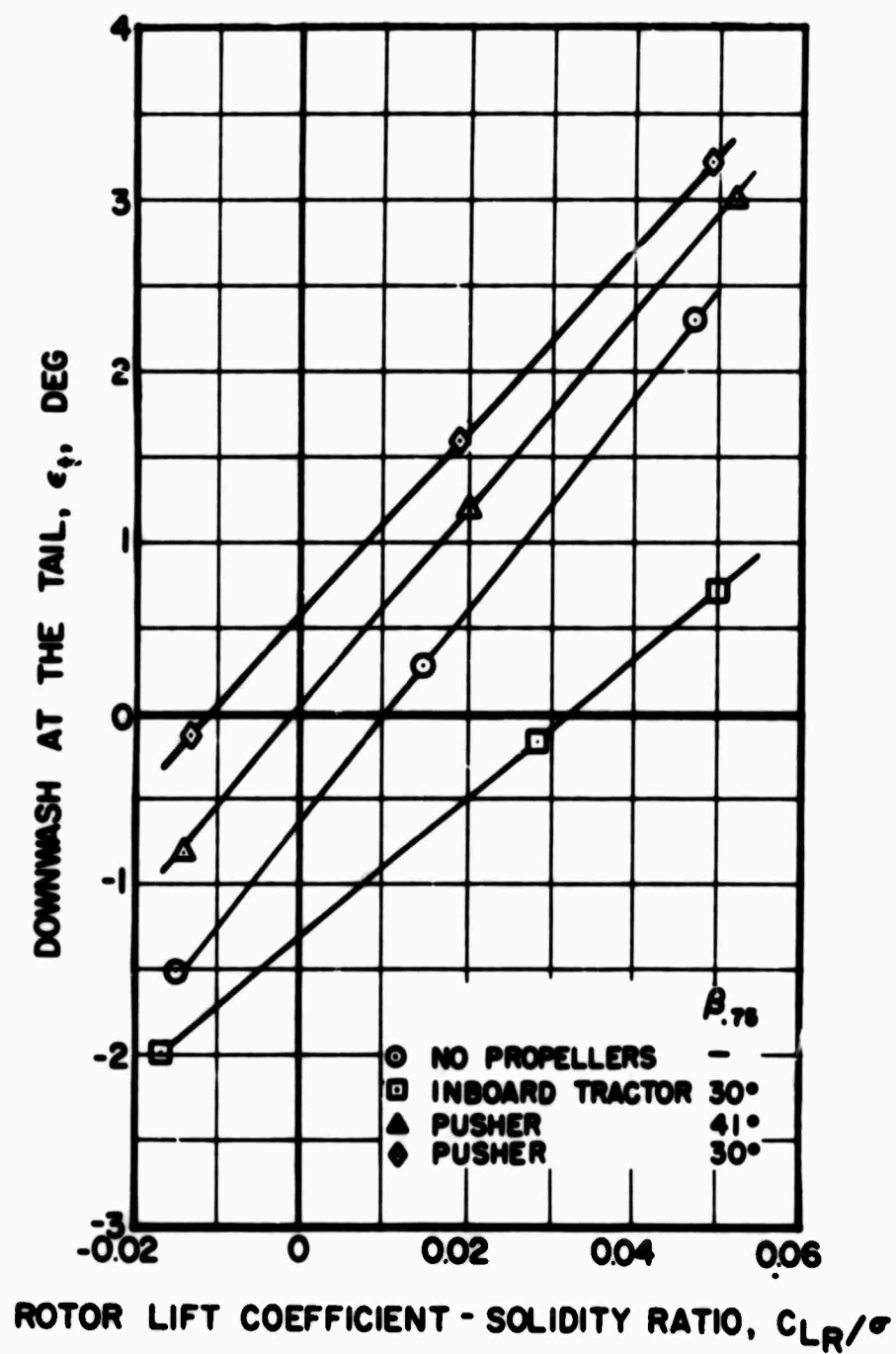


Figure 155. Effect of Propeller Thrust and Rotor Lift on Downwash Angle at the Tail for the Pusher and Inboard Tractor Propellers at $V_s = 120$ Knots, $\alpha_f = -4^\circ$.

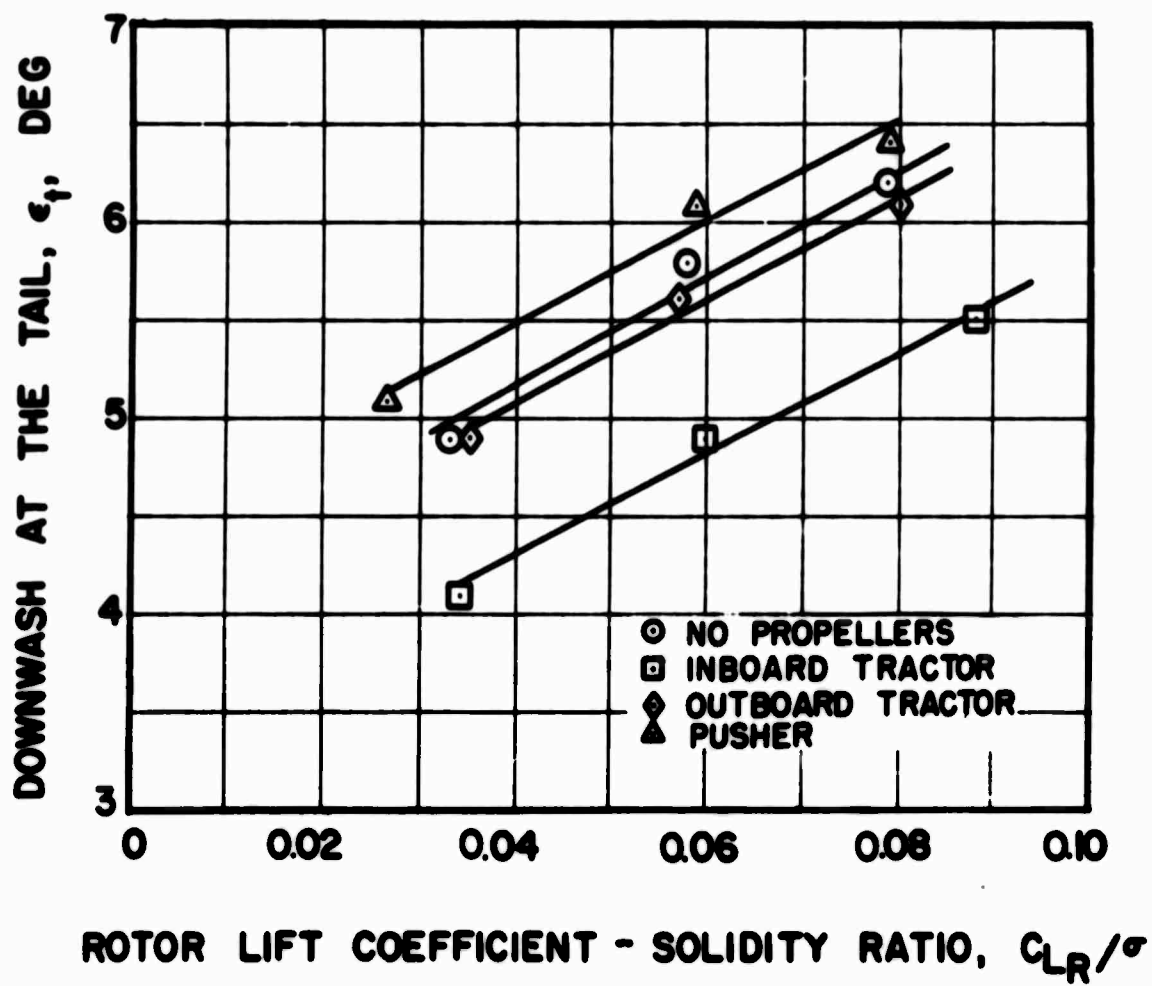
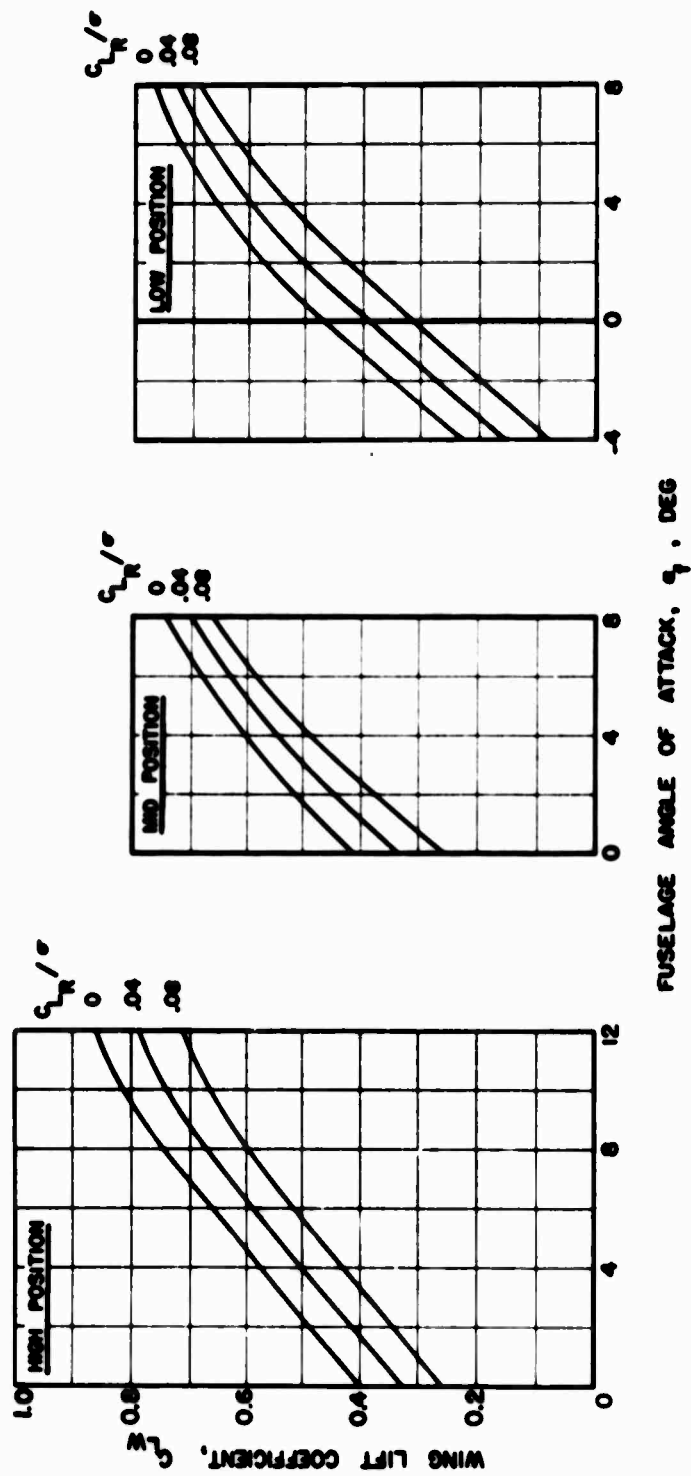


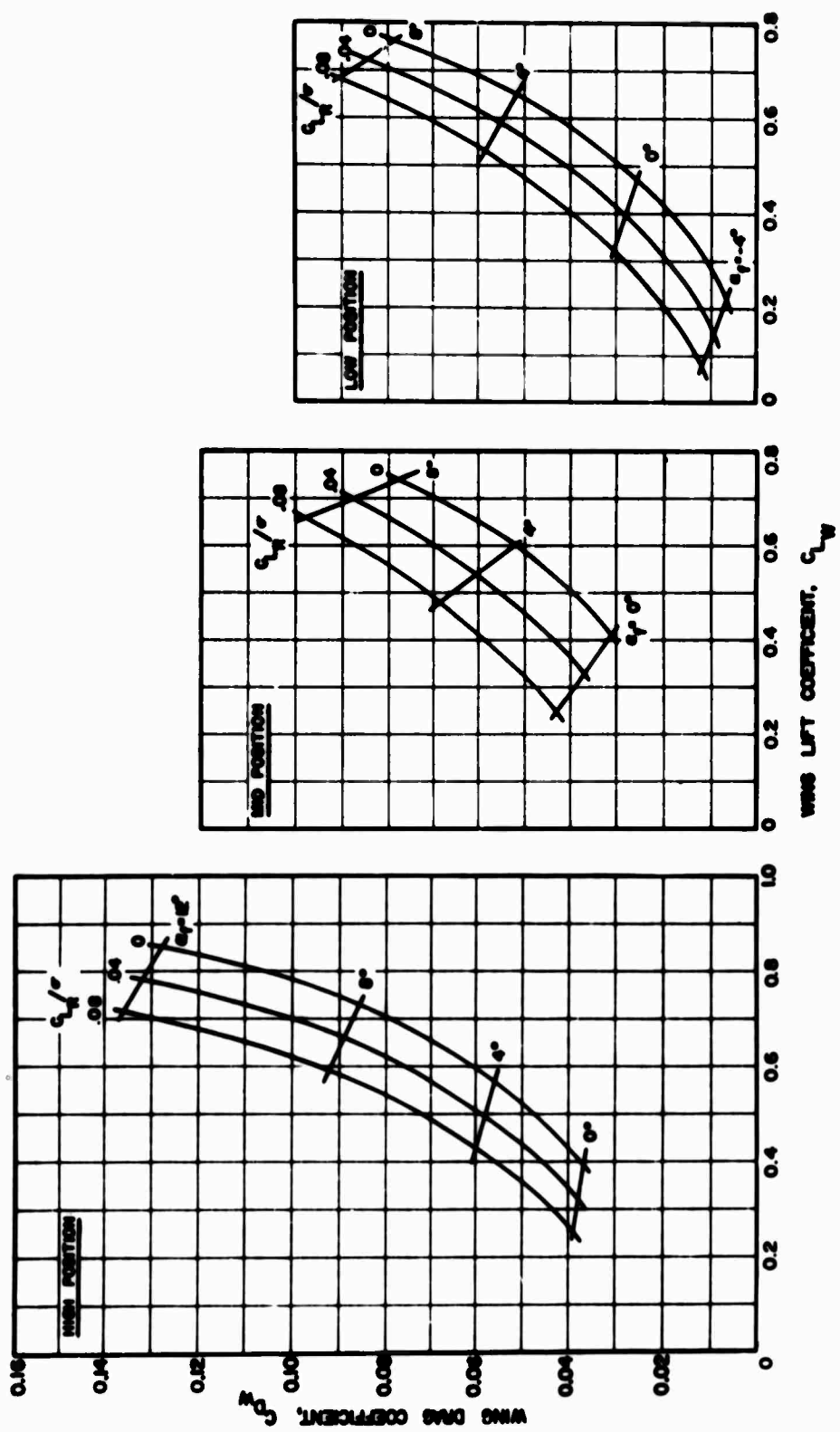
Figure 156. Effect of Propeller Location and Rotor Lift on Downwash Angle at the Tail at $V_s = 200$ Knots, $\alpha_f = 8^\circ$, $\beta_{.75} = 41^\circ$.

APPENDIX I WING AERODYNAMIC CHARACTERISTICS



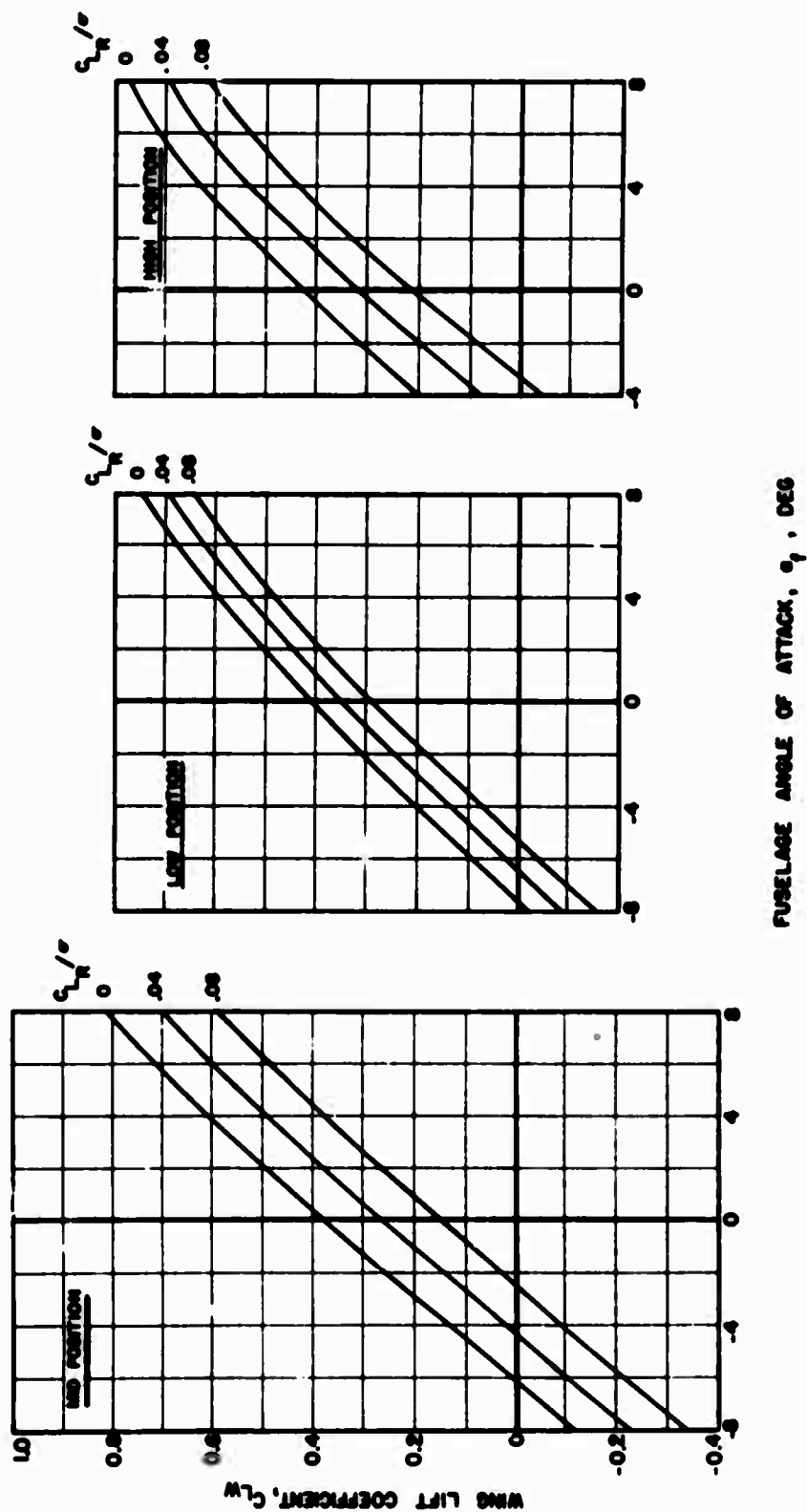
(a) Wing Lift

Figure 157. Effect of Fuselage Angle of Attack and Wing Position on Wing Lift and Drag at Various Rotor Lifts, Medium Wing, $V_S = 120$ Knots.



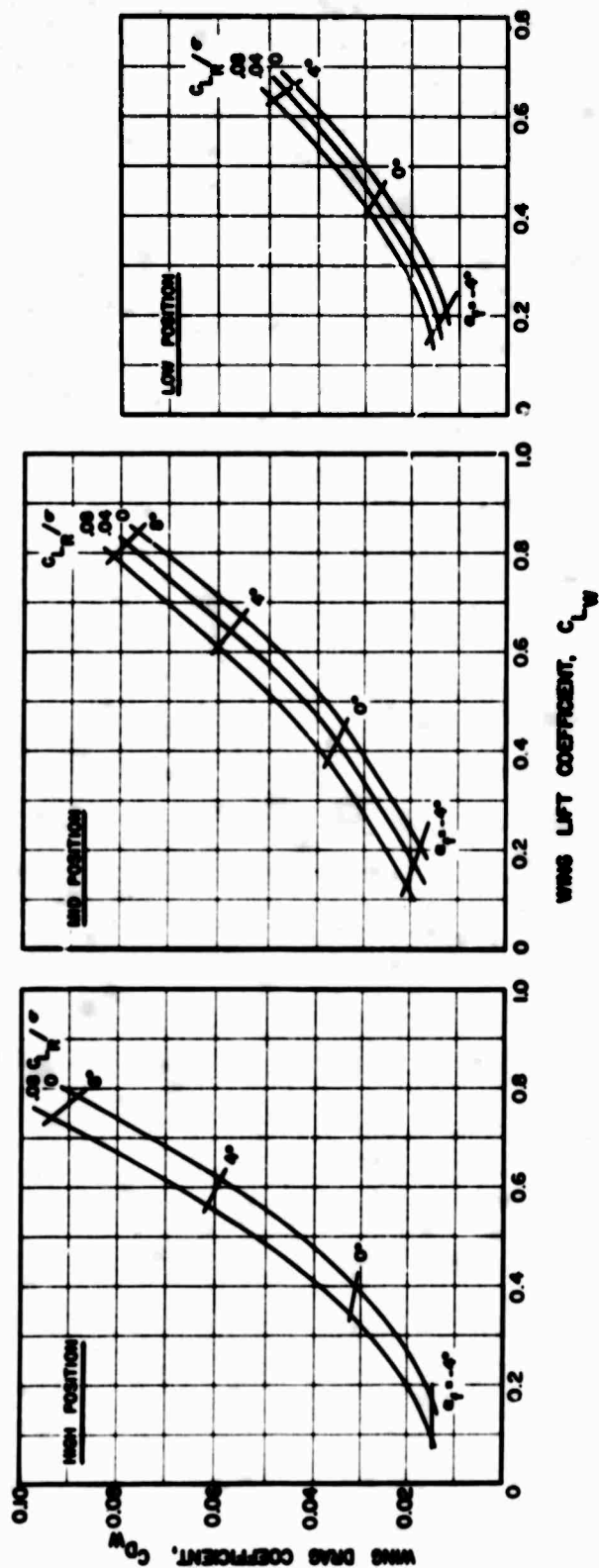
(b) Wing Lift - Drag Polar

Figure 157. Concluded.



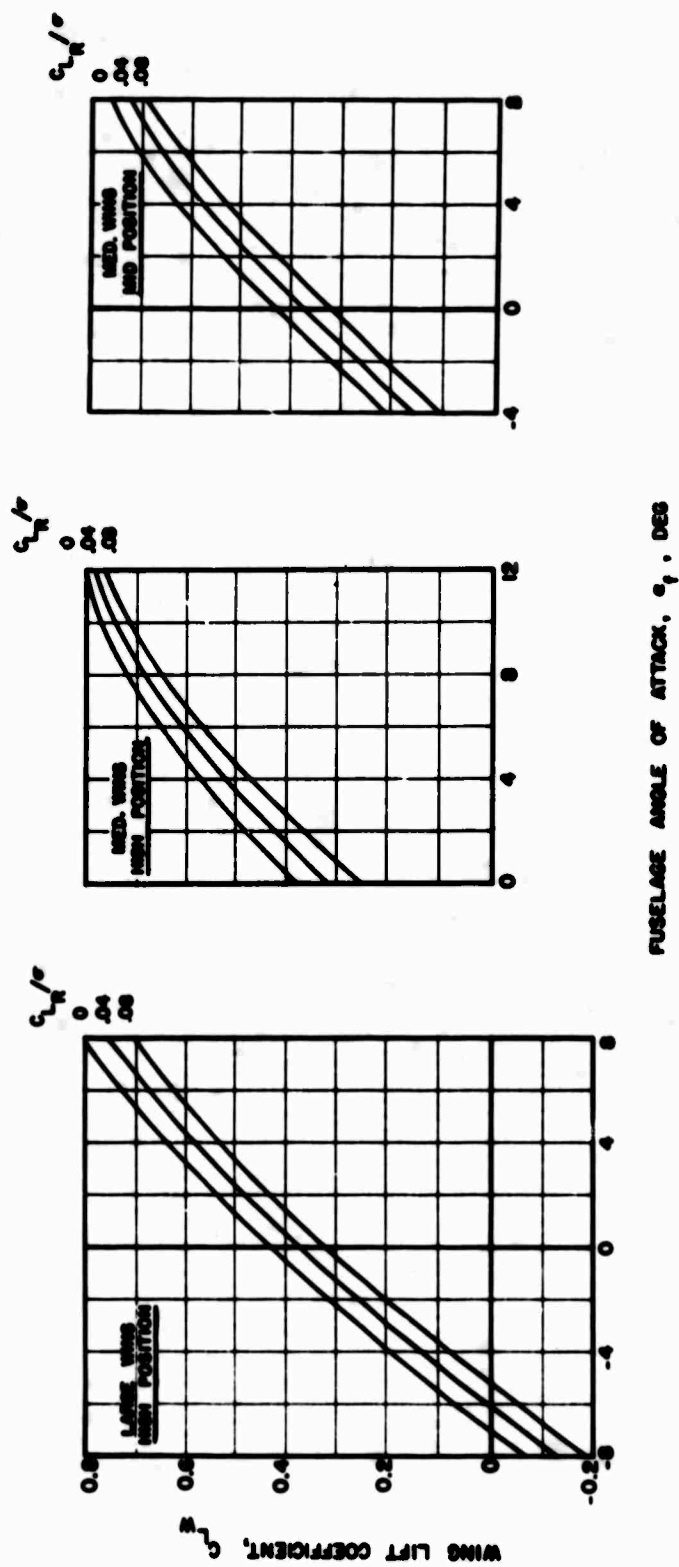
(a) Wing Lift

Figure 158. Effect of Fuselage Angle of Attack and Wing Position on Wing Lift and Drag at Various Rotor Lifts, Large Wing, $V_S = 120$ Knots.



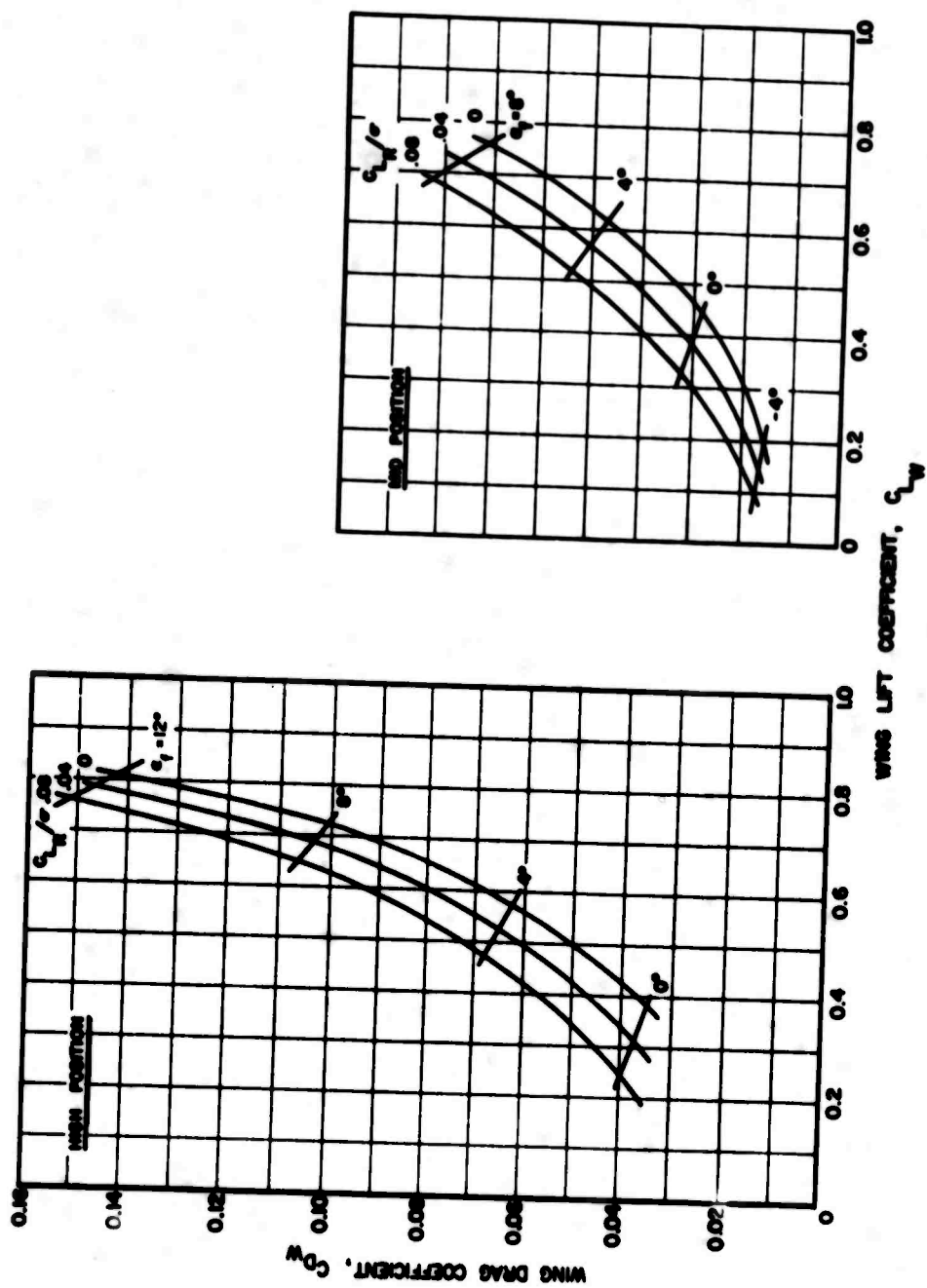
(b) Wing Lift - Drag Polar

Figure 158. Concluded.



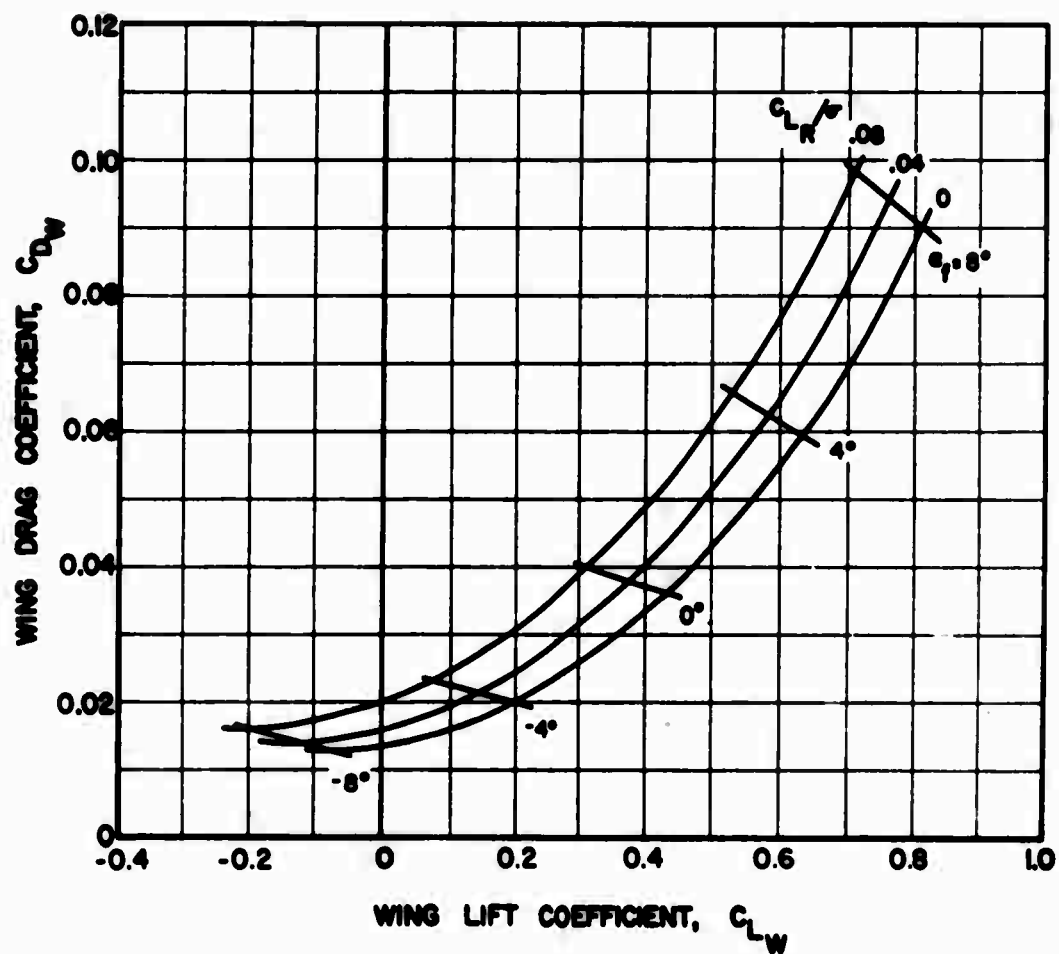
(a) Wing Lift

Figure 159. Effect of Fuselage Angle of Attack and Wing Position on Wing Lift and Drag at Various Rotor Lifts, Large and Medium Wings, $V_s = 160$ Knots.



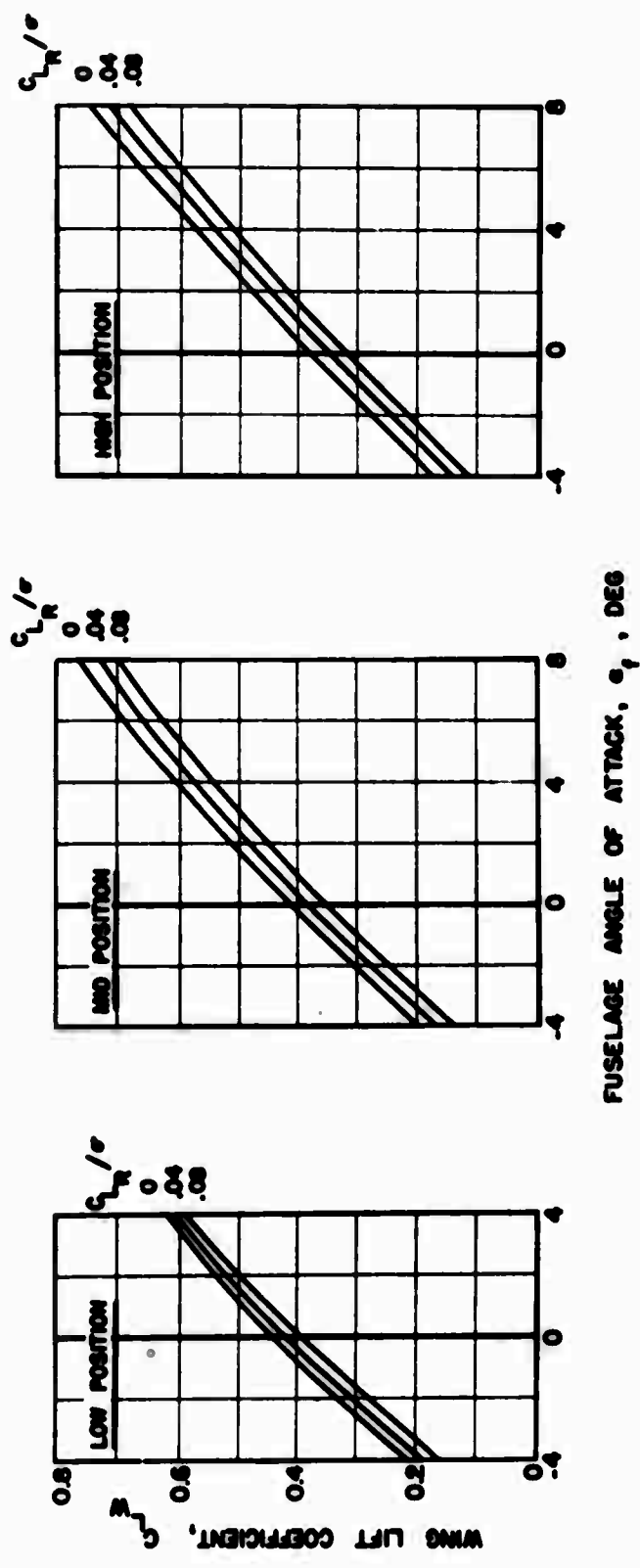
(b) Wing Lift - Drag Polar, Medium Wing

Figure 159. Continued.



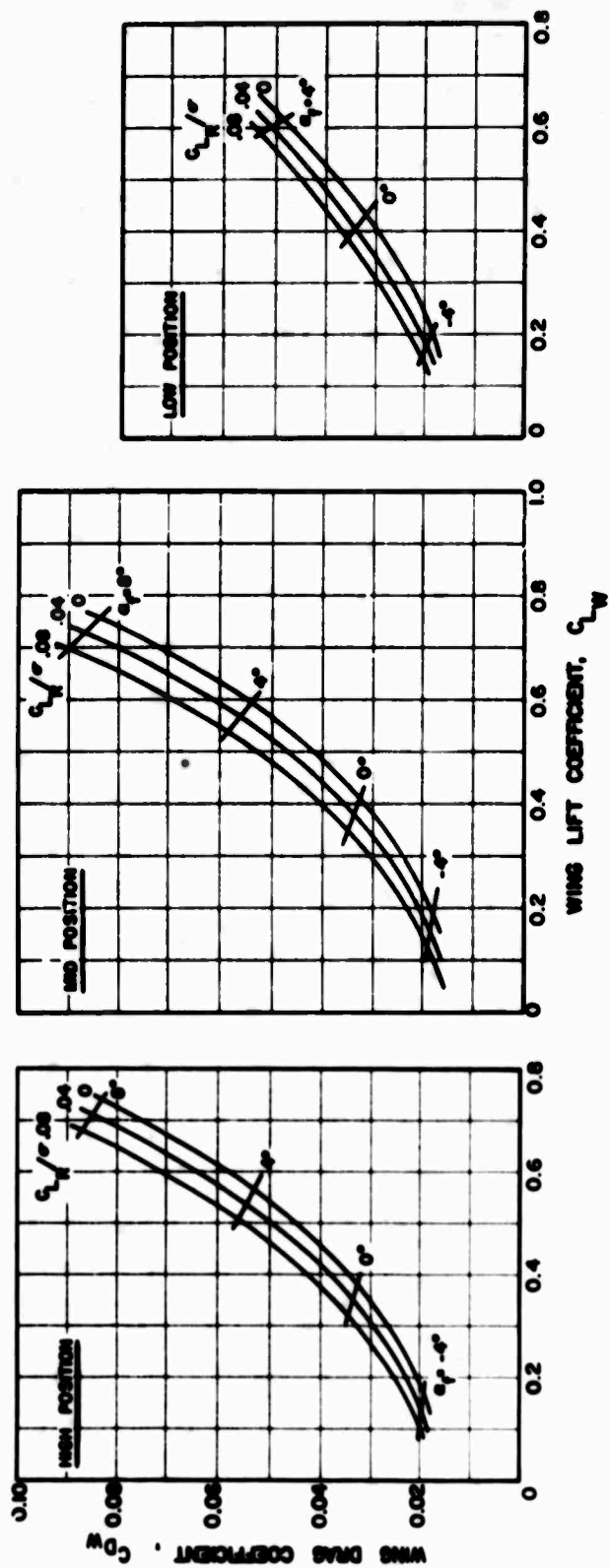
(c) Wing Lift - Drag Polar, Large Wing, High Position

Figure 159. Concluded.



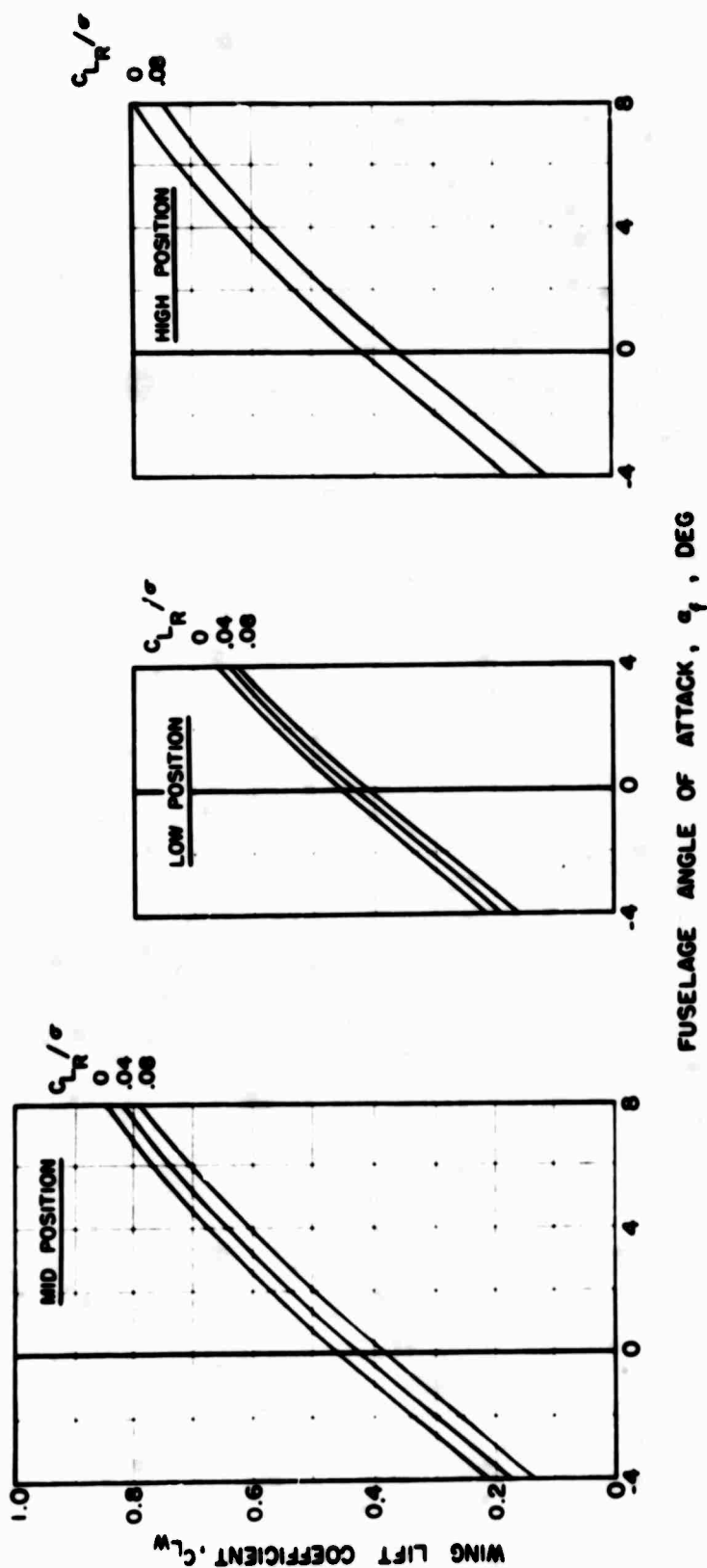
(a) Wing Lift

Figure 160. Effect of Fuselage Angle of Attack and Wing Position on Wing Lift and Drag at Various Rotor Lifts, Medium Wing, $V_s = 200$ Knots.



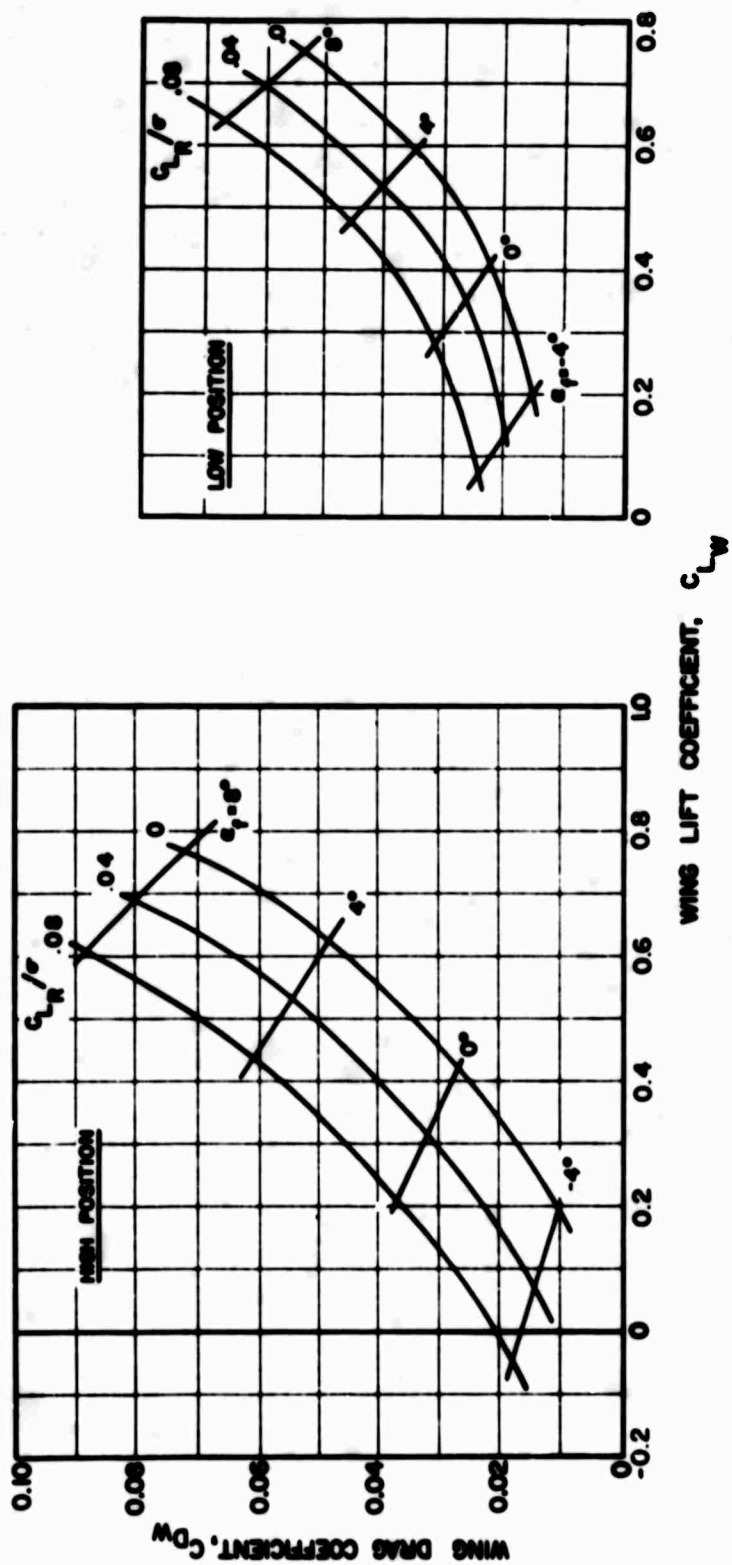
(b) Wing Lift - Drag Polar

Figure 160. Concluded.



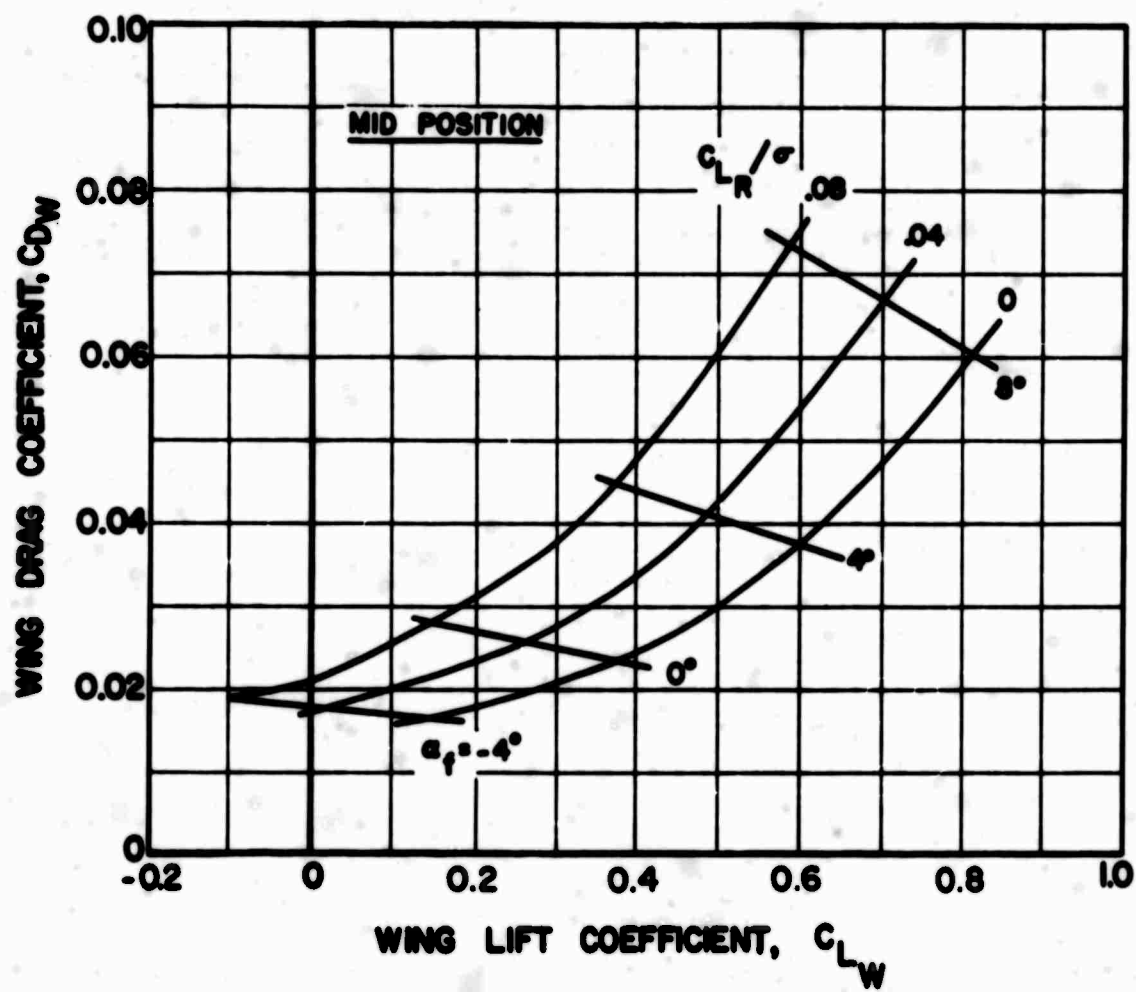
(a) Wing Lift

Figure 161. Effect of Fuselage Angle of Attack and Wing Position on Wing Lift and Drag at Various Rotor Lifts, Large Wing, $V_S = 200$ Knots.



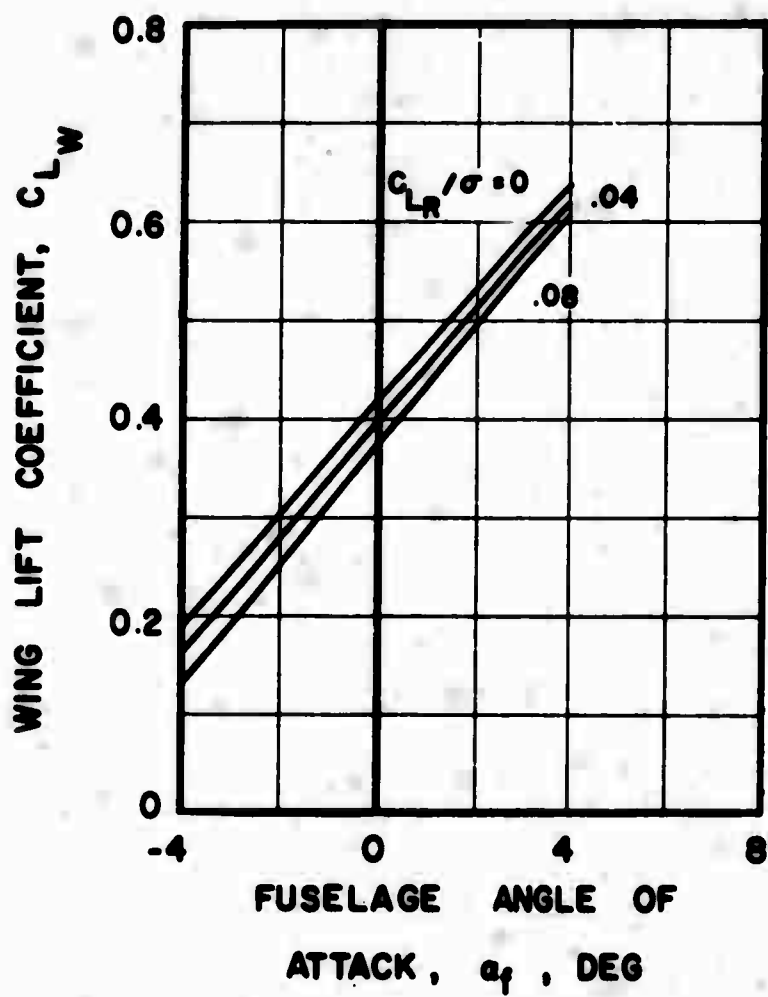
(b) Wing Lift - Drag Polar

Figure 161. Continued.



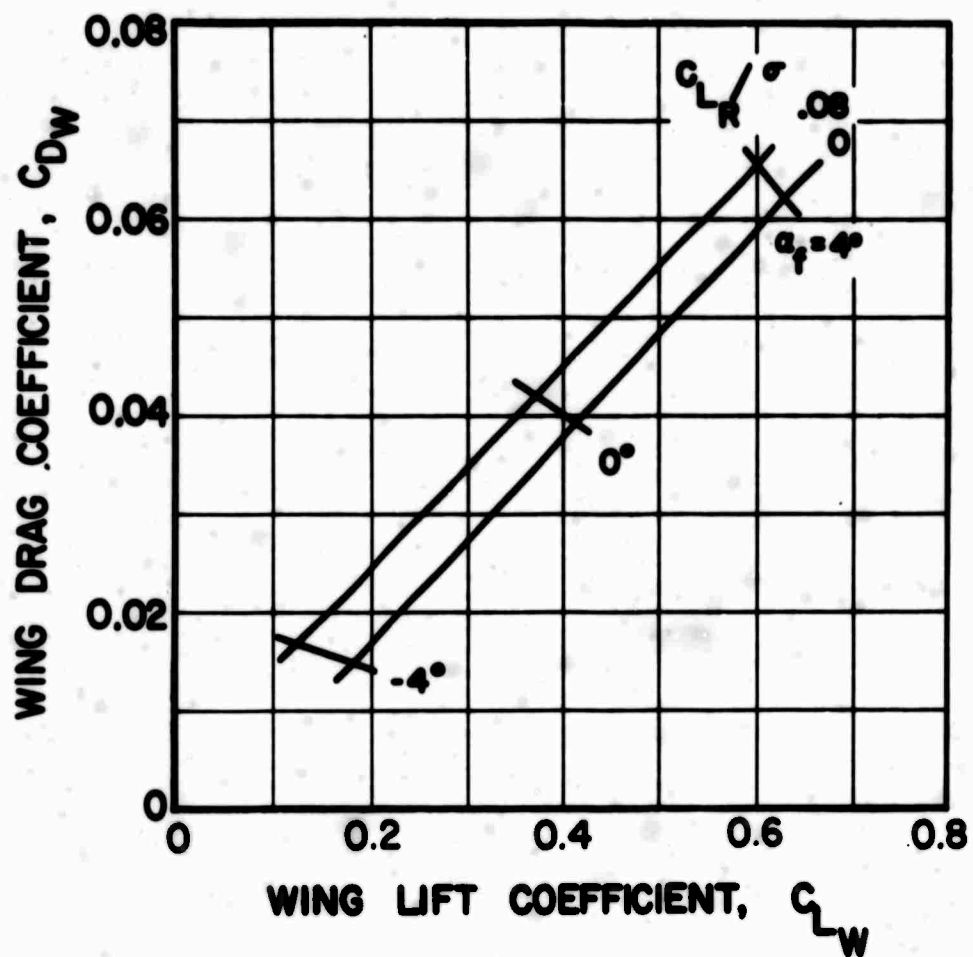
(b) Concluded

Figure 161. Concluded.



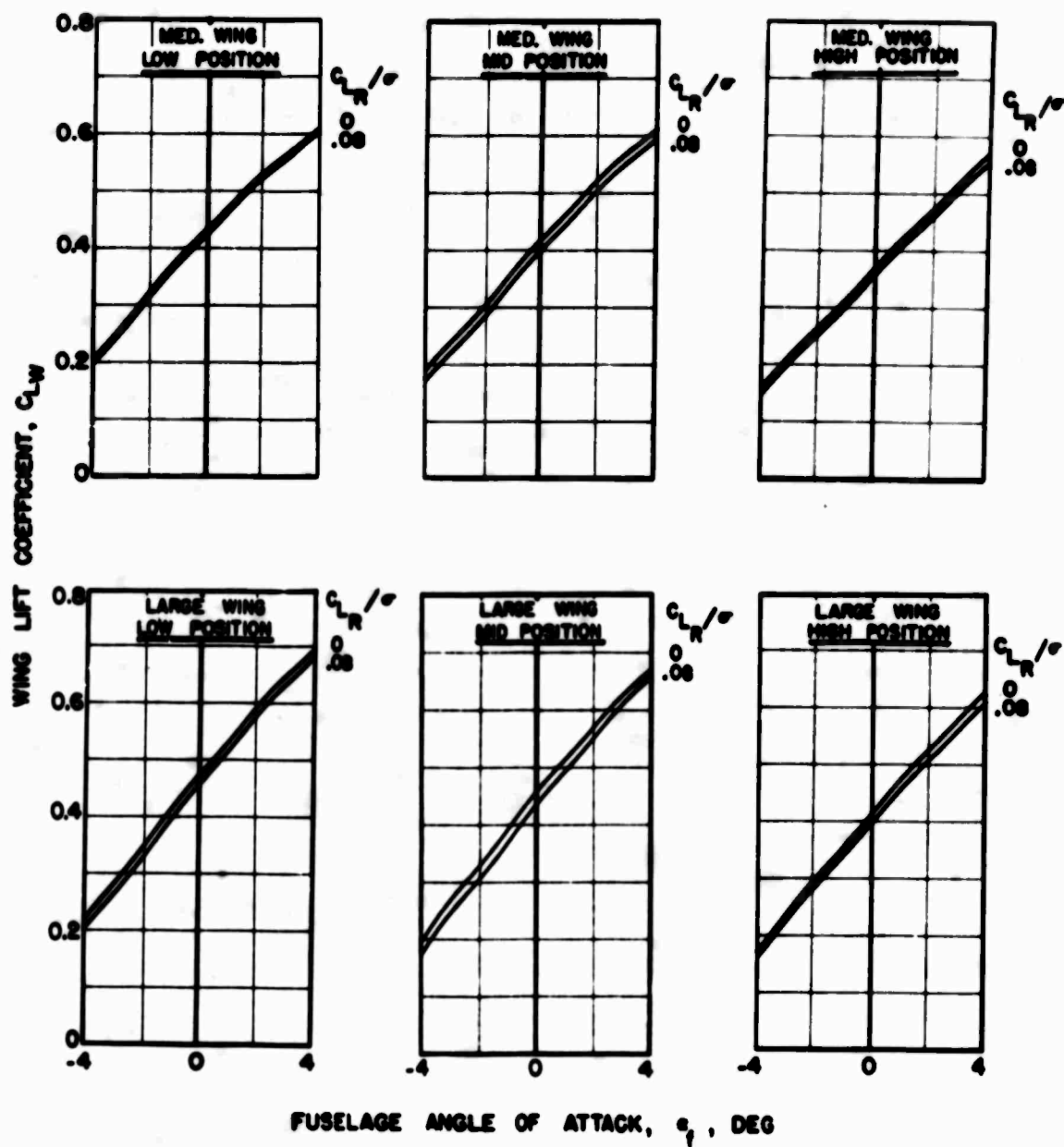
(a) Wing Lift

Figure 162. Effect of Fuselage Angle of Attack on Wing Lift and Drag at Various Rotor Lifts, Large Wing, High Position, $V_s = 232$ Knots.



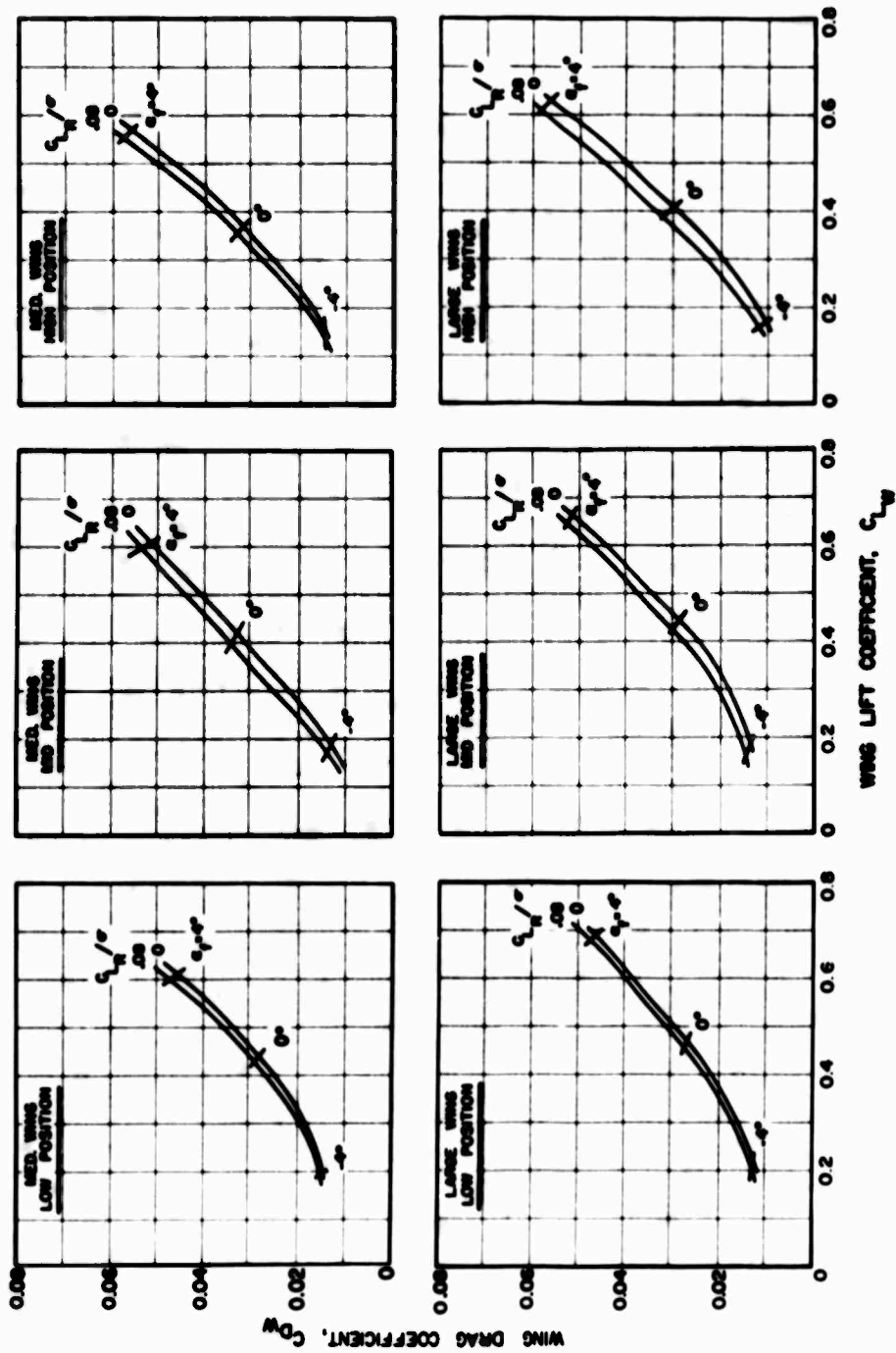
(b) Wing Lift - Drag Polar

Figure 162. Concluded.



(a) Wing Lift

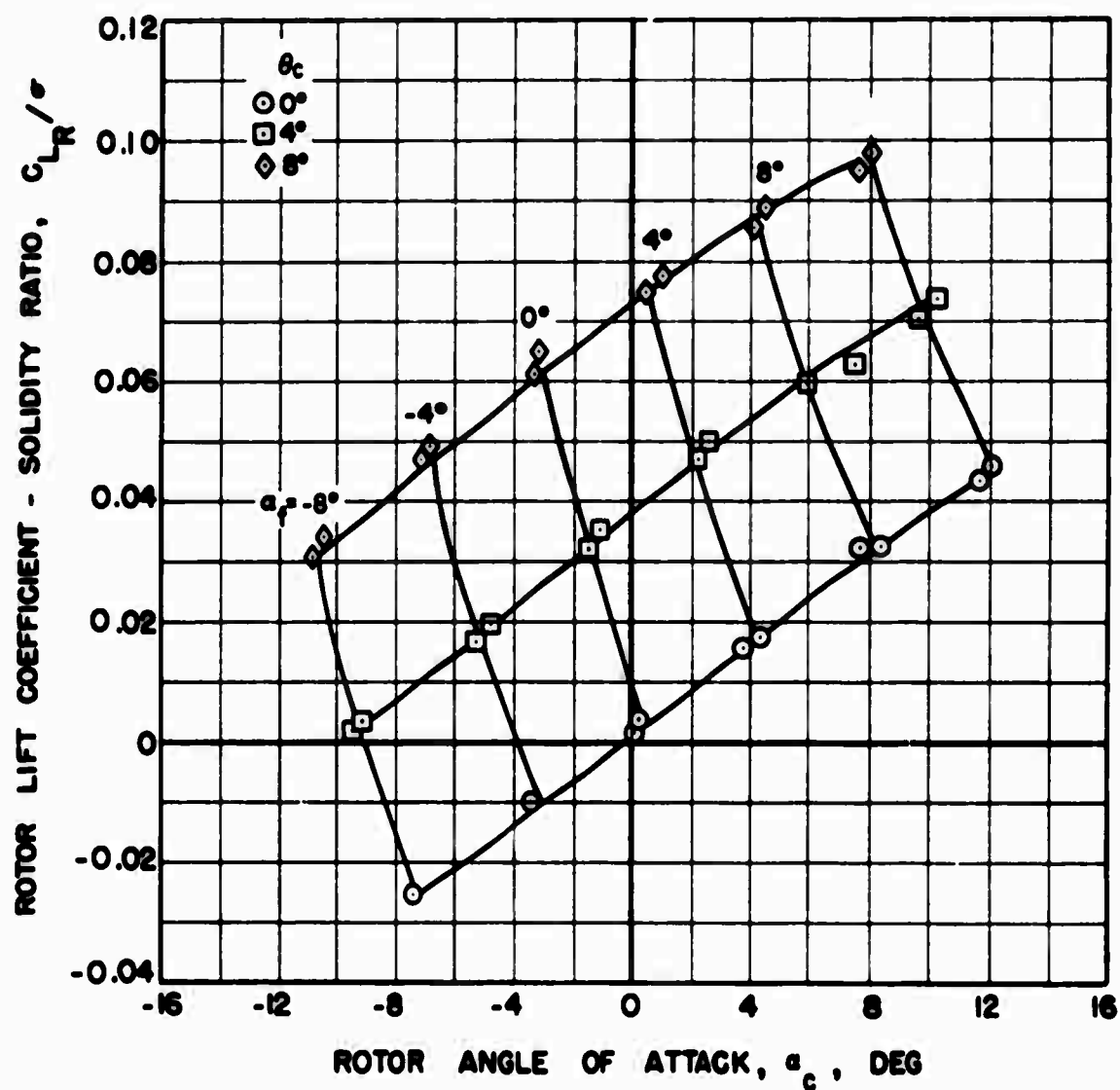
Figure 163. Effect of Fuselage Angle of Attack and Wing Position on Wing Lift and Drag at Various Rotor Lifts, Large and Medium Wings, $V_s = 300$ Knots.



(b) Wing Lift - Drag Polar

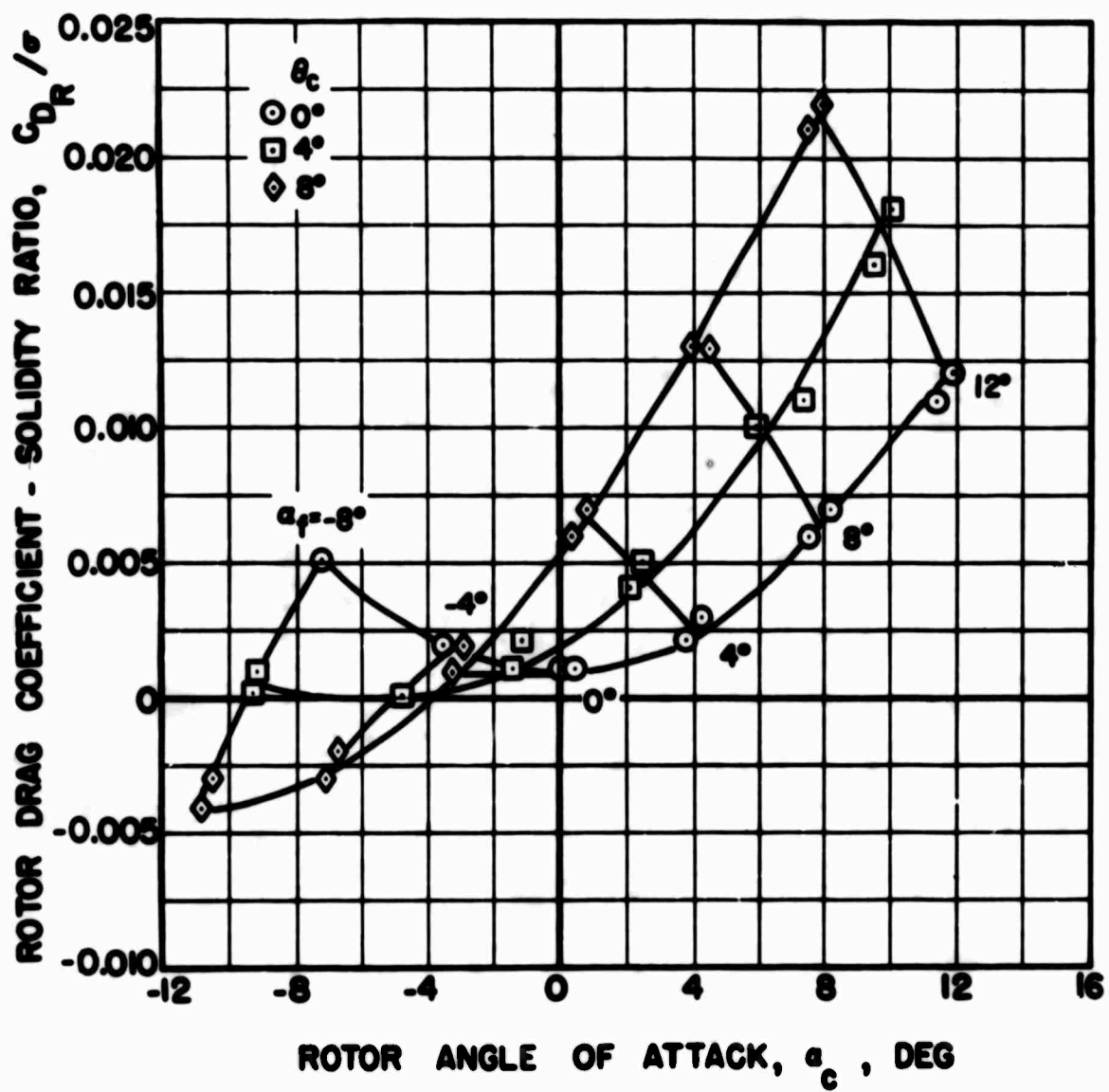
Figure 163. Concluded.

APPENDIX II ROTOR AERODYNAMIC CHARACTERISTICS



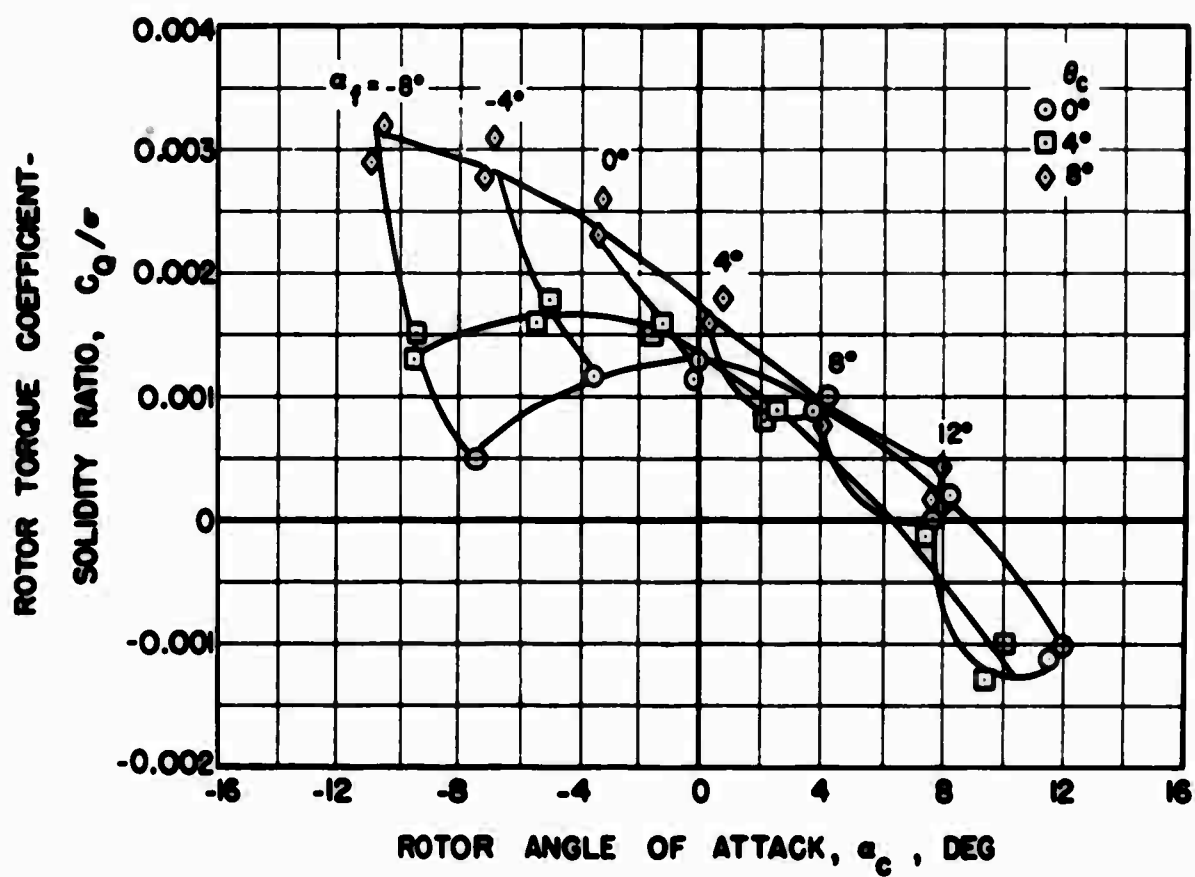
(a) Rotor Lift

Figure 164. Effect of Rotor Angle of Attack and Collective Pitch Setting on Rotor Aerodynamic Characteristics at $V_s = 120$ Knots.



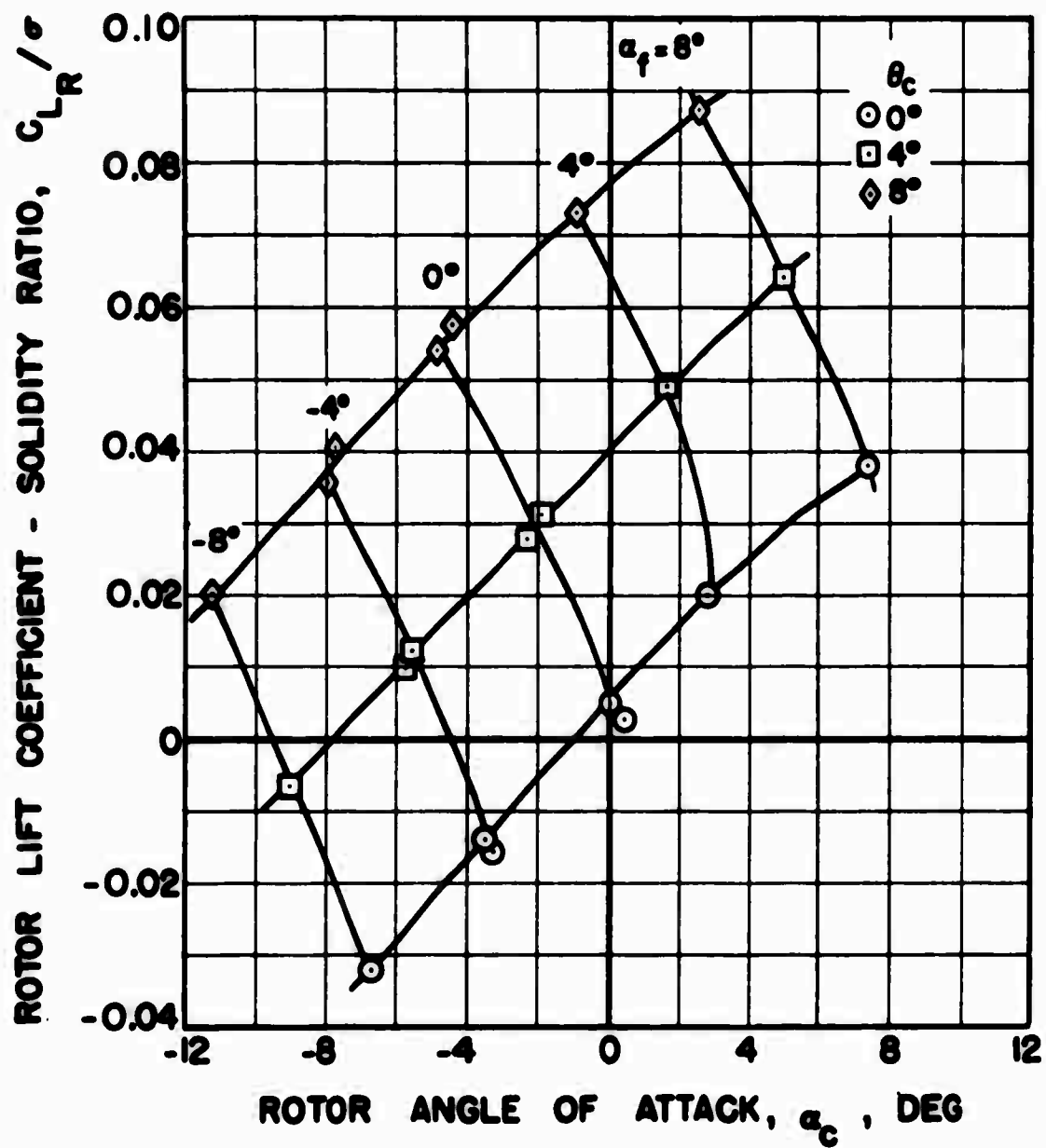
(b) Rotor Drag

Figure 164. Continued.



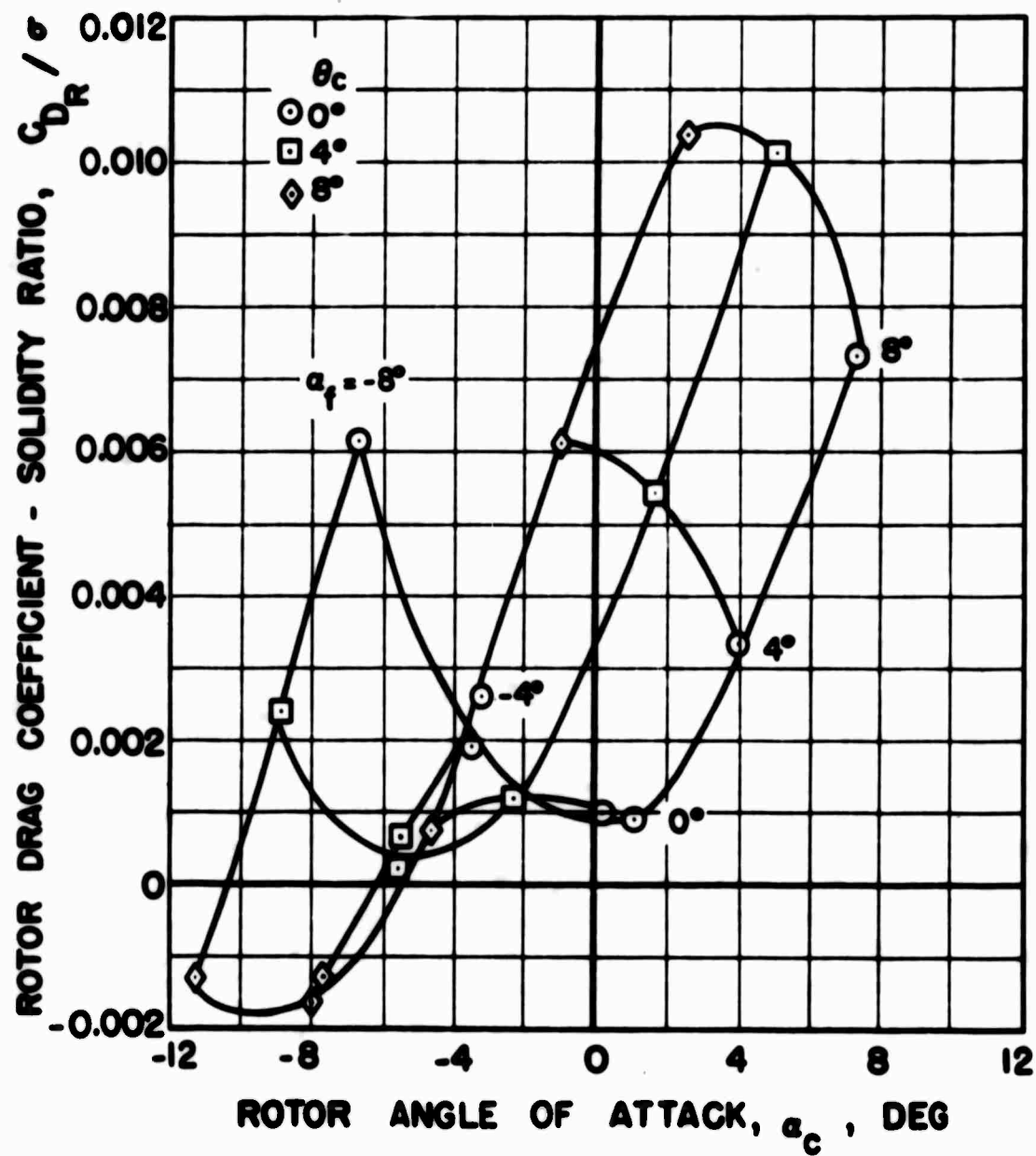
(c) Rotor Torque

Figure 164. Concluded.



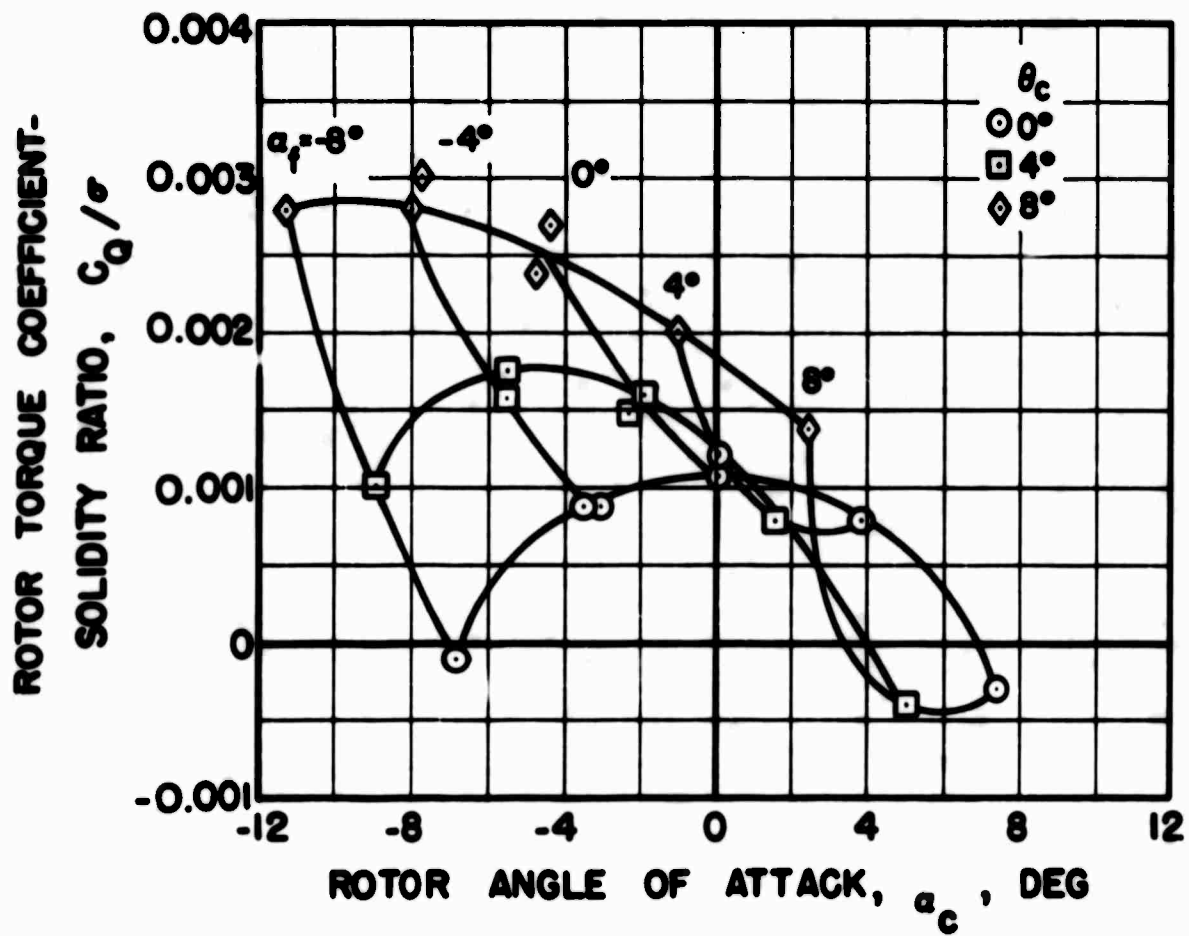
(a) Rotor Lift

Figure 165. Effect of Rotor Angle of Attack and Collective Pitch Setting on Rotor Aerodynamic Characteristics at $V_s = 160$ Knots.



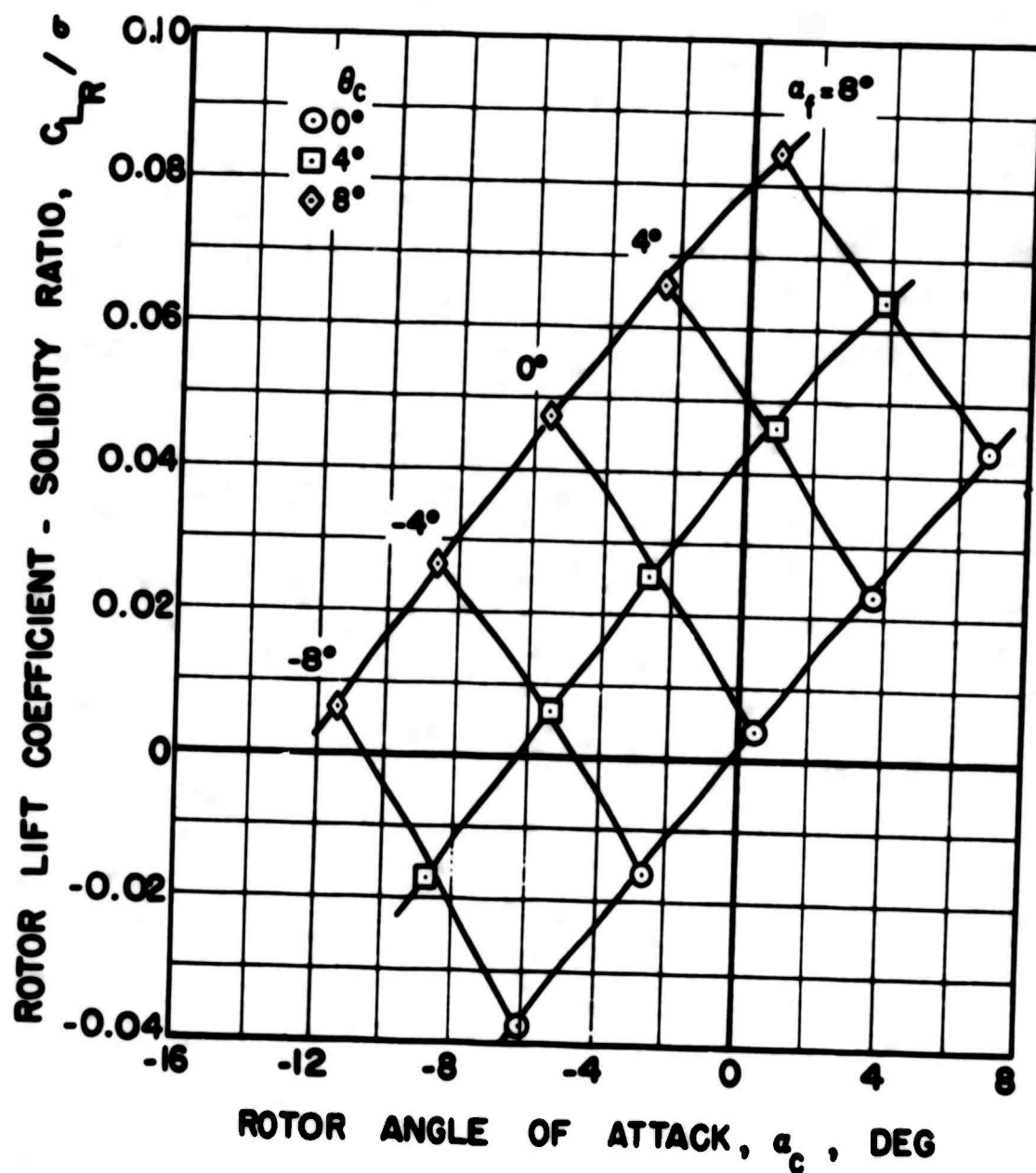
(b) Rotor Drag

Figure 165. Continued.



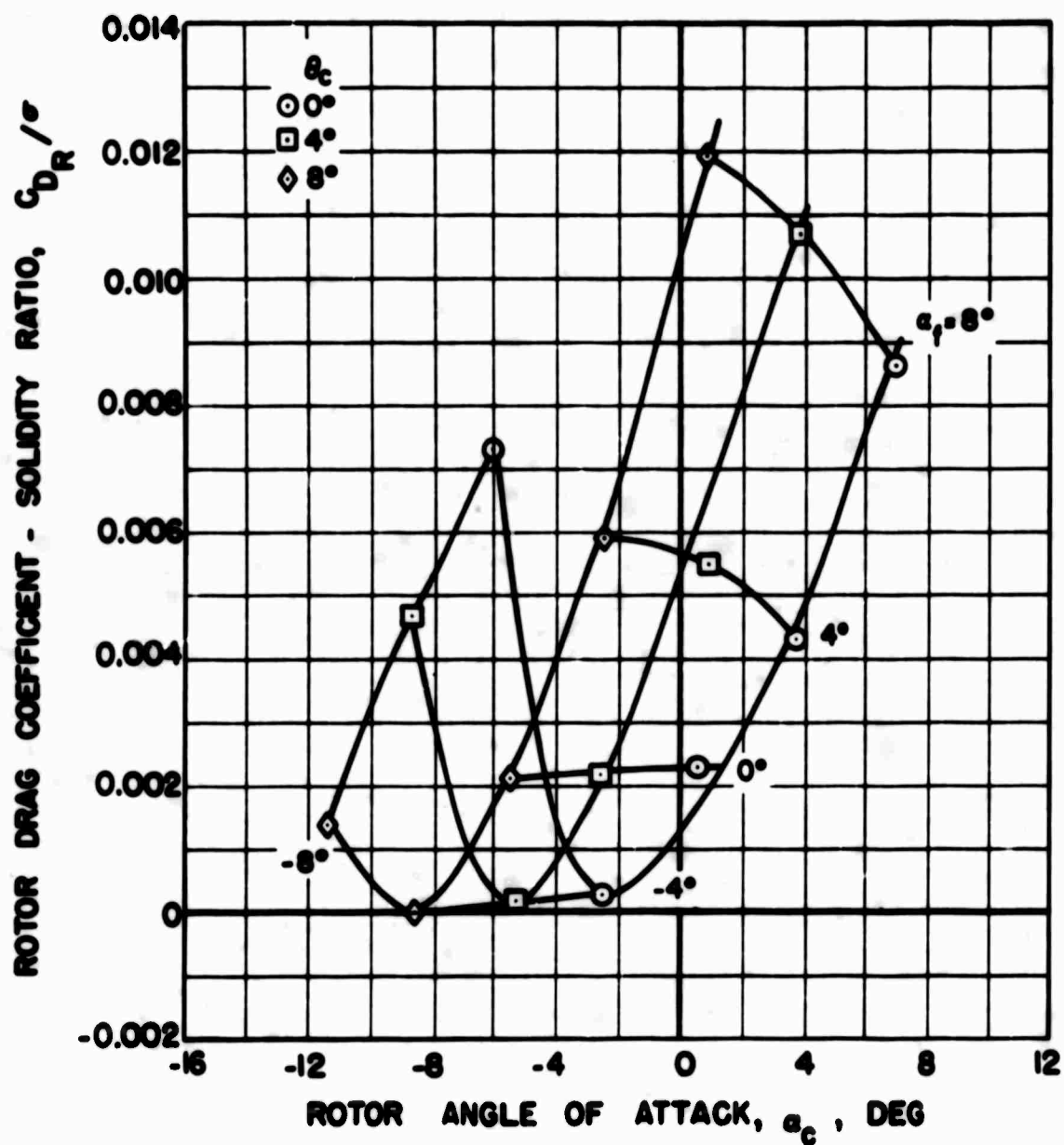
(c) Rotor Torque

Figure 165. Concluded.



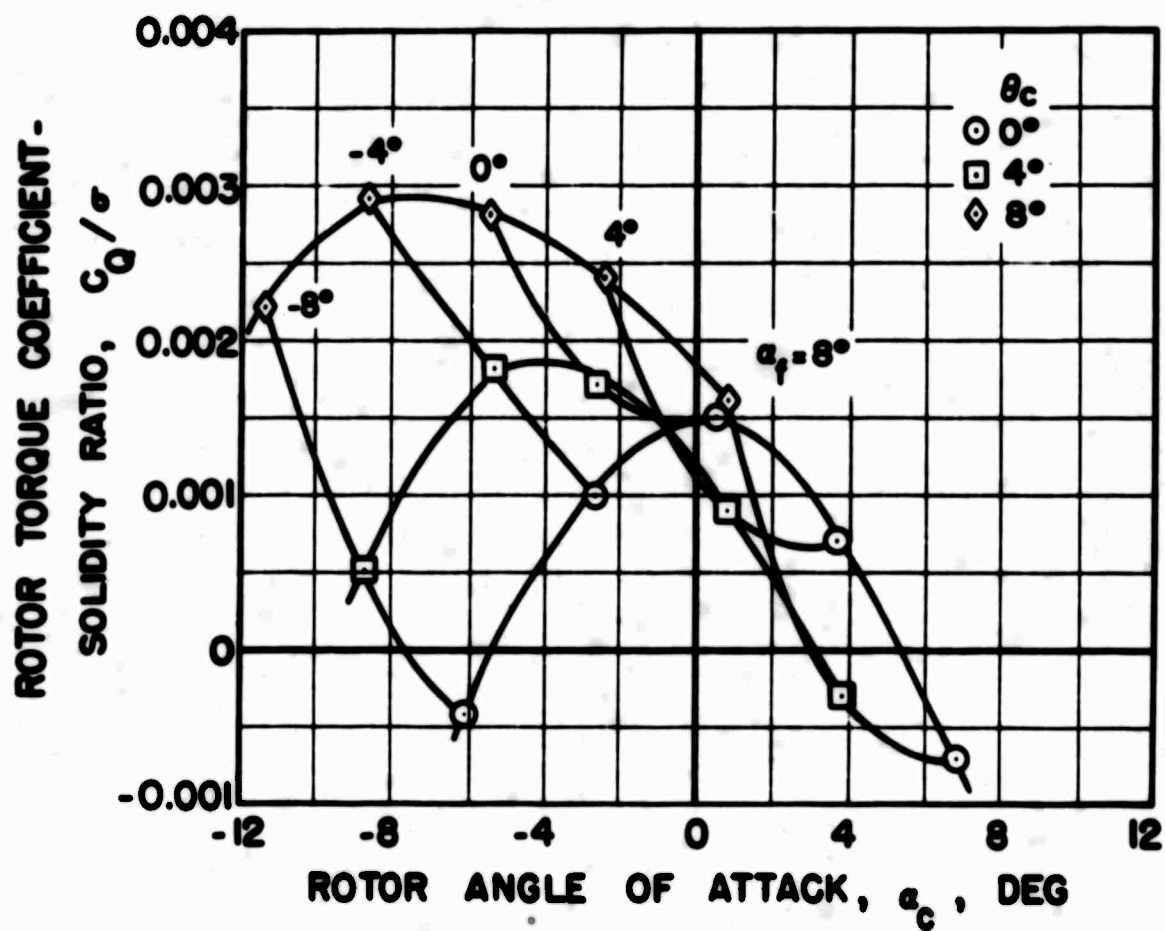
(a) Rotor Lift

Figure 166. Effect of Rotor Angle of Attack and Collective Pitch Setting on Rotor Aerodynamic Characteristics at $V_s = 200$ Knots.



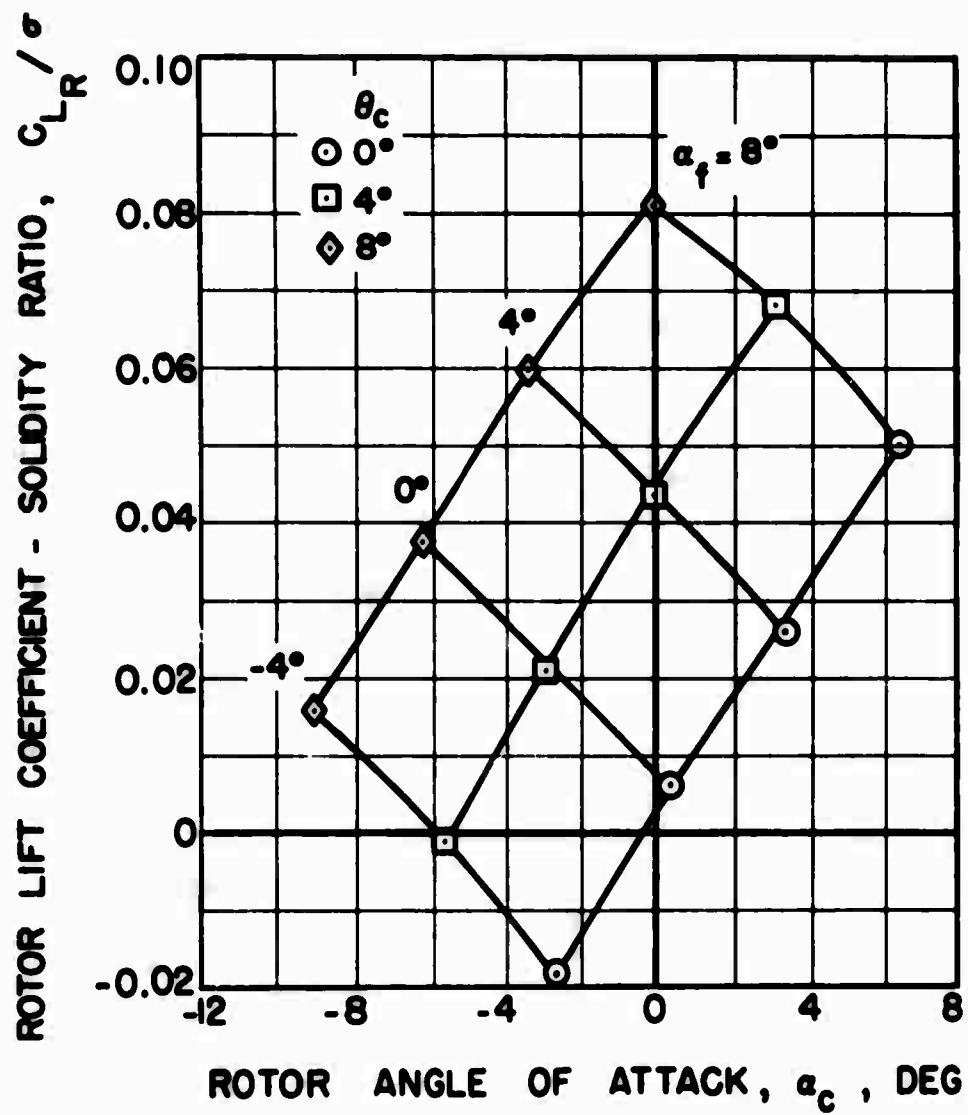
(b) Rotor Drag

Figure 166. Continued.



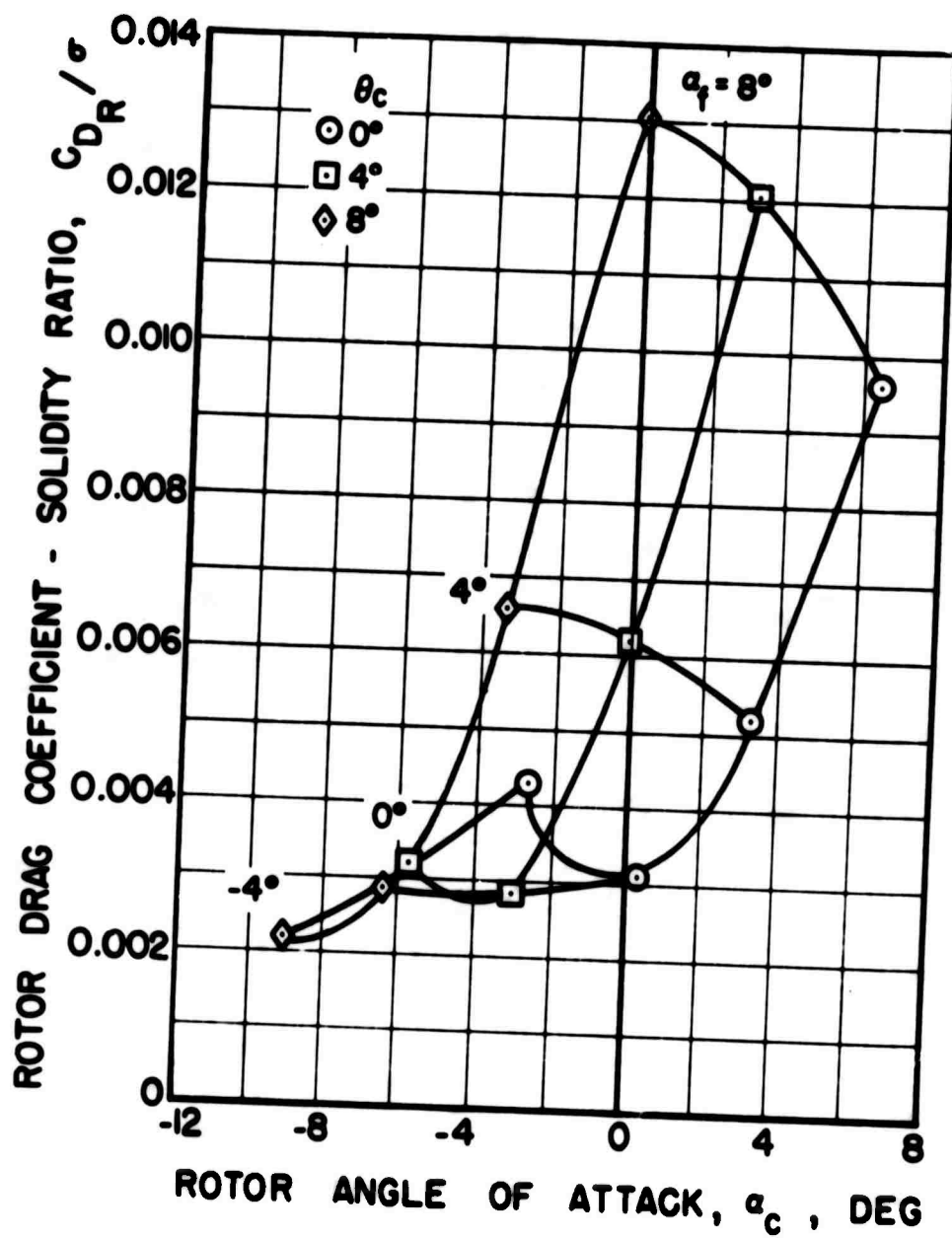
(c) Rotor Torque

Figure 166. Concluded.



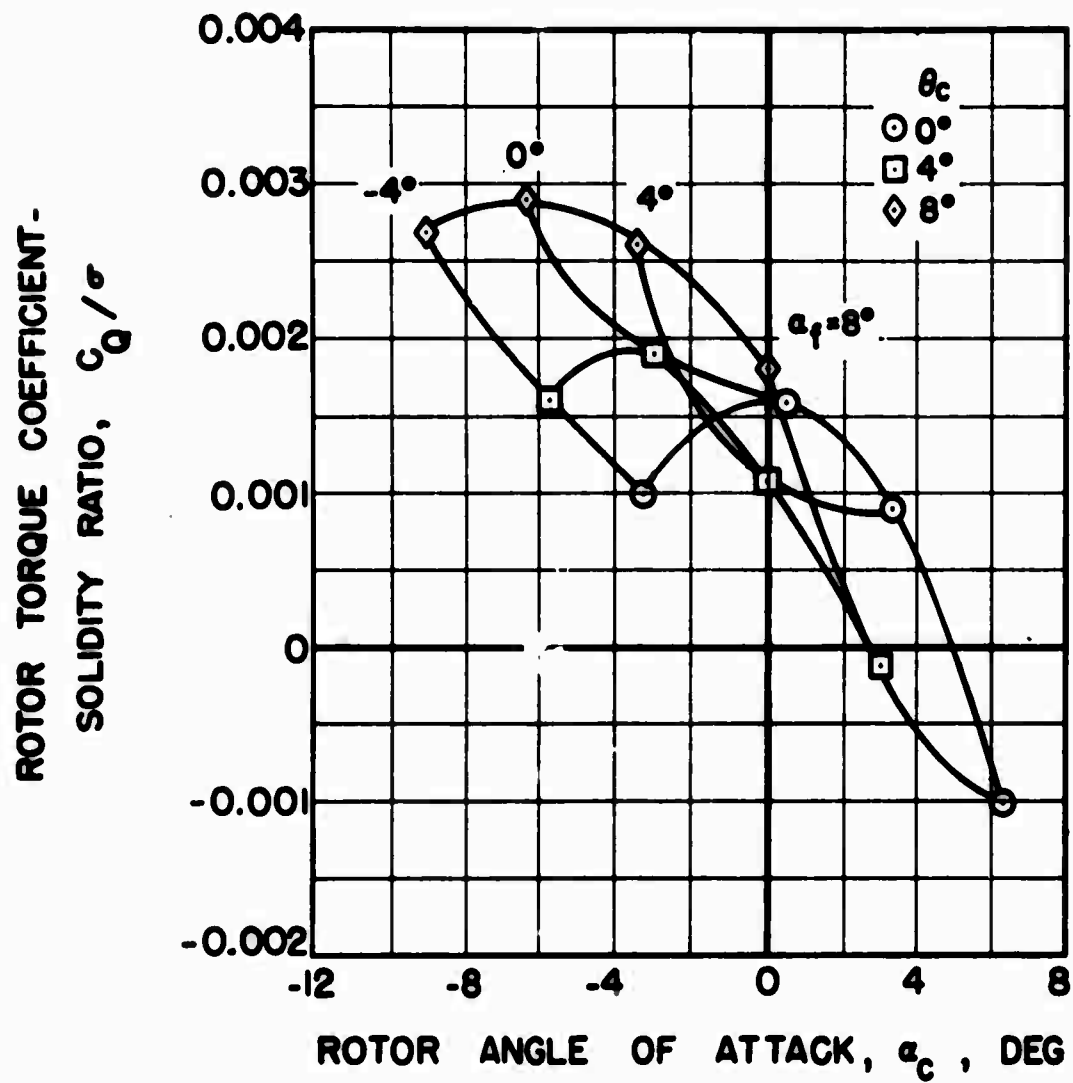
(a) Rotor Lift

Figure 167. Effect of Rotor Angle of Attack and Collective Pitch Setting on Rotor Aerodynamic Characteristics at $V_s = 232$ Knots.



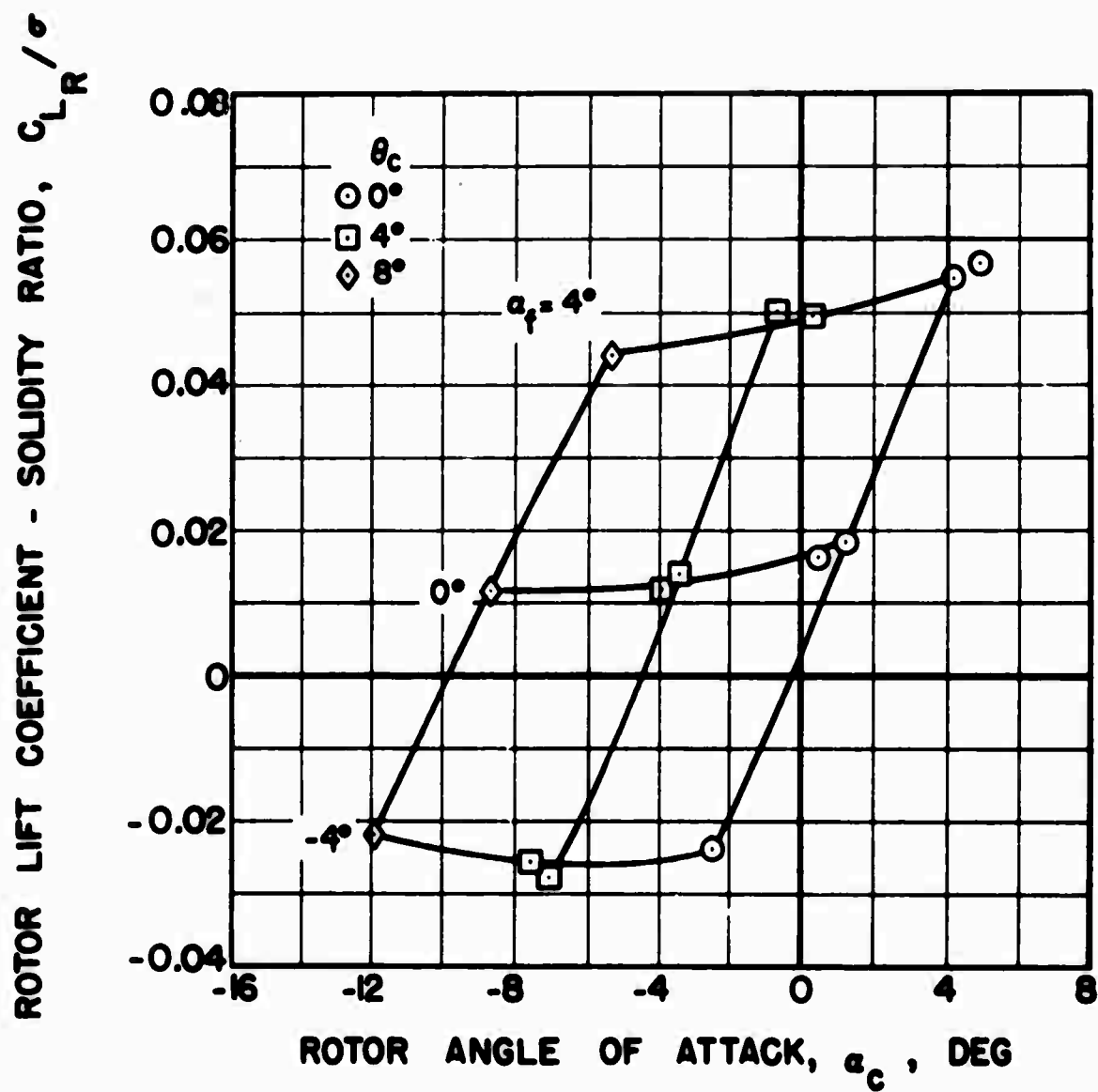
(b) Rotor Drag

Figure 167. Continued.



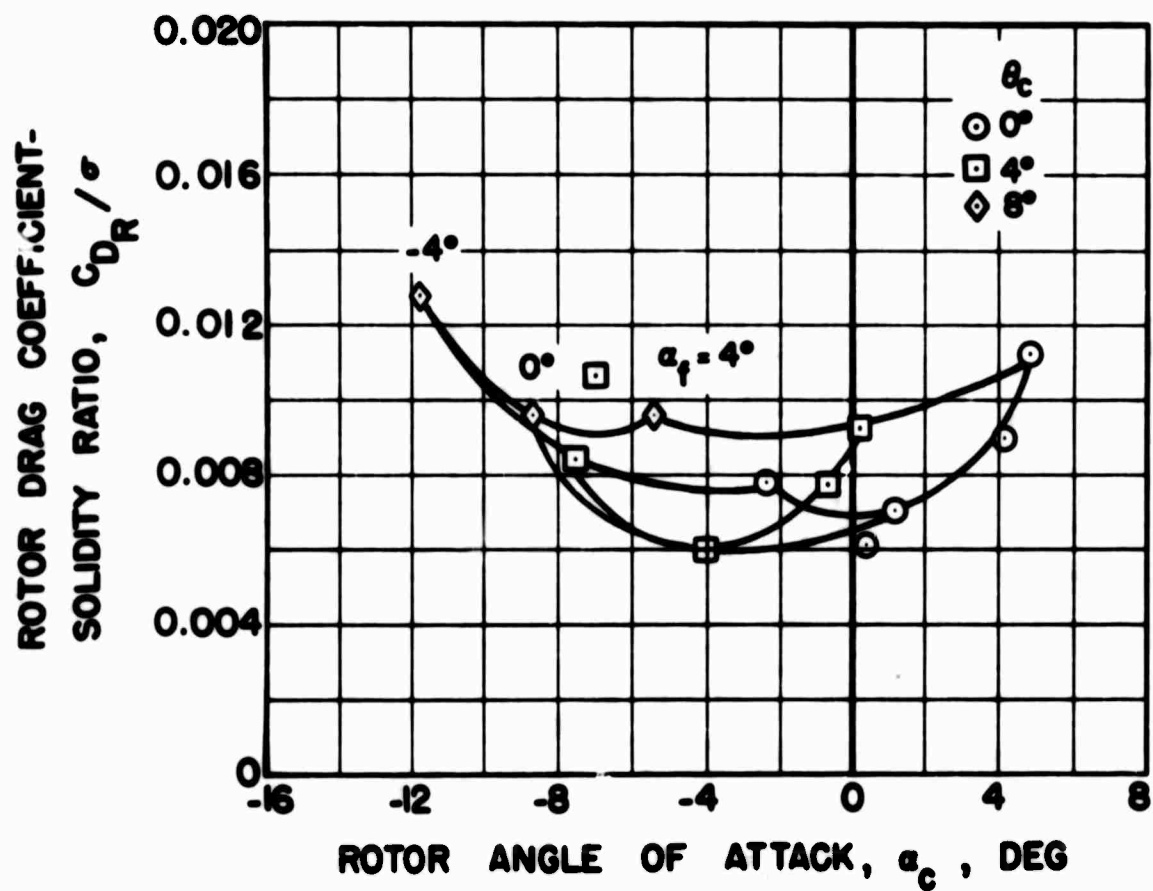
(c) Rotor Torque

Figure 167. Concluded.



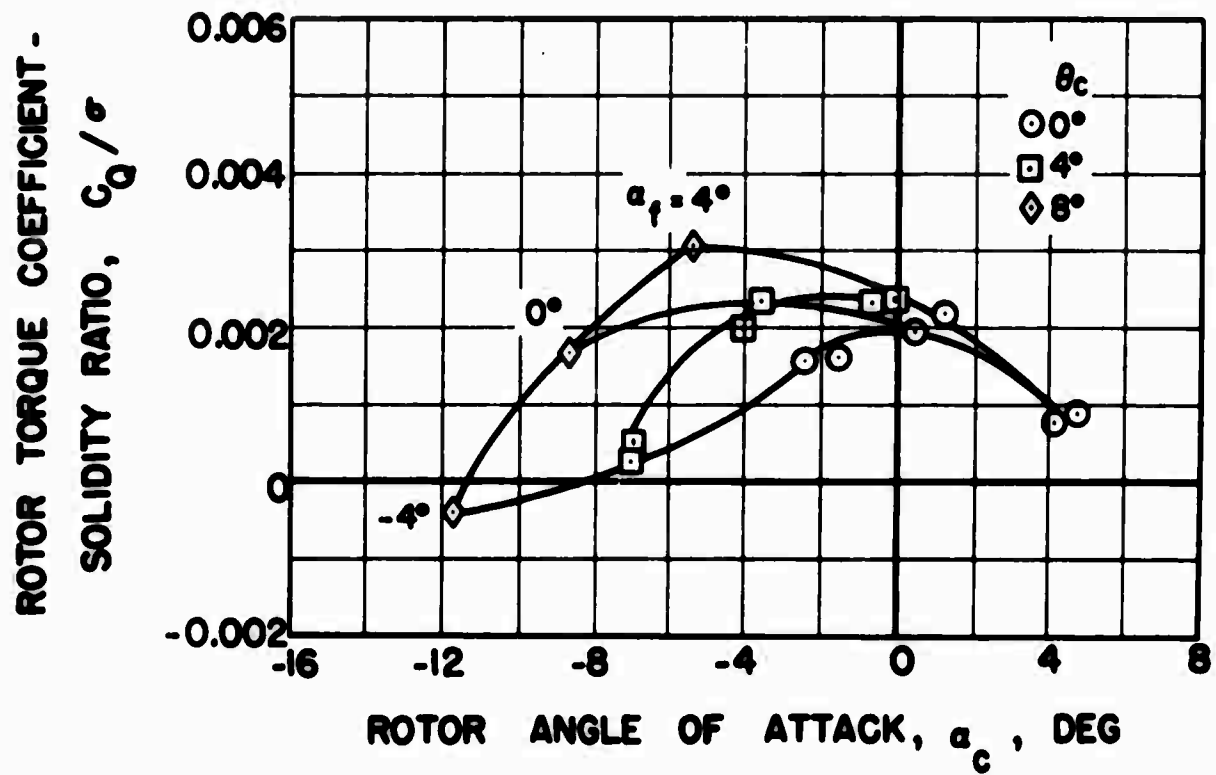
(a) Rotor Lift

Figure 168. Effect of Rotor Angle of Attack and Collective Pitch Setting on Rotor Aerodynamic Characteristics at $V_s = 300$ Knots.



(b) Rotor Drag

Figure 168. Continued.



(c) Rotor Torque

Figure 168. Concluded.

APPENDIX III AERODYNAMIC CHARACTERISTICS OF WING WITH PROPELLERS

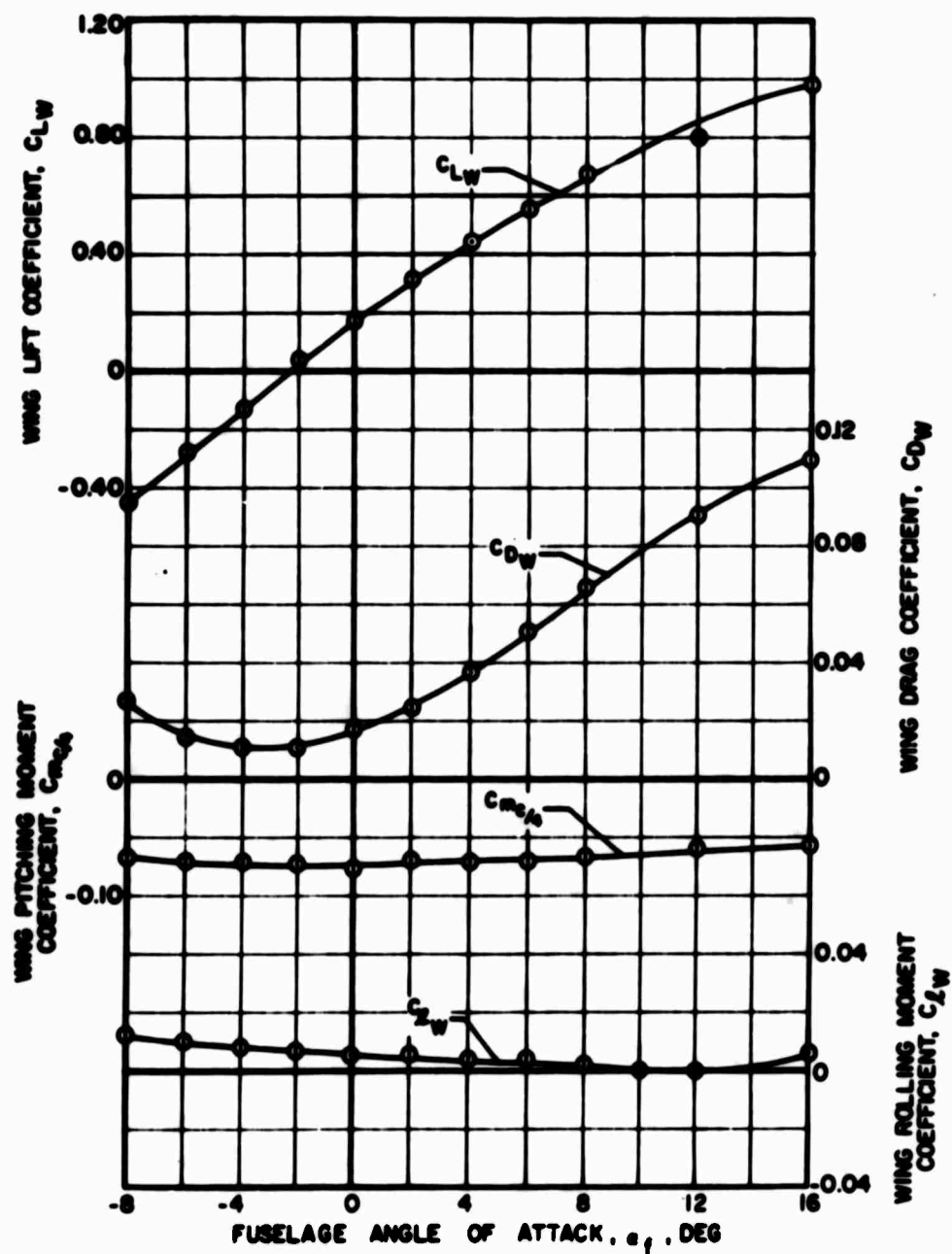
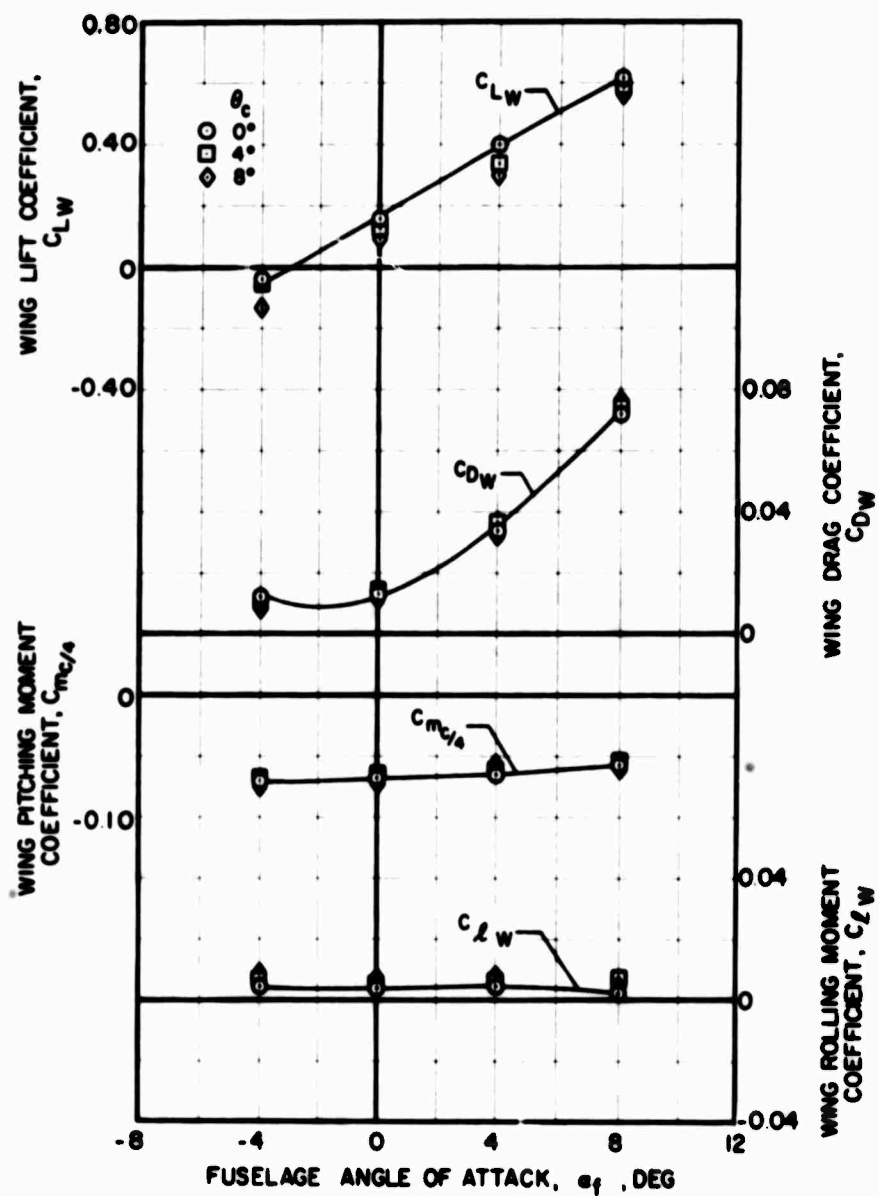
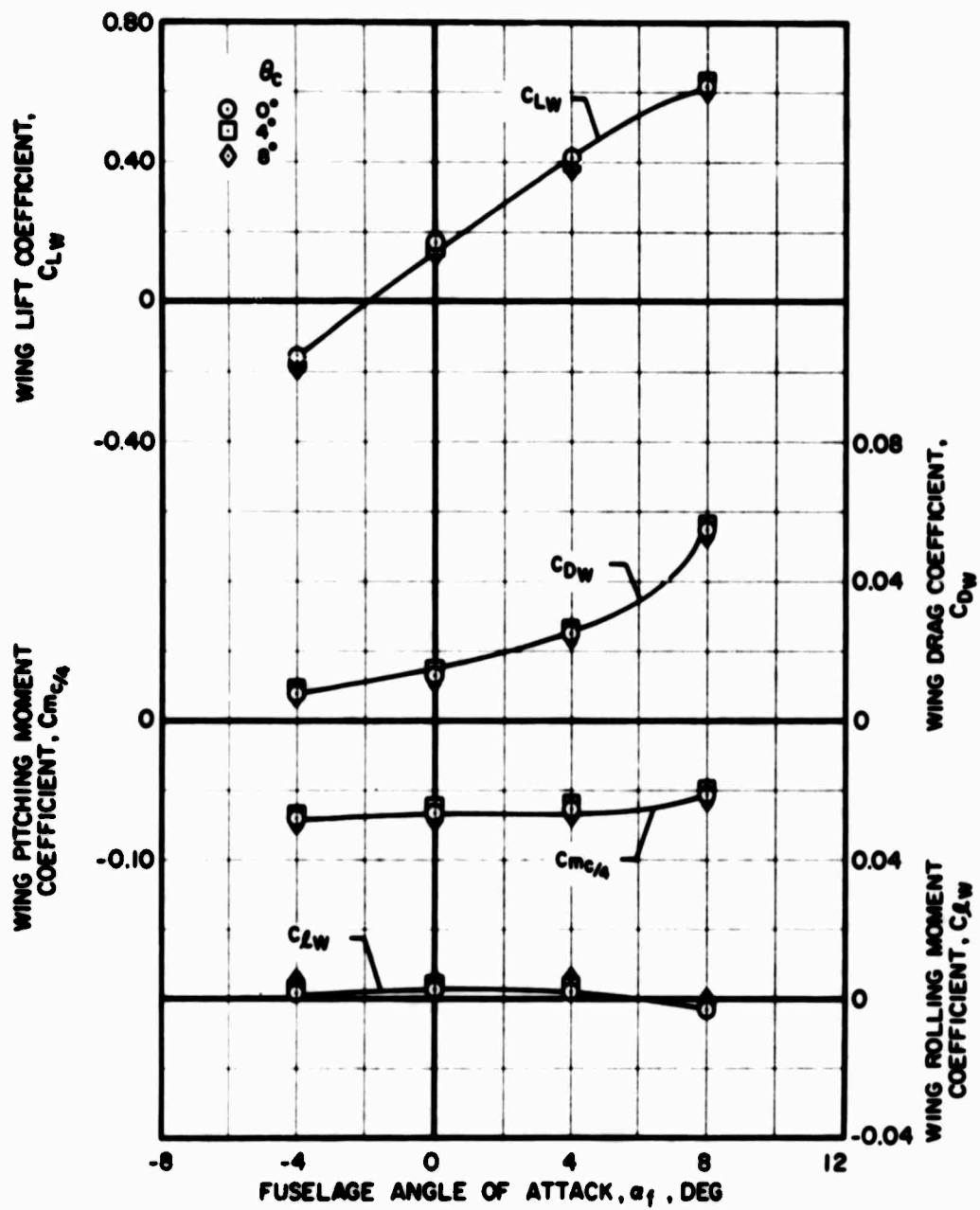


Figure 169. Effect of Fuselage Angle of Attack on the Aerodynamic Characteristics of the Large Wing, Without Rotor, Nacelles, or Propellers, $i_w = 0^\circ$.



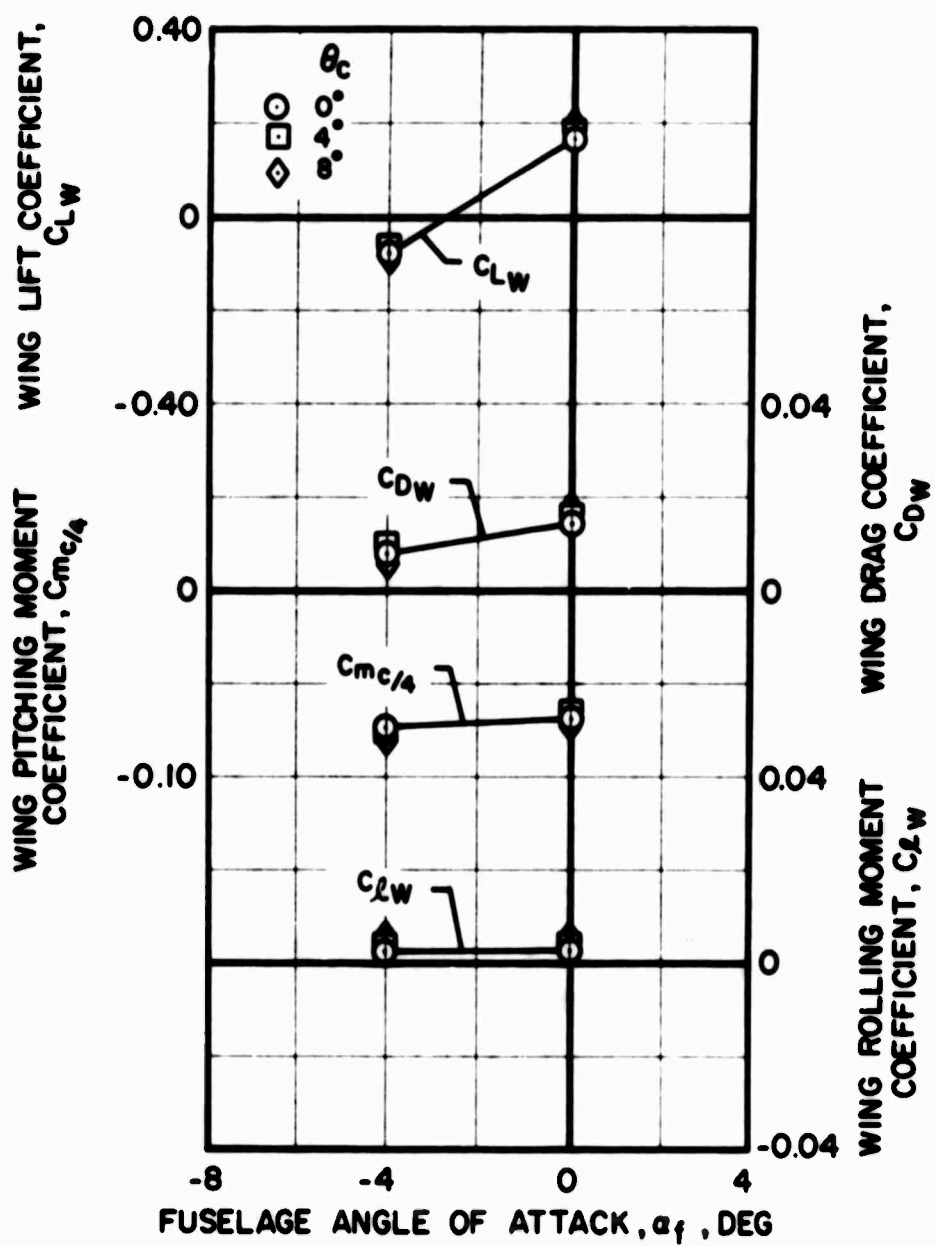
(a) $V_s = 120$ Knots

Figure 170. Effect of Fuselage Angle of Attack on the Aerodynamic Characteristics of the Large Wing, Without Propellers or Nacelles and With Rotor at Various Collective Pitch Settings and Forward Speeds, $i_w = 0^\circ$.



(b) $V_s = 200$ Knots

Figure 170. Continued.



(c) $V_s = 300$ Knots

Figure 170. Concluded.

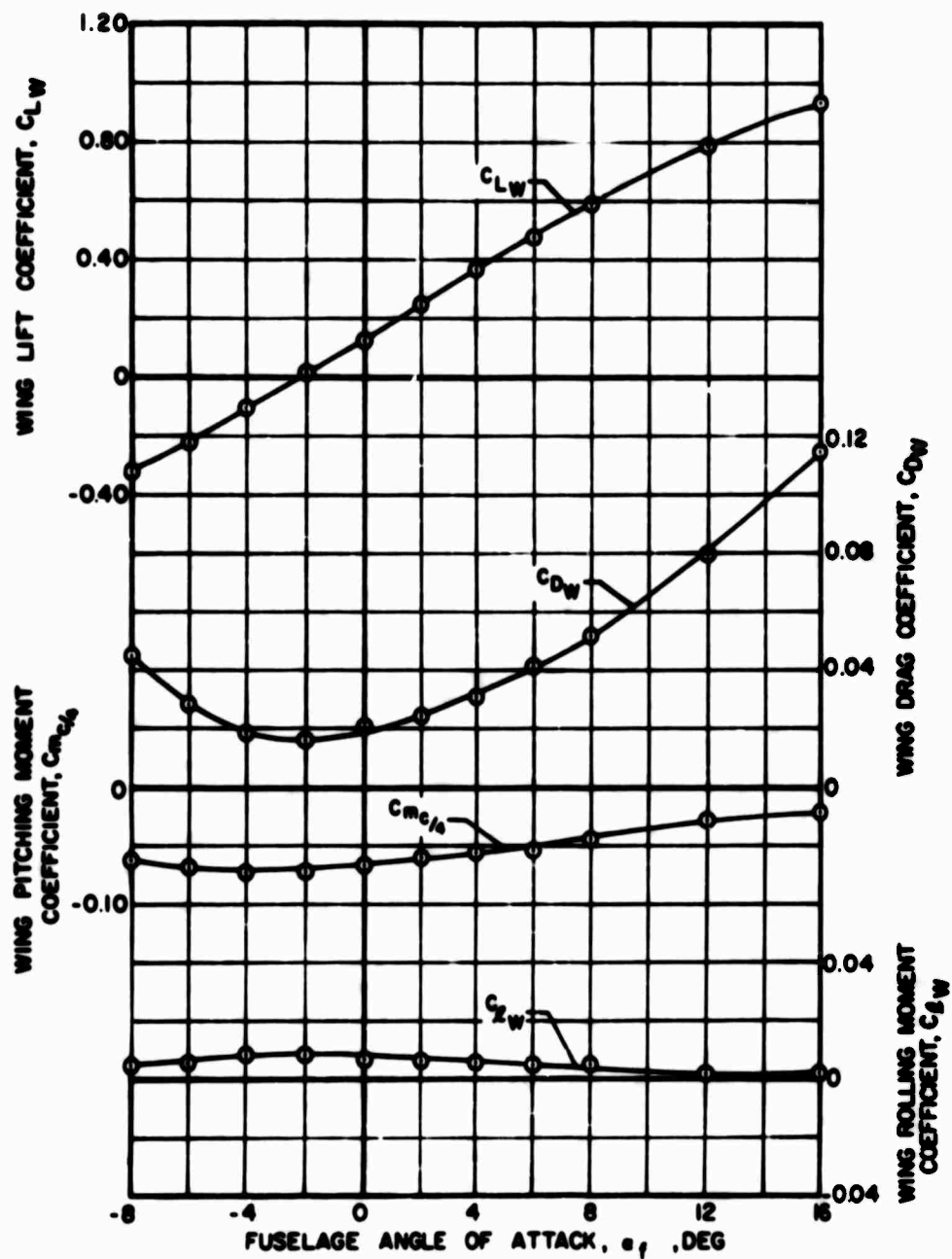
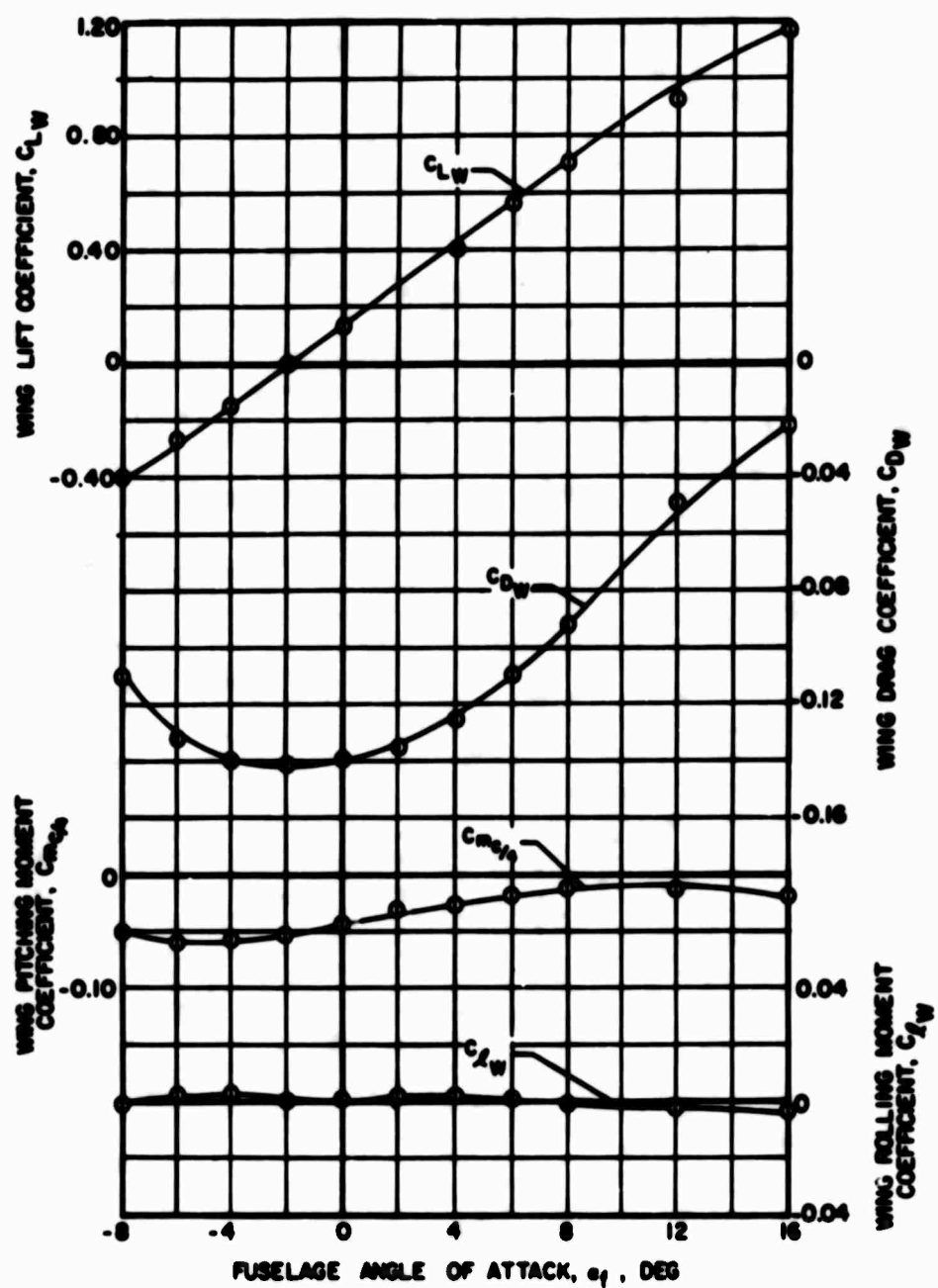
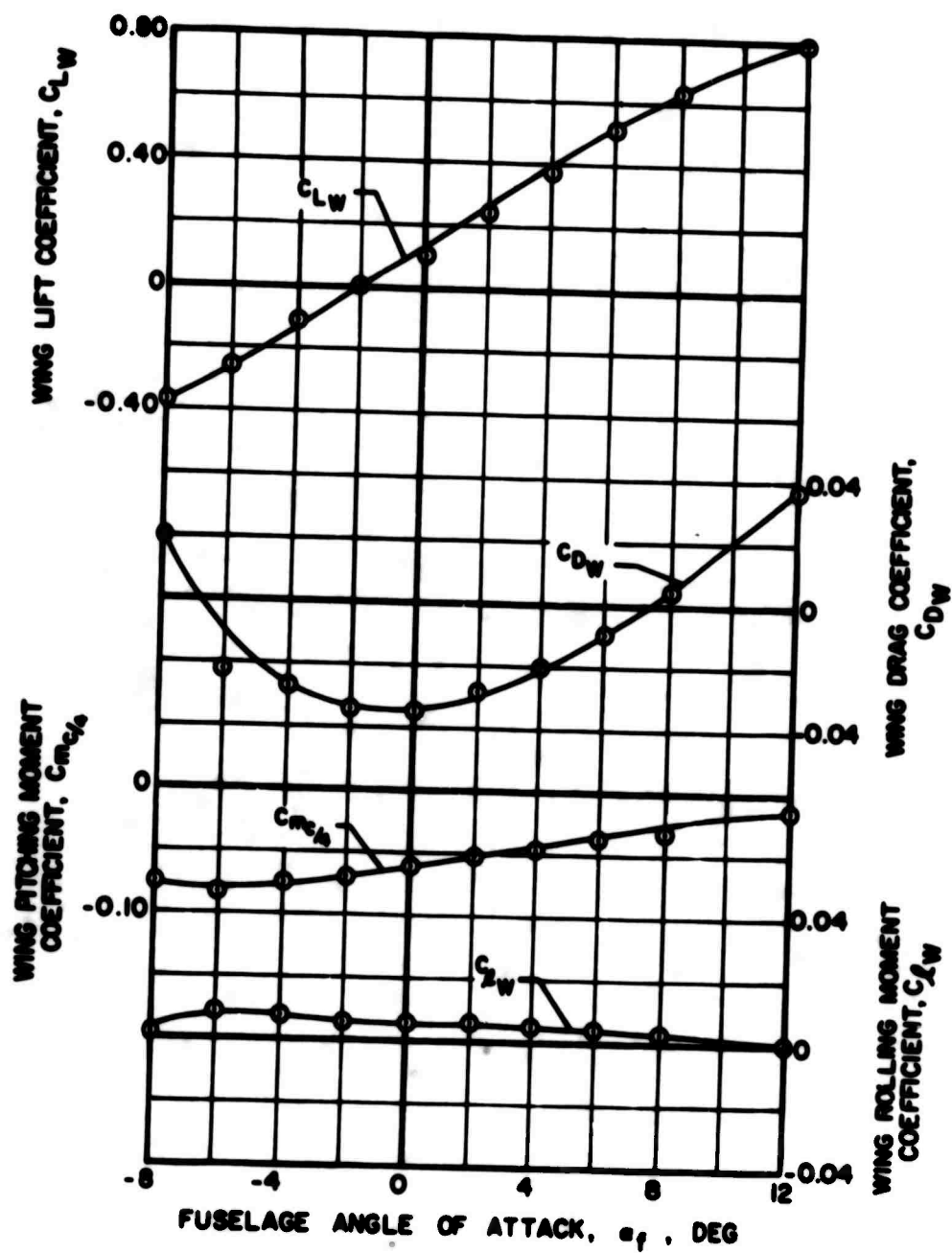


Figure 171. Effect of Fuselage Angle of Attack on the Aerodynamic Characteristics of the Large Wing, Without Propellers or Rotor and With Inboard Nacelles, $i_w = 0^\circ$.



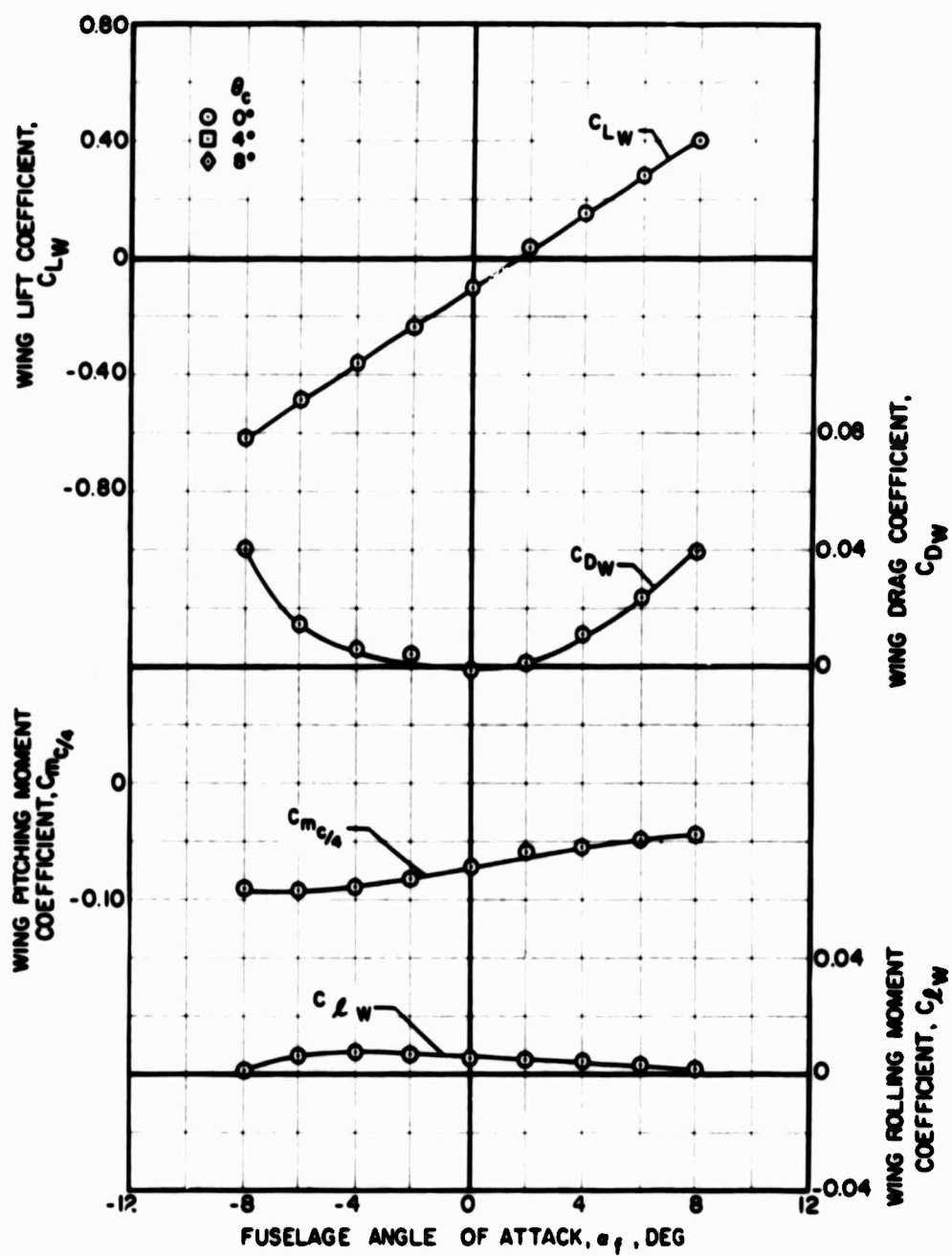
(a) $V_S = 120$ Knots

Figure 172. Effect of Fuselage Angle of Attack on the Aerodynamic Characteristics of the Large Wing. Without Rotor and With Inboard Tractor Propellers at Various Forward Speeds, $\beta_{.75} = 41^\circ$. $i_w = 0^\circ$.



(b) $V_S = 200$ Knots

Figure 172. Continued.



(c) $V_s = 300$ Knots

Figure 172. Concluded.

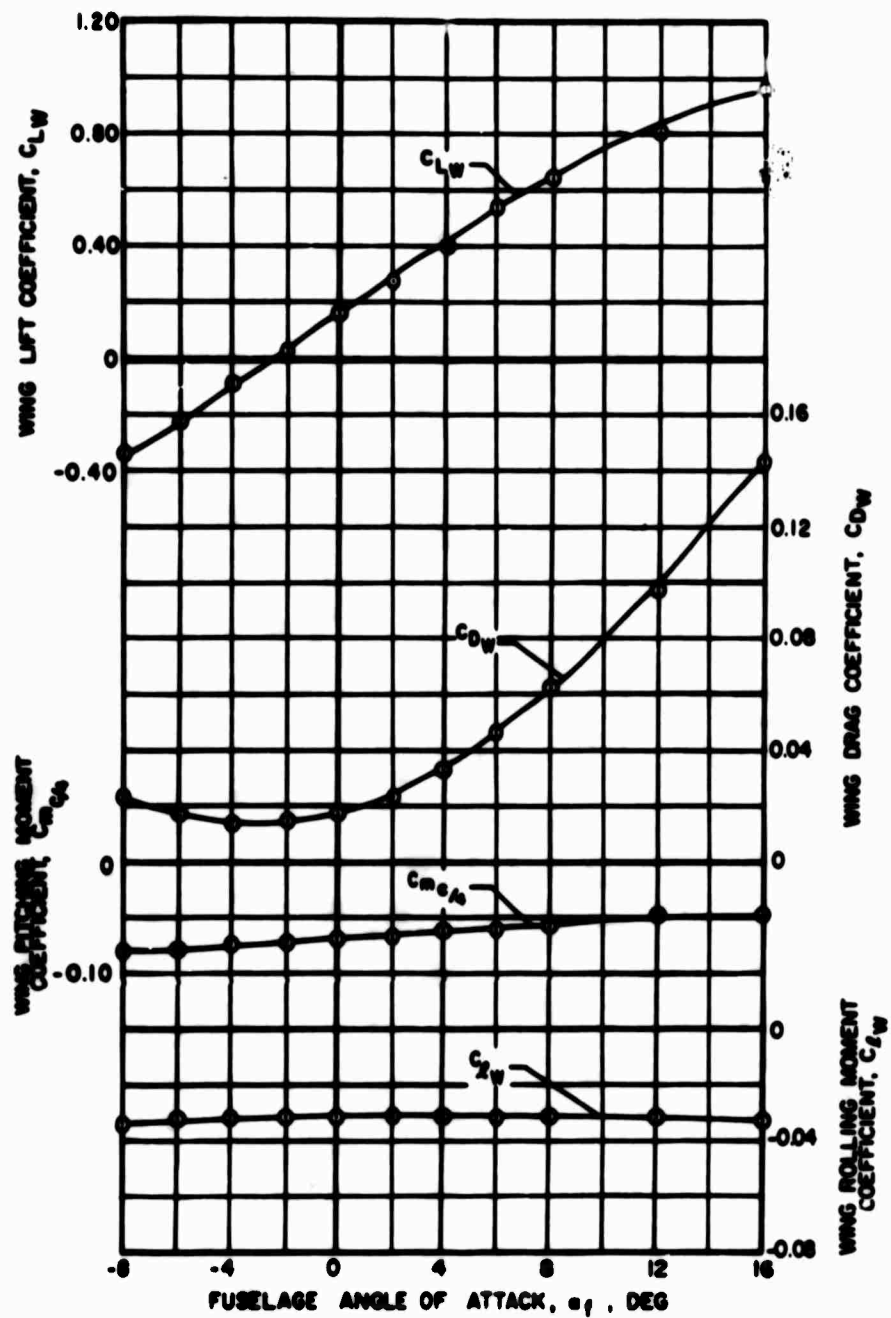
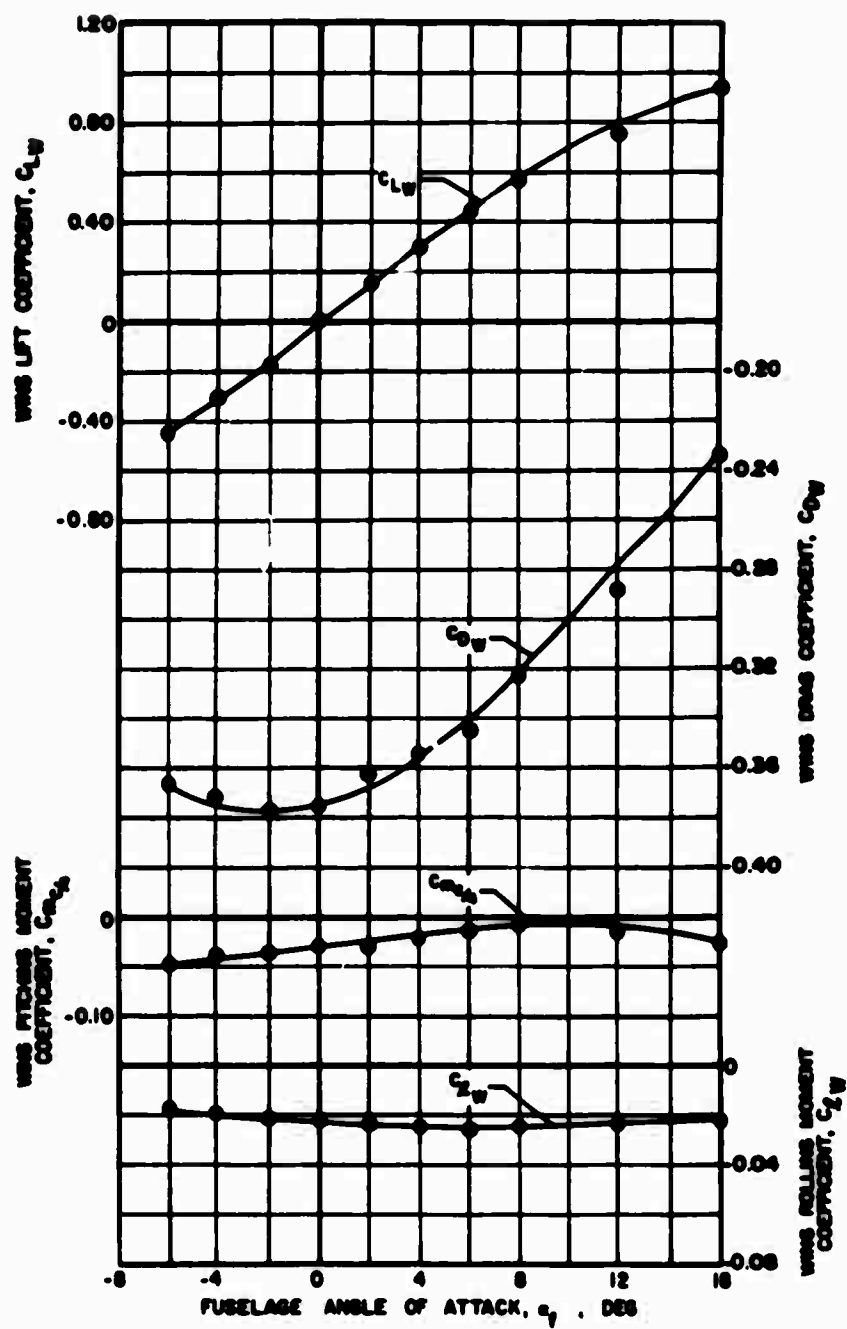
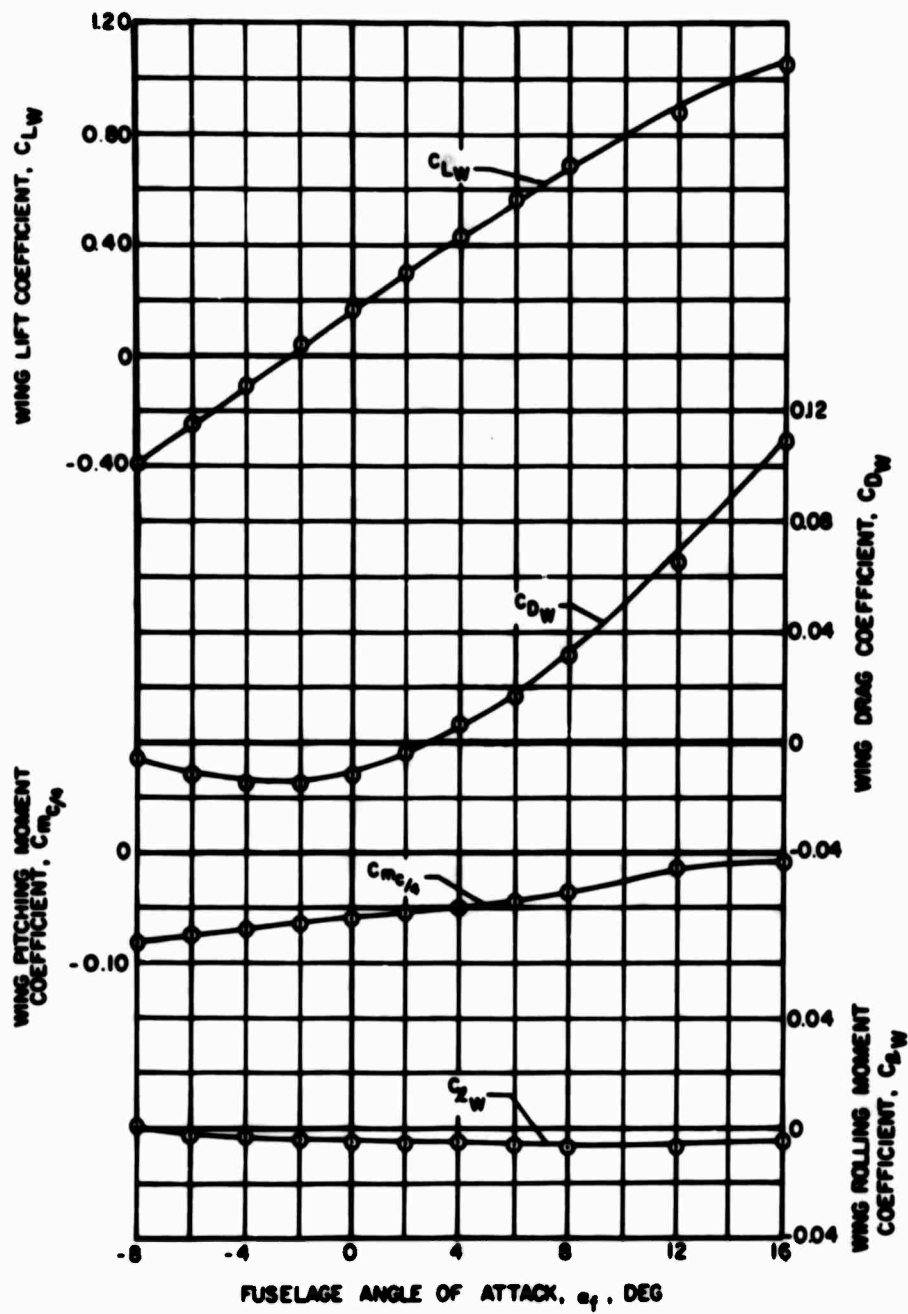


Figure 173. Effect of Fuselage Angle of Attack on the Aerodynamic Characteristics of the Large Wing. Without Propellers or Rotor and With Outboard Nacelles, $i_w = 0^\circ$.



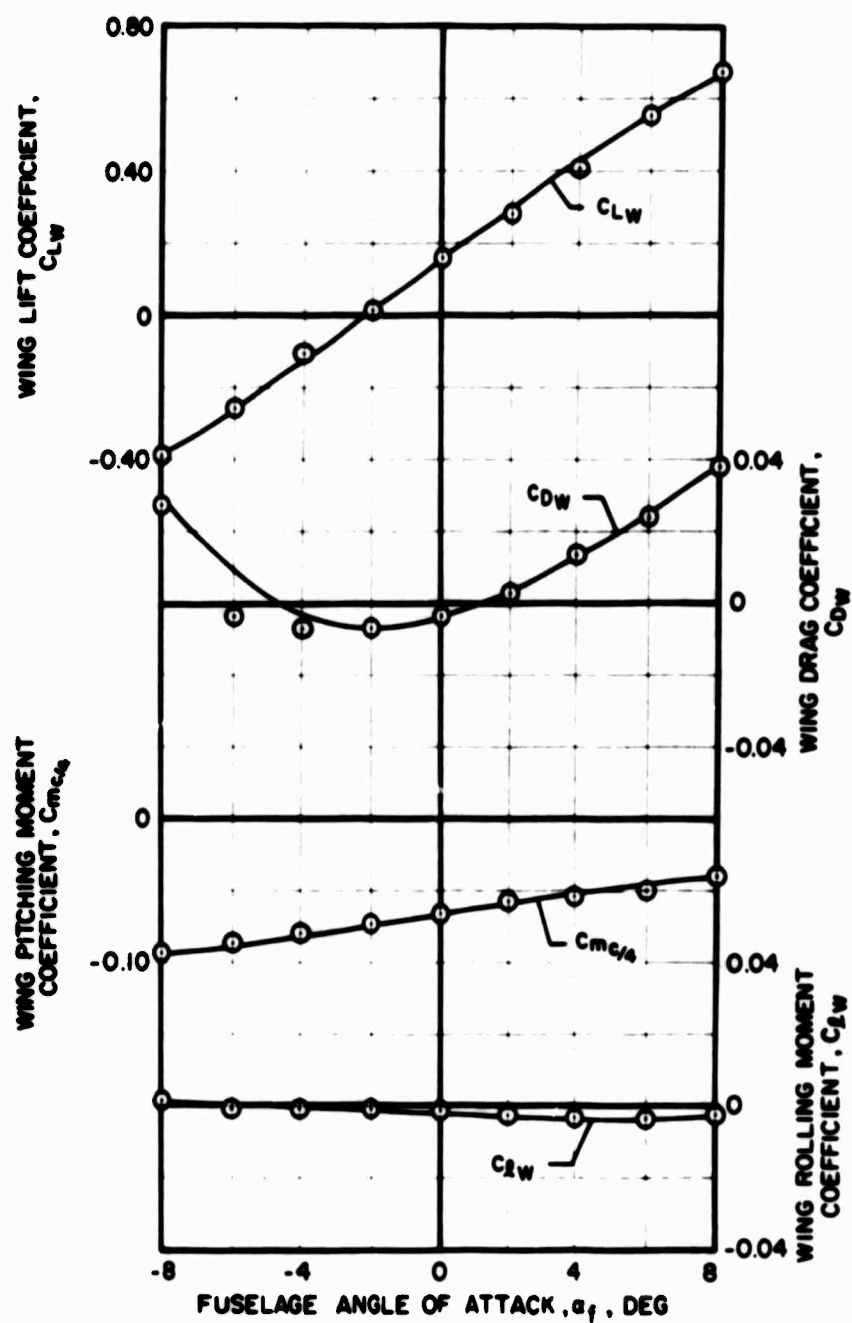
(a) $V_S = 120$ Knots

Figure 174. Effect of Fuselage Angle of Attack on the Aerodynamic Characteristics of the Large Wing, Without Rotor and With Outboard Tractor Propellers at Various Forward Speeds, $\beta_{75} = 41^\circ$, $i_w = 0^\circ$.



(b) $V_S^* = 200$ Knots

Figure 174. Continued.



(c) $V_s = 300$ Knots

Figure 174. Concluded.

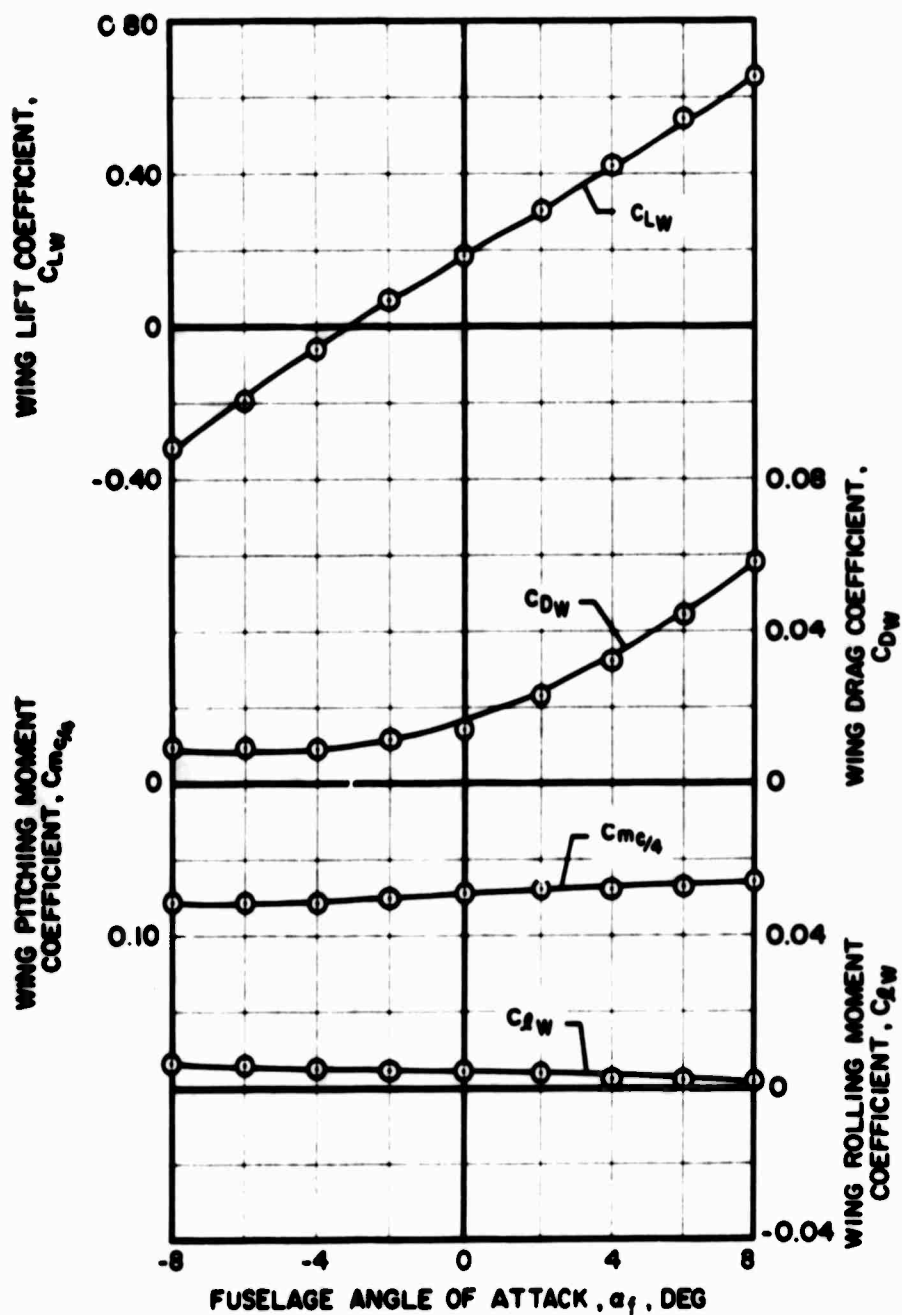
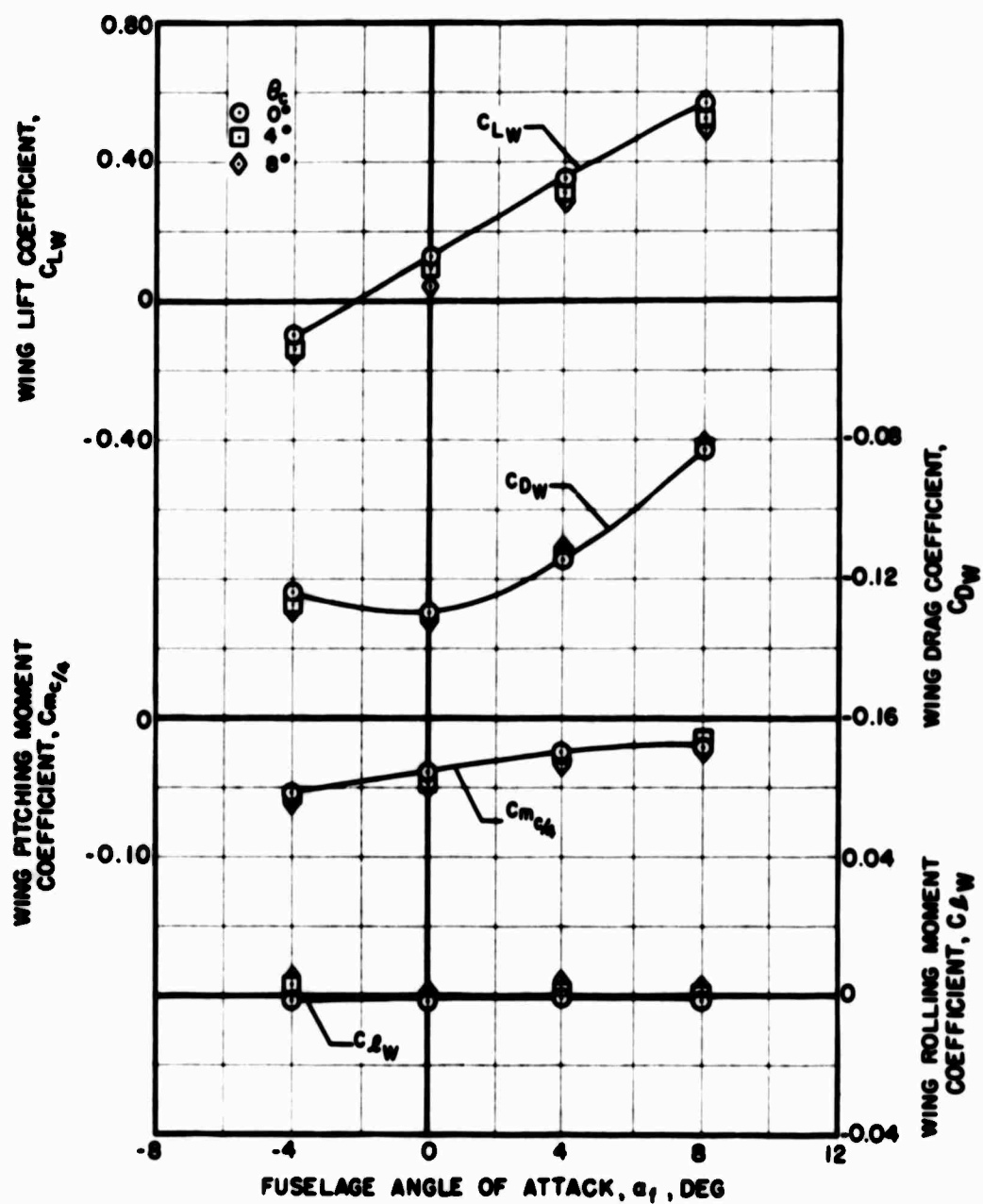
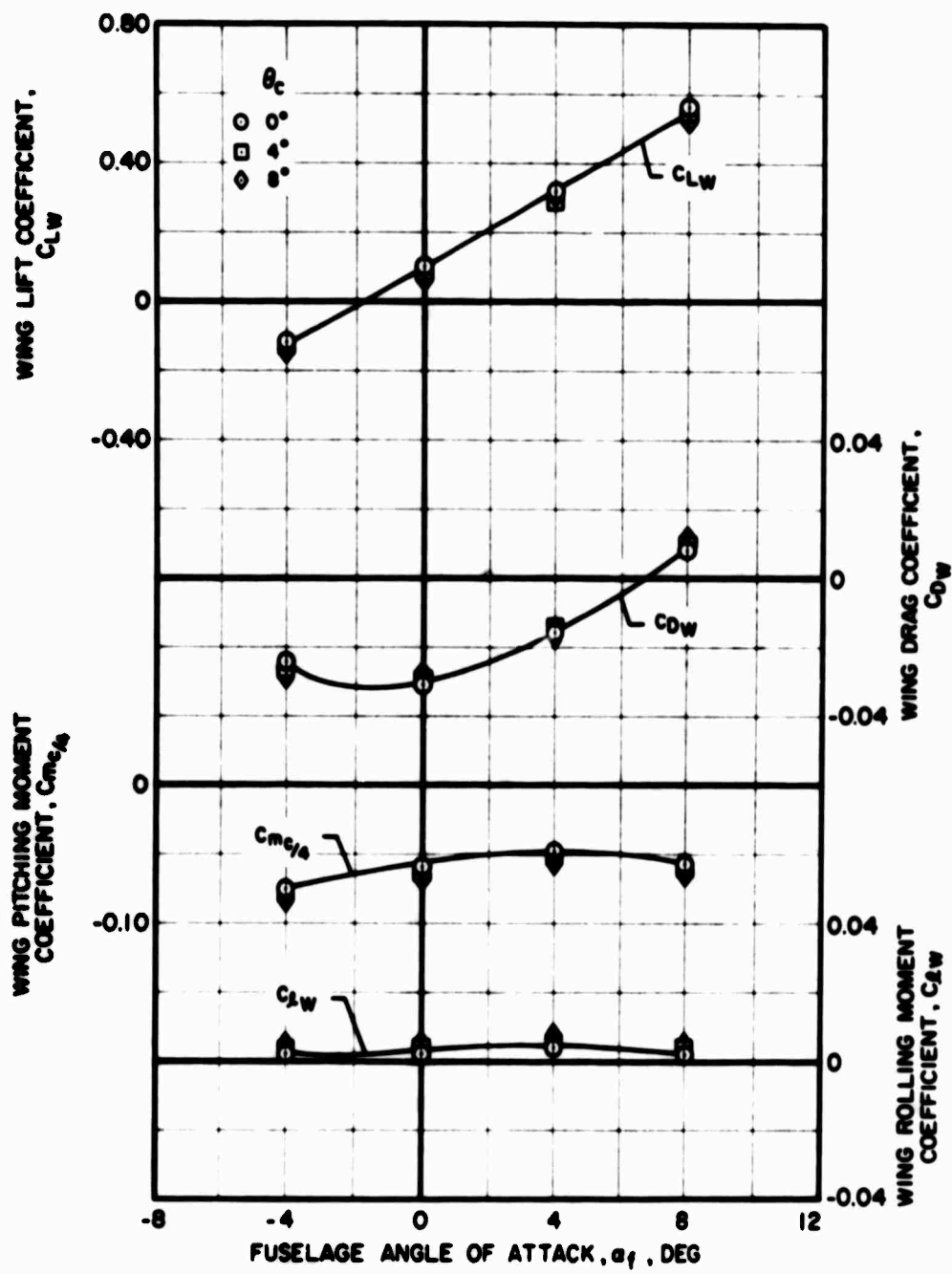


Figure 175. Effect of Fuselage Angle of Attack on the Aerodynamic Characteristics of the Large Wing, Without Rotor and With Pusher Propeller Without Empennage at $V_s = 300$ Knots, $\beta_{.75} = 41^\circ$, $i_w = 0^\circ$.



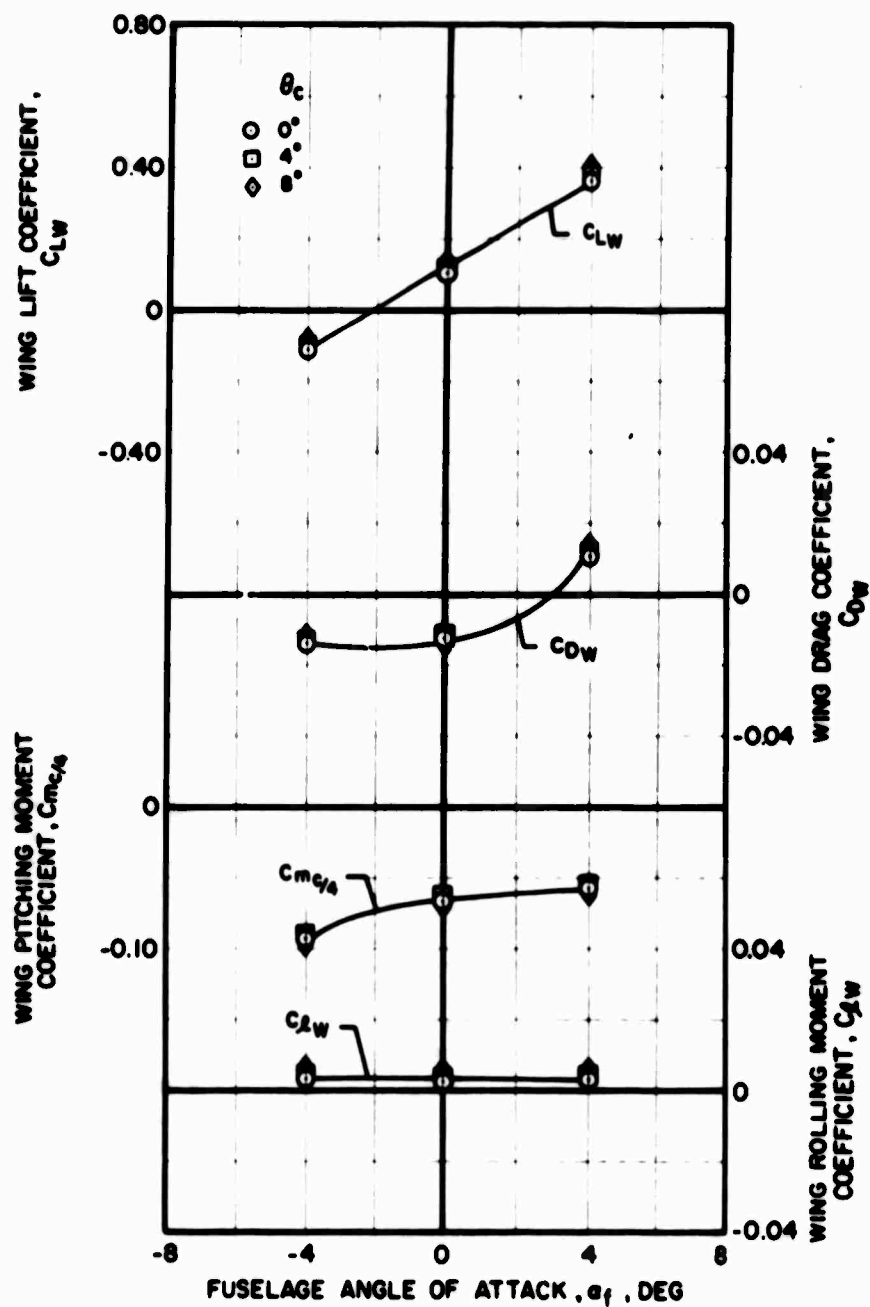
(a) $V_s = 120$ Knots

Figure 176. Effect of Fuselage Angle of Attack on the Aerodynamic Characteristics of the Large Wing, With Rotor and Inboard Tractor Propellers at Various Forward Speeds and Collective Pitch Settings, $\beta_{.75} = 41^\circ$, $i_w = 0^\circ$.



(b) $V_s = 200$ Knots

Figure 176. Continued.



(c) $V_s = 300$ Knots

Figure 176. Concluded.

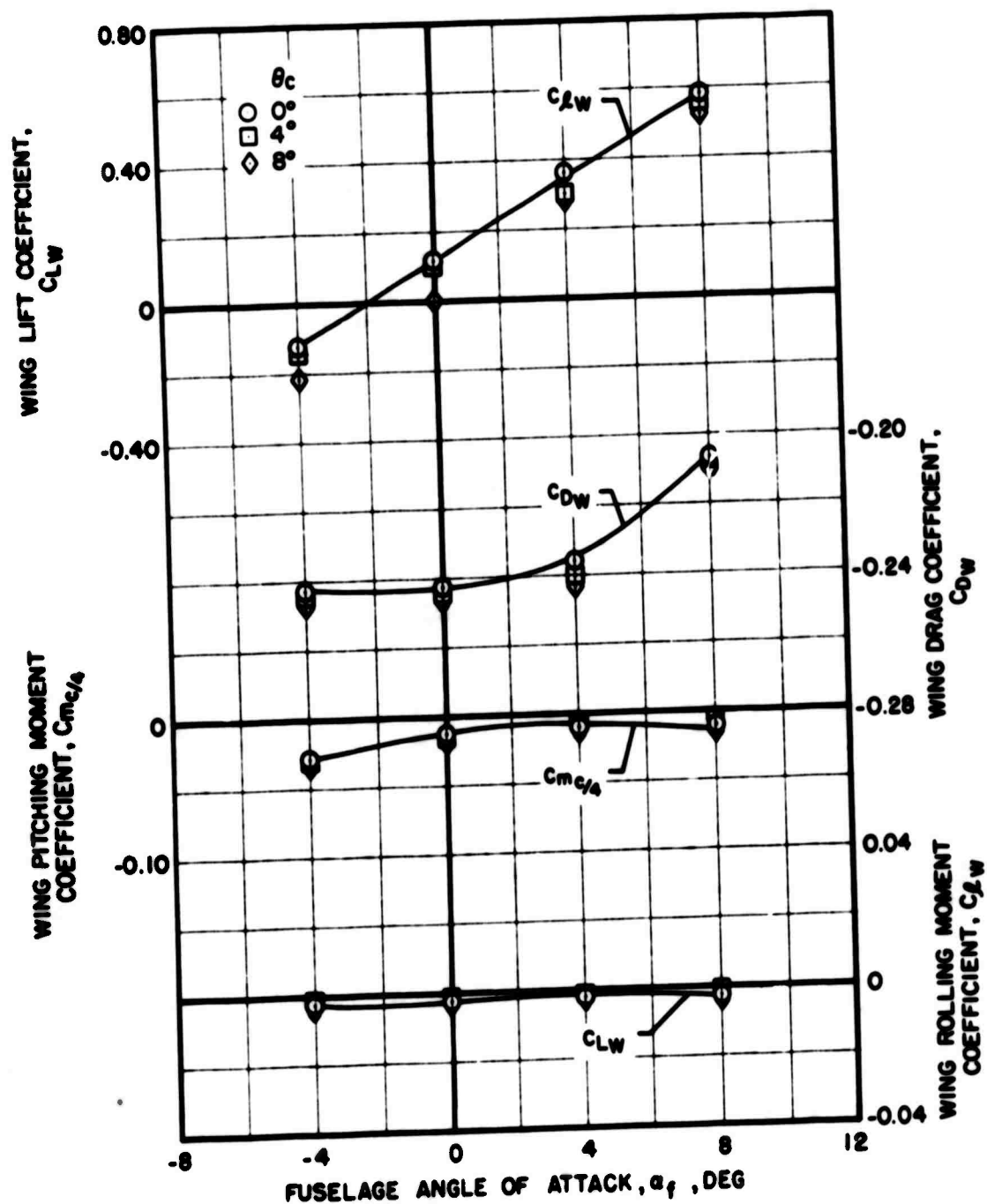
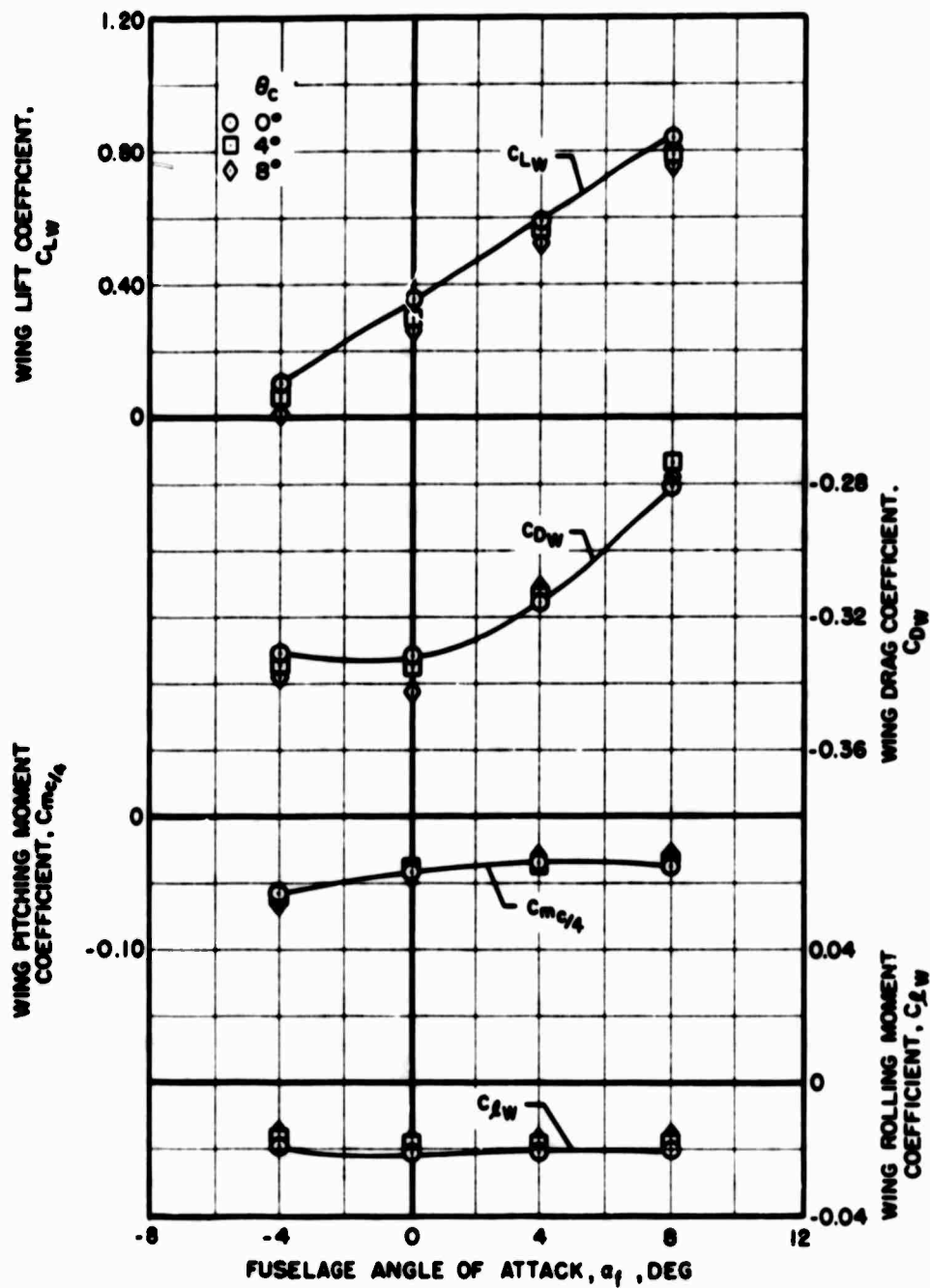
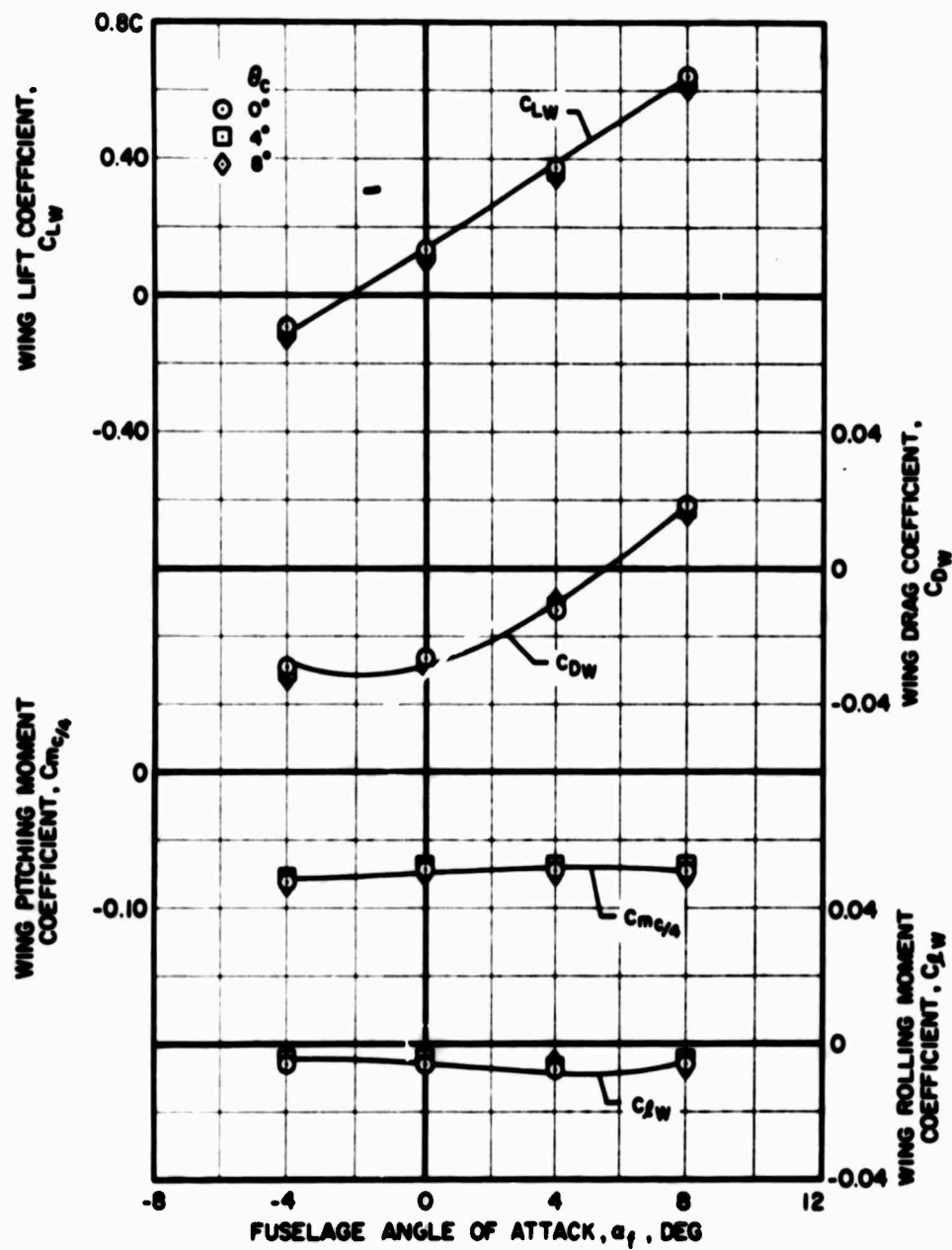


Figure 177. Effect of Fuselage Angle of Attack on the Aerodynamic Characteristics of the Large Wing, With Rotor and Inboard Tractor Propellers at $V_s = 120$ Knots and Various Collective Pitch Settings, $\beta_{75} = 30^\circ$, $i_w = 0^\circ$.



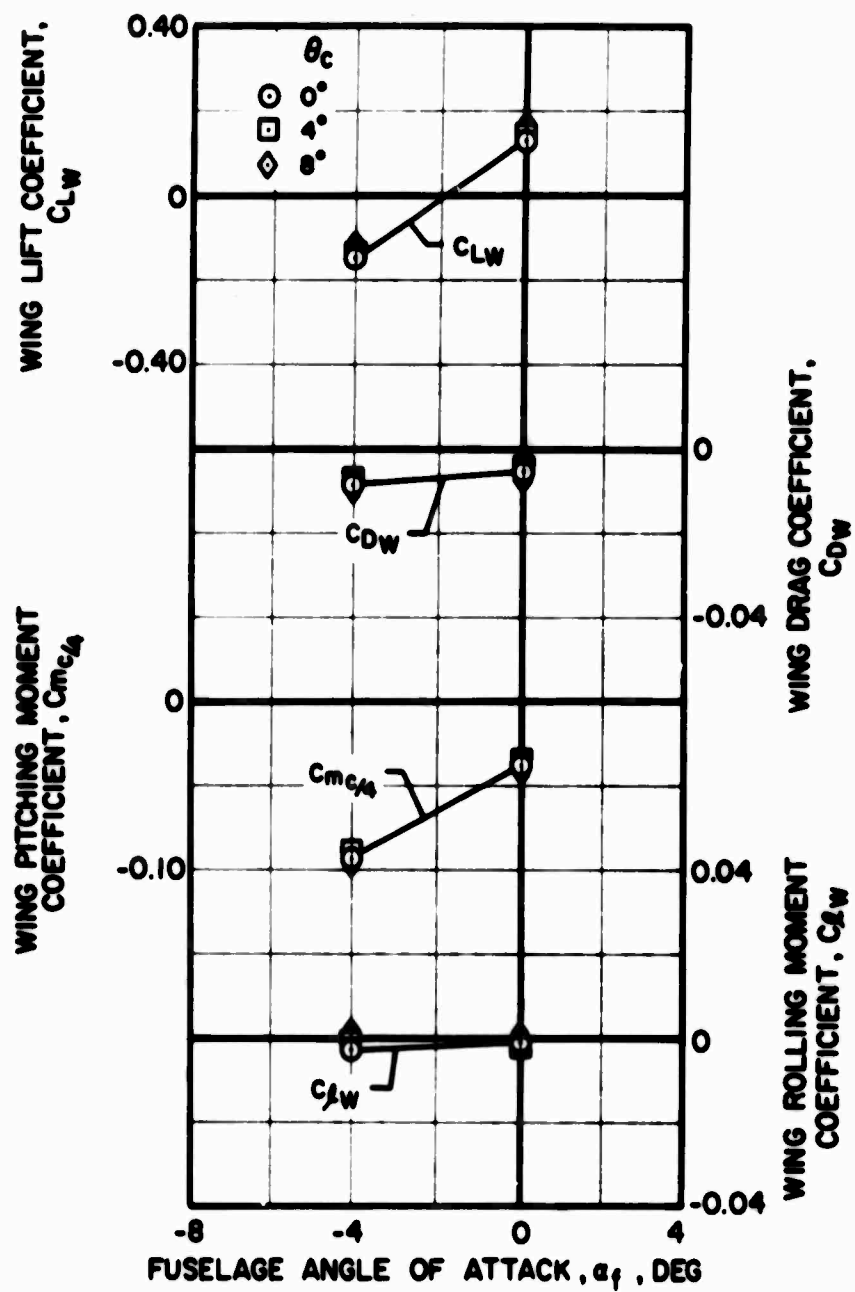
(a) $V_s = 120$ Knots

Figure 178. Effect of Fuselage Angle of Attack on the Aerodynamic Characteristics of the Large Wing, With Rotor and Outboard Tractor Propellers at Various Forward Speeds and Collective Pitch Settings, $\beta_{75} = 41^\circ$, $i_w = 0^\circ$.



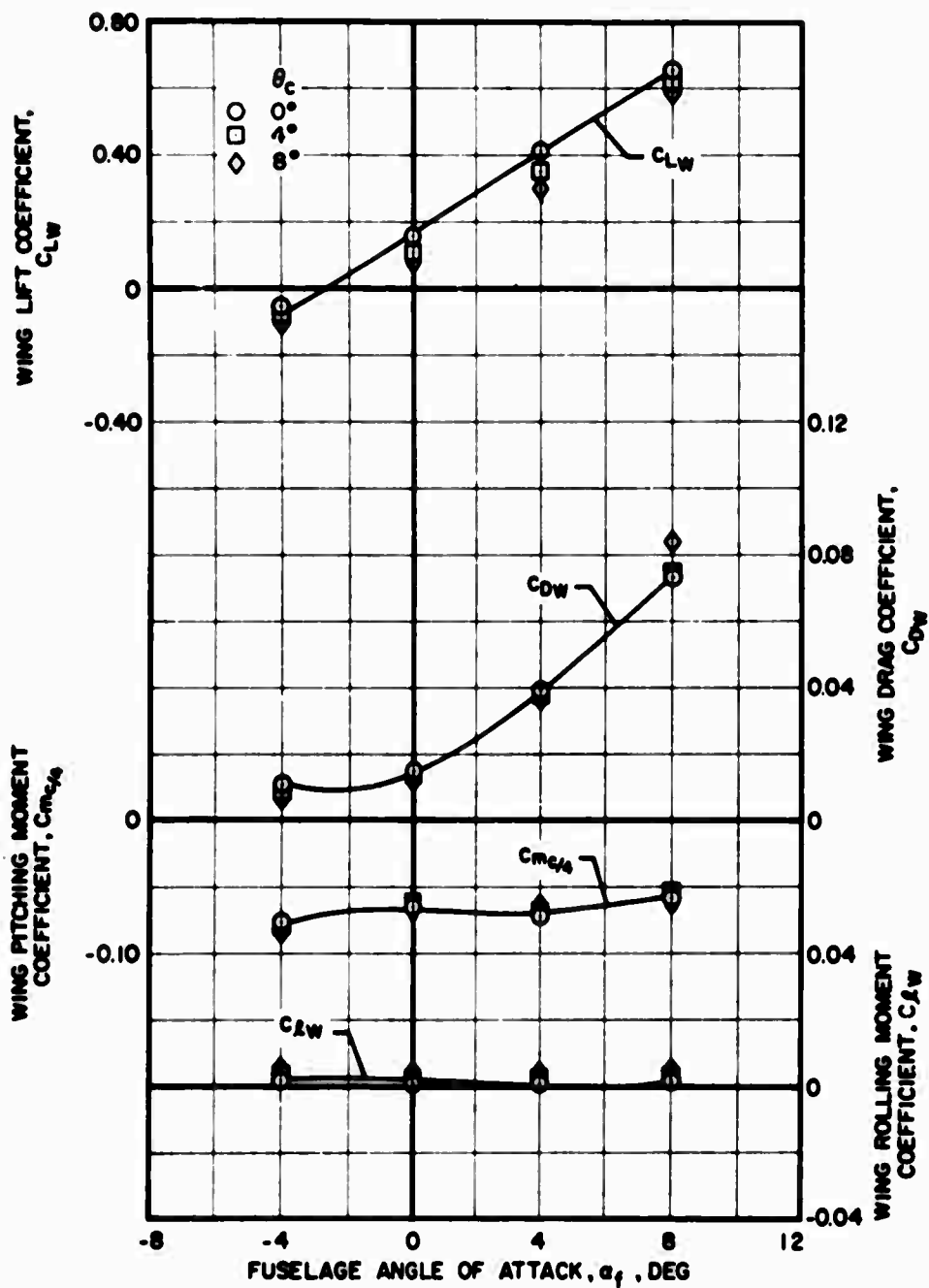
(b) $V_s = 200$ Knots

Figure 178. Continued.



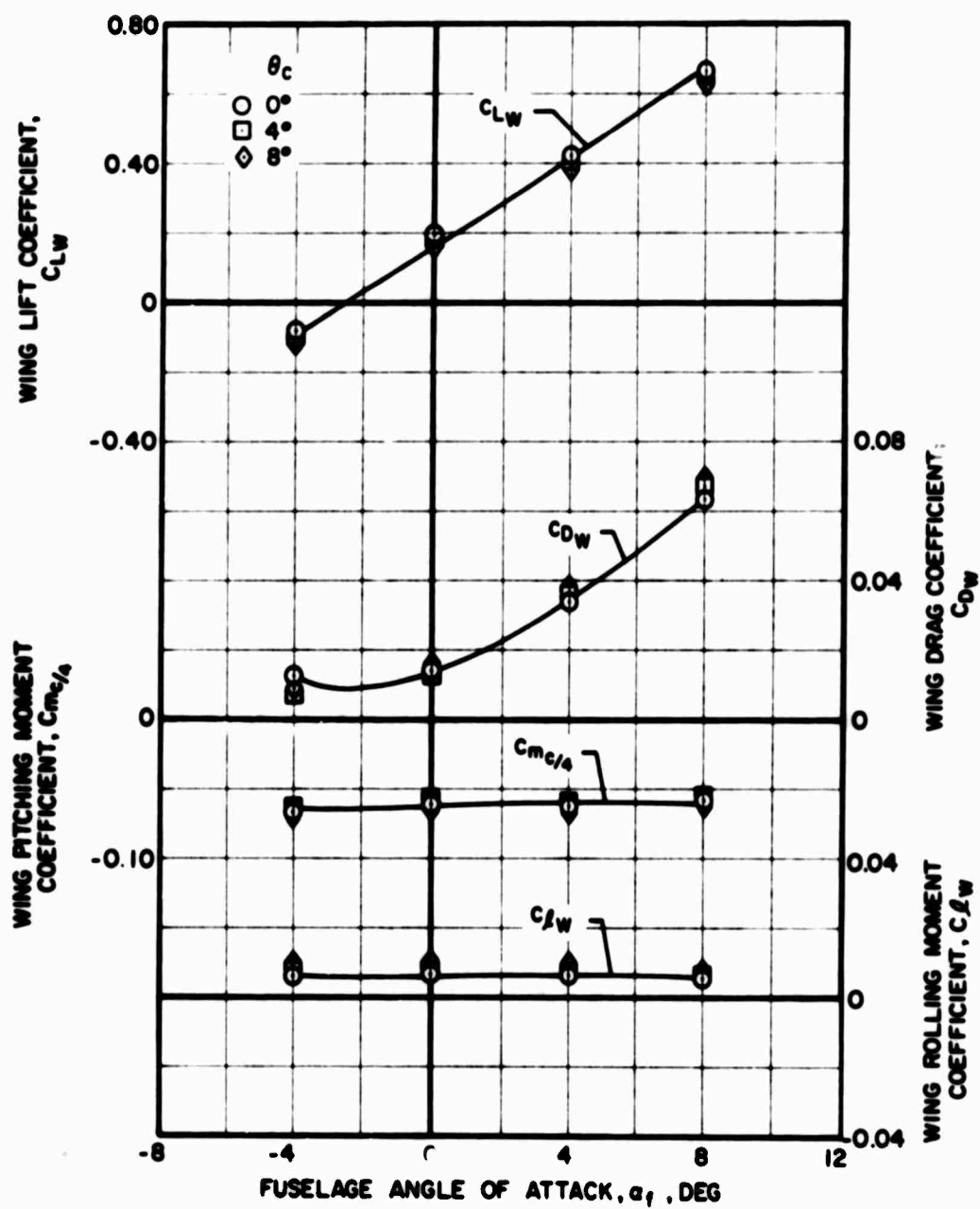
(c) $V_s = 300$ Knots

Figure 178. Concluded.



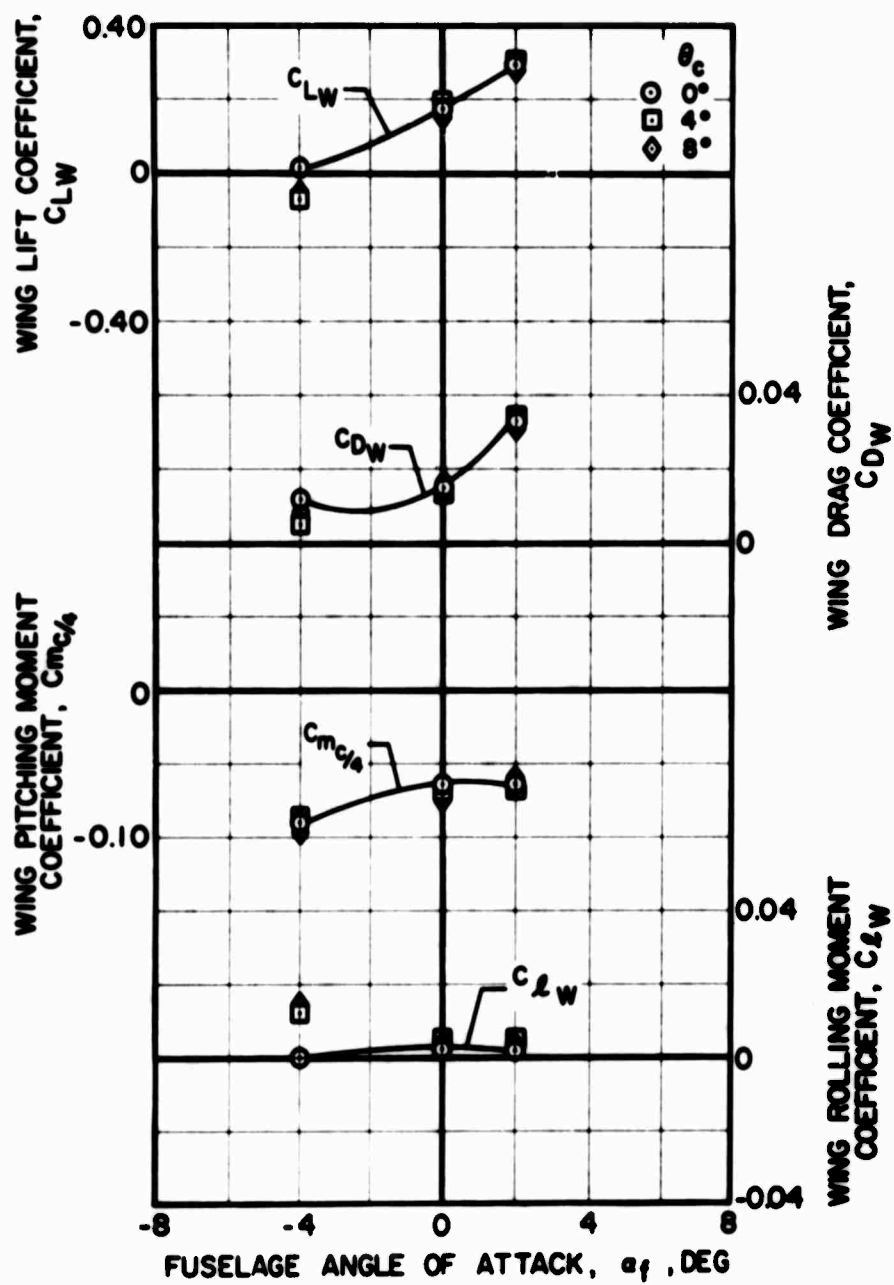
(a) $V_s = 120$ Knots

Figure 179. Effect of Fuselage Angle of Attack on the Aerodynamic Characteristics of the Large Wing, With Rotor, Pusher Propeller, and Empennage at Various Forward Speeds and Collective Pitch Settings, $\beta_{.75} = 41^\circ$, $i_w = 0^\circ$.



(b) $V_S = 200$ Knots

Figure 179. Continued.



(c) $V_s = 300$ Knots

Figure 179. Concluded.

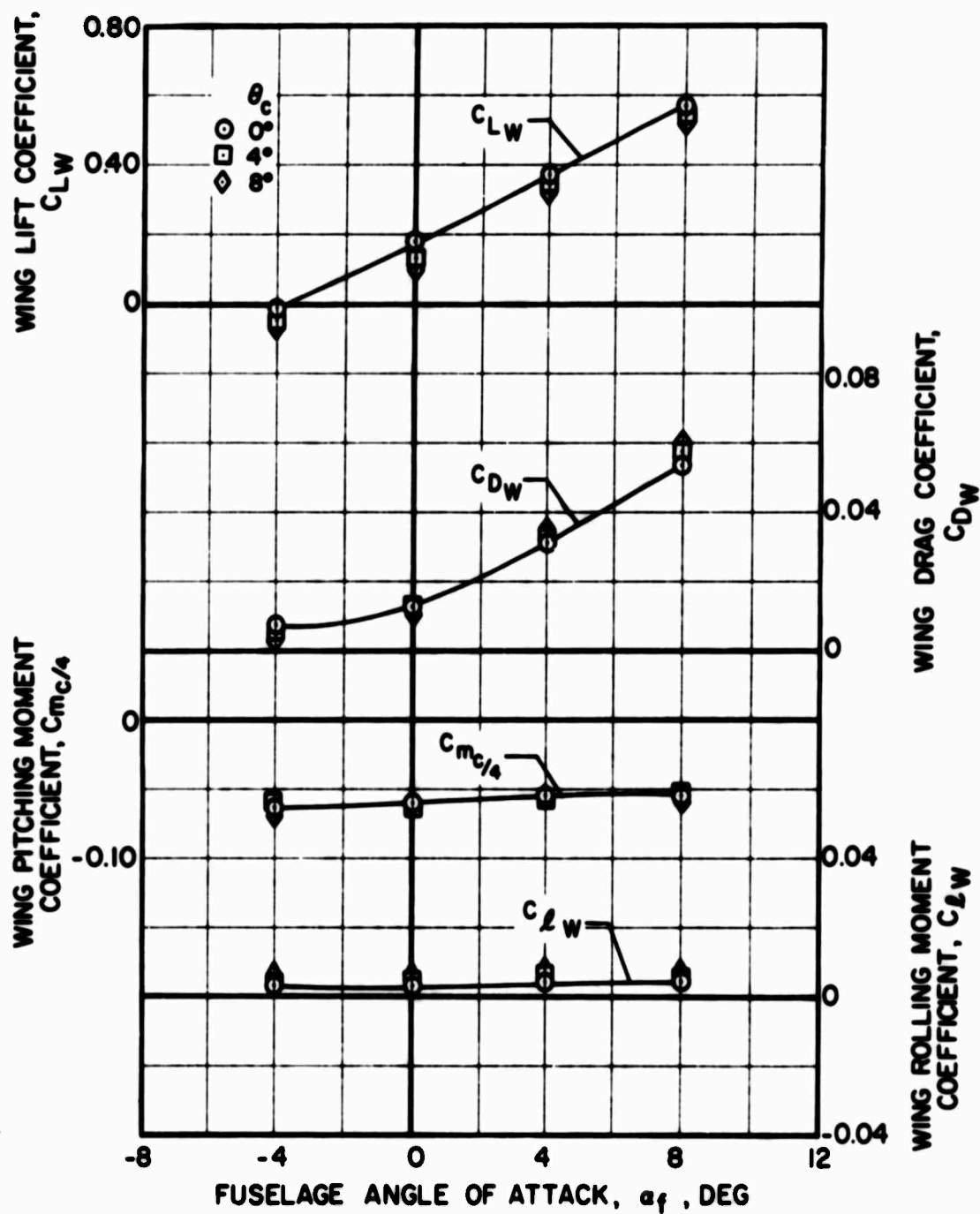


Figure 180. Effect of Fuselage Angle of Attack on the Aerodynamic Characteristics of the Large Wing, With Rotor, Pusher Propeller, and Empennage at $V_s = 120$ Knots and Various Collective Pitch Settings, $\beta_{75} = 30^\circ$, $i_w = 0^\circ$.

DISTRIBUTION

US Army Materiel Command	5
US Army Aviation Materiel Command	5
United States Continental Army Command	1
United States Army, Pacific	1
Chief of R&D, DA	2
Director of Defense Research and Engineering	2
US Army R&D Group (Europe)	2
US Army Aviation Materiel Laboratories	24
US Army Limited War Laboratory	1
US Army Human Engineering Laboratories	1
Army Aeronautical Research Laboratory, Ames Research Center	1
US Army Research Office-Durham	1
Plastics Technical Evaluation Center	1
US Army Test and Evaluation Command	1
US Army Electronics Command	2
US Army Combat Developments Command, Fort Belvoir	2
US Army Combat Developments Command Transportation Agency	1
US Army Combat Developments Command Aviation Agency	1
US Army Ordnance Weapons Command	1
Ordnance Special Weapons- Ammunitions Command	1
US Army Aviation School	1
Assistant Chief of Staff for Force Development	1
US Army Tank-Automotive Command	2
US Army Aviation Test Activity, Edwards AFB	2
Air Force Flight Test Center, Edwards AFB	2
US Army Field Office, AFSC, Andrews AFB	1
Air Force Materials Laboratory, Wright-Patterson AFB	2
Air Force Flight Dynamics Laboratory, Wright-Patterson AFB	2
Systems Engineering Group, Wright-Patterson AFB	3
Naval Air Systems Command, DN	9
Office of Naval Research	10
US Naval Research Laboratory	1
US Naval Air Test Center, Patuxent River	1
Commandant of the Marine Corps	1
Marine Corps Liaison Officer, US Army Transportation School	1
Testing and Development Division, US Coast Guard	1
Manned Spacecraft Center, NASA	1
NASA Scientific and Technical Information Facility	2
NASA-LRC	1
NAFEC Library (FAA)	2
US Army Aviation Human Research Unit	1
US Army Board for Aviation Accident Research	1
Bureau of Safety, Civil Aeronautics Board	2
US Naval Aviation Safety Center, Norfolk	1

UNCLASSIFIED

Security Classification

DOCUMENT CONTROL DATA - R & D

(Security classification of title, body of abstract and indexing annotation must be entered when the overall report is classified)

1. ORIGINATING ACTIVITY (Corporate author) Sikorsky Aircraft Division of United Aircraft Corporation Stratford, Connecticut		2a. REPORT SECURITY CLASSIFICATION UNCLASSIFIED	
		2b. GROUP	
3. REPORT TITLE INVESTIGATION OF COMPOUND HELICOPTER AERODYNAMIC INTERFERENCE EFFECTS			
4. DESCRIPTIVE NOTES (Type of report and inclusive dates) FINAL REPORT			
5. AUTHOR(S) (Last name, middle initial, first name) Lawrence J. Bain Anton J. Landgrebe			
6. REPORT DATE October 1967	7a. TOTAL NO. OF PAGES 388	7b. NO. OF REFS 20	
8a. CONTRACT OR GRANT NO. DA 44-177-AMC-203(T)		8b. ORIGINATOR'S REPORT NUMBER(S) USAAVLABS Technical Report 67-44	
a. PROJECT NO. Task 1F125901A13903		8c. OTHER REPORT NO(S) (Any other numbers that may be assigned this report) SER-50474	
c.			
d.			
10. DISTRIBUTION STATEMENT This document has been approved for public release and sale; its distribution is unlimited.			
11. SUPPLEMENTARY NOTES		12. SPONSORING MILITARY ACTIVITY U.S. Army Aviation Materiel Laboratories Fort Eustis, Virginia	
13. ABSTRACT A generalized model of a compound helicopter was tested in the United Aircraft 18-foot wind tunnel to determine the nature of aerodynamic interferences between the rotor, the fuselage, and various wings, as well as the effects of these components on the downwash at the tail. A number of the results of this test were correlated with published theories. In addition, a theoretical method for calculating the wing induced flow through the rotor is presented, and the theoretical results are correlated with the experimental results. It was concluded from this work that definite measurable interferences do exist, although none were found that would seriously compromise the compound helicopter concept; and in general, existing theories for predicting aerodynamic interference effects due to a wing produce reasonable correlation with measured effects. Correlation is lacking for rotor induced interference effects. In a second test the mutual interferences between a rotor and various propeller configurations were investigated. It was concluded from this work that the vibratory bending moments on wing-mounted tractor propellers are a direct function of the sum of the rotor momentum downwash angle and the geometric angle of attack while the vibratory bending moments on a tail-mounted pushed propeller have a relationship to the rotor lift which depends on the presence or absence of empennage forward of the propeller. It was also found that increasing thrust on wing-mounted tractor propellers generally causes increased rotor blade vibratory bending moments.			

DD FORM 1473 1 NOV 66 REPLACES DD FORM 1473, 1 JAN 64, WHICH IS OBSOLETE FOR ARMY USE.

UNCLASSIFIED
Security Classification

UNCLASSIFIED

Security Classification

10. KEY WORDS	LINK A		LINK B		LINK C	
	ROLE	WT	ROLE	WT	ROLE	WT
Compound Helicopter Aerodynamic Interference						

UNCLASSIFIED

Security Classification